UNIVERSITY OF KWAZULU-NATAL

THE MINERALOGY, PETROLOGY AND PGE GEOCHEMISTRY OF THE UG2 CYCLIC UNIT AT LEBOWA PLATINUM MINE (ATOK), NORTH-EASTERN BUSHVELD COMPLEX

Clifford Fitzhenry (200270766)

School of Geological Sciences

University of KwaZulu-Natal

Durban

4041

Submitted in partial fulfillment for the requirements for the degree of Master of Science.

I declare that this is my own unaided work except where referenced or suitably acknowledged.

Signature…… Date……..

Abstract

This project is an investigation of the UG2 cyclic unit of the Upper Critical Zone at Lebowa (Atok) Platinum Mine, North Eastern Bushveld Complex. It combines a fieldwork study, carried out at Lebowa, with a drill core study, carried out on the ZG219 intersection at the University of KwaZulu-Natal. The Atok UG2 is a ~60 cm thick layer of chromitite underlain by a pegmatoidal pyroxenite and overlain by a medium grained feldspathic pyroxenite, and which is located near the base of the differentiated UG2 cyclic unit. The UG2 cyclic unit is shown to comprise an upward evolving lithological sequence of chromitite→feldspathic pyroxenite→norite→anorthosite, which is also punctuated by several mm scale chromitite stringers. The combination of density measurements, whole-rock geochemical analysis on 210 closely spaced samples and normative mineralogical profiles revealed the UG2 cyclic unit to contain a normal fractionation trend overlain by a reverse fractionation trend at the level of the UG2 leuconorite (thereby indicating an increased influx of magma into the chamber during the formation of the UG2 cyclic unit). High precision ICP-MS geochemical data revealed both the base-metal sulphide and platinum group element mineralization to be concentrated in a bottom-loaded triple peaked profile pattern through the UG2 chromitite. The sulphide assemblage comprises mainly pentlandite, chalcopyrite and pyrite with lesser pyrrhotite whilst the platinum group mineralogy comprises a PGE-sulphide dominated assemblage with lesser amounts of PGE-tellurides.

A model is proposed to account for the petrogenesis of the UG2 cyclic unit as well as of the platinum group element mineralization. The UG2 cyclic unit is an excellent example of an open magma chamber system and is suggested to represent a dynamic interplay of evolving, cooling and fractionating resident liquids within the chamber along with repetitive influxes of fresh, undifferentiated primitive magma. These primary processes were then superseded by later postcumulus processes of compaction, metasomatization and recrystallization to form the pegmatoidal feldspathic pyroxenite unit. The chromitite stringers are suggested to represent the product of a magma injection (coupled with subsequent mixing with the resident liquid) into the chamber. The mechanism of mineralization is suggested to be the result solely of primary magmatic processes with little or no role played by late stage postcumulus processes. It is envisaged that a segregated sulphide liquid would have scavenged and extracted base and precious metals from the silicate magma as it percolated through. The metal impregnated sulphide liquid would have then become concentrated in the chromite slurry and become mixed in with the chromite crystals.

Table of Contents

1. Introduction

1.1 Objective of Study

This project involves two broad objectives – the first is to document the geochemistry, mineralogy and petrology of the UG2 orebody (i.e. the UG2 chromitite layer and its hanging wall and footwall), as well as the variation of these properties vertically through the orebody. The second objective is to investigate the mechanism of formation of the chromitite stringers present in the UG2 hanging wall sequence, and to apply these findings to the Bushveld, and layered intrusions, in general.

In terms of the first objective – there is very little detailed geochemical data available on the UG2 chromitite layer. The major reason for this is the difficulty involved in dissolving the chromitite for analysis using ICP-MS solution techniques and in standard fusions for XRF major element analysis. It is in this regard that this project bears its importance - in that it provides the first account of the trace element distribution in the UG2. This project also provides the first detailed account of the geochemical, mineralogical and petrological variations through the UG2 chromitite layer and its hanging wall and footwall. This data will prove invaluable in understanding both the mechanisms of mineralization and petrogenesis of the UG2 ore body of the north-eastern Bushveld.

In terms of the second objective – the formation of chromitite layers in layered intrusions remains an, essentially, unsolved issue. The Bushveld Complex provides the perfect vantage point in order to investigate this phenomenon in that it contains numerous, laterally extensive chromitite layers ranging from <1 mm up to several metres in width. The feldspathic pyroxenitic UG2 hanging wall sequence, in particular, provides an ideal study section in that it hosts several chromitite stringers in a relatively closely spaced succession. Detailed sampling through this succession will provide geochemical data which can be used to interpret the changes occurring in the magma chamber at the time of their formation.

1.2 Regional Geology

1.2.1 Overview of the Bushveld Complex

The Bushveld Complex (Figures 1.1 and 1.2) is the worlds largest layered mafic to ultramafic intrusion with a maximum thickness estimated at 13 000 m and an aerial extent of approximately 65 000 km^3 (Eales and Cawthorn, 1996), and it is the main constituent of the multi-complex Bushveld Magmatic Province (Irvine, 1982, Kruger, 1990; 1991). The Complex is centrally located within the northern portion of South Africa and is almost entirely surrounded and underlain by older sedimentary and volcanic successions of the Transvaal Supergroup, which is dated at 2224 ± 21 Ma (Burger and Coertze, 1975; Rb – Sr).

The Bushveld Complex intruded into the Pretoria Group of the Transvaal Supergroup at 2054 ± 2 to 2061 ± 2 Ma (Walraven, 1986). The Complex has been dated by various authours – all yielding an approximately similar overall result i.e. 2049 ± 152 Ma, and 2057 ± 24 Ma respectively (Von Gruenewaldt *et al,* 1986; Sm –

Nd), 2050 ± 22 Ma (Hamilton, 1977; Rb – Sr), 2050 ± 25 Ma (Harmer and Sharpe, 1985; Rb – Sr), 2025 ± 40 Ma (Lee and Butcher, 1990; Rb – Sr) and 2050 Ma (Buick *et al,* 2001).

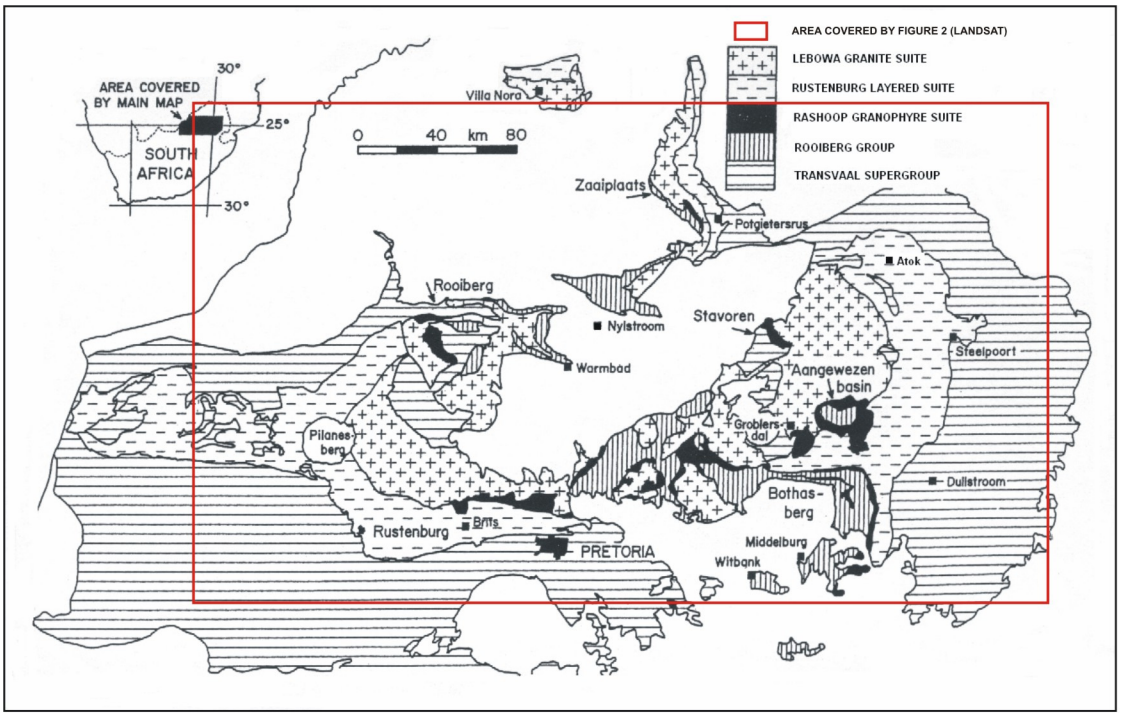

Figure 1.1: The Bushveld Complex, with red box indicating extent of Figure 1.2 (after Walraven, 1986).

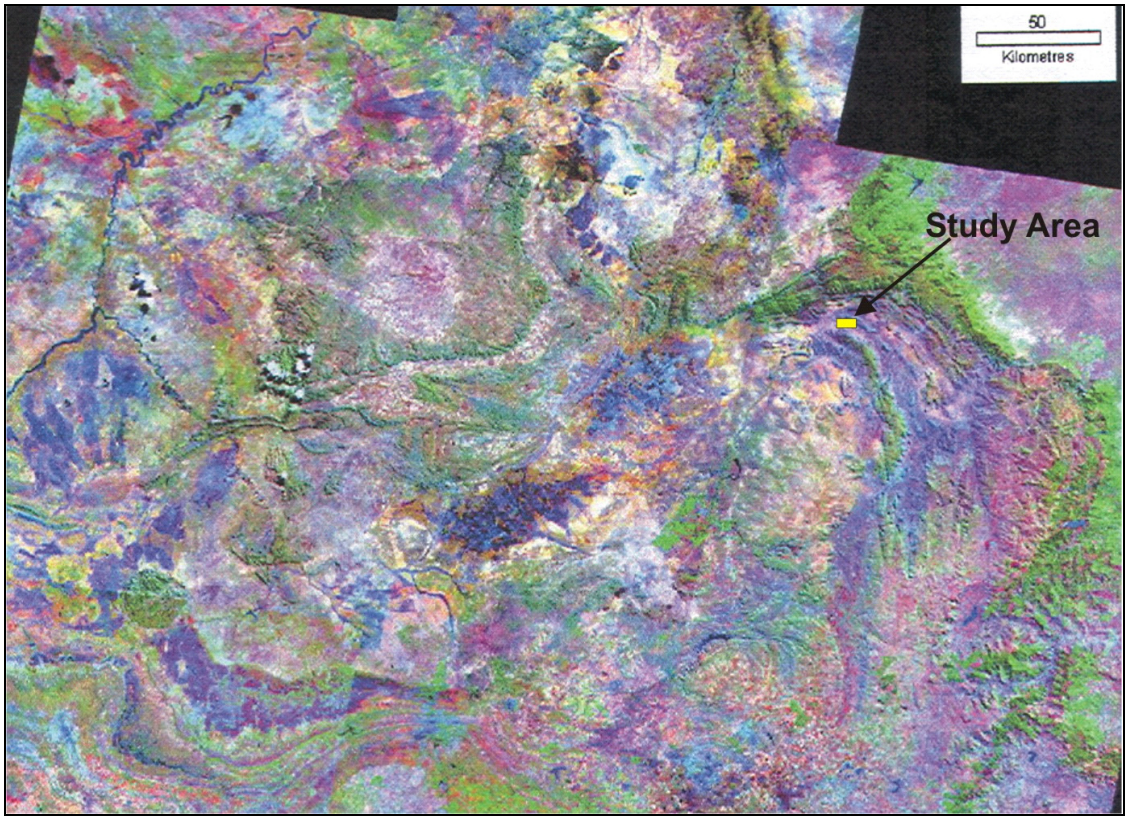

Figure 1.2: Enhanced LandSat image of the Bushveld Complex clearly showing the study area (from Brown, 2004)

Its outcrop pattern is characterized by four distinct lobes, namely, the western lobe, which is centred on Rustenburg, the eastern lobe, situated south of Polokwane, the northern lobe, which outcrops south of Mokopane to Villa Nora, and the far western limb, which is an eroded remnant extending toward Botswana (Eales and Cawthorn, 1996). A fifth unexposed lobe, the south eastern lobe, exists near Bethal (Eales and Cawthorn, 1996).

The Bushveld Complex layered succession (termed the Rustenburg Layered Suite) dips inwards towards the central granite and granophyre suites, with the exception of the northern lobe, which dips in an independently westerly direction (Tankard *et al*., 1982). Geophysical studies indicate that the eastern and western limbs are not connected at depth beneath the central granites, granophyres and sedimentary cover, but rather that the Complex instead consists of several feeder compartments (Tankard *et al*., 1982), as was originally suggested by Cousins (1959). It is proposed that there are at least four, possibly five, intrusive centres coincident with the lobes (Tankard *et al.,* 1982). Due to the remarkable similarities in crystallization sequences between the eastern and western lobes, Sharpe (1981) suggested that the compartments were interconnected to a large master chamber at depth during the early stages of crystallization.

The central portion of the Bushveld Complex has been extensively intruded by the Rashoop Granophyre Suite, which is dated at 2000 ± 30 Ma (Fourie and von Gruenewaldt, 1979; U – Pb) and the Lebowa Granite Suite, which is dated at 2010 ± 20 Ma (Von, Gruenewaldt *et al,* 1986; U – Pb), whilst the western limb of the Complex has been intruded by the alkaline Pilanesberg Complex. Irvine (1982) and Kruger (1990, 1991) have recommended that the complete array of ultramafic to acid plutonic, hyabyssal and volcanic rocks that formally comprise the Bushveld Complex (including the Rustenburg Layered Suite, the Rashoop Granophyre Suite and the Lebowa Granite Suite), the Bushveld – related Losberg (Coetzee and Kruger, 1989) and the Molopo Farms Complexes (Von Gruenewaldt *et al,* 1986), be collectively termed the Bushveld Magmatic Province.

It is the layered mafic portion of the Bushveld Magmatic Province, i.e. the Rustenburg Layered Suite, which forms the focus of this study.

1.2.2 The Rustenburg Layered Suite

The Rustenburg Layered Suite (Figure 1.3) forms the economically important layered mafic portion of the complex. A distinctive characteristic of the Rustenburg Layered Suite, as the name suggests, is the extremely well developed, laterally extensive layering which is present on a variety of scales ranging from a few mm (termed laminations) up to hundreds of metres thick (termed macro cyclic units). Several types of layering are suggested by Eales and Cawthorn (1996) to exist, including modal layering, in which layering is defined by homogenous lithologies and which gives rise to cyclic units, textural layering, in which layering is defined by changes in crystal size, crystal habit or fabric, phase layering, which is defined by the appearance or

disappearance of cumulus phases, and finally cryptic layering, which is defined by the changes in mineral or whole-rock composition (as controlled by mineral composition).

The intrusive mechanism of the Rustenburg Layered Suite is suggested by Eales and Cawthorn (1996) to involve a series of magma pulses injected into the chamber from a primitive source. It is these repeated injections of magma into the chamber that are suggested by Eales and Cawthorn (1996) to be responsible for the formation of cyclic units, within the Rustenburg Layered Suite. The simplified process would involve an injection of primitive magma into the chamber followed by a process of re-equilibration in which the dormant, more evolved magma in the chamber mixed with the new primitive magma. This process of re-equilibration would have to be extremely efficient to account for the vast lateral extent of the layering within the Rustenburg Layered Suite (Eales and Cawthorn, 1996). The processes of crystallization and fractionation would then gradually drive the magma towards more evolved compositions, until a new batch of primitive magma is injected into the chamber which will result in the process being repeated. This continually repeated process is suggested by Eales and Cawthorn (1996) to produce cyclic units varying from tens of metres up to hundreds of metres thick (termed macro cyclic units). These cyclic unit patterns are superimposed on an overall normal fractionation trend of the Rustenburg Layered Suite which is defined by ultramafic and mafic compositions at the base which gives way to a more evolved, intermediate composition at the top.

Therefore the mechanism of formation of the Rustenburg Layered Suite is a complex process involving a delicate interplay between two distinct processes – that of continuous, repeated injections of primitive magma into the chamber, followed by mixing and fractionation (forming cyclic units), superimposed on a larger scale fractionation trend of gradual evolution of magma compositions within the chamber.

In terms of stratigraphy, the Rustenburg Layered Suite is divided into five zones distinguished by the dominant cumulus phase in each zone:

The Marginal Zone constitutes the base of the Rustenburg Layered Suite and it comprises up to 800 m of heterogeneous noritic rocks (Vermaak, 1976). Eales and Cawthorn (1996) interpret the Marginal Zone as representing composite sills of the initial sill phase of the intrusion.

The Lower Zone overlies the Marginal Zone and it comprises up to 1 700 m of alternating dunite, harzburgite and pyroxenite (Eales and Cawthorn, 1996).

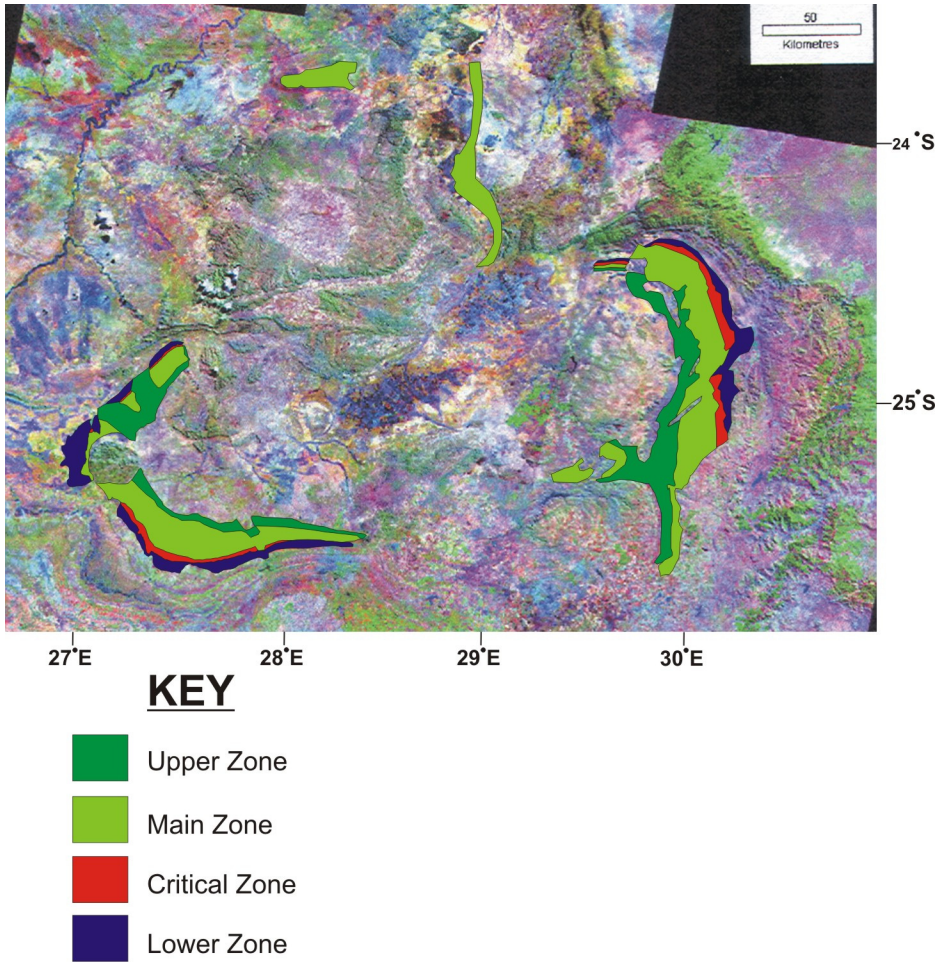

Figure 1.3: LandSat image overlain with Bushveld Complex zonal (Rustenburg Layered Suite) geology (from Brown, 2004).

The Critical Zone is host to the sequence under investigation in this study. It can be subdivided into lower and upper subzones, with the boundary between the two marked by the first appearance of cumulus plagioclase in the Rustenburg Layered Suite (Cameron, 1980). The Lower Critical Zone comprises mainly pyroxenites, with the Upper Critical Zone comprising mainly pyroxenites, norites and anorthosites (Eales and Cawthorn, 1996). The Critical Zone is host to three groups of chromitite layers – the Lower (LG), Middle (MG) and Upper Groups (UG) (Hatton and von Gruenewaldt, 1989). The individual chromitite layers are labeled from the base upwards i.e. LG 1 – 7, MG 1 – 4, and UG 1 – 2 (and UG3 only in the eastern limb) (Eales and Cawthorn, 1996). The Upper Critical Zone is also host to the platiniferous Merensky and UG2 layers. Eight cyclic units have been identified within the Upper Critical Zone, consisting of partial or complete sequences from a base of ultramafic cumulates (chromitite, harzburgite, or pyroxenite) through norite to anorthosite (Eales and Cawthorn, 1996). The base of each of these units is sharp, whilst internal contacts within the units may be sharp or gradational (Eales and Cawthorn, 1996).

A satisfactory mineralogical boundary is difficult to determine for between the Critical and Main Zone. The boundary is currently taken as the top of the Giant Mottled Anorthosite, which caps the Bastard Cyclic Unit (Eales and Cawthorn, 1996; Kruger, 1990; Kruger, 1991). The Main Zone is a thick succession of cumulates devoid of olivine and chromium spinel, and is generally lacking both the fine-scale layering and the extreme lithological diversity characteristic of the Critical Zone (Eales and Cawthorn, 1996). In general, the Main Zone comprises predominantly gabbronorite with subordinate norite and anorthosite (Eales and Cawthorn, 1996).

The Upper Zone is approximately 2300 m thick and comprises mainly ferrogabbro with minor anorthosite (Eales and Cawthorn, 1996). The most distinguishing characteristic of this zone is the presence of 25 magnetite cumulate layers, which attain a thickness of up to 6 m (Eales and Cawthorn, 1996).

1.2.3 The UG2 Chromitite Layer

The Upper Group 2 chromitite, or the UG2 chromitite (or even simply referred to as the UG2) as it is more commonly known, comprises a chromitite layer developed near the base of the differentiated UG2 cyclic unit within the Upper Critical Zone of the Rustenburg Layered Suite. It exists at a varying distance beneath the Merensky reef (from <30 m in the North-Western Bushveld to ~400 m in the Eastern Bushveld) and averages about 60 cm thick throughout the Complex (Viljoen *et al*., 1986, Brown and Nowack, 2003). Apart from a few local interruptions the UG2 displays remarkable continuity along strike in both the eastern and western limbs of the Bushveld Complex (Mclaren and De Villiers, 1982; Davey, 1992; Maier and Eales, 1994; Maier and Bowen, 1996).

A number of chromitite stringers, of variable width, commonly occur at a range of distances (from a few mm to over 7 m above) above the UG2 reef. These layers only contain very low PGE (platinum group elements) contents and relatively high Pt/Pd ratios (Brown, 2004). It is the UG2 chromitite layer and its overlying chromitite-rich hanging wall sequence which forms the focus of this study.

1.3 Locality and Geology of the Study Area

This project was carried out at the Lebowa Platinum Mine (LPM) Middelpunt Hill UG2 operation which is situated on the north-eastern extremity of the eastern limb of the Bushveld Complex (Figures 1.4, 1.5 and 1.6). The overall mining operation (both Merensky and UG2 portions) is better known as ‘Atok’, the name being derived from when it was first commissioned, which is what it will be referred to in this report.

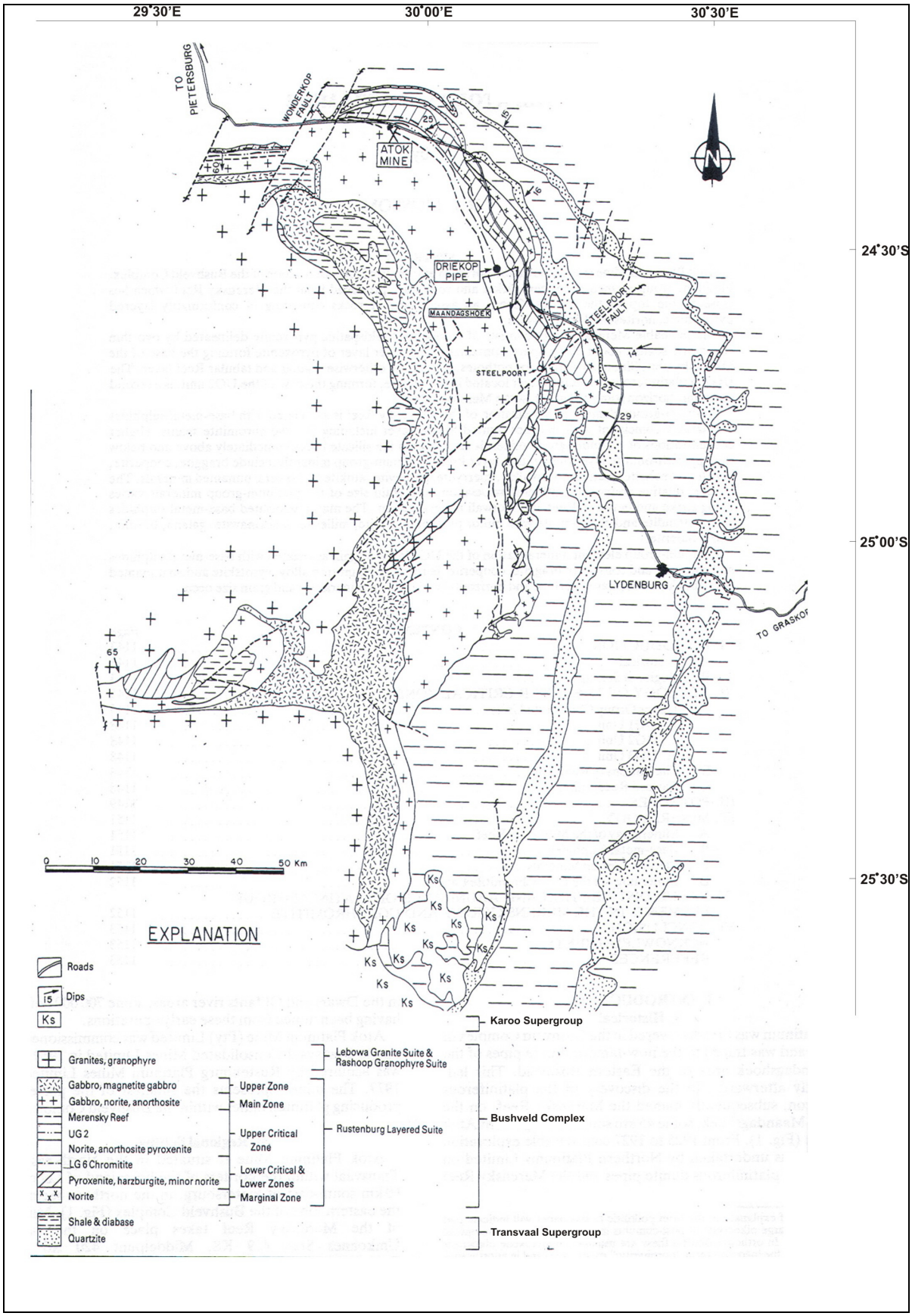

Figure 1.4: Geological map of the Eastern Bushveld Complex showing the location of Atok Mine (Mossom, 1986).

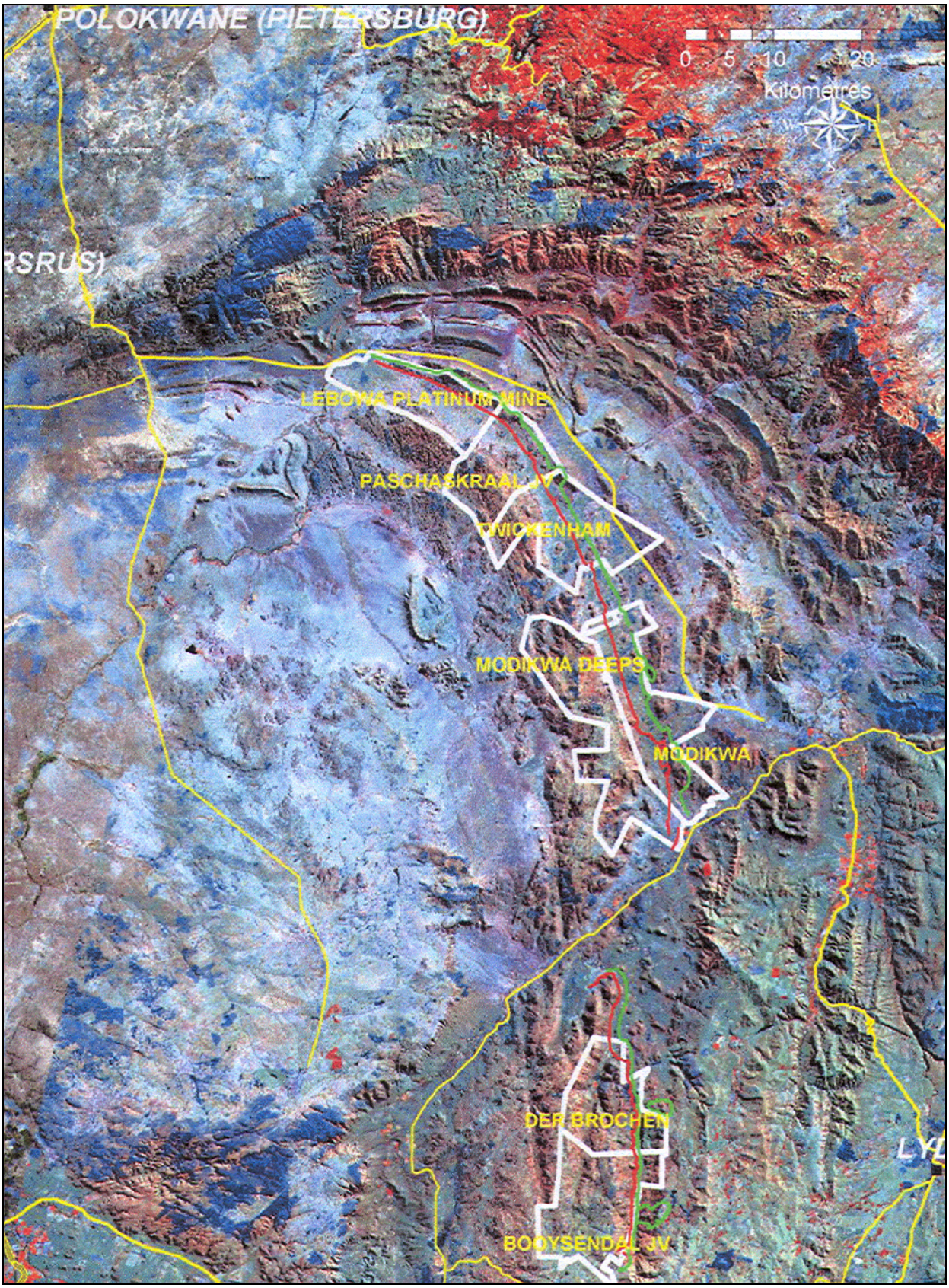

Figure 1.5: LandSat image of the Eastern Bushveld Complex. Current Anglo Platinum mining and project areas are shown with the study area i.e. Lebowa (Atok) Platinum Mine clearly visible as the most northerly of the Anglo Platinum operations. The red line indicates the Merensky reef outcrop and the green line the UG2 outcrop.

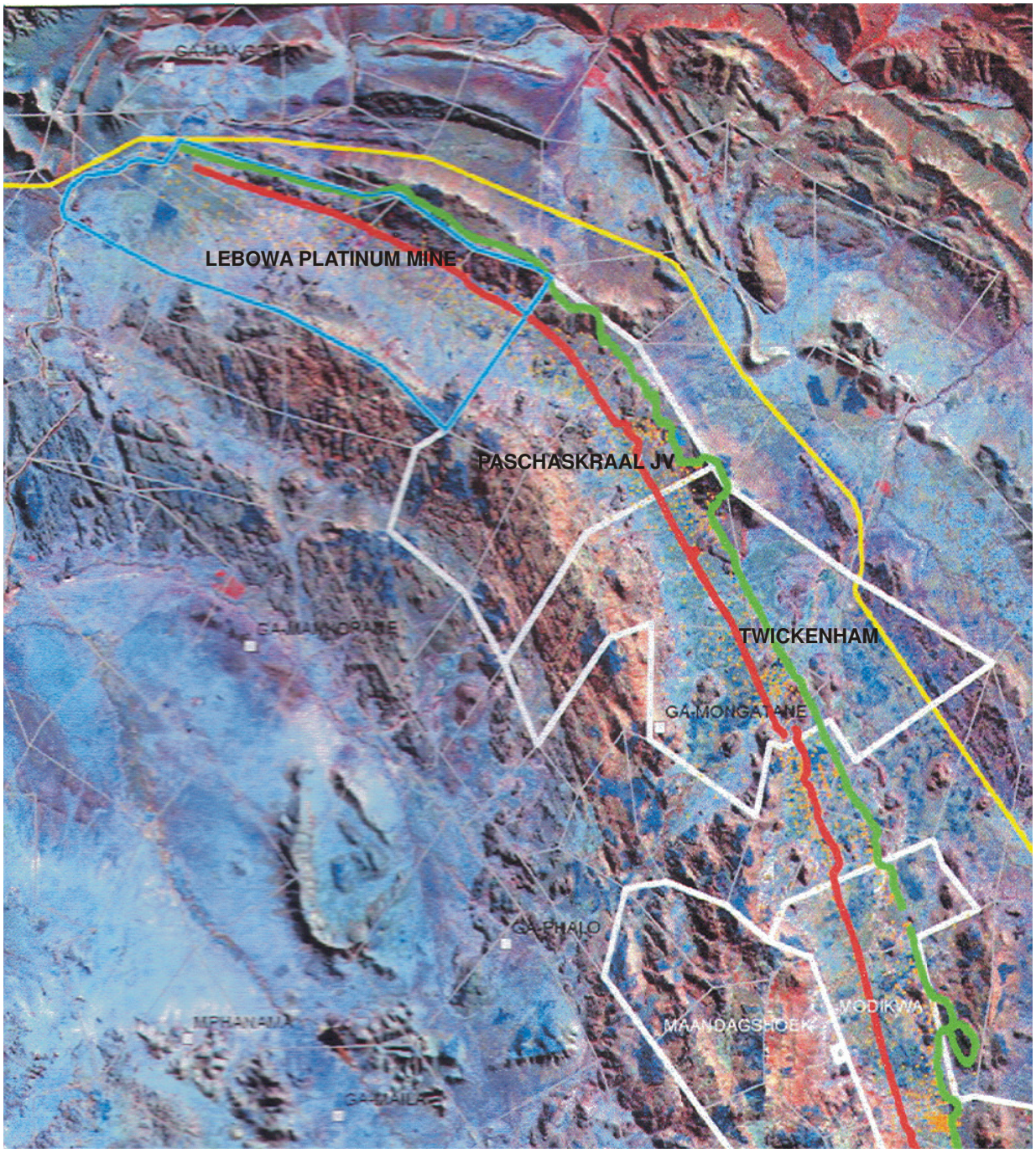

Figure 1.6: LandSat TM Spacemap of the north-eastern Bushveld Complex. The Lebowa (Atok) Platinum Mine is outlined in blue (Brown, 2004).

1.3.1 Overview and History of the Atok Mine

The Atok Mine is situated in the Limpopo Province some 60 km south-west of Polokwane and it comprises the farms Zeekoegat 421KS, Diamand 422 KS, Middelpunt 420 KS, Umkoanesstad 419 KS and Brakfontein 404 KS. It is situated in the Olifants River valley on the north-eastern edge of the eastern limb of the Bushveld Complex (Figure 1.7).

The mine was initially commissioned through a partnership between Anglo Transvaal and OK Bazaars (hence the derivation of the name *Atok*) in 1969. It is now owned by Lebowa Platinum Mines Ltd, a wholly owned subsidiary of Anglo Platinum Plc. Ltd. The Atok mine has long been one of the principal Bushveld PGM mines and has been exploiting the Merensky Reef for over 30 years. Mining of the UG2 on the Atok mining property, however, only commenced in 1999 due to technological advances in metallurgical processing of the platiniferous chromitite layer. A rigorous evaluation and expansion programme was commenced in 2001 and, to date, approximately 700 diamond drill boreholes have been drilled on the property (investigating both the Merensky and UG2 reefs), resulting in a total of about 240 km of drill core to date. This is quite substantial considering the property area measures some 17 km along strike and amounts to 10 938 Ha in area.

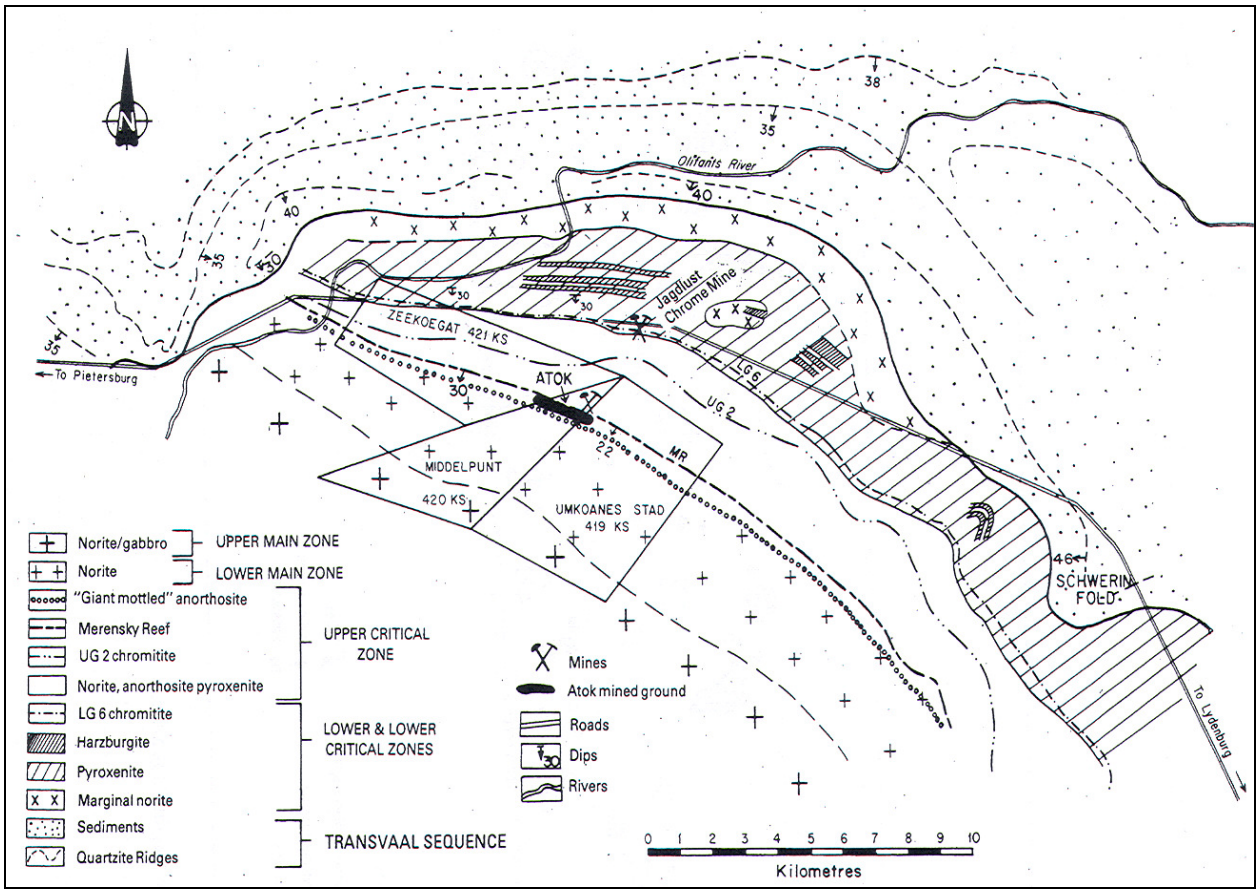

Figure 1.7: Detailed geological map of the Atok area (Mossom, 1986).

1.3.2 The Atok Middelpunt Hill UG2 Operation

The Atok Middelpunt Hill UG2 operation accesses the UG2 reef via four adits which intersect the western portion of the Middelpunt Hill and are developed some 3 km into the hill. These footwall drives are developed into footwall norite and they are each separated vertically by ~100 m.

From these drives a series of horizontal cross cuts branch off perpendicular to regional dip (south westerly direction). On intersecting the UG2 reef a reef-raise is developed which follows the chromitite up – dip. The raise proceeds until it intersects the equivalent cross – cut developed from footwall drive higher up i.e. The different levels are interconnected by raises. A series of panels (stopes), some 30 m in width, are then developed off the raise along strike and it is within these panels that the blasting and removal of the reef (the term reef is a mining term which refers to the extent of economic mineralization) occurs. The mining operation takes place by way of breast mining with strike stabilizing pillars. The mining cut is taken from the first hanging wall chromitite stringer (if the stringer occurs within 30 cm of the top reef contact) 90 cm downwards. The fieldwork portion of this project involved detailed mapping of one of the underground reef raises (3.23) as well as of a surface exposure of the entire UG2 cyclic unit.

1.3.3 Local Geology

The Atok Mine is located on the north-eastern edge of the Rustenburg Layered Suite on the eastern limb of the Bushveld Complex (Figure 1.7). The Rustenburg Layered Suite of the eastern limb forms an arcuate outcrop pattern from the Oliphants River Valley to the Steelpoort fault, 70 km along strike to the south-east. The stratigraphy of the critical zone of the eastern limb is well known from the classic works of Cameron (Cameron 1977, 1978, 1980, 1982).

The Atok Mine is underlain by an alternating succession of anorthosites, gabbronorites and pyroxenites of the upper Critical Zone, overlain by gabbronorites of the main zone. This layered stratigraphy forms an arcuate outcrop pattern with regional dip varying from 16° on the Brakfontein farm increasing north-westwards to 30° on the Zeekoegat farm (Figure 1.7). The structure of the area is relatively simple with the UG2 ore body existing as a tabular, continuous horizon across the entire mine property.

Figure 1.8 illustrates the average lithostratigraphic column for the Eastern Bushveld whilst Figure 1.9 provides a more focused stratigraphic column of just the upper Critical Zone for Atok. The average UG2 stratigraphy for the Zeekoegat farm (which is where the study borehole, ZG219, was drilled) is provided in Figure 1.10.

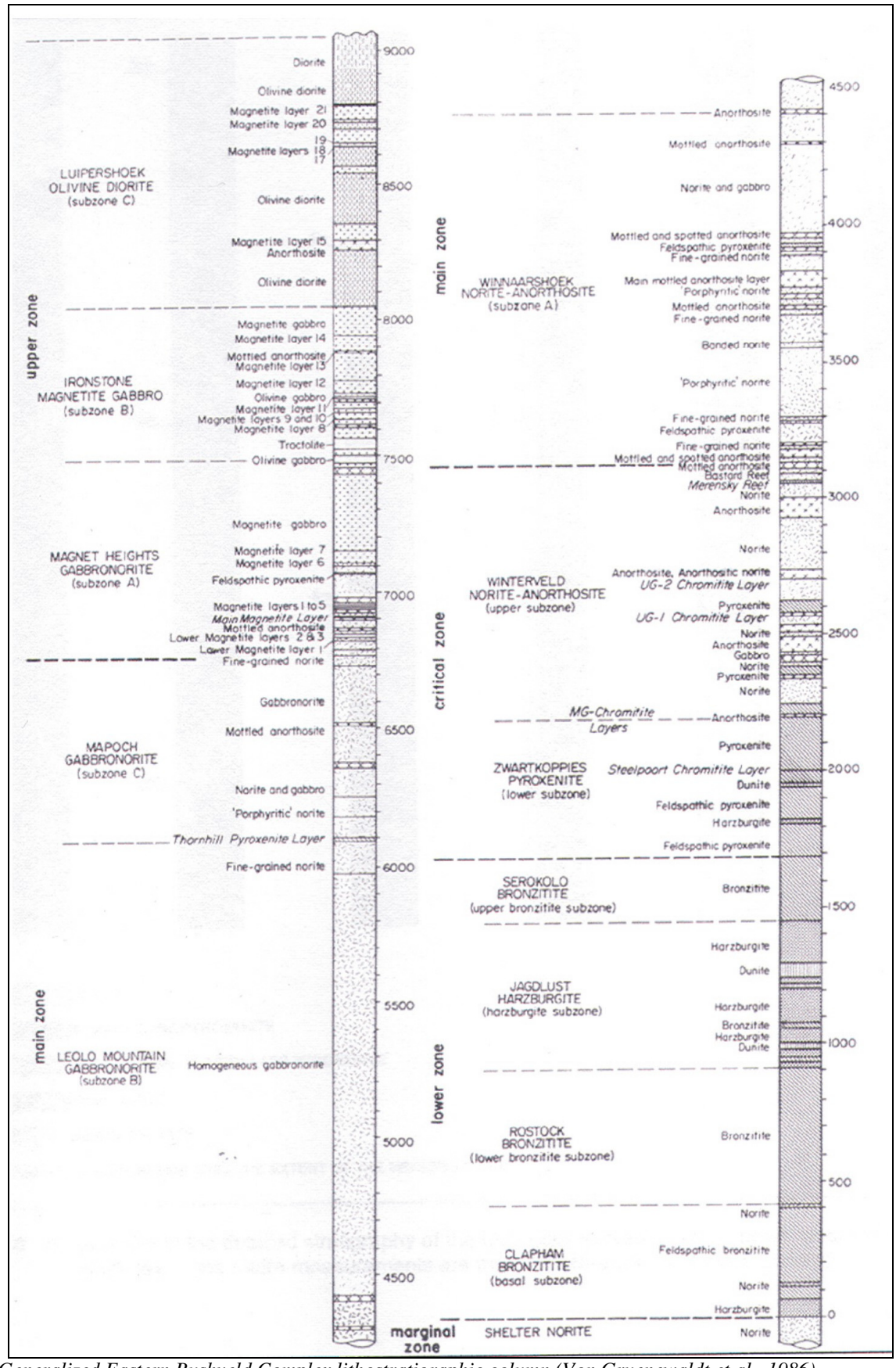

Figure 1.8: Generalized Eastern Bushveld Complex lithostratigraphic column (Von Gruenewaldt et al., 1986).

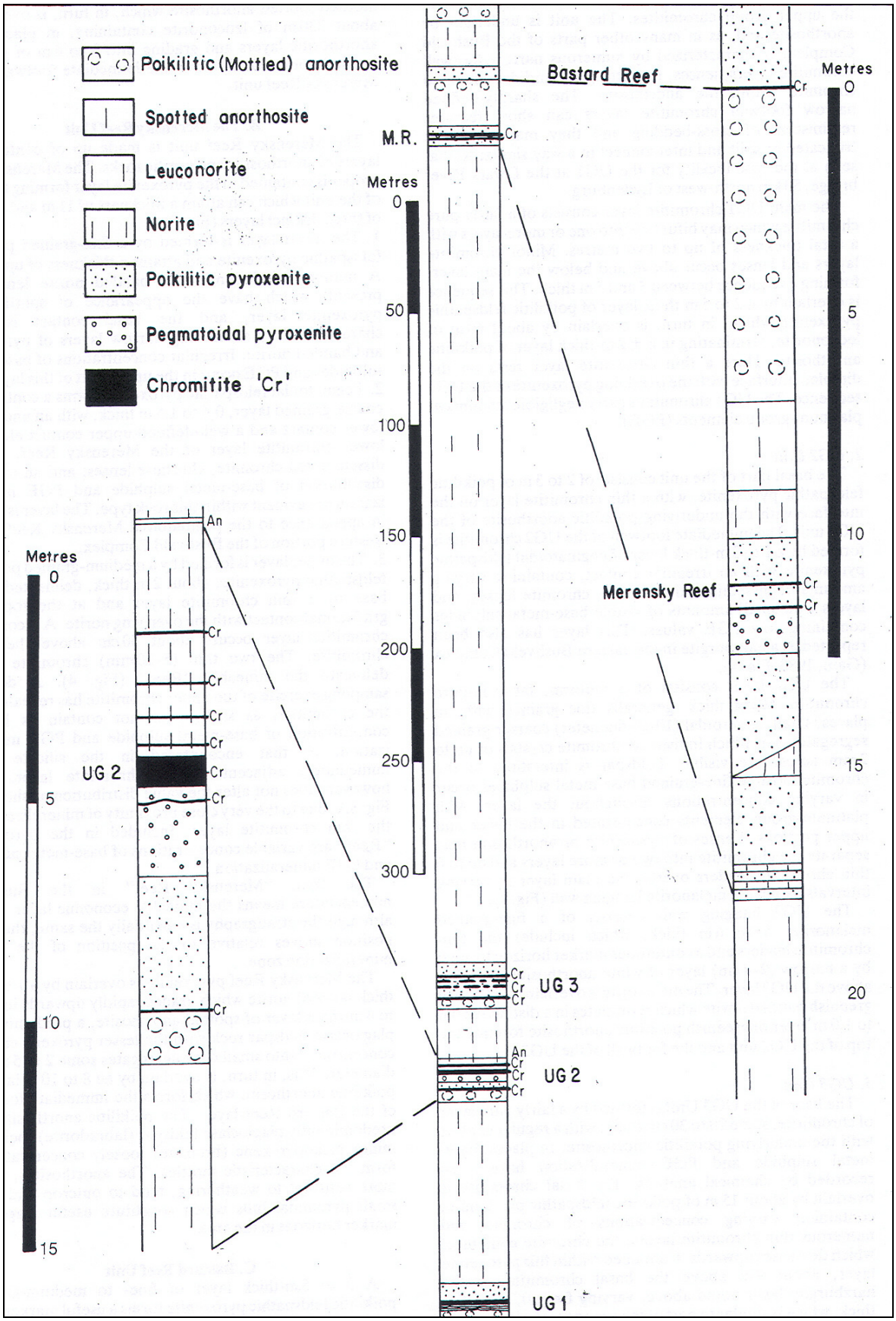

Figure 1.9: Upper Critical Zone stratigraphy at Atok (Mossom, 1986).

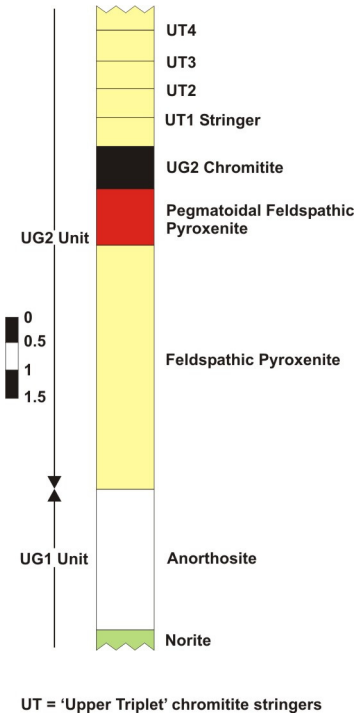

Figure 1.10: Average 'normal' UG2 succession stratigraphy for the Zeekoegat farm (modified from Brown, 2004).

There is some small variation in stratigraphy across the property with the thickness of the UG2 varying from an average of 63 cm on Brakfontein farm to 74 cm on Zeekoegat with a general range between 20 cm and 140 cm (average for the entire mine property is 70 cm). There is thus a systematic westerly thickening and steepening of the UG2 ore body across the mine property. Although the Anglo Platinum Exploration Geology Department considers that this variation does not warrant separation into individual geozones, this work shows that subdivisions are possible on the basis of structural characteristics:

1.3.3.1 Normal UG2

Normal, or undisturbed, UG2 chromitite comprises predominantly chromite (70 – 90 %) within an intercumulate matrix of plagioclase feldspar and orthopyroxene and is generally 0.6 to 1.1 m thick. It is overlain by a medium-grained poikilitic feldspathic pyroxenite which hosts a variable number (0 to 4) of mm to cm-scale chromitite stringers (Figure 1.10). The UG2 chromitite is most commonly underlain by a pegmatoidal feldspathic pyroxenite layer of about 1 m in width that is commonly host to disseminated chromite and some base-metal sulphide (BMS) mineralization. A second pegmatoidal feldspathic pyroxenite layer of approximately the same thickness is often developed a few metres below this layer (although sporadically so at Atok), and the two are separated by a medium grained feldspathic pyroxenite unit. This feldspathic pyroxenite unit occurs below the lowermost pegmatoidal feldspathic pyroxenite layer and is separated from the UG1 anorthosite by a mm-scale chromitite stringer which forms the base of the UG2 cyclic unit.

1.3.3.2 Potholed UG2

Potholes are magmatic disturbances to the reef plane manifested as deep depressions that interrupt reef continuity, and hence has mineability implications (Brown and Nowack, 2003). In plan view, potholes are roughly circular structures, and cause the UG2 to occur below its normal stratigraphic elevation. Although the abundance of UG2 potholes at the Atok mine appear to be far less than for the Merensky Reef, the average diameter of potholes intersected from mining excavations is ~50 m, which indicates that they are substantially larger than for the Merensky Reef which averages ~30 m in diameter. Also unlike the Merensky Reef there is no thinning of the UG2 within potholes, but rather a transgression into the footwall lithologies. In some cases this can be as low as the UG1 anorthosite.

1.3.3.3 Felsic Pegmatite Replaced UG2

Pegmatites are late-stage, discordant replacement bodies which have formed as a result of metasomatic allochemical recrystallization of the primary cumulate lithology (Irvine, 1982). Four varieties exist, namely ultramafic, mafic, intermediate and felsic (Brown and Nowack, 2003). In certain areas of the Atok Mine the UG2 is found to contain irregular bodies of felsic pegmatites often less than 2 m in diameter. These minor occurrences show no indication of being particularly iron-rich and are not suggestive of any extensive replacement (Brown and Nowack, 2003). These pegmatite occurrences are minor both in abundance and extent compared to the better known and highly destructive mafic and ultramafic pegmatites that occur elsewhere in the Bushveld Complex.

1.3.3.4 Dolerite Dyke Intruded UG2

Fieldwork carried out at the Atok mine has revealed the UG2 to have been intruded by a NE – SW striking dolerite dyke swarm ranging from a few cm up to 10 m wide. These dykes tend to be surrounded by a cm-scale alteration zone, which is a result of the host rock being altered by migrating late-stage fluids. Dense jointing and faulting (see next geozone) often accompany these dolerite dykes rendering the UG2 in the immediate vicinity unmineable.

1.3.3.5 Faulted and Jointed UG2

In certain areas joint and fault density can be relatively high (i.e. in the joint zone which often surrounds dolerite dykes) and can have a major disruption on the reef. Highly jointed and faulted UG2 tends to display a massive, friable texture and can be highly altered (joints create pathways for late-stage fluids to migrate and react with the host mineralogy).

1.3.3.6 Oxidised UG2

Oxidation of the reef is seen to occur where it is close to the surface. Brown and Nowack (2003) calculated the average oxidation depth to range from 40 to 55 m in the Atok Mine Valley down to 25 to 35 m in the Middelpunt and Umkoannestad mountains.

1.4 Aims and Objectives

This investigation comprises an approach that combines both a fieldwork study, carried out at the Atok Middelpunt UG2 operation, and a drillcore study, carried out at the University of KwaZulu-Natal. This two-pronged approach was used to tackle two broad objectives i.e. to document the geochemistry, mineralogy and petrology of the UG2 orebody (i.e. the UG2 chromitite layer and its hanging wall and footwall), as well as the variation of these properties vertically through the orebody. The second objective is to investigate the mechanism of formation of the chromitite stringers present in the UG2 hanging wall sequence, and to apply these findings to the Bushveld, and to layered intrusions, in general.

The fieldwork study incorporated underground mapping of the UG2 chromitite layer (and its immediate hanging wall and footwall) in the reef raises of the Atok Middelpunt UG2 mine, along with surface mapping of the entire UG2 unit. The high degree of weathering of the surface road section outcrop served to greatly accentuate subtle textural changes of the individual lithological units thus allowing them to be identified and mapped. Surface mapping of the weathered UG2 unit complemented the drill core study on unaltered rock of the same unit, enabling primary layers and textures to be identified and documented

The drill core study first involved investigating the stratigraphy of the UG2 unit through core logging and density measurements. Logging included the identification of individual lithological units as well as documenting the primary mineralogical and textural characteristics of the units. Much attention was paid to identifying the hanging wall chromitite stringers (which can be as thin as half a millimetre) as well documenting any textural, mineralogical or structural changes with depth through the study section. Density measurements were carried out through the entire study section. This allowed the identification of individual lithological units based on the variation of the dominant primary cumulus minerals (which directly affect the density). The combination of detailed geological logging and density measurements proved to be a highly successful method of investigating the stratigraphy of the study section.

The geochemical investigation formed the crux of this investigation and it included both whole-rock and PGE geochemistry. The geochemistry results were then used to identify the presence of any cyclic units and evaluate the extent of any magma recharge of the chamber. The mechanism of formation of the chromitite layers in the UG2 hanging wall were also investigated using geochemistry.

The UG2 chromitite layer of the ZG219 deflection 2 was then identically sampled as the motherhole section (i.e. 3 cm continuous sampling through the entire layer). These samples were then mineralogically analyzed at the Anglo Platinum Research Centre in Johannesburg using a combination of MLA (mineral liberation analyzer) and Qem-Scan (quantitative evaluation of materials using scanning electron microscopy) techniques. The MLA and Qem-Scan machines are both forms of automated scanning electron microscopes and they were used to characterize the platinum group mineralogy (PGM) and base metal sulphide (BMS) assemblages within the study intersection. Both techniques are described further in Section 2.

Finally, all lithologies were analyzed petrographically using transmitted light microscopy in the form of the Optimas (optical image analyzer) microscope. This involved identifying the mineralogy and textural characteristics of the different lithological units. Microphotographs were taken and were used to document the general primary mineralogical and textural characteristics of the different units. The different lithologies were then classified according to Streckeison (1973) based on their primary mineralogy.

2. Methods of Investigation

The methods used in this investigation are briefly described here. As noted previously, this project combines two major investigative approaches i.e. a fieldwork study, carried out at the study area, and a laboratory based drill core study.

2.1 Fieldwork Study

The fieldwork study was carried out at the study area (i.e. at the Atok Mine) during the period January to July 2004. The fieldwork portion of this project was aimed at documenting the field relations and outcrop styles of the various individual units which make up the UG2 cyclic unit. Combining both underground and surface mapping of the UG2 cyclic unit allowed both fresh (through underground mapping) and weathered rock exposures (through surface mapping of weathered outcrop material) of the UG2 unit to be mapped and studied. This proved ideal in that certain subtle primary igneous textures that were not easily identifiable in the fresh rock underground were greatly accentuated through weathering and were thus able to be studied in the surface outcrop.

2.2 Drill Core Study

The drill core study is based on the ZG219 mother hole (MH) and its two deflections (hereon termed D1 and D2), which were drilled on the Zeekoegat Farm of the Atok Mine lease area (Figure 4.1). The drill core study was carried out during various stages of 2004 and 2005. The ZG219 motherhole core (30.34m in length) was selected for the geochemical analysis as well as for the petrographic study (with some petrographic samples derived from the D2 core as well) whilst the D1 core (29.60m in length) was used for the mineralogical portion of this study. The D2 core (18.35m in length) was therefore retained as a 'reserve' deflection.

2.2.1 Drill Core Logging

Borehole ZG219 (mother hole, deflection 1 and 2) was logged in detail. Logging involved producing a qualitative description of the rock types through a detailed visual inspection of the core. Apart from noting all lithological contacts and changes, estimations of colour, crystal size, texture, modal proportions, alteration and core loss were determined.

The colour of the core material directly reflects the relative mafic or felsic nature of the core. The main mafic mineral is orthopyroxene whilst the main felsic mineral is plagioclase; therefore the colour allows an estimation of the pyroxene/plagioclase ratio to be made. Describing the texture involved noting the size, type and nature of oikocrysts (if present), estimating the size and general nature of the cumulus phases, as well as determining the nature and amount of intercumulus material.

An important part of the logging process involved the identification of thin (1 – 5 mm) chromitite layers present in the section (as these could reveal an insight into the process of chromite precipitation). Apart from identifying the chromitite layers, careful attention was paid to any changes in colour, texture, modal proportions and crystal size across the layers. Cyclic units and evidence of fractionation trends were identified, which could later be compared to the geochemistry results.

Photos of the core are provided in appendix A whilst the geological log is present in appendix B.

2.2.2 Density Measurements

2.2.2.1 Sample Selection

The main aim of the density sample selection process was to allow for a continuous run of density through the entire core. Therefore every single piece of core material from all three deflections was measured for density i.e. with density samples ranging in length from 1 to 10cm. In certain areas i.e. specifically around the chromitite stringers and at other lithological boundaries the core had to be cut in order to improve rock type and density resolution. The final product of this strict sample selection process is a continuous, high resolution run of density through the entire drill core deflection.

2.2.2.2 Method

The density of the samples were measured using the standard immersion technique in which the dry core samples were first weighed in air (weight in air) followed by the sample being weighed in a bucket of water (weight in water). The density of the sample was then calculated through the following equation: wt. in air / (wt. in air – wt. in water). This method required the use of a scale from which fishing line was used to suspend the core samples in either air or water. Repetition of the same sample indicated an error of less than 0.1 %.

These density results were used to study the stratigraphic variation through the core. A discussion of the density results is provided in section 4 with all the density data presented in appendix C.

2.2.3 Geochemistry

2.2.3.1 Sample Selection

The main aim of the geochemistry sample process was two fold: the first was to provide a continuous geochemical profile through the entire motherhole drill core (in order to be able to interpret trends and possible fractionation processes), and the second was to provide a more detailed geochemical (including PGE) profile through the UG2 chromitite as well as its immediate footwall and hanging wall up to the topmost chromitite stringer. A ‘flexible’ sample selection method was therefore required.

The UG2 hanging wall section from the UG3 footwall anorthosite down to the topmost chromitite stringer was continuously sampled using a sample length of 15 cm (half core). This strategy was also used for the UG2

footwall section from below the pegmatoidal feldspathic pyroxenite down to the base of the feldspathic pyroxenite. The sampling interval was then extended to 1 x 15 cm sample every 15 cm (not continuous as before) through the anorthosite and gabbronorite units of the UG1 hanging wall.

A more detailed sampling strategy was used for the UG2 chromitite, its footwall pegmatoidal feldspathic pyroxenite and hanging wall feldspathic pyroxenite up to the topmost chromitite stringer. A continuous run of sampling using a sample length of 5 cm (full core) was therefore used for the hanging wall feldspathic pyroxenite and footwall pegmatoidal feldspathic pyroxenite units. The chromitite stringers in the hanging wall were sampled separately using 2 or 3 cm long samples (just long enough to only include the stringer and minimal pyroxenite material). The UG2 chromitite was sampled continuously using 3 cm long samples.

In total, 240 samples were submitted for bulk rock XRF analysis (major and trace elements) with 54 of these samples also analysed for PGE using the ICP-MS technique (see appendix D)

2.2.3.2 Sample Preparation

The geochemistry sample preparation followed established procedures which involved first cleaning the samples, followed by crushing and finally milling each sample to a very fine powder.

Firstly, any altered material was trimmed off the core. The core was then scrubbed to clear any debris and then rinsed with ionized water. It was then subject to ultrasonic cleaning in the ultrasonic bath for 2 to 3 minutes. After cleaning, the sample was then crushed in the jaw crusher. Very close attention was paid to cleaning the jaw crusher (i.e. brushing, vacuuming and then rinsing with acetone) between samples in order to prevent cross contamination between samples.

After crushing the samples were then milled in a C-steel swing mill for one minute (coarse mill). One hundred grams of the 'coarsely milled' material was then subjected to another minute of milling (normal mill). Finally, 20 grams of the 'normally milled' material was subject to a further 2 minutes of milling (fine mill). After each stage of milling the samples were coned and quartered to ensure that a statistically representative sample was obtained. Much attention was paid to thoroughly cleaning all equipment with acetone after each sample to avoid contamination.

2.2.3.3 Methods

Both the X-Ray fluorescence (XRF) and the Inductively Coupled Plasma Mass Spectrometry (ICP-MS) analytical techniques were used for the bulk rock geochemical analysis. Details are as follows:

A. <u>XRF Major Elements</u>

The major elements were determined using the Norrish Fusion technique (Norrish and Hutton, 1969) using in-house correction procedures and analyzed using a Philips PW2404 X-ray fluorescence spectrometer. Sample

weight used was 350 gm and flux weight 2.5 gm. Calibration standards were primary International Reference Materials USGS series (USA) and NIM series (South Africa). Precision was taken as 1% for elements in abundance of greater than 5% by weight, and 5% for elements in abundance less than 5%.

B. XRF Trace Elements

Trace elements were determined on pressed pellets using a Moviol solution binder and analyzed using a Philips PW2404 X-ray fluorescence spectrometer. Standardization was carried out using International Reference Materials USGS series (USA) and NIM series (South Africa). Precision was determined on the basis of counting time and was taken as 5% for elements in abundance greater than 100 ppm, and 10% for elements in abundance between 10 and 100 ppm.

C. PGE Analyses

The platinum group elements (Pt, Pd, Rh, Ru, Ir and Os; also to include Au) were determined by standard fire assay methods using a S based flux and collected in NiS. Final analysis was by ICP-MS. Detection limits of the PGE and Au are as follows (all in ppb): Pt 2; Pd 2; Rh 1; Ru 2; Ir 2; Os 2; Au 5. Repeated analyses were carried out on 10% of all samples and repeatability was in all cases better than 10%. The instrument used was a Perkin Elmer DRC-e.

D. ICP-MS Trace Elements

Trace elements were determined using the Perkin Elmer DRC-e and analyzed against certified primary solution standards. International reference materials AGV-2, BCR-1 and BR-1 were analyzed with every run. Agreement to accepted values of the standards was better than 10% for all elements and in many cases better than 5%. Dissolution of 50 mg of sample was carried out with high purity HF-HNO3 using a MARS microwave digester.

2.2.4 Petrography

2.2.4.1 Sample Selection

A selection of representative samples were selected from through the mother hole and D2 drill core for the petrographic analysis. In total, 31 samples were selected for the petrographic study.

2.2.4.2 Method

The 31 thin sections were analyzed petrographically using transmitted light microscopy in the form of the Optimas at Anglo Research (see appendix E). The Optimas is a regular Zeiss Axioscope light microscope with a Media Cybernetics Evoltion 5 Mp colour camera and a Marzhauser Wetzler robotic stage.

Emphasis was placed on estimating modal proportions, crystal size, crystal shape and habit, and the degree of alteration as well as describing any textures present. The samples were then classified according to the nomenclature and recommendations of the IUGS subcommission on Igneous Rocks (Streckeisen, 1973).

Three of the UG2 mineralogical samples (see below) were then uncoated and analysed on the Optimas using reflected light microscopy. Emphasis here was placed on identifying and documenting the base-metal sulphide (BMS) assemblages.

2.2.5 Mineralogy

2.2.5.1 Sample Selection

Only the UG2 chromitite was mineralogically analysed and the sampling strategy corresponded exactly with that used in the geochemistry selection i.e. continuous 3 cm sampling through the chromitite. This therefore allowed various mineralogical and geochemical characteristics to be compared closely with each other and it also allowed the platinum-group and base-metal sulphide mineralogy as well as their variations through the UG-2 to be documented.

2.2.5.2 Sample Preparation

Rock slab mounts were prepared from the core material at the Anglo Research Sample Preparation laboratory (see appendix F). This allowed the original rock textures and structure to be preserved and therefore analyzed. Detailed textural characteristics of the base-metal sulphides (BMS) and platinum-group minerals (PGM) were carefully documented. These rock slabs were mounted on normal blocks (used at Anglo Research) and run on the MLA (mineral liberation analyzer) and Qem*Scan (quantitative evaluation of minerals by scanning electron microscopy) machines.

2.2.5.3 Method

The Anglo Research Mineralogy department in Johannesburg (Figure 2.1) is one of the most technologically advanced mineralogical research laboratory in the world. It was therefore an important benefit to this project that this sophisticated mineralogical equipment was made available for use. This proved invaluable in characterizing both the BMS and PGM assemblages present within the UG2.

In terms of qualitative techniques the Optimas (optical image analyzer) was used for the petrographic study (transmitted light microscopy) as well as for documenting the BMS assemblages within the UG2 (reflected light microscopy).

Figure 2.1: The Anglo Research 'Beam Room' – the worlds most technologically advanced mineralogical laboratory. On the left are the 4 QemScans and on the right are 5 MLAs.

Quantitative mineralogical data was obtained using state-of-the-art automated SEM (scanning electron microscopy) techniques in the form of the MLA (mineral liberation analyser) and the Qem-Scan (quantitative evaluation of materials using scanning electron microscopy). Both these instruments are normal SEMs equipped with highly advanced and specific software packages which enable them to function in a fully automated state. The individual techniques are briefly discussed here:

(1) Qem-Scan (Quantitative Evaluation of Materials using Scanning Electron Microscopy)

The Qem-Scan consists of a Leo 1450 SEM, equipped with four light element energy dispersive X-ray detectors, a microanalyser and an electronic processing unit (software package) developed by CSIRO in Melbourne, Australia. At Anglo Research the Qem-Scan technique is primarily used for bulk modal and BMS characterization. For this project, however, it was used for textural mapping – the mapping of rock slabs using X-ray analysis to produce a detailed mineralogical map exhibiting the in-situ textures as well as the mineralogical distribution.

(2) MLA (Mineral Liberation Analyzer)

The MLA comprises an XL40 SEM (Figure 2.2) and Edax energy dispersive X-ray analysis system combined with a software package developed at JKMRC in Brisbane, Australia. The MLA is ideal for characterizing the PGMs – which occur only in trace amounts the Bushveld ore-bodies (i.e. the Merensky reef, Platreef and the UG2 reef). The MLA technique relies on BSE (back scattered electron) imaging (i.e. the difference in BSE grey levels, which is a direct function of the atomic number) to search and to locate the PGMs (which, due to their much larger atomic number, appear much brighter compared to the silicate, chromite and BMS minerals). Once

the PGMs have been located, x-ray spectra are collected in centroid positions from the different BSE grey level zones (i.e. the PGM and its associated minerals). Due to the PGMs being very small (~ 5µm) the MLA, once it has located the PGM due to its BSE brightness, zooms into a higher resolution before proceeding with the x-ray collection. The x-ray spectra are then later compared to the in-house set of PGM standards and the minerals classified accordingly.

Figure 2.2: The XL-40 (or 'MLA 1') MLA which was used to characterize the PGMs in ZG219.

There are a variety of different MLA measurement types – all using varying combinations of BSE imaging and x-ray analysis. Due to the fact that whole rock slabs were analysed (as opposed to crushed and milled material) it was decided that the sparse phase liberation lite (spl-lite) PGM-characterization method be used. This method is used for coarse-grained material or for rock slabs (as in this case). Once the machine has identified and located a PGM (on the basis of BSE grey levels) it draws a block around it so that only the PGM and its directly surrounding particles are analysed. The surrounding particles are also analysed and classified according to an in-house set of x-ray standards. These include the oxide and silicate minerals. The final result from this measurement is a series of mineral maps (Figure 2.3) from which quantitative modal mineralogy, mineral size and association data are obtained.

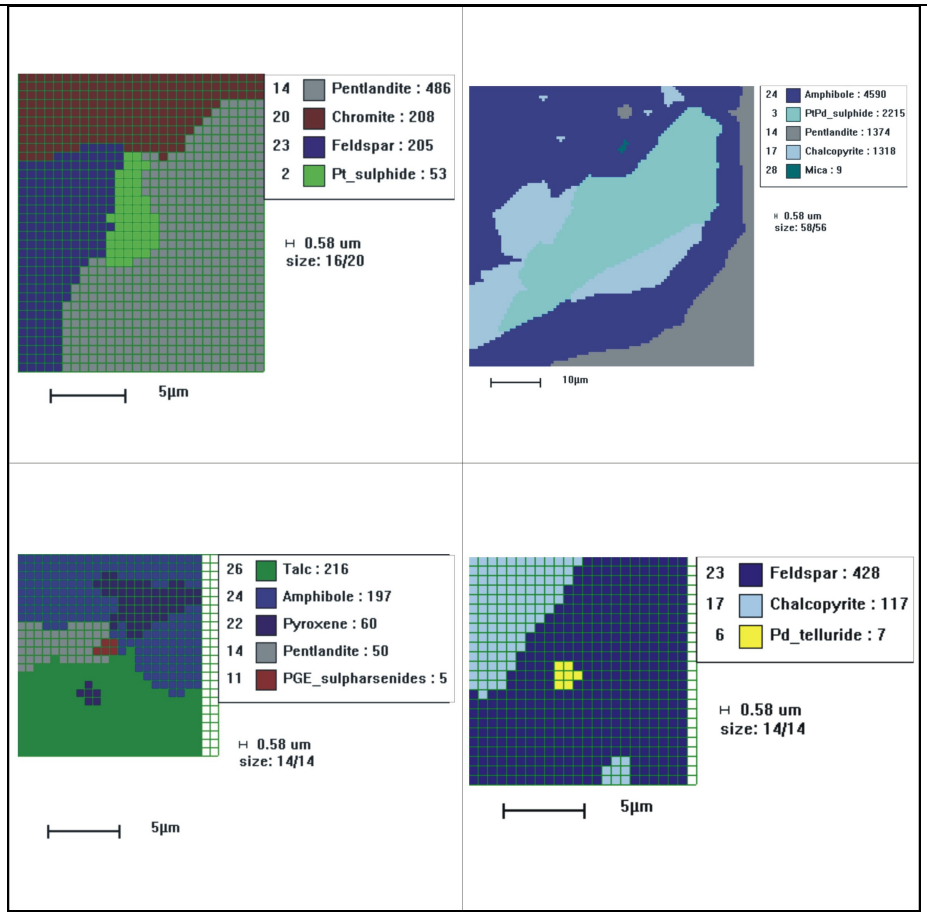

Figure 2.3: MLA spl-lite mineral maps from the ZG219 samples. Note the fine grain size of the PGMs.

This section has served as a brief introduction to these two forms of automated SEMs, as well as the measurement types utilized. Both these techniques are extremely important for applied mineralogy i.e. identifying metallurgical process problems, optimizing concentrator circuit design and characterizing in-situ exploration and ore body material (as carried out in this project). The reader is, however, referred to the literature for further detailed information regarding these techniques and their applications (i.e. Jones, 1987; Petruk, 1986, 1988, 2000; King, 1993, Gu, 2003).

3. Fieldwork

3.1 Introduction

Fieldwork was carried out at the Atok Middelpunt UG2 operation during the periods December 2002 – January 2003 and January to June 2004. The fieldwork study complemented the drill core investigation as it enabled both fresh (drill core material) and weathered (Adit 3 road section) exposures of the UG2 unit to be observed and studied.

Another major aspect of the fieldwork was to study the field relations and structural characteristics of the individual lithological units that make up the UG2 cyclic unit. This data is invaluable in deciphering the petrogenetic evolution of the study section.

The fieldwork portion of this project can be subdivided into two sections: (1) underground mapping of the UG2 chromitite layer and its immediate hanging wall (HW) and footwall (FW), and (2) surface mapping of the entire UG2 cyclic unit.

3.2 Underground Mapping

Underground mapping of the UG2 chromitite layer, and its immediate hanging wall and footwall, was carried out in several reef raises within the Middelpunt Hill UG2 mine. The results of the mapping carried out in raise 3.24 is presented here, as raise 3.24 provided the best representation of the UG2 layer and its hanging wall and footwall. Raise 3.24 was accessed via adit 3 and it extends in a south-westerly direction (top to bottom) and provides a 43 m exposure of normal UG2 along dip. The stratigraphic variability of the UG2, its hanging wall and footwall as well as the primary mineralogy and textures (due to the fresh underground exposures) of the rocks were examined and are documented here. Figure 3.1 shows an averaged stratigraphic column for the section (UG2 as well as its hanging wall and footwall) exposed in the panel side wall. Figure 3.2 provides a full profile of the entire mapped side-wall face of the raise, whilst Figure 3.3 shows individual sections of the raise in greater detail.

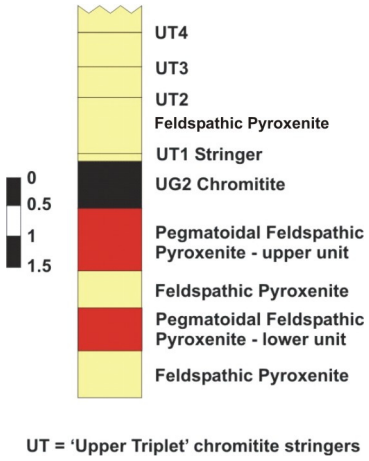

Figure 3.1: Average stratigraphic column for the Atok UG2 and its immediate hanging wall and footwall.

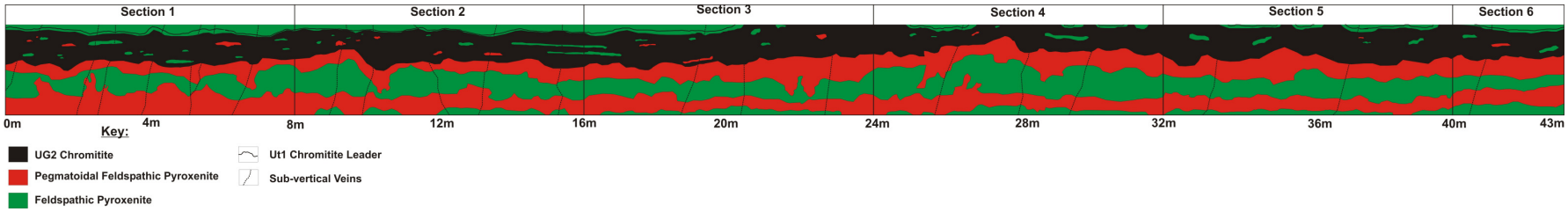

Figure 3.2: Geological profile of the entire mapped raise 3.24 section (note vertical scale = horizontal scale).

(A)

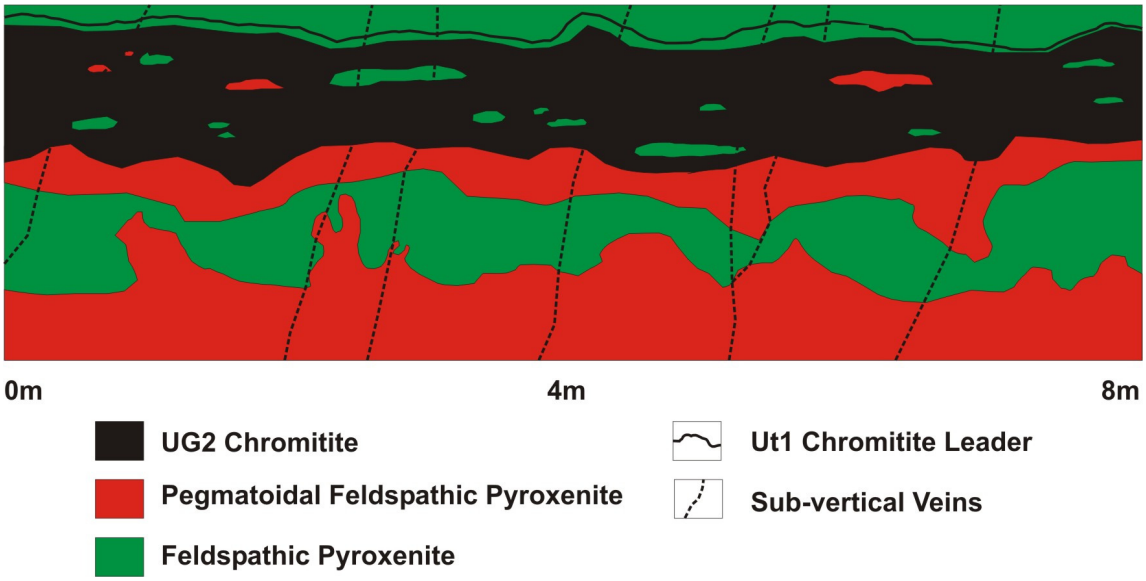
0m
4m
8m
UG2 Chromitite
Pegmatoidal Feldspathic Pyroxenite
Feldspathic Pyroxenite
Ut1 Chromitite Leader
Sub-vertical Veins

(B)

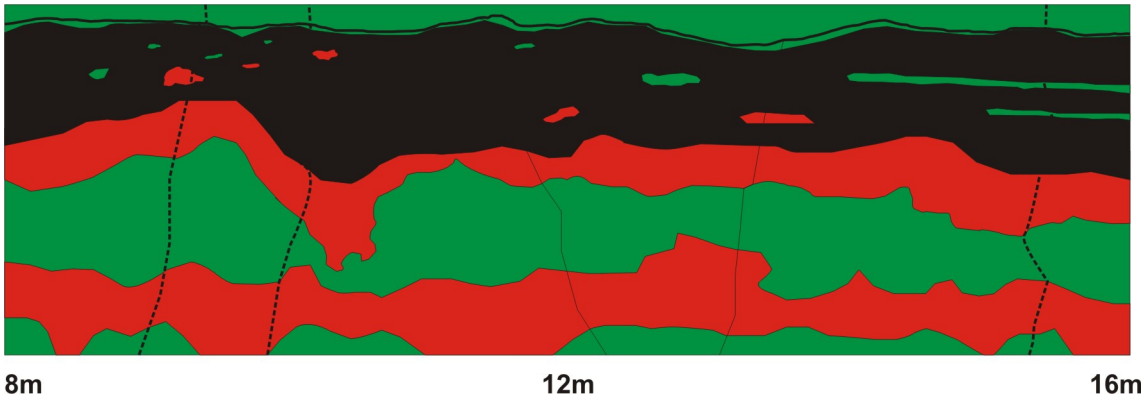
8m
12m
16m

(C)

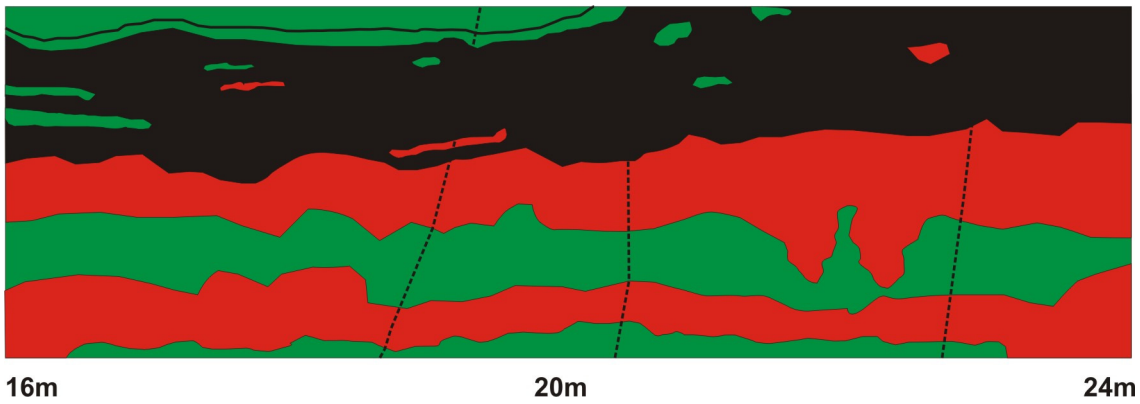
16m
20m
24m

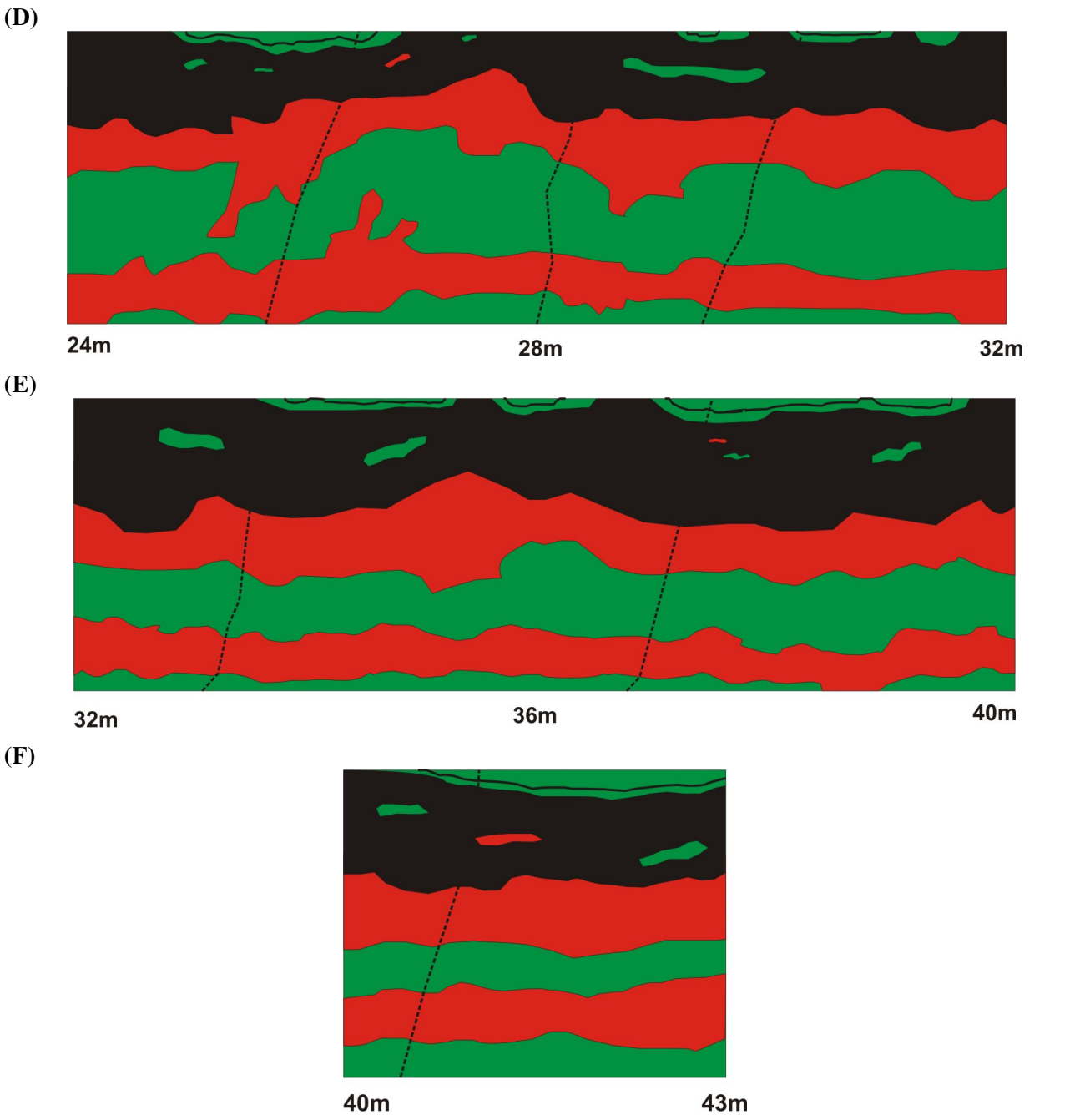

Figure 3.3: Cross-sections of the side-wall face of raise 3.24 within the Atok Middelpunt UG2 mine (note: vertical scale = horizontal scale).

3.2.1 The UG2 Chromitite Layer

The UG2 chromitite layer occurs as a ~60 cm thick (varying between 72 and 47 cm), planar layer of chromitite. The primary mineralogy comprises a cumulate framework of chromite grains within an intercumulus matrix of plagioclase feldspar and orthopyroxene. The UG2 is also known to be fairly sulphide rich in the Atok area (Mossom, 1986) and sulphide blebs were indeed observed in the underground exposures. The sulphides tend to be intercumulus in nature and are generally less than 3 mm in size.

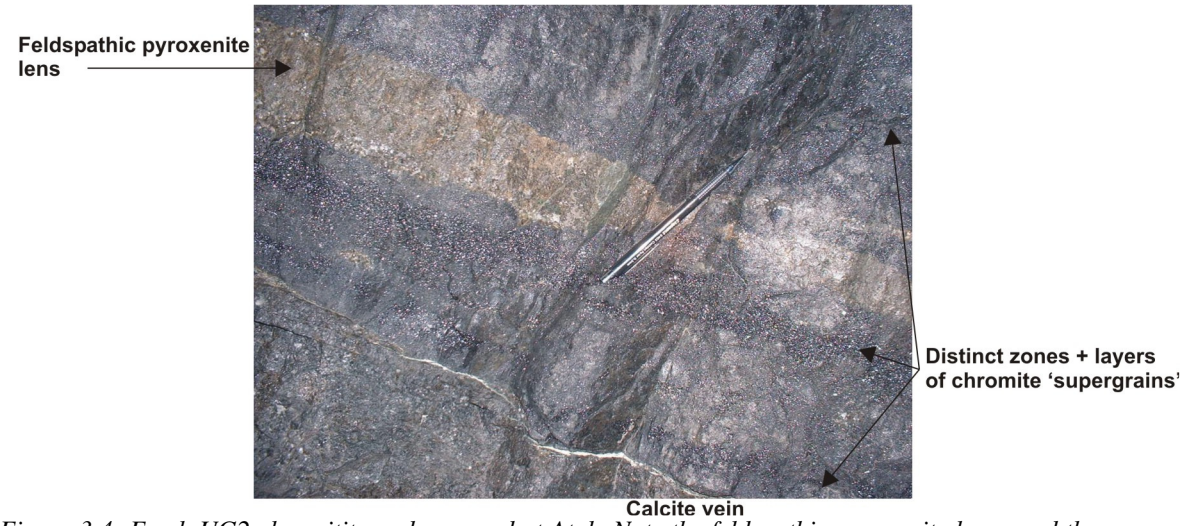

Figure 3.4: Fresh UG2 chromitite underground at Atok. Note the feldspathic pyroxenite lense and the zones of euhedral chromite supergrains.

The bulk of the UG2 is made up of fine grained, subhedral chromite. A particularly interesting texture was identified with segregations of pure, coarse euhedral chromite crystals (heron termed 'supergrains') existing in distinct irregular patches (Figure 3.4) against the background of 'regular' subhedral, finer grained chromite. The patches are highly variable and irregular and are mainly concentrated in the lower portion of the layer.

There is a substantial variation between the planarity of the top reef contact (TRC) and the bottom reef contact (BRC). The TRC is generally planar and regular with only minor slight undulations. The BRC, however, is highly irregular and erratic (Figure 3.5). Sharp transgressions into the footwall (over a scale of 10 to 30 cm) were observed and are termed 'micropotholes' in this study. These micropotholes are defined by the BRC only and are highly irregular (i.e. no set size or shape).

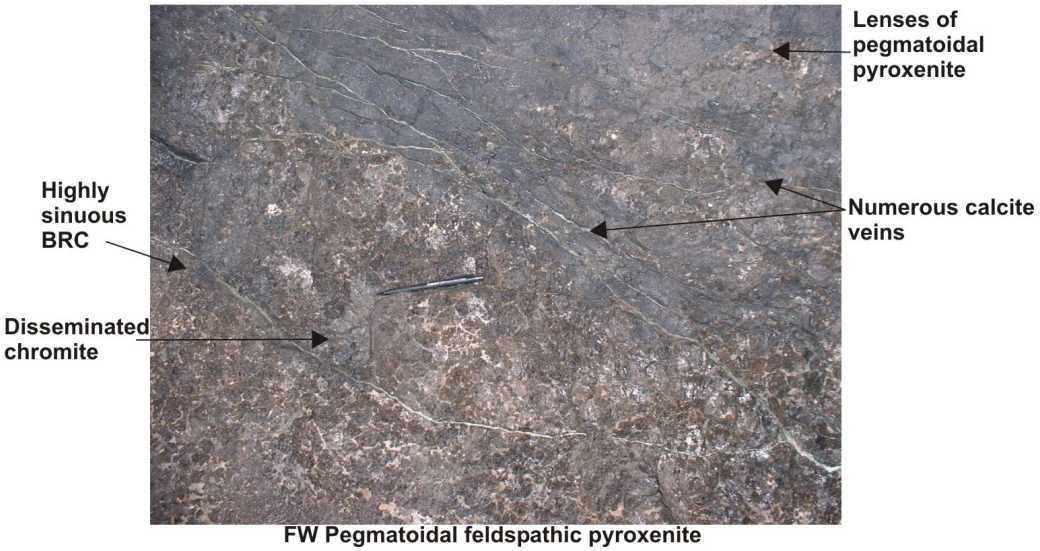

Figure 3.5: Disturbed UG2 containing a highly sinuous BRC, numerous pegmatoidal lenses as well as numerous calcite veins. Fluid flow accompanying the veining has disturbed and altered the reef.

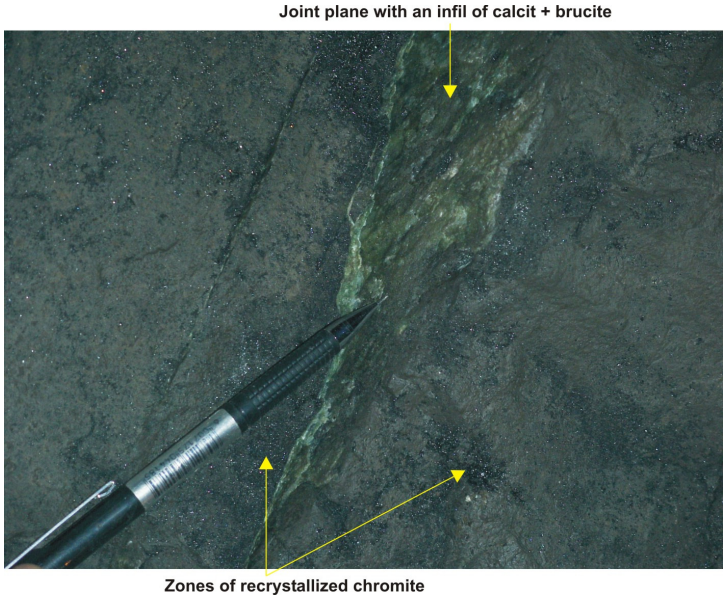

Figure 3.6: A calcite vein cutting through the UG2. Note the zones of recrystallized chromite surrounding the joint.

The chromitite layer also contains numerous layer parallel lenses of both medium-grained feldspathic pyroxenite and pegmatoidal feldspathic pyroxenite (Figure 3.4). The lenses range in size from 5 cm up to 1.5 m in length and average 5 to 10 cm in width. The layer, in general, is planar and regular with only slight undulations observed. The UG2 is also seen to be cut be a number of calcite and pegmatoidal veins and unfilled joints and factures (Figures 3.5 and 3.6). The calcite joints tend to be thin (<3 mm) and vary greatly in dip and strike. One particular calcite joint, the 'undulating calcite break' (UCB), has a hazardous affect on mining due to the fact that it cuts through the chromitite and hanging wall at a low angle (leading to potential hanging wall failure). The pegmatite joints, however, tend to be thicker (0.5 to 2 cm) and maintain a steepish dip (~75°) and regular strike.

3.2.2 The UG2 Footwall

The footwall to the UG2 is a pegmatoidal feldspathic pyroxenite unit (Figure 3.7) and, rarely, a medium-grained feldspathic pyroxenite. The latter generally occurs below the pegmatoidal feldspathic pyroxenite layer and only forms the immediate footwall to the UG2 when the pegmatoidal feldspathic pyroxenite dips down and occurs up to a metre below the UG2.

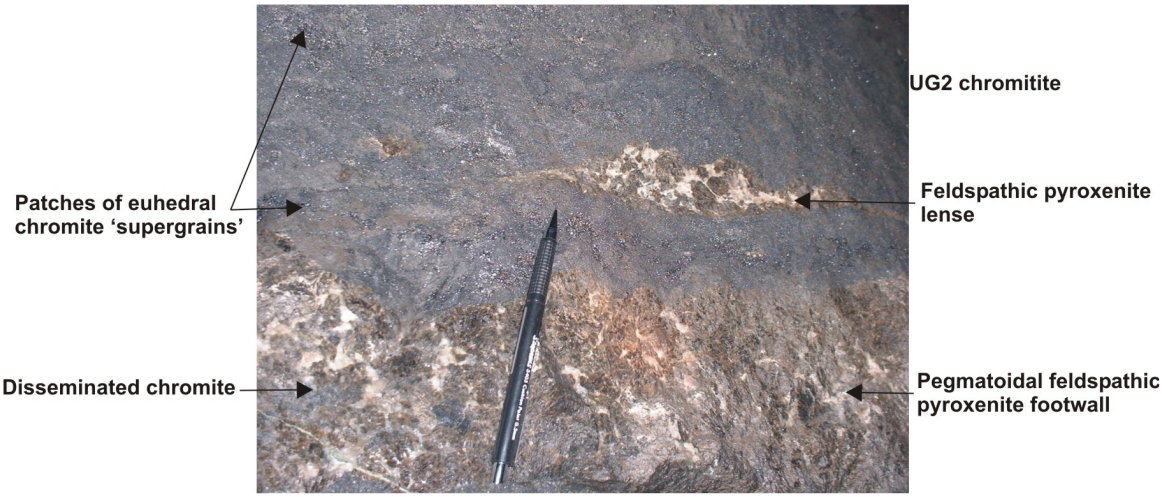

Figure 3.7: The UG2 and its underlying pegmatoidal feldspathic pyroxenite FW. Note the sinuous nature of the BRC.

The pegmatoidal feldspathic pyroxenite comprises large ortho – and clinopyroxene, as well as plagioclase, oikocrysts in an intercumulate matrix of plagioclase feldspar. The size of these oikocrysts tend to be largest at the very top of the unit i.e. just below the BRC. There is a distinctive decrease in the cumulus crystal size downward through the unit.

Another major aspect of the footwall pegmatoidal feldspathic pyroxenite layer is the occurrence of chromite within it. Chromite occurs both in a disseminated form as well as as distinctive layers in the footwall unit. The disseminated chromite occurs in the footwall in a highly irregular form i.e. both the amount and distribution of the chromite is variable. The disseminated chromite occurs in the footwall down to a depth of 80 cm below the BRC, but is generally concentrated in the topmost 30 cm of the pegmatoidal feldspathic pyroxenite layer. A distinctive chromite stringer also occurs in the footwall some 10 to 20 cm below the BRC (Figure 3.8). This stringer is sometimes joined by a second stringer.

Figure 3.8: The UG2 and its FW being cut by a reverse fault. Note the chromitite stringer within the FW.

Below the pegmatoidal feldspathic pyroxenite unit is a medium – grained feldspathic pyroxenite layer. This unit has a poikilitic texture and occasionally exists as the immediate footwall to the UG2. This unit

varies slightly from the hanging wall feldspathic pyroxenite unit in that it is coarser grained and slightly more feldspathic.

A second pegmatoidal feldspathic pyroxenite unit exists below the medium – grained feldspathic pyroxenite layer – some 1 to 2 m below the uppermost pegmatoidal feldspathic pyroxenite unit. This lower pegmatoidal pyroxenite exhibits the same coarse grained texture as the upper unit. The only observable difference is the lack of any chromite mineralization within it.

3.2.3 The UG2 Hanging Wall

The UG2 hanging wall unit was identified as being a medium-grained feldspathic pyroxenite. The top contact of this unit is not exposed within the reef panels. The general mineralogy of the unit comprises cumulus orthopyroxene and clinopyroxene with interstitial plagioclase. The first of the triplet chromitite leaders (UT1 – upper triplet 1) occurred regularly about 1 cm above the TRC (Figure 3.1 and 3.9). This feldspathic pyroxenite unit formed the hanging wall to the UG2 chromitite at all the observed underground exposures. The TRC, although sometimes slightly sinuous in nature (Figure 3.9), is mostly planar, which is in stark contrast to the BRC (Figure 3.7).

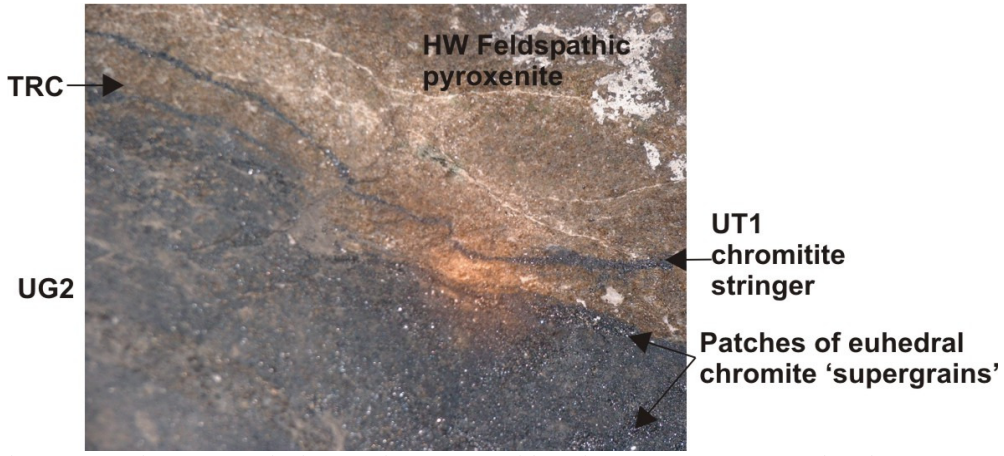

Figure 3.9: The TRC of the UG2 with the overlying HW feldspathic pyroxenite. Note the close proximity of the UT1 stringer to the TRC.

3.3 Surface Mapping

The mine road leading up to Adit 3 provides an excellent exposure of the entire UG2 cyclic unit (Figure 3.10). The section that was mapped extends from the parking entrance (top of the road) outside Adit 3, down to the first sharp corner (which is to the right) in the road. This road cutting exposure averages 4 m in height and is 165 m in length. It provides a spectacular outcrop of the UG2 basal pyroxenite unit up to the UG3 chromitite layer (Figures 3.11 and 3.12).

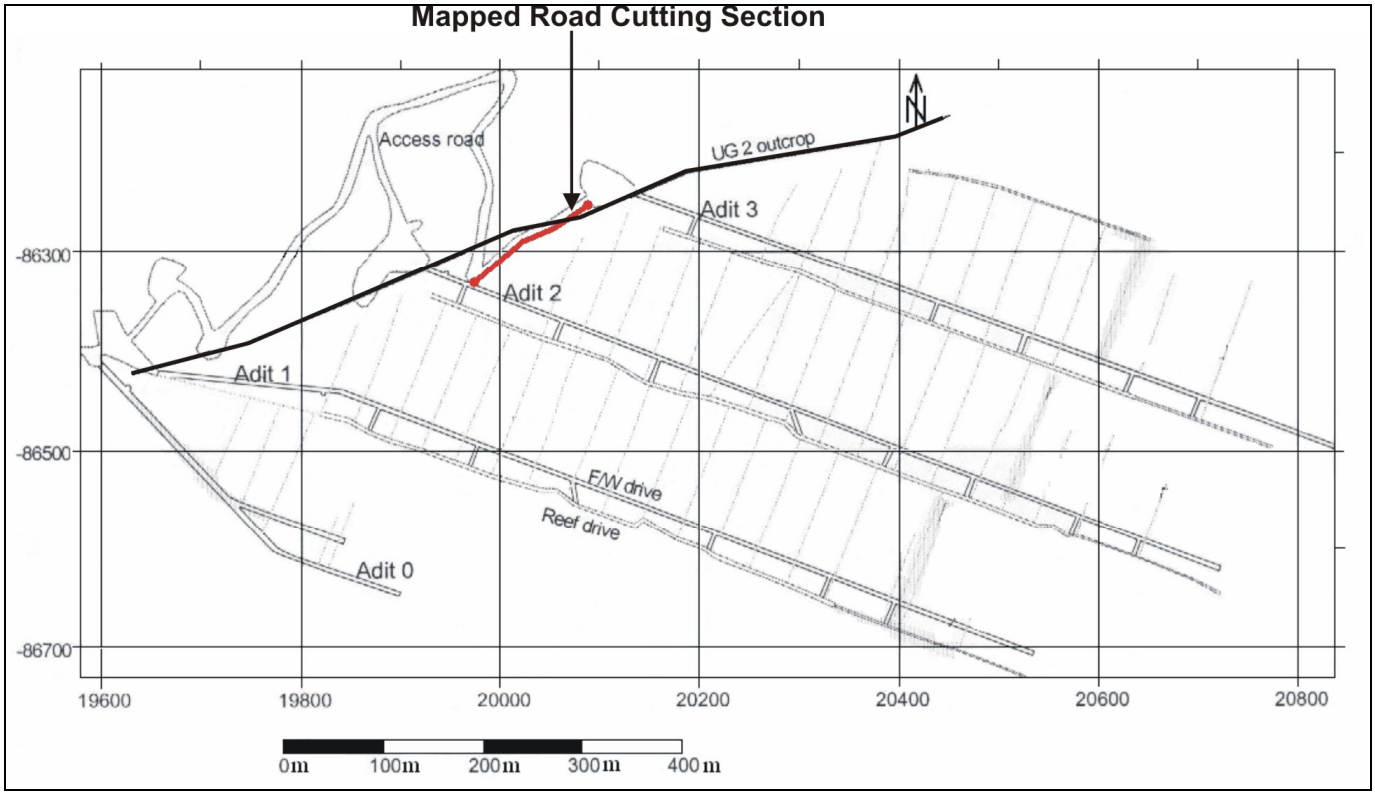

Figure 3.10: Plan view of the Atok Middelpunt UG2 operation (showing only the main adit and reef drive tunnels) with the mapped road cutting outcrop depicted in red (modified after Snowden, 2003).

A photographic collage of the section (Figures 3.13 and 3.14) was produced in order to document the field relations of the section. This was done by taking a series of photos of the section and then stitching them together in CorelDraw. The final result proved highly successful and it provides a superb visual of the outcrop which can then be correlated to the field maps. It also allows one to view the intricate details of the field relations and outcrop styles of the different lithologies in the differentiated layered UG2 cyclic unit.

The high degree of weathering of the road cutting exposure has accentuated the subtle primary igneous textures of the exposed material (which are otherwise difficult to identify in fresh rock), thereby highlighting each individual unit. The degree of weathering of each unit is a direct function of its primary composition, in that more mafic material will prove more resistant to weathering, whilst feldspathic material tends to weather more easily. It is therefore the variation in the pyroxene/plagioclase ratio (as pyroxene is the dominant mafic

mineral and plagioclase the dominant felsic mineral) between the different units that results in some units being more weathered and altered compared to others. This differential weathering of the individual units allowed each and every unit to be identified and mapped. This was particularly helpful during mapping of the pyroxenite sequences in which several units (defined by differing pyroxene/plagioclase ratios) often exist within a single sequence. It is very difficult to discriminate between different pyroxenite units in a whole pyroxenite sequence in fresh drill core material (as it was found during the core logging of ZG219).

The weathering has thus had the influence of drawing out subtle mineralogical and textural characteristics of individual units which, otherwise, would not have been identifiable. Therefore, mapping of the highly weathered adit 3 road section exposure complemented the drill core study ideally in that it allowed a comparison of fresh material (drill core) with weathered material (road section) of the same UG2 cyclic unit.

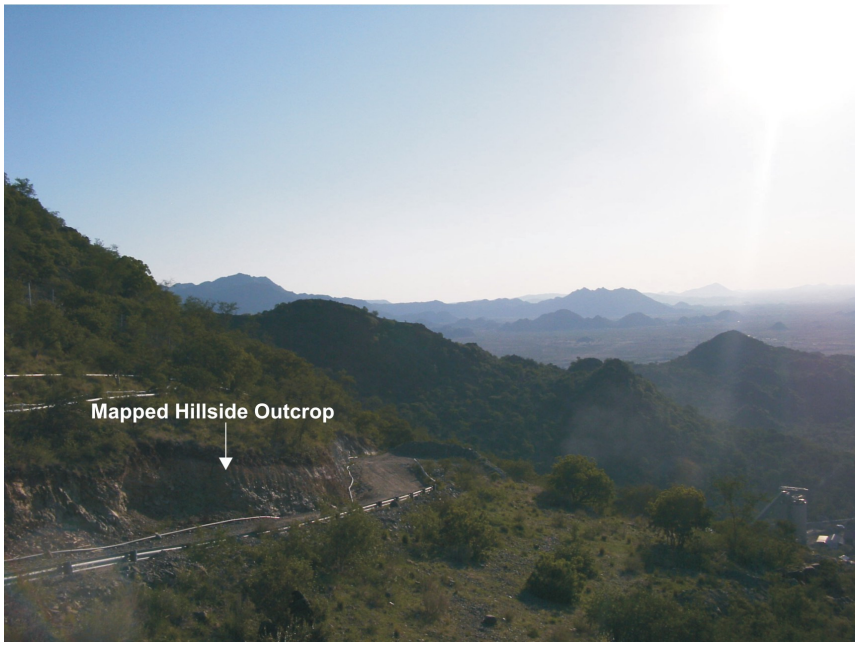

Figure 3.11: View south across Middelpunt with the mapped road section in the foreground.

Figure 3.12: View northwards showing the layered stratigraphy outcropping in the road section. Note the HW gabbronorites in the foreground and the UG2 in the background.

The section was drawn using field maps which were drawn out neatly and then scanned into CorelDraw, where they were traced over. Due to the length of the mapped road section a simplified section was produced of the entire exposure (Figure 3.15), and to then break up the entire mapped section into 15 m long, detailed sections (Figures 3.16 – 3.19).

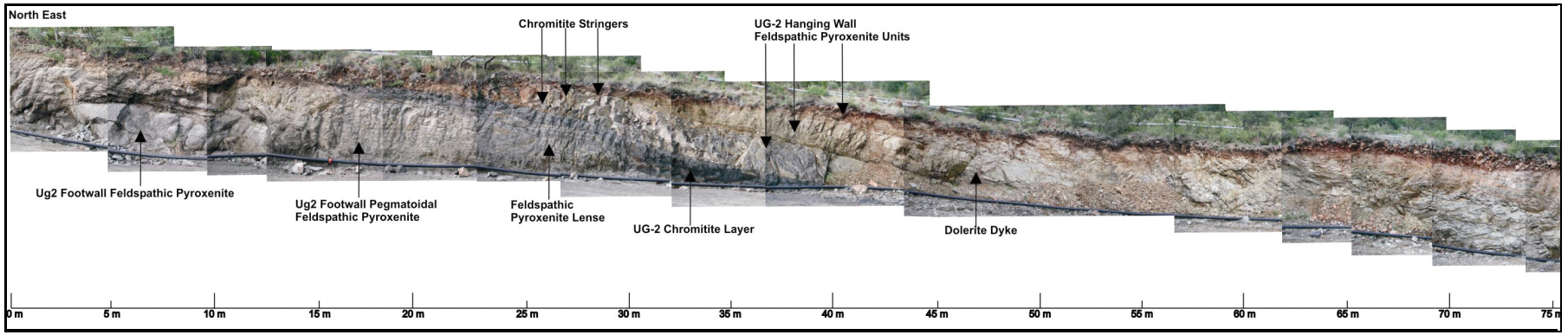

Figure 3.13: Photographic collage of the first 85 m of the mapped Adit 3 road cutting section.

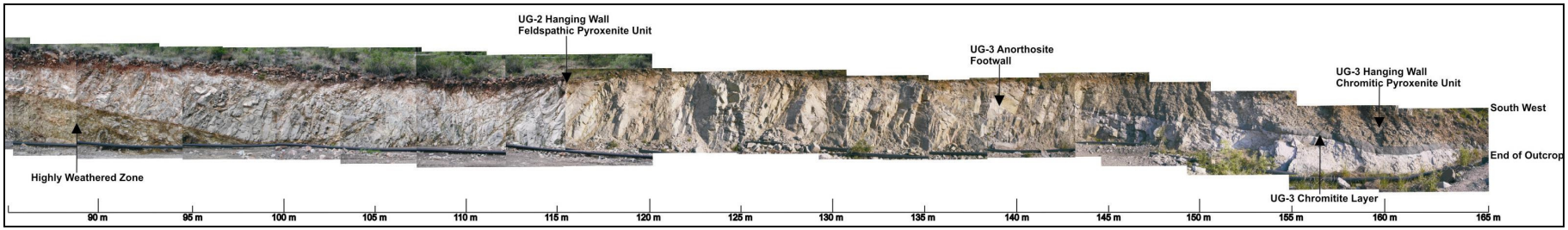

Figure 3.14: Photographic collage of the second 85 m of the mapped Adit 3 road cutting section.

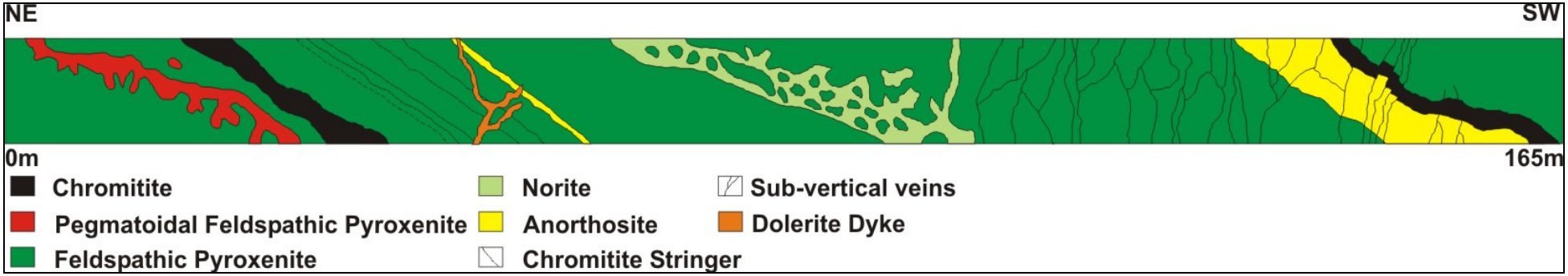

Figure 3.15: Geological profile of the entire mapped Adit 3 road cutting section (0 to 165 m).

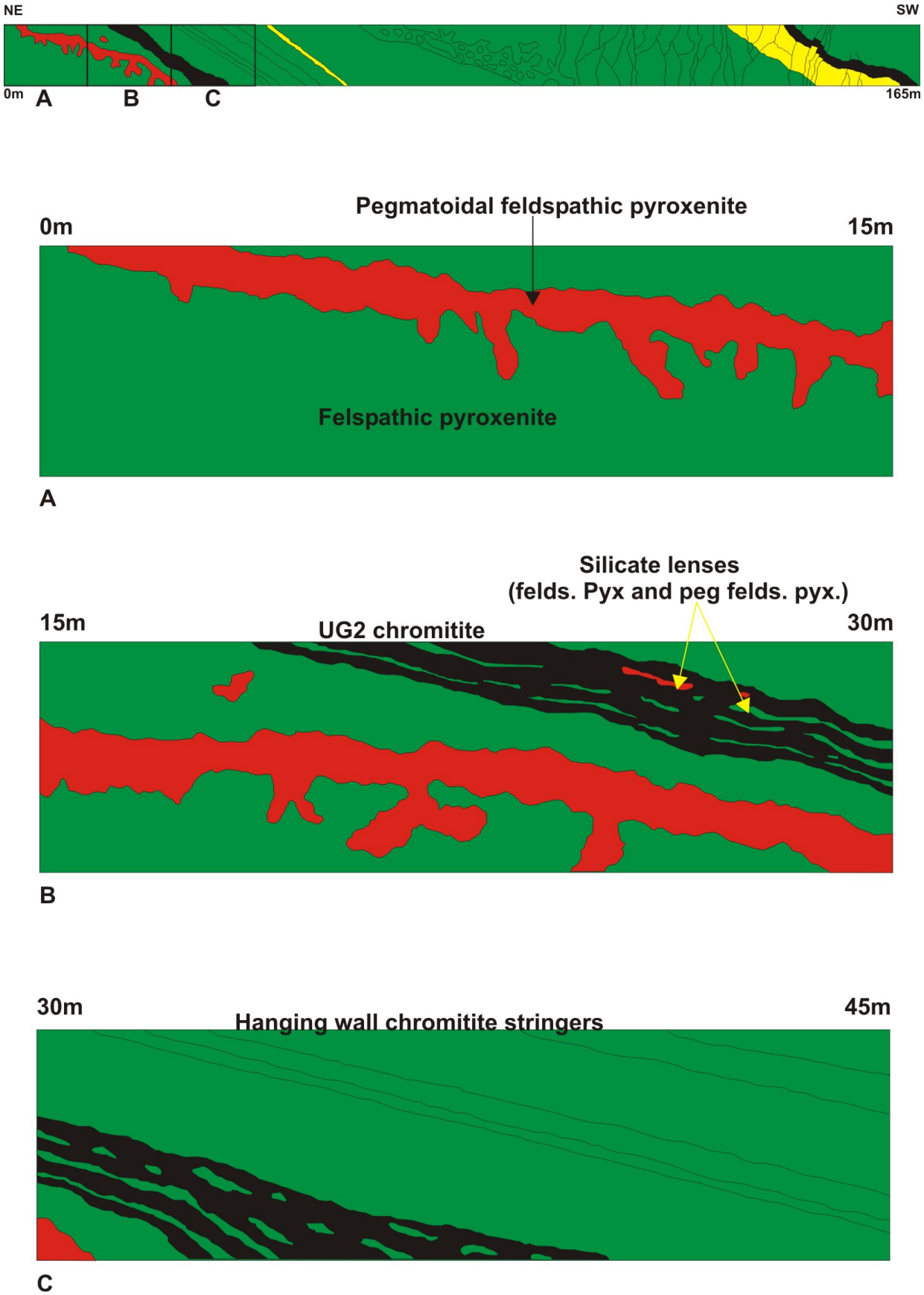

Figure 3.16: Mapped sections for 0 to 45 m of the road cutting outcrop.

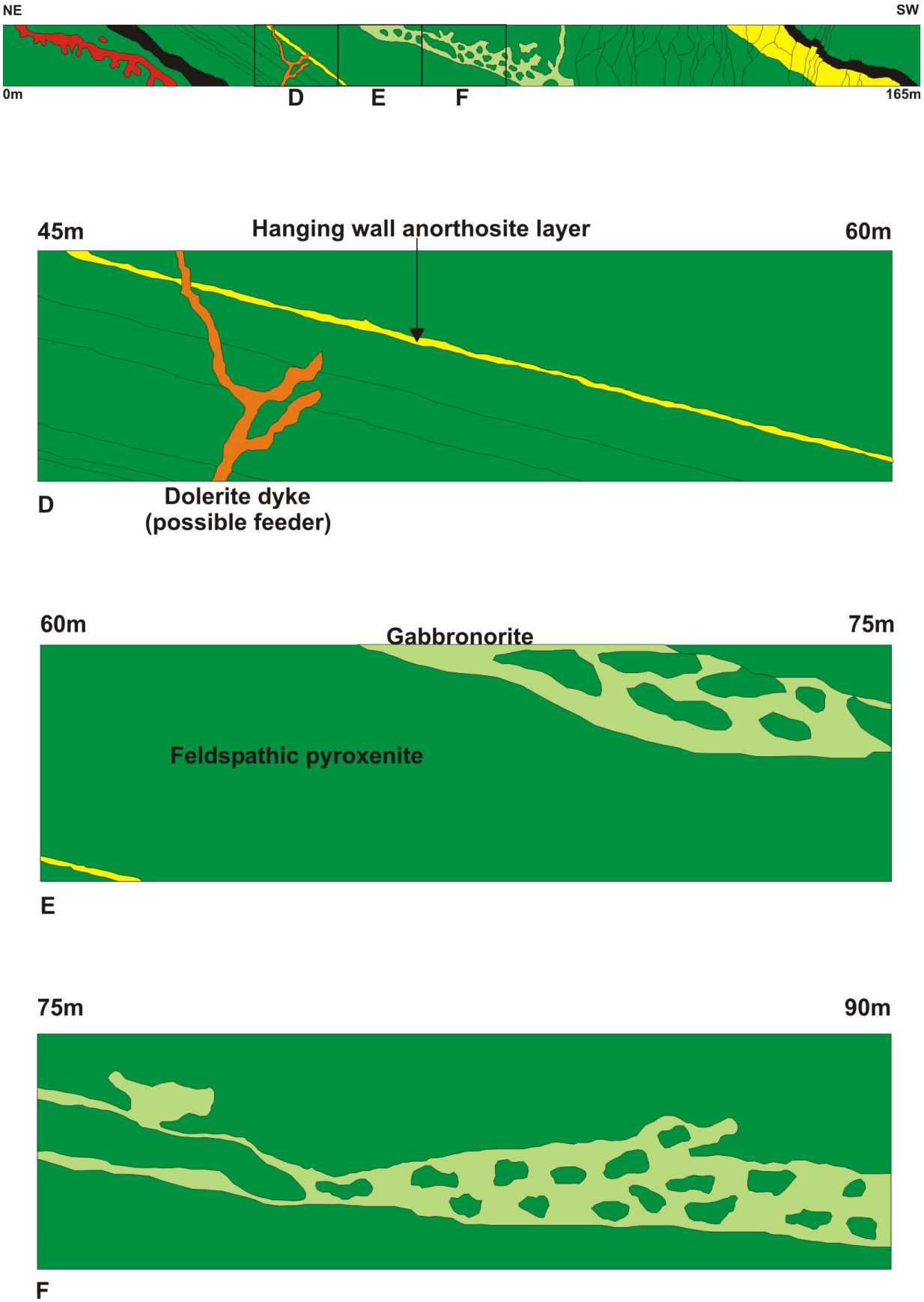

Figure 3.17: Mapped sections for 45 to 90 m of the road cutting outcrop.

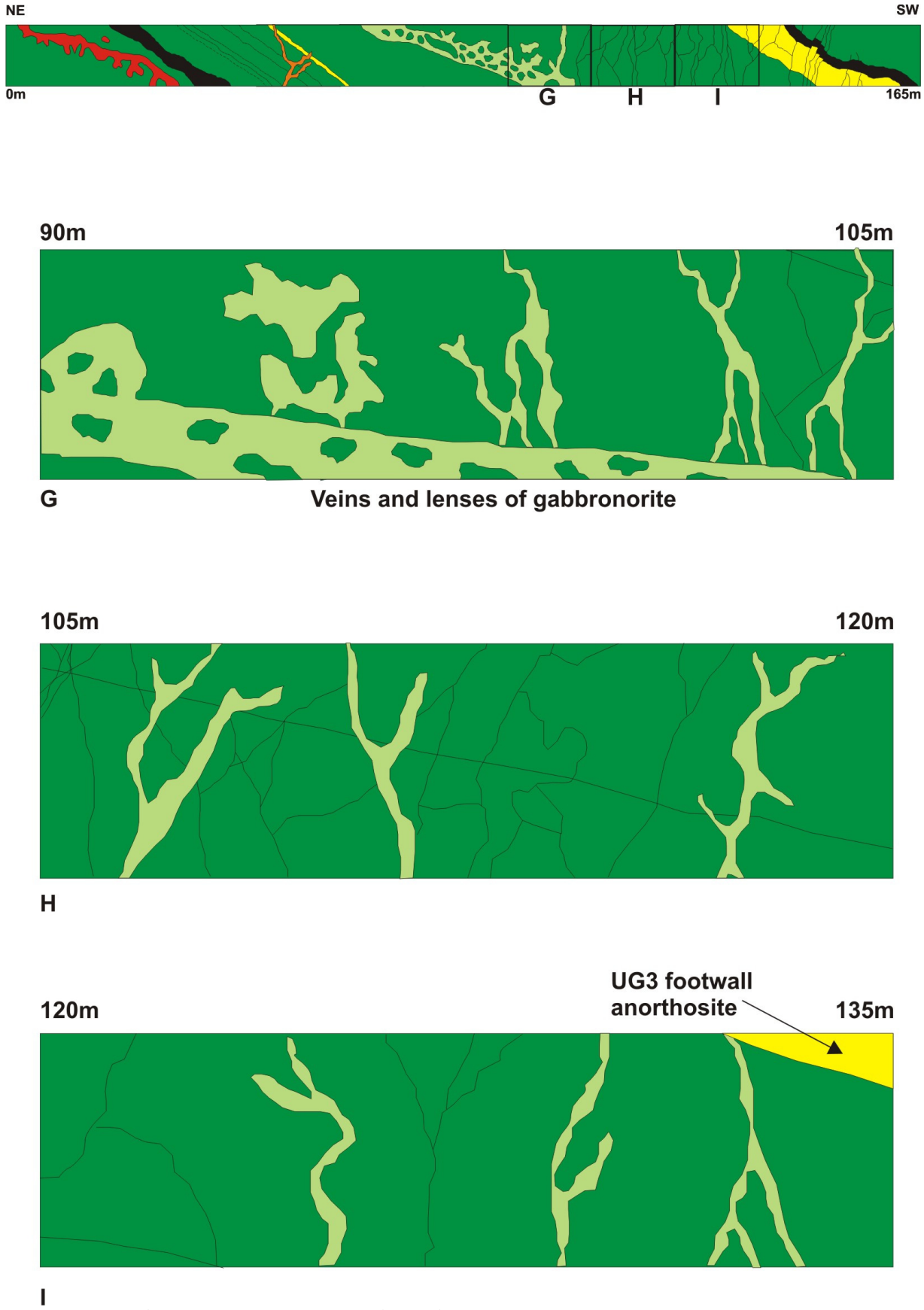

Figure 3.18: Mapped sections for 90 to 135 m of the road cutting outcrop.

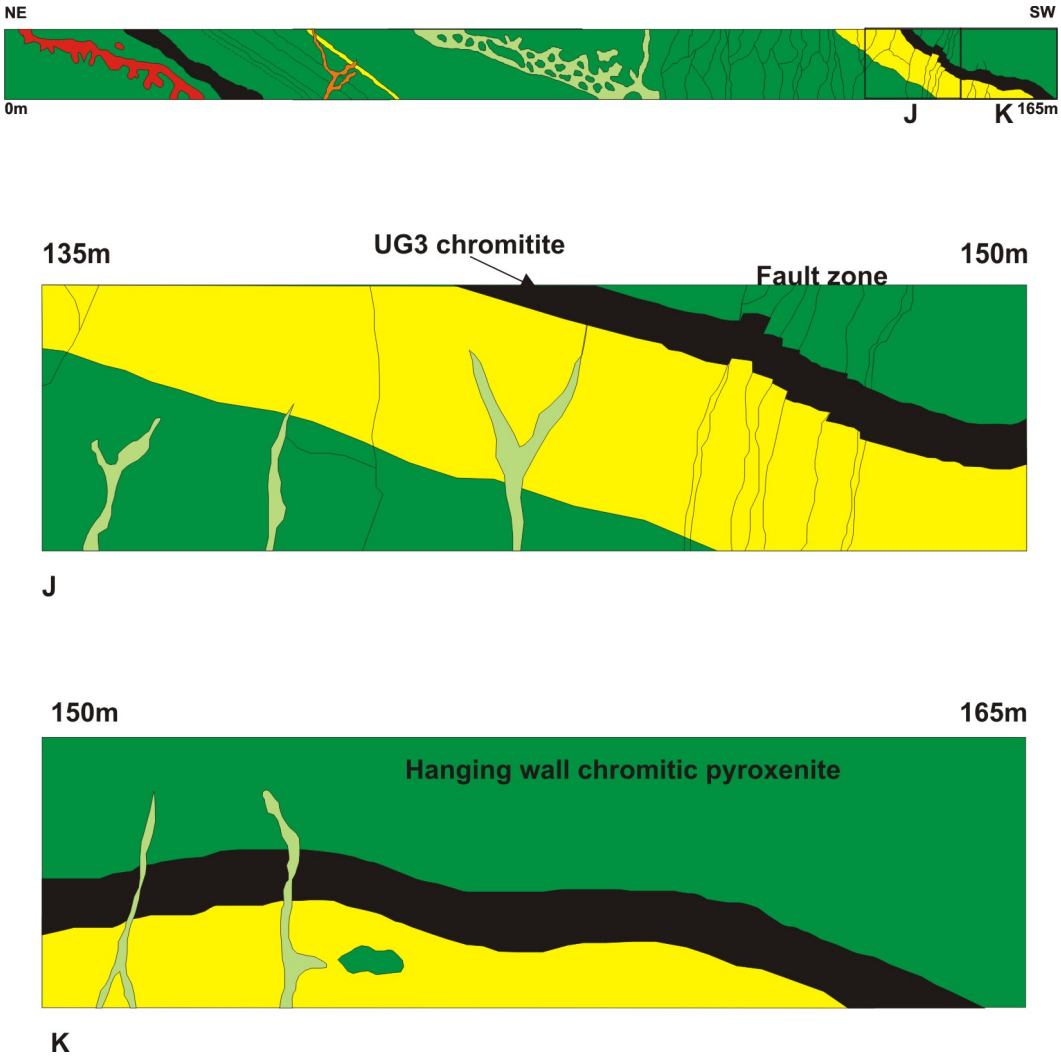

Figure 3.19: Mapped sections for 135m to 165 m of the road cutting outcrop.

Section A (Figure 3.16) shows the basal pyroxenite unit of the UG2 cyclic unit. The bottom contact with the UG1 anorthosites is not exposed. The basal feldspathic pyroxenite is highly weathered (because it contains appreciable amounts of plagioclase) and it contains 0.5 to 2 cm large clinopyroxene oikocrysts. Overlying this basal pyroxenite is a highly undulating pegmatoidal pyroxenite layer which on average is 0.5 m thick. An interesting characteristic of this layer is that the bottom contact is highly irregular and undulating, whilst the top contact is more planar. Similar characteristics were found in the underground exposures of the UG2 chromitite layer.

The footwall to the UG2 chromitite layer (Figure 3.16 section B) is a feldspathic pyroxenite unit. The chromitite layer itself contains numerous pyroxenite and pegmatoid lenses, resulting in bifurcation of the chromitite. A distinctive nodular texture is identified within the chromitite (Figure 3.20). This texture has been accentuated by intensive weathering. The nodules were identified as being round, resistant orthopyroxene oikocrysts which range in size from 0.5 to 2 cm. This texture was not identifiable in the fresh

underground exposures or in the fresh drill core material, thereby underlining the importance of the mapped road section. A significant amount of copper staining was identified within the chromitite (Figure 3.21). This can be attributed to the oxidation of base metal sulphides such as chalcopyrite, which occur in anomalous amounts in the Atok UG2 layer.

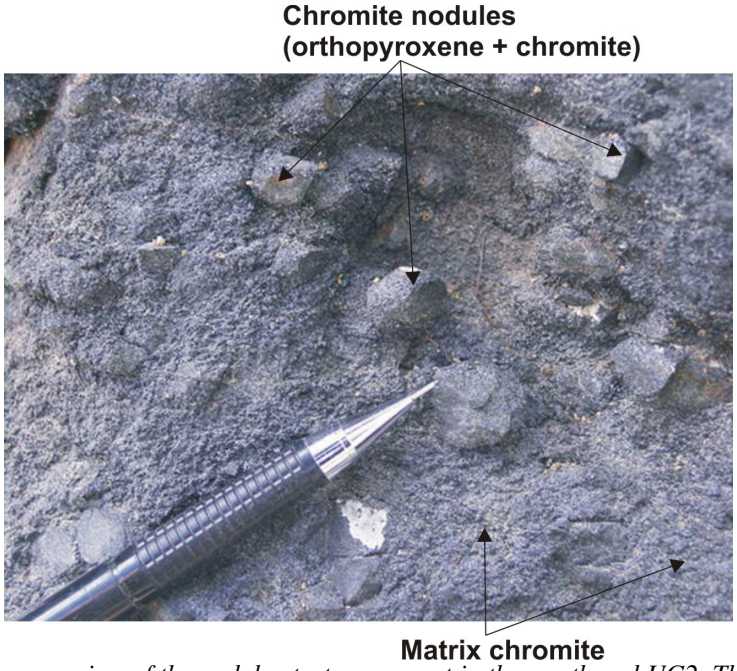

Figure 3.20: Close up view of the nodular texture present in the weathered UG2. These are oikocrysts of orthopyroxene and chromite and are more resistant to weathering than the normal fine grained chromite matrix.

Figure 3.21: Highly weathered UG2 displaying chromite nodules and copper staining.

The hanging wall to the chromitite layer is a feldspathic pyroxenite unit (Figure 3.16 section C). This unit is much fresher than the footwall pyroxenite. Therefore, the hanging wall pyroxenite unit is more mafic in composition than the footwall unit (more feldspathic). Approximately 3 m above the UG2 layer is the UT1 (upper triplet 1) chromitite leader. The UT2 and UT3 leaders occur within 1 m above the UT1 leader. A further two chromitite leaders are present approximately 5 m above the triplets (Figure 3.22). These chromitite leaders are as thin as 1 mm, but are entirely continuous through the section. Several growth-fault structures (cm scale) were identified in the leaders (Figures 3.23 and 3.24). These are interpreted to be a result of brittle failure (slip) of the semi-solid chromitite layer in response to stress during crystallization.

Figure 3.22: View of the HW section with the UG2 in the background. Note different pyroxenite units.

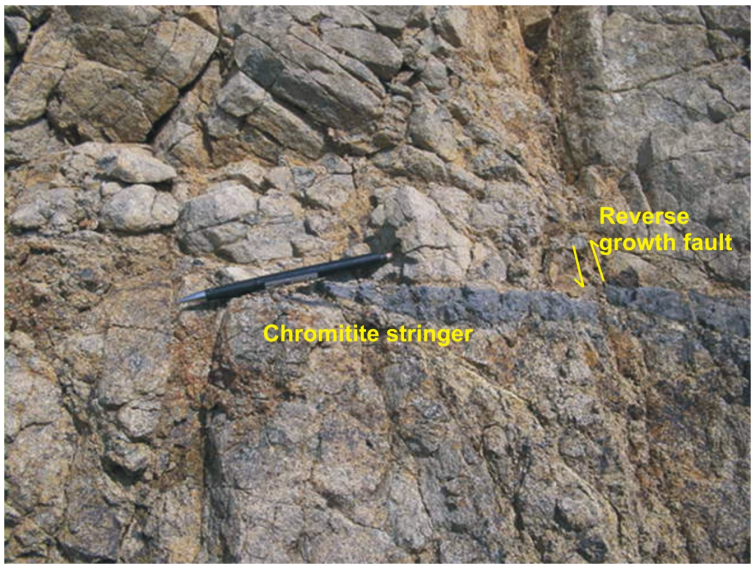

Figure 3.23: Chromitite stringer affected by a growth fault.

Figure 3.24: Chromitite stringer affected by a reverse growth fault with associated thickening.

Figure 3.25: Two separate hanging wall feldspathic pyroxenite units separated by a chromitite stringer.

An interesting feature of this chromitite-rich sequence is that there is a sharp textural change across each of the chromitite leaders (Figure 3.25). This indicates a compositional change in each of the pyroxenites below and above the chromitite leaders. Therefore each of these pyroxenites are representative of different individual units, with the chromitite leaders occurring at the breaks between successive pyroxenite units.

Two features were used to identify different pyroxenite units within this pyroxenite sequence: 1) crystal size and, 2) plagioclase content (which largely controls the degree of weathering). Therefore, the pyroxenite package has been subdivided into several individual units based on textural characteristics which are absent in fresh material.

Approximately 10 m above the UG2 layer is a 2 cm thick anorthosite layer (Figure 3.17 section D). This layer has been referred to by Mossom (1986) as a marker horizon. Also evident in section D is a dolerite

dyke which intrudes the layered stratigraphy (Figure 3.17 section D, Figure 3.26). The dyke is either part of the Karoo Supergroup (much later than the Bushveld Complex) or it may represent a feeder to the Rustenburg Layered Suite, in which case it provides the initial liquid composition of the magma from which the Rustenburg Layered Suite crystallized (Wilson pers. Comm., 2003). Although the dyke does not follow any lithological contacts, it does display a slight deviation across the fourth chromitite leader. The fact that the dyke does not follow any lithological contacts could possibly suggest that the dyke intruded whilst the material was semi-solid (during crystallization of the Rustenburg Layered Suite) and that it therefore represents a possible feeder conduit to the Rustenburg Layered Suite.

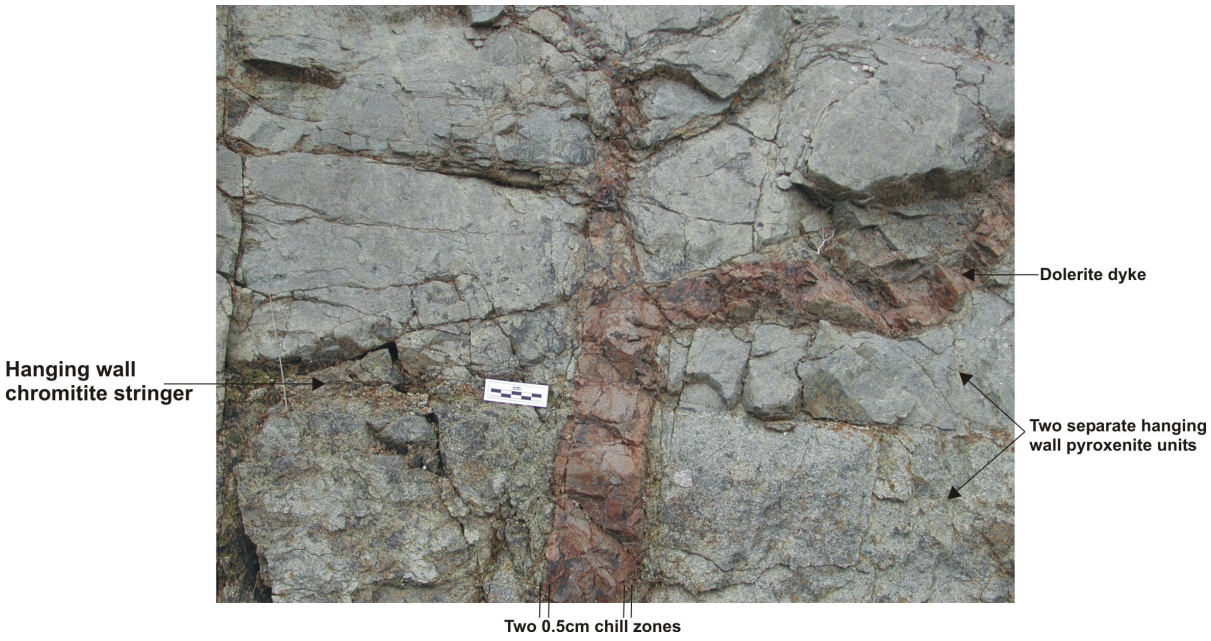

Figure 3.26: Suspected feeder dolerite dyke intruding the layered hanging wall stratigraphy.

Figure 3.17 section E shows the first appearance of greenish, banded norite in the sequence. This norite unit displays an unusual texture in that it contains numerous lenses of pyroxenite. Several other structures are evident in this unit including columnar jointing, as well as very well developed mm to cm scale layering and cross bedding. Very peculiar vein-type structures extend upward from the norite unit. The veins are generally highly weathered. The peculiar textures present in the norite unit are likely to be simply a result of intensive weathering. Two lithological contacts separating three individual pyroxenite units are shown in sections H and I within Figure 3.18.

The immediate footwall to the UG3 chromitite is an anorthosite unit (Figure 3.19 section J). This anorthosite unit varies from pure anorthosite (cumulate plagioclase) in places to pyroxene anorthosite (contains cm-scale pyroxene-rich layers) in others. The base of this unit is characterized by cm-scale layered, cross-bedded anorthosite and pyroxene anorthosite (Figure 3.27). The UG3 chromitite layer comprises a 30 cm thick, solid band of chromitite (very different to the UG2). In the exposure it displays an undulating

structure (similar to a 'roll' structure). A fault zone comprising one normal and five reverse faults displace the layer (maximum displacement is 14 cm) (Figure 3.28). The hanging wall to the UG3 chromitite is a chromitic feldspathic pyroxenite unit. This unit contains an appreciable amount chromite, both as blebs of chromitite and as individual chromite crystals within the euhedral clinopyroxene oikocrysts. This pyroxenite unit is notably feldspathic and it contains numerous, well-formed euhedral clinopyroxene oikocrysts (up to 5 cm in size).

Figure 3.27: Cross-bedded layers of anorthosite and pyroxene anorthosite.

Figure 3.28: The UG3 chromitite affected by a fault zone.

3.4 Discussion

The detailed mapping of the weathered UG2 cyclic unit in the field complements the drill core study carried out on fresh drill core material. It enables subtle primary textures, otherwise unidentifiable in fresh exposures, of the rock types, through accentuation by weathering, to be studied. In this instance, detailed mapping of the weathered road section proved an effective way of discriminating individual pyroxenite units within the thick pyroxenite package. This would have been difficult to do through ordinary core logging. The weathered road section also allowed numerous other mineralogical, compositional and textural features of the UG2 cyclic unit to be identified and studied (due to their accentuation by weathering processes).

The underground field mapping was carried out on fresh exposures of the UG2 chromitite, and several features were identified:

- Irregular zones of recrystallized euhedral coarse chromite exist throughout the UG2 against a background of fine grained chromite. It is suggested that these segregations represent areas of recrystallized chromite.
- The planarity of the TRC and the BRC differ greatly with the TRC highly planar whilst the BRC is irregular, sinuous and often contains micropotholes.
- The footwall pegmatoidal feldspathic pyroxenite is highly irregular and commonly exists as the direct footwall to the reef. There are also often two units of pegmatoidal feldspathic pyroxenite below the UG2.
- It is evident that there was abundant interaction between the footwall and the lower portion of the UG2 through the highly irregular nature of the BRC as well as the irregular, nevertheless, abundant, distribution of disseminated chromite in the footwall. This lithological contact shows signs of erosion and reworking as well as redistribution of chromite from the UG2. These features are only present where the pegmatoidal feldspathic pyroxenite forms the footwall and do not exist where the UG2 is supported by a medium-grained pyroxenite. These observations, coupled with the fact that the size of the orthopyroxene oikocrysts in the pegmatoid are largest near its top contact and decrease systematically downward, lend themselves to the suggestion that the pegmatoidal feldspathic pyroxenite unit is a late-stage crystallization product of an upward percolating volatile rich melt. It is likely that this late-stage melt percolated up through the cumulate pile during the late primary stage i.e. The cumulate pile was already at an advanced stage of crystallization. It then most likely ponded beneath the impermeable UG2 chromitite barrier where it attempted to erode its way through. The erosive effect, however, was negligible and only the BRC, in places, was disrupted with some chromite being reworked into the pegmatoid. Eventually it too crystallized out in its final position beneath the UG2.

Conclusions from the surface mapping include:

- The highly weathered nature of the outcrop assisted in identifying distinct individual units within seemingly monotonous sequences. This is due to the weatherability of the lithologies being a direct function of its pyroxene:plagioclase ratio (ie. the amount of interstitial plagioclase present). In this respect the hanging wall feldspathic pyroxenite was seen to be more mafic (higher pyroxene:plagioclase ratio) than the footwall feldspathic pyroxenite unit. The hanging wall sequence also shows slight variations in pyroxene:plagioclase ratio across the chromite stringers – confirming the hanging wall pyroxenite sequence to be composed of several individual units bound by chromite stringers.
- The UG2 itself appears bifurcated and comprises numerous lenses. The weathering has affected the reef by oxidizing the base-metal sulphides (producing copper staining) as well as by accentuating a nodular texture in the chromitite. This texture comprises oikocrysts of orthopyroxene and chromite which have formed resistant, circular nodules which stand out against the more friable, fine-grained matrix.
- The UG3, however, differs from the UG2 by not containing any nodular type texture or any sulphide oxidation. Overall, the UG3 also contained no lenses (in contrast to the UG2) and it exists as a solid planar band of fine-grained chromite.
- The highly weathered hanging wall gabbronorite sequence is seen to contain a relatively high amount of interstitial material (with a lower pyroxene:plagioclase ratio).

The combination of surface and underground field mapping has proved highly successful in documenting both the fresh and weathered characteristics of the study sequence. These characteristics wouldn't have been documented if only fresh drill core material was studied in this project.

.

4. Stratigraphy of ZG219

One of the main aspects of this project is a detailed drill core study involving geochemical, mineralogical and petrographical work carried out on a borehole intersection from the Atok mine property – namely ZG219. The ZG219 borehole was drilled on the farm Zeekoegat (Figures 4.1 and 4.2), which is the north-westerly most farm of the Atok mine property, and the core comprises a motherhole (MH) and two deflections (D1 and D2) of the UG2 chromitite (with an estimated separation of 1 – 3 m). The core was drilled to a depth of ~382 m and the section logged extended from ~350 m to ~382 m (incorporating portions of the UG1 and UG3 units as well as the entire UG2 unit). As already mentioned, the MH core was used for the geochemical analysis (see Appendix A) whilst the D1 deflection was used for the mineralogical and petrographic examination. The D2 core was retained as a reserve deflection for possible future further work. All three deflections, however, were logged in detail and density was measured throughout their length.

4.1 Introduction

Each of the deflections were studied in order to interpret and document the layered stratigraphy in each. This was done by using a combination of detailed geological logging and density measurements. The combination of these two techniques provides a highly accurate examination of the igneous stratigraphy within the sections.

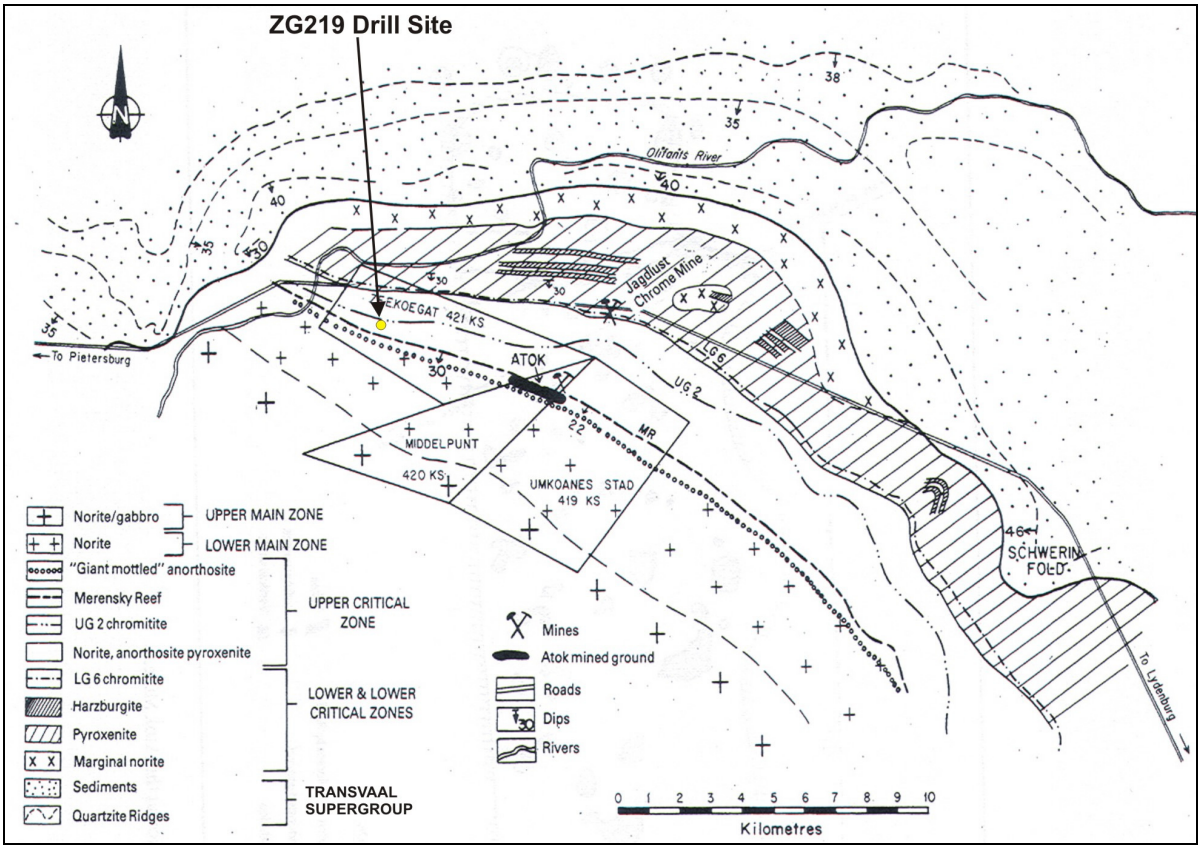

Figure 4.1: Geological map of the Atok mine property showing the drill site of ZG219 (modified after Mossom, 1986).

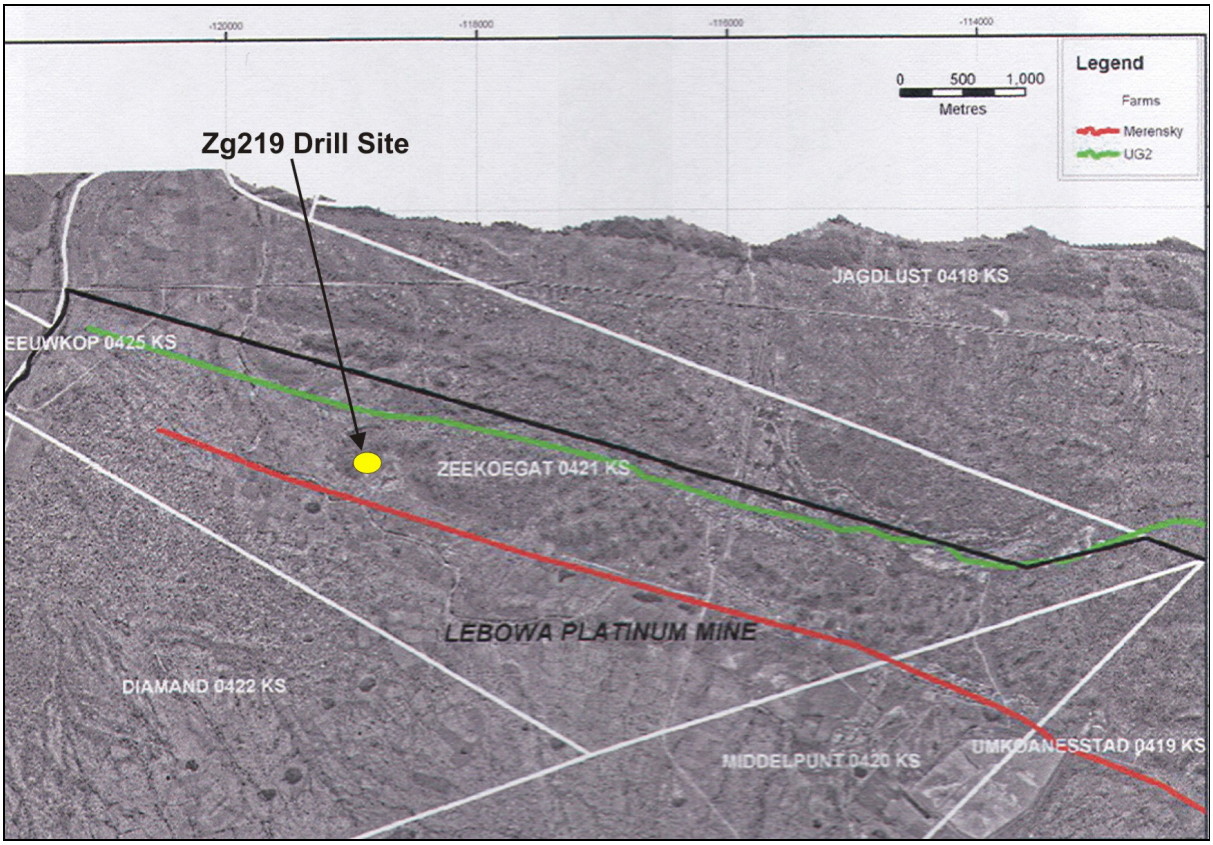

Figure 4.2: LandSat map of the Zeekoegat farm showing the UG2 and Merensky reef outcrops as well as the ZG219 drill site (modified after Brown, 2004).

The geological logs and the density profiles for the entire study sections are discussed first in section 4.2. This gives a suitable setting and context for discussing the ore zone within the intersections in section 4.3.

4.2 Entire ZG219 Study Section

The entire ZG219 MH core study section extends from ~350 m to ~382 m and it intersects the basal portion of the UG3 unit, the entire UG2 unit as well as the topmost portion of the UG1 unit. The results of the geological logging and the density measurements for the entire ZG219 MH study section are discussed in detail (and are available in Appendix B and C respectively). Following this the local stratigraphic variation of the study section between the three intersections (2 – 3 m apart) will be briefly discussed.

A graphical display of the ZG219 MH study section log is provided in Figure 4.3 whilst the full density profile is shown in Figure 4.4. The different rock types found within the study section are discussed in detail using the graphical log, density profile as well as a series of representative core photos (Figures 4.5 – 4.7). All unique mineralogical and textural characteristics of each of the different rock types, as well as the overall logging and density results, are further discussed here.

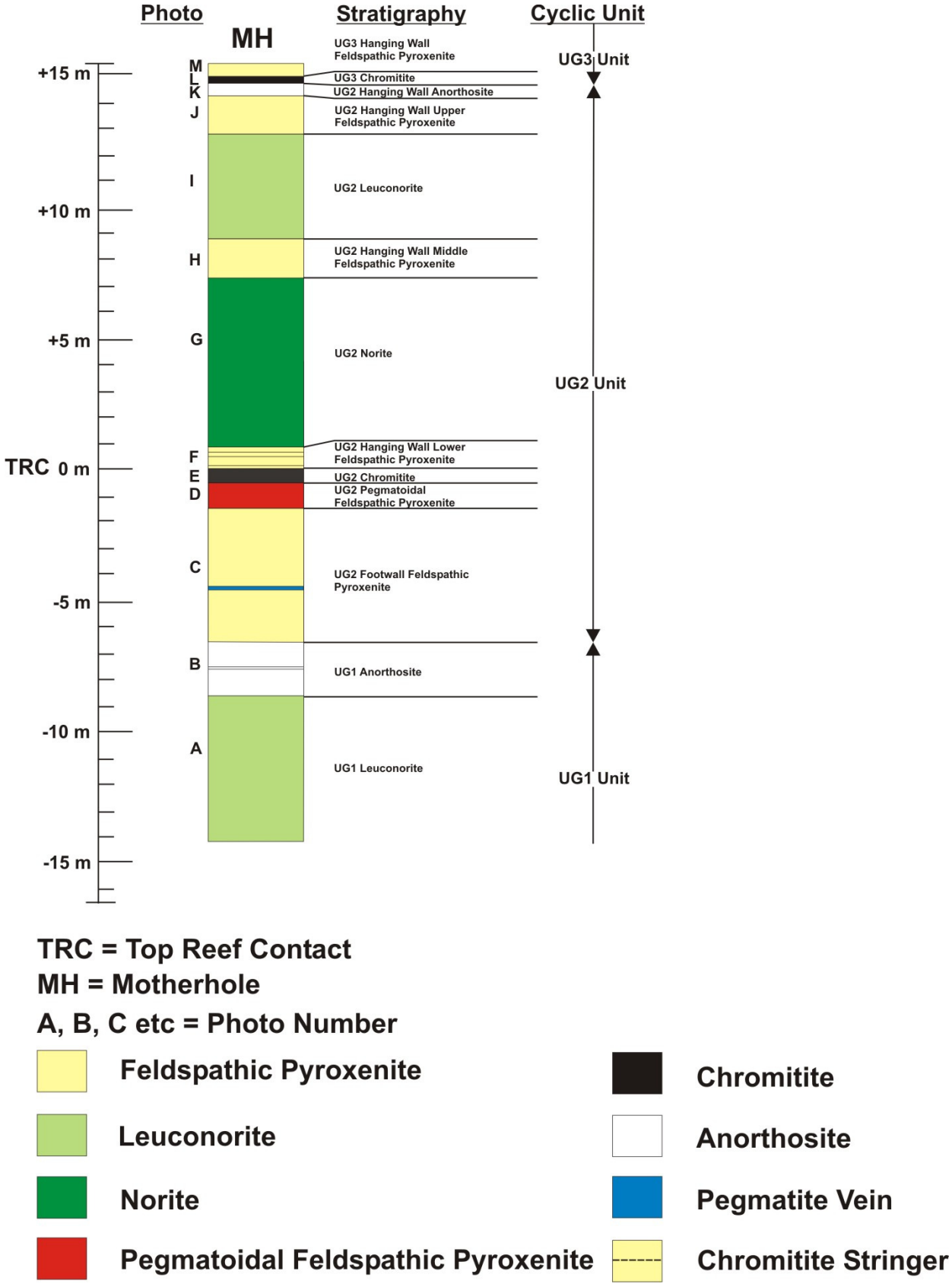

Figure 4.3: Geological log of the ZG219 MH. The official stratigraphic nomenclature for each of the rock types used in this study is provided.

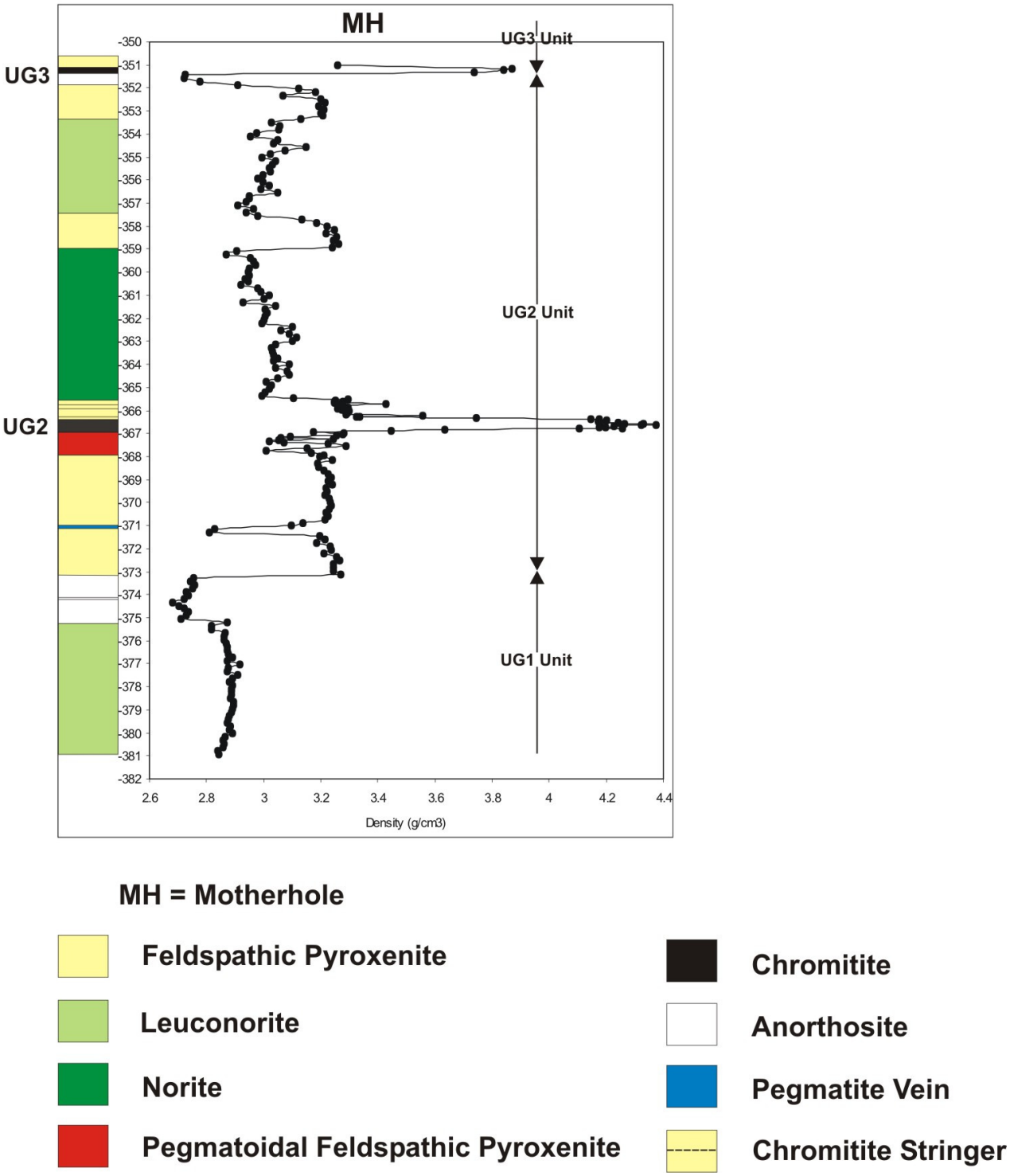

Figure 4.4: Density profile of ZG219 MH.

Both Figures 4.3 and 4.4 show that the study section covers 3 cyclic units, namely, from the base up, the UG1, UG2 and UG3 units (with only the UG2 unit intersected in full). Each of these units are discussed separately whilst moving stratigraphically up through the core section (in order of UG1 – UG2 – UG3).

4.2.1 The UG1 Cyclic Unit

Only the upper portion of the UG1 cyclic unit is exposed in the core including the two topmost units - the UG1 leuconorite and the UG1 anorthosite.

The UG1 leuconorite (Figure 4.5 A) displays a well-developed granular texture with a pyroxene : plagioclase ratio of 30:70. It exhibits a constant density profile (2.8 – 2.9 g/cm^3) with negligible small-scale variation, thereby indicating it to be texturally homogeneous and containing a constant degree of interstitial plagioclase throughout.

The UG1 anorthosite (Figure 4.5 B) is oikocrystic and is a pure plagioclase cumulate. It hosts a prominent chromitite stringer which appears somewhat irregular and is affected by several mm scale reverse faults. The textures and structures exhibited here are similar to those observed, albeit on a smaller scale, at the Dwars River site where the UG1 chromitite itself displays spectacular outcrop styles and structural relations with its anorthositic foot- and hanging wall. The density differences between the chromitite and anorthosite are thought to form such structures (Nex, 2004). This unit displays a constant density profile (~2.7 g/cm^3) reflecting its homogeneous texture.

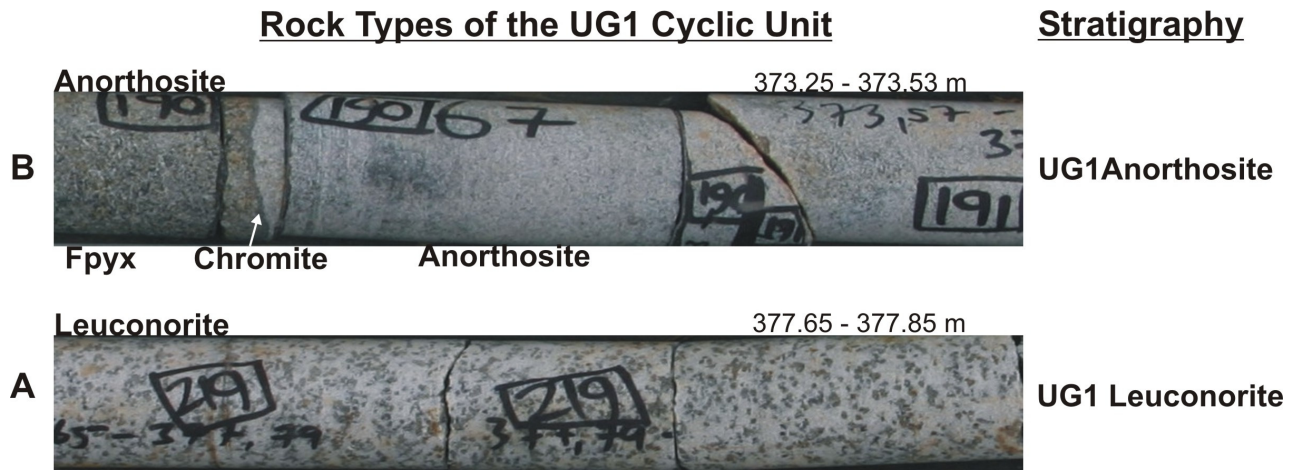

Figure 4.5: Representative core photos of the different rock types found within the UG1 cyclic unit. Note that the letters A and B refer to which unit the sample is derived from in Figure 4.3.

4.2.2 The UG2 Cyclic Unit

The UG2 cyclic unit in the ZG219 MH comprises a basal feldspathic pyroxenite unit (Figure 4.6 C) which is separated from the underlying UG1 unit by a mm scale chromitite stringer (Figure 4.5 B). This UG2 footwall feldspathic pyroxenite unit has a pyroxene:plagioclase ratio of 80:20 and it displays a typical poikolytic texture. It also exhibits a coarser crystal size when compared to the hanging wall feldspathic pyroxenite units. The unit displays very constant density values of ~3.2 g/cm^3 throughout its entire length,

thereby indicating it to be texturally homogeneous and containing a constant degree of trapped interstitial plagioclase throughout. A single sharp drop in density in this unit does occur and is attributed to a pegmatite vein which cuts through the pyroxenite. The vein comprises coarse grained felsic minerals and is surrounded by an alteration zone where fluid activity has affected the host pyroxenite.

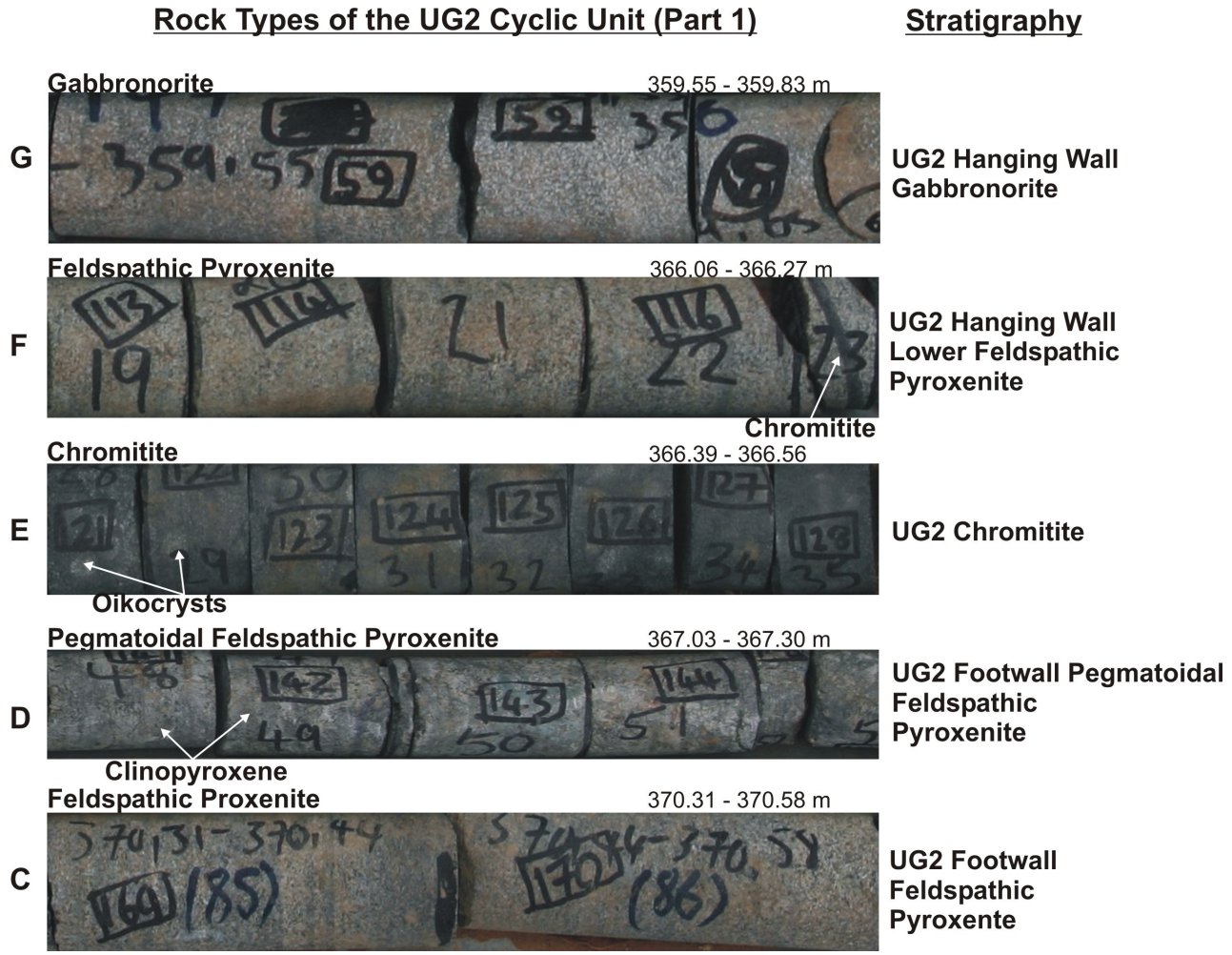

Figure 4.6: Representative core photos of the different rock types found within the UG2 cyclic unit. Note that the letters C – G refer to which unit the sample is derived from in Figure 4.3.

Overlying the medium grained feldspathic pyroxenite unit is a pegmatoidal feldspathic pyroxenite (Figure 4.6 D) which forms the immediate footwall to the UG2 chromitite. This lithology has a pyroxene : plagioclase ratio of 30:70 and contains very coarse cumulus clinopyroxene (1 – 5 cm), and minor orthopyroxene, in a plagioclase matrix. The pegmatoidal feldspathic pyroxenite also has highly sinuous top and bottom contacts (although the bottom contact is a lot more sinuous and irregular than the top) and commonly contains irregular pods and blebs of chromite in its upper portions. The density values are somewhat variable, although still averaging around 3.1 – 3.2 g/cm^3, throughout the unit. This variability is a

result largely of the pegmatoidal texture, in which irregular zones containing an enriched amount of intercumulus plagioclase exist throughout the unit, as well as the presence of irregular, disseminated sulphide and chromite mineralization (especially near the top of the unit).

Resting on the pegmatoidal feldspathic pyroxenite is the UG2 chromitite (Figure 4.6 E) which is ~50 cm thick and comprises a solid band of chromitite with interspersed orthopyroxene oikocrysts. Also present are zones of coarser chromite supergrains against the background of ordinary fine grained chromite. In certain areas there is also visible, disseminated, fine grained sulphide mineralization present. The top reef contact (TRC) is also distinctly planar whilst the bottom reef contact (BRC) is irregular with some footwall interaction in certain areas. The UG2 chromitite displays the highest density values of the study section of ~4.1 - ~4.4 g/cm^3. There appears to be an intricate variation pattern of the density through the chromitite, and this is investigated further in section 4.3.

The UG2 chromitite is overlain by a hanging wall of feldspathic pyroxenite (Figure 4.6 F) which hosts several chromitite leader seams. The hanging wall feldspathic pyroxenite is finer-grained, and more mafic in character, compared to the footwall feldspathic pyroxenite. This unit is the first (lowermost) of 3 feldspathic pyroxenites developed within the UG2 hanging wall and therefore its official designation in this study is 'UG2 hanging wall lower feldspathic pyroxenite'. The chromitite stringers (Figure 4.6 F) range from 1 mm up to ~5 mm in thickness and are classified, from the lowermost one up, UT1 (upper triplet) through to UT4. An interesting observation is that there are visible changes in textural and lithological characteristics across the chromitite stringers. Therefore the UG2 hanging wall lower feldspathic pyroxenite should be regarded as individual small-scale units separated by distinct chromitite stringers, rather than as one single package.

From the density profile of the UG2 hanging wall lower feldspathic pyroxenite several points are important to consider: (1) the hanging wall lower feldspathic pyroxenite shows slightly higher values than compared to the footwall pyroxenite sequence (thereby indicating it to be more mafic than the footwall sequence), (2) the chromitite stringers, to a certain extent, are picked out in the density profile, and finally, (3) the values appear to decrease slightly toward the top of the unit in a systematic fashion (thereby indicating the unit to become more leucocratic further up).

Above the hanging wall lower feldspathic pyroxenite is a major development of gabbronorite (Figure 4.6 G) together with several cm scale anorthosite and leuconorite layers. This gabbronorite sequence shows a much higher degree of density variation compared to the previous units (with values around 3 – 3.1 g/cm^3). The irregular, ragged density profile of this sequence reflects the presence of the subordinate cm-scale interlayered leuconorite and anorthosite layers. Definite zones of higher and lower density exist and these relate directly to the amount of cumulus plagioclase present. Another major point is that there is a distinct systematic decrease in density up through the unit (thereby indicating the gabbronorite unit to become more leucocratic further up).

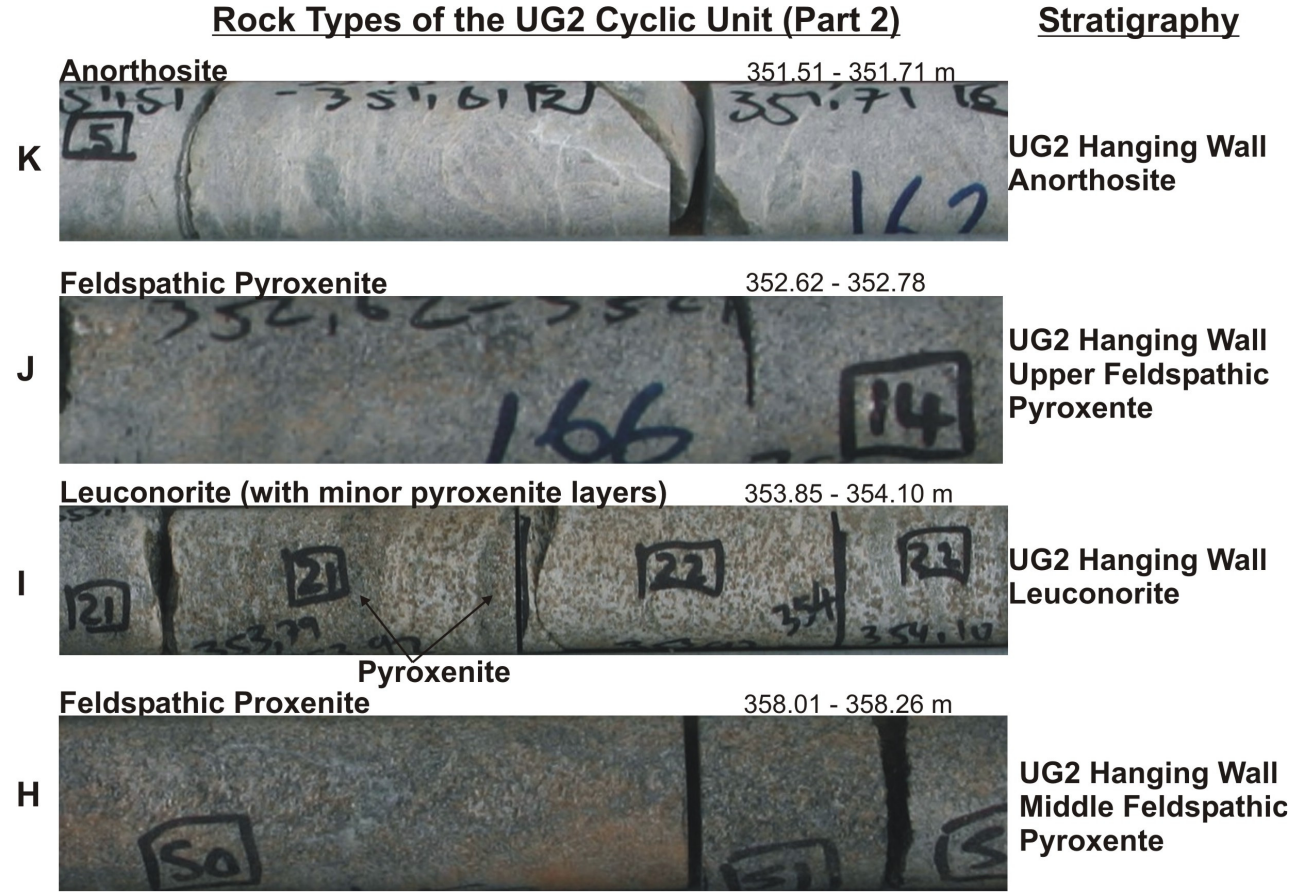

Figure 4.7: Representative core photos of the different rock types found within the UG2 cyclic unit. Note that the letters H – K refer to which unit the sample is derived from in Figure 4.3.

Overlying this well-layered package is the hanging wall middle feldspathic pyroxenite unit (Figure 4.7 H) which is ~2 m thick and displays a well-developed oikocrystic texture and a pyroxene : plagioclase ratio of 80:20. This unit exhibits similar density values to the UG2 footwall pyroxenite sequence but appears to be slightly less dense than the hanging wall sequence. Even within this unit (~2 m thick) there appears to be a systematic drop off in density toward the top of the unit (thereby defining a trend toward a more leucocratic composition higher up).

Resting on the hanging wall middle feldspathic pyroxenite is a well-layered leuconorite package which comprises interlayered subordinate cm scale feldspathic pyroxenite layers (Figure 4.7 I). The irregular density profile exhibited for this unit can be attributed to these cm scale, feldspathic pyroxenite layers. The leuconorite unit also displays a reverse density trend with density values increasing systematically upwards through the unit (thereby indicating a trend toward a more mafic composition further up through the unit).

Overlying the UG2 leuconorite is the UG2 hanging wall upper feldspathic pyroxenite (Figure 4.7 J). This unit is a ~1.5 m thick feldspathic pyroxenite unit which shows a constant density profile (~3.2 g/cm^3) with negligible small-scale variation. An interesting point is that this particular unit exhibits slightly lower

density values than both the UG2 hanging wall middle and lower feldspathic pyroxenite units, and is instead similar (in density) to the UG2 footwall feldspathic pyroxenite unit.

Above the UG2 hanging wall upper pyroxenite is the topmost, and final, unit of the UG2 cyclic unit - the UG2 anorthosite (Figure 4.7 K). Within this unit there is an upward gradational succession (on a cm scale) from pyroxene anorthosite to massive anorthosite. The pyroxene anorthosite comprises fine scale pyroxenite layering (which also define spectacular cross-beds) within anorthosite, whilst the massive anorthosite is devoid of any pyroxenite layering and is a pure plagioclase cumulate. The density profile confirms this succession and exhibits a systematic upward decrease in values through the unit (on a cm scale).

4.2.3 The UG3 Cyclic Unit

The UG3 unit rests on the UG2 unit and its base is marked by the UG3 chromitite layer. The UG3 chromitite (Figure 4.8 L) is a solid band of chromitite which contains no silicate lenses or oikocrystic textures as found in the UG2. It displays a granular texture with very little interstitial silicate and no visible BMS or copper staining. The UG3 chromitite exhibits a density of ~3.8 g/cm^3 which is somewhat less than for the UG2 (~ 4.2 g/cm^3). This is most likely a result of the greater BMS and PGE content of the UG2.

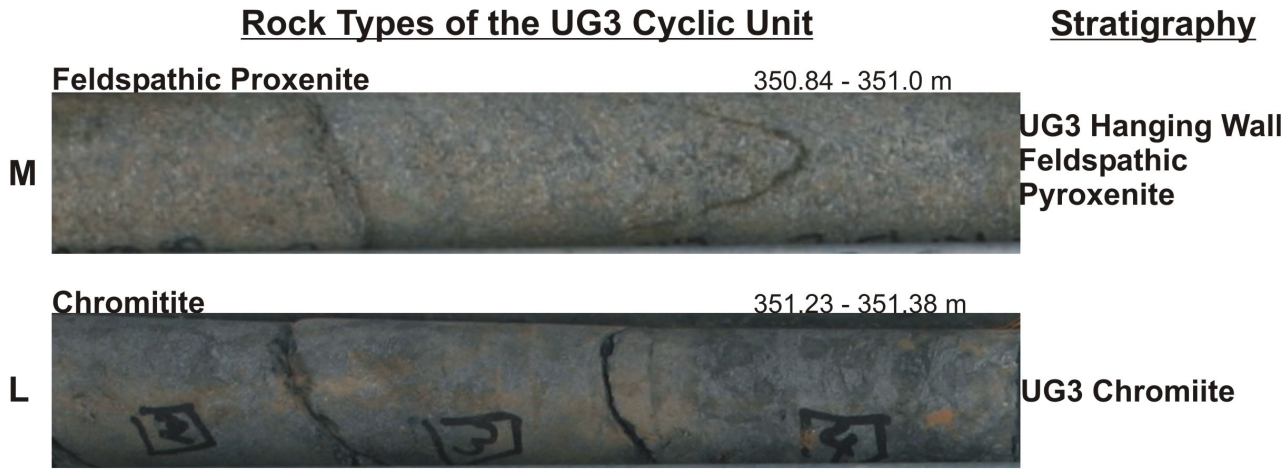

Figure 4.8: Representative core photos of the different rock types found within the UG3 cyclic unit. Note that the letters L – M refer to which unit the sample is derived from in Figure 4.3.

Overlying the UG3 chromitite, and which forms the topmost unit of the study section, is a chromitic feldspathic pyroxenite (Figure 4.8 M). This unit exhibits lenses and pods of chromite as well as spectacular euhedral clinopyroxene oikocrysts. Although it does appear felsic in nature in the core (thereby indicating a high degree of interstitial plagioclase) it displays a density of ~3.25 g/cm^3, which corresponds closely with the other pyroxenite units within the study section.

4.2.4 Local Stratigraphic Variation

Plotting the graphical geological logs (Figure 4.9) and the full density profiles (Figures 4.10 and 4.11) for each of the ZG219 MH, D1 and D2 intersections next to each other gives us a good vantage point to study the local stratigraphic variation of the study section. Each of the deflections has an estimated horizontal separation of 1 – 3 m with the geological logs and density profiles of Figures 4.9 and 4.11 respectively plotted relative to each other using the TRC (top reef contact) as a datum line.

The graphical geological logs (Figure 4.9) show that only the MH intersects the UG2 cyclic unit in full (as well portions of the UG1 and UG3 units) whilst the D1 and D2 cores intersect the upper portion of the UG1 unit and the vast majority of the UG2 unit. They also show that there is a strong stratigraphic correlation across all 3 cores. Even the mm scale chromitite stringers (including the UG1 anorthosite hosted stringer as well as the series of stringers hosted by the UG2 hanging wall lower feldspathic pyroxenite) can be traced across all 3 sections with precision. The only visible lithological change across the cores is in the UG2 footwall pegmatoidal feldspathic pyroxenite which appears thickened in the D1 core, whilst the D2 section exhibits 2 thinner upper pegmatoidal developments and 2 lower units, which aren't present in the other cores. Apart from this unit, however, all other units show negligible change and correlate closely across the sections (for example the UG2 chromitite shows only a 2 cm difference in thickness across the 3 sections).

The relative density profiles (Figures 4.10 and 4.11) all show a similar systematic variation pattern through the different rock types. More importantly, the multitude of density trends and systematic variations identified in the MH core are reflected accurately in the D1 and D2 cores. The normal density trends exhibited by the UG2 hanging wall lower and middle feldspathic pyroxenite and gabbronorite units as well as the reverse trend present in the UG2 leuconorite are all clearly visible in the D1 and D2 intersections. This serves to confirm the integrity of these density trends. They are therefore a distinct characteristic of the respective rock types (and not just a nugget-affect) and are representative of certain processes (discussed later).

Therefore the three intersections show a strong correlation, not just of stratigraphic units and rock types, but also of delicate density trend patterns across the three cores. The UG2 footwall pegmatoidal feldspathic pyroxenite showed some irregularity and local stratigraphic variation (which is confirmed by fieldwork), and this is attributed to its emplacement by post-cumulus recrystallization (discussed later).

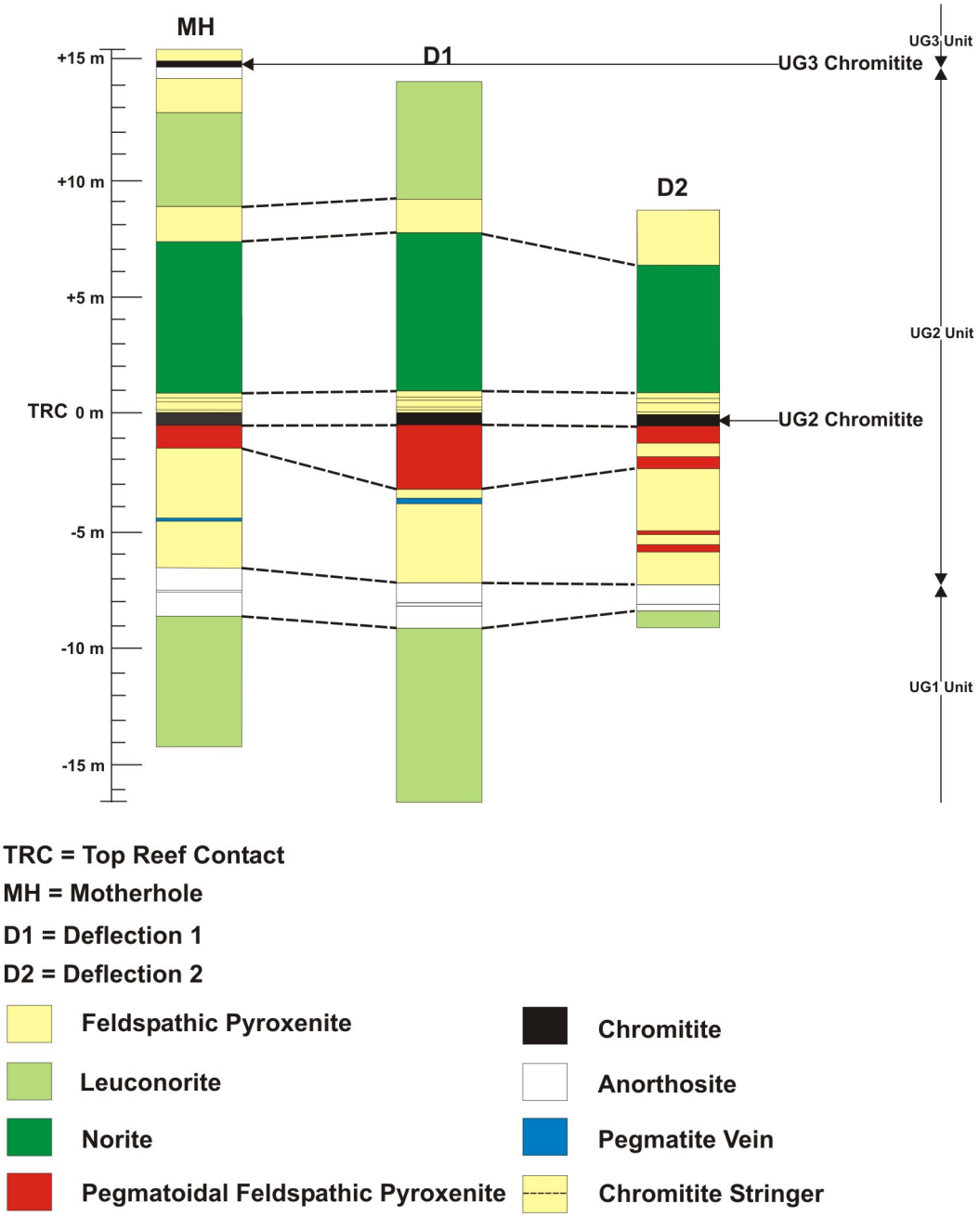

Figure 4.9: Geological logs of ZG219 MH, D1 and D2.The spacing between the cores is estimated at 1 – 3m.

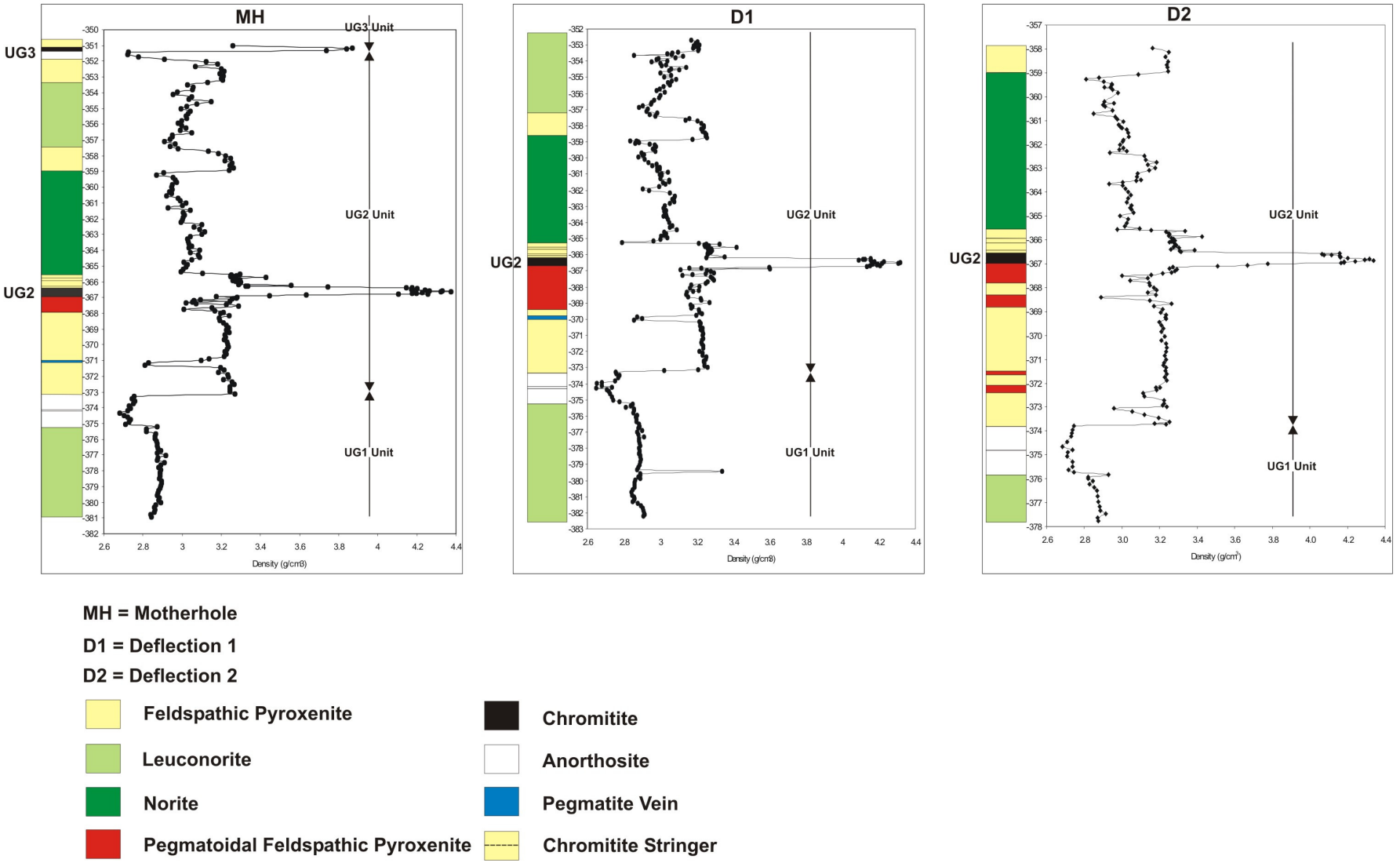

Figure 4.10: Full density profiles for the ZG219 MH, D1 and D2. Note that each core has an individual scale and are not relative to each other.

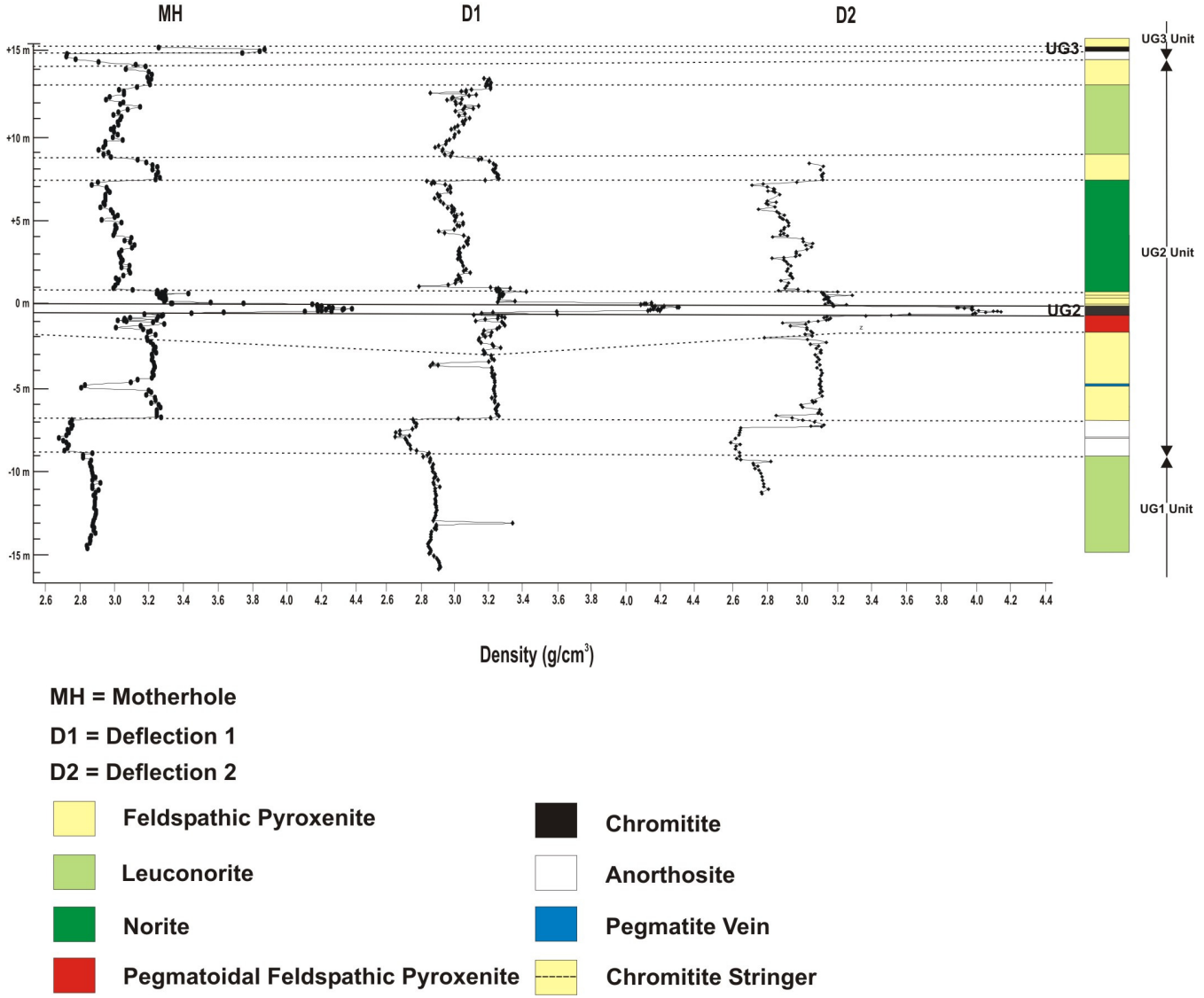

Figure 4.11: Relative density profiles of the ZG219 MH, D1 and D2. The profiles are plotted using the TRC (top reef contact) as a datum line.

4.3 ZG219 Ore Zone Section

The ore zone section (Figure 4.12) is a term used in this study for the lithological package comprising the UG2 chromitite and the entire hanging wall lower feldspathic pyroxenite unit as well as the entire UG2 footwall pegmatoidal feldspathic pyroxenite (upper unit only for the D2 section). Although the UG2 chromitite is the main host of BMS (base-metal sulphide) and PGE (platinum-group element) mineralization, there is a degree of mineralization associated with the chromitite stringers as well as with the pegmatoidal feldspathic pyroxenite unit. The ore zone section therefore includes the entire mineralized section and is not restricted to the zone of economic grade as in the mining cut. The upper and bottom contacts of the ore zone section are therefore marked by the upper contact of the hanging wall lower feldspathic pyroxenite unit (or the UT5 stringer) and the bottom contact of the UG2 footwall pegmatoidal feldspathic pyroxenite respectively.

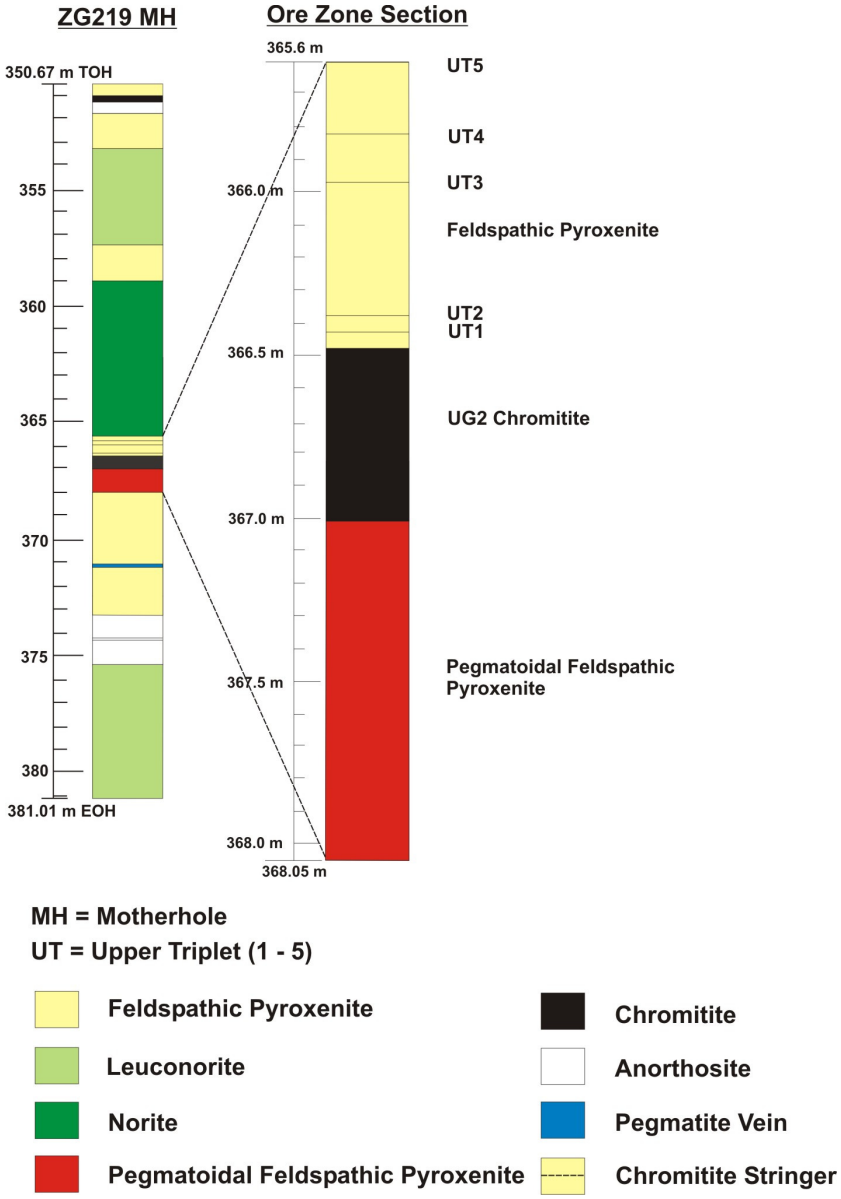

Figure 4.12: ZG219 motherhole ore zone section.

The graphical geological log of the ore zone sections are presented in Figure 4.13 whilst full density profiles for the sections are provided in Figures 4.14 and 4.15.

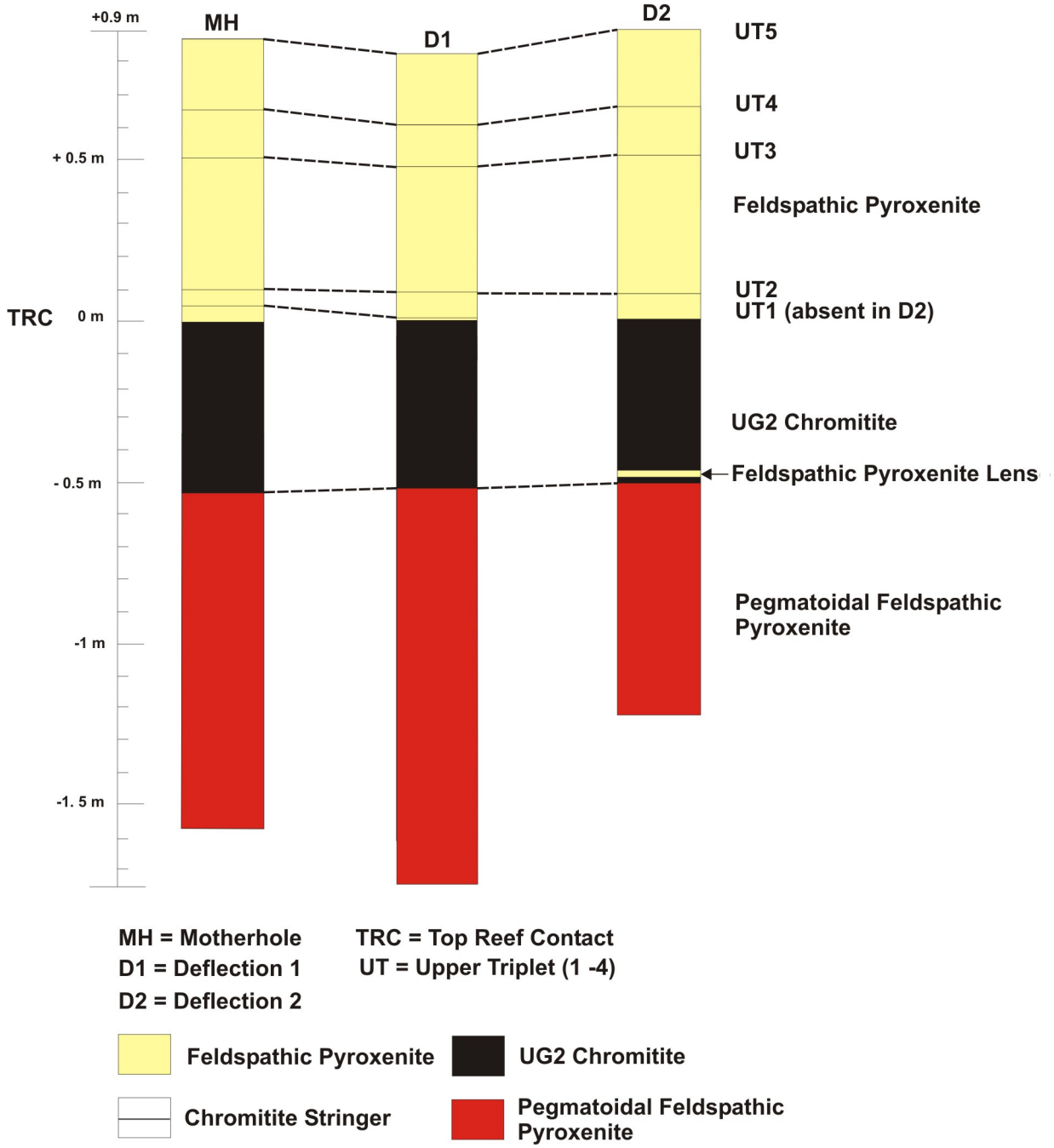

Figure 4.13: Geological logs of the ore zones (up to the topmost HW chromitite stringer) in the 3 cores.

Starting from the base, the pegmatoidal feldspathic pyroxenite footwall ranges in thickness from 1.1 m (D2) to 2 m (D1). This lithology contains very coarse cumulus clinopyroxene (1 – 5 cm), and minor orthopyroxene, in a plagioclase matrix. The density profiles for this unit are irregular, although still averaging around 3.1 – 3.2 g/cm^3, throughout the unit. This variability is a result largely of the pegmatoidal texture, in

which irregular zones containing an enriched amount of intercumulus plagioclase exist throughout the unit, as well as the presence of irregular, disseminated sulphide and chromite mineralization (especially near the top of the unit).

The UG2 chromitite has an average thickness of ~51 cm (MH shows the maximum thickness of 53 cm). The only distinct difference between the 3 reef intersections is the 2 cm thick feldspathic pyroxenite lens present near the base of the D2 reef. The density values for the chromitite range between 4.1 and 4.3 g/cm^3. There is also a distinctive 'bottom heavy' density profile pattern through the reef. This intricate profile pattern is mimicked through the three cores and is expected to be a result of base-metal sulphides and/or platinum-group metal mineralization concentrated within this portion of the reef (i.e. bottom loaded grade profiles). This will be further investigated in chapter 7.

The UG2 hanging wall lower feldspathic pyroxenite hanging wall extends to 1.5 m above the reef. Five chromitite stringers each are present in the MH and D1 sections and only four in D2. Correlating each stringer between the cores shows that the UT1 stringer appears to dip downward from the MH to the D1 and appears to not be present in D2. It is possible that in this section the UT1 stringer is not developed (and hence the UT2 is labeled UT1 etc). The remaining stringers correlate very well across the three cores. The density measurements have done an excellent job of picking out the fine chromitite stringers. Therefore, carrying out closely spaced density measurements through a seemingly monotonous pyroxenite package greatly assists in picking out fine chromitite stringers, which are often <1 mm thick. Overall however, the hanging wall feldspathic pyroxenite shows a systematic upward decrease in density values (a normal density trend).

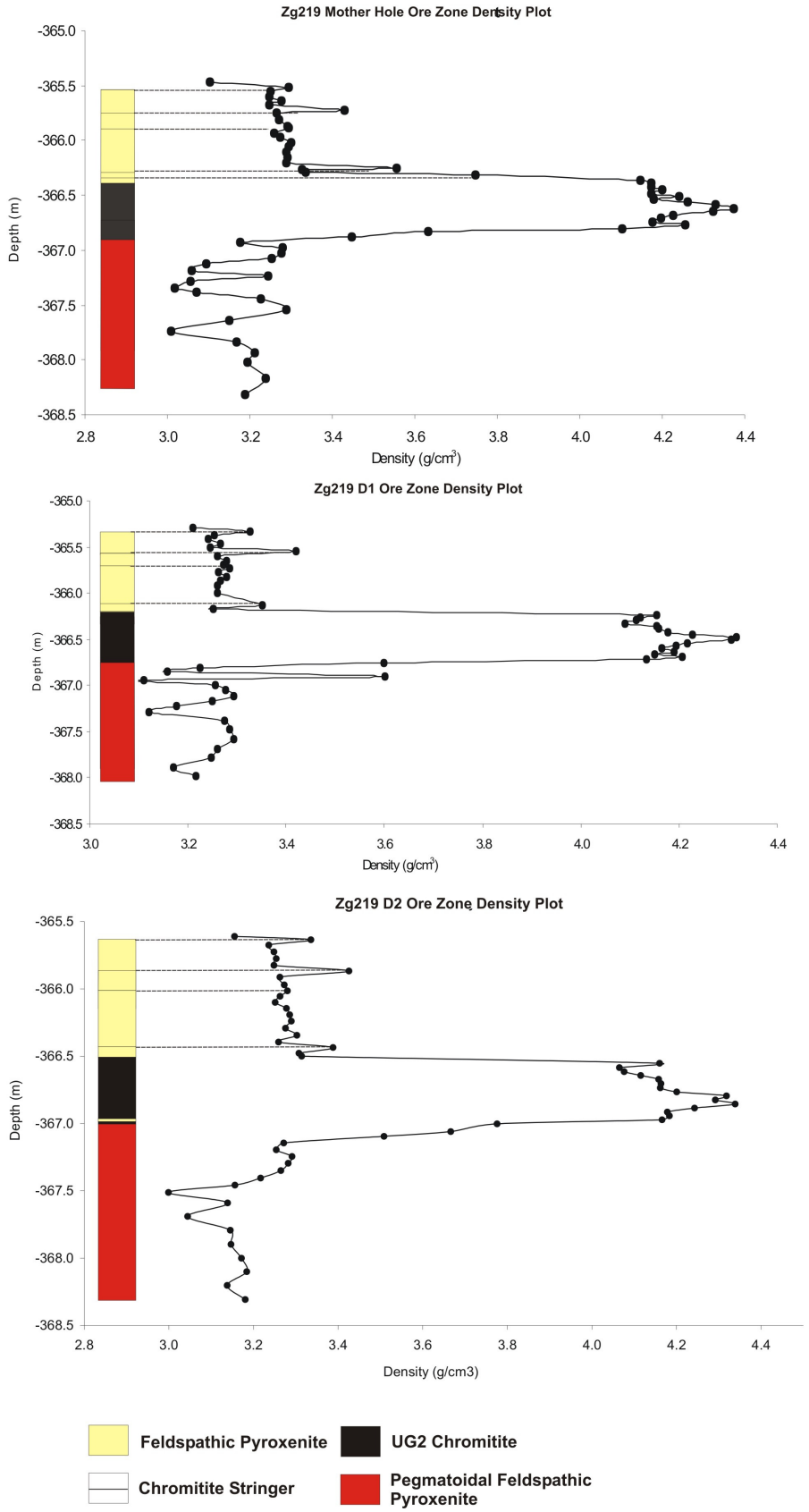

Figure 4.14: Density profiles of the ore zones of the three cores.

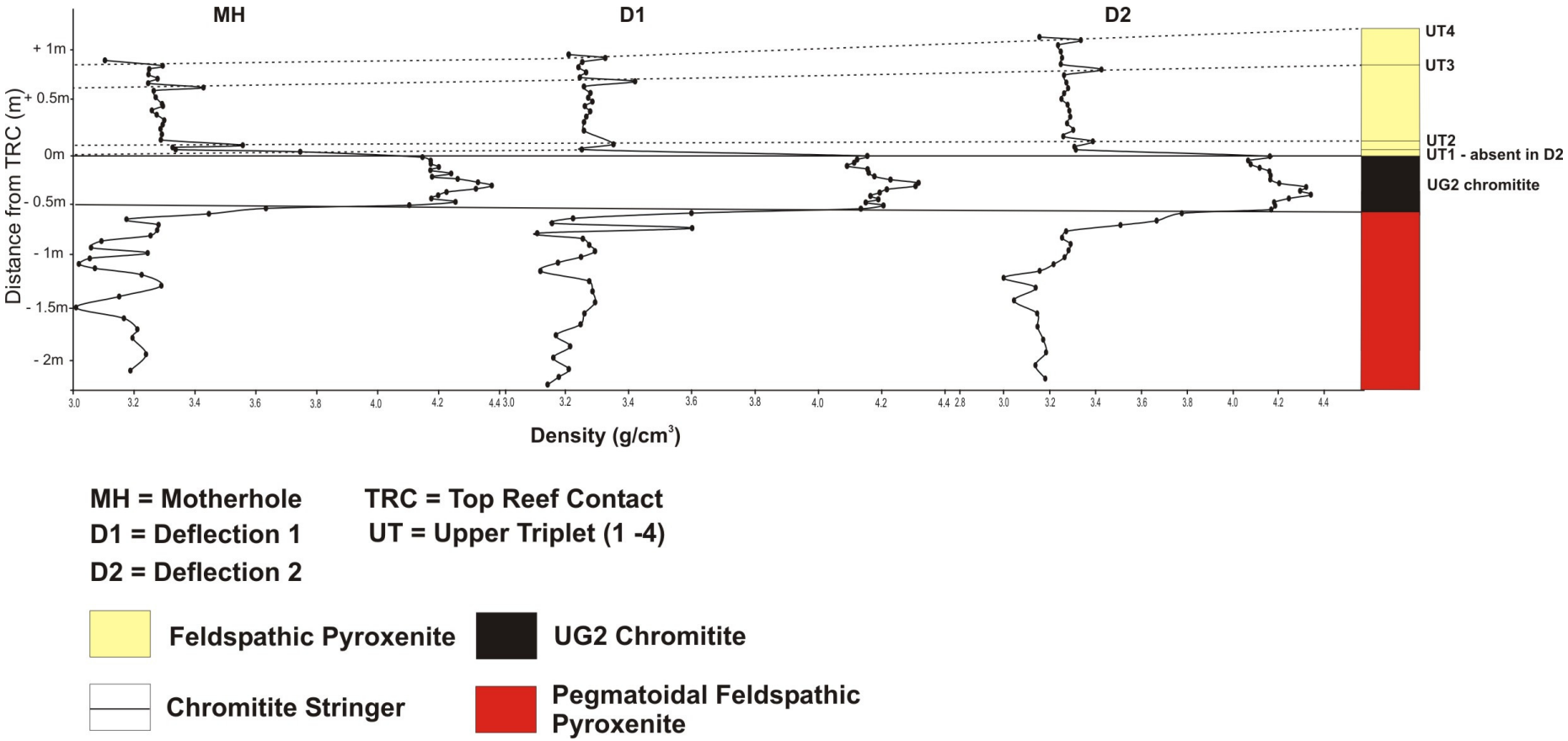

Figure 4.15: Relative density profiles of the ore zones of the three cores. The TRC (top reef contact) has been used as a datum line.

4.4 Discussion

The decision to investigate the stratigraphy of the ZG219 borehole using a combination of geological logging and density measurements proved highly successful. The accurate logging enabled visual traits/trends to be identified, with the final product being a qualitative log. The closely spaced density measurements generated quantitative information and allowed the accurate identification of trends in seemingly monotonous units (i.e. pyroxenites/gabbronorites). These two methods complemented each other and allowed both detailed logs and density profiles to be produced. The following conclusions can be made from both sets of results:

The geological logging revealed the cores to contain a strongly differentiated cumulate package comprising the topmost portion of the UG1 cyclic unit, as well as the entire UG2 cyclic unit. Both cyclic units contain normal fractionation sequences, i.e. an upward evolving sequence that tends to become more felsic further upsection, and both display an upward evolving lithological sequence of chromitite→feldspathic pyroxenite→gabbronorites→anorthosite. Several mm scale chromite stringers have also been identified in the hanging wall feldspathic pyroxenite. Small changes in texture, grain size and pyroxene : plagioclase ratio were seen to occur across these chromite stringers in the pyroxenite. These visual characteristics will be important in deciphering the petrogenetic history of these stringers and associated units.

It was also possible, with careful logging, to identify visual changes in pyroxene : plagioclase ratio within a single pyroxenite/gabbronorite sequence. This allows us to identify whether the unit trends to more leucocratic or, conversely, melanocratic compositions further up, or down, through the unit. Also the presence of well developed, cm scale interlayered feldspathic pyroxenite and leuconorite layers in the leuconorite sequence, as well as cm scale anorthosite and leuconorite layers within the gabbronorite package were identified. The formation of such well developed lithological layering may possibly be either a result of multiple magma injections into the chamber over a short time period or even the possible emplacement of crystal mushes into the magma pile.

The three intersections all show a strong correlation, not just of stratigraphic units and rock types, but also of delicate density trend patterns across the three cores. Only the UG2 footwall pegmatoidal feldspathic pyroxenite showed some irregularity and local stratigraphic variation (which is confirmed by fieldwork), and this is attributed to its late-stage emplacement mechanism. It is suggested in chapter 3 that based on field evidence, the pegmatoidal feldspathic pyroxenite unit represents a late-stage crystallization product of an upward percolating volatile rich melt. It is postulated that this late-stage melt percolated up through the cumulate pile during the late primary stage i.e. the cumulate pile was already at an advanced stage of crystallization. This suggestion is confirmed by the geological logs with the pegmatoidal feldspathic pyroxenite unit showing a high degree of irregularity and stratigraphic variation across the cores, whilst the remaining primary magmatic units all show a high degree of correlation with negligible variation.

The density measurements allowed the identification of several features which were not visible during logging. The density of the layered mafic units in the study section is reliant on the proportion of denser mafic minerals to the less dense felsic minerals. Because orthopyroxene is the dominant mafic mineral and plagioclase the dominant felsic mineral, the density of the units is a direct function of the pyroxene : plagioclase ratio of the different units (i.e. is controlled by the major cumulus mineralogy of the rock types). Therefore the detailed density profiles reflect changes in major mineral proportions through the study section – and is therefore modal dependant i.e. assumes no effect of mineral compositions. This is manifested as density trends where the systematic change in mineral proportions through a section exhibits a systematic change in density known as a density trend. The changes in mineral proportions, as quantified by the density measurements, are suggested to be reflecting primary fractionation processes.

Several conclusions were made from the density work: Firstly, the overall UG2 unit is seen to display a normal fractionation trend (as defined by a normal density trend), although, superimposed on this overall normal fractionation trend are a number of well developed local trends present with certain individual units i.e. the UG2 hanging wall lower and middle feldspathic pyroxenite, and UG2 gabbronorite, units also display well developed local normal fractionation trends. Above the hanging wall middle feldspathic pyroxenite, however, the UG2 leuconorite shows a well developed reverse fractionation trend – possibly indicating increased magma injections into the chamber at this level. This could also explain the largely disruptive stratigraphy within this unit – which comprises well developed interlayered lithologies (leuconorite and feldspathic pyroxenite).

The variation in density regularity of the hanging wall units compared with the footwall units (i.e. the footwall units display relatively constant density variations whilst the hanging wall exhibits a more ragged, irregular profile) possibly indicates an increased intensity of magma replenishment during the formation of the hanging wall sequence. The denser, and hence more mafic, character of the hanging wall feldspathic pyroxenite units compared with the footwall units could also indicate that the hanging wall sequence is a crystallization product of a larger, more primitive magma batch – possible at the level of the UG2. This is entirely consistent with the fieldwork observations in that the hanging wall feldspathic pyroxenite was found to be more mafic in character than compared to the footwall feldspathic pyroxenite unit.

Overall it is evident that the UG2 cyclic unit, despite displaying an overall normal fractionation trend, comprises a great deal of small-scale variation i.e. local normal trends within individual units as well as a reverse trend near the top of the unit. It also appears that the chamber underwent increased repetitions of magma injections up through the sequence. This is shown by the regular profiles of the footwall sequence whilst the hanging wall units are largely disruptive and irregular and show a reverse fractionation trend near the top. Therefore this is interpreted as the intensity of the injections had increased up through the hanging wall sequence.

Overall, the stratigraphic analysis of the study section has revealed the possible magma processes, and the variation of these processes over time, that took place during the crystallization of the sequence. It has also shown that the crystallization of the UG2 cyclic unit is more complex than originally thought, with an increased intensity of magma addition to the chamber experienced during the formation of the hanging wall sequence. It has also served to provide further evidence which is suggestive that the pegmatoidal feldspathic pyroxenite represents a late primary stage crystallization product of an upward percolating volatile-rich melt (i.e. Mathez and Mey, 2005).

Overall, the results display an excellent example of an open magma chamber and they reveal the complexities and intricacies involved in the formation of a layered cumulate pile.

5. Petrography and Rock Types

5.1 Introduction

Thirty one samples for petrographic studies were taken from the entire length of the core section (Appendix E), and included all the lithologies encountered, apart from chromitite (Table 5.1). A detailed petrographic examination of each of these lithologies was carried out using transmitted light microscopy. Emphasis was placed on estimating the modal proportions (using a visual examination) as well as describing the textures present. The lithologies were classified according to the IUGS classification scheme of Strieckeison (1973) for coarse to medium grained igneous rocks. By taking several samples from individual lithological units it is possible, using petrography, to identify any trends or variations in either the modal mineralogy or the textural characteristics within the single unit, thereby identifying possible fractionation trends.

Table 5.1: List of petrographic samples taken from ZG219 MH (the list is in stratigraphic order).

Sample #	From (m)	To (m)	Lithology	Unit
5	351.42	351.57	Anorthosite	UG2 Anorthosite
8	351.87	352.02	Leuconorite (joint at base)	UG2 Upper Leuconorite
10	352.17	352.32	Feldspathic Pyroxenite	UG2 Hanging Wall Upper Feldspathic Pyroxenite
14	352.77	352.92	Feldspathic Pyroxenite	
18	353.37	353.52	Leuconorite	UG2 Leuconorite
19	353.52	353.67	Norite	
21	353.82	353.97	Feldspathic Pyroxenite (with leuconorite layers)	
24	354.27	354.42	Leuconorite (with feldspathic pyroxenite layers)	
29	355.02	355.17	Leuconorite	
32	355.47	355.62	Feldspathic Pyroxenite (with leuconorite layers)	
37	356.22	356.37	Leuconorite	
48	357.87	358.02	Feldspathic Pyroxenite	UG2 Hanging Wall Middle Feldspathic Pyroxenite
52	358.47	358.62	Feldspathic Pyroxenite	
59	359.52	359.67	Norite	UG2 Norite
75	361.92	362.07	Norite (with minor anorthosite band)	
91	364.32	364.47	Norite	
142	365.65	365.70	Feldspathic Pyroxenite	UG2 Hanging Wall Lower Feldspathic Pyroxenite
147	365.89	365.94	Feldspathic Pyroxenite	
156	366.32	366.37	Feldspathic Pyroxenite	
181	367.22	367.27	Pegmatoidal Feldspathic Pyroxenite	UG2 Pegmatoidal Feldspathic Pyroxenite
185	367.43	367.49	Pegmatoidal Feldspathic Pyroxenite	
150	367.54	367.64	Pegmatoidal Feldspathic Pyroxenite	
152	367.74	367.84	Pegmatoidal Feldspathic Pyroxenite	
160	368.77	368.92	Fine- Grained Feldspathic Pyroxenite	UG2 Footwall Feldspathic Pyroxenite
170	370.27	370.42	Fine- Grained Feldspathic Pyroxenite	
182	372.07	372.22	Fine- Grained Feldspathic Pyroxenite	
191	373.42	373.57	Anorthosite	UG1 Anorthosite
198	374.47	374.62	Anorthosite	
208	375.97	376.12	Norite	UG1 Norite
220	377.77	377.92	Norite	
234	379.87	380.02	Norite	

All the lithologies are characterized by a mineral assemblage of mainly orthopyroxene, plagioclase and clinopyroxene. Accessory minerals include quartz, orthoclase, phlogopite and chromite.

5.2 Petrographic Descriptions

This section provides the results of the petrographic descriptions of each of the different lithologies. Each lithology contained a minimum of two petrographic samples and the final modal proportions were calculated as an average from all the samples examined from that particular unit.

5.2.1 Anorthosites

Anorthosites contain plagioclase as the dominant cumulus phase (minimum 90 %), with minor ortho- and clinopyroxene. Two anorthosite units are present within the study section – the lowermost one which forms the topmost unit of the UG1 cyclic unit (UG1 anorthosite), and a second one higher up which forms the immediate footwall to the UG3 chromitite (UG2 anorthosite).

5.2.1.1 UG1 Anorthosite

This unit forms the topmost unit of the UG1 cyclic unit.

Average modal composition (samples 191 and 198):

- Plagioclase 95 %
- Orthopyroxene 1 %
- Clinopyroxene 1 %
- Calcite (vein material) 3 %

This unit is almost a pure plagioclase cumulate. There is no layering or crystal alignment present and the texture can be described as massive. Overall it comprises closely packed cumulus plagioclase with minor accessory minerals (see Figure 5.1A). The plagioclase crystals are subhedral to euhedral in form and up to 6 mm in size. Some of the larger plagioclase crystals poikilitically enclose smaller plagioclase grains. A late stage calcite vein is seen to cut through the cumulate lithology. It has had a negligible affect on the lithology however.

5.2.1.2 UG2 Anorthosite

This unit forms the immediate footwall to the UG3 chromitite layer.

Average modal composition (sample 5):

- Plagioclase 98 %
- Calcite 2 %

This unit comprises solely of cumulus plagioclase with no other cumulus minerals present. The most striking difference between this unit and the UG1 anorthosite is that this anorthosite is finer grained than the UG1

anorthosite (see Figure 5.1B) with the plagioclase crystals <2 mm in length. There is also some local calcite veining (as in the previous anorthosite).

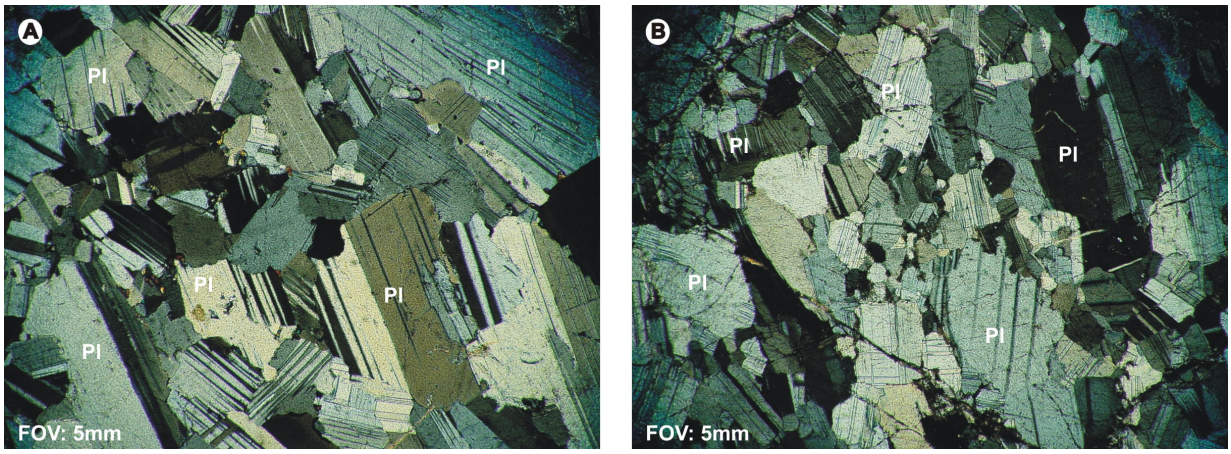

Figure 5.1: Petrographic characteristics of the anorthosite units found within the core section; pl = plagioclase, FOV = field of view. (A) UG1 anorthosite (sample 191). Massive anorthosite with plagioclase crystals <6 mm. (B) UG2 anorthosite (sample 5). Massive anorthosite with plagioclase crystals <2 mm.

5.2.2 Norites

Schurmann (1993) describes norite as containing both plagioclase (10 – 90 %) and orthopyroxene (90 – 10 %) as cumulus phases. Accessory phases include clinopyroxene and phlogopite. Norites also tend to have both melanocratic and leucocratic varieties, based on the proportion of the plagioclase to orthopyroxene. Two norite units (UG1 norite, Figure 5.2 A – C), and the UG2 norite, Figure 5.2 D - F) and two leuconorite units (both present within the UG2 hanging wall sequence, Figure 5.3A - F).

5.2.2.1 UG1 Norite

This unit forms the base of the core section and it is part of the UG1 hanging wall.

Average modal composition (samples 208, 220 and 234):

- Plagioclase 60 %
- Orthopyroxene 33 %
- Clinopyroxene 5 %
- Phlogopite 2 %

This unit comprises cumulus plagioclase and orthopyroxene with an intercumulate matrix of clinopyroxene and phlogopite (see Figure 5.2 A – C). The plagioclase crystals are sub to euhedral in form and <5 mm in length whilst the orthopyroxenes are subhedral and <3 mm in length. The orthopyroxene crystals also display blebby clinopyroxene exsolution lamellae. Clinopyroxene occurs as an interstitial phase along with phlogopite. A well developed oikocrystic texture exists with large (~3 – 5 mm) optically continuous clinopyroxene grains poikilitically enclosing both orthopyroxene and plagioclase crystals.

Figure 5.2: Petrographic characteristics of the norites within the study section; opx = orthopyroxene, pl = plagioclase, phlg = phlogopite, FOV = field of view. (A) UG1 norite (sample 208). Norite comprising cumulate plagioclase and orthopyroxene. (B) UG1 norite (sample 220). Norite with intercumulus phlogopite. (C) UG1 norite (sample 234). Regular norite. (D) UG2 norite (sample 59). Fine grained norite from top portion of unit (note higher plagioclase content and finer grain size than base of unit i.e. F). (E) UG2 norite (sample 75). Fine grained norite. (F) UG2 norite (sample 91). Fine grained norite from base of unit.

5.2.2.2 UG2 Norite

This unit forms part of the UG2 hanging wall sequence and exists immediately above the UG2 lower feldspathic pyroxenite unit. It also comprises cm scale subordinate leuconorite (plagioclase rich) layers within the well layered norite package.

Average modal composition (samples 59, 75 and 91):

	Bottom of unit:	**Top of unit:**
• Plagioclase	40 %	60 %
• Orthopyroxene	55 %	35 %
• Clinopyroxene	3 %	3 %
• Phlogopite	2 %	2 %

This unit comprises a cumulus framework of plagioclase and orthopyroxene with a minor interstitial matrix of clinopyroxene and phlogopite (see Figure 5.2 D – F). There is a large difference in grain size between this unit and the UG1 norite, with this norite being finer grained than the UG1 norite. The orthopyroxene and plagioclase crystals are <3 mm in size. The plagioclase crystals (lath shaped) are moderately well aligned to define a layering fabric.

There is a visible trend through the unit with the top of the unit being more plagioclase rich and finer grained than the base (see Figure 5.2 D vs. F). This is consistent with a normal fractionation trend.

5.2.2.3 UG2 Leuconorite

This unit forms part of the UG2 hanging wall sequence and comprises an interlayered package of leuconorite and subordinate feldspathic pyroxenite (Figure 5.3A – E). Therefore petrographic characteristics range from pure feldspathic pyroxenite to leuconorite over a mm scale. The feldspathic pyroxenite layers, however, are minor and have a negligible affect on the general modal composition of the unit.

Average modal composition (Samples 37, 32, 29, 24, 21, 19 and 18):

- Plagioclase 70 – 80 %
- Orthopyroxene 18 - 25 %
- Clinopyroxene 2 - 10 %
- Phlogopite 1 - 4 %

Several differences exist between this leuconorite unit and the previous norite units. Firstly, it is coarser grained than the previous units. Apart from being more plagioclase rich it also has a higher clinopyroxene abundance. Clinopyroxene exists as a cumulus phase along with plagioclase and orthopyroxene. The orthopyroxene crystals are <4.5 mm in size, the plagioclase <3 mm and the clinopyroxene crystals are generally smaller (~1 mm), although they do sometimes occur as large (~4 mm) oikocrysts where they poikilitically enclose orthopyroxene and plagioclase. The plagioclase crystals define a well developed layered fabric. The mm scale, sub-horizontal feldspathic pyroxenite layers are evident in thin section where textural changes across a few mm range from a typical feldspathic pyroxenite to a well layered leuconorite (Figure 5.3B).

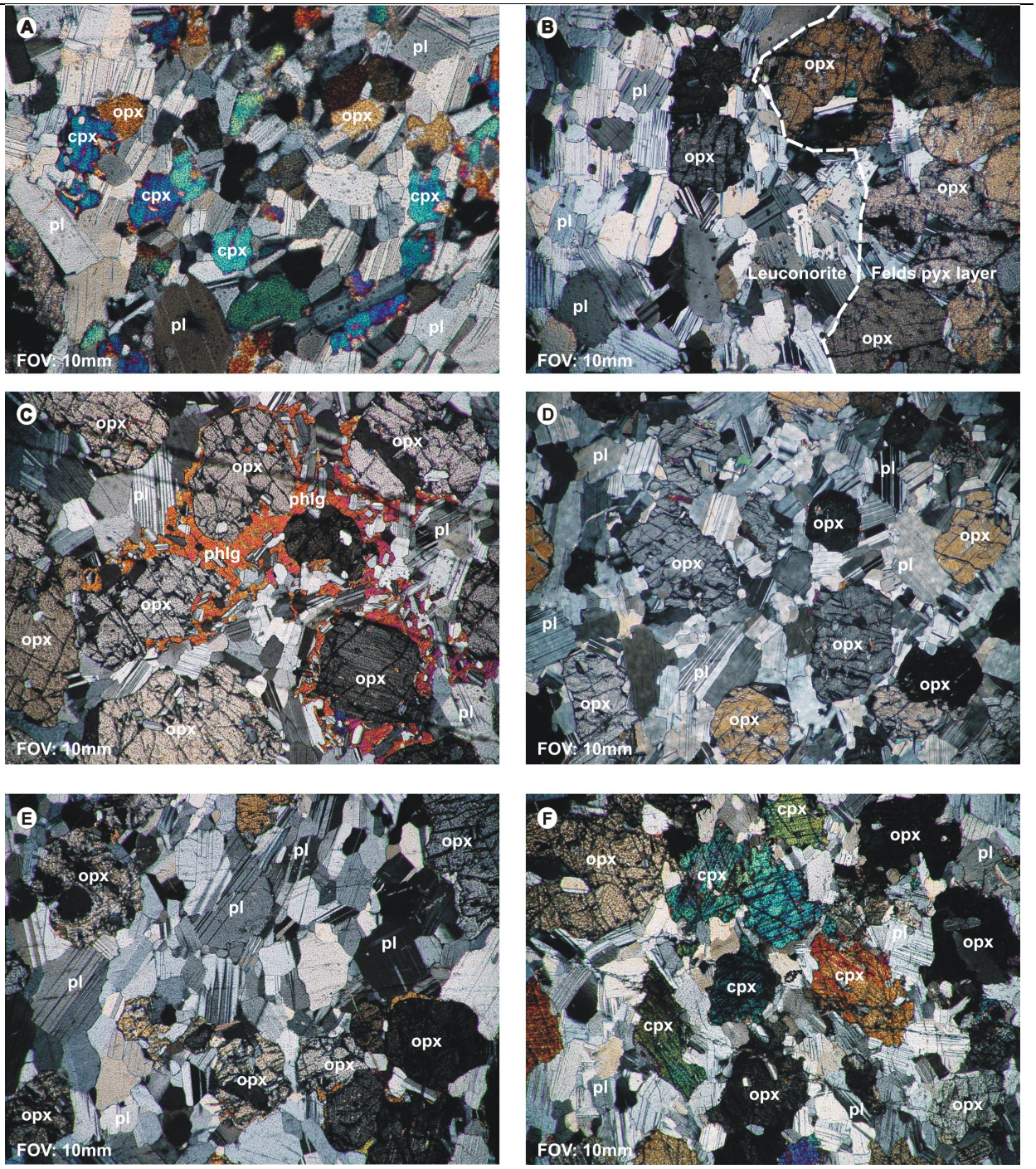

Figure 5.3: Petrographic characteristics of the leuconorites within the core section; pl = plagioclase, opx = orthopyroxene, cpx = clinopyroxene, phlg = phlogopite, FOV = field of view. (A) UG2 leuconorite (sample 37). Leuconorite with cumulus plagioclase, orthopyroxene and clinopyroxene. (B) UG2 leuconorite (sample 32). Leuconorite with subordinate feldspathic pyroxenite layer. (C) UG2 leuconorite (sample 18). Leuconorite with intercumulus phlogopite. (D) UG2 leuconorite (sample 24). Regular leuconorite. (E) UG2 leuconorite (sample 24). Regular leuconorite with well defined layering fabric. (F) UG2 upper leuconorite (sample 8). Leuconorite with cumulus plagioclase, orthopyroxene and clinopyroxene.

5.2.2.4 UG2 Upper Leuconorite

This unit occurs beneath the UG2 anorthosite and it is a narrow transition zone between the underlying UG2 upper feldspathic pyroxenite and the UG2 anorthosite (Figure 5.3F).

Average modal composition (sample 8):

- Plagioclase 65 %
- Orthopyroxene 20 %
- Clinopyroxene 15 %

This leuconorite unit is slightly more mafic than the other leuconorites. It also has a higher clinopyroxene content compared to the previous norite units. The plagioclase crystals define a layering fabric and there appears to be mm scale layers of leuconorite and regular norite.

5.2.3 Feldspathic Pyroxenites

Schurmann (1993) explains that the term 'feldspathic pyroxenite' is a traditional descriptive name of Bushveld rocks used to describe a pyroxenite unit with approximately 10 % feldspar.

5.2.3.1 UG2 Footwall Feldspathic Pyroxenite

This feldspathic pyroxenite unit is the stratigraphically lowest of four feldspathic pyroxenite units found in the study section, and it is the only one below the UG2. It is also the basal unit of the UG2 cyclic unit (Figure 5.4A – C).

Average modal composition (Samples 182, 170 and 160):

- Plagioclase 15 – 20 %
- Orthopyroxene 70 - 80 %
- Clinopyroxene 5 - 10 %
- Phlogopite 0 - 1 %

This unit is a mesocumulate comprising cumulus orthopyroxene and clinopyroxene with an interstitial matrix of plagioclase and clinopyroxene. There is a large amount of intercumulus material. Much of the interstitial plagioclase is optically continuous. Orthopyroxene (< 7mm) is the dominant phase and in some cases it displays almost total clinopyroxene replacement exsolution lamellae. This unit can therefore be classified as a plagioclase orthopyroxenite.

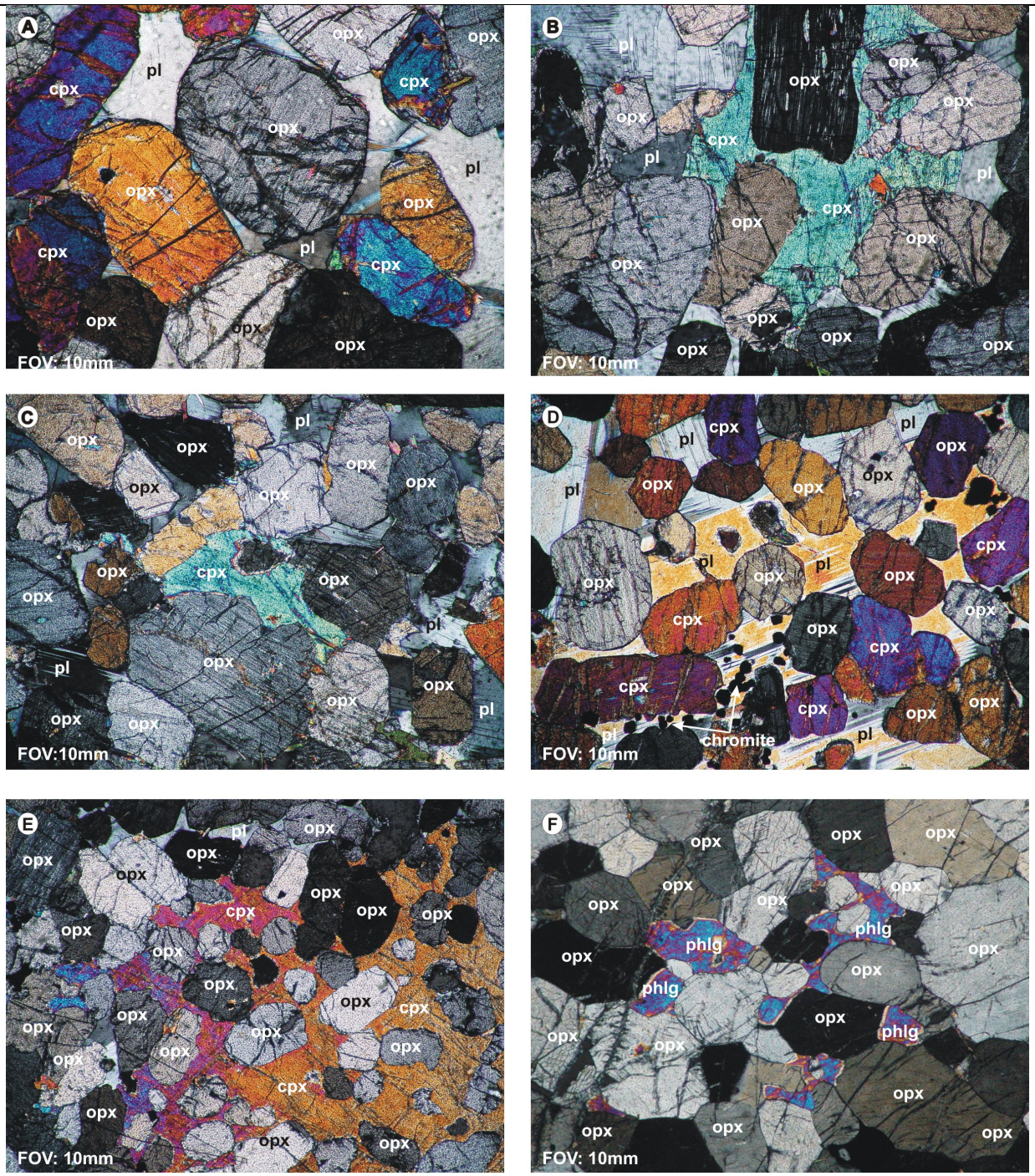

Figure 5.4: Petrographic characteristics of the UG2 footwall and the UG2 hanging wall feldspathic pyroxenites; pl = plagioclase, opx = orthopyroxene, cpx = clinopyroxene, phlg = phlogopite, cr = chromite, FOV = field of view. (A) UG2 footwall feldspathic pyroxenite (sample 160). Feldspathic pyroxenite with cumulus orthopyroxene and clinopyroxene in interstitial plagioclase. (B) UG2 footwall feldspathic pyroxenite (sample 170). Feldspathic pyroxenite with intercumulus clinopyroxene. (C) UG2 footwall feldspathic pyroxenite (sample 182). Feldspathic pyroxenite with intercumulus plagioclase and clinopyroxene. ((D) UG2 hanging wall lower feldspathic pyroxenite – top of unit (sample 142). Feldspathic pyroxenite with cumulus orthopyroxene and clinopyroxene in an optically continuous plagioclase matrix. Note also chromite grains in interstitial matrix. (E) UG2 hanging wall lower feldspathic pyroxenite (sample 147). Large oikocrystic clinopyroxene poikilitically enclosing orthopyroxene. (F)UG2 hanging wall lower feldspathic pyroxenite – base of unit (sample 156). Feldspathic pyroxenite with intercumulus phlogopite.

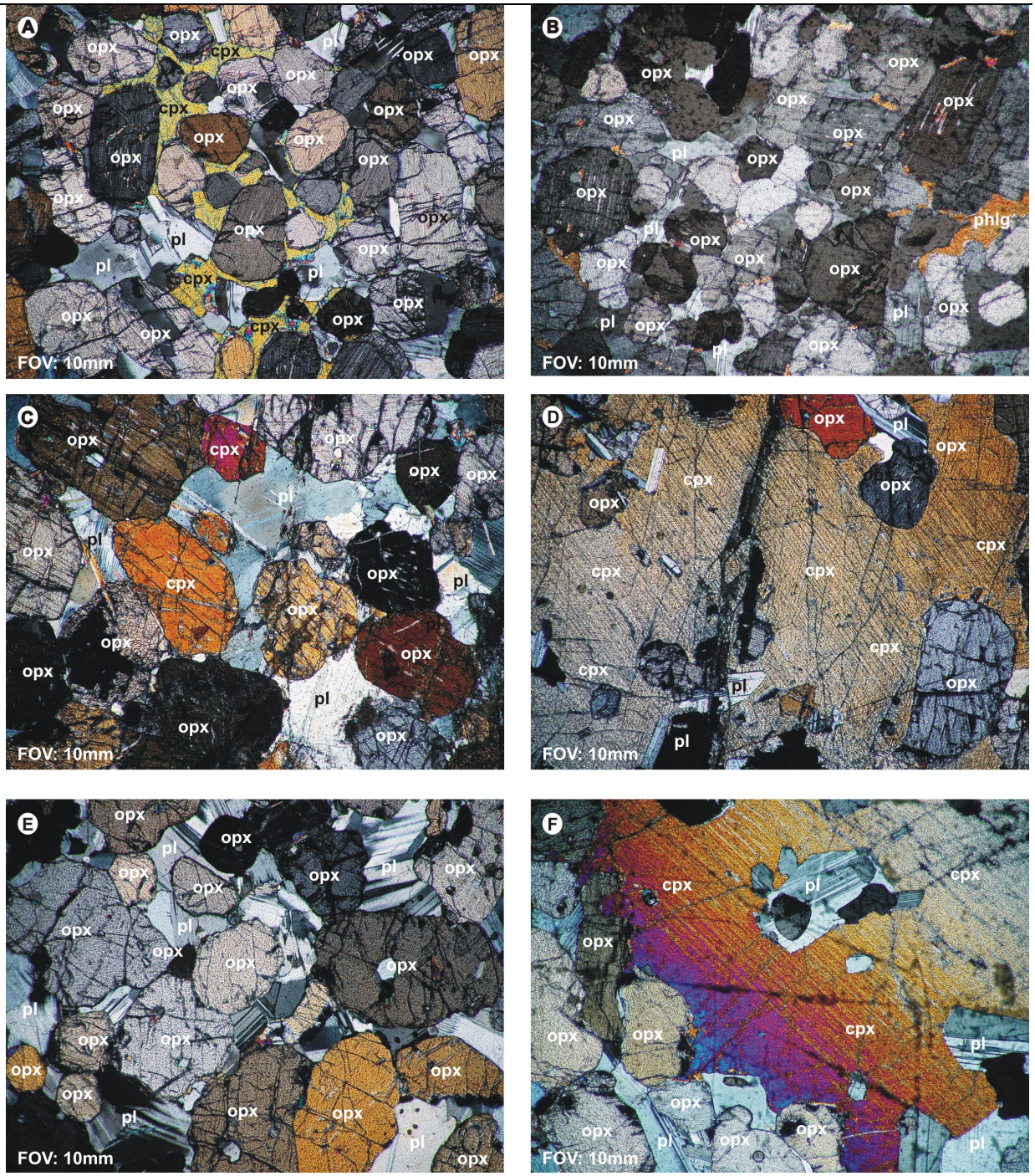

Figure 5.5: Petrographic characteristics of UG2 hanging wall middle and upper feldspathic pyroxenites; pl = plagioclase, opx = orthopyroxene, cpx = clinopyroxene, phlg = phlogopite, cr = chromite, FOV = field of view. (A)UG2 hanging wall middle feldspathic pyroxenite (sample 48). Large optically continuous clinopyroxene oikocrysts enclosing cumulus orthopyroxene. (B)UG2 hanging wall middle feldspathic pyroxenite (sample 52).Regular feldspathic pyroxenite. (C) UG2 hanging wall upper feldspathic pyroxenite (sample 10). Feldspathic pyroxenite with optically continuous intercumulus plagioclase matrix. (D) UG2 hanging wall upper feldspathic pyroxenite (sample 10). Large clinopyroxene oikocryst poikilitically enclosing cumulus orthopyroxene. (E) UG2 hanging wall upper feldspathic pyroxenite (sample 14). Regular feldspathic pyroxenite. (F) UG2 hanging wall upper feldspathic pyroxenite (sample 14).). Large clinopyroxene oikocryst poikilitically enclosing cumulus plagioclase.

5.2.3.2 UG2 Hanging Wall Lower Feldspathic Pyroxenite

This unit forms the immediate hanging wall to the UG2 chromitite and it comprises several mm scale chromite stringers (Figure 5.4D – F).

Average modal composition (Samples 156, 147 and 142):

	Bottom of unit:	**Top of unit:**
• Plagioclase	6 %	15 %
• Orthopyroxene	90 %	70 %
• Clinopyroxene	3 %	10 %
• Phlogopite	0 %	3 %
• Chromite	3 %	3 %

Petrographically there are several differences between this unit and the footwall pyroxenite. Firstly, this unit is finer grained with the orthopyroxenes < 2 mm in size. This pyroxenite is also more mafic with a higher pyroxene : plagioclase ratio than the footwall unit. Texturally the hanging wall unit is close to being classified as an adcumulate and it contains much less intercumulus plagioclase. There is a trend toward a more plagioclase rich composition up through the unit, consistent with a normal fractionation trend (see Figure 5.4D vs. F).

5.2.3.3 UG2 Hanging Wall Middle Feldspathic Pyroxenite

This pyroxenite unit is the middle pyroxenite within the UG2 hanging wall sequence (Figure 5.5A – B).

Average modal composition (Samles 48 and 52):

	Bottom of unit:	**Top of unit:**
• Plagioclase	5 %	15 %
• Orthopyroxene	80 %	80 %
• Clinopyroxene	15 %	5 %

This unit is more mafic (contains less intercumulus plagioclase) and is slightly finer grained than the lower hanging wall pyroxenite. It also contains well developed clinopyroxene oikocrysts (Figure 5.5A). There is a trend toward slightly more plagioclase rich compositions at the top of the unit.

5.2.3.4 UG2 Hanging Wall Upper Feldspathic Pyroxenite

This is the upper feldspathic pyroxenite of the UG2 hanging wall sequence (Figure 5.5C – F)..

Average modal composition (Samples 10 and 14):

	Bottom of unit:	**Top of unit:**
• Plagioclase	20 %	5 %
• Orthopyroxene	75 %	80 %
• Clinopyroxene	3 %	13 %
• Phlogopite	2 %	2 %

This unit is coarser grained than the middle pyroxenite unit. It also contains well developed, large clinopyroxene oikocrysts. However, as opposed to the previous pyroxenite it shows a trend toward more mafic compositions up through the unit. This is consistent with a reverse fractionation trend.

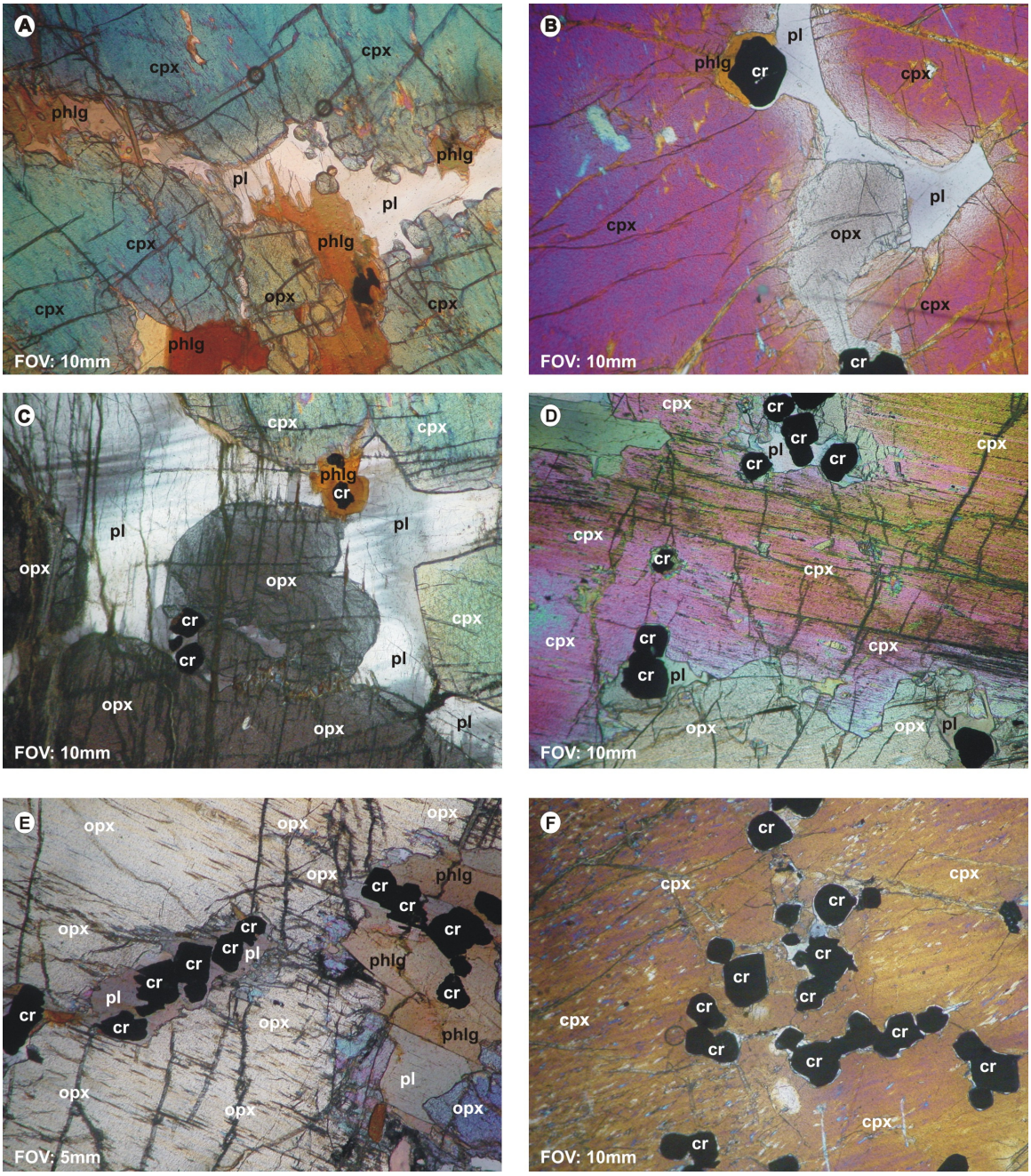

Figure 5.6: Petrographic characteristics of UG2 pegmatoidal feldspathic pyroxenite; pl = plagioclase, opx = orthopyroxene, cpx = clinopyroxene, phlg = phlogopite, cr = chromite, FOV = field of view. (A)Sample 152. Pegmatoidal feldspathic pyroxenite with large cumulus clinopyroxene and pockets of interstitial phlogopite and plagioclase. (B) Sample 150. Pocket of intercumulus plagioclase in between cumulus clino and orthopyroxene. Note chromite grains. (C) Sample 181. Pocket of interstitial plagioclase in between ortho and clinopyroxene. Note optical continuity of plagioclase matrix. (D) Sample 185. Large clinopyroxene poikilitically enclosing chromite. (E) Sample 181. Cumulus orthopyroxene with interstitial phlogopite and chromite. (F) Sample 150. Large clinopyroxene poikilitically enclosing chromite grains.

5.2.354 UG2 Pegmatoidal Feldspathic Pyroxenite

This unit is texturally distinct from the previous regular feldspathic pyroxenites. It also forms the direct footwall to the UG2 chromitite (Figure 5.6A – F).

Average modal composition (Samples 150, 152, 181 and 185):

- Plagioclase 10 – 20 %
- Orthopyroxene 10 - 15 %
- Clinopyroxene 60 - 70 %
- Phlogopite 0 - 5 %
- Chromite 2 – 10 %
- Orthoclase 0 – 5 %

This unit is texturally distinctive from the regular pyroxenites. It contains extremely large clinopyroxene oikocrysts (< 20 mm) and large cumulus orthopyroxene crystals, with a series of 'trapped' liquid enclosures where intercumulus plagioclase and phlogopite exist. Intercumulus material is restricted to minor pockets or fissures of trapped liquid (Figure5.6A – C). Chromite occurs as euhedral crystals and are present within the intercumulus matrix as well as locked within the cumulus clinopyroxenes. Due to the large amount of intercumulus plagioclase, the IUGS system classifies the rock as a gabbronorite. However, because of the large grain size of the pyroxenes, the absence of cumulus plagioclases and the appreciable amount of intercumulus plagioclase, the author favours the term 'pegmatoidal feldspathic pyroxenite' for this unit.

5.3 Discussion

This section has served to describe the petrographic characteristics of all the different silicate lithologies encountered within the study section. The dominant cumulus minerals found in these lithologies are orthopyroxene, plagioclase and clinopyroxene with accessory phases such as phlogopite and chromite also present. Modally there is a series ranging from pure plagioclase cumulates (anorthosites) through progressively more mafic, pyroxene-rich leuconorites, norites and eventually feldspathic pyroxenites which still contain ~10 % plagioclase. Apart from the modal abundances there are also pronounced variations in crystal size and the general texture between the different lithologies. Certain units also show slight variations in these characteristics up through the unit (defining possible fractionation trends).

6. Whole-Rock Geochemistry

6.1 Introduction

The main aim of the whole-rock geochemical analysis was to provide a continuous geochemical profile through the entire mother hole drill core through a succession of chromitite, feldspathic pyroxenite, norite and anorthosite. The behaviour of the major and trace elements were investigated through the study section (Appendix D). The elemental profile patterns were then used to investigate the processes occurring within the chamber during the formation of the UG2 unit.

The geochemistry study comprises three investigative approaches: Firstly, the major elements present in the study section monitor the major cumulus phases present in the section. These elements are compatible to the main cumulus minerals and they partition actively into these phases during fractional crystallization. Therefore, the major (compatible) element profile patterns through the section are used to monitor the variation of the cumulus minerals.

During fractional crystallization a certain amount of residual liquid becomes trapped in the pore spaces between the cumulus minerals and becomes enriched in incompatible elements and water. Incompatible elements are those which do not partition into the crystallizing phases and, instead, remain behind in the residual liquid (i.e. Zr, TiO_2 and K_2O). Therefore, the incompatible trace element patterns through the section are used to monitor the amount of trapped liquid.

Finally, the base metals (Cu, Ni, Zn and S) are used to investigate the processes of mineralization operating within the study section.

6.2 Geochemical Techniques

A flexible sampling method was used to select a number (240) of representative samples from throughout the study section. A continuous run of sampling using a sample length of 15 cm was used to sample the UG2 hanging wall section from the UG2 hanging wall anorthosite down to the topmost chromitite stringer. This strategy was also used for the UG2 footwall section from below the UG2 footwall pegmatoidal feldspathic pyroxenite down to the base of the UG2 footwall feldspathic pyroxenite. The sampling interval was then extended to 1 x 15 cm sample every 15 cm (not continuous as before) through the anorthosite and gabbronorite units of the UG1 hanging wall.

A more detailed sampling strategy was used for the UG2 chromitite, its footwall pegmatoidal feldspathic pyroxenite and hanging wall lower feldspathic pyroxenite up to the topmost chromitite stringer. A continuous run of sampling using a sample length of 5 cm (full core) was therefore used for the hanging wall feldspathic pyroxenite and footwall pegmatoidal feldspathic pyroxenite units. The chromitite stringers in the hanging wall were sampled separately using 2 or 3 cm long samples (just long enough to only include the

stringer and minimal pyroxenite material). The UG2 chromitite was sampled continuously using 3 cm long samples (totaling 17 samples).

In total, 240 samples were analyzed for bulk rock major and trace elements with 54 of these samples also analyzed for PGE (chapter 7). The X-Ray fluorescence (XRF) analytical technique was used for the bulk rock geochemical analysis. The major element analyses were determined using 350 mg of sample by the Norrish fusion method (Norrish and Hutton, 1969) method and analyzed using a Philips PW1404 X-ray fluorescence spectrometer. The following elements were analyzed by this method and expressed as oxides: SiO_2, Al_2O_3, FeO (Fe_2O_3 recalculated as 10% total Fe), MnO, MgO, CaO, Na_2O, K_2O, TiO_2, Cr_2O_3, NiO and P_2O_5. The trace elements were analyzed against certain standards using pressed powder pellets. The following trace elements were analyzed using the XRF technique: Zr, Sr, Zn, Cu, Ni, and S. Correction software for the XRF major and trace elements was that developed within the Geology Department. All analyses were compared to certified international reference materials.

6.3 Major Elements

Figure 6.1 exhibits the variation of SiO_2 through the section, whilst Figure 6.2 shows the variation of MgO and Al_2O_3 through the study section.

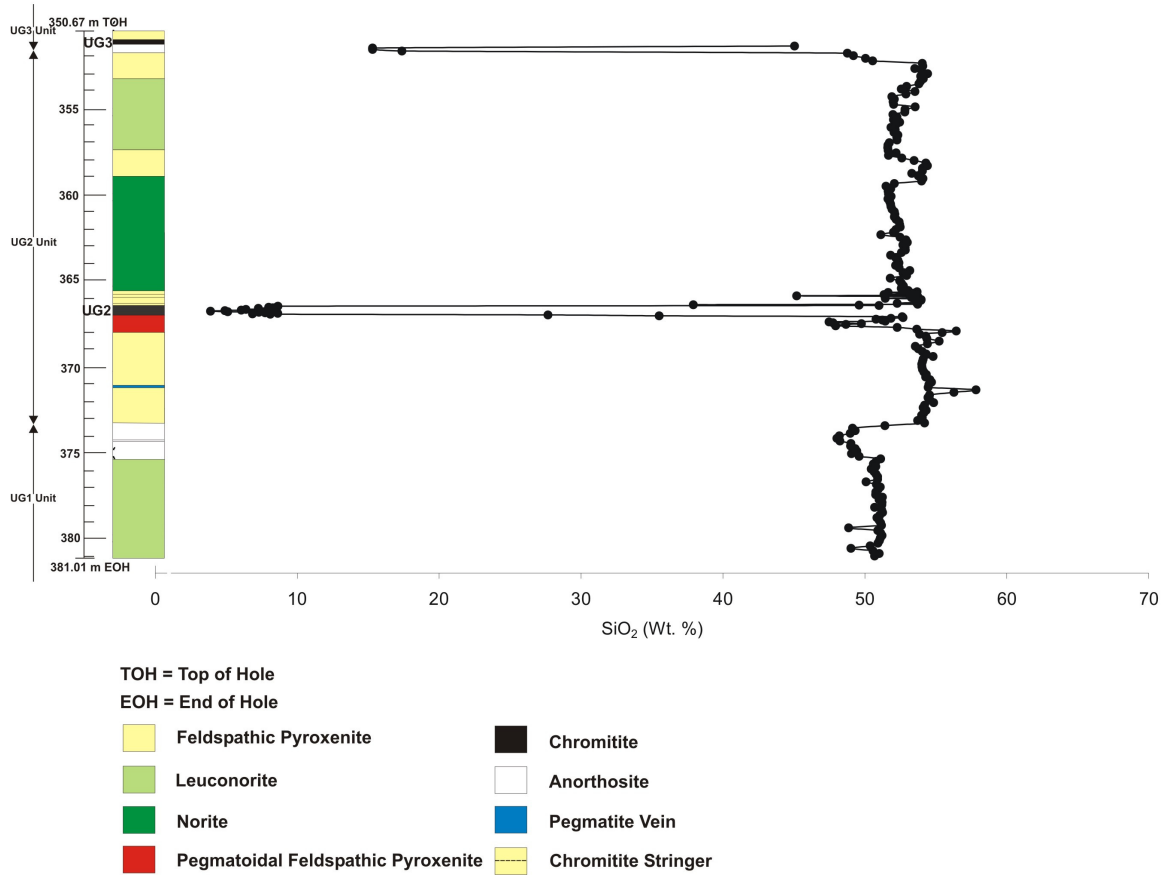

Figure 6.1: Variation of SiO_2 (wt. %) through the study section.

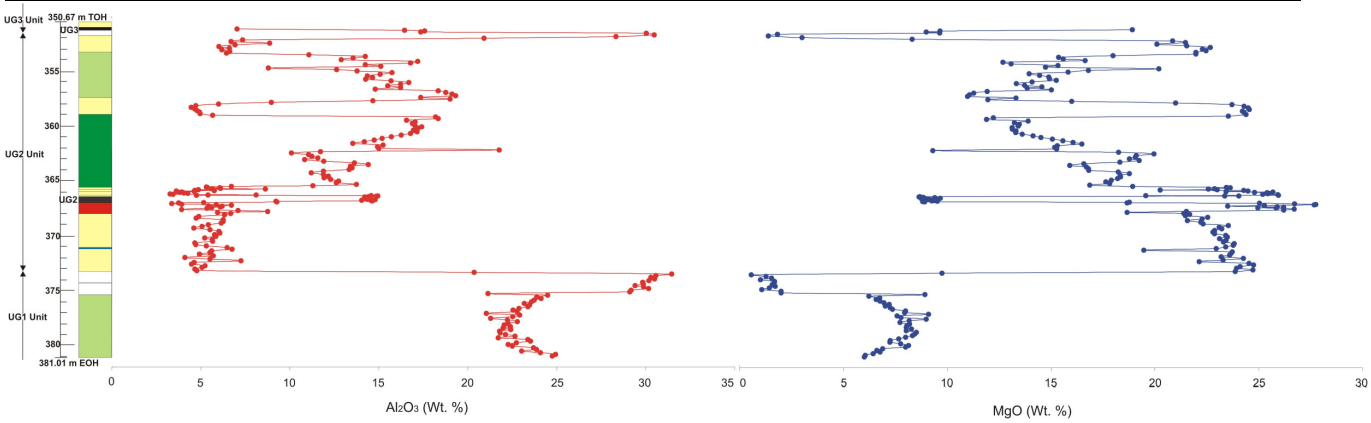

Figure 6.2: Variation of MgO (Wt. %) and Al_2O_3 (Wt. %) through the study section.

The profile pattern of SiO_2 through the study section (Figure 6.1) shows an enrichment through the pyroxenite units with a decreasing abundance through the norite and anorthosite units. Although SiO_2 partitions into both orthopyroxene and plagioclase, it does so more favourably into the former. Therefore, the SiO_2 content is seen to track the modal variation of orthopyroxene through the section. The general profile pattern shows an overall upward decreasing trend through the study section with a reversal to an upward increasing trend at the level of the UG2 leuconorite.

The Al_2O_3 and MgO profile patterns are perfectly contrasted (Figure 6.2). These elements partition very strongly into plagioclase and orthopyroxene respectively and hence monitor the modal abundances of these two minerals. Because plagioclase and orthopyroxene form the dominant mineral assemblage, the Al_2O_3 and MgO variation patterns through the section can be used to define the lithological units as well as to identify possible fractionation trends. The two profile patterns clearly indicate a lower normal fractionation trend (straddling the UG1 unit – UG2 unit boundary) passing upwards into a reverse fractionation trend (with the base of the UG2 leuconorite marking the boundary between the two).

The profile patterns of CaO and Na_2O (Figure 6.3) are essentially monitoring the modal variation of plagioclase through the section (due to the fact that they both partition strongly into it). Both the patterns define the different lithological units in the section i.e. progressively higher abundances in the more plagioclase rich lithologies (norite – leuconorite – anorthosite) and lower abundances in the more mafic pyroxenite units. The patterns also exhibit a normal fractionation trend (defined by upward increasing abundances) overlain by a reverse trend (marked by upward decreasing abundances) at the level of the UG2 leuconorite.

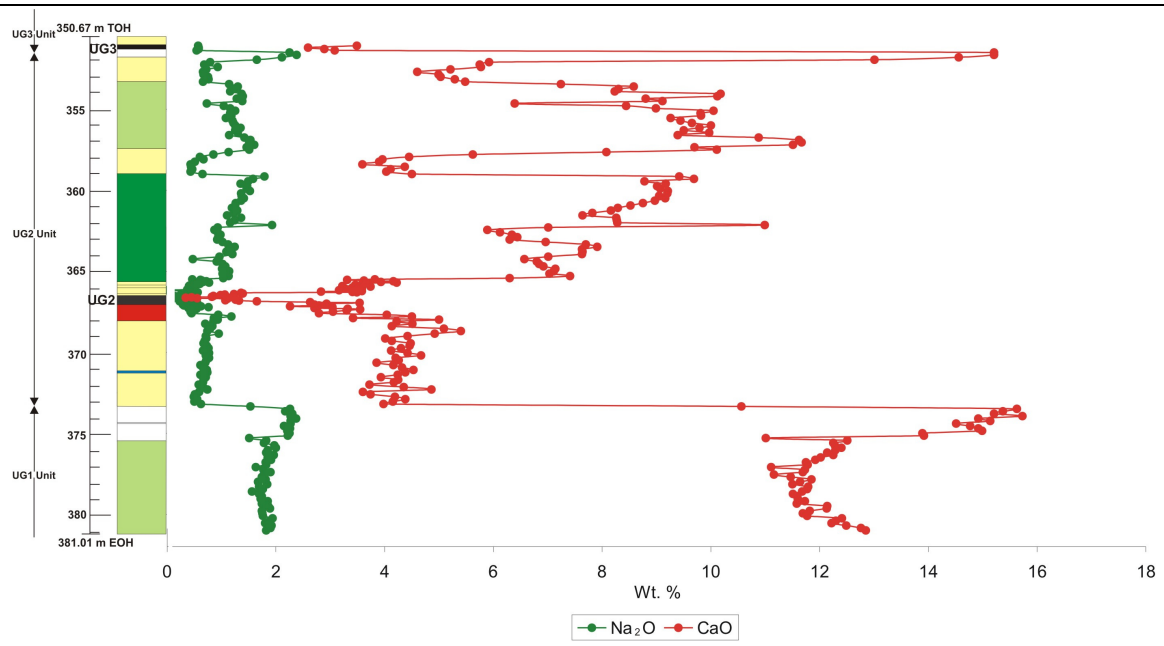

Figure 6.3: Variation of Na_2O (Wt. %) and CaO (Wt. %) through the study section.

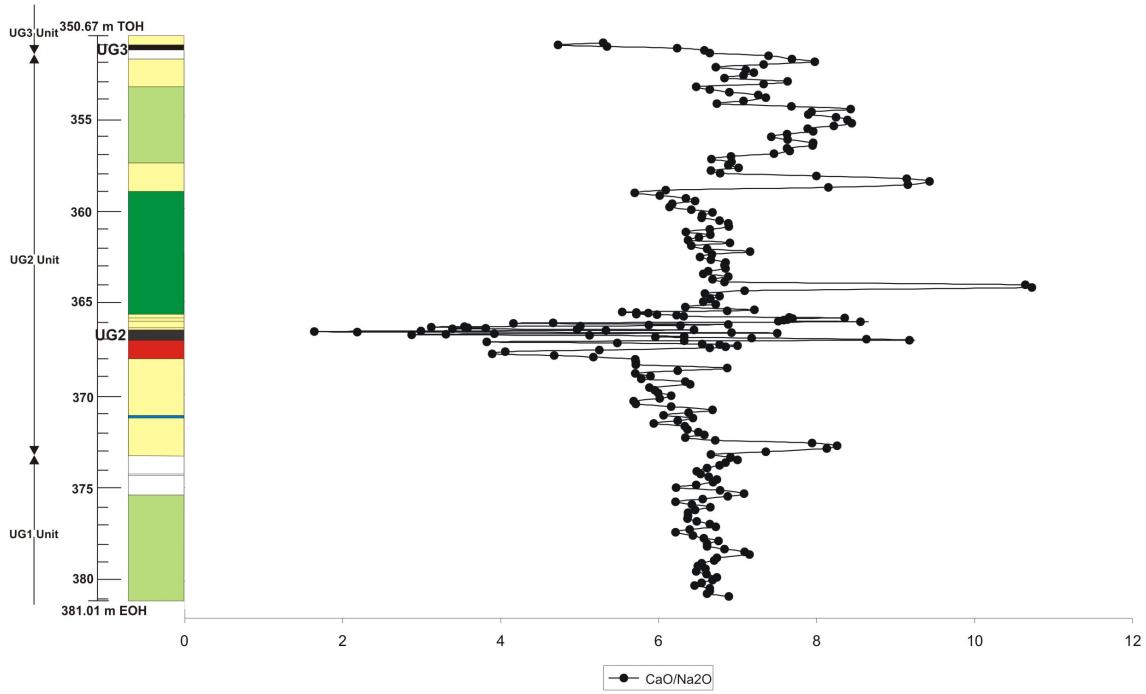

Figure 6.4: Variation of CaO/Na_2O (two point moving average) through the study section.

The profile pattern of the CaO/Na_2O ratio (Figure 6.4) is used to monitor the compositional variation of plagioclase through the study section. The values are relatively constant and show a sharp increase at the base of the UG2 unit (footwall pyroxenite). In the UG2 footwall feldspathic pyroxenite the plagioclase compositions tend to become more sodic up through the unit. There is then a greater deal of variation through the footwall

pegmatoidal pyroxenite whilst the UG2 chromitite exhibits the most calcic plagioclase compositions of the entire study section. This is terminated by a sharp change to more sodic plagioclase compositions within the UG2 hanging wall feldspathic pyroxenite. Relatively constant values exist through the UG2 norite unit and, as for the UG2 footwall and hanging wall feldspathic pyroxenite units, a sharp increase toward more sodic plagioclase compositions is exhibited at the base of the UG2 hanging-wall middle feldspathic pyroxenite unit. Overlying this, the UG2 leuconorite unit exhibits a well defined upward trend toward more sodic compositions. This trend, however, only exists for the basal portion of this unit and there is a sharp change toward more regular, constant values within the middle and upper portions of the UG2 leuconorite. A sharp change toward more sodic compositions exists within the overlying UG2 hanging wall upper feldspathic pyroxenite unit and is overlain by a trend toward more calcic plagioclase compositions through the UG3 anorthosite and chromitite.

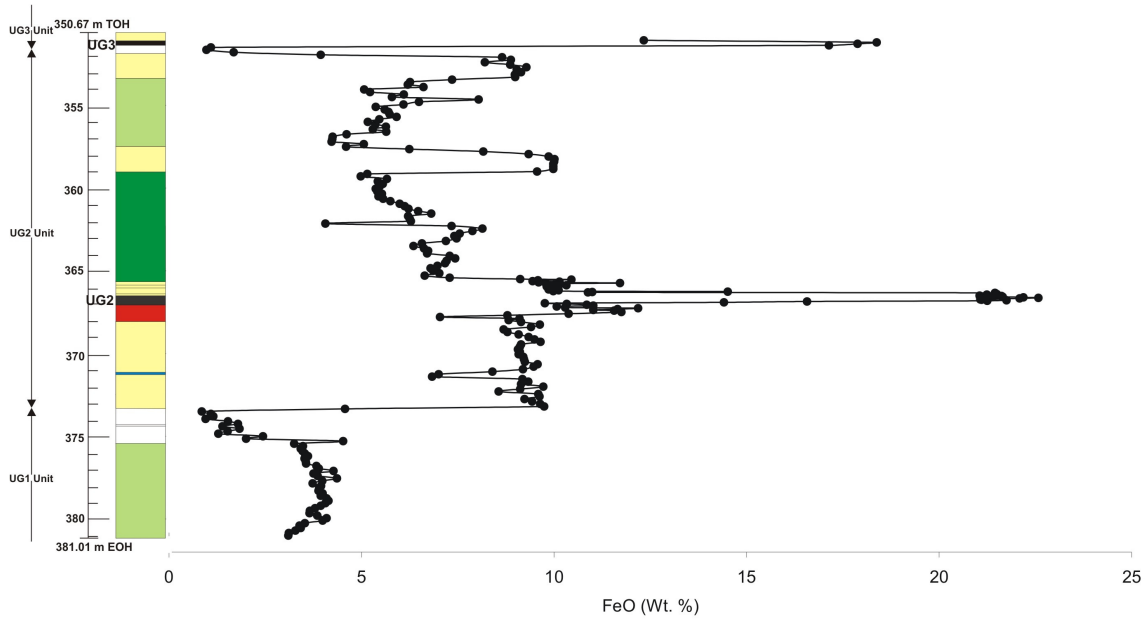

Figure 6.5: Variation of FeO (Wt. %) through the study section.

The profile pattern of FeO (Figure 6.5) is very similar to the MgO trend (Figure 6.2). This is due to FeO, like MgO, partitioning strongly into orthopyroxene the modal variation of which thus controlling the variation of FeO through the section. An overall normal trend, capped by a reverse trend at the base of the UG2 leuconorite, is thus exhibited in this profile pattern.

There is a greater small-scale and layer-scale variation in the calcium number (Ca #)[1] as opposed to the magnesium number (Mg #)[1] through the section (Figure 6.6). The Mg #, in particular, is remarkably constant

[1] Ca# = $CaO/(CaO + Na_2O)$; Mg# = $MgO / (MgO + Fe_2O_3)$

through the section, showing a decrease only within the anorthosite units as well as in the footwall pegmatoidal pyroxenite and the UG2 and UG3 chromitites. There is only a very slight upward increasing trend within the UG2 leuconorite. This therefore reflects an essentially constant orthopyroxene composition through the study section. The Ca #, however, shows upward evolving compositions (as defined by a decreasing Ca #) through the UG2 footwall feldspathic pyroxenite as well as an upward trend toward more sodic plagioclase compositions (increasing Ca #) through the basal portion of the UG2 leuconorite. There are also, as mentioned earlier, sharp increases toward more sodic compositions at the base of major feldspathic pyroxenite units.

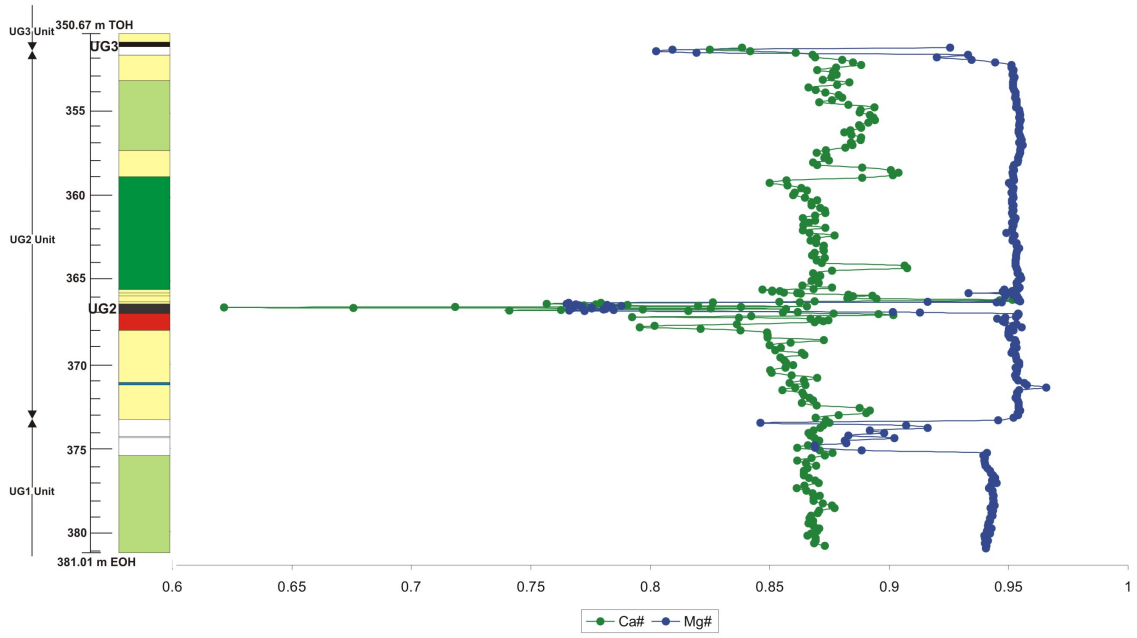

Figure 6.6: Variation of Ca # (two point moving average) and Mg # through the study section.

The profile pattern of Cr_2O_3 (Figure 6.7) essentially monitors the variation of orthopyroxene (due to Cr_2O_3 being moderately compatible to it) as well as clinopyroxene (due to Cr_2O_3 displaying a moderately strong partition coefficient into clinopyroxene) through the study section in portions where chromite is not a major mineral. There is an increasing Cr_2O_3 trend up through the upper portion of the UG2 footwall feldspathic pyroxenite into the overlying footwall pegmatoidal pyroxenite (which does contain disseminated chromite) and UG2 chromitite units. The enriched values persist through the hanging wall feldspathic pyroxenite unit and show an upward decreasing trend (normal trend) through the UG2 norite and middle pyroxenite units. A reversal to an upward increasing trend then occurs through the UG2 leuconorite unit (reverse trend). The Cr_2O_3 pattern reflects the normal and overlying reverse trends, as defined by other elements, but only within the UG2 hanging wall sequence. This is because the normal trend (marked by upward decreasing Cr_2O_3 values as a result of upward decreasing amounts of normative orthopyroxene) in the UG2 footwall sequence is 'cancelled out' by

a contrasting trend of upward increasing Cr_2O_3 abundances due to an upward increasing modal clinopyroxene trend (Figure 8.7).

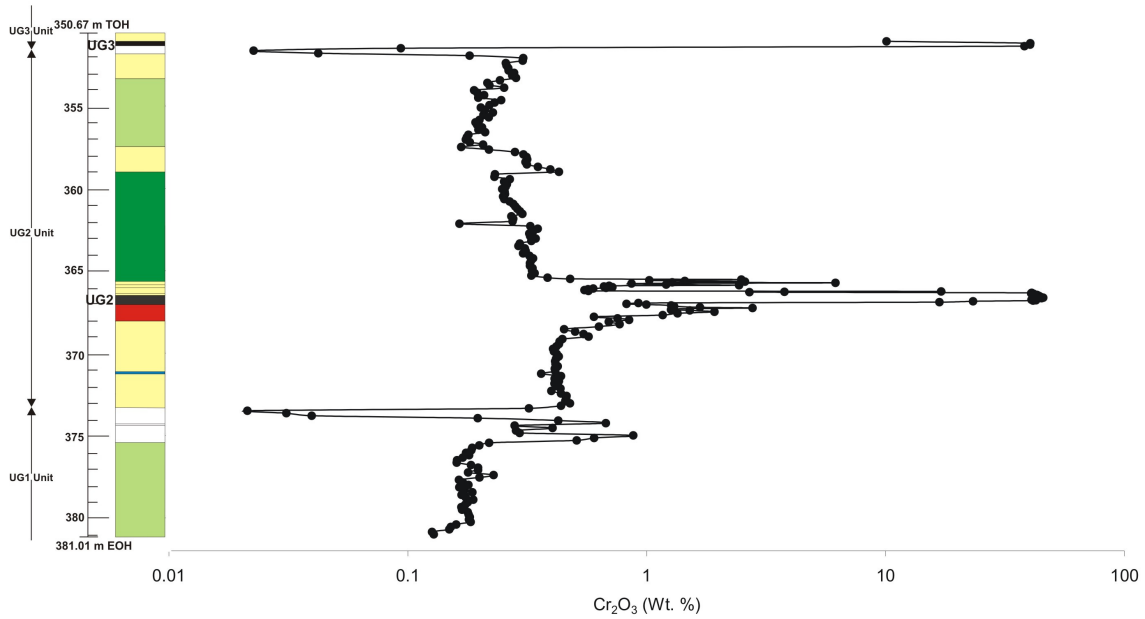

Figure 6.7: Variation of Cr_2O_3 (Wt. %) through the study section.

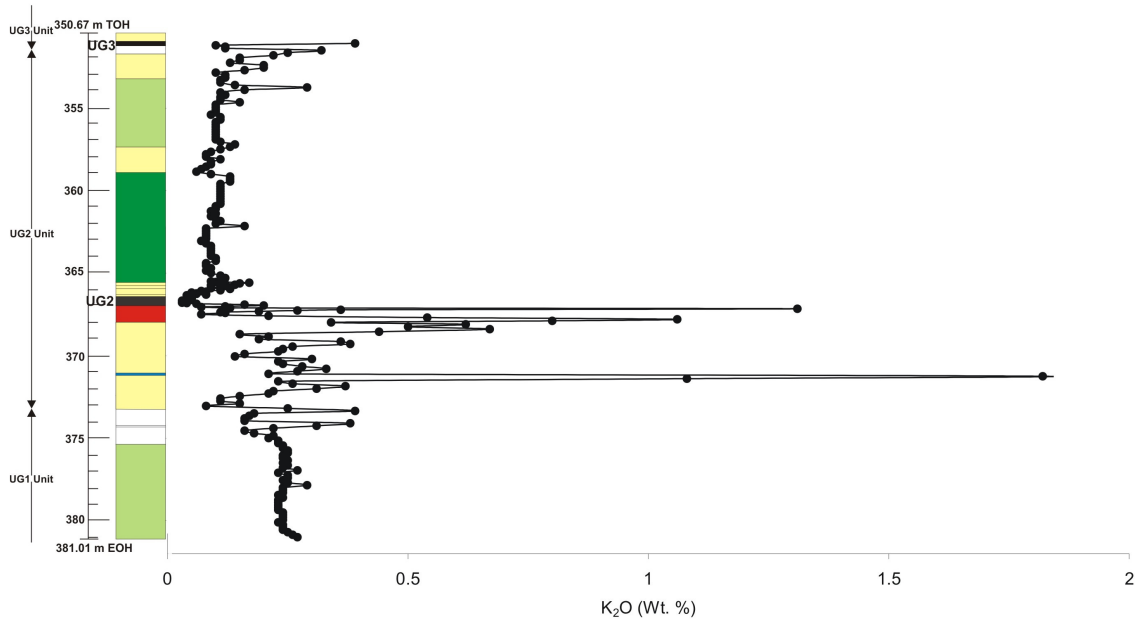

Figure 6.8: Variation of K_2O (Wt. %) through the study section.

The profile pattern of K_2O (Figure 6.8) shows no distinct lithologically controlled variations. This is because K_2O is an incompatible element and it therefore does not partition strongly into any cumulus mineral but is rather concentrated within the trapped intercumulus liquid during crystallization. Its abundance through

the section is therefore used to monitor the abundance of trapped liquid within the cumulates. A consistent abundance exists throughout the section apart from in the UG2 footwall feldspathic pyroxenite where higher, and more irregular, values are exhibited. This pattern also exists in the UG2 hanging wall upper feldspathic pyroxenite unit, which shows increasing values through into the overlying UG3 anorthosite and chromitite units. The UG2 hanging wall lower feldspathic pyroxenite exhibits a well defined trend of upward increasing values (also entirely regular and constant) through the unit.

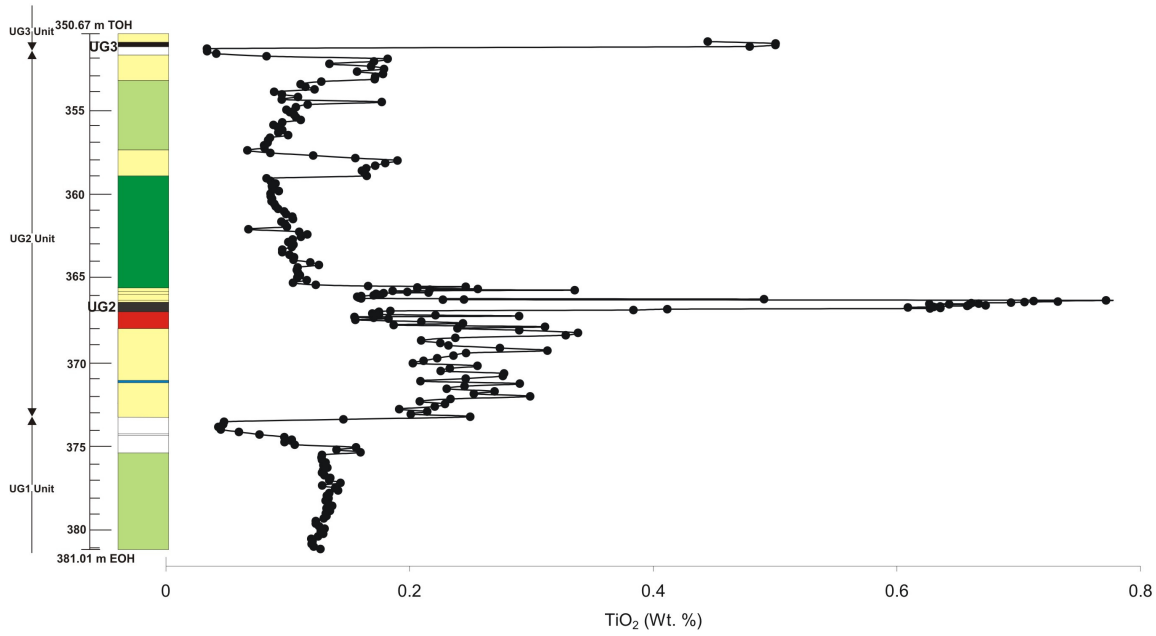

Figure 6.9: Variation of TiO_2 (Wt. %) through the study section.

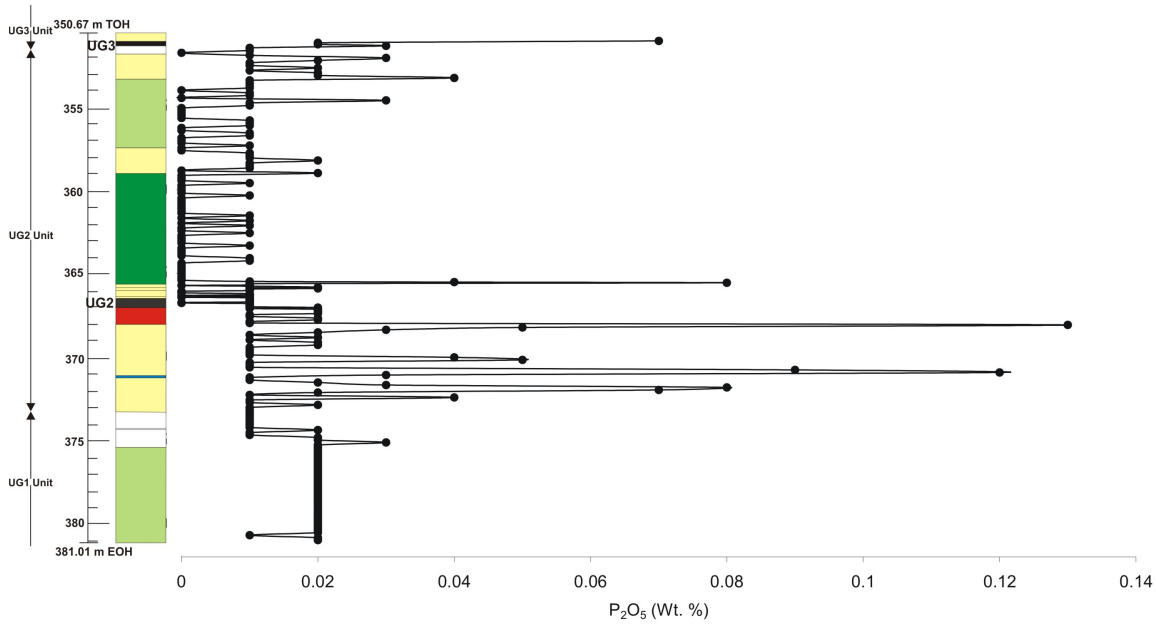

Figure 6.10: Variation of P_2O_5 (Wt. %) through the study section.

Both TiO_2 and P_2O_5 are incompatible elements which, like K_2O, are concentrated into the trapped interstitial liquid (which means they can therefore be used to monitor trapped liquid behaviour through the section). Both the profile patterns (Figures 6.9 and 6.10 respectively) exhibit higher, more irregular values through the UG2 footwall feldspathic pyroxenite unit. This confirms the K_2O pattern that the UG2 footwall feldspathic pyroxenite unit contains the highest abundance of trapped interstitial liquid in the study section. TiO_2, however, is also strongly compatible in chromite and therefore shows sharp increased abundances through both the UG2 and UG3 chromitite layers.

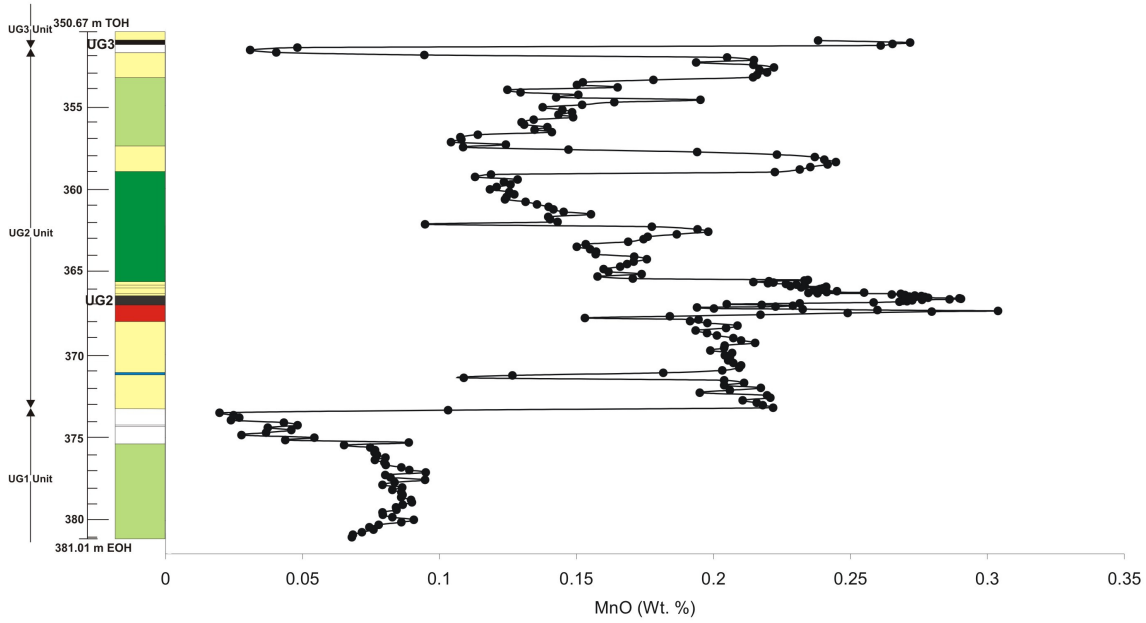

Figure 6.11: Variation of MnO (Wt. %) through the study section.

The profile pattern of MnO (Figure 6.11) is very similar to that for FeO. This is because, like FeO, MnO is compatible in orthopyroxene and therefore tracks its modal abundance through the section. Similar to the other compatible elements the MnO pattern reveals a normal fractionation trend (straddling the UG1 unit – UG2 unit boundary) overlain by a reverse trend (at the level of the UG2 leuconorite unit).

6.4 XRF Trace Elements

The profile pattern of Zr (Figure 6.12) is very similar to those of K_2O (Figure 6.8) and TiO_2 (Figure 6.9). This is a result of Zr also being a strongly incompatible element and thus also being concentrated into the trapped interstitial liquid. It confirms the earlier findings that the highest amounts of trapped liquid are found within the UG2 footwall feldspathic pyroxenite unit.

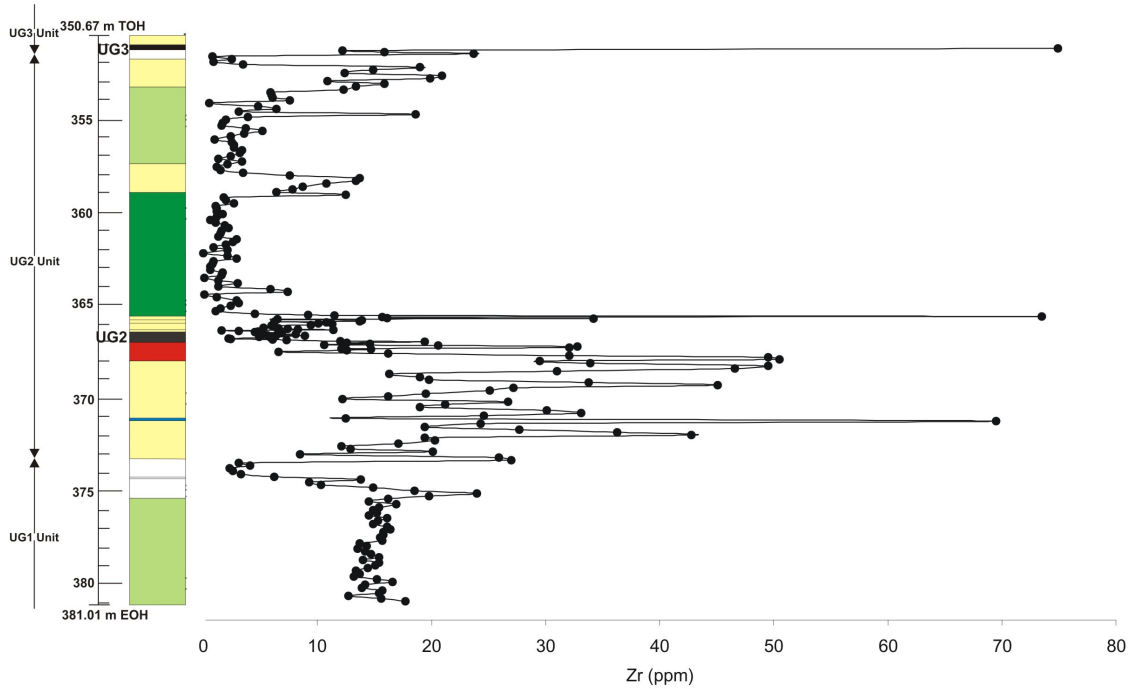

Figure 6.12: Variation of Zr (ppm) through the study section.

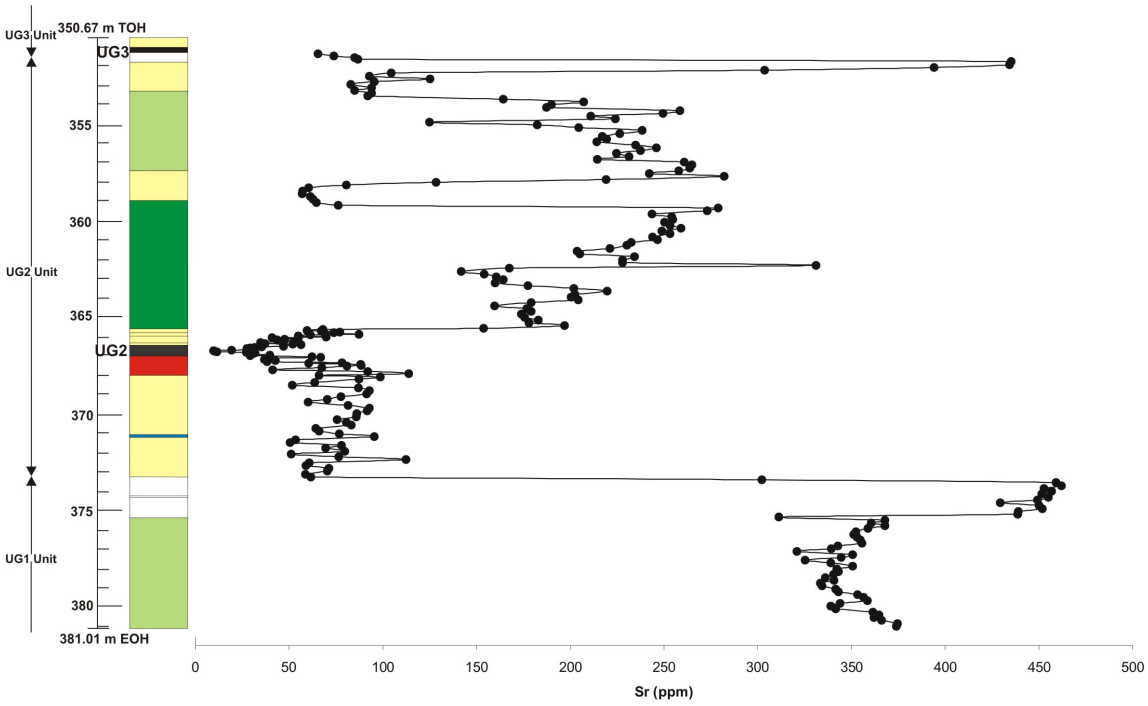

Figure 6.13: Variation of Sr (ppm) through the study section.

As opposed to Zr, the trace element Sr is not an incompatible element and it is strongly compatible to plagioclase. Its profile pattern, like that of Al_2O_3, reflects the modal variation of plagioclase through the section (Figure 6.13).

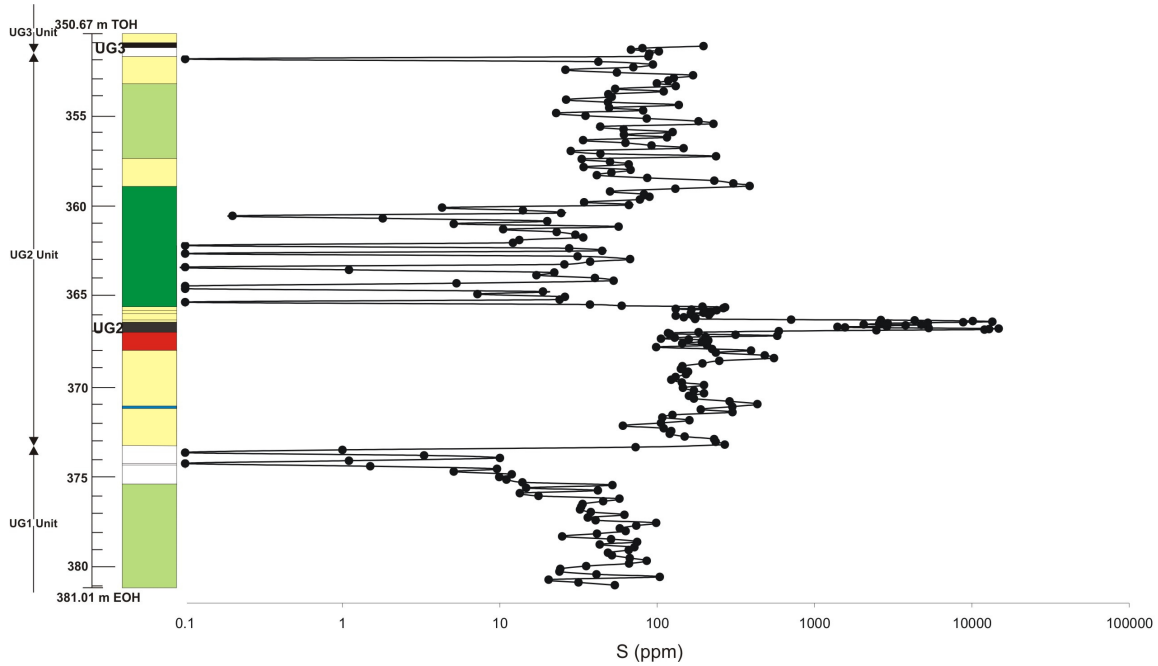

Figure 6.14: Variation of S (ppm) through the study section.

The profile pattern of S (Figure 6.14) is monitoring solely the amount of sulphide mineralization through the section. This is because S is completely incompatible in the silicate minerals and partitions, along with the base metals, only into base-metal sulphide minerals. There is a trend of upward increasing concentration through the UG2 footwall feldspathic pyroxenite, which leads up to the highest values in the section within the footwall pegmatoidal pyroxenite and the UG2 chromitite. The hanging wall lower pyroxenite also exhibits relatively high S values in the same region as the footwall feldspathic pyroxenite. The UG2 norite, however, shows low S values throughout the unit whilst the hanging wall middle feldspathic pyroxenite shows an increase in S values, which continues through into the overlying UG2 leuconorite unit. The UG2 leuconorite unit exhibits higher, as well as notably more irregular, values as opposed to, in particular, the UG1 leuconorite unit.

Figures 6.15 (Zn and Cu) and 6.16 (Ni and S) provide the profile patterns of the major base metals (i.e. Zn, Cu and Ni) along with that of S. Because S is completely incompatible in the silicate minerals and that it partitions only into (and is thus monitoring the variation of) the sulphide minerals, means that the variation of the base-metal profile patterns from the S pattern provides a measure of their compatibility in certain silicate minerals.

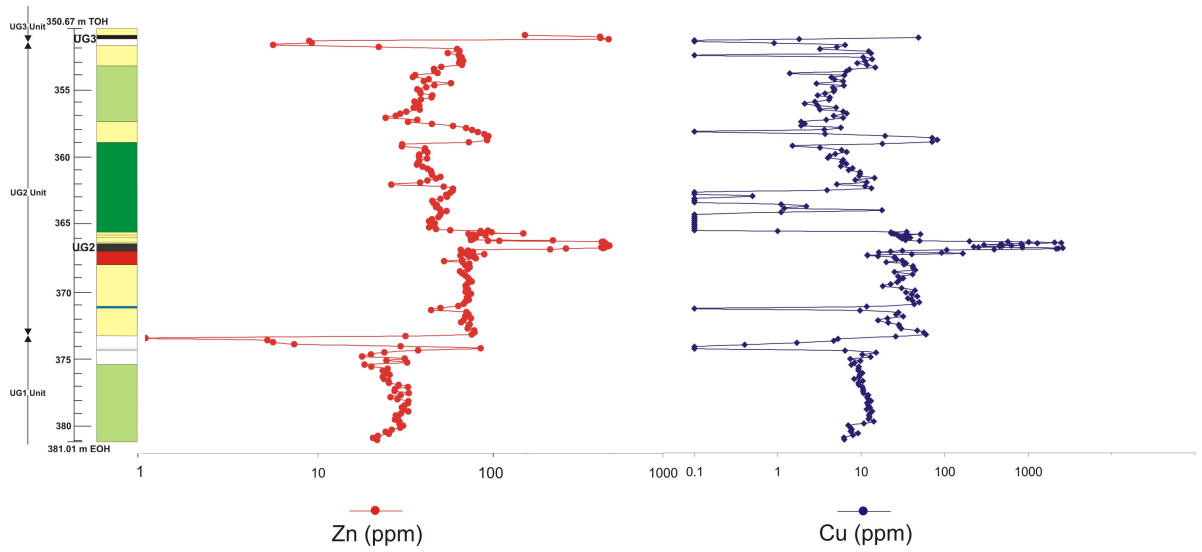

Figure 6.15: Variation of Zn (ppm) and Cu (ppm) through the study section.

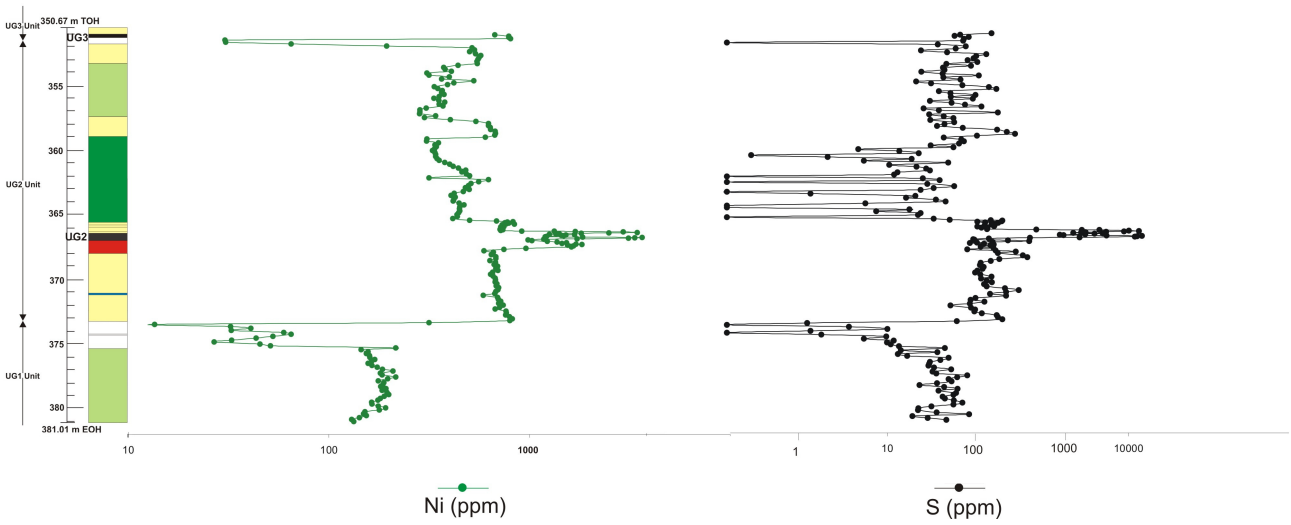

Figure 6.16: Variation of Ni (ppm) and S (ppm) through the study section.

The patterns of Cu, Ni and Zn all show certain similarities as well as distinct differences to that of S, thereby indicating that they are monitoring the variation of both the sulphide minerals as well as that of certain silicate minerals through the study section. All three of the base metals show highest values through the UG2 chromitite and the pegmatoidal pyroxenite footwall. This is a result of the enriched sulphide mineralization found within these two units. The three base metals also, however, show higher values through the pyroxenite units and lower values through the less mafic norite and anorthosite units. This is also true, to a certain extent, for the S profile pattern, although there are certain differences.

A normal fractionation trend is present in the entire section below the UG2 leuconorite. This is defined by an upward decreasing abundance of orthopyroxene (as well as those compatible elements which partition strongly into it). This is especially evident in the UG2 footwall feldspathic pyroxenite unit. The S profile, however, shows a contrasting pattern and exhibits an upward increasing abundance (leading up to the UG2 chromitite) through the footwall feldspathic pyroxenite unit. The base metal profile patterns through the footwall feldspathic pyroxenite unit are therefore a result of the dynamic interplay between decreasing modal abundances of orthopyroxene, coupled with increasing modal abundances of sulphide minerals, upward through the unit. The Zn pattern appears to be approximately equally modified by these two processes and shows no change in abundance through the unit whilst the Ni pattern appear to be biased toward, and more strongly controlled by, the decreasing orthopyroxene modal abundance through the unit as they show an upward decrease in abundance through the unit (in contrast to the S trend but sympathetic toward to the modal orthopyroxene trend). Cu, like S, is completely incompatible in the silicate minerals and partitions only into the sulphide minerals. Its profile pattern is, therefore, a result of the quantity as well as the compositional variation of the base-metal sulphide minerals. The upward decreasing trend in Cu through the footwall feldspathic pyroxenite, for example, is a result of systematic decreasing amounts of Cu-sulphide minerals (i.e. chalcopyrite) through the unit.

The base metal profile patterns have shown how they are monitoring both the quantity and compositional variation (i.e. S and Cu) of the sulphide minerals as well as of orthopyroxene (Zn and Ni) through the study section. Both Zn and Ni therefore partition favourably into orthopyroxene (as well as chromite), albeit on a scale of a few to several tens ppm. The S and Cu profiles, however, only monitor the amount and compositional variation of the sulphide minerals through the section.

6.5 Inter-Element Plots

This section presents a series of inter-element graphical plots (variation diagrams). Inter-elements plots are used to plot one element against another and can be used to evaluate the degree of correlation between the two elements. The diagrams presented show considerable detail with each of the different lithological units depicted by a different symbol and colour. This allows lithological trends (and mineral mixing lines) to be clearly exhibited. On each of the figures the idealized mineral compositions are provided (simple estimations).

The first set of plots are termed 'Harker' plots and they consist of SiO_2 plotted against another element. Figure 6.1 has already shown that SiO_2 exhibits the highest abundance in the pyroxenite units along with a systematic decrease through the norite units, the leuconorite units and into the anorthosite units as well as a sharp decrease in the chromitite layers (thereby indicating it to be controlled by the modal variation of orthopyroxene through the section). Plotting it against another element will show whether that element corresponds to this lithologically controlled variation (either positively or negatively) or not at all.

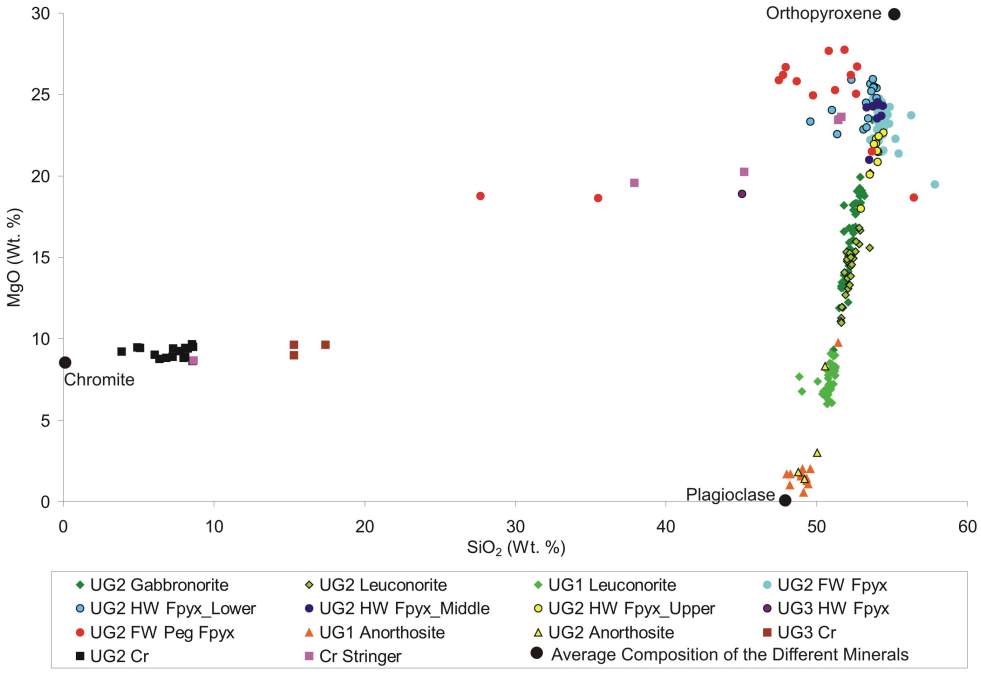

Figure 6.17: Plot of SiO_2 (Wt. %) vs. MgO (Wt. %).

The plot of MgO vs. SiO_2 (Figure 6.17) reveals a well defined kinked trend. A kinked trend is where the values are present in two different groups (or mixing lines), thereby indicating two controls on the distribution of the elements. Figure 6.17 shows that two positive trends are present. One showing a systematic increase in both the elements from the anorthosite units, through the leuconorite and norite units and finally into the feldspathic pyroxenite units (the plagioclase – orthopyroxene mixing line). The second trend is far less well defined and shows a decrease in both elements from the footwall pegmatoidal pyroxenite unit through the chromite stringers and into the UG3 and UG2 chromitite layers (chromite – orthopyroxene mixing line). Both these trends are controlled by the abundance of orthopyroxene through the section.

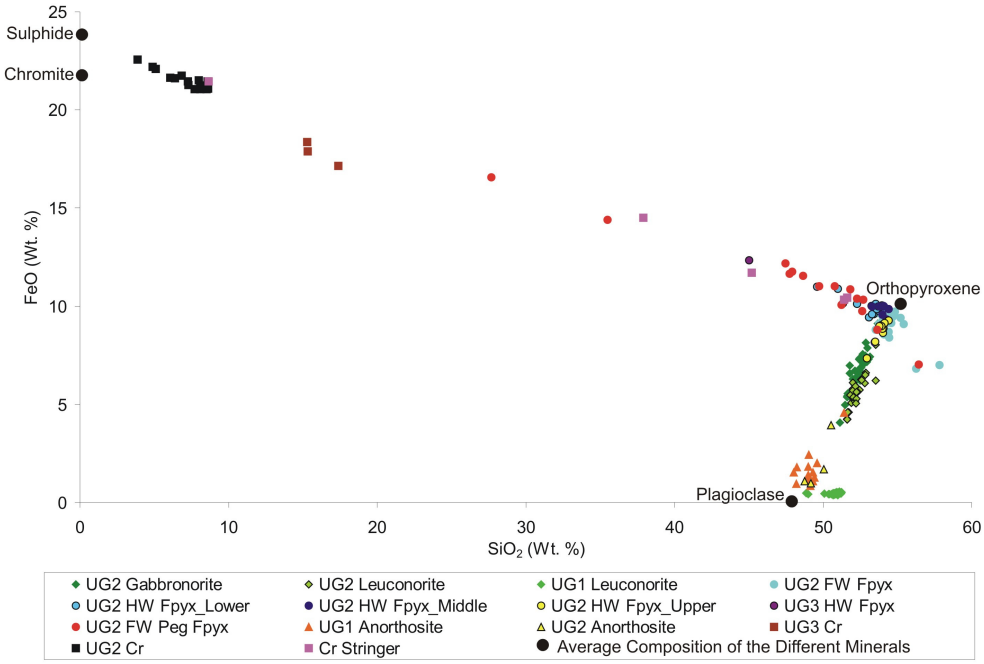

Figure 6.18: Plot of SiO_2 (Wt. %) vs. FeO (Wt. %).

The plot of SiO_2 vs. FeO (Figure 6.18) shows another well defined kinked trend, however this time it comprises one positive and one negative trend. The positive trend is controlled by the variation of orthopyroxene through the different lithologies (as with MgO). The negative trend, however, is a result of FeO also partitioning into chromite. This results in an increase in FeO (due to an increase in chromite) as well as a decrease in SiO_2 (due to decreasing orthopyroxene abundances) through the footwall pegmatoidal pyroxenite and into the chromitite layers. FeO is thus controlled by the distribution of both orthopyroxene and chromite as it partitions strongly into both these minerals.

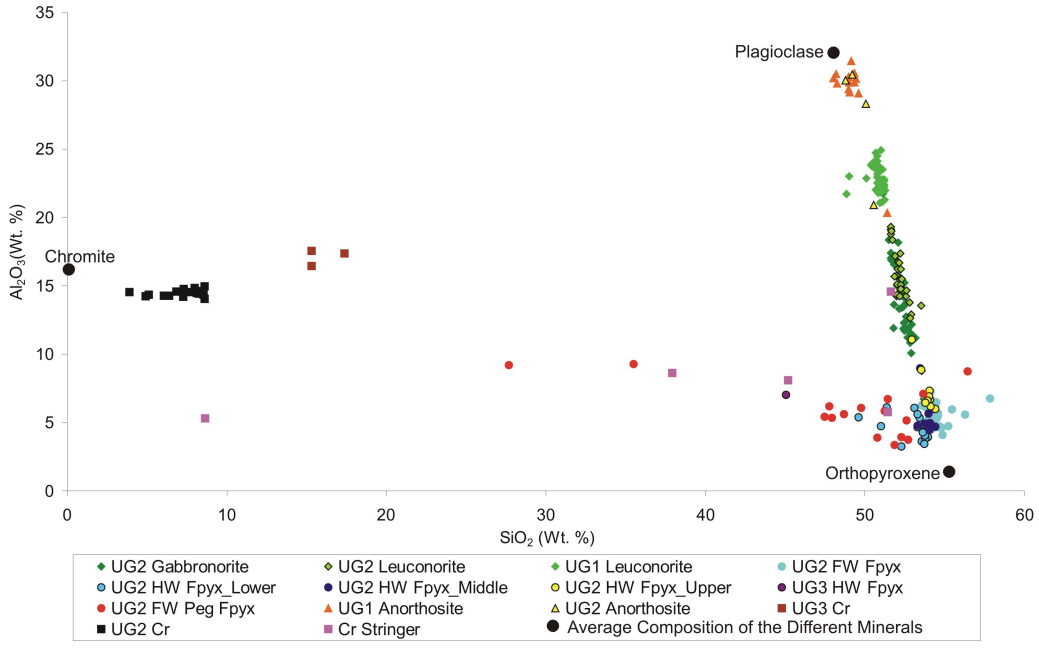

Figure 6.19: Plot of SiO_2 (Wt. %) vs. Al_2O_3 (Wt. %).

The plot of Al_2O_3 vs. SiO_2 (Figure 6.19) shows two kinked negative trends. One is well defined and is a result of Al_2O_3 partitioning strongly into plagioclase (whilst SiO_2 partitions less favourably into plagioclase than for orthopyroxene). The second trend is more poorly defined and it shows an increase of Al_2O_3 into the chromitite layers (along with a decrease in SiO_2). This reveals that Al_2O_3 partitions into (and is thus controlled by the variation of) both plagioclase and chromite.

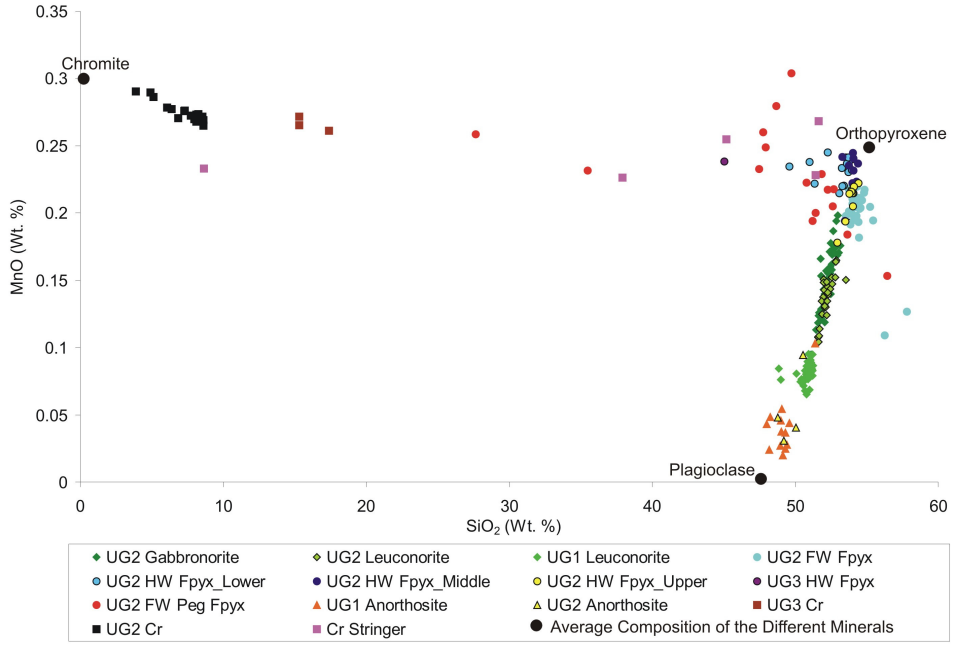

Figure 6.20: Plot of SiO_2 (Wt. %) vs. MnO (Wt. %).

The plot of MnO vs. SiO_2 (Figure 6.20) is very similar to that of FeO vs. SiO_2 (Figure 6.18) thereby indicating MnO to be partitioning into (and thus controlled by) both orthopyroxene and chromite (albeit in much lower abundances than FeO).

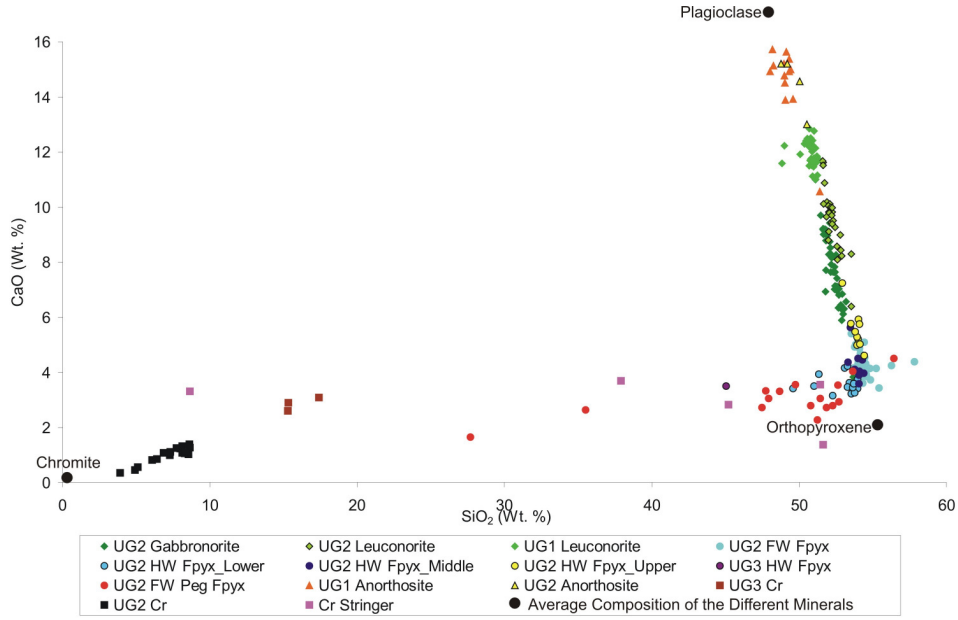

Figure 6.21: Plot of SiO_2 (Wt. %) vs. CaO (Wt. %).

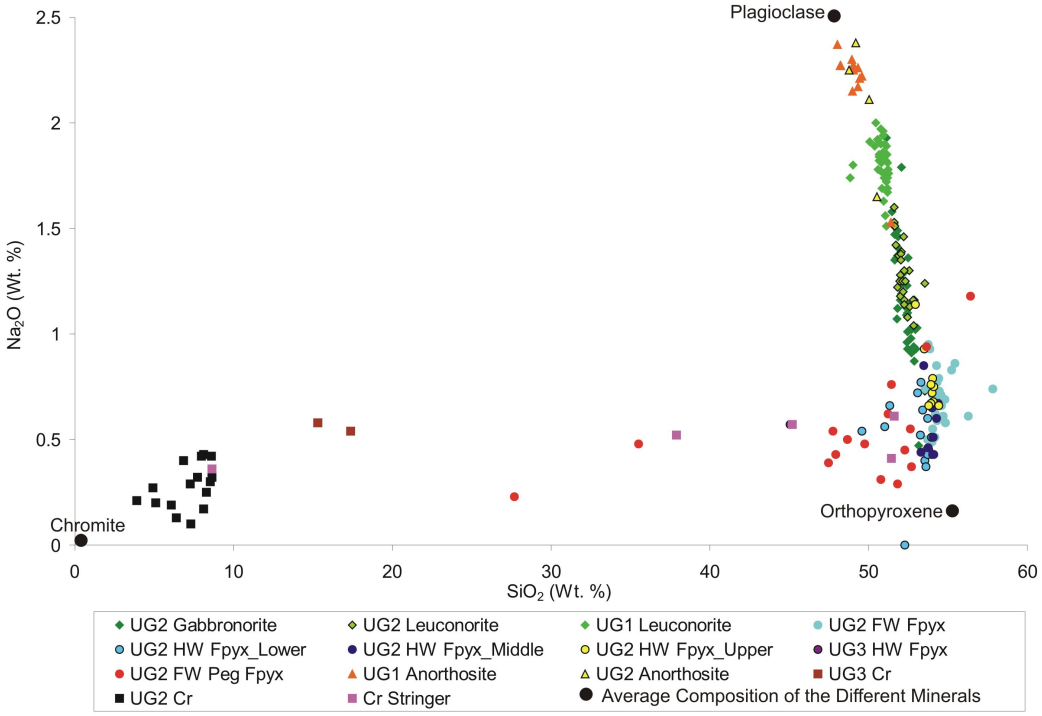

Figure 6.22: Plot of SiO_2 (Wt. %) vs. Na_2O (Wt. %).

Figures 6.21 and 6.22 (CaO and Na_2O respectively vs. SiO_2) show similar kinked positive and negative trends. These indicate both CaO and Na_2O to be solely controlled by the presence of plagioclase (i.e. they both partition into only plagioclase) i.e. they show a decrease from anorthosite through norite into pyroxenite (along with an increase in SiO_2) as well as a decrease into the chromitite layers (along with a decrease in SiO_2).

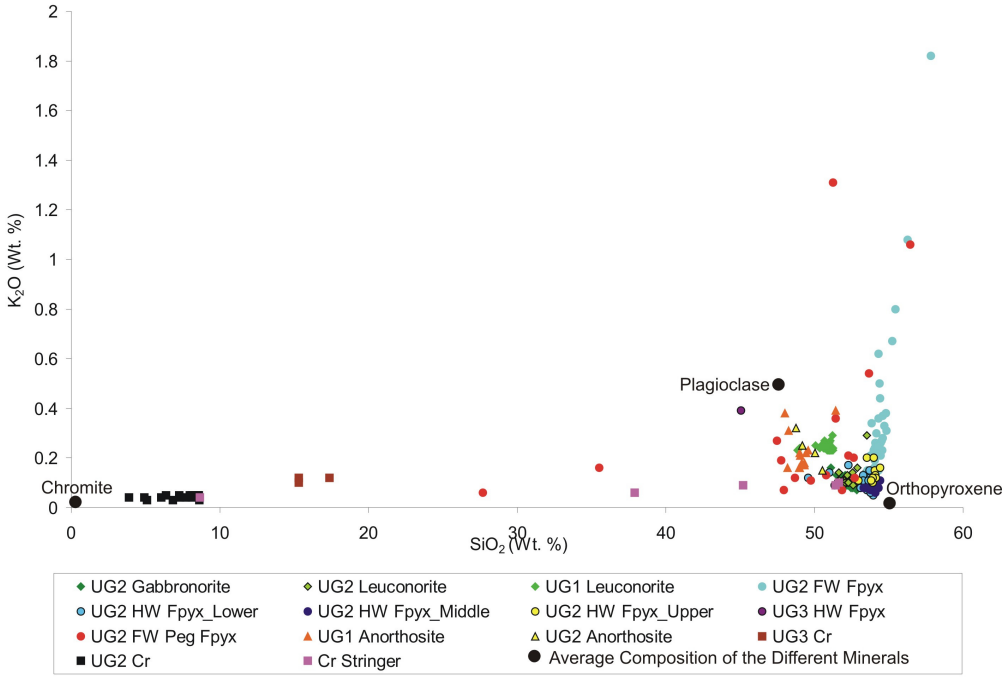

Figure 6.23: Plot of SiO_2 (Wt. %) vs. K_2O (Wt. %).

Figure 6.23 (SiO_2 vs. K_2O) shows two broad groups of values and no well defined trends (as opposed to the previous elements). K_2O is, as mentioned earlier, an element which is largely incompatible in the main cumulus minerals and thus remains behind to form part of the trapped interstitial liquid. It is therefore used to monitor the variation of the intercumulus liquid through the section. From Figure 6.23 it is evident that most of the lithological units contain only very small amounts of K_2O (and thus intercumulus matrix). Only the UG2 footwall feldspathic pyroxenite unit reveals a trend of increasing K_2O values, along with a slight increase in SiO_2 through it. This unit thereby contains a greater proportion of interstitial matrix (representing crystallized trapped interstitial liquid) as opposed to the other lithological units (and more interestingly other pyroxenite units).

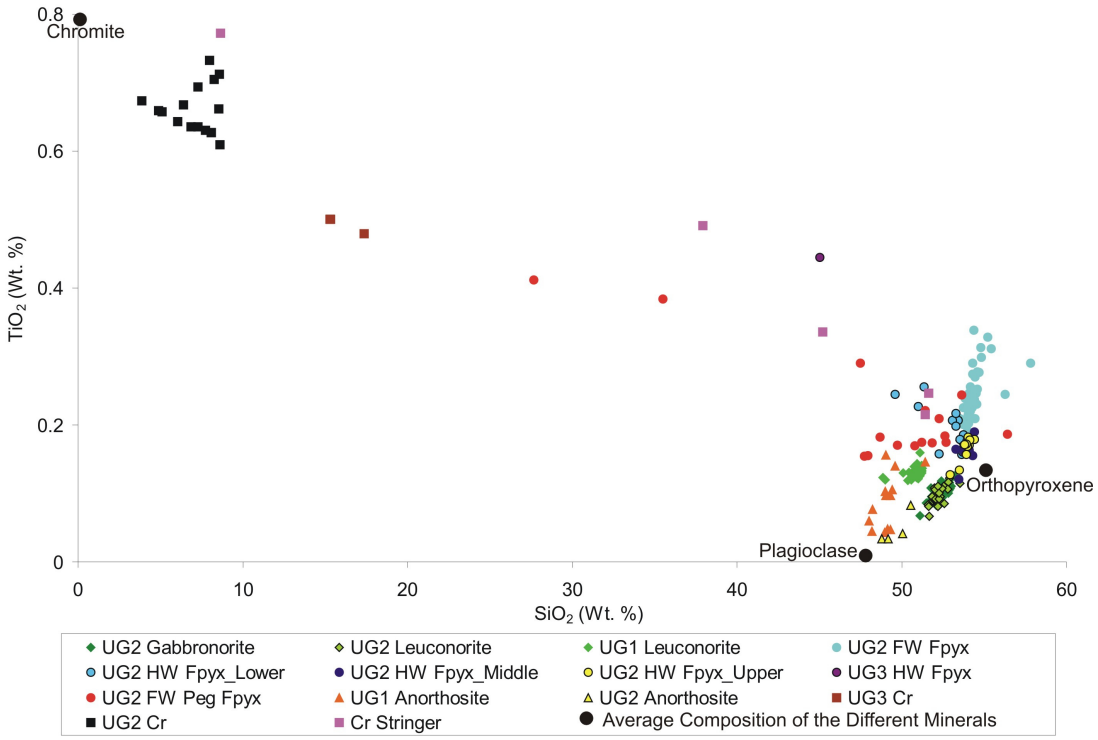

Figure 6.24: Plot of SiO_2 (Wt. %) vs. TiO_2 (Wt. %).

Both TiO_2 (Figure 6.24) and Zr (Figure 6.25) behave in a similar fashion to K_2O and, due to their incompatibility in the main cumulus minerals, remain behind and are concentrated in the trapped interstitial liquid. Both these plots confirm the observation from Figure 6.23 in that the UG2 footwall feldspathic pyroxenite unit contains the highest amount of interstitial matrix. Figure 6.24, however, also shows an enrichment of TiO_2 into the chromitite layers thereby indicating it to partition strongly into chromite.

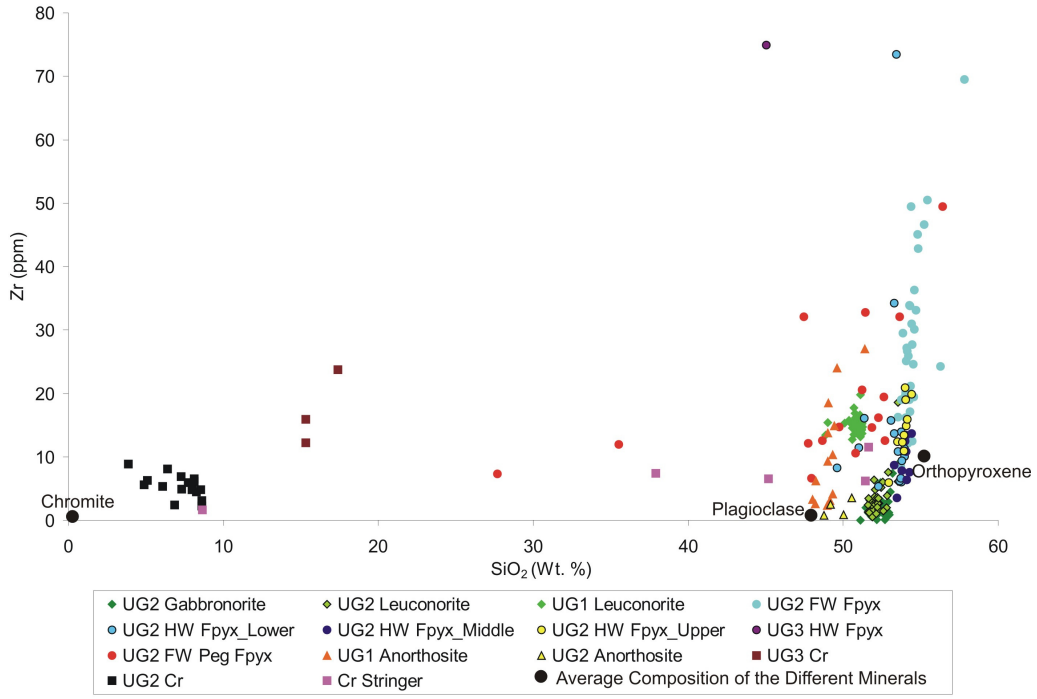

Figure 6.25: Plot of SiO_2 (Wt. %) vs. Zr (ppm).

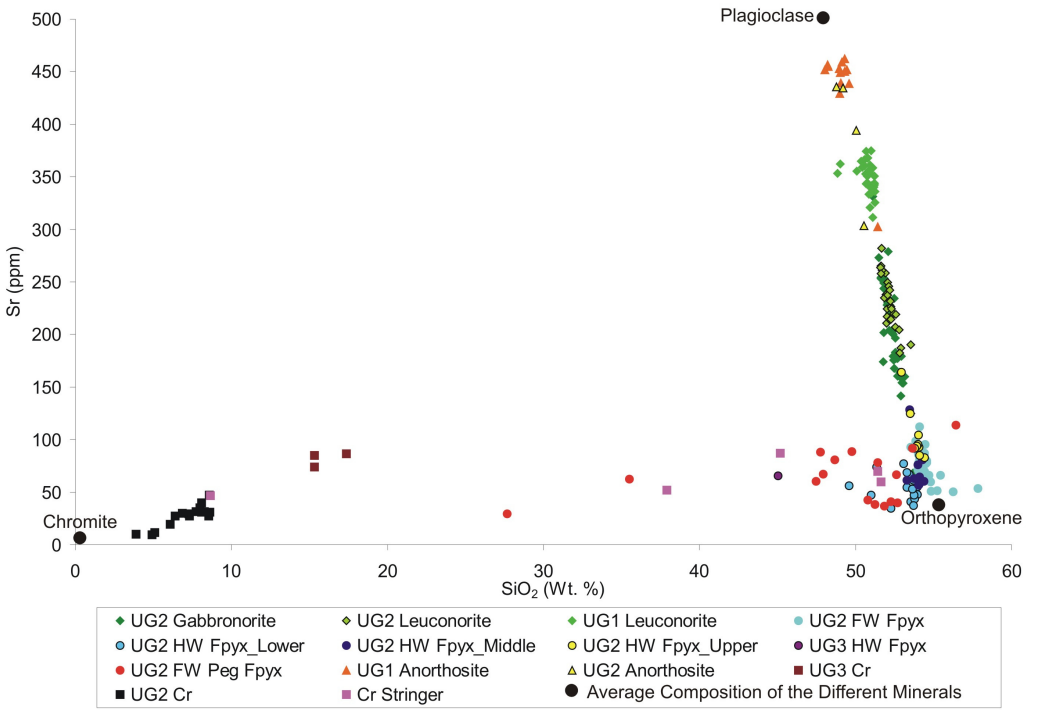

Figure 6.26: Plot of SiO_2 (Wt. %) vs. Sr (ppm).

Although Sr is a trace element it has been shown earlier (Figure 6.13) to partition strongly into plagioclase. This is confirmed by Figure 6.26 in which a negative and a positive trend are exhibited. This is due to Sr monitoring plagioclase variation whilst SiO_2 monitors orthopyroxene variation (as it partitions more strongly into it than plagioclase) through the section.

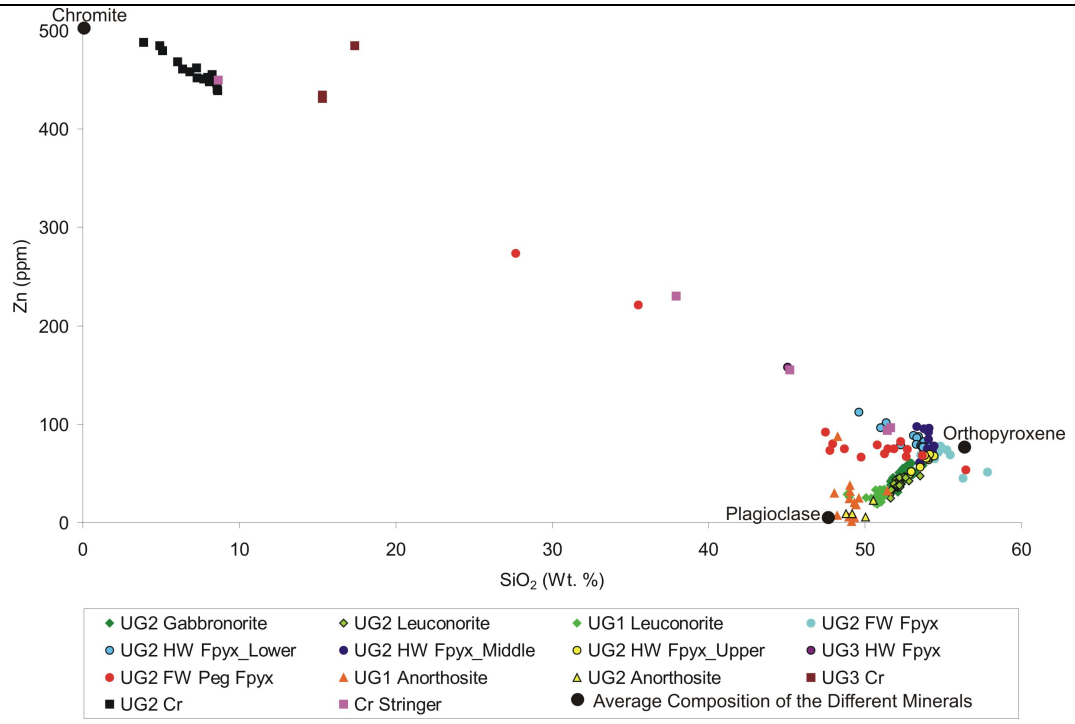

Figure 6.27: Plot of SiO_2 (Wt. %) vs. Zn (ppm).

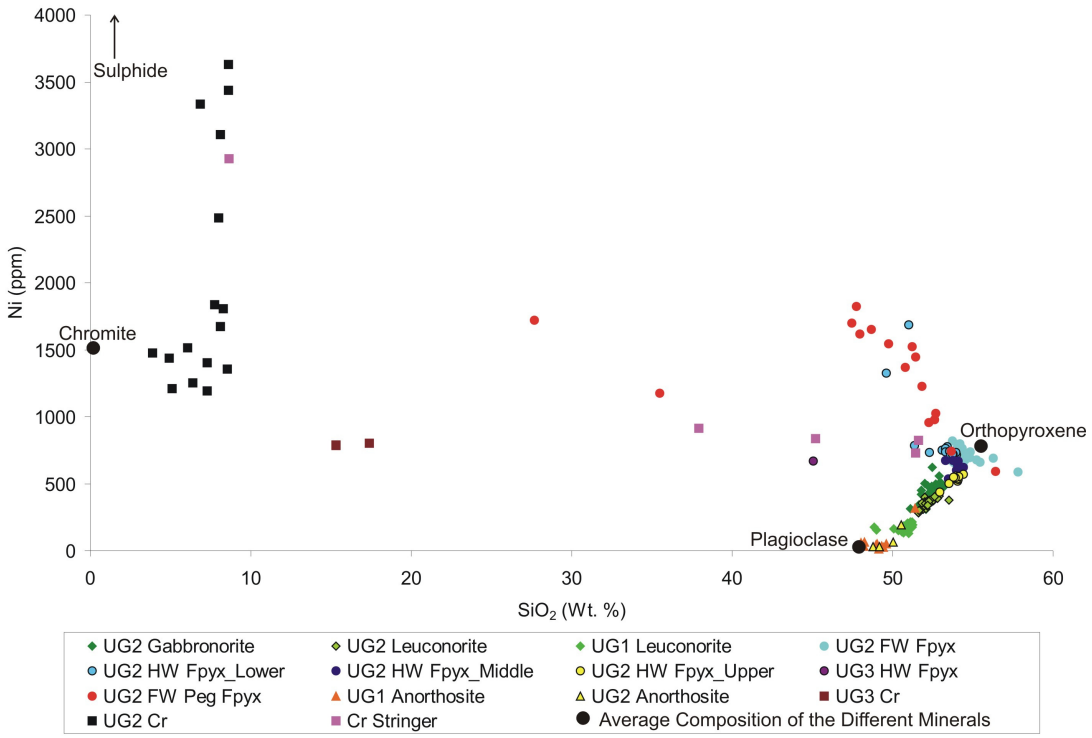

Figure 6.28: Plot of SiO_2 (Wt. %) vs. Ni (ppm).

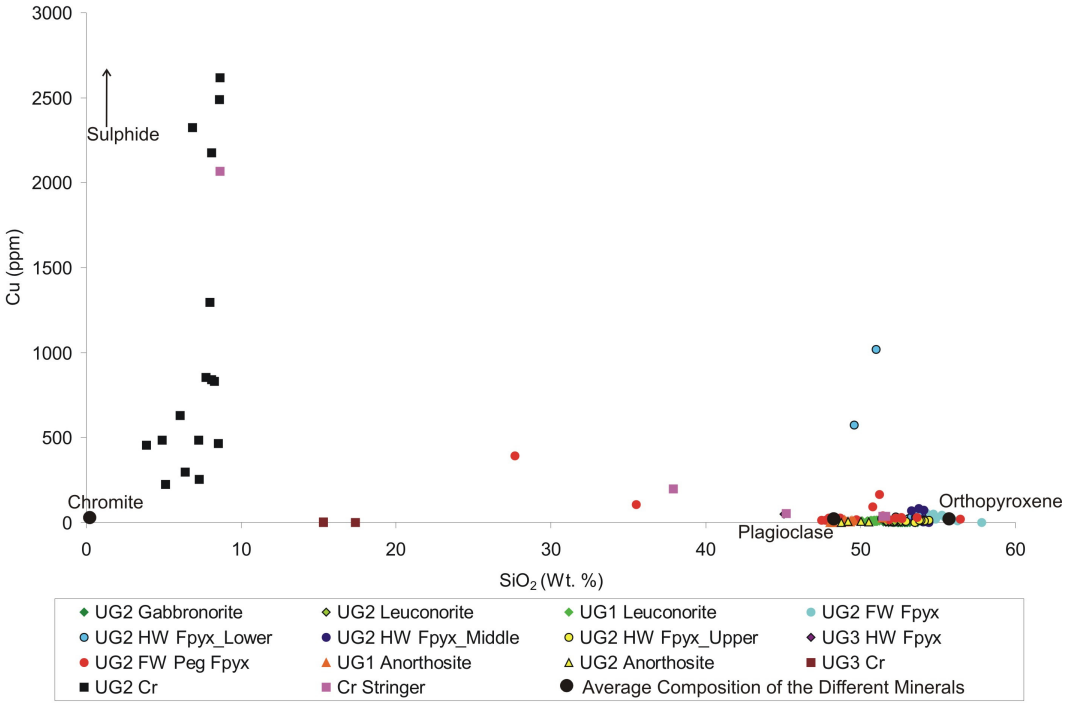

Figure 6.29: Plot of SiO_2 (Wt. %) vs. Cu (ppm).

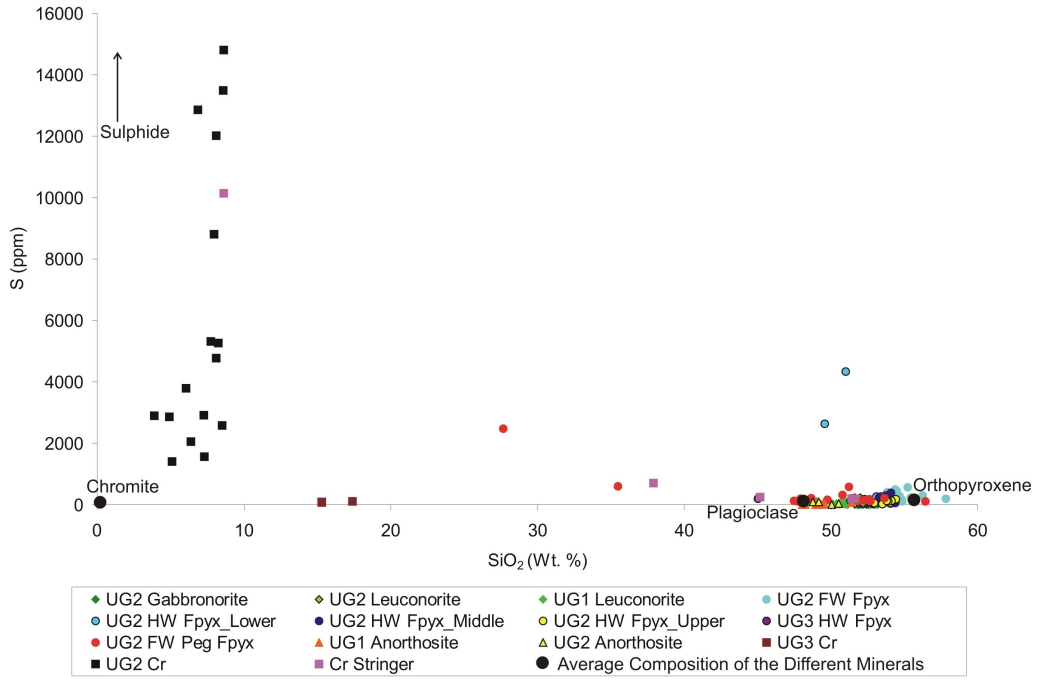

Figure 6.30: Plot of SiO_2 (Wt. %) vs. S (ppm).

The Harker plots of Zn (Figure 6.27), Ni (Figure 6.28), Cu (Figure 6.29) and S (Figure 6.30) reveal some interesting patterns. The plots of Zn and Ni confirm earlier observations that these elements are controlled by more than one factor. Both elements partition into orthopyroxene, albeit in small abundances, as is exhibited by the well defined positive trend in both the plots (Figures 6.27 and 6.28). Figure 6.27 then

exhibits a second, well defined negative trend which confirms that Zn partitions into chromite. The well defined negative trend is defined by increasing Zn and decreasing SiO_2 through those units containing cumulus chromite. The Ni plot, Figure 6.28, however, shows a range of Ni values through the UG2 chromitite but at no relation to SiO2 variation. Therefore the variation of Ni through the chomitite is controlled not by cumulus chromite abundance, as with Zn, but rather base-metal sulphide mineralization. Therefore the Zn pattern is controlled by cumulus orthopyroxene and chromite whilst Ni abundance is controlled by orthopyroxene and base-metal sulphide variation (and composition).

In contrast to both Zn and Ni, Cu and S (Figures 6.29 and 6.30 respectively) are completely incompatible to the silicate minerals and partition only into, and are controlled solely by, the base-metal sulphide minerals. Therefore, both the Cu and S distributions, as well as the Ni distribution within the chromitite layers, are controlled solely by the quantity, and compositional variation, of the base-metal sulphides. Conversely, both Zn and Ni partition into orthopyroxene, whilst Zn also partitions strongly into chromite.

The plots of MgO vs. FeO (Figure 6.31), MnO vs. FeO (Figure 6.32) and MgO vs. MnO (Figure 6.33) all exhibit well defined positive trends for the silicate lithologies as well as a separated group of values, showing no distinct trends, for the chromitite layers. MgO, FeO and MnO all partition strongly into orthopyroxene resulting in a well defined positive trend, when plotted against each other, for the silicate lithologies. For the chromitite layers, however, only Figure 6.32 reveals a positive trend (due to both FeO and MnO partitioning into chromite) whilst both Figures 6.31 and 6.33 show only a separate group of values.

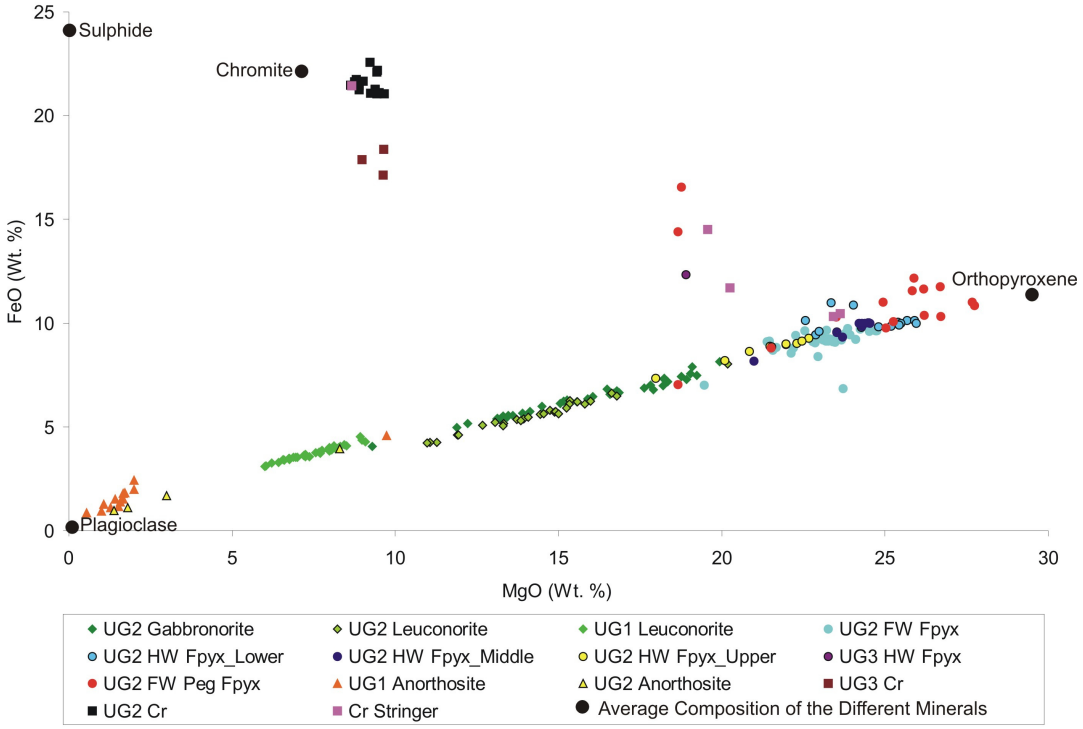

Figure 6.31: Plot of MgO (Wt. %) vs. FeO (Wt. %).

It is also important to note that the linear mixing relationship between plagioclase and orthopyroxene exhibited in Figure 6.31 illustrates an almost uniform Mg# regardless of the ratio of plagioclase to orthopyroxene in the rocks, with the UG1 anorthosite and leuconorite units deviating slightly from this trend due to a slightly lower Mg#.

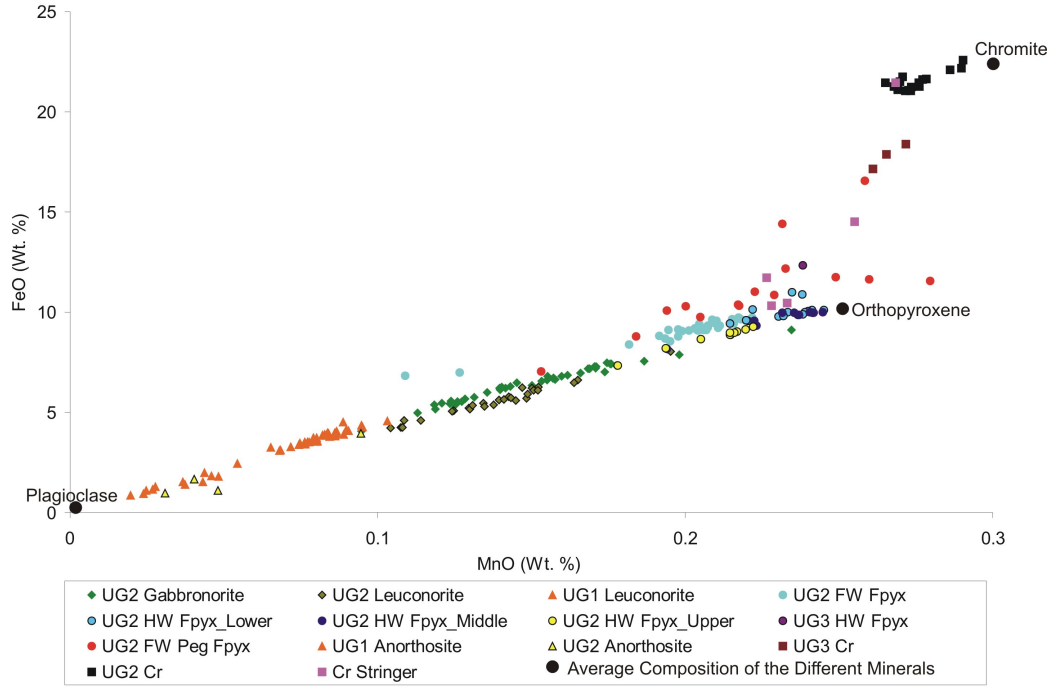

Figure 6.32: Plot of MnO (Wt. %) vs. FeO (Wt. %).

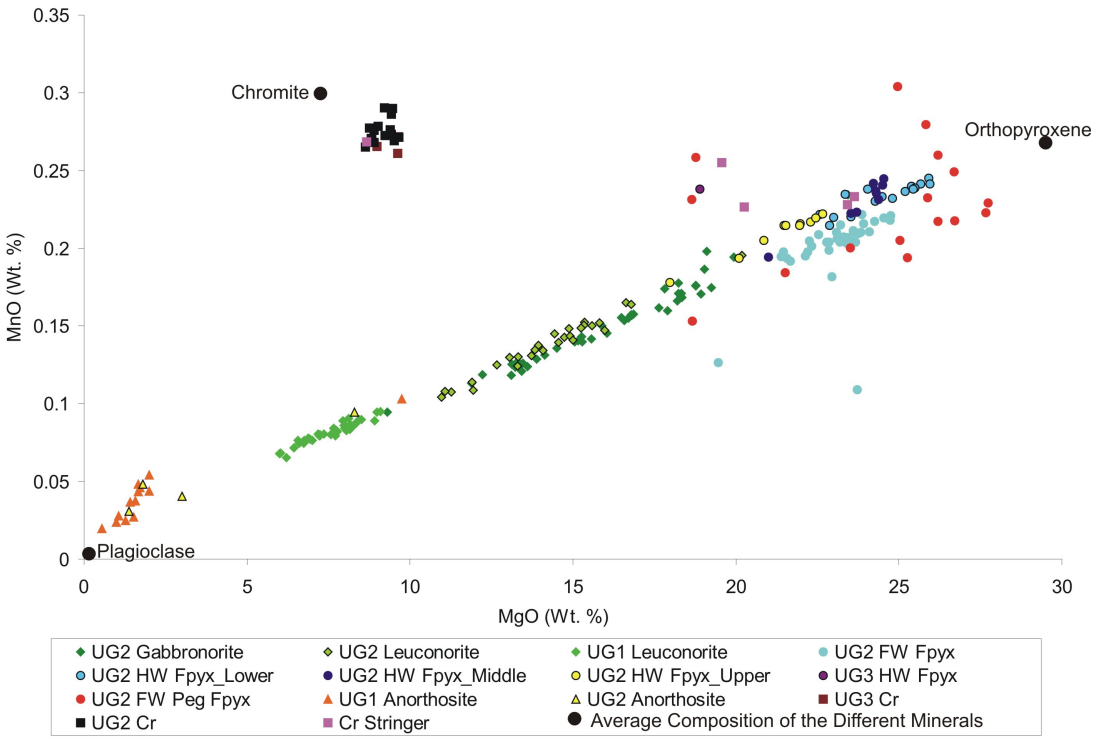

Figure 6.33: Plot of MgO (Wt. %) vs. MnO (Wt. %).

The plots of MnO vs. Al_2O_3 (Figure 6.34), MgO vs. Al_2O_3 (Figure 6.35) and FeO vs. Al_2O_3 (Figure 6.36) all show well defined negative trends for the silicate lithologies as well as a separate group of values, showing no trend, for the chromitite layers. This is because Al_2O_3 partitions strongly into plagioclase whilst FeO, MnO and MgO all partition strongly into orthopyroxene.

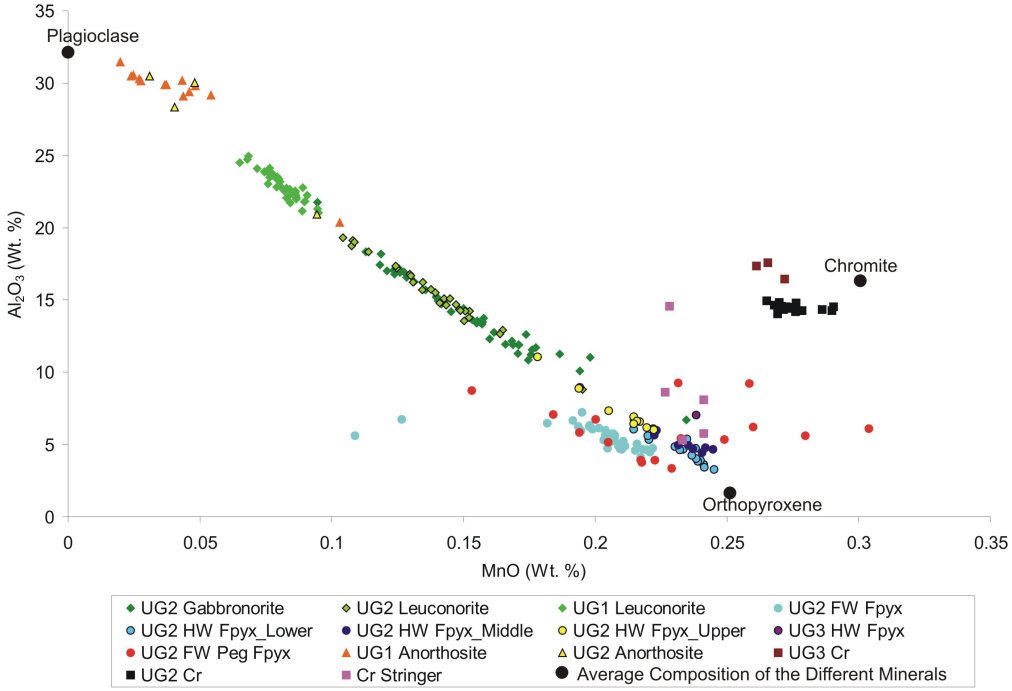

Figure 6.34: Plot of Al_2O_3 (Wt. %) vs. MnO (Wt. %).

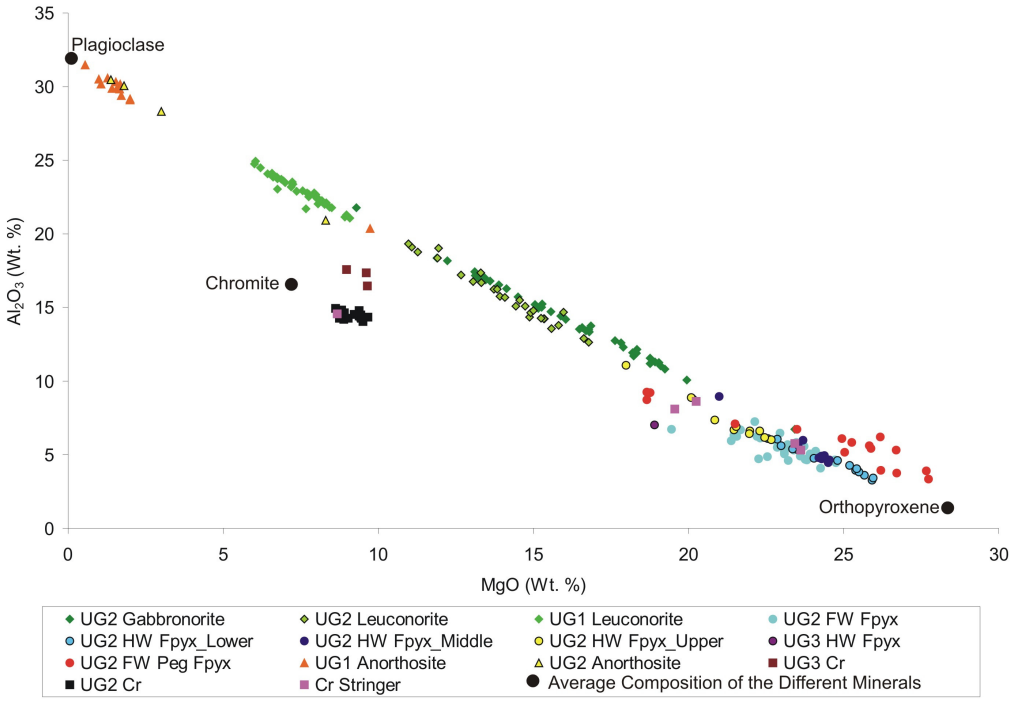

Figure 6.35: Plot of Al_2O_3 (Wt. %) vs. MgO (Wt. %).

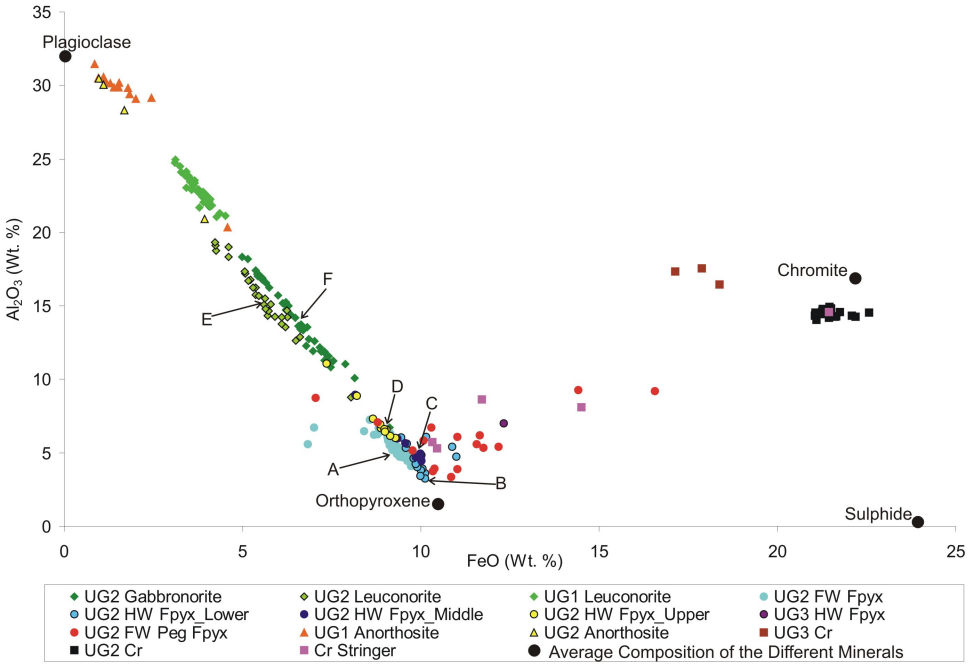

Figure 6.36: Plot of Al_2O_3 (Wt. %) vs. FeO (Wt. %); A = UG2 FW feldspathic pyroxenite, B = UG2 HW lower feldspathic pyroxenite, C = UG2 HW middle feldspathic pyroxenite, D = UG2 HW upper feldspathic pyroxenite. Note the distinct separation of the above units into groups.

Both the plots of Al_2O_3 vs. CaO (Figure 6.37) and Al_2O_3 vs. Na_2O (Figure 6.38) show strong positive trends. This is because Al_2O_3, CaO and Na_2O all partition strongly into plagioclase. The positive trend, however, shows a greater degree of variation and irregularity as opposed to the positive trends defined by those elements which partition into orthopyroxene (i.e. FeO and MnO). This confirms earlier conclusions in that the plagioclase composition evolves through the section (and thus show a greater range of CaO and Na_2O values).

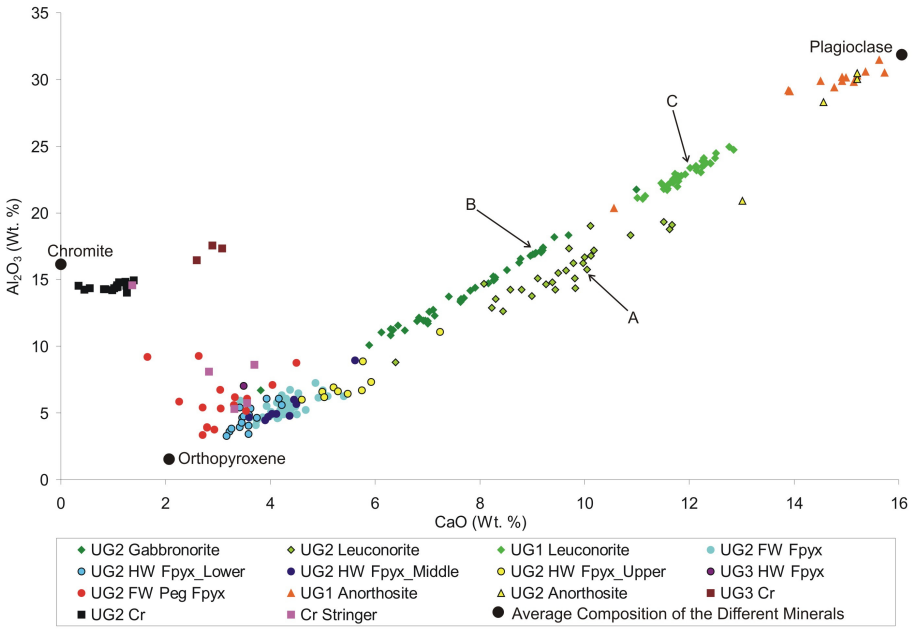

Figure 6.37: Plot of Al_2O_3 (Wt. %) vs. CaO (Wt. %); A = UG2 leuconorite, B = UG2 gabbronorite, C = UG1 leuconorite. Note the distinct separation of these units into well defined groups.

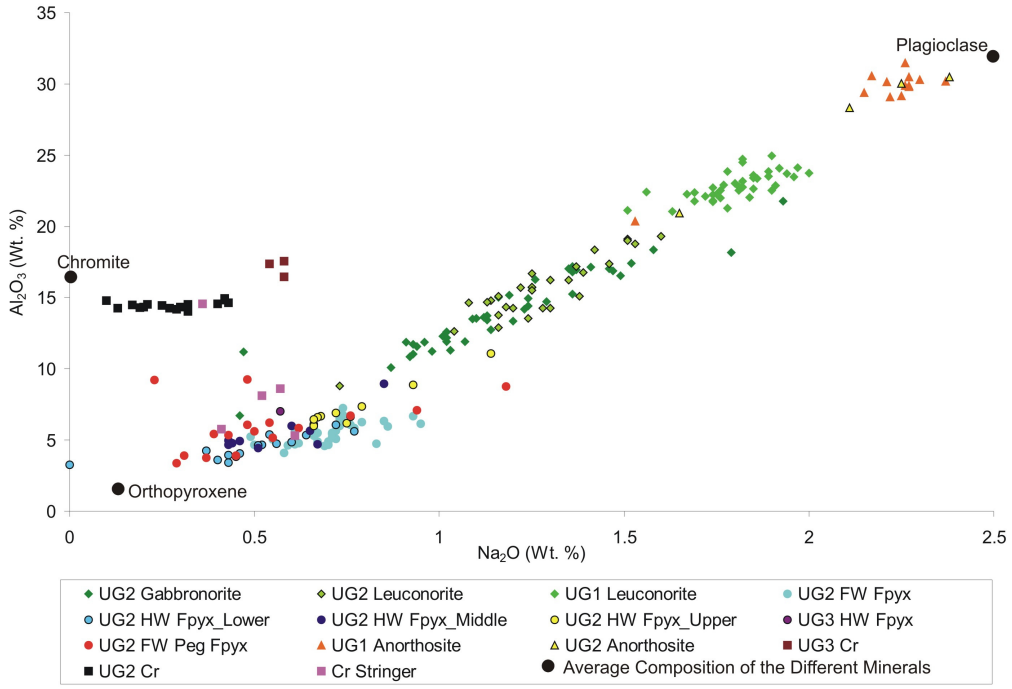

Figure 6.38: Plot of Al_2O_3 (Wt. %) vs. Na_2O (Wt. %).

The plots of FeO vs. CaO (Figure 6.39), FeO vs. Na_2O (Figure 6.40) and MnO vs. CaO (Figure 6.41) all exhibit well defined negative trends. This is due to CaO and Na_2O partitioning favourably into plagioclase whilst FeO and MnO partition strongly into orthopyroxene. An interesting point is that, for the CaO plots, the negative trend continues through into the chromitite layers. This is most likely a result of there being appreciable amounts of plagioclase present in the chromitites.

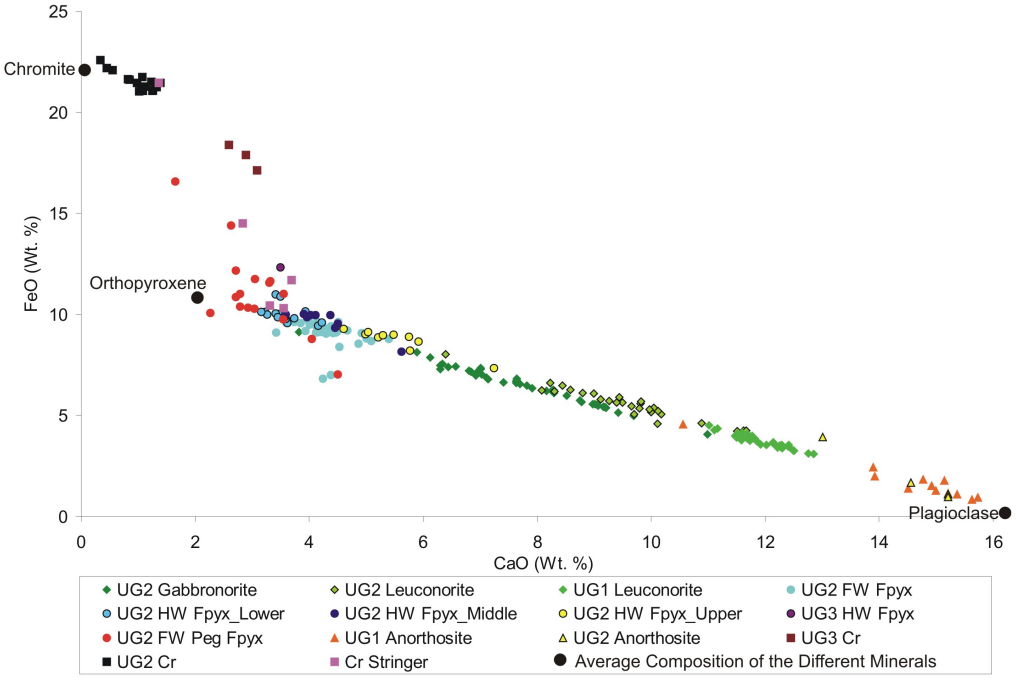

Figure 6.39: Plot of FeO (Wt. %) vs. CaO (Wt. %).

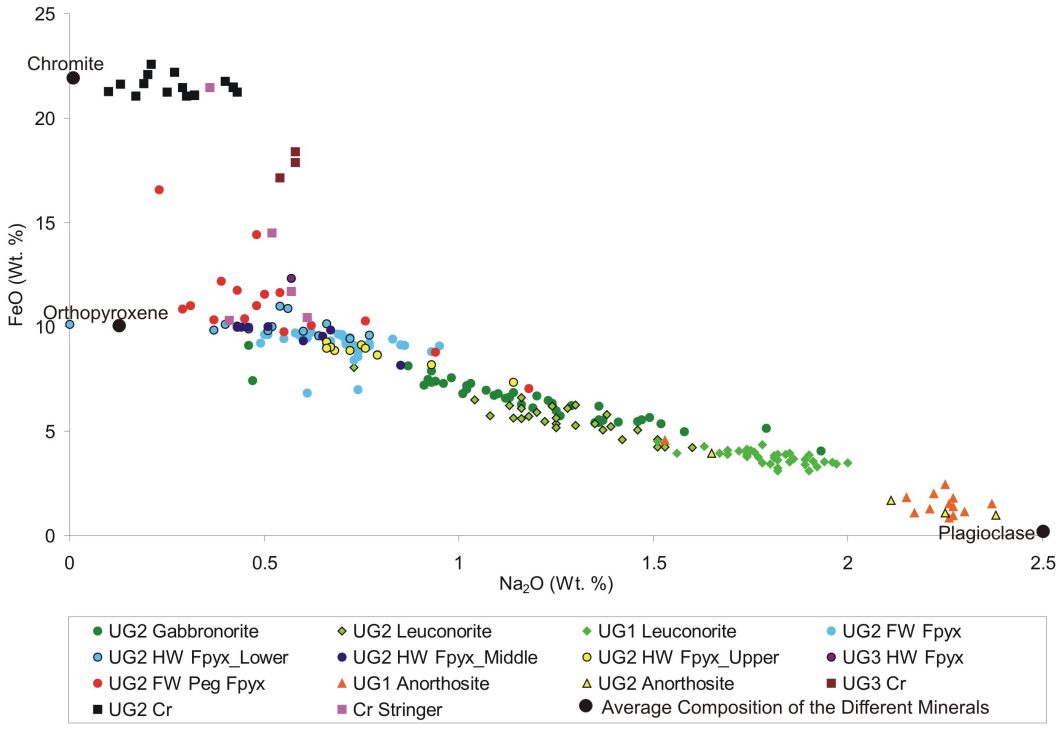

Figure 6.40: Plot of FeO (Wt. %) vs. Na_2O (Wt. %).

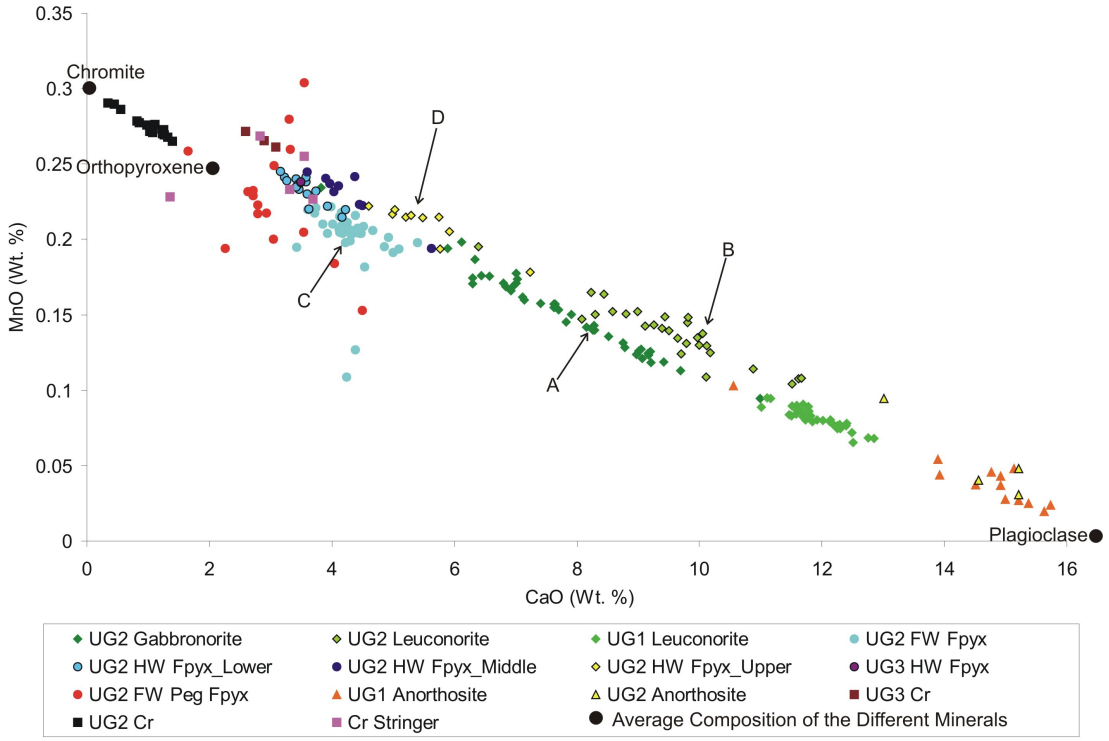

Figure 6.41: Plot of MnO (Wt. %) vs. CaO (Wt. %); A = UG2 gabbronorite, B = UG2 leuconorite, C = UG2 FW feldspathic pyroxenite, D = UG2 HW upper feldspathic pyroxenite. The above units exhibit values which tend to plot in distinct groups.

The plots of MnO vs. Na_2O (Figure 6.42), MgO vs. CaO (Figure 6.43) and MgO vs. Na_2O (Figure 6.44) all show strong negative trends. Figures 6.43 and 6.44 both confirm that MgO does partition into chromite.

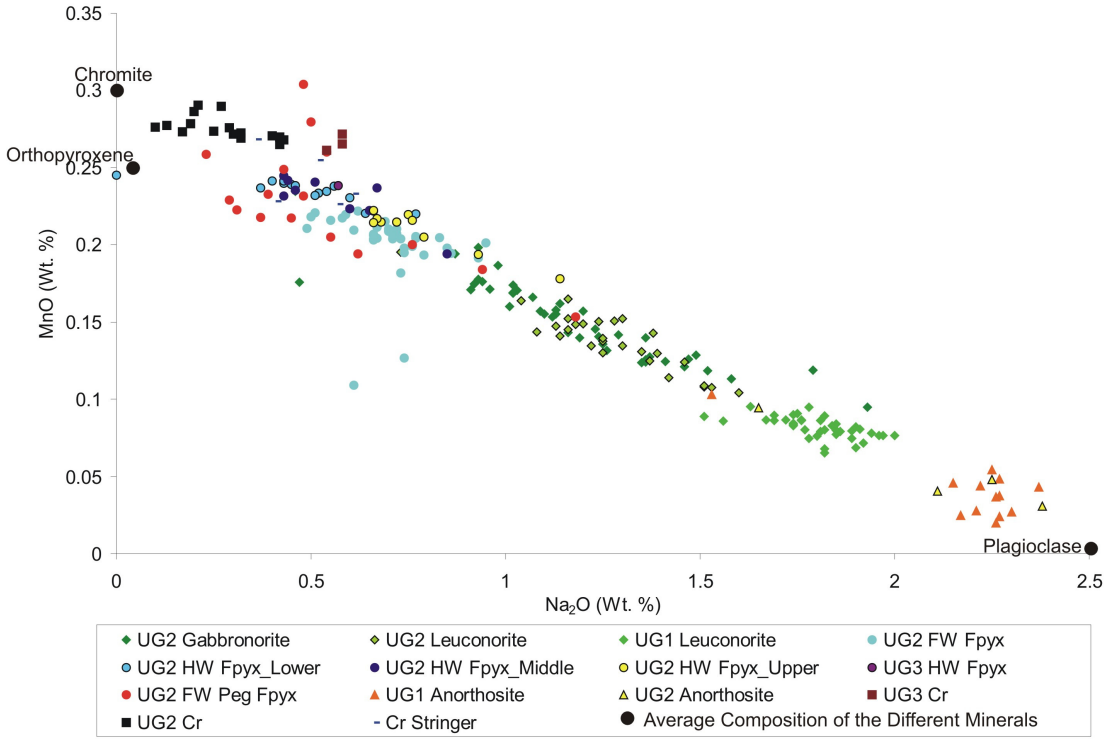

Figure 6.42: Plot of MnO (Wt. %) vs. Na_2O (Wt. %).

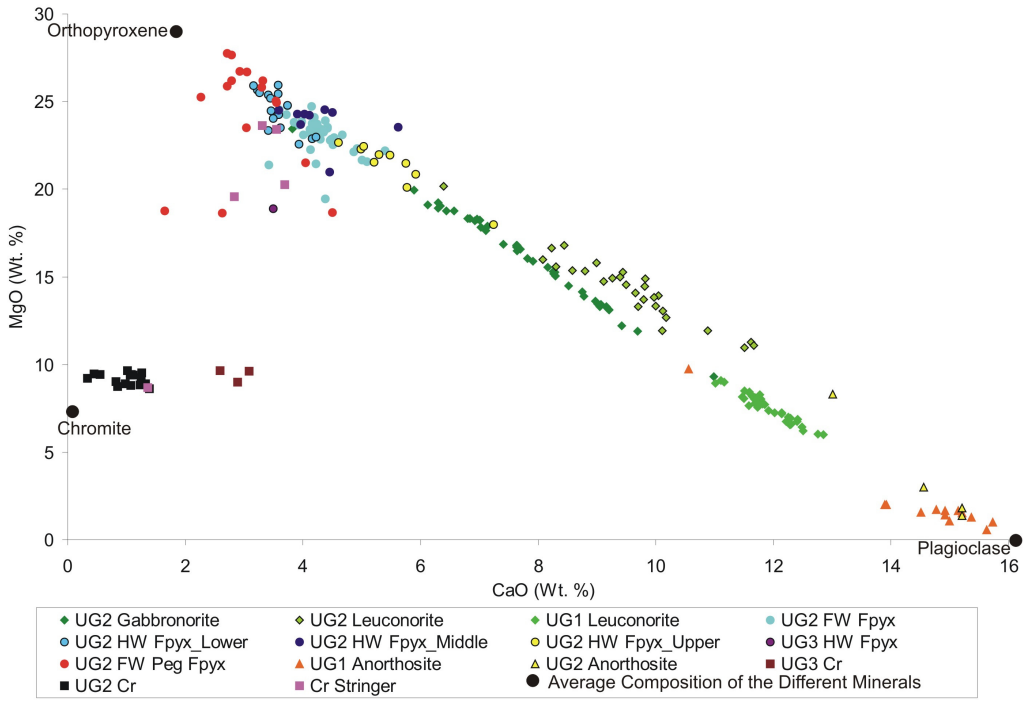

Figure 6.43: Plot of MgO (Wt. %) vs. CaO (Wt. %).

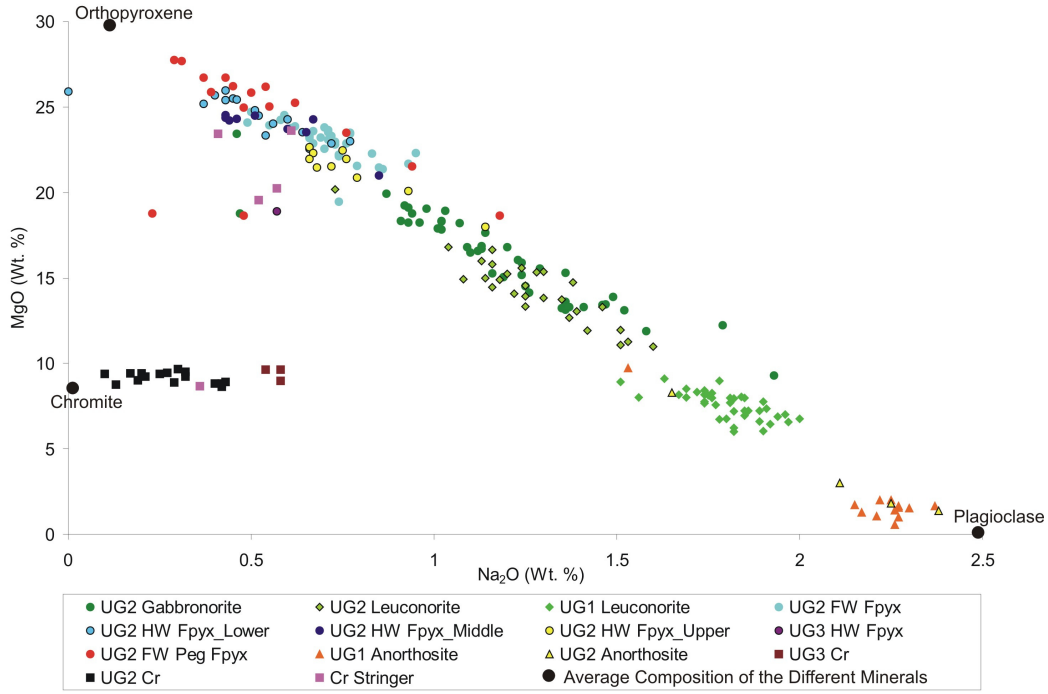

Figure 6.44: Plot of MgO (Wt. %) vs. Na_2O (Wt. %).

Figures 6.45 (CaO vs. Na_2O) and 6.46 (Al_2O_3 vs. Sr) both show positive trends. As mentioned earlier, there is a greater range in Na_2O and CaO values probably due to evolving plagioclase compositions through the study section. Conversely, the Al_2O_3 and Sr values are well constrained and show little variation apart from for the chromitite samples due to Al_2O_3 also partitioning strongly into chromite.

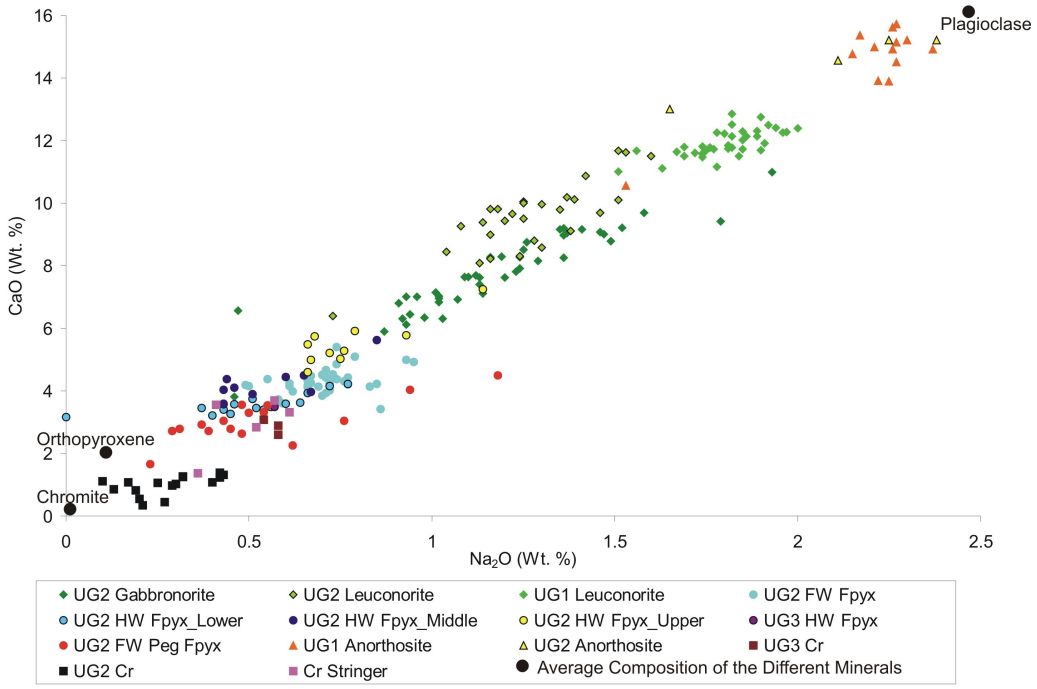

Figure 6.45: Plot of CaO (Wt. %) vs. Na_2O (Wt. %).

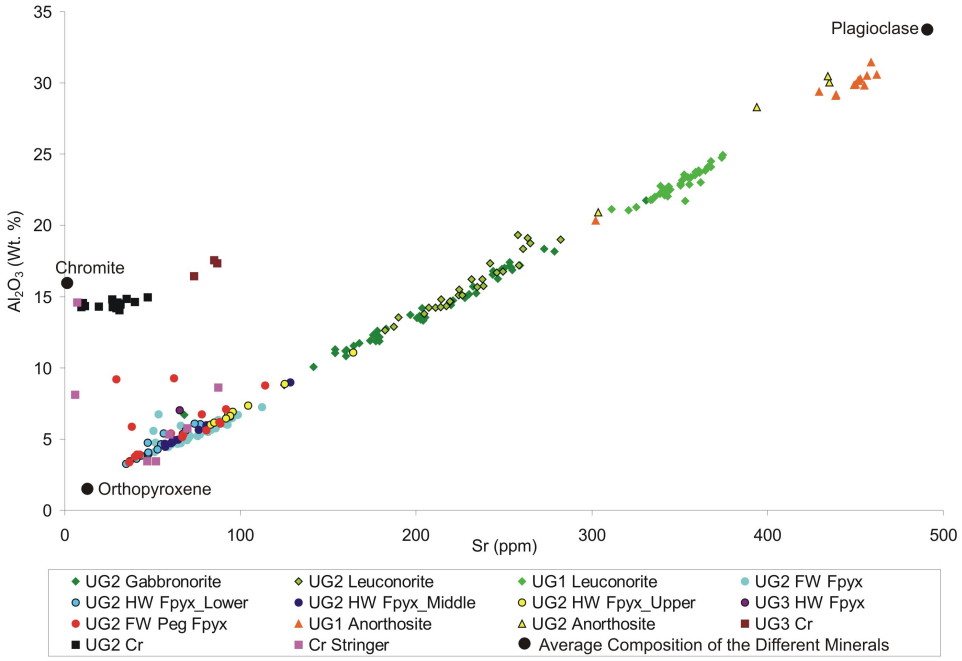

Figure 6.46: Plot of Al_2O_3 (Wt. %) vs. Sr (ppm).

The plots of FeO vs. Sr (Figure 6.47), MnO vs. Sr (Figure 6.48) and MgO vs. Sr (Figure 6.49) all show strong negative trends. What is interesting with these three plots though is that they highlight the varying partitioning strength of FeO, MnO and MgO into chromite. MgO does partition (not strongly) into chromite (defined by a displaced range of low values for the chromitites), MnO does partition into chromitite (defined by a continuous trend through the silicates and chromitites) and FeO partitions very strongly into chromite (defined by displaced high values for the chromitites).

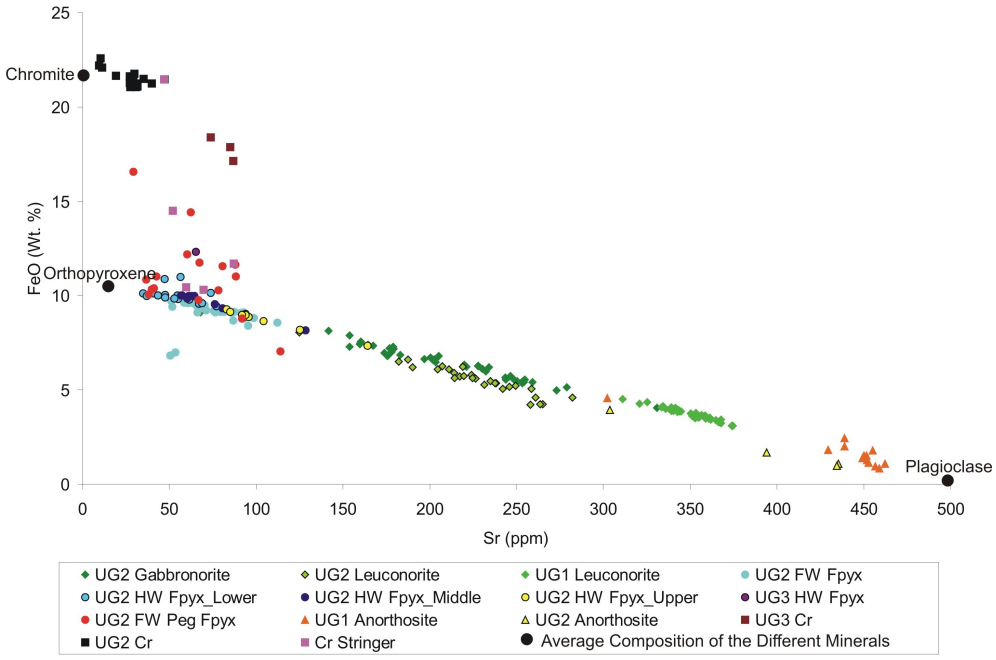

Figure 6.47: Plot of FeO (Wt. %) vs. Sr (ppm).

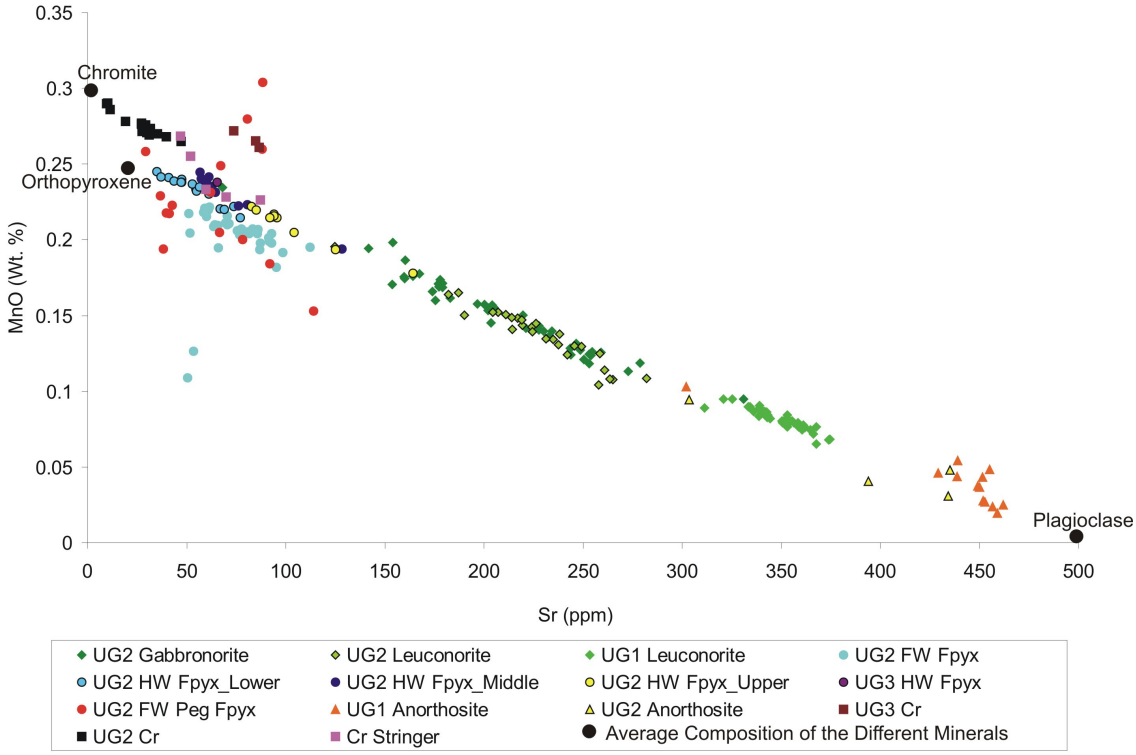

Figure 6.48: Plot of MnO (Wt. %) vs. Sr (ppm).

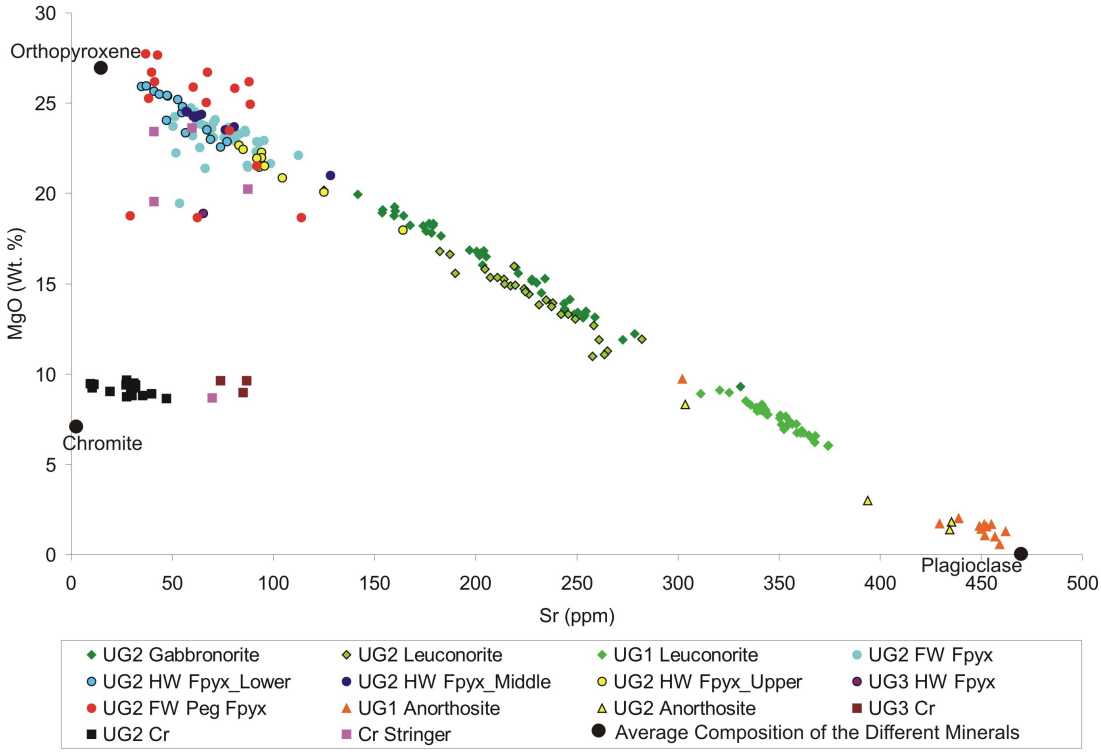

Figure 6.49: Plot of MgO (Wt. %) vs. Sr (ppm).

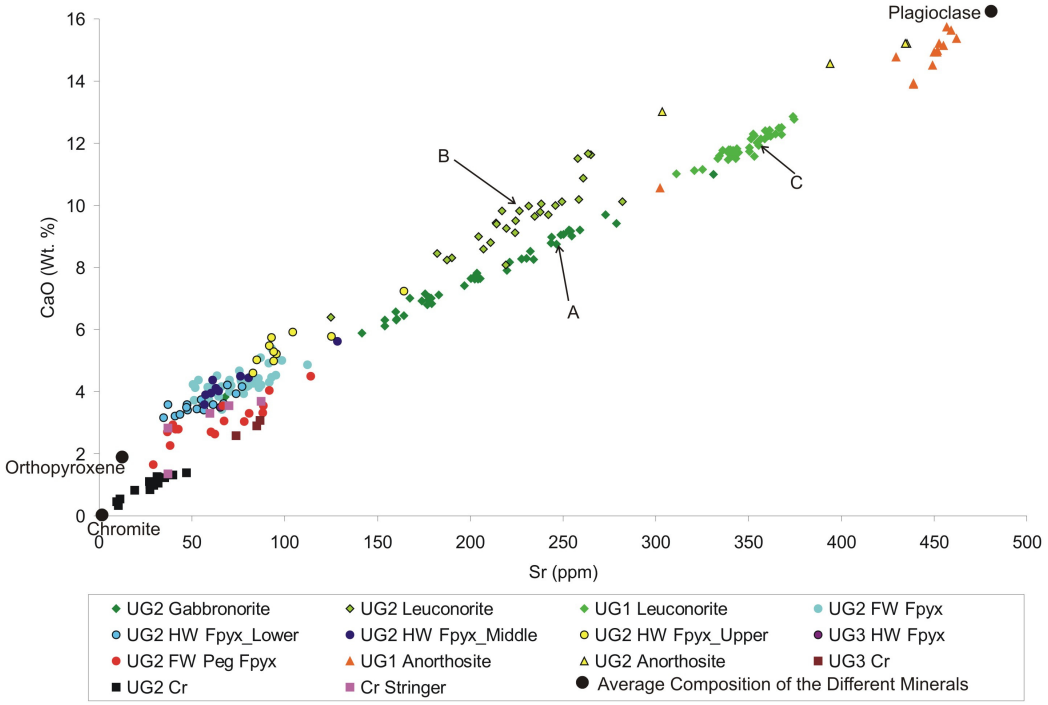

Figure 6.50: Plot of CaO (Wt. %) vs. Sr (ppm); A = UG2 gabbronorite, B = UG2 leuconorite, C = UG1 leuconorite. Note the separate groups of these units.

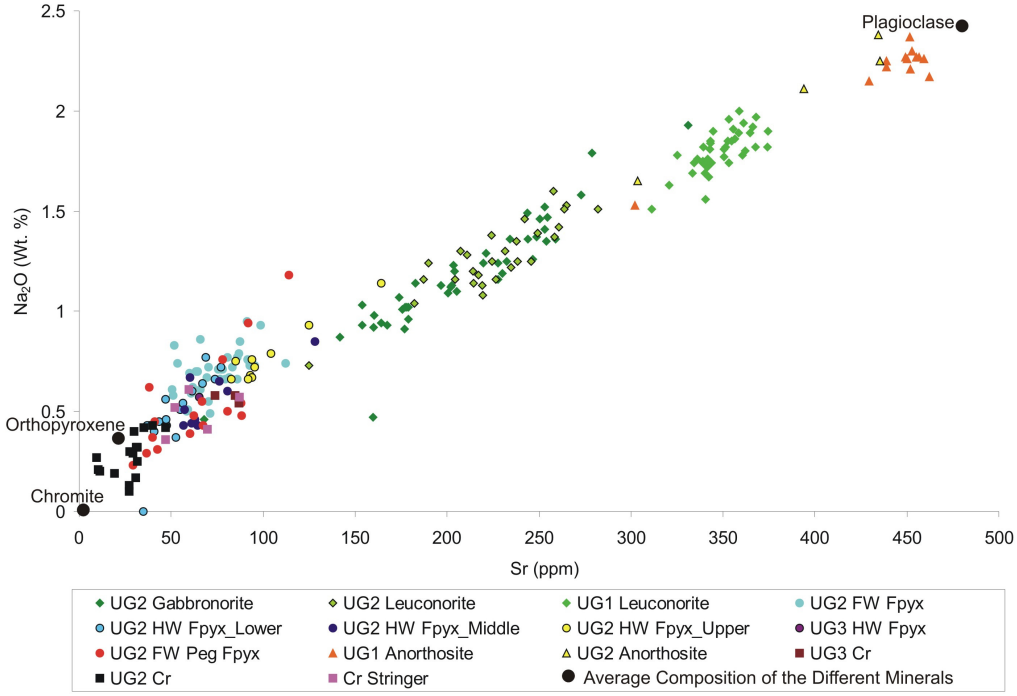

Figure 6.51: Plot of Na_2O (Wt. %) vs. Sr (ppm).

Figures 6.50 (CaO vs. Sr) and 6.51 (Na_2O vs. Sr) both show positive trends which are characterized by a wider range of values as opposed to the Al_2O_3 vs. Sr (Figure 6.46) plot due to the evolving CaO/Na_2O ratio in plagioclase through the section. The UG2 leuconorite group of values (Figure 6.50) is defined by higher relative CaO contents – most likely due to it containing a higher proportion of clinopyroxene (to be investigated later).

As mentioned earlier Zr, TiO_2 and K_2O are incompatible elements (although TiO_2 is also compatible to chromite) and can be used to monitor the amount of trapped liquid through the section. Figures 6.52 (Zr vs. TiO_2), 6.53 (K_2O vs. Zr) and 6.54 (K_2O vs. TiO_2) all show positive trends (with the chromitite values forming outliers in Figures 6.52 and 6.54 due to TiO_2 partitioning into chromite). What is consistent in all three plots is that the UG2 footwall feldspathic pyroxenite unit shows the highest values (forms the 'end portion' of the positive trends) and thus is seen to contain the highest proportion of trapped liquid in the section.

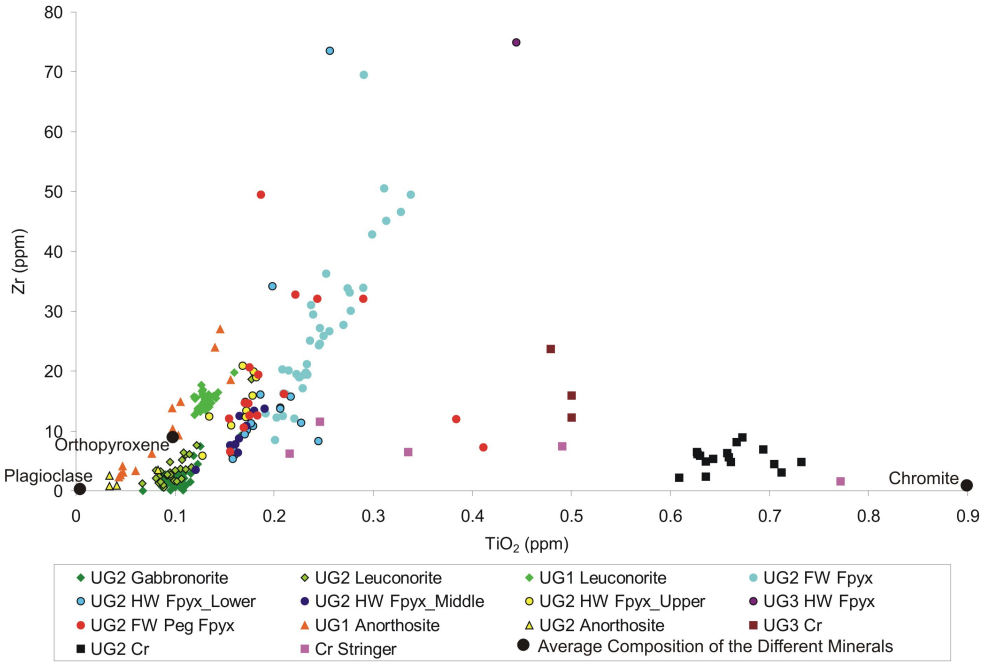

Figure 6.52: Plot of Zr (ppm) vs. TiO_2 (ppm).

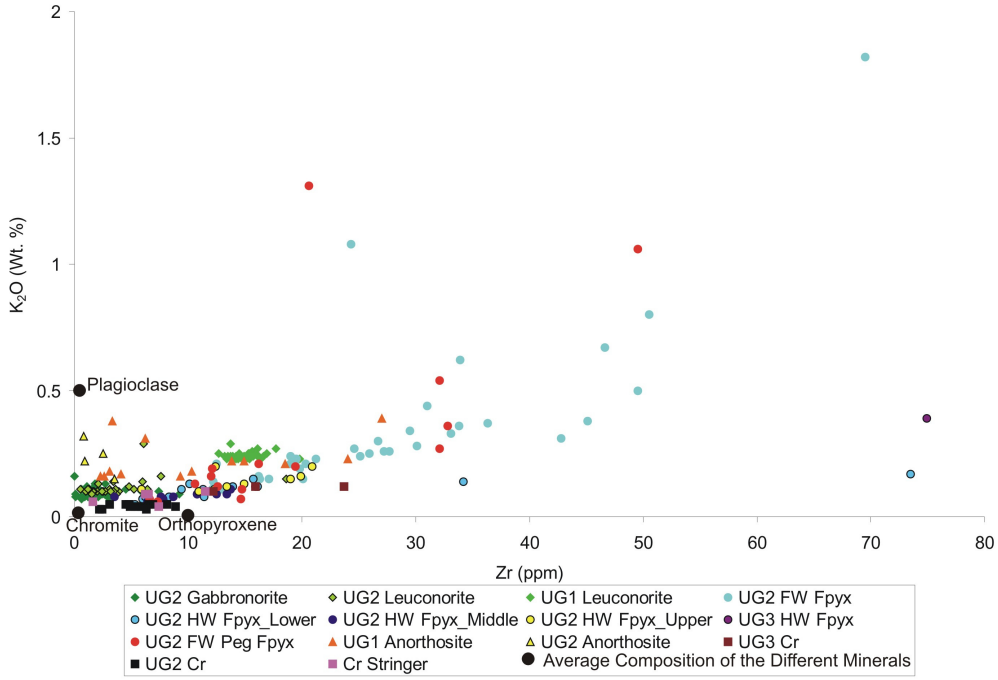

Figure 6.53: Plot of K_2O (Wt. %) vs. Zr (ppm).

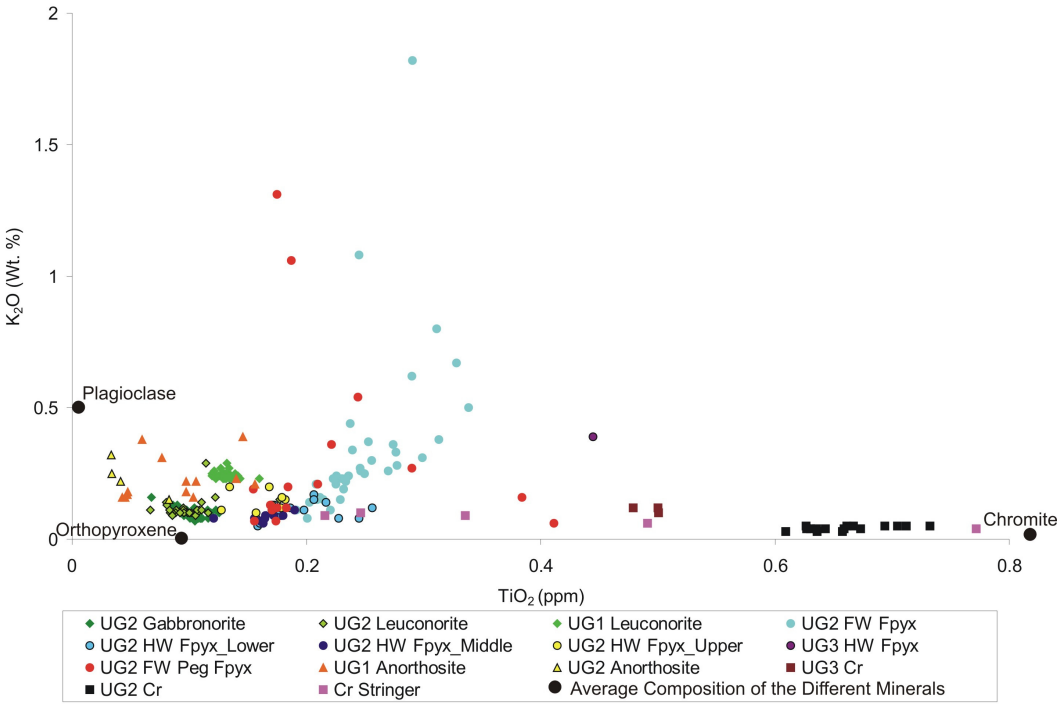

Figure 6.54: Plot of K_2O (Wt. %) vs. TiO_2 (ppm).

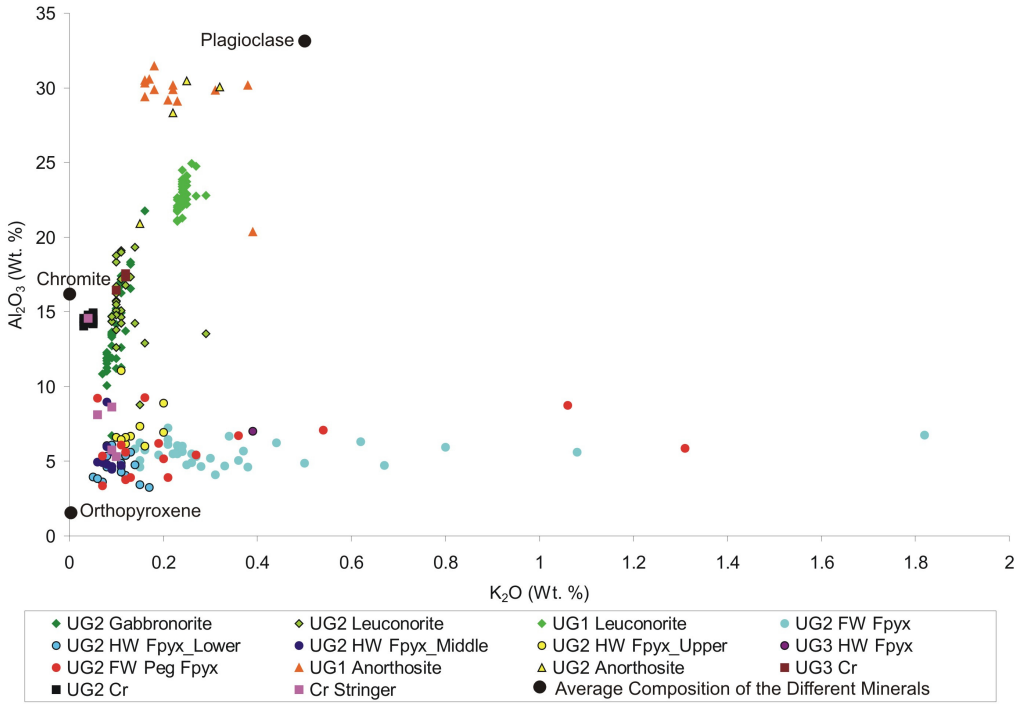

Figure 6.55: Plot of Al_2O_3 (Wt. %) vs. K_2O (ppm).

Figures 6.55 (Al_2O_3 vs. K_2O), 6.60 (Na_2O vs. K_2O) and 6.61 (K_2O vs. Sr) all show positive trends whilst Figures 6.56 (Al_2O_3 vs. TiO_2), 6.57 (FeO vs. K_2O), 6.58 (MnO vs. K_2O), 6.59 (MgO vs. K_2O) all display negative trends. A consistent trend through all these figures is that the incompatible element (i.e. Zr, TiO_2 or K_2O) values for the UG1 leuconorite and UG2 footwall feldspathic pyroxenite units are higher than

expected resulting in these units showing values which are displaced from the, often well defined, trends. This therefore means that the UG2 footwall feldspathic pyroxenite and the UG1 leuconorite units both show enriched incompatible element abundances due to their high proportion of trapped intercumulus liquid (with the UG2 footwall feldspathic pyroxenite containing the highest abundance of trapped liquid in the study section and the UG1 leuconorite the second most).

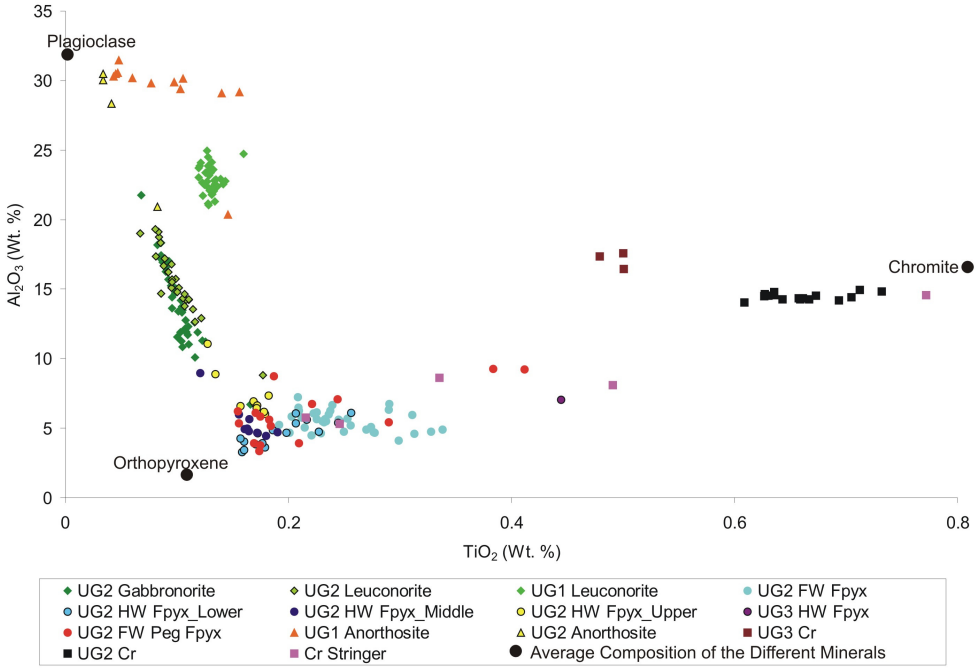

Figure 6.56: Plot of Al_2O_3 (Wt. %) vs. TiO_2 (ppm).

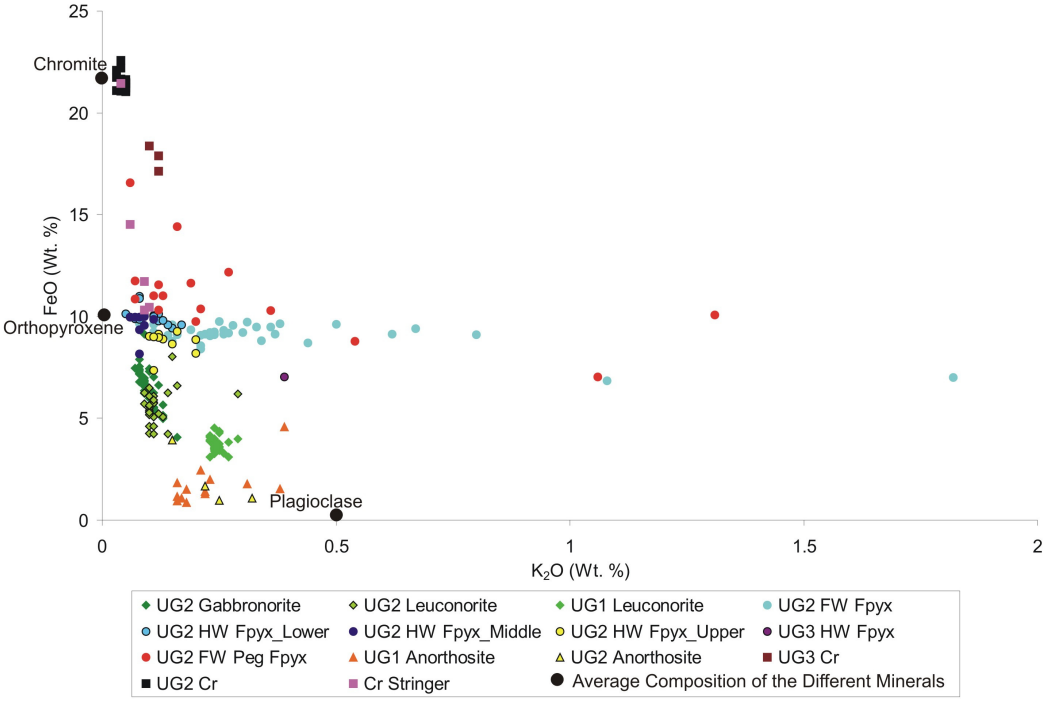

Figure 6.57: Plot of FeO (Wt. %) vs. K_2O (ppm).

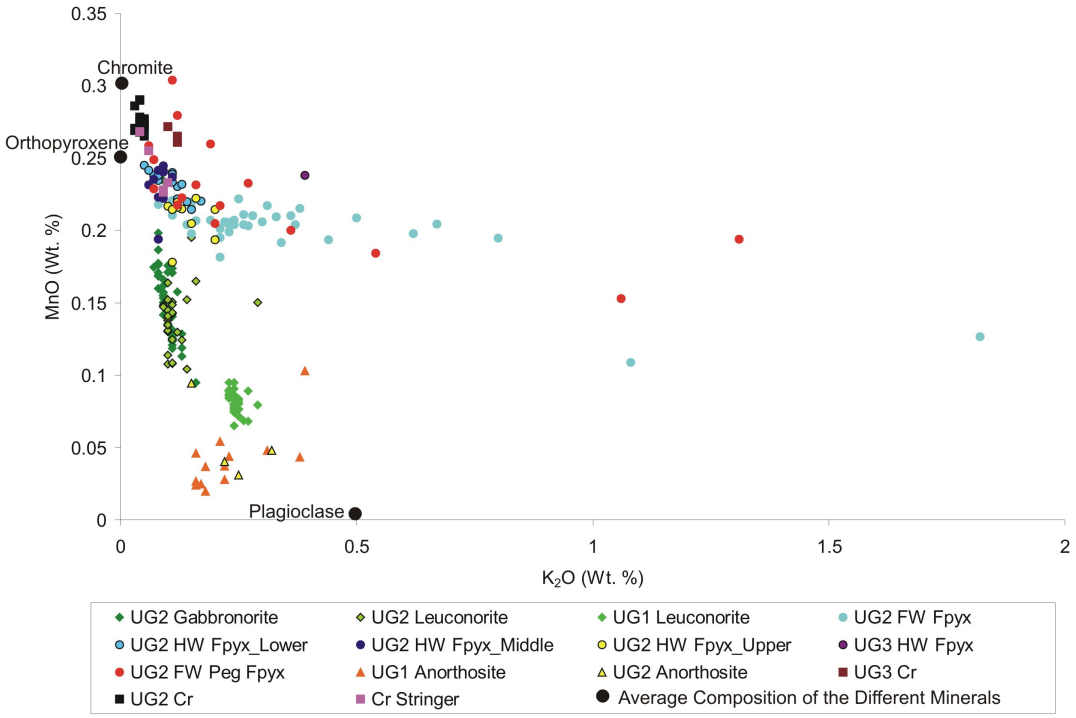

Figure 6.58: Plot of MnO (Wt. %) vs. K_2O (ppm).

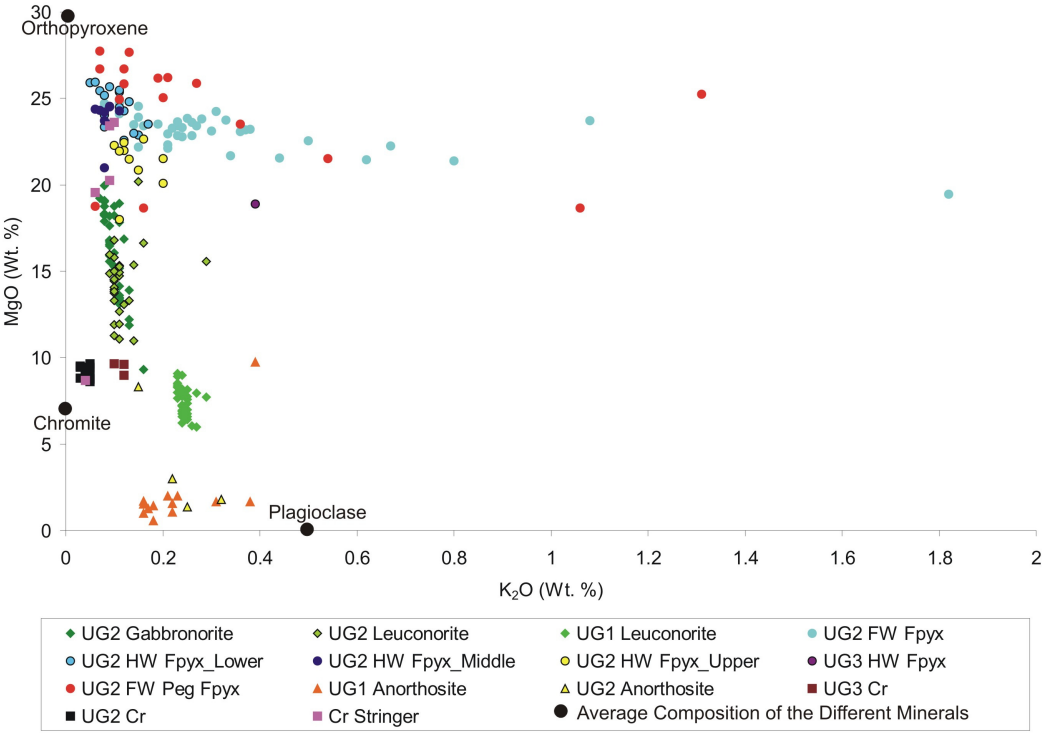

Figure 6.59: Plot of MgO (Wt. %) vs. K_2O (ppm).

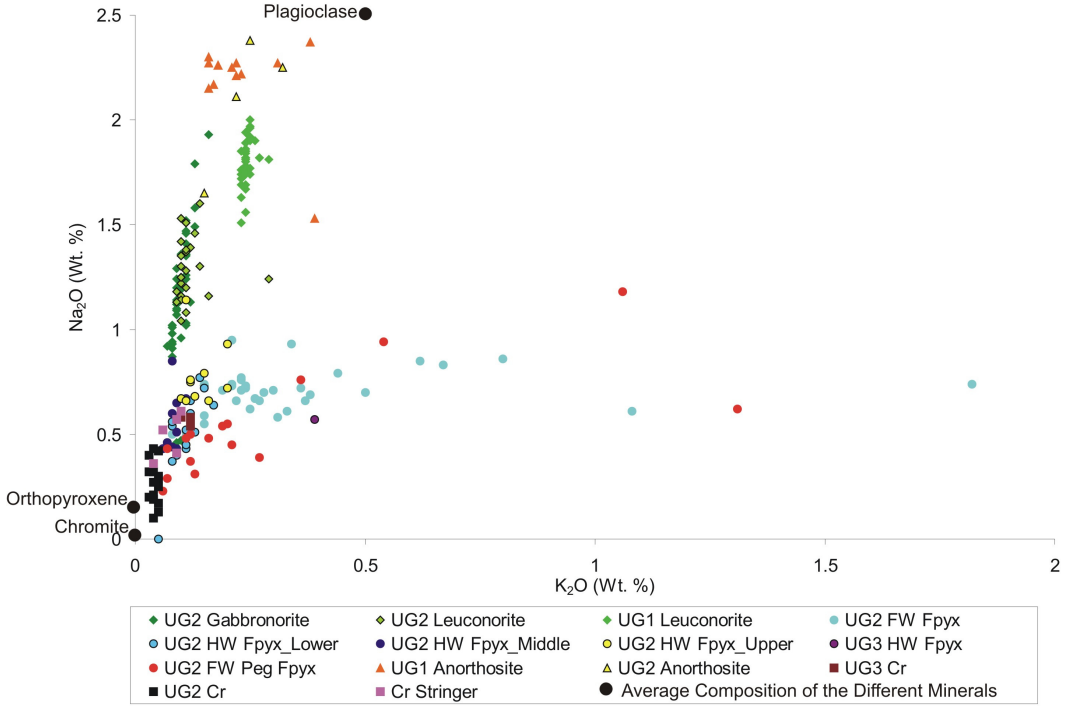

Figure 6.60: Plot of Na_2O (Wt. %) vs. K_2O (ppm).

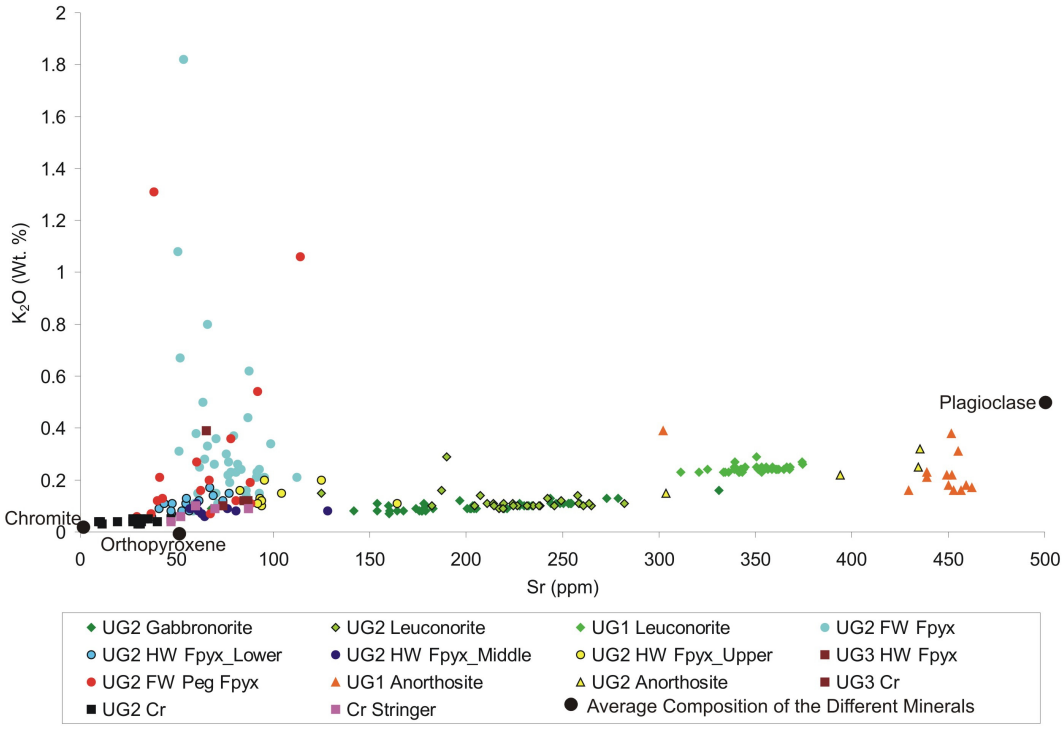

Figure 6.61: Plot of K_2O (Wt. %) vs. Sr (ppm).

Figures 6.62 (Ni vs. MgO) and 6.63 (Zn vs. MgO) both show well defined positive trends whilst, conversely, Figures 6.64 (Ni vs. Al_2O_3) and 6.65 (Zn vs. Al_2O_3) exhibit well defined negative trends. These respective trends are a result of both Ni and Zn partitioning into orthopyroxene. The variable chromitite and pegmatoidal pyroxenite values in Figures 6.62 and 6.64 are a direct result of elevated amounts of BMS mineralization (thereby showing higher Ni values), whilst the variable chromitite and pegmatoidal pyroxenite values in Figures 6.63 and 6.65 are a result of Zn partitioning strongly into chromite and BMS.

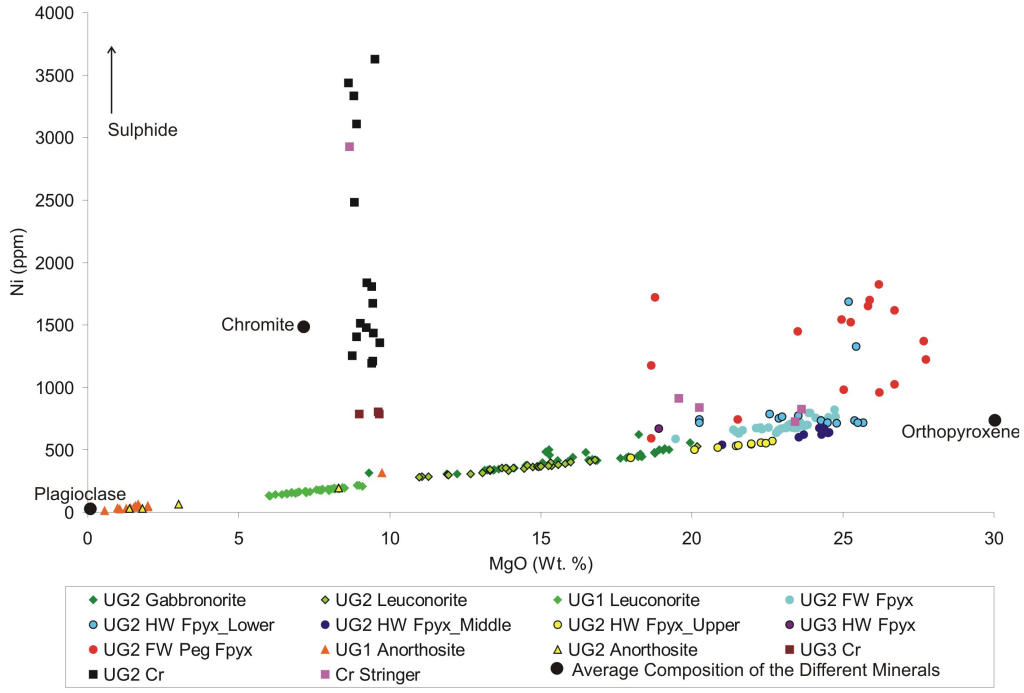

Figure 6.62: Plot of Ni (ppm) vs. MgO (Wt. %).

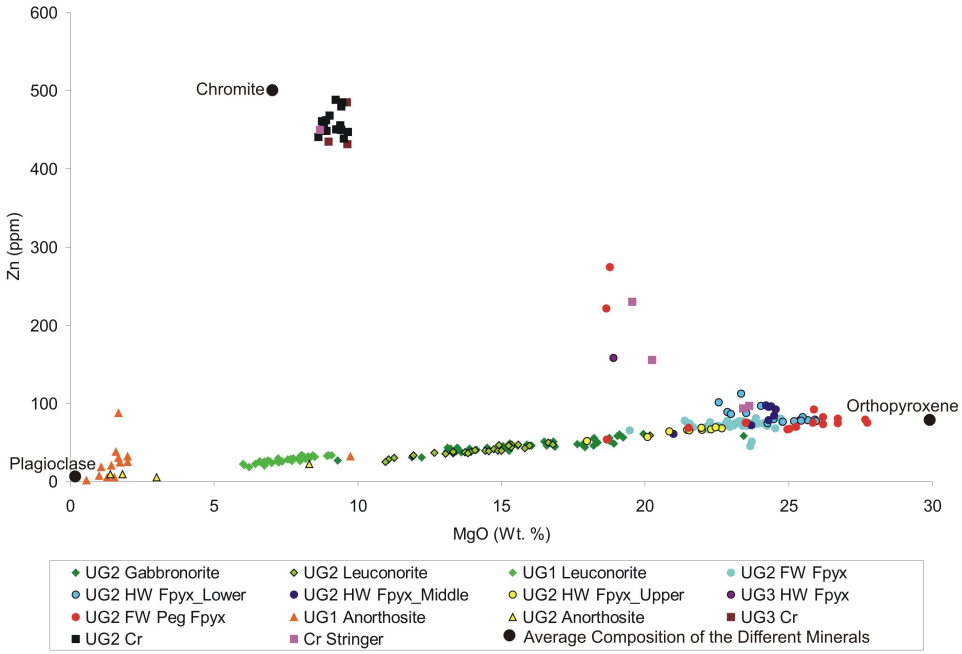

Figure 6.63: Plot of Zn (ppm) vs. MgO (Wt. %).

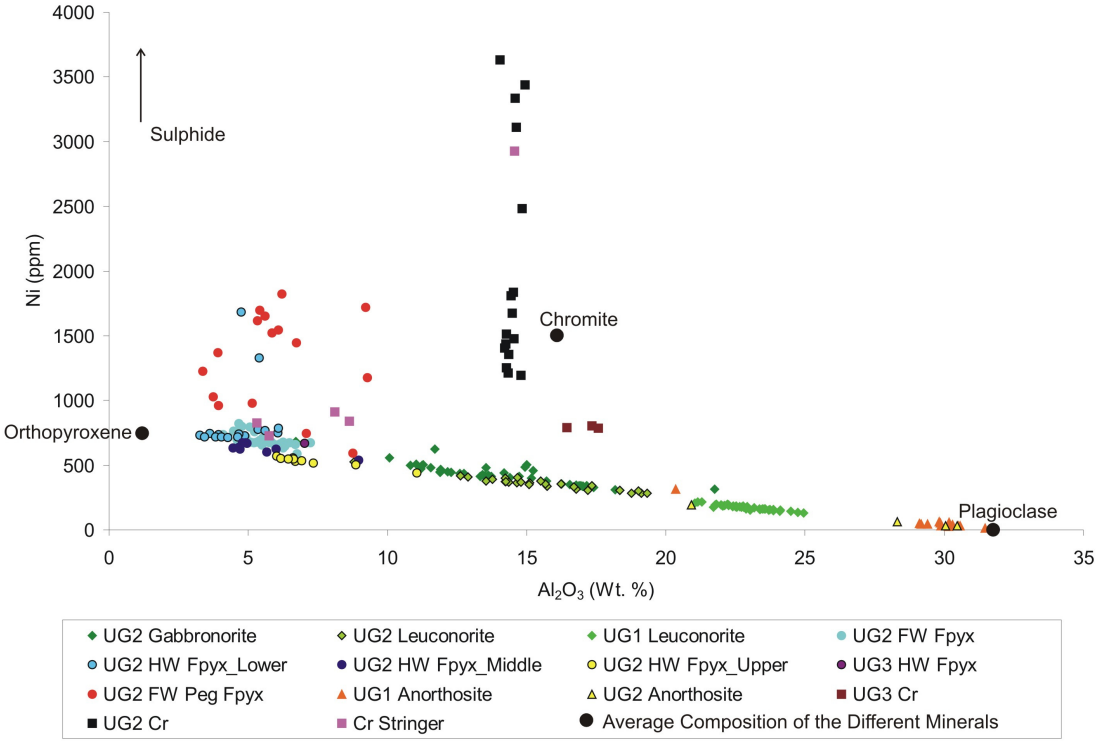

Figure 6.64: Plot of Ni (ppm) vs. Al_2O_3 (Wt. %).

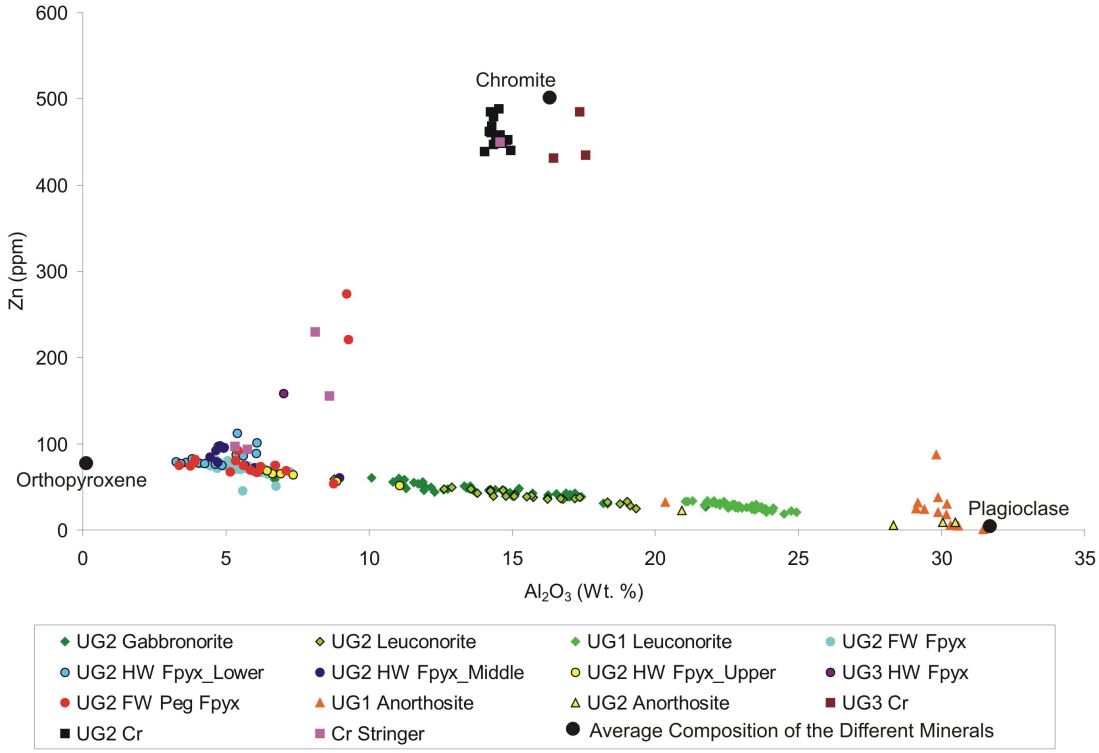

Figure 6.65: Plot of Zn (ppm) vs. Al_2O_3 (Wt. %).

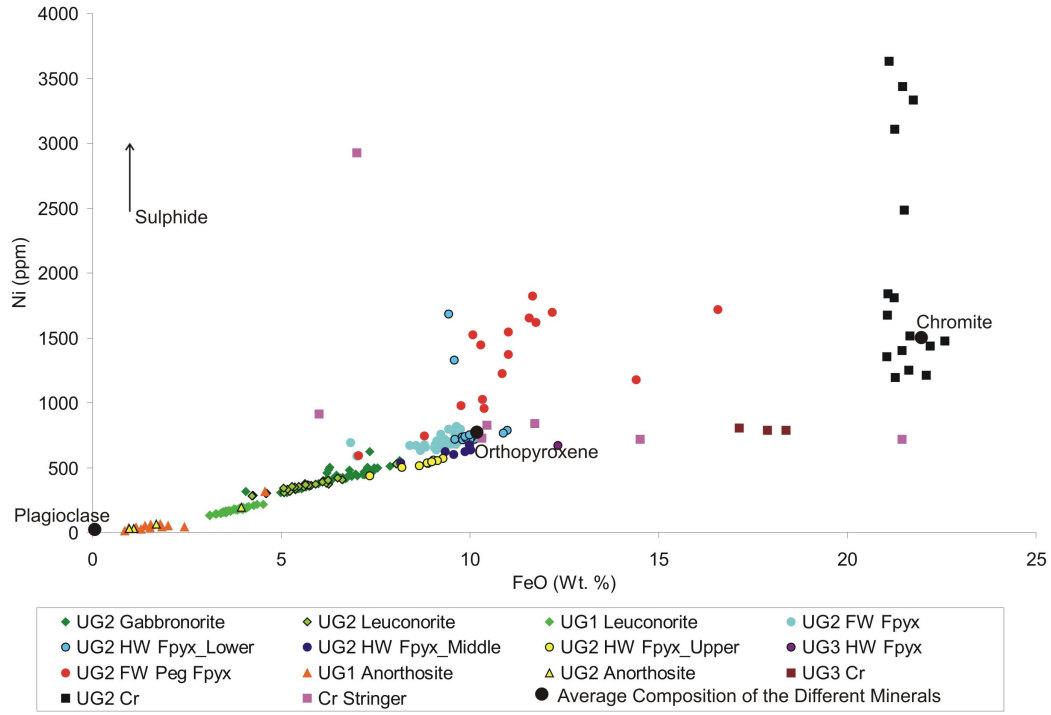

Figure 6.66: Plot of Ni (ppm) vs. FeO (Wt. %).

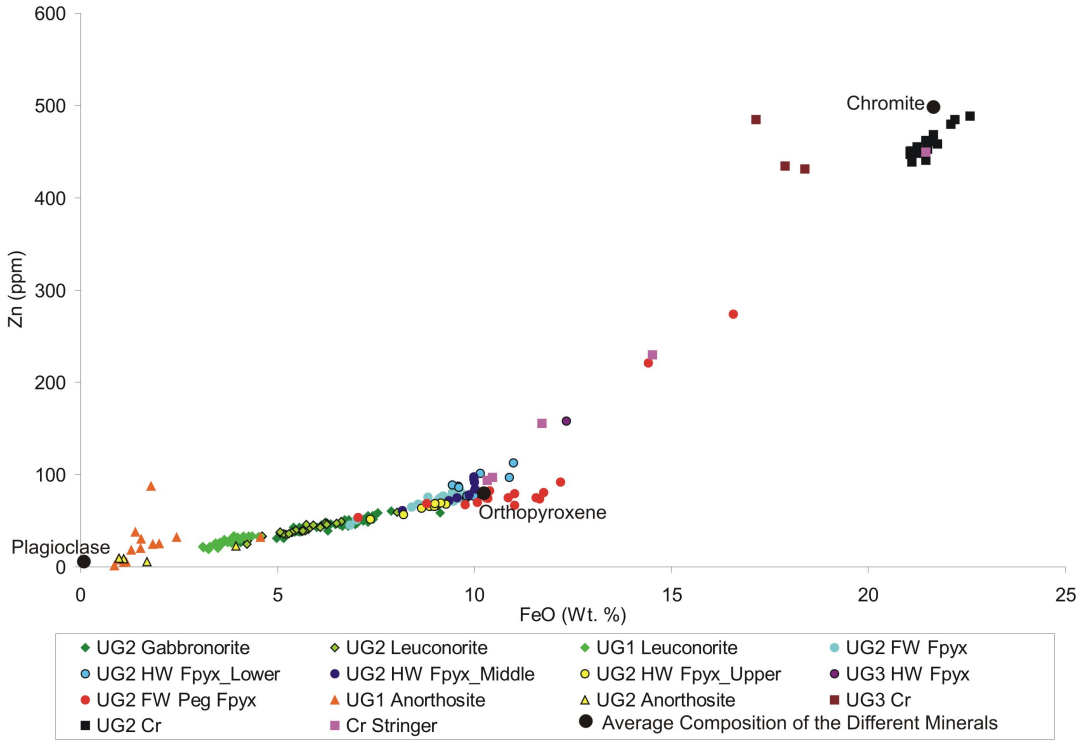

Figure 6.67: Plot of Zn (ppm) vs. FeO (Wt. %).

Figures 6.66 (Ni vs. FeO) and 6.67 (Zn vs. FeO) both show kinked positive trends. A well defined initial trend is exhibited by the silicates due to all of Zn, MnO and FeO partitioning into orthopyroxene. The well defined second trend in Figure 6.67 is a result of Zn and FeO both partitioning into chromite whilst the

irregular values in Figure 6.66 are due to Ni monitoring the BMS abundance and FeO monitoring the chromite. Figure 6.68 (Zn vs. Ni) also shows a positive trend coupled with a range or irregular values for the chromitites and the pegmatoidal pyroxenite due to Zn partitioning into chromite and BMS and Ni into BMS.

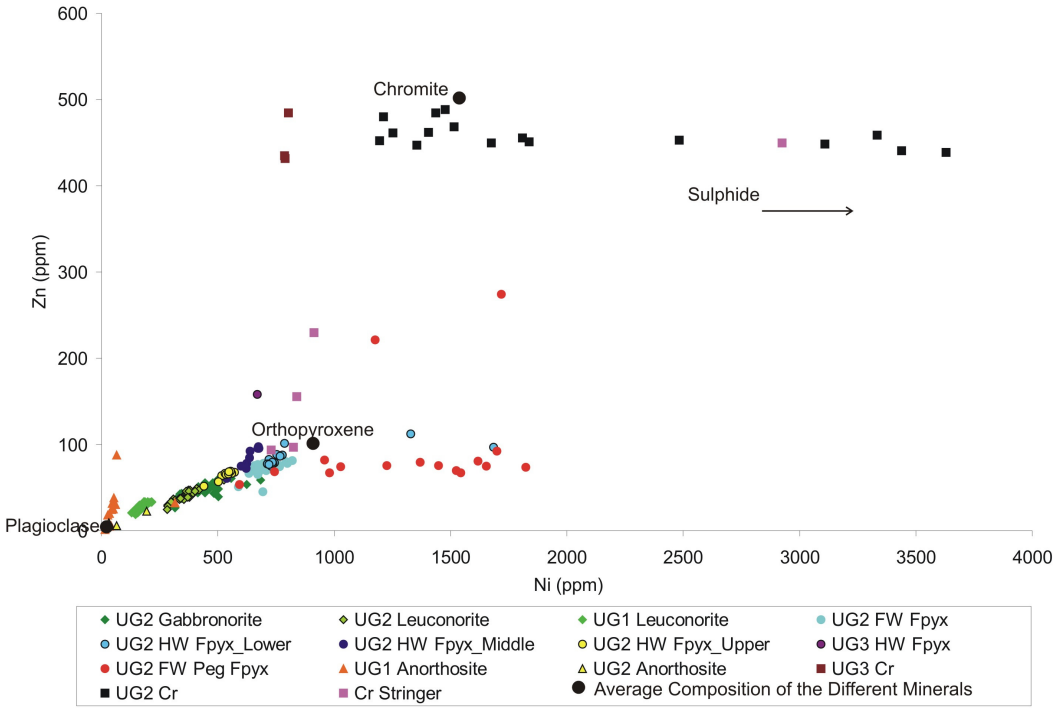

Figure 6.68: Plot of Zn (ppm) vs. Ni (ppm).

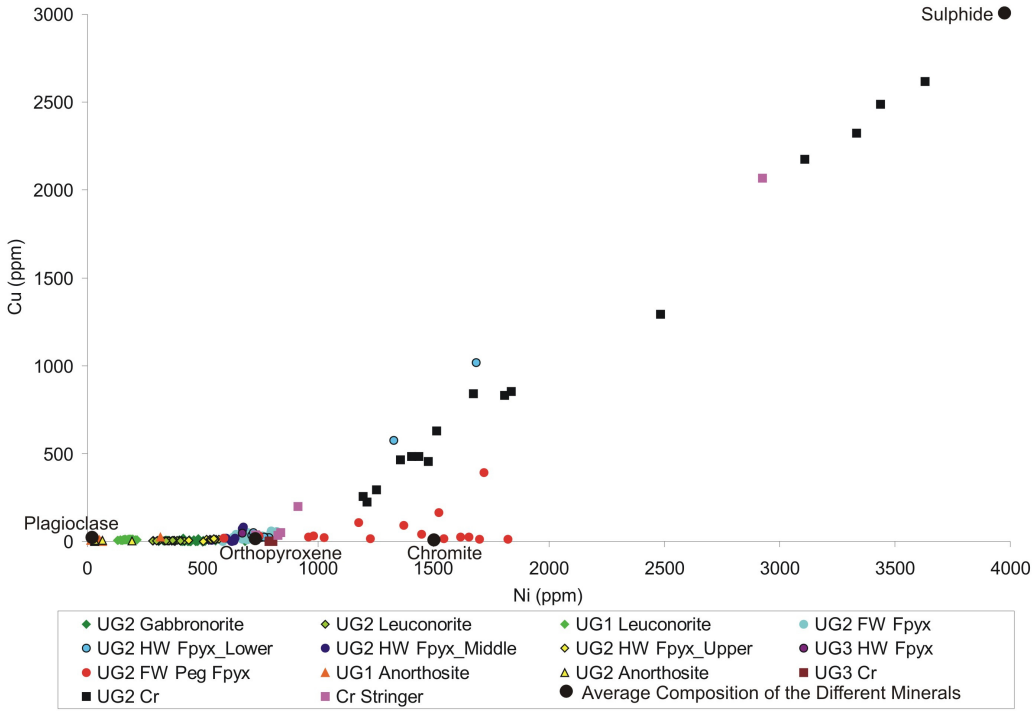

Figure 6.69: Plot of Cu (ppm) vs. Ni (ppm).

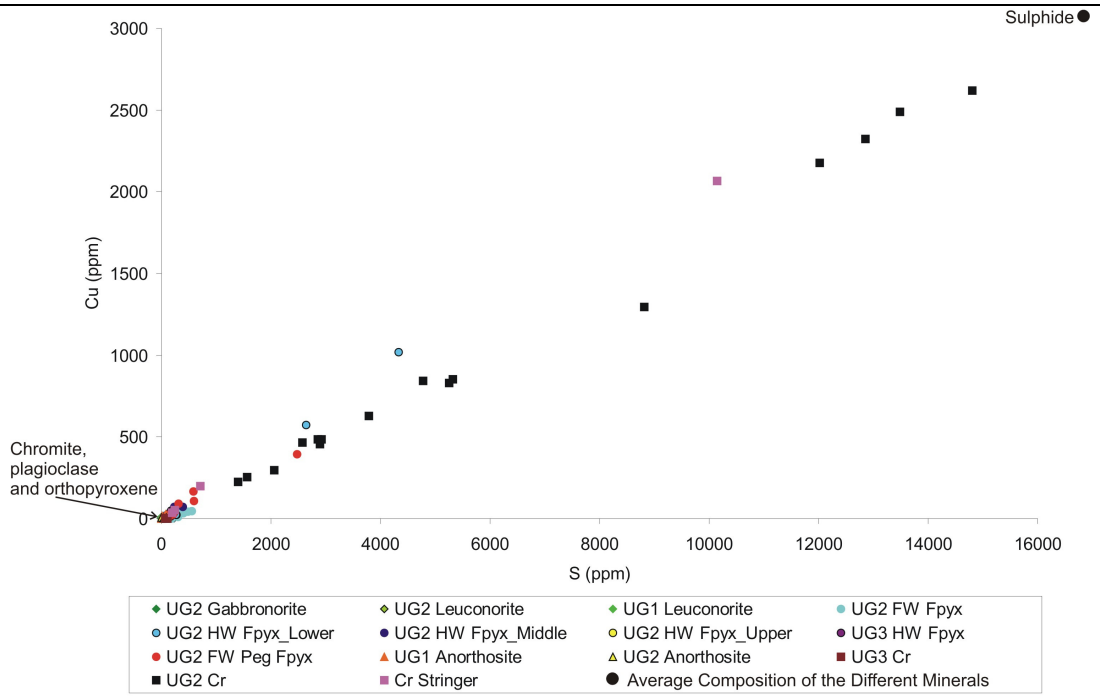

Figure 6.70: Plot of Cu (ppm) vs. S (ppm).

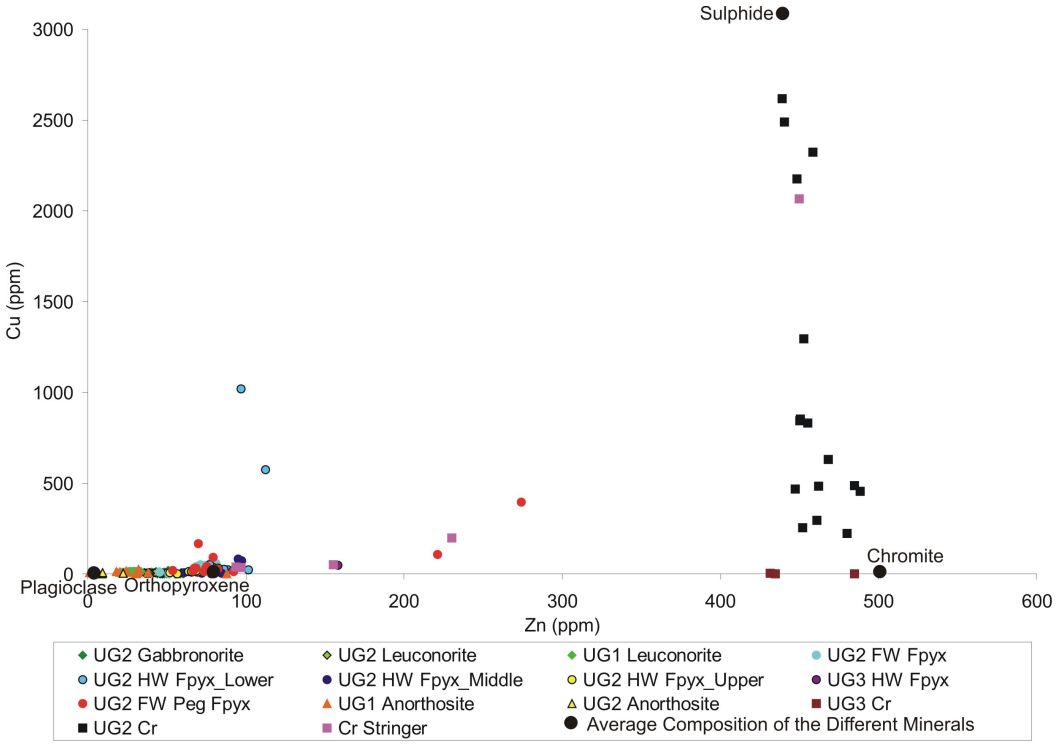

Figure 6.71: Plot of Cu (ppm) vs. Zn (ppm).

Due to Cu, Ni and S mainly partitioning into, and thus monitoring, the BMS mineralization Figures 6.69 (Cu vs. Ni), 6.70 (Cu vs. S) and 6.72 (Ni vs. S) show only positive trends for all the chromitite and pegmatoidal pyroxenite values (due to these two lithologies hosting the BMS mineralization). The plots with

Zn (Figures 6.71 and 6.73) show no trends but rather a set of elevated values for the chromitites (due to Zn partitioning into chromite).

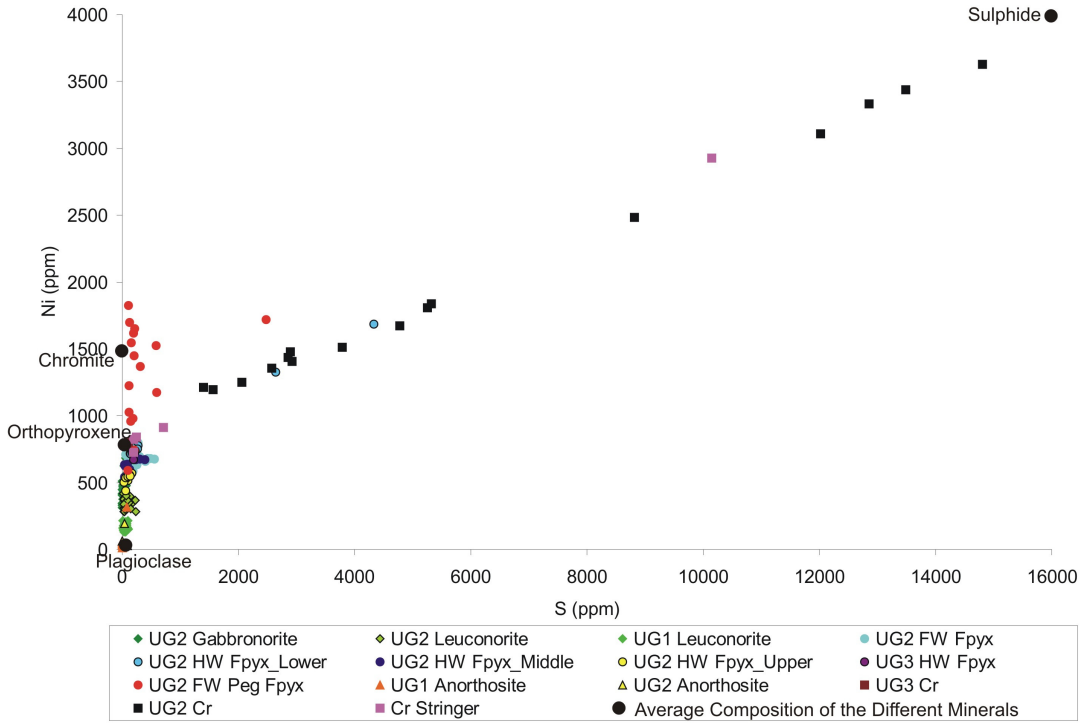

Figure 6.72: Plot of Ni (ppm) vs. S (ppm).

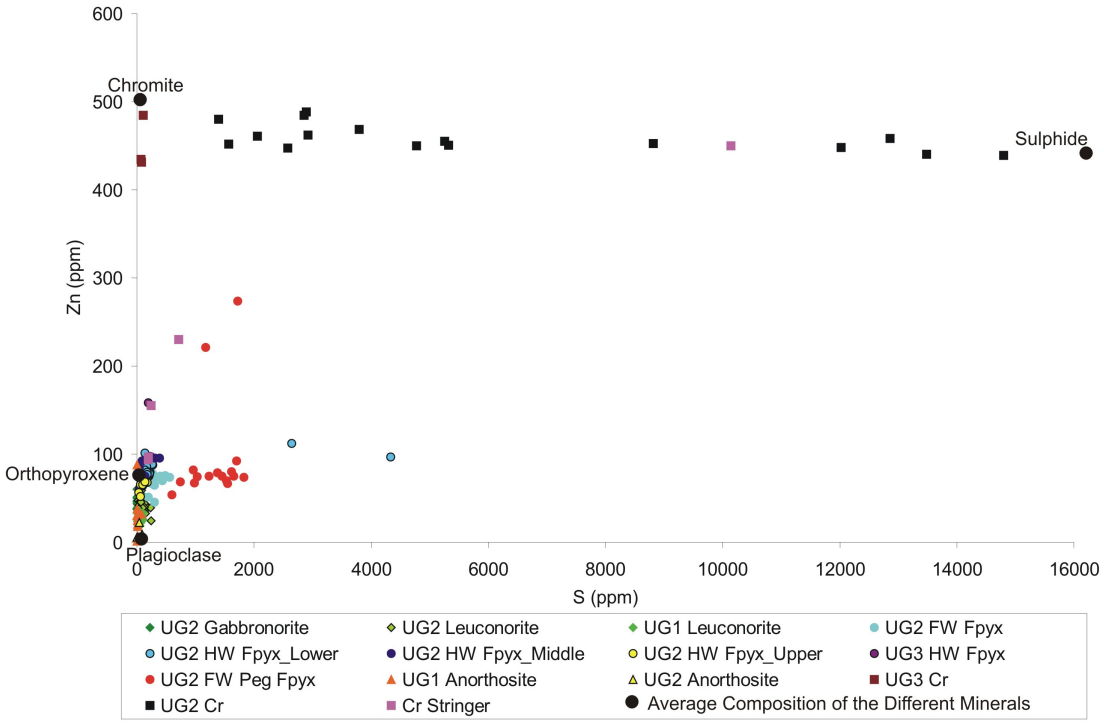

Figure 6.73: Plot of Zn (ppm) vs. S (ppm).

6.6 Conclusions

The following broad conclusions can be made from the whole rock geochemistry section:

- The major element profiles (i.e. MgO, Al_2O_3 etc) are seen to define a lower normal fractionation trend (which straddles the UG1 – UG2 boundary) and an overlying reverse fractionation trend (at the level of the UG2 leuconorite).
- The UG2 footwall feldspathic pyroxenite and the UG1 leuconorite units both show enriched incompatible element abundances (Zr, K_2O, TiO_2) due to their high proportion of trapped intercumulus liquid (with the UG2 footwall feldspathic pyroxenite containing the highest abundance of trapped liquid in the study section and the UG1 leuconorite the second most).
- Cu, Ni and S all show strong relationships with each other and define elevated levels of BMS mineralization within the UG2 chromitite, the hanging wall chromitite stringers and, to a lesser extent, the footwall pegmatoidal pyroxenite.

The whole rock geochemical results can be used to interpret the processes occurring within the Bushveld chamber during the formation of the UG2 cyclic unit. A petrogenetic model for the UG2 cyclic unit (and hence chromitite layers in general) is hereby formulated (based on the geochemical result provided):

There were repeated, episodic influxes of magma into the chamber during the formation of the lower and critical zones (Eales *et al.,* 1990). It is this process of magma mixing that has been suggested by Irvine (1977) to have initiated chromite crystallization and hence being responsible for the formation of chromitite layers. Evidence for this includes the fact that chromitite layers are intimately associated with cyclical layering (Naldrett *et al.,* 1983), and often occur at, or near, the base of cyclic units (i.e. Jackson, 1970; Naslund and McBirney, 1996). The UG2 cyclic unit exhibits several chromitite layers: a basal chromitite stringer, the UG2 chromitite layer itself (which occurs near the base of the cyclic unit), several hanging wall chromitite stringers and the UG3 chromitite layer (which exists at the base of the UG3 cyclic unit. The whole rock geochemistry results reveal the UG2 unit to contain a normal fractionation trend overlain by a reverse trend.

Therefore it is envisaged that the evolving Bushveld chamber would have been crystallizing out the UG1 anorthosite (Nex, 2004), when a number of minor magma pulses were injected into the chamber (i.e. Eales *et al.,* 1990). The crystallizing system would have been forced into the chromite field for a short period, thereby initiating precipitation of the mm scale basal chromitite stringer (i.e. Irvine, 1977; Naldrett, 1989). This chromitite stringer forms the base of the UG2 cyclic unit. Chromite crystallization then drove the system back into the orthopyroxene phase field from where the system resumed orthopyroxenite crystallization (Irvine, 1977). During this time the UG2 footwall feldspathic pyroxenite was built up.

The system was then forced back into the chromite phase field either by a single large injection or by a build up of several, rapid injections of magma into the system (Irvine, 1977). The system would have been forced further into the chromite phase field than the last occurrence thereby resulting in a longer period of chromite crystallization and eventually producing a thicker final chromitite layer (than the previous occurrence). Crystallization solely of chromite would have then forced the system back into the orthopyroxene field, where orthopyroxenite crystallization, as well as repetitive influxes of magma, resumed. The hanging wall sequence therefore represents a classic continuous evolving fractionating open magma system in which normal evolutionary cooling and fractionation processes were punctuated by small, sharp injections of primitive magma, thereby resulting in the formation of mm scale chromitite stringers (i.e. Irvine, 1977; Eales *et al*., 1990).

Therefore, during the early stages of crystallization of the UG2 unit the resident liquid within the chamber, despite still been replenished by intermittent injections of more primitive magma, as a result of fractional crystallization, trended toward more evolved compositions. This overall normal trend is mirrored by local intra-lithological normal fractionation trends within the UG2 footwall and UG2 hanging wall middle and upper feldspathic pyroxenite units.

At the level of the upper contact of the UG2 hanging wall middle feldspathic pyroxenite unit a reversal in fractionation trends occurred. Through the overlying UG2 leuconorite and upper feldspathic pyroxenite units an upward trend toward more primitive compositions existed (as reflected by a more mafic mineral distribution). This is suggested to represent a period of increased magma addition into the chamber (i.e. Irvine, 1977). Therefore the process of magma replenishment of the chamber is suggested to now be the dominant process – as opposed to that of acquiescence and fractional crystallization (punctuated by intermittent injections) - during the normal trend. The UG2 unit thus experienced an increased influx of more primitive magma during its formation. Nevertheless, the chromitite layers (including the UG2 and the stringers present in its hanging wall) are suggested to represent injections of batches of more primitive magma into the chamber (as described in chapter 9).

In conclusion, the whole rock geochemistry results from this work show the UG2 cyclic unit to represent a dynamic interplay of evolving, cooling and fractionating resident liquids within the chamber along with repetitive influxes of fresh, undifferentiated primitive magma.

7. PGE Geochemistry

7.1 Introduction

One of the major aims of this project is the investigation of the PGE mineralization within the UG2 chromitite and its immediate hanging wall and footwall. This chapter presents high precision PGE compositional data (Appendix D) for 54 closely spaced samples from throughout the ZG219 MH 'ore zone' (which heron refers to the UG2 chromitite, its footwall pegmatoidal feldspathic pyroxenite unit, as well as its hanging wall feldspathic pyroxenite unit, including the chromitite stringers). This allows detailed PGE distribution profiles through the ore zone to be constructed. A variety of geochemical tools (including inter-element plots, PGE ratios and chondrite normalized patterns) are used to investigate the PGE mineralization within the ore zone. Finally a model for the PGE mineralization hosted within the UG2 ore zone is presented.

For the purposes of this project the PGE (also called the precious metals) will be abbreviated as follows: Pt = platinum, Pd = palladium, Rh = rhodium, Ru – ruthenium, Os = osmium, Ir = iridium, Au = gold.

7.2 Geochemical Techniques

A more detailed sampling strategy was used for the UG2 ore zone (i.e. the UG2 chromitite, its footwall pegmatoidal feldspathic pyroxenite and hanging wall lower feldspathic pyroxenite up to the topmost chromitite stringer). A continuous run of samples using a sample length of 5 cm (full core) was used for the hanging wall feldspathic pyroxenite and footwall pegmatoidal feldspathic pyroxenite units. The chromitite stringers in the hanging wall were sampled separately using 2 or 3 cm long samples (just long enough to only include the stringer and minimal pyroxenite material). The UG2 chromitite was then sampled continuously using 3 cm long samples.

The platinum-group elements (PGE) and gold were analyzed using a Perkin Elmer Elan 6100 ICP-MS. Sample preparation involved preparation of a NiS pre-concentrate using 25 grams of sample, followed by milling of the sulphide pellet. Fifty milligrams of sample was dissolved in an HNO_3-HCl mix using the Anton Paar microwave digestor. Along with gold the following PGE were analyzed against certified standards: Pt, Pd, Rh, Ru, Ir and Os.

7.3 PGE Distributions

The concentration profile for the total PGE plus Au is presented in Figure 7.1.

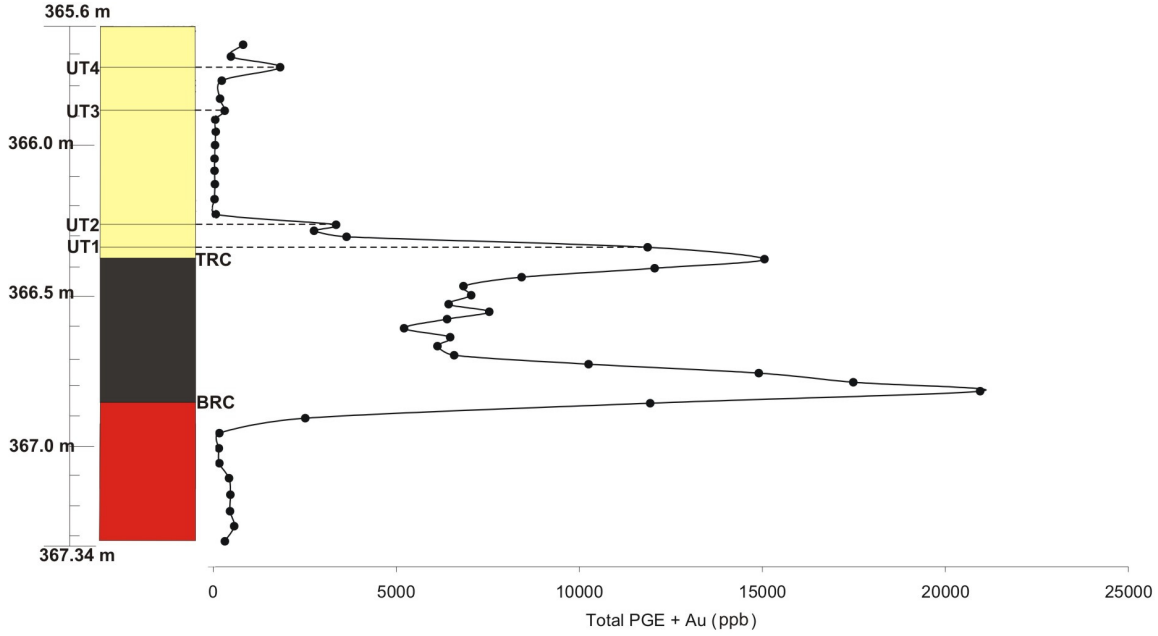

Figure 7.1: Stratigraphic variation of total PGE plus Au through the ZG219 MH ore zone section.

The grouped PGE + Au concentration profile reveals a distinct triple-peaked mineralization pattern through the UG2 chromitite. The precious metal abundances are low through the footwall pegmatoidal pyroxenite but show a sharp peak at the level of the BRC (bottom reef contact) followed by a trough through the middle of the chromitite (which shows a small peak within the trough) and ending off with another peak (although slightly smaller than the BRC peak) at the level of the TRC (top reef contact). The hanging wall pyroxenite shows low mineralization levels that are punctuated by small peaks at the levels of the chromitite stringers. The precious metal mineralization profile pattern through the UG2 ore zone can therefore be described as predominantly bottom loaded with two major peaks (at the top and bottom contacts of the chromitite) separated by a trough through the middle of the layer. A third lesser peak is seen to occur within this middle trough (although is not as well developed as in the total sulphide profile (Figure 7.2).

By overlaying the total base metal plus sulphur (Cu + Ni + S) profile on the PGE + Au profile (Figure 7.2) it is clear that the patterns are almost identical and clearly sympathetic. The major difference is that the lower base metal plus sulphur peak is slightly offset (and is slightly above) to the PGE + Au peak. Apart from this, the base metal plus sulphur profile pattern is also triple-pronged and displays a clearly defined peak in the middle of the layer. The upper and bottom peaks of the base metal plus sulphur profile are approximately equal (unlike the PGE + Au which has a stronger bottom peak) and the hanging wall and footwall units have a higher base metal plus sulphur abundance than PGE + Au (although the base metal plus sulphur peaks at the chromitite stringers are less pronounced).

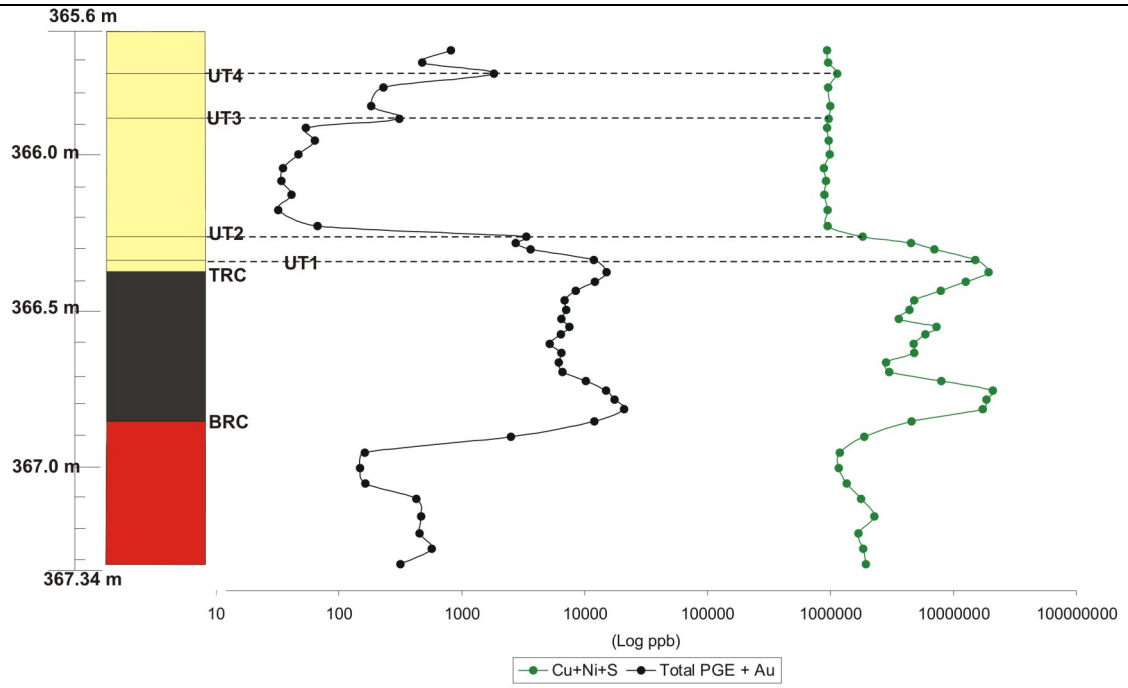

Figure 7.2: Stratigraphic variation of total base metal plus sulphur (i.e. Cu + Ni + S) and total PGE plus gold through the ZG219 MH ore zone section.

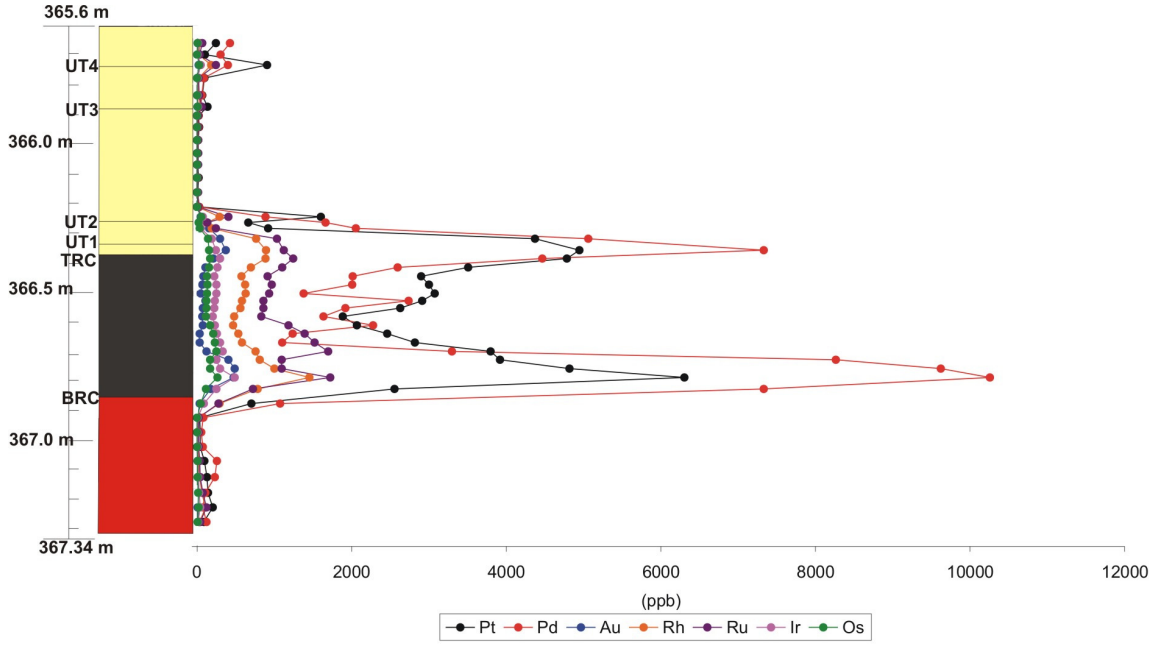

Figure 7.3: Stratigraphic variation of the individual PGE (as well as gold) through the ZG219 MH ore zone section.

The individual PGE profile patterns (Figure 7.3) are broadly similar although differences do exist and are investigated further at a later stage. All the PGE profiles are bottom loaded (have a stronger bottom peak) and display two major peaks (at the bottom and top layer contacts) separated by a trough which too hosts a minor peak. Within the trough (which makes up most of the layer) the precious metal order of decreasing abundance is Pt→Pd→Ru→Rh→Ir→Os→Au whilst in the upper and bottom peaks it is

Pd→Pt→Ru→Rh→Au→Ir→Os. Therefore, within the peaks Pd overtakes Pt as the most abundant PGE whilst Au and Ir both show sharp increases. This reflects a higher chalcophile character of these elements in the upper peak.

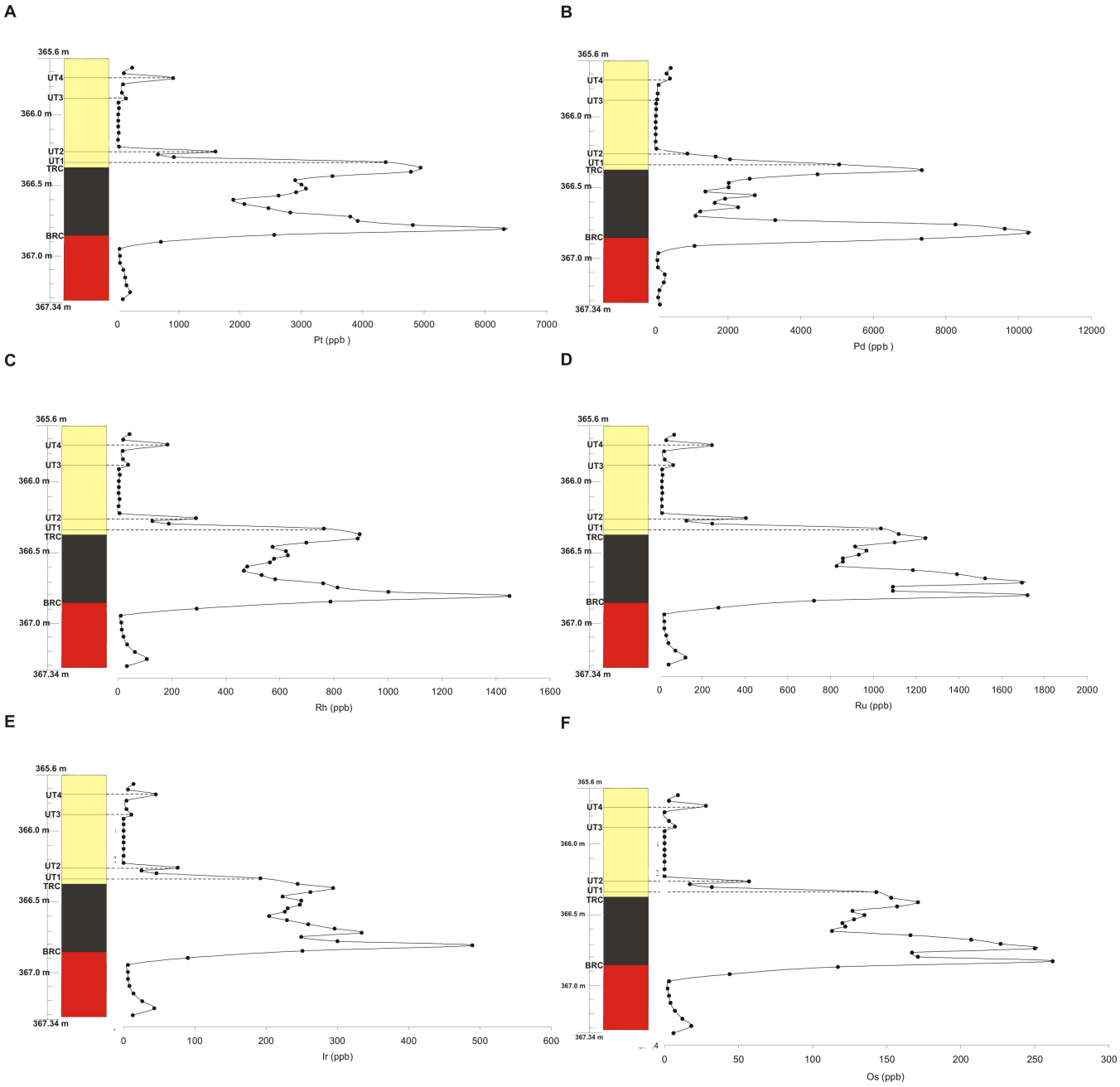

Figure 7.4: Vertical distribution plots showing the stratigraphic variation of all the individual PGE through the ZG219 MH ore zone section.

The individual PGE (Figure 7.4) and Au (Figure 7.5) have profile patterns that are broadly similar. All have a lower and upper peak separated by a trough, with the lower peak slightly stronger than the upper one. The main differences between the individual profiles exist in the shape of the bottom peak as well as of the trough (or middle) zone. The upper peak remains largely unchanged for all the profiles.

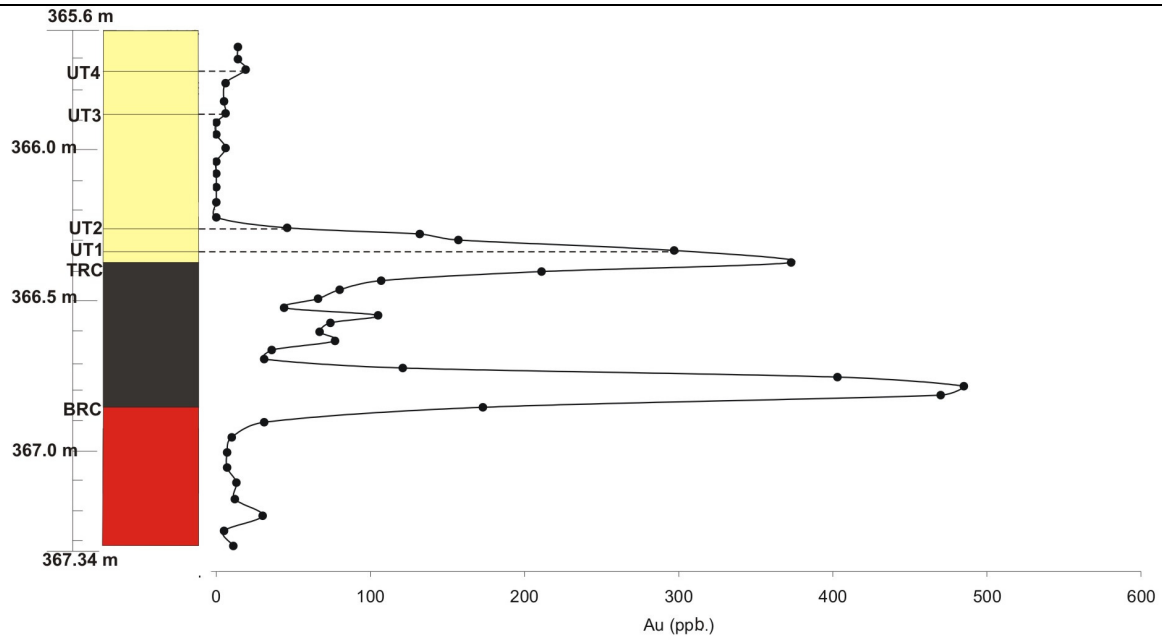

Figure 7.5: Stratigraphic variation of gold through the ZG219 MH ore zone section.

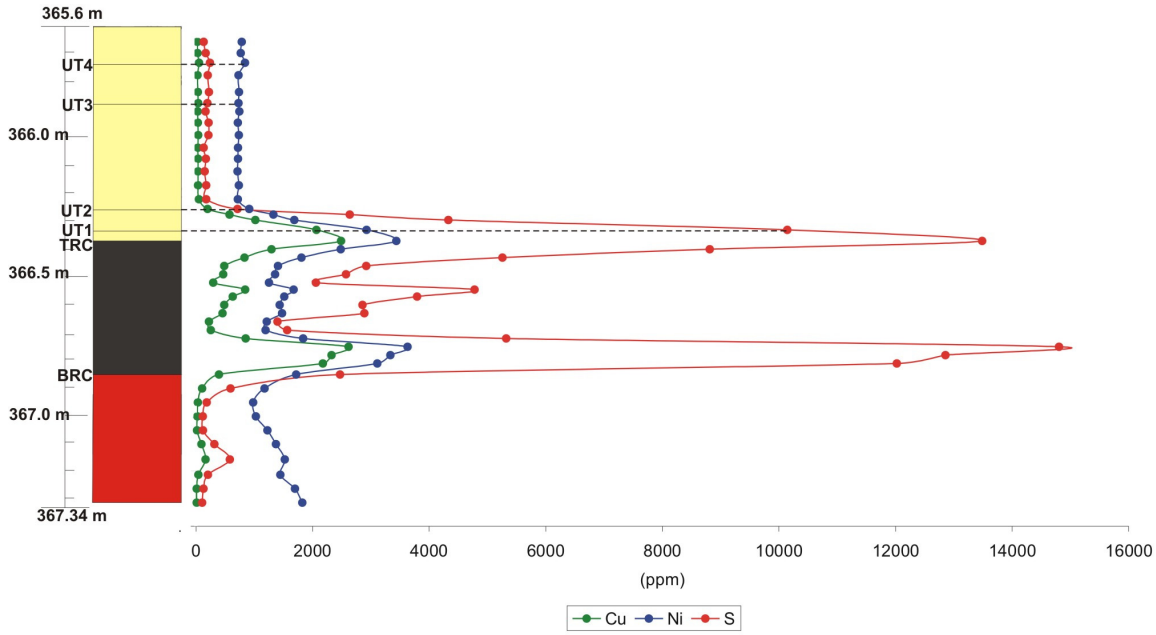

Figure 7.6: Stratigraphic variation of Cu, Ni and S through the ZG219 MH ore zone section.

The individual base metals plus sulphur (Cu, Ni and S) profiles (Figure 7.6) also show a triple-pronged pattern with two major peaks separated by a middle trough and a lesser peak. S shows the greatest enrichment through the ore zone whilst Ni has a higher background level through the hanging wall and footwall due to it partitioning into orthopyroxene.

7.4 PGE Ratios

A variety of PGE ratios have been calculated and plotted against the stratigraphic log of the ore zone. These ratios can provide information on magma compositions as well as primary processes such as fractional segregation of sulphides from the magma (Naldrett and Wilson, 1990)

The stratigraphic variation of (total PGE + Au)/S (an expression of the precious metal tenor) is provided in Figure 7.7. High precious metals tenors exist as a peak in the footwall pegmatoidal pyroxenite as well as three distinct peaks within the chromitite. These peaks correspond to the troughs in the Cu, Ni and S profiles in Figure 7.6. A systematic upward decreasing trend in precious metals tenors exists through the chromitite and into the overlying pyroxenite. This trend is then reversed about halfway up through the pyroxenite and shows an upward increasing trend in precious metals tenor in the upper half of the hanging wall pyroxenite. All the chromitite stringers are marked by sharp peaks in precious metals tenors.

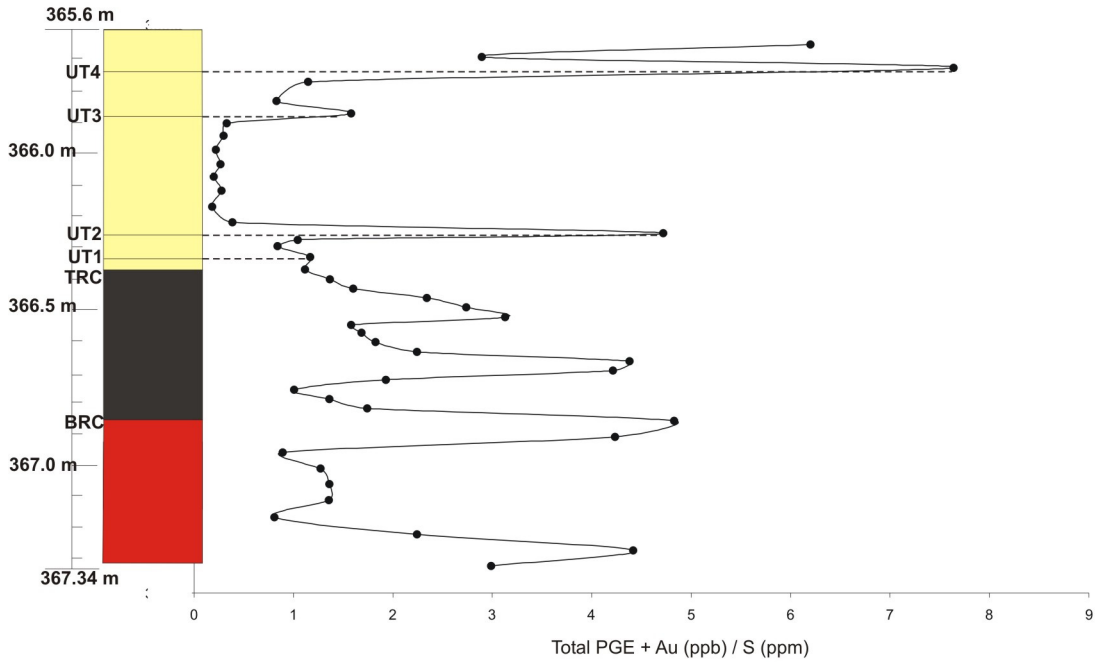

Figure 7.7: Stratigraphic variation of the total PGE plus gold (in ppb) to S (in ppm) ratio through the ZG219 MH ore zone section.

The individual PGE (Figure 7.8) and Au (Figure 7.9) tenors profile patterns through the ore zone reveal broadly similar patterns. All the plots show the three peaks through the chromitite – although they vary in size between the PGE i.e. Pd, Au and, to a lesser exent, Rh display stronger bottom peaks (at the BRC) whilst the remaining PGE all have larger middle peaks. Also, all PGE apart from Au and Pd show systematic sharp drop

offs in tenors through the upper portion of the chromitite whilst all the PGE show increases through the hanging wall pyroxenite and show sharp peaks at the chromitite stringers.

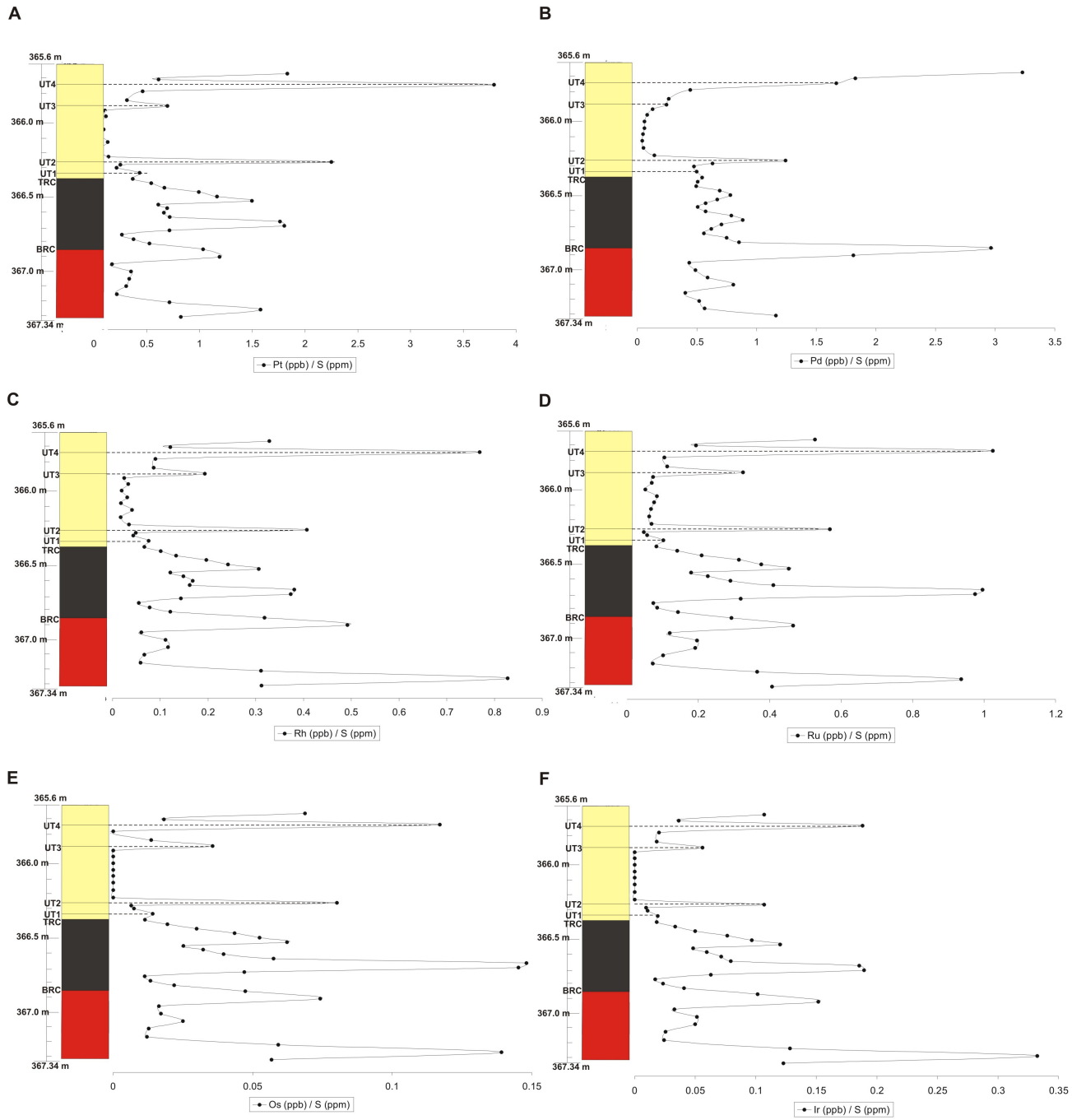

Figure 7.8: Vertical distribution plots showing the stratigraphic variation of all the individual PGE to S ratios through the ZG219 MH ore zone section.

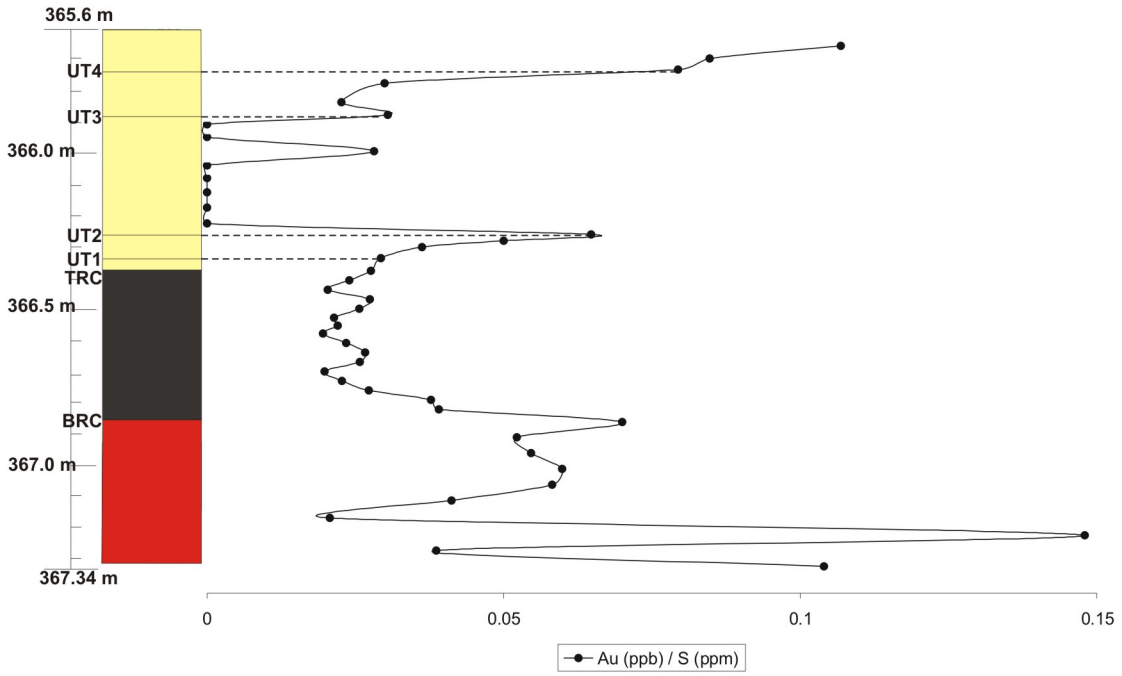

Figure 7.9: Stratigraphic variation of the Au to S ratio through the ZG219 MH ore zone section.

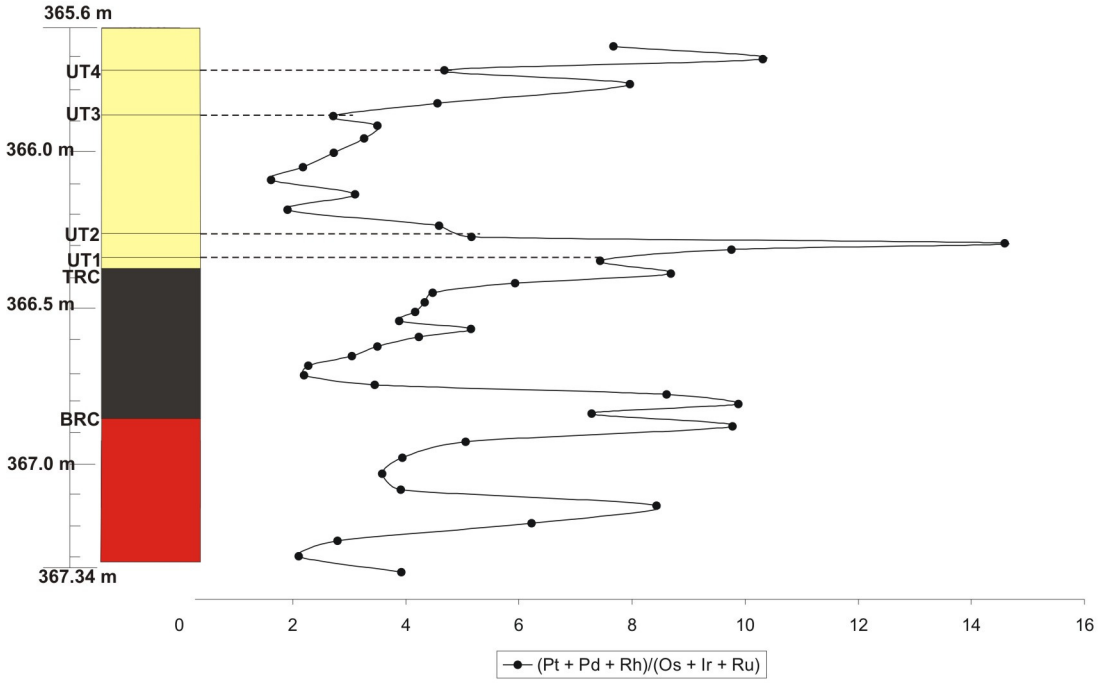

Figure 7.10: Stratigraphic variation of (Pt + Pd + Rh)/(Os + Ir + Ru) through the ZG219 MH ore zone section.

The ratio (Pt + Pd + Rh)/(Os + Ir + Ru) is used to compare the PGE of relative chalcophile character to those of relative siderophile character (Eales *et al.,* 1993; Scoon and Teigler, 1994; Maier and Barnes, 1999; Kruger, 2005). The values shown through the ZG219 MH UG2 ore zone typically range from 2 – 10, with a peak at 16 for the UT2 stringer. These values are in line with values, i.e. 1 – 20, used to characterize the

Critical Zone (Maier and Barnes, 1999). Stratigraphic variations of this value (Figure 7.10) through the ZG219 MH ore zone show a peak in the footwall pegmatoidal pyroxenite as well, once again, the 3 peaks within the chromitite. There is then a systematic increase through the upper portion of the layer up to the UT2 stringer. This is followed by a drop off into the overlying feldspathic pyroxenite and then another systematic increase through the upper portion of the pyroxenite (through both the UT4 and UT5 stringers).

The stratigraphic variation of the Pt/Pd ratio (Figure 7.11) through the ore zone section shows a sawtooth type profile. Despite a peak near the base the footwall shows lower values. The three peaks are once again present in the chromitite but the bottom peak appears to have migrated further up and is not at the BRC (as for other ratio plots). There is then a systematic decrease through the upper portion of the chromitite up to the UT2 stringer. The hanging wall pyroxenite shows moderately high values and is characterized by sharp peaks at the level of the chromitite stringers.

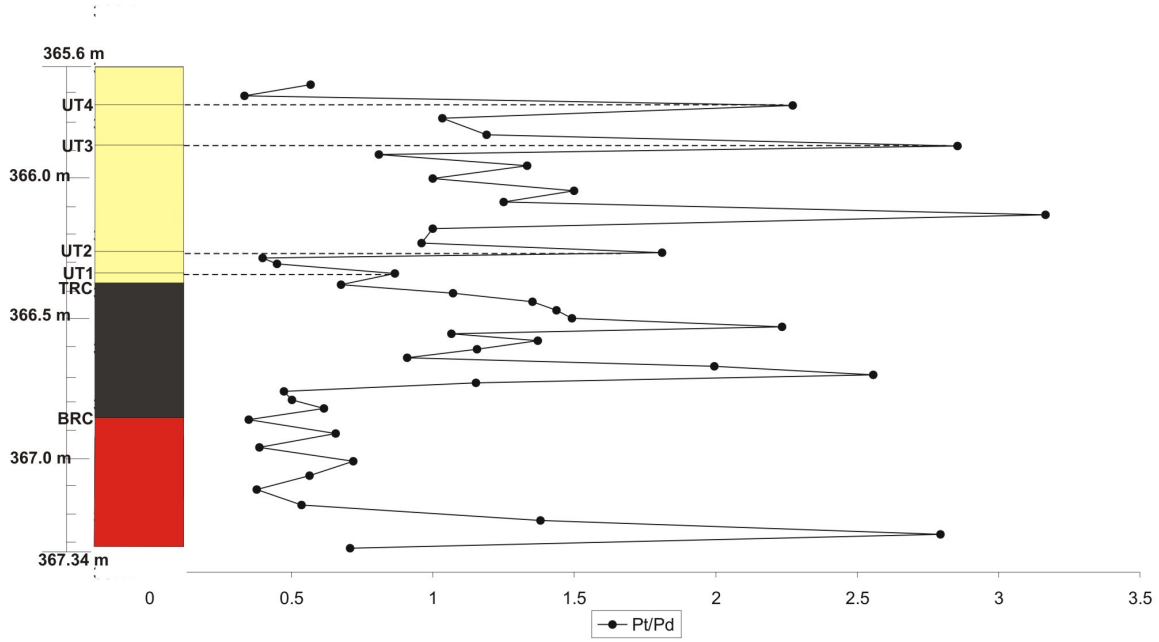

Figure 7.11: Stratigraphic variation of the Pt/Pd ratio through the ZG219 MH ore zone section.

Several representative PGE ratio distribution plots which showed systematic trends were selected and are provided in Figure 7.12. There are distinct similarities in the Au/Pd, Ir/Pt, Os/Pt, Rh/Pt and Ru/Pt plots with all plots exhibiting high values in the footwall followed by a systematic decrease through the chromitite up to the UT2 stringer. Higher values are typically shown in these plots above the UT2 along with an upward decrease through the hanging wall pyroxenite. The only difference is in the Au/Pd plot where there is an increase through the chromitite followed by a sudden drop at the UT2 stringer. The Os/Ir profile, however, shows a contrasting pattern and it exhibits low footwall values along with a systematic increase through the ore zone up to the UT2 stringer.

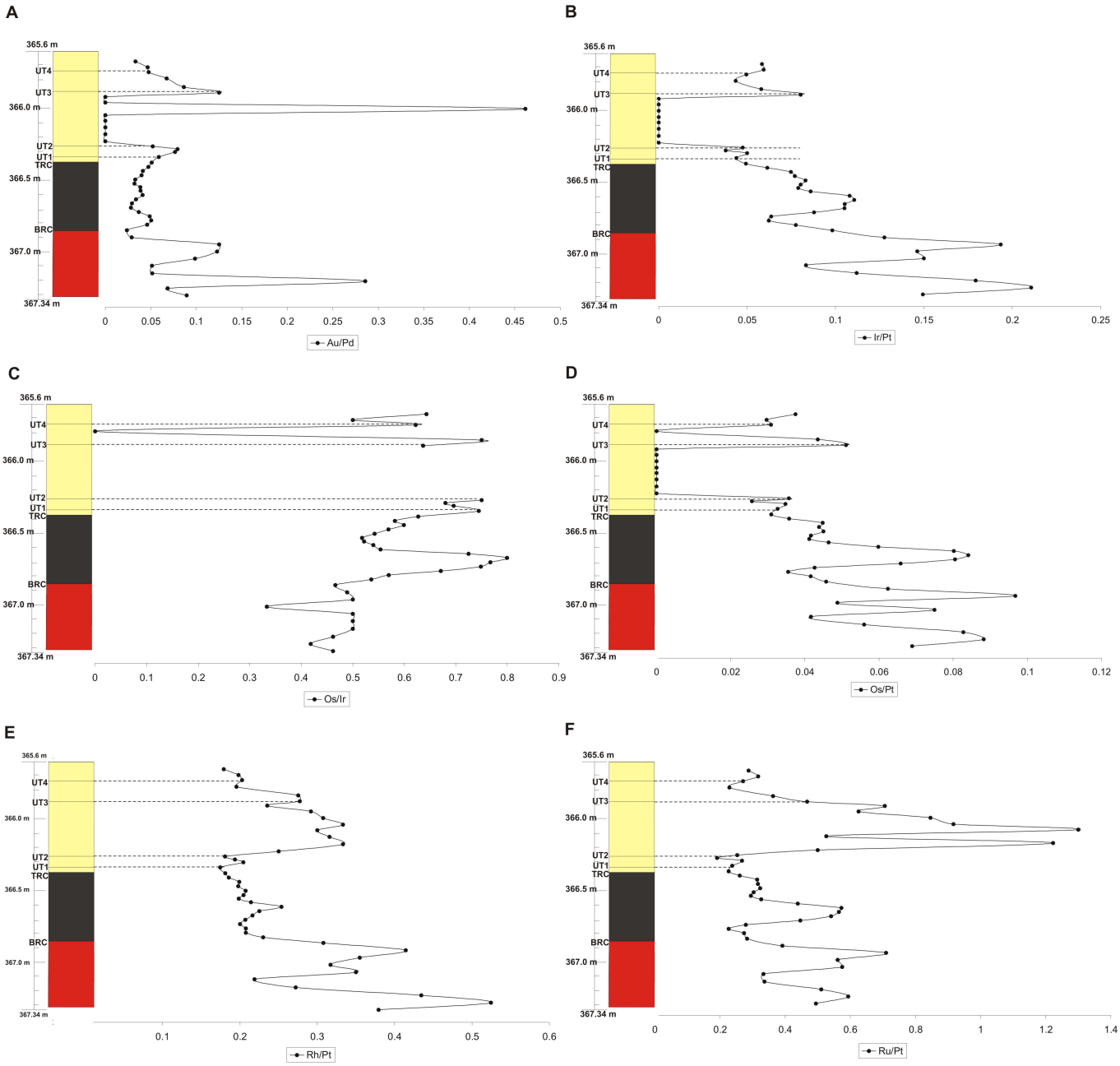

Figure 7.12: Vertical distribution plots showing the stratigraphic variation of a variety of selected PGE-ratios through the ZG219 MH ore zone section. (A) Au/Pd. (B) Ir/Pt. (C) Os/Ir. (D) Os/Pt. (E) Rh/Pt. (F) Ru/Pt. The blank zone in C is due to both Os and Ir being below the detection limit through this zone.

Chondrite normalized PGE patterns are provided for the different lithologies of the ZG219 MH ore zone in Figures 7.13 (UG2 chromitite), 7.14 (hanging wall chromitite stringers), 7.15 (footwall pegmatoidal pyroxenite) and 7.16 (hanging wall felspathic pyroxenite). Several differences are seen to exist between the different lithological PGE patterns. Pd occurs as the peak value for the UG2 chromitite, the UT1 stringer and the hanging wall feldspathic pyroxenite whilst Rh forms the peak value for the rest (i.e. the pegmatoidal

pyroxenite and chromitite stringers UT2 – UT4). The UG2 chromitite shows the most constrained pattern whilst the pegmatoidal pyroxenite and, especially, the hanging wall pyroxenite show a greater variation in pattern. The UT1 stringer exhibits a pattern similar to the UG2 chromitite whilst the UT2 – UT4 stringers show a pattern similar to that of the pegmatoidal pyroxenite.

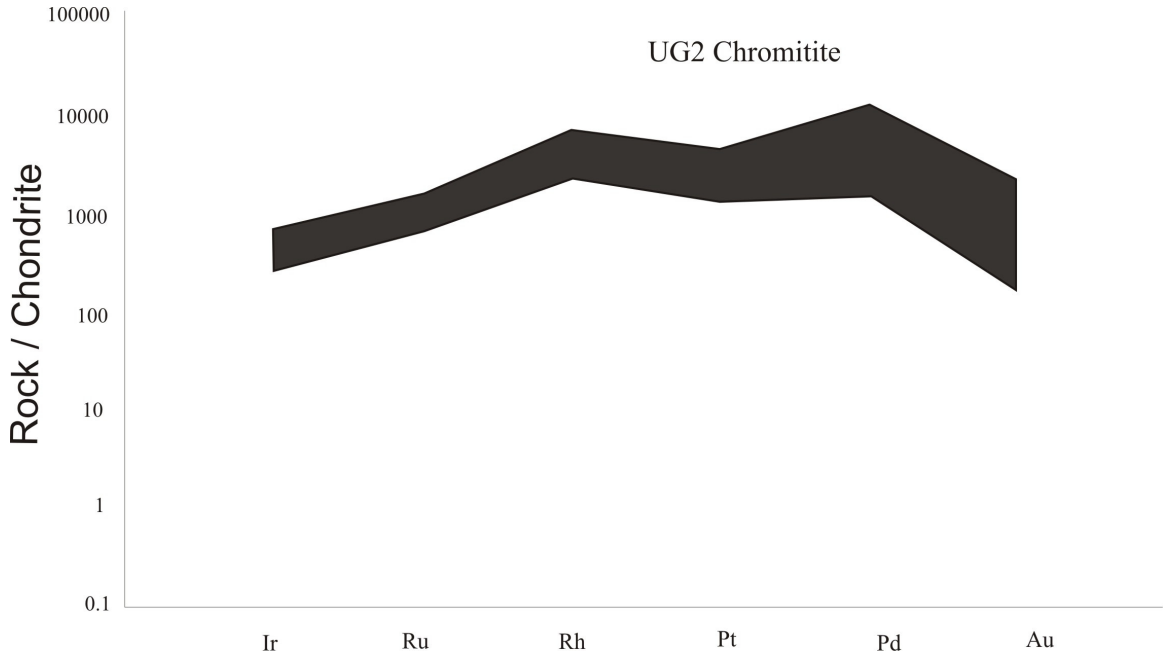

Figure 7.13: Chondrite (C1) normalized PGE pattern for the ZG219 MH UG2 chromitite.

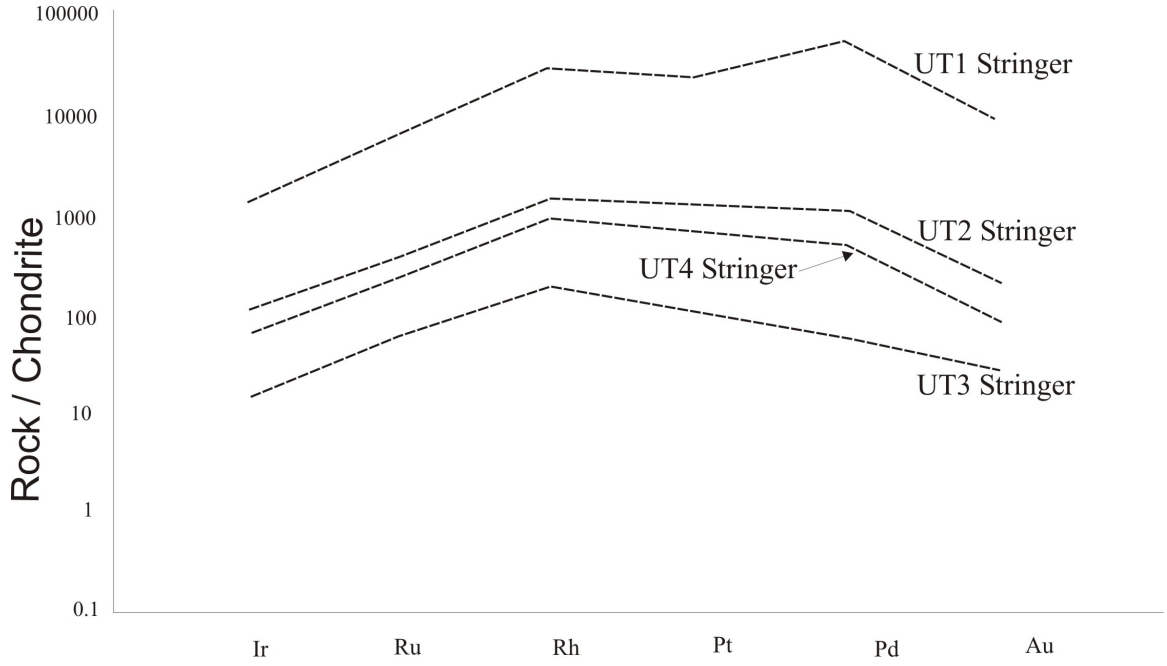

Figure 7.14: Chondrite (C1) normalized PGE patterns for the four ZG219 MH hanging wall chromitite stringers.

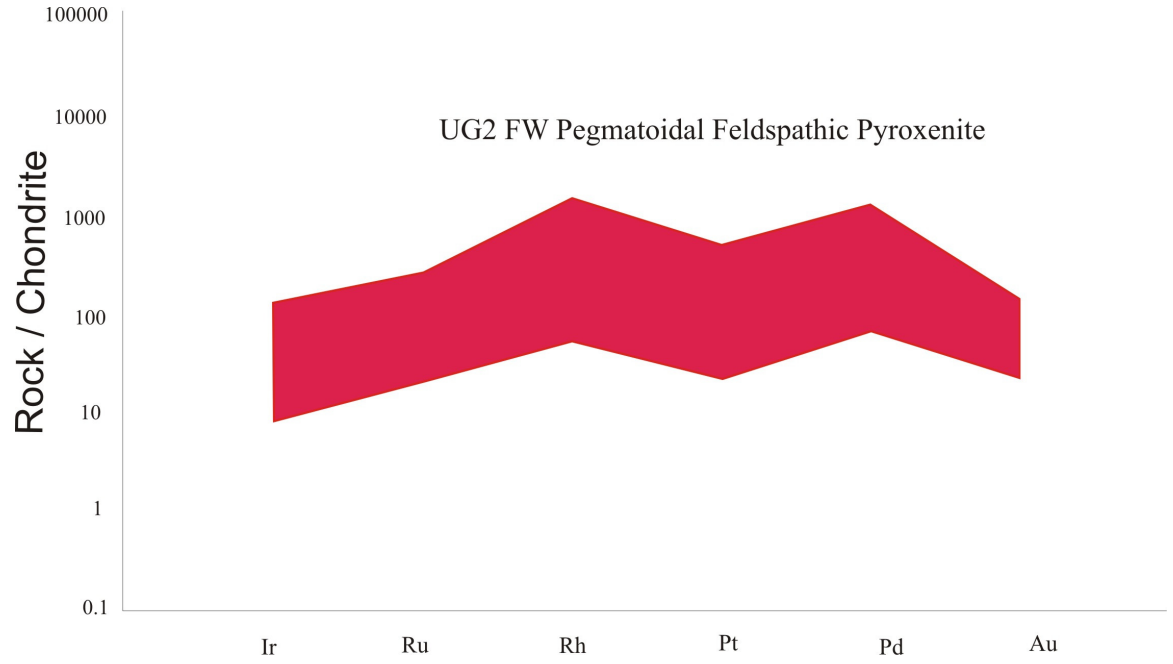

Figure 7.15: Chondrite (C1) normalized PGE pattern for the ZG219 MH UG2 footwall pegmatoidal feldspathic pyroxenite.

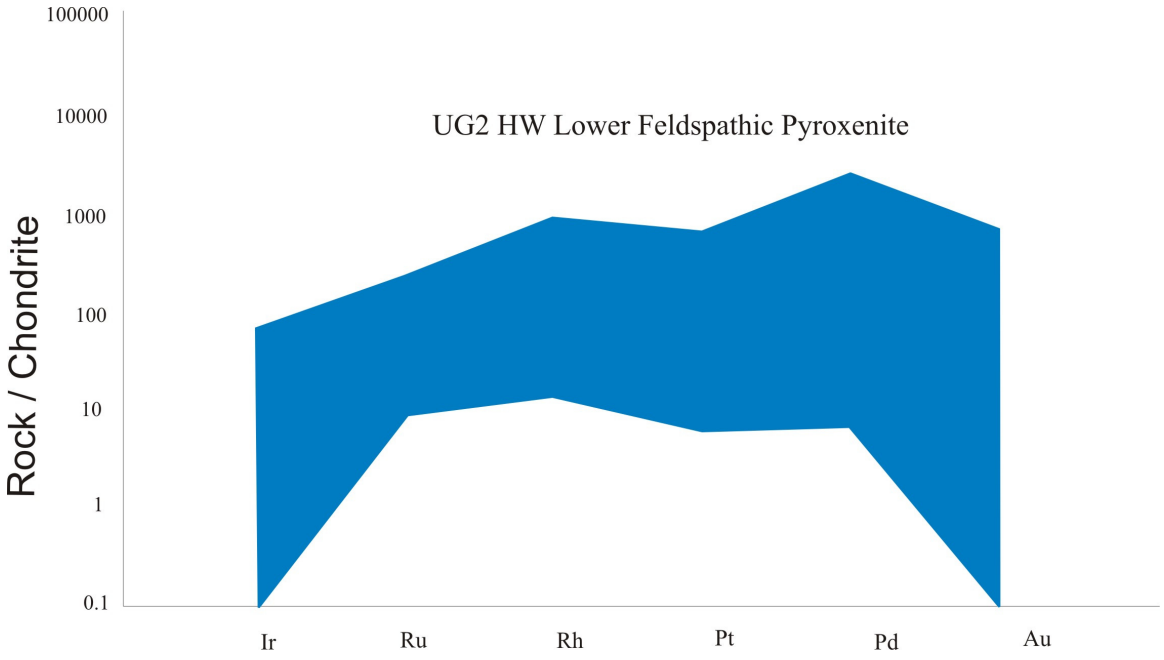

Figure 7.16: Chndrite (C1) normalized PGE pattern for the ZG219 MH UG2 hanging wall lower feldspathic pyroxenite.

7.5 Inter-Element PGE Plots

A series of inter – element plots are shown in Figures 7.17 – 7.23. These are used to test the dependencies (or controls) of one element on another. This can be used to test the controls on the PGE and can provide important information relating to the mineralization process of the PGE.

From Figure 7.17 it is clear that there is a moderately strong correlation between the BMS and the total PGE (especially through the UG2 chromitite). This indicates a degree of control on the PGE by the BMS through the UG2 chromitite.

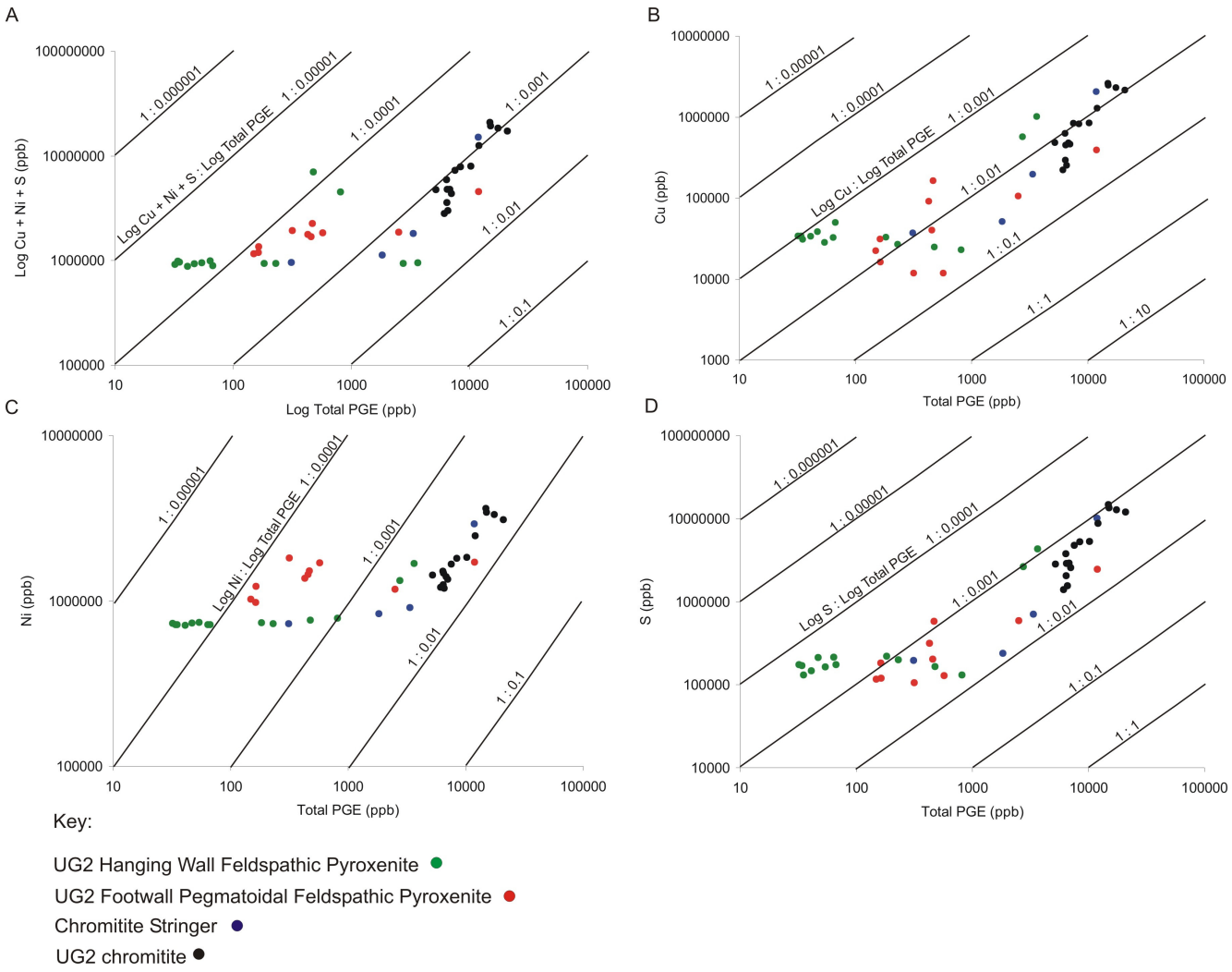

Figure 7.17: A variety of selected inter-element plots. (A) Log Cu + Ni + S (ppb) vs. log total PGE (ppb). (B) Log Cu (ppb) vs. log total PGE (ppb). (C) Log Ni (ppb) vs. log total PGE (ppb). (D) Log S (ppb) vs. log total PGE (ppb).

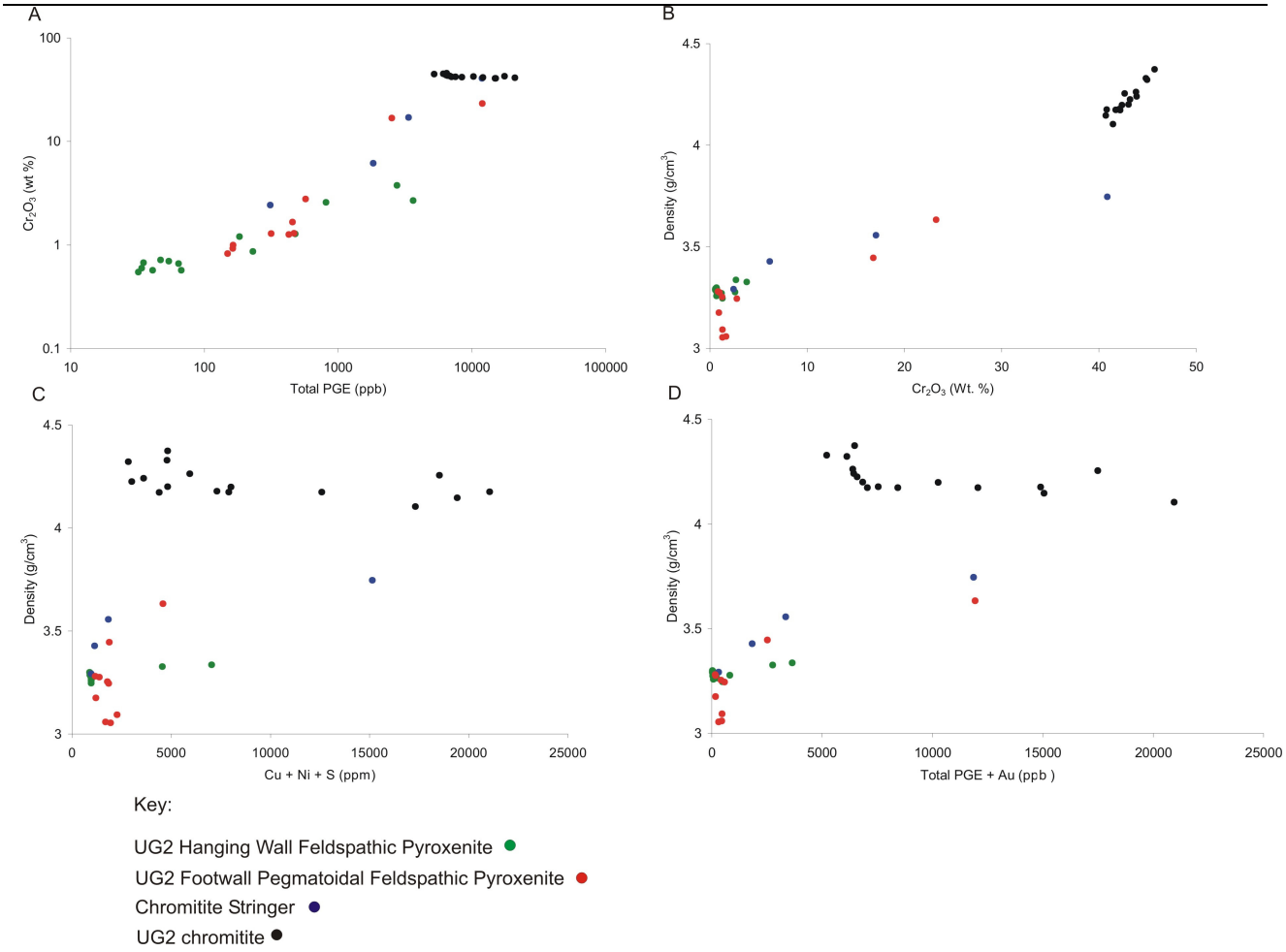

Figure 7.18: A variety of selected inter-element plots. (A) Log Cr_2O_3 (Wt. %) vs. log total PGE (ppb). (B) Density (g/cm^3) vs. Cr_2O_3 (Wt. %). (C) Density (g/cm^3) vs. Cu + Ni + S (ppm). (D) Density (g/cm^3) vs. total PGE plus Au (ppb).

Figure 7.18 exhibits a variety of inter element plots related to the density of the UG2 chromitite. Figure 7.18 A shows a positive correlation to exist between the Cr_2O_3 and the PGE abundance within the silicate lithologies, whilst a slight negative relationship exists between the two in the UG2 chromitite. The positive relationship is due to PGE mineralization within the silicates mostly linked to the hanging wall chromitite stringers or to areas of disseminated chromite mineralization within the footwall pegmatoidal pyroxenite. The negative relationship is possibly linked to intercumulate framework of the chromitite and the textural setting of the PGE. The PGM and BMS (which both host the PGE) have been identified as occurring mainly within the interstitial framework of the cumulus chromites (Chapter 8). Therefore, where the chromitite displays a closed packing framework there will be limited intercumulate space available and thus minimal PGM or BMS mineralization. Where the chromitite displays an open framework a larger amount of intercumulate space is available and thus greater amounts of PGM and BMS mineralization is expected.

Figure 7.18 B shows that in the UG2 chromitite and other chromitite bearing rocks (i.e. the chromitite stringers and portions of the footwall pegmatoidal pyroxenite) the density is very much controlled by the chromite abundance. This is also evident in Figure 7.1 C and D where the UG2 chromitite shows a negative relationship between density and both BMS and PGE abundance, due to these elements displaying a negative relationship to the chromite abundance, which is the major control on the density.

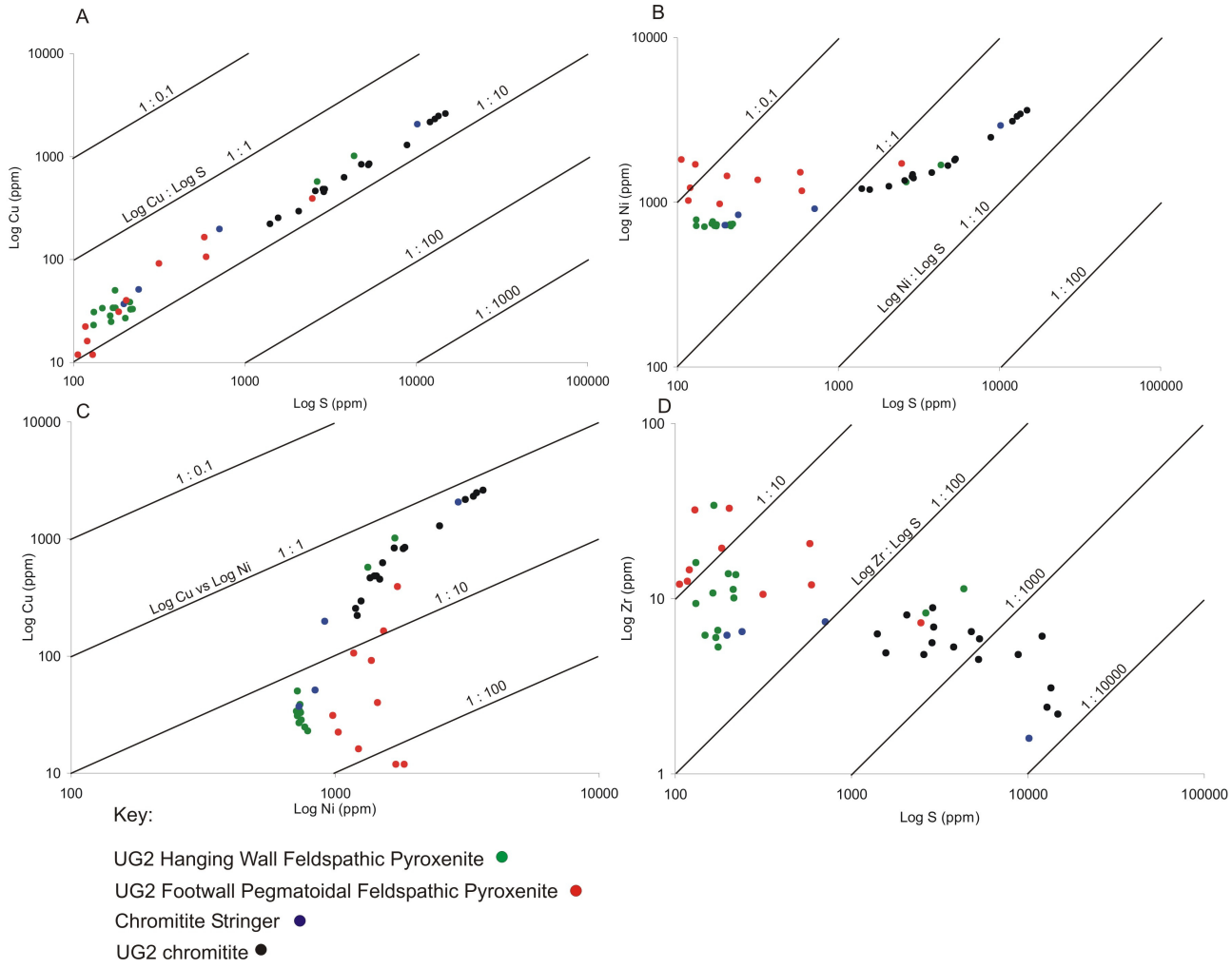

Figure 7.19: A variety of selected inter-element plots. (A) Log Cu (ppm) vs. log S (ppm). (B) Log Ni (ppm) vs. log S (ppm). (C) Log Cu (ppm) vs. log Ni (ppm). (D) Log Zr (ppm) vs. log S (ppm).

Figure 7.19 shows several BMS inter-element plots. Very strong positive relationships are seen to exist between each of the base metals. The high background values of Ni are due to it partitioning into orthopyroxene. Figure 7.19 D exhibits a broad negative correlation between Zr and S. Zr is used to monitor the amount of trapped interstitial liquid (see chapter 6) whilst S monitors solely the amount of BMS mineralization. Because both the trapped liquid and the BMS mineralization both inhabit the intercumulus pore space in the chromitite the negative correlation provides evidence that the trapped liquid and the BMS mineralization must have competed for interstitial space during crystallization. It is possible that either one

may have displace the other from its original position (the rising late-stage, postcumulus liquid or the percolating, primary sulphide melt) or that one took up position first and the other occupied what was left of the intercumulus pore space at a later stage.

Table 7.1 provides a qualitative degree of correlation between the PGE and the BMS. It is based on a visual examination of the respective inter-element plots and is solely a qualitative indication. All the 'very good' correlation plots, as well a few other select plots, are provided in Figures 7.20 to 7.23.

Table 7.1: The qualitative degree of correlation between the different PGE, BMS and gold (based on a visual examination of the inter-element plots).

	Pt	Pd	Rh	Ir	Os	Ru	Au	Cu	Ni	S
Pt		Average	Very good	Good	Good	Good	Average	Average	Average	Average
Pd	Average		Average	Poor	Poor	Poor	Very good	Very good	Very good	Good
Rh	Very good	Average		Good	Good	Good	Average	Average	Average	Average
Ir	Good	Poor	Good		Very good	Very good	Very poor	Very poor	Poor	Poor
Os	Good	Poor	Good	Very good		Very good	Very poor	Very poor	Poor	Poor
Ru	Good	Poor	Good	Very good	Very good		Very poor	Poor	Poor	Poor
Au	Average	Very good	Average	Very poor	Very poor	Very poor		Very good	Good	Very good
Cu	Average	Very good	Average	Very poor	Very poor	Poor	Very good		Good	Very good
Ni	Average	Very good	Average	Poor	Poor	Poor	Good	Good		Very good
S	Average	Good	Average	Poor	Poor	Poor	Very good	Very good	Very good	

Key

Very good	
Good	
Average	
Poor	
Very poor	

Figure 7.20 exhibits the inter-element plots between S and all the individual PGE. Figure 7.20 B stands out distinctly as it shows a 'good' correlation between S and Pd whilst the remaining plots range from poor to average. Pd, due to its markedly chalcophile nature, therefore differs from the remaining PGE in that it shows a good correlation with S.

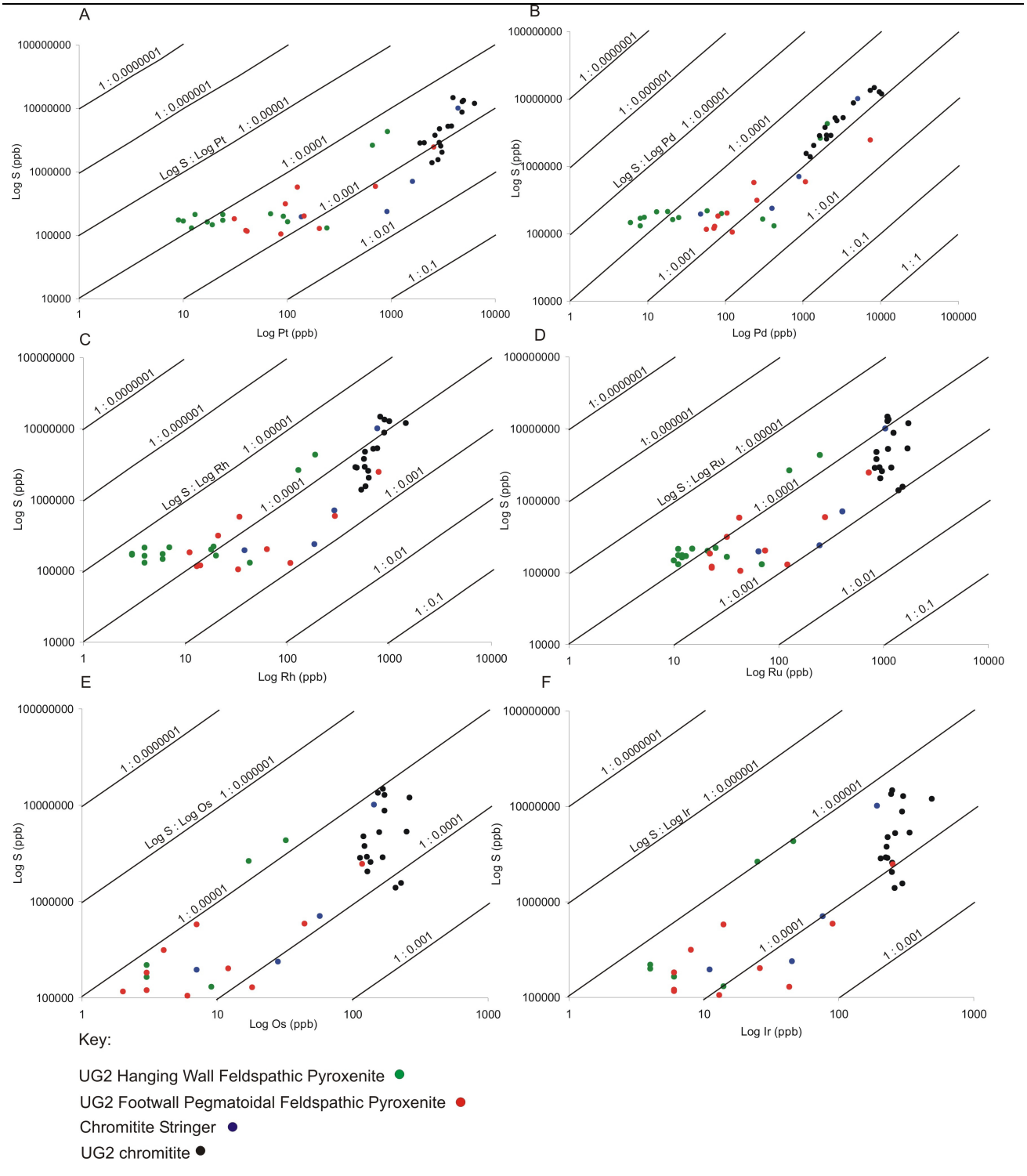

Figure 7.20: A variety of selected inter-element plots. (A) Log S (ppb) vs. log Pt (ppb). (B) Log S (ppb) vs. log Pd (ppb). (C) Log S (ppb) vs. log Rh (ppb). (D) Log S (ppb) vs. log Ru (ppb). (E) Log S (ppb) vs. log Os (ppb). (F) Log S (ppb) vs. log Ir (ppb).

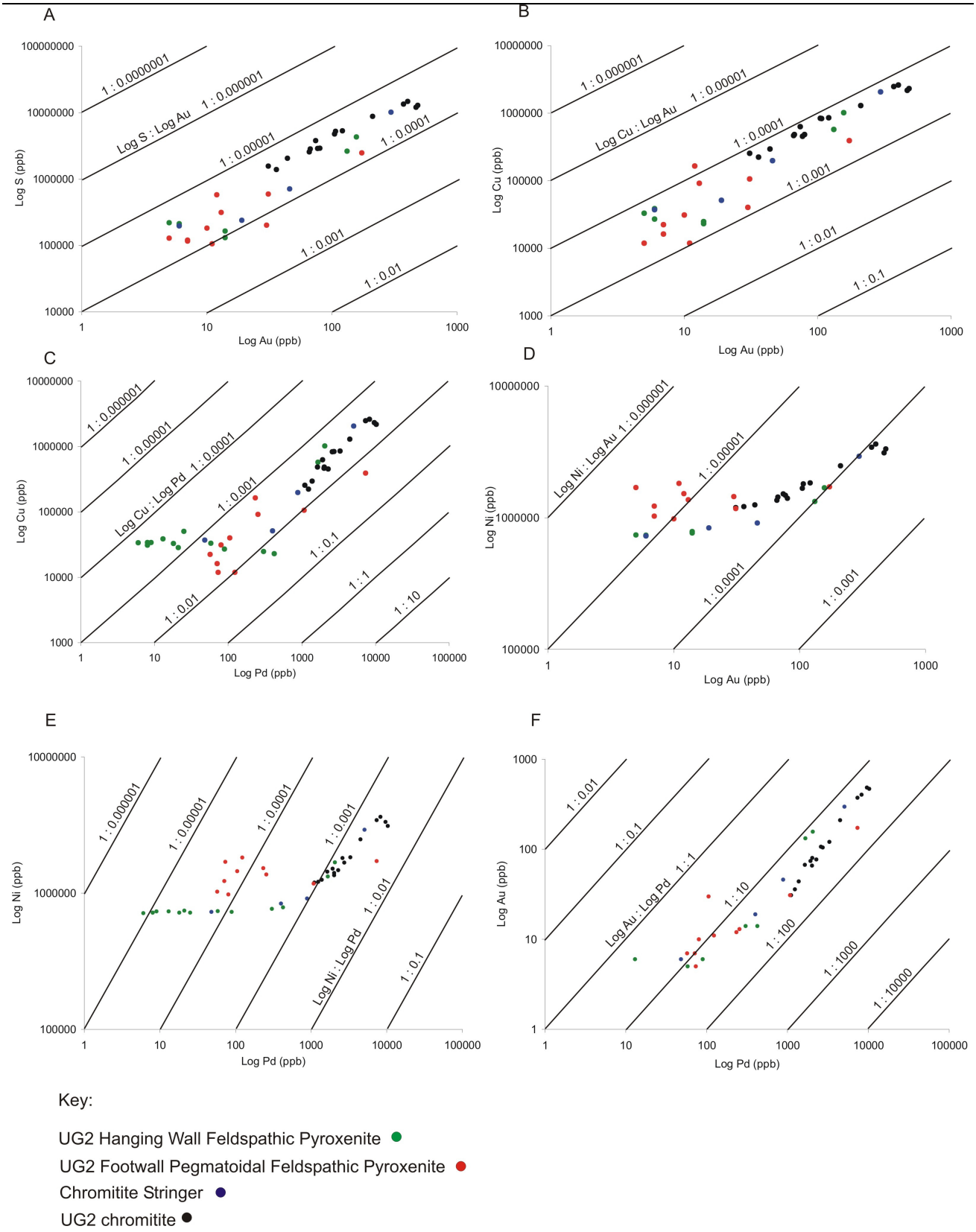

Figure 7.21: A variety of selected inter-element plots. (A) Log S (ppb) vs. log Au (ppb). (B) Log Cu (ppb) vs. log Au (ppb). (C) Log Cu (ppb) vs. log Pd (ppb). (D) Log Ni (ppb) vs. log Au (ppb). (E) Log Ni (ppb) vs. log Pd (ppb). (F) Log Au (ppb) vs. log Pd (ppb).

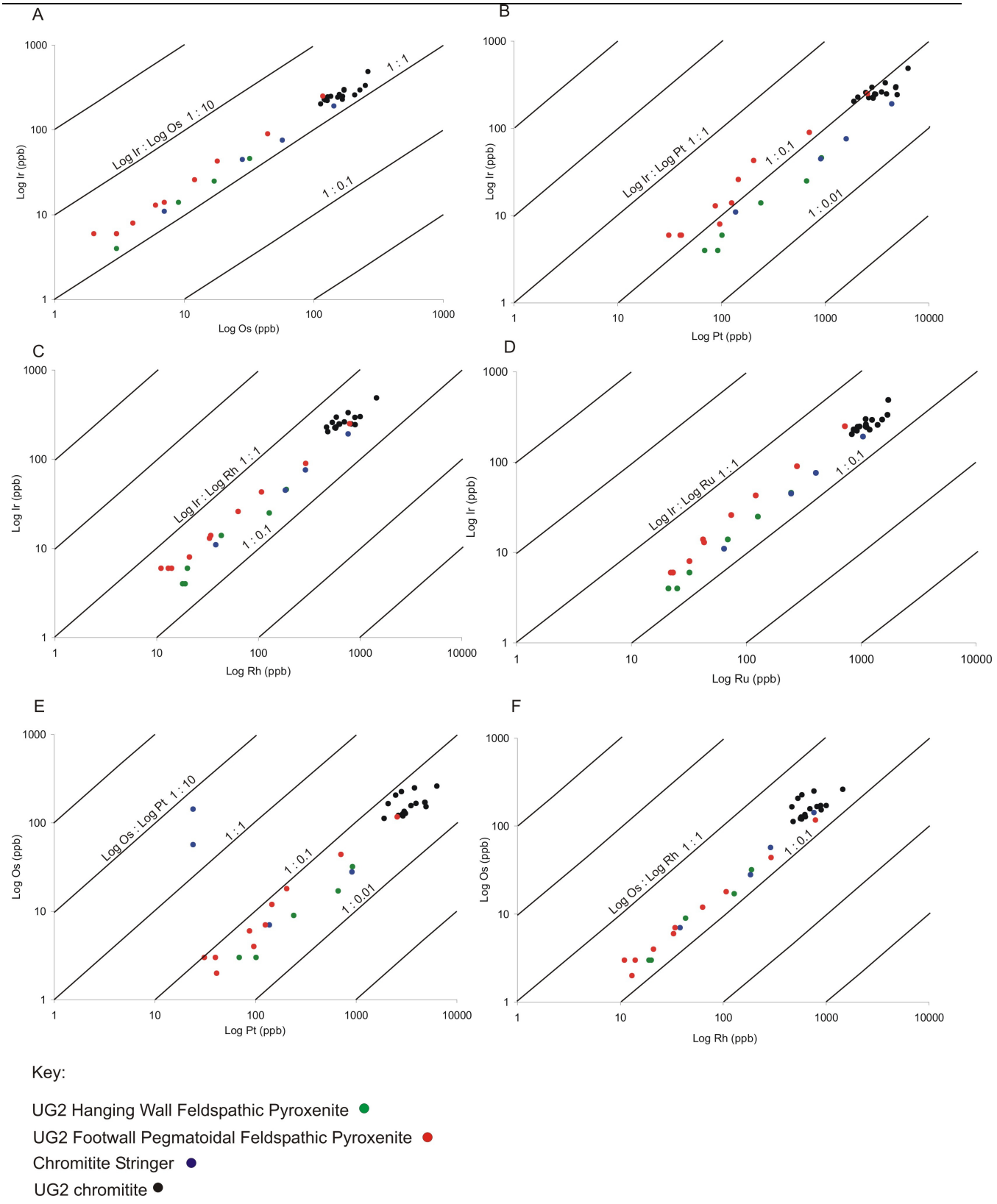

Figure 7.22: A variety of selected inter-element plots. (A) Log Ir (ppb) vs. log Os (ppb). (B) Log Ir (ppb) vs. log Pt (ppb). (C) Log Ir (ppb) vs. log Rh (ppb). (D) Log Ir (ppb) vs. log Ru (ppb). (E) Log Os (ppb) vs. log Pt (ppb). (F) Log Os (ppb) vs. log Rh (ppb).

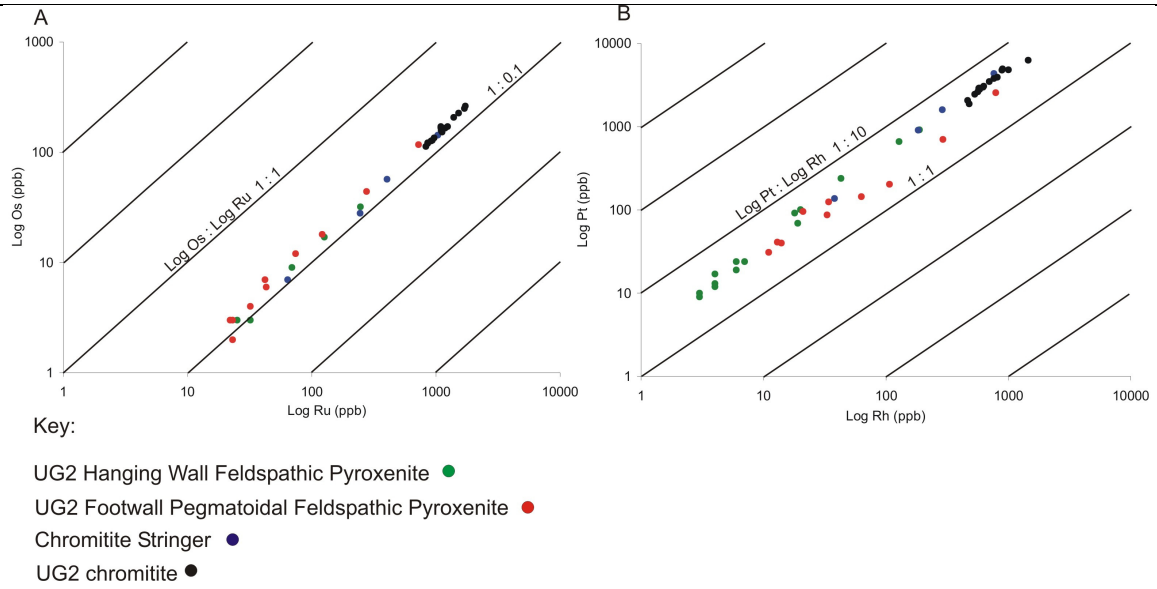

Figure 7.23: Selected inter-element plots. (A) Log Os (ppb) vs. log Ru (ppb). (B) Log Pt (ppb) vs. log Rh (ppb).

Figure 7.21 shows a series of inter-element plots involving base metals plus sulphur as well as Pd and Au. As expected the base metals plus sulphur show very strong positive relationships with each other. It is also clear from Figure 7.21 that both Pd and Au exhibit 'good' to 'very good' correlations with the base metals plus sulphur. Therefore both Pd and Au differ from the other PGE in that they exhibit, due to their chalcophile nature, good correlations with the base metals plus sulphur. The remaining PGE tend to be siderophile in character and show only strong correlations with other PGE (and not base metal plus sulphur). This is exhibited in Figures 7.22 and 7.23 where the PGE of a dominantly siderophile nature, i.e. all the PGE minus Pd, show strong relationships with each other. Therefore both Pd and Au appear to be controlled by the BMS and whilst the remaining PGE are controlled by PGM (i.e. all partition strongly into the different PGMs).

7.6 Conclusions

The following conclusions can be made regarding the PGE geochemistry:

- The PGE + Au grade is concentrated in a (bottom loaded) triple pronged profile pattern through the ore zone.
- The individual PGE profiles differ somewhat from each other, although all show a strong bottom peak (at the BRC) and an upper peak at the TRC (separated by a zone of lower abundance).
- The base metal plus sulphur distribution is similar to the PGE + Au pattern apart from the bottom peak which is slightly higher up than the PGE + Au bottom peak.
- The individual base metals plus sulphur (Cu, Ni and S) show an almost identical pattern as the total BMS pattern (Cu + Ni + S).
- High precious metals tenors (expressed as (PGE + Au)/S) exist in the footwall and also occur as three distinct peaks within the chromitite. These three peaks in the chromitite coincide with troughs in the Cu, Ni and S profiles. There is also a systematic upward decreasing trend through the chromitite and the hanging wall. This trend is reversed midway up through the hanging wall pyroxenite.
- The individual PGE and Au tenors show similar patterns with three peaks present within the chromitite although Pd, Au and Rh have a stronger bottom peak whilst the other PGE have larger middle peaks.
- The ratio (Pt + Pd + Rh)/(Os + Ir + Ru) shows a peak in the footwall as well as the characteristic triple peaks within the chromitite. There is a systematic upward increase through the upper portion of the chromitite up to the UT2 stringer. A trough then exists followed by a second upward increasing trend through the hanging wall pyroxenite.
- The Pt/Pd ratio shows a sawtooth type profile with the three peaks present within the chromitite, although the bottom peak is slightly higher than for the previous plots. There is a systematic upward decreasing trend through the upper portion of the chromitite up to the UT2 with the overlying hanging wall pyroxenite exhibiting relatively high values.
- The chondrite normalized PGE patterns reveals four sets of pattern types (lithologically related). The UG2 chromitite shows the most constrained pattern whilst the pegmatoidal pyroxenite and, especially, the hanging wall pyroxenite, show a larger variation. Pd forms the peak element for the UG2 chromitite, the UT1 stringer and the hanging wall pyroxenite whilst Rh is the peak for the pegmatoidal pyroxenite and stringers UT2 – 4.

- There is a negative correlation between the PGE and the Cr_2O_3 abundance (as well as with density). This is related to the textural framework of the rock, as the PGE (and BMS) are interstitial to the chromite. Therefore when the packing of the chromitite is more 'open' there is a greater amount of 'available' interstitial space for the PGE and BMS. This is reflected in the lower abundance of Cr_2O_3 and a greater amount of interstitial PGE and BMS.
- The base metal plus sulphur show very strong positive correlations with each other.
- Of the PGE only Pd and Au show strong correlations with the base metals and sulphur. This is attributed to their chalcophile character. The remaining PGE are all siderophile in nature and show poor to average correlations with the base metals and sulphur and good overall relationships with each other.

It is clear from the delicate trends exhibited by the metal distribution profiles that the mechanism of mineralization was most likely one of a primary magmatic origin. The author suggests that only primary magmatic processes could be responsible for producing such delicate metal profile patterns and trends. The triple peaked base metal plus sulphur and PGE profiles (Figure 7.2) show good correlation as well as a clearly defined triple peaked shape. It is possible that this pattern could suggest a multi pronged PGE mineralization event (i.e. a three stage process). Nevertheless it is clear (from the intricate chemical patterns) that the PGE and BMS mineralization present in the UG2 ore body were a result of primary magmatic processes with negligible subsequent postcumulus alteration or reworking.

There are a variety of suggested mechanisms for PGE mineralization in layered intrusions, and these are summarized in Chapter 9. Based on the PGE geochemical evidence the authour favours a primary magmatic model, of which there are two main theories: that of sulphide scavenging (i.e. Naldrett, 1989) and that where the PGE exist as metallic clusters in the melt (Tredoux *et al.,* 1995). The close mineralogical association between the PGM and BMS and the good chemical correlation between the PGE and BMS (especially between Pd and Au and the BMS) suggest the sulphide scavenging model to be the most likely mineralization mechanism.

Therefore a sulphide liquid would be responsible for scavenging and extracting the base and precious metals from the silicate melt (i.e. Naldrett, 1989). One point that needs to be addressed, however, is what caused sulphur supersaturation in the magma. Due to the fact that frequent magma injections into the chamber (with subsequent mixing) were seen to be occurring at this stage (Eales *et al.,* 1990), and that magma mixing is hereby suggested have generated the chromitite layers, the authour suggests that these influxes of new magma into the chamber were responsible for initiating sulphur supersaturation. This would provide a close

link between the formation of chromitite layers and the genesis of PGE mineralization, thereby explaining their close association (Scoon and Teigler, 1994; Kruger, 2002).

The mechanism of PGE enrichment into the sulphide liquid was therefore most likely a result of sulphide scavenging i.e. as the immiscible sulphide liquid separated from the silicate liquid and percolated downward through the pile it scavenged and collected PGE from the magma (Naldrett, 1989).

At magmatic temperatures the segregated sulphide melt, enriched in PGMs, would have begun to crystallize *mss* (monosulphide solid solution) (i.e. von Gruenewaldt *et al.,* 1990). During cooling, the PGE originally incorporated into the *mss* diffused to the sulphide grain boundaries to form PGMs (mainly PGE-sulphides and PGE-tellurides) (i.e. von Gruenewaldt *et al.,* 1990). This explains the close sulphide-PGM association, as well as the propensity of the PGMs to be located at phase boundaries (especially triple point junctions) (see Chapter 8). Some of the PGM remained in solid solution in the sulphide phases (i.e. Pd in pentlandite). During this stage, appreciable amounts of Pd and Au partitioned into the BMS minerals (due to their strong chalcophile tendencies) to occur in a solid solution state within the BMS minerals. Therefore, the remaining PGE all partitioned strongly into the PGM. This explains the close relationship between Pd and Au and the BMS as well as the remaining PGE with each other (see Chapter 7). Negligible geochemical evidence for any postcumulus alteration or remobilization exists (i.e. higher concentrations of more mobile elements such as K_2O). The PGE geochemical results of this work therefore point to a primary magmatic mineralization model for the UG2 ore body

8. Mineralogy and Mineral Distributions

8.1 Introduction

A mineralogical investigation was carried out on the ZG219 D1 (deflection 1) UG2 intersection. This core is a deflection from the ZG219 borehole and it is used in both the mineralogy and petrography portions of this study. The ZG219 D1 UG2 chromitite section was sampled in detail by taking continuous 3 cm samples throughout its length. These samples were then examined using a variety of sophisticated mineralogical techniques from basic ore microscopy through to automated electron beam technology such as the Qem-Scan (quantitative evaluation of materials using scanning electron microscopy) and MLA (mineral liberation analyser) (Appendix F). These techniques generated quantitative data on the overall bulk mineralogy of the ZG219 D1 UG2 as well as on the base-metal sulphide (BMS) and platinum-group mineral (PGM) assemblages within the chromitite.

8.2 Mineralogical Techniques

In terms of qualitative techniques the Optimas (optical image analyzer) was used for documenting the BMS assemblages within the UG2 (reflected light microscopy).

Quantitative data was obtained for the BMS and PGM assemblages using state-of-the-art automated SEM (scanning electron microscopy) techniques in the form of the MLA (mineral liberation analyser) and the Qem-Scan (quantitative evaluation of materials using scanning electron microscopy). Both these instruments are ordinary SEMs equipped with highly advanced and specific software packages which enable them to function in a fully automated state. The individual techniques are briefly discussed here:

(1) Qem-Scan (Quantitative Evaluation of Materials using Scanning Electron Microscopy)

The Qem-Scan consists of a Leo 1450 SEM, equipped with four light element energy dispersive X-ray detectors, a microanalyser and an electronic processing unit (software package) developed by CSIRO in Melbourne, Australia. At Anglo Research the Qem-Scan technique is primarily used for bulk modal and BMS characterization. For this project, however, it was used for textural mapping – the mapping of rock slabs using X-ray analysis to produce a detailed mineralogical map exhibiting the in-situ textures as well as the overall mineralogical distribution.

(2) MLA (Mineral Liberation Analyzer)

The MLA comprises an XL40 SEM (Figure 2.2) and Edax energy dispersive X-ray analysis system combined with a software package developed at JKMRC in Brisbane, Australia. The MLA is ideal for characterizing the PGMs – which occur only in trace amounts the Bushveld ore-bodies (i.e. the Merensky reef, Platreef and the UG2 reef). The MLA technique relies on BSE (back scattered electron) imaging (i.e. the difference in BSE

grey levels, which is a direct function of the atomic number) to search and to locate the PGMs (which, due to their larger atomic number, appear much brighter compared to the silicate, chromite and BMS minerals). Once the PGMs have been located, x-ray spectra are collected in centroid positions from the different BSE grey level zones (i.e. the PGM and its associated minerals). Due to the PGMs being very small (~ 5µm) the MLA, once it has located the PGM due to its BSE brightness, zooms into a higher resolution before proceeding with the x-ray collection. The x-ray spectra are then later compared to the in-house set of PGM standards and the minerals classified accordingly.

There are a variety of different MLA measurement types – all using varying combinations of BSE imaging and x-ray analysis. Due to the fact that whole rock slabs were analyzed (as opposed to crushed and milled material) it was decided that the sparse phase liberation lite (spl-lite) PGM-characterization method be used. This method is used for coarse-grained material or for rock slabs (as in this case). Once the machine has identified and located a PGM (on this basis of BSE grey levels) it draws a block around it so that only the PGM and its directly surrounding particles are analyzed. The final result from this measurement is a series of mineral maps (Figure 8.1) from which quantitative modal mineralogy, mineral size and association data are obtained.

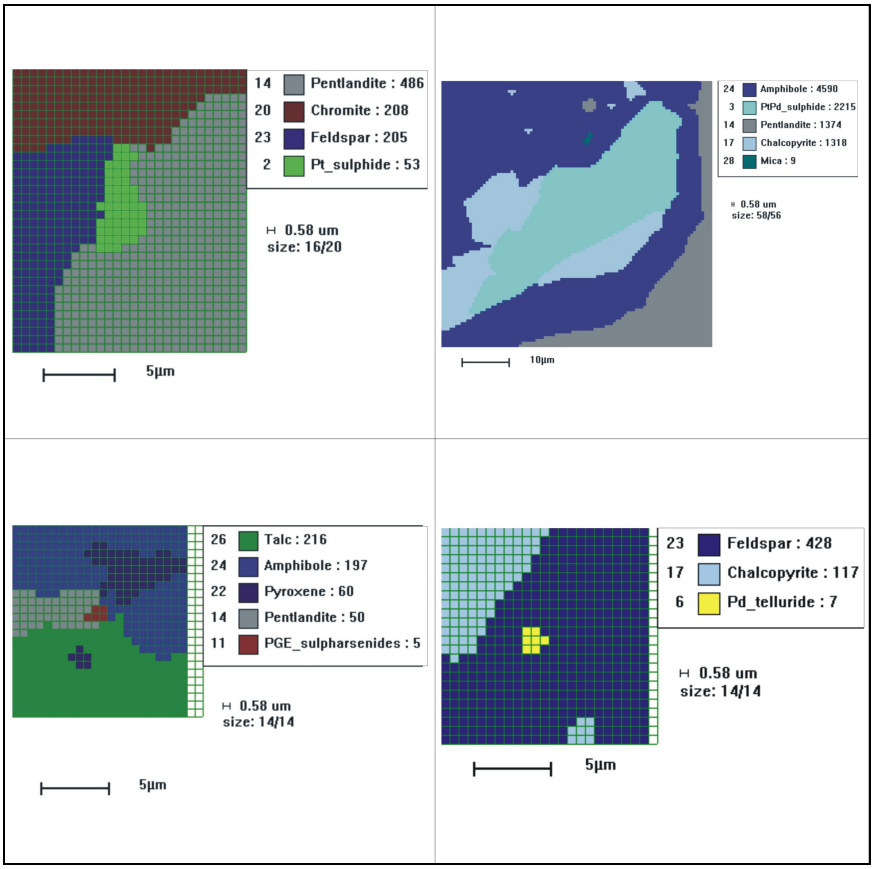

Figure 8.1: MLA spl-lite mineral maps from the ZG219 samples. Note the fine grain size of the PGMs.

This section has served as a brief introduction to these two forms of automated SEMs, as well as the measurement types utilized. Both these techniques are extremely important for applied mineralogy i.e. identifying metallurgical process problems, optimizing concentrator circuit design and characterizing in-situ exploration and ore body material (as carried out in this project). The reader is, however, referred to the literature for further detailed information regarding these techniques and their applications (i.e. Jones, 1987; Petruk, 1986, 1988, 2000; King, 1993, Gu, 2003).

8.3 Bulk Mineralogy

8.3.1 Bulk Mineralogical Composition

The bulk mineralogical composition of the ZG219 D1 UG2 was characterized using a Qem-Scan bulk modal measurement (a form of automated point counting). This generated quantitative data on the overall bulk mineralogical composition of the ZG219 D1 UG2 (Table 8.1 and Figure 8.2) as well as the vertical mineralogical variation through the chromitite (Tables 8.2 and 8.3, Figures 8.3 and 8.4).

Table 8.1: Bulk mineralogical composition of the ZG219 D1 UG2.

Mineral Type	ZG219 D1 UG2
Chromite	85.4
Plagioclase	7.6
Orthopyroxene	1.0
Clinopyroxene	0.7
Hydrous Minerals	4.4
Talc	3.1
Amphibole	0.3
Chlorite	0.6
Phlogopite	0.4
BMS	1.0
Total	100.0

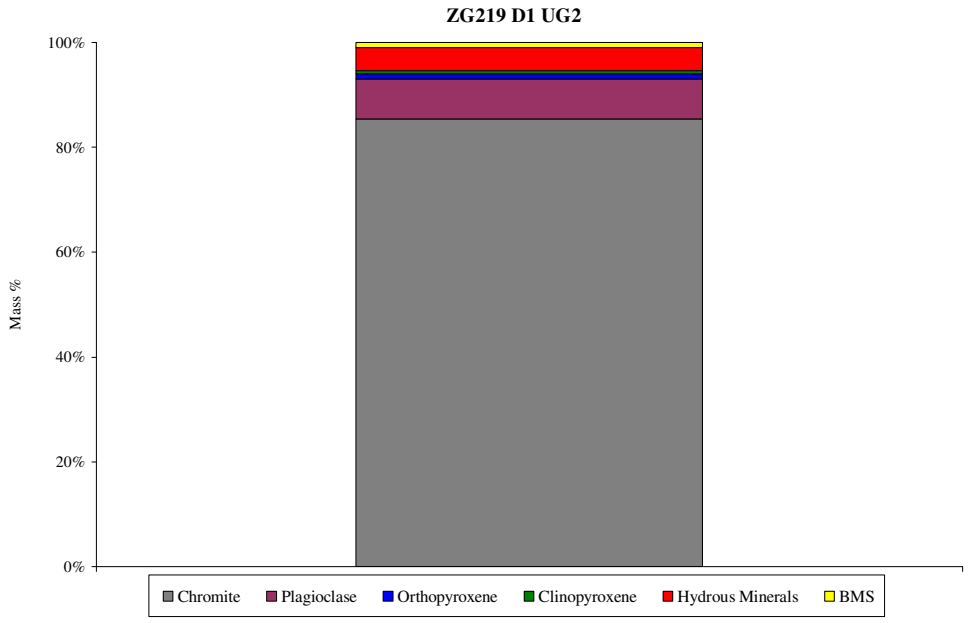

Figure 8.2: Bulk mineralogical composition of the ZG219 D1 UG2.

The overall bulk mineralogical composition of the ZG219 D1 UG2 chromitite comprises mainly chromite (~85 %), with lesser plagioclase (~7.5 %) and orthopyroxene (~1 %), with a total BMS content of ~1 %. Variable amounts of primary hydrous minerals also exist and include talc, amphibole, chlorite and phlogopite. These hydrous phases are suggested to represent postcumulus primary minerals which have formed by primary entrapment of the final liquid during the advanced (postcumulus) stages of fractionation. A variety of incompatible elements (including water) have become trapped within this interstitial liquid and have eventually crystallized out to form these hydrous phases. These phases can therefore be used to monitor the degree of trapped liquid through the chromitite.

Table 8.3: Bulk mineralogical composition of the upper half of the ZG219 D1 UG2.

Mineral Type	161	162	163	164	165	166	167	168
Chromite	84.1	76.1	80.0	78.5	78.0	88.3	88.9	92.5
Plagioclase	11.6	11.2	11.8	11.0	6.2	9.5	4.8	3.6
Orthopyroxene	0.2	2.1	1.4	2.2	3.5	0.2	1.0	0.3
Clinopyroxene	0.1	0.5	0.4	0.5	1.1	0.1	0.4	0.1
Hydrous Minerals	1.3	7.2	5.4	7.6	11.0	1.4	4.0	2.9
Talc	0.6	5.9	4.2	6.2	9.5	0.5	3.2	1.9
Amphibole	0.1	0.3	0.2	0.4	0.5	0.1	0.3	0.1
Chlorite	0.2	0.6	0.3	0.3	0.5	0.2	0.3	0.5
Phlogopite	0.5	0.5	0.7	0.7	0.4	0.7	0.2	0.4
BMS	2.7	2.8	1.0	0.2	0.2	0.5	0.9	0.6
Total	100.0	100.0	100.0	100.0	100.0	100.0	100.0	100.0

Table 8.4: Bulk mineralogical composition of the lower half of the ZG219 D1 UG2.

Mineral Type	169	170	171	172	173	174	175	176
Chromite	88.6	95.7	95.2	87.0	89.2	89.5	80.8	76.6
Plagioclase	3.4	0.5	1.6	8.5	6.0	5.3	11.8	12.3
Orthopyroxene	1.3	0.5	0.4	0.5	0.6	0.3	0.6	0.4
Clinopyroxene	0.4	0.1	0.1	0.6	0.4	0.8	0.9	3.9
Hydrous Minerals	4.6	2.8	2.5	3.2	3.4	2.8	4.0	5.9
Talc	3.7	2.2	1.7	1.8	2.2	1.8	2.1	1.7
Amphibole	0.2	0.0	0.1	0.4	0.4	0.4	0.6	0.7
Chlorite	0.4	0.5	0.4	0.4	0.5	0.5	1.0	2.8
Phlogopite	0.2	0.1	0.3	0.6	0.3	0.2	0.4	0.7
BMS	1.7	0.3	0.2	0.1	0.4	1.3	1.9	0.8
Total	100.0	100.0	100.0	100.0	100.0	100.0	100.0	100.0

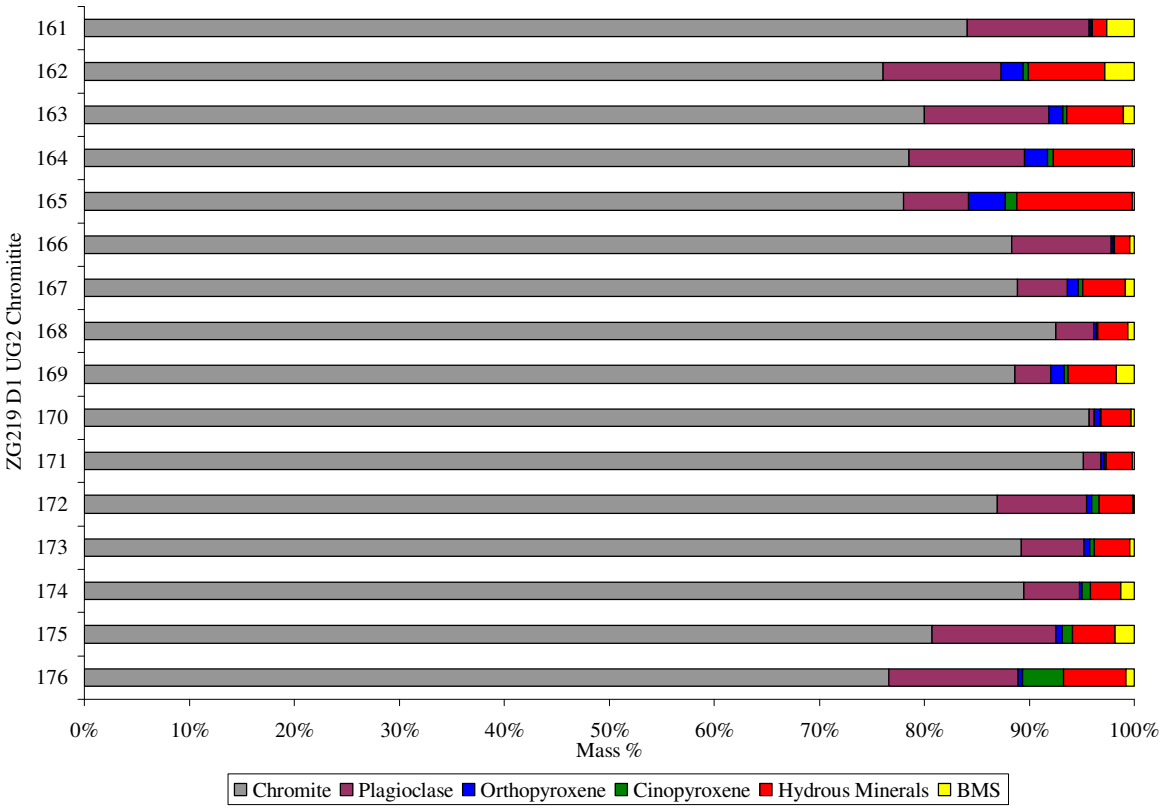

Figure 8.3: Vertical bulk mineralogical composition through the ZG219 D1 UG2.

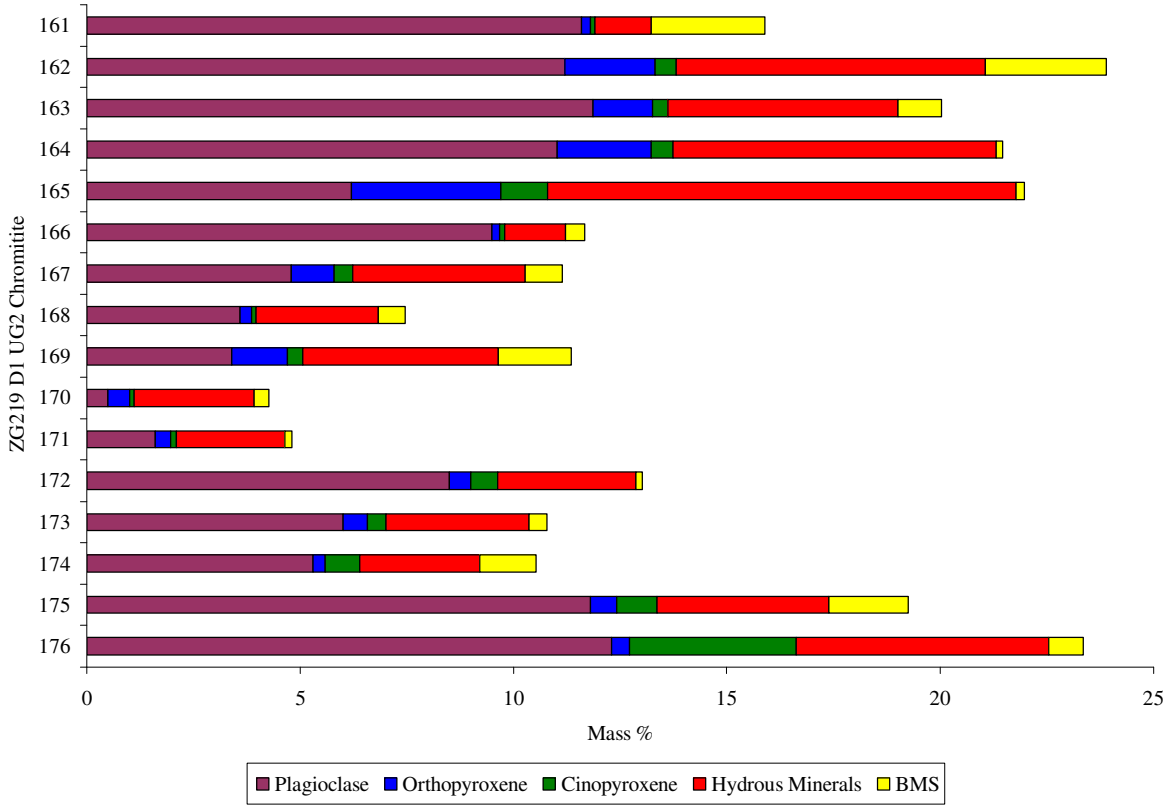

Figure 8.4: Vertical relative bulk mineralogical composition through the ZG219 D1 UG2 excluding chromite.

Figure 8.3 represents the total bulk mineral compositional profile for the ZG219 D1 UG2 whilst Figure 8.4 is the same as Figure 8.3 except that it excludes chromite (in order to better display the trends of the accessory phases). These profiles indicate that there is some distinct variation in the distribution and the amounts of all the major and accessory minerals through the UG2 (note numbers 161 to 176 are the sample numbers). This is especially true for the hydrous minerals and the BMS profiles. The distribution profile of both the BMS and the hydrous minerals (which are indicative of trapped interstitial liquid) will be important when attempting to decipher the mineralization and crystallization history of the UG2. The BMS profile will be discussed in the next section whilst the profile of the hydrous mineral distribution through the UG2 is presented in Figure 8.5.

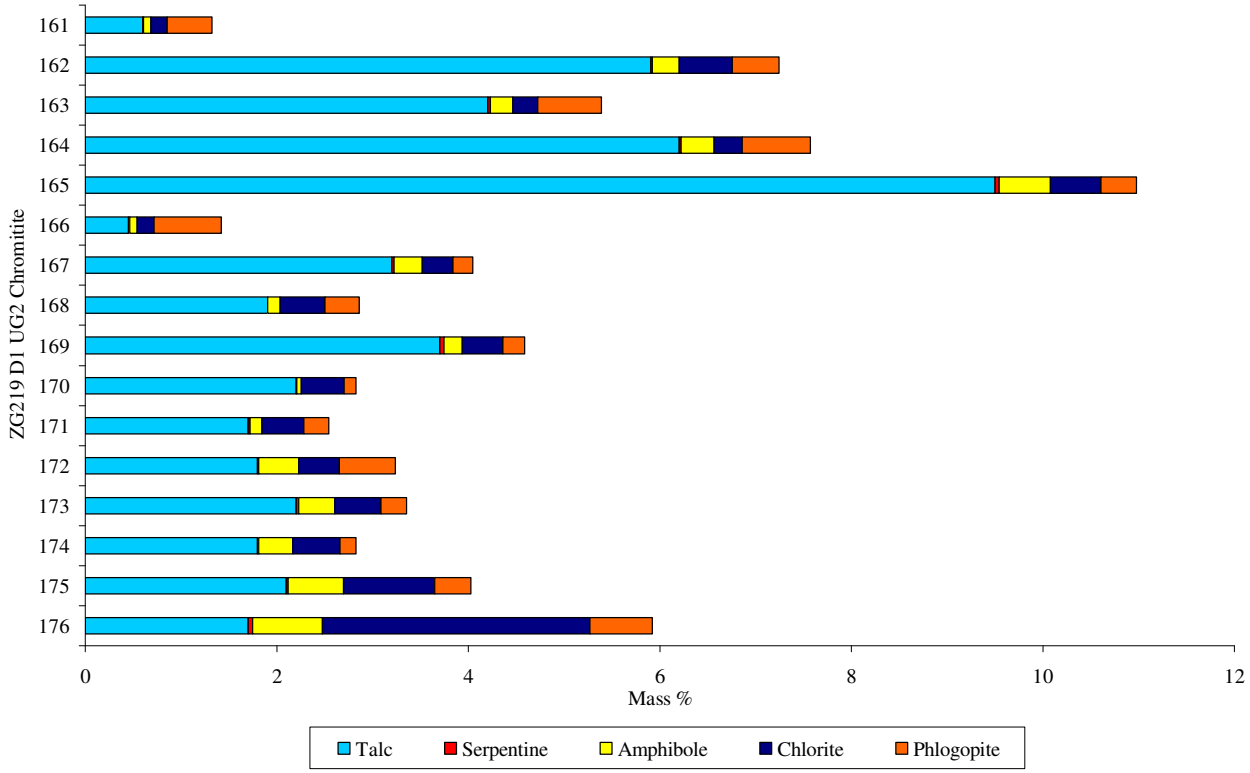

Figure 8.5: Vertical hydrous mineral distribution through the ZG219 D1 UG2.

The hydrous mineral profile shows that the hydrous minerals appear to be mainly concentrated near the upper portion of the reef and are also concentrated in two other lesser zones - one at the bottom of the reef and another near the middle. These zones of higher concentrations show levels of >3 % whilst the general background for the reef is approximately 2 – 2.5 %. These zones could be presumed to represent areas of greater amounts of trapped liquid. The possible affect or relationship between the amount and distribution of hydrous minerals in the UG2 (and hence degree of trapped liquid) and BMS and PGM mineralization will be investigated in the discussion section.

8.3.2 CIPW Normative Mineralogy

The norm calculation is used to estimate the bulk mineralogy of a rock using a whole-rock chemical analysis (Rollinson, 1990). It is the most commonly used calculation scheme and it used here on all 242 chemically analyzed samples taken from throughout the ZG219 MH study section in order to generate a bulk mineralogical profile for the entire study section. While it is not a completely true portrayal of the actual mineralogy it is a highly comparative and wholly correct relative representation of the mineralogical assemblages through the section. Profiles of the major minerals (orthopyroxene, plagioclase, clinopyroxene, olivine, orthoclase and chromite) found in the study section are plotted against the graphical geological log (Figures 8.6 to 8.11).

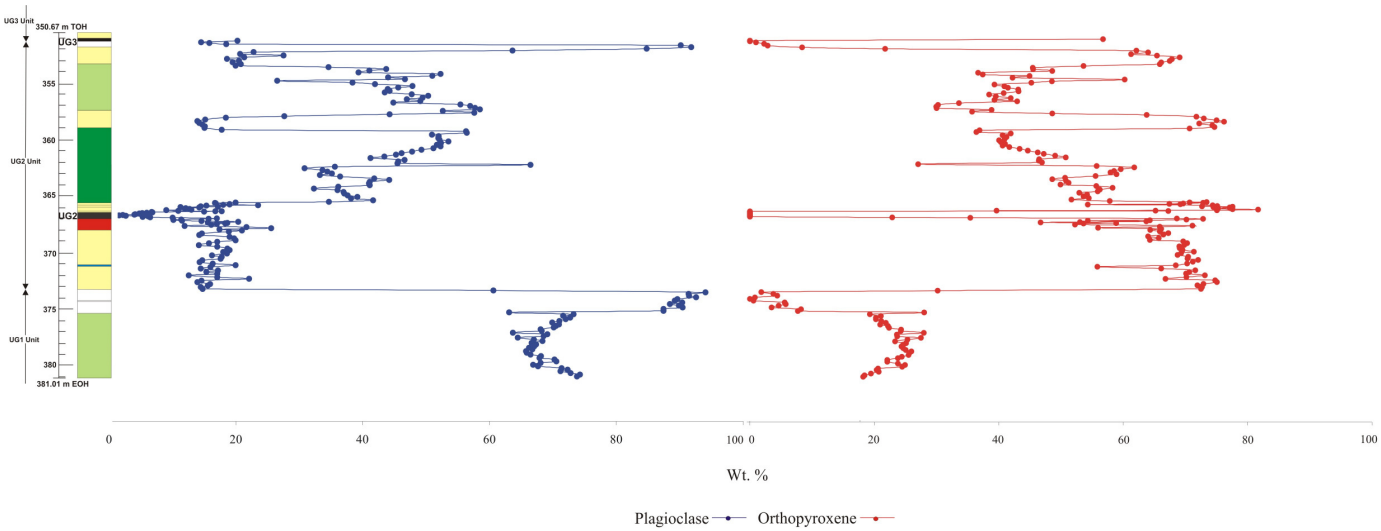

Figure 8.6: Normative plagioclase and orthopyroxene profiles through the ZG219 MH study section.

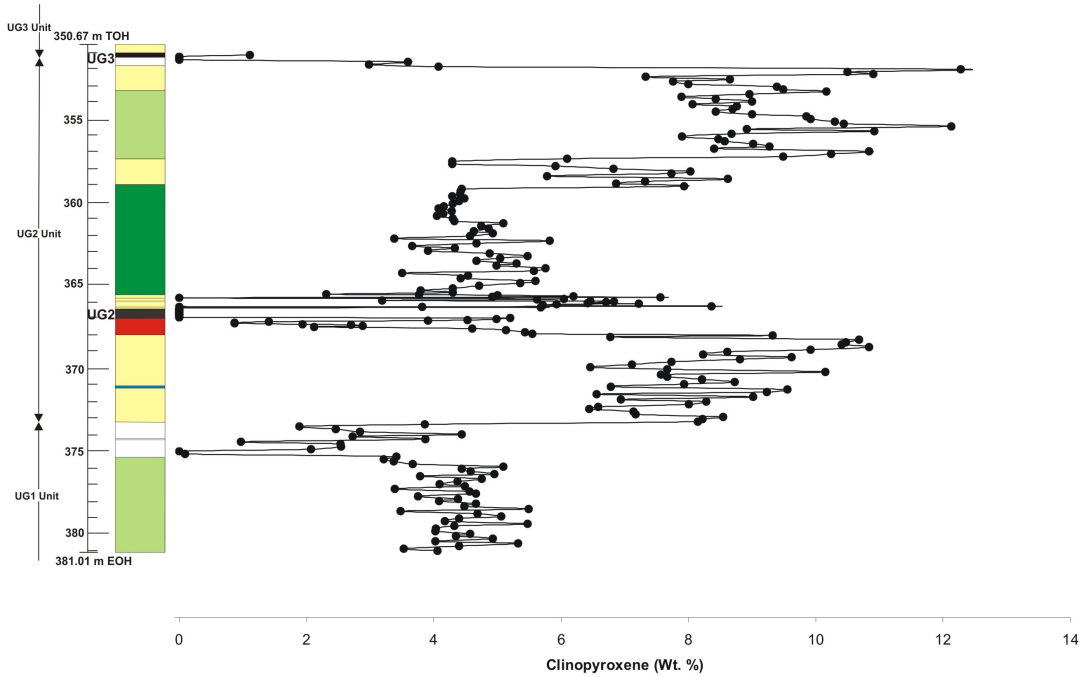

Figure 8.7: Normative clinopyroxene profile through the ZG219 MH study section.

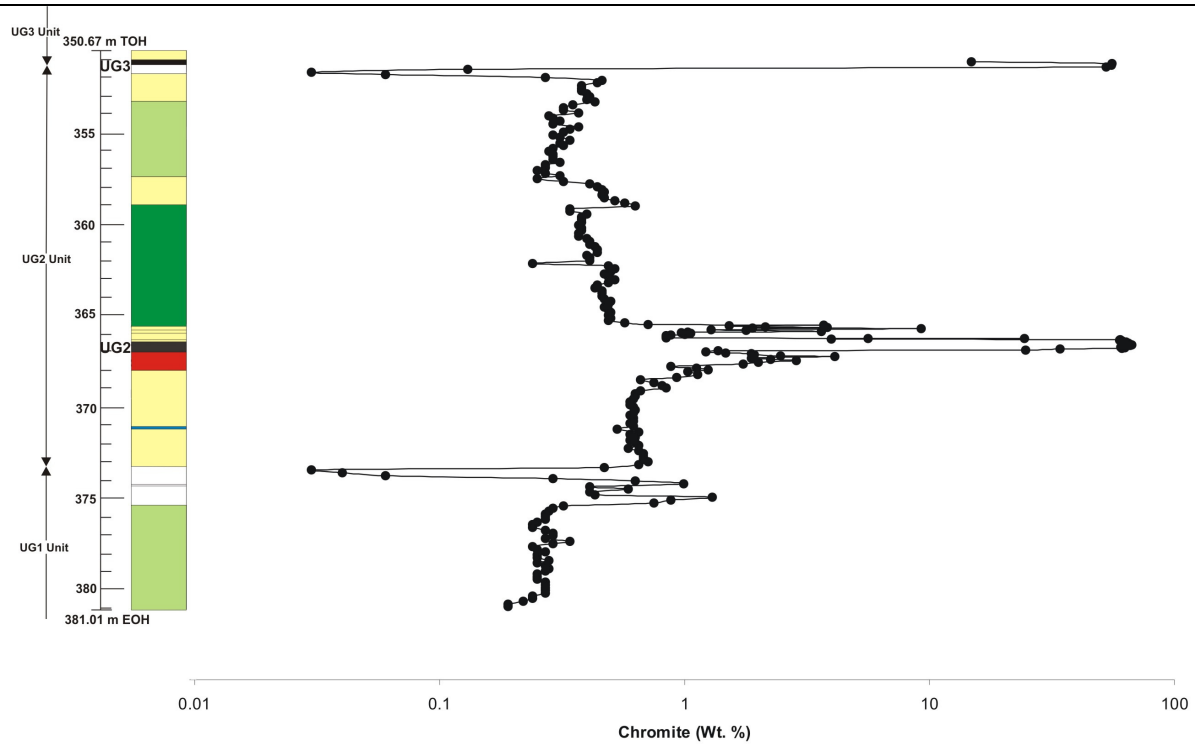

Figure 8.8: Normative chromite profile through the ZG219 MH study section.

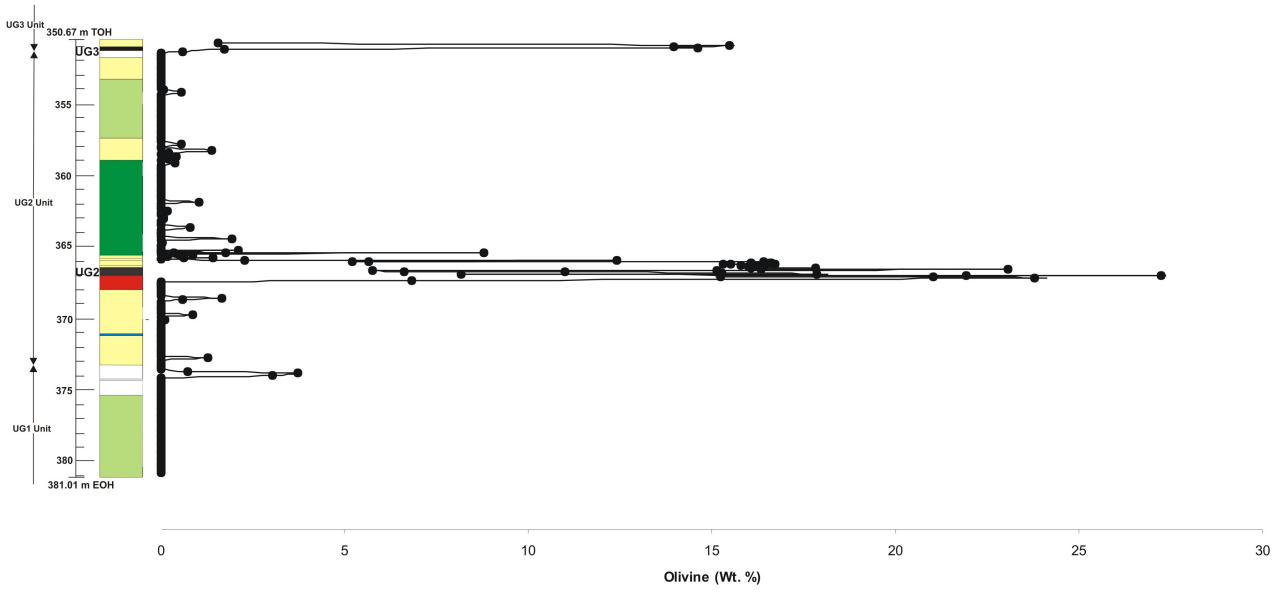

Figure 8.9: Normative olivine profile through the ZG219 MH study section.

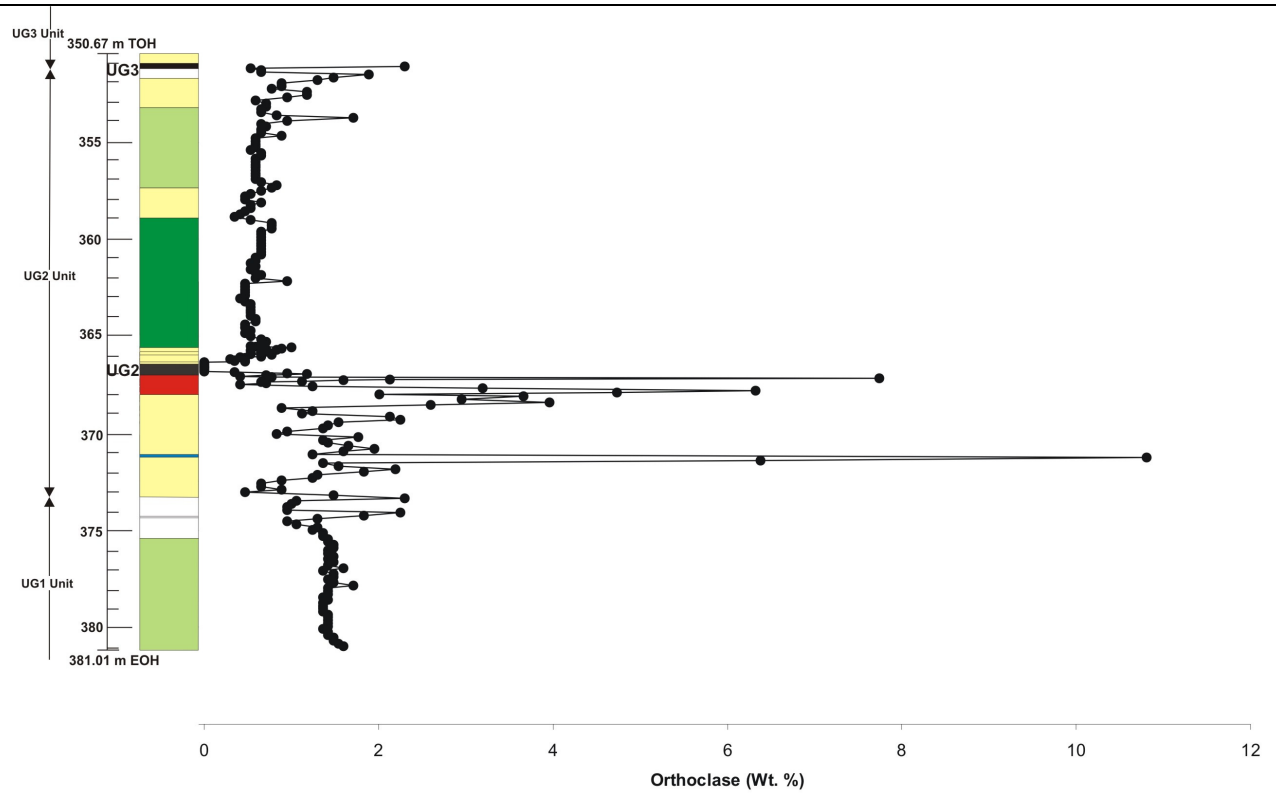

Figure 8.10: Normative orthoclase profile through the ZG219 MH study section.

The two most dominant silicate minerals present in the study section are plagioclase and orthopyroxene, and they have perfectly contrasted profiles (Figure 8.6). Their profiles define the lithological units present as well as can be used to identify intralithological trends. Because they form the dominant mineral assemblage the vertical distribution of the minerals through the sections is a good method of identifying possible fractionation trends.

Three distinct lithological trends can be identified within the study section (and are defined by all the normative mineralogical profiles). A normal trend is exhibited by the upper portion of the UG1 cyclic unit i.e. the bottom of the study section up to the top of the UG1 anorthosite unit. The UG2 cyclic unit comprises two lithological trends: a normal trend from the base of the unit (UG2 footwall feldspathic pyroxenite) up to the top of the hanging wall middle feldspathic pyroxenite unit, as well as a reverse trend from the base of the UG2 leuconorite unit up to the top of the section.

The normal trend comprises an upward compositionally evolving system which is defined by an increase in plagioclase and a corresponding decrease in orthopyroxene. This trend is defined by upward evolving lithologies (from pyroxenite to norite to anorthosite) as well as by intra-lithological trends (i.e. the UG2 footwall and hanging wall lower feldspathic pyroxenite units as well as the UG2 gabbronorite unit all

exhibit distinct normal trends). Conversely, the UG2 leuconorite exhibits a distinct reverse trend in that it tends to become more mafic up through the unit.

The plagioclase and orthopyroxene distributions also allows us to distinguish between different units of the same lithological type i.e. the feldspathic pyroxenite units have variable plagioclase and orthopyroxene contents of 15 – 25 % as well as 60 – 80 % respectively.

The clinopyroxene distribution (Figure 8.7) is notably more irregular compared to the plagioclase and orthopyroxene profiles. This is a result of it occurring mainly as an interstitial phase as well as as exsolution lamellae within orthopyroxene. The clinopyroxene distribution is less lithologically controlled than the orthopyroxene and plagioclase distributions. For example, the highest amounts of clinopyroxene in the section occur in the UG2 hanging wall upper feldspathic pyroxenite and UG2 leuconorite units, with the UG2 leuconorite unit containing higher amounts than more mafic lithologies lower down in the section. Apart from exhibiting the same two trends as defined by the orthopyroxene and plagioclase profiles, the clinopyroxene distribution shows a distinct enrichment up through the UG2 footwall feldspathic pyroxenite unit (thereby defining a reverse trend).

The chromite profile (Figure 8.8) is plotted on a log scale as the majority of the study section comprise <1 wt. % abundance, whilst the two chromitite layers have abundances of >80 wt. %. A smooth profile is present with, once again, the same two trends present as defined by the previous mineral distribution profiles. The UG2 hanging wall lower and UG3 hanging wall feldspathic pyroxenite units are the most chromite enriched silicate lithologies. Their presence directly above major chromitite layers suggest that the processes that formed the chromite may still be continuing here albeit on a less major scale (especially with the numerous chromitite stringers present in the UG2 hanging wall lower feldspathic pyroxenite).

The olivine profile (Figure 8.9) reveals that only the UG3 and UG2 chromitite layers as well as the UG2 footwall pegmatoidal feldspathic pyroxenite unit contain the highest normative olivine abundances (5 – 30 %) in the study section.

The orthoclase profile (Figure 8.10) shows a smooth trend for the majority of the study section apart from the UG2 footwall feldspathic pyroxenite and pegmatoidal feldspathic pyroxenite units where an irregular distribution exists.

The CIPW norm programme has provided an accurate method of calculating the theoretical bulk mineralogy for the study section using chemistry data. This data reveals the presence of two major trends within the UG2 unit – a basal normal trend capped by a reverse trend at the level of the UG2 leuconorite.

8.3.3 Bulk Mineralogical Textural Characteristics

Apart from examining mineral abundances and distribution profiles through the UG2 chromitite it is also important to take note of the textural characteristics of the minerals. This can also provide information of the genetic and mineralization history of the layer. Several MLA (mineral liberation analyzer) BSE (back-scattered electron) microphotos were used to document the general bulk rock texture of the ZG219 D1 UG2. A Qem-Scan mapping measurement technique was then used to map the rock slab samples from the ZG219 D1 UG2 and to quantify the texture. This data should prove entirely complementary to the fieldwork section of the project where the textural characteristics (macro-textures) of the UG2 in the field, in both a weathered and a fresh state, were documented. Where the fieldwork concentrated on macro textures within the layer this section serves to document the micro textures present as well as to establish the association and distribution of both the major and accessory minerals. A variety of whole mapped rock slab microphotos are presented from different levels within the UG2 chromitite. The aim was to obtain an overall representation of the chromitite layer as well as to highlight any local textural variations.

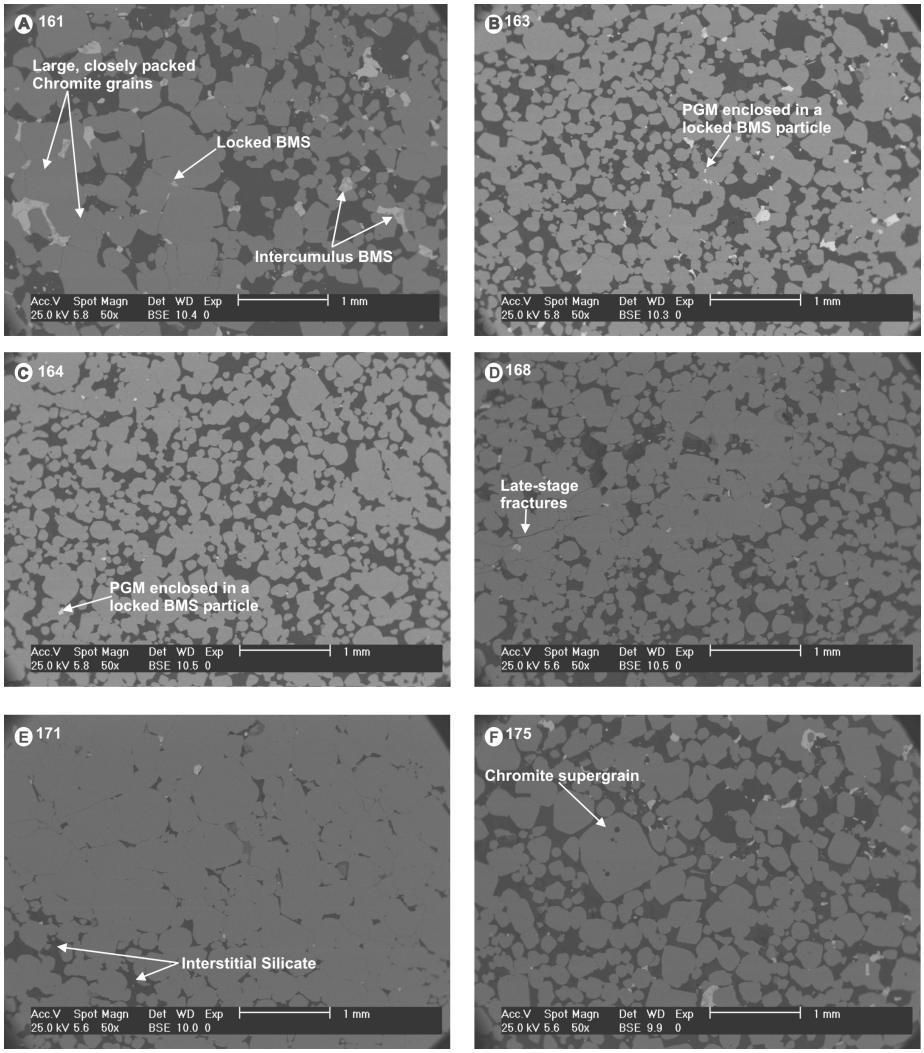

Figure 8.11: Several MLA BSE microphotos from different heights within the UG2 (arranged in order of height starting at the top of the layer in A and then working downwards to F). All photos are of the same scale.

Samples 163 (B) and 164 (C) exhibit a well-developed open-packing structure (matrix-supported) (Figure 8.11). Samples 161 (A), 168 (D) and 175 (F), however, exhibit more of a tighter packing structure (although still not a closed-packing structure). Note the general coarse size of the chromite grains (5 - 250 µm) as well as the presence of some chromite supergrains (~500 µm). Sample 171 (E), however, shows a perfect closed-packing structure and is fully chromite grain supported. Note how the sulphide particles occur interstitially to the chromite and occasionally locked within the chromites.

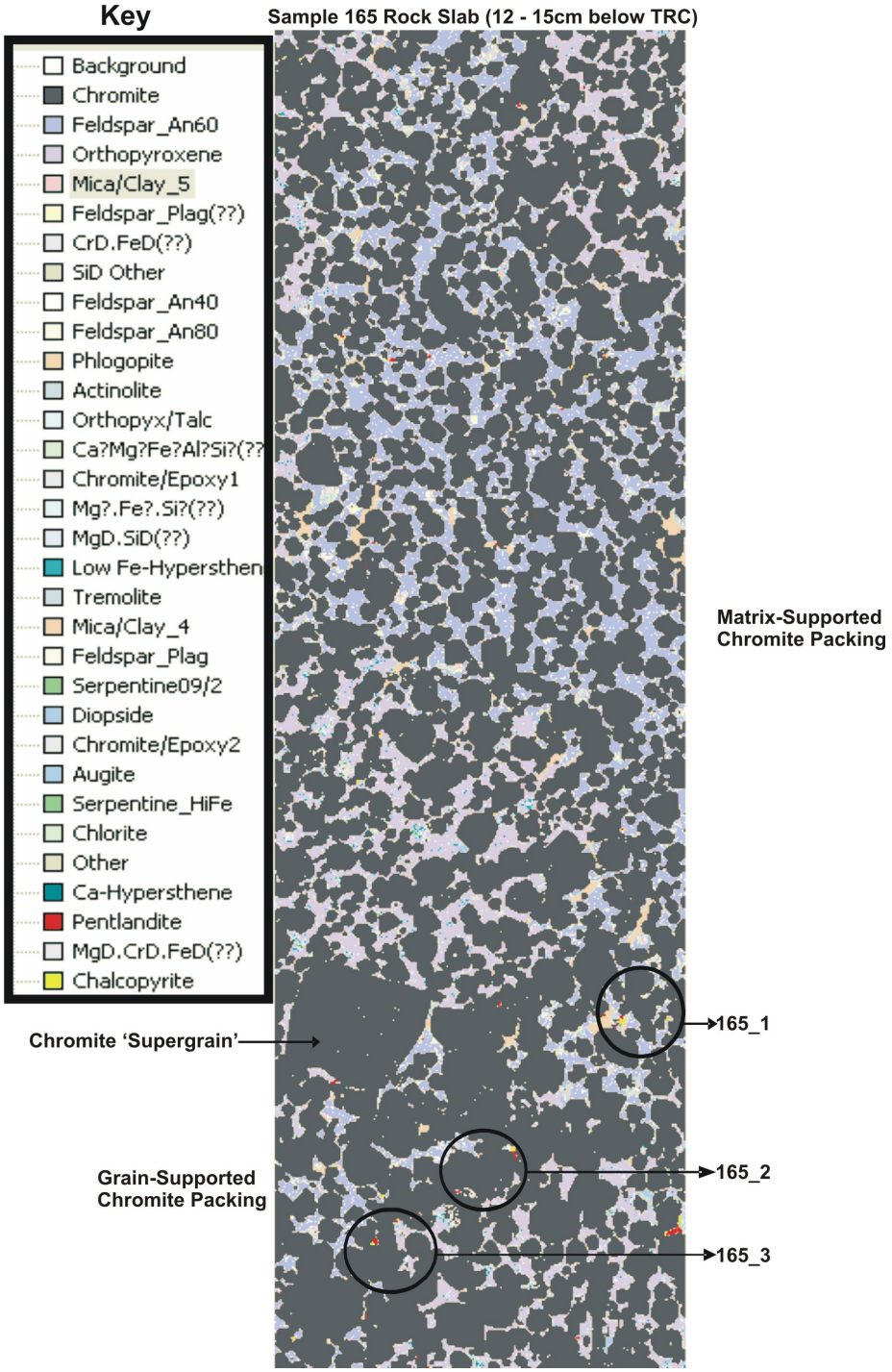

Figure 8.12: Qem-scan texture mapping results of a rock slab from sample 165 (Area is ~2mm across).

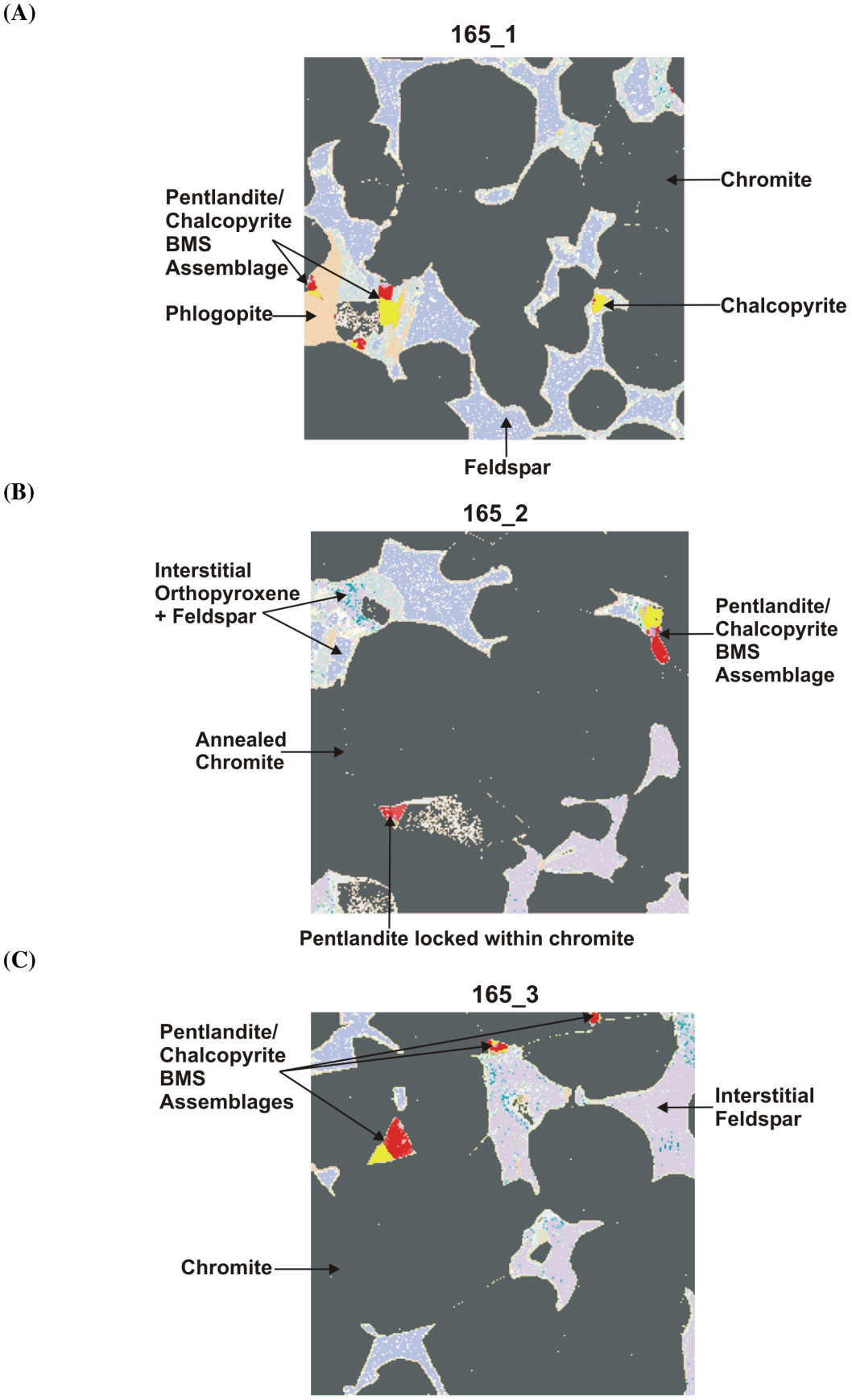

Figure 8.13: Zoomed in Qem-scan map images from sample 165 (Area is ~0.5mm across).

Figure 8.12 represents a mapped rock slab from sample 165. The general texture comprises medium to large chromite grains in an interstitial matrix of feldspar and orthopyroxene. Orthopyroxene exists both in an interstitial form as well as in a cumulus form. For most of the section the chromite packing exists as a matrix-supported one (where the chromite grains are mostly surrounded by interstitial material, but near the base of the section the chromite grains appear to have joined and coalesced to form a grain-supported packing structure. Also within this area exist several 'supergrains' of chromite – the formation of which are discussed later.

Three zoomed in images from this rock slab are then presented in Figure 8.13. In 8.13A sulphide particles, comprising mainly pentlandite and chalcopyrite, are shown to exist freely within the intercumulus matrix. In 8.13 B and C, however, the sulphide particles exist both within the chromites (locked within the chromite) and in interstitial gaps and joints between the chromite grains. A good example of an annealed chromite (supergrain) grain exists in 8.13 B.

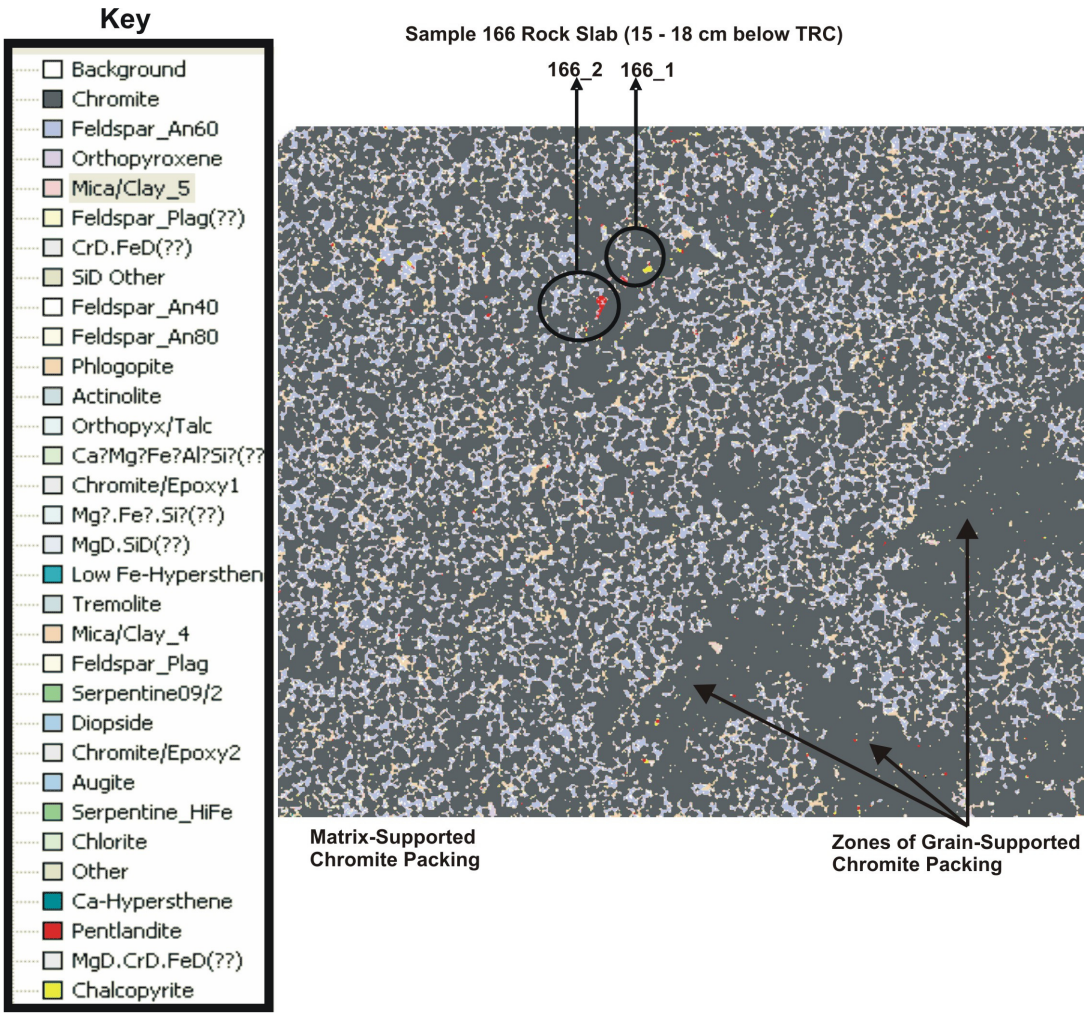

Figure 8.14: Qem-scan texture mapping results of a rock slab of sample 166(Area is ~10mm across)..

(A)

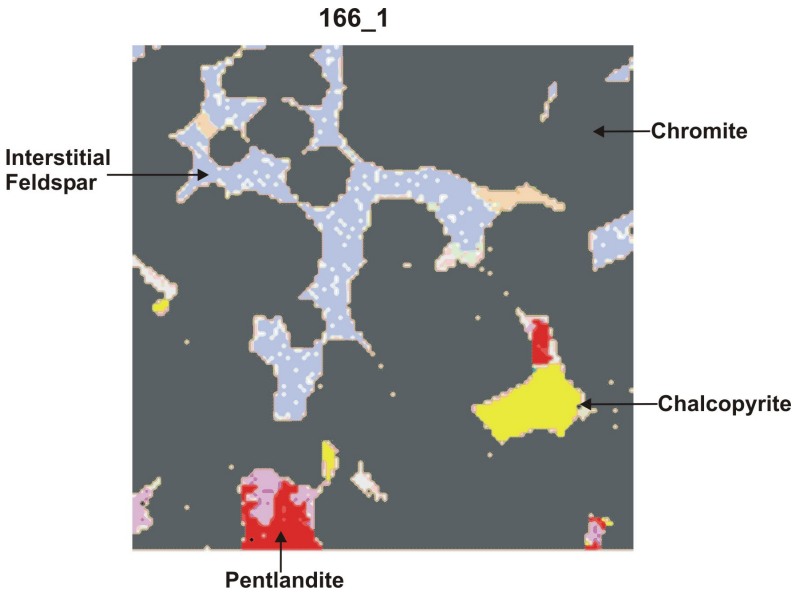

(B)

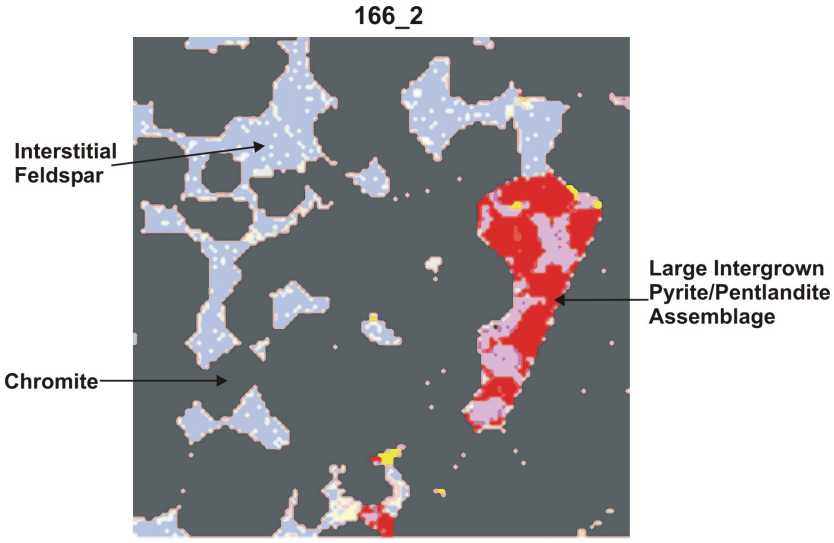

Figure 8.15: Zoomed in Qem-scan map images from sample 166 (Area is 0.5mm across).

Figure 8.14 (section from sample 166) once again shows (as with sample 165) a dominant matrix-supported chromite packing structure with lesser, distinct zones of grain-supported chromite packing. These zones are distinct and contrast sharply with the surrounding texture. They are seen to comprise 'clumps' of chromite which have coalesced together. During this process particles of sulphide and/or silicate can become trapped within the chromite as is shown in Figure 8.15 A. Figure 8.15 B shows a well-developed particle exhibiting a delicate pyrite-pentlandite assemblage. This large sulphide particle has also become trapped within the chromite.

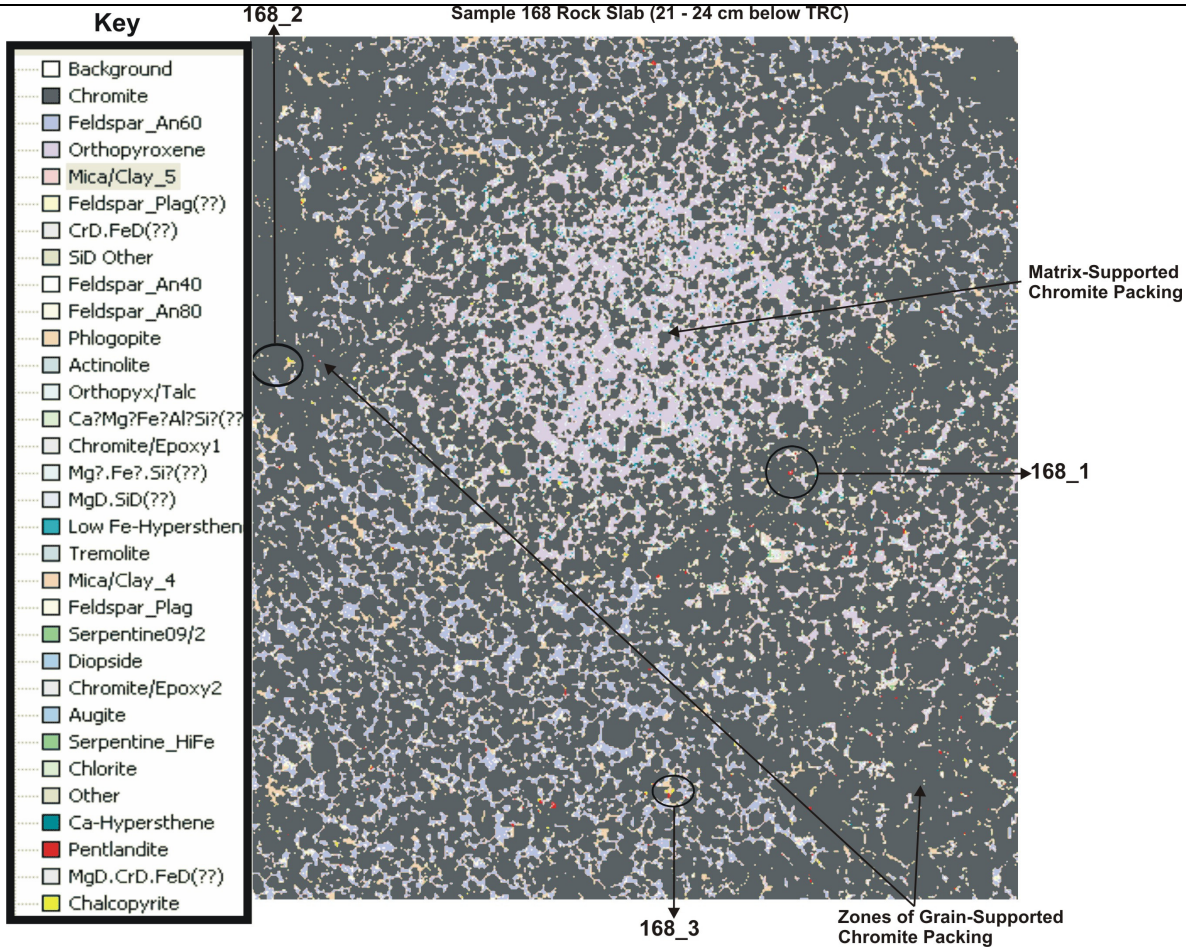

Figure 8.16: *Qem-scan texture mapping results of a rock slab of sample 168 (Area is ~15mm across).*

(A)

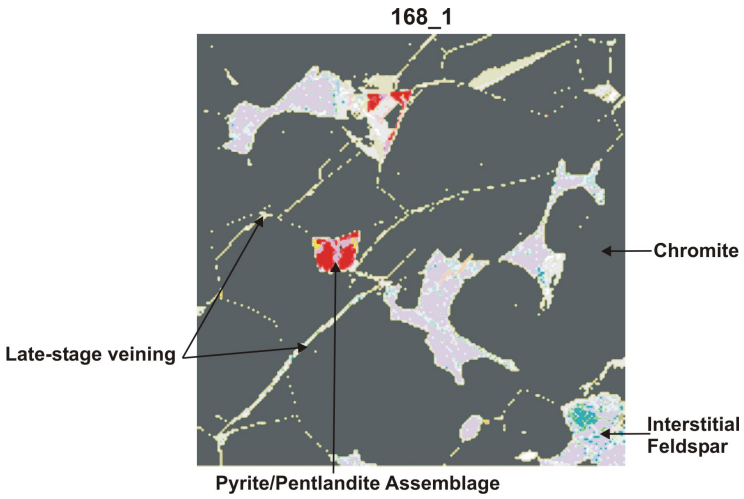

(B)

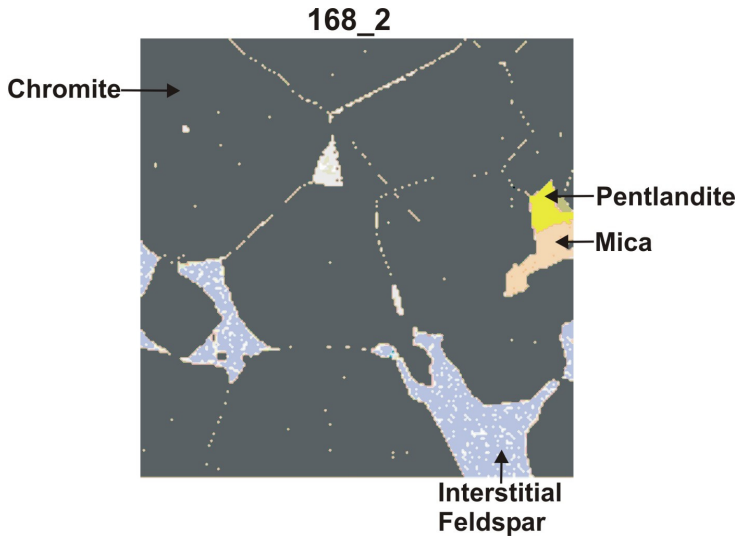

(C)

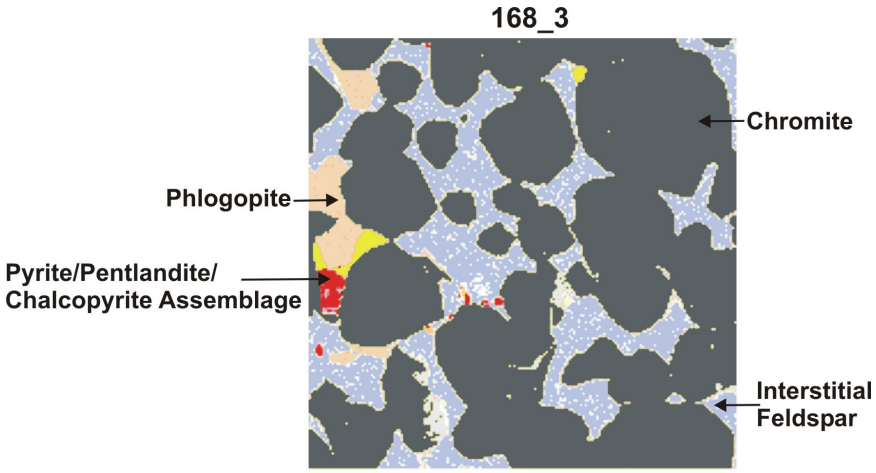

Figure 8.17: Zoomed in Qem-scan map images from sample 168 (Area is ~0.5mm across).

Sample 168 (Figure 8.16) appears to have more of a grain-supported structure with lesser zones of matrix-supported areas. Figure 8.17 A shows a pyrite-pentlandite composite sulphide particle locked within chromite which, in turn, has been affected by late-stage veining. The veining runs diagonally across the image. The veining appears to be of silicate composition. There is no sulphide mineralization associated with the veining, with the sulphide particles concentrated rather in the matrix or locked within the chromites (i.e. Figure 8.17 B). Figure 8.17 C exhibits a pyrite-pentlandite-chalcopyrite assemblage which is interstitial to the surrounding cumulus chromite and phlogopite.

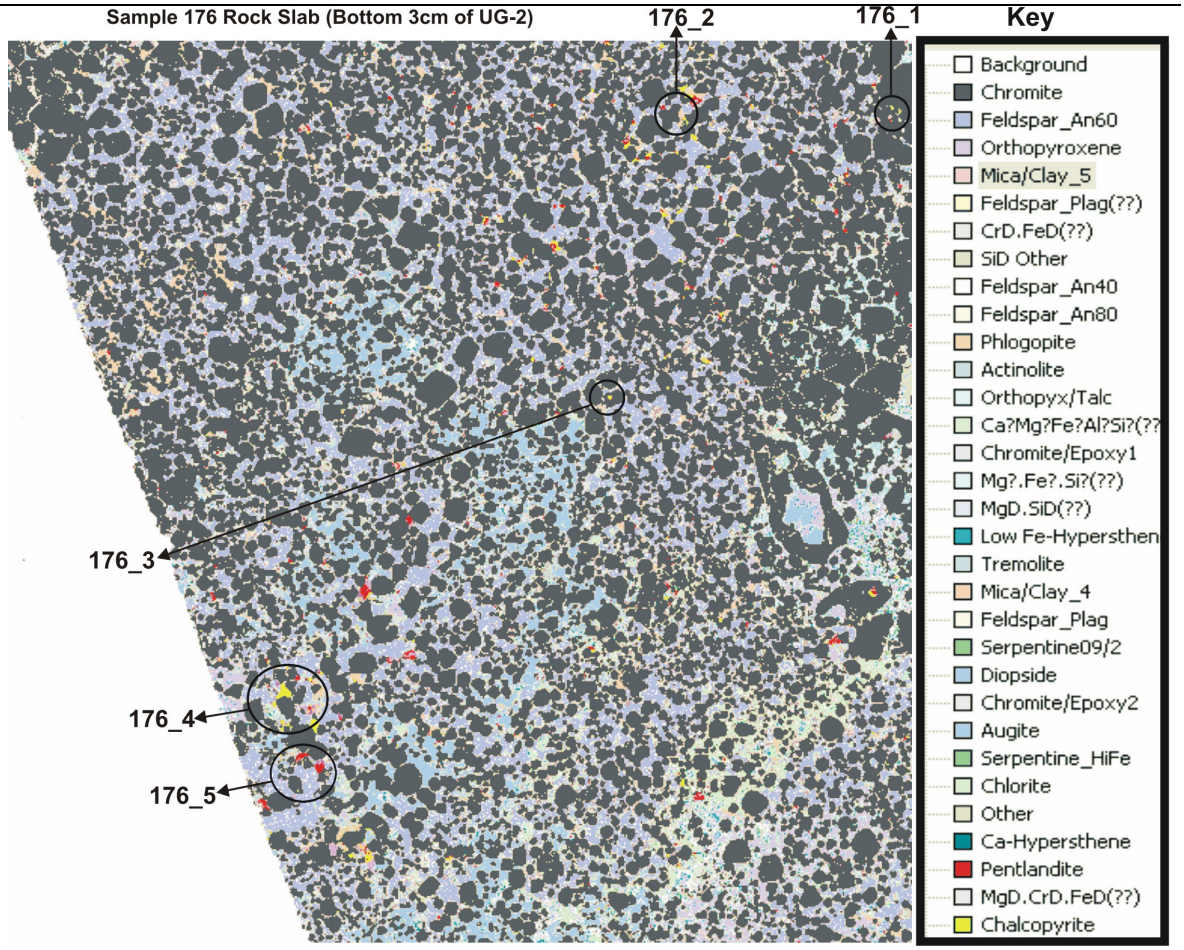

Figure 8.18: Qem-scan texture mapping results of a rock slab of sample 176 (Area is ~10mm across).

(A)

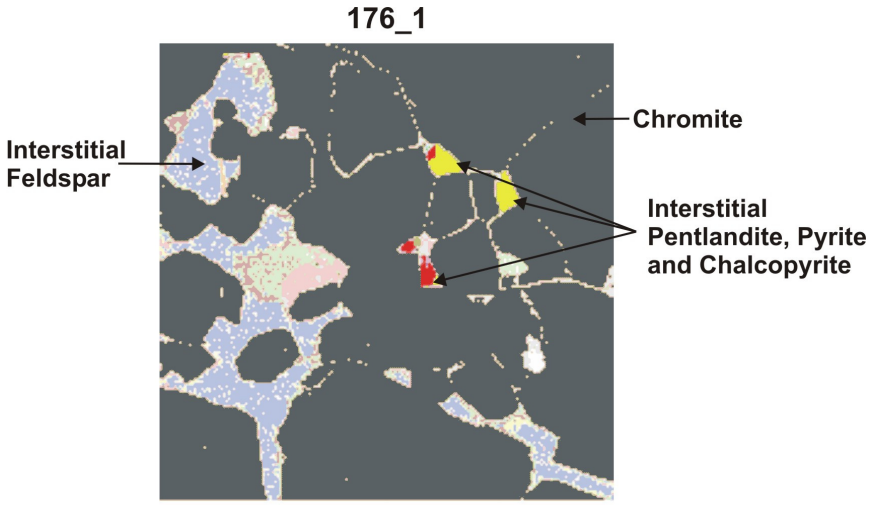

(B)

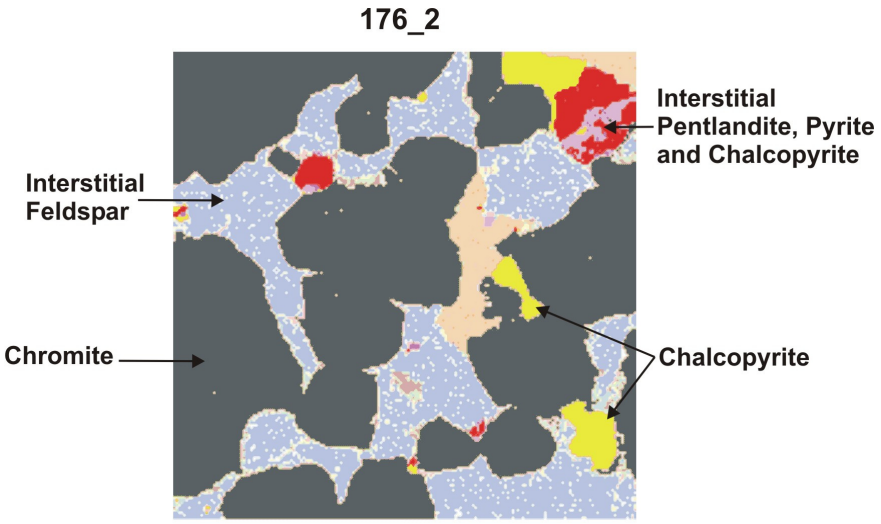
176_2
Interstitial
Pentlandite, Pyrite
and Chalcopyrite
Interstitial
Feldspar
Chromite
Chalcopyrite

(C)

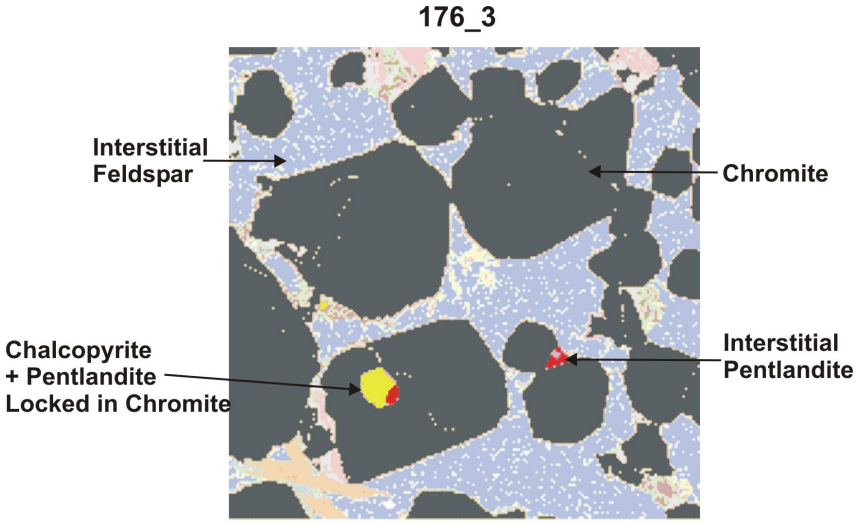
176_3
Interstitial
Feldspar
Chromite
Chalcopyrite
+ Pentlandite
Locked in Chromite
Interstitial
Pentlandite

(D)

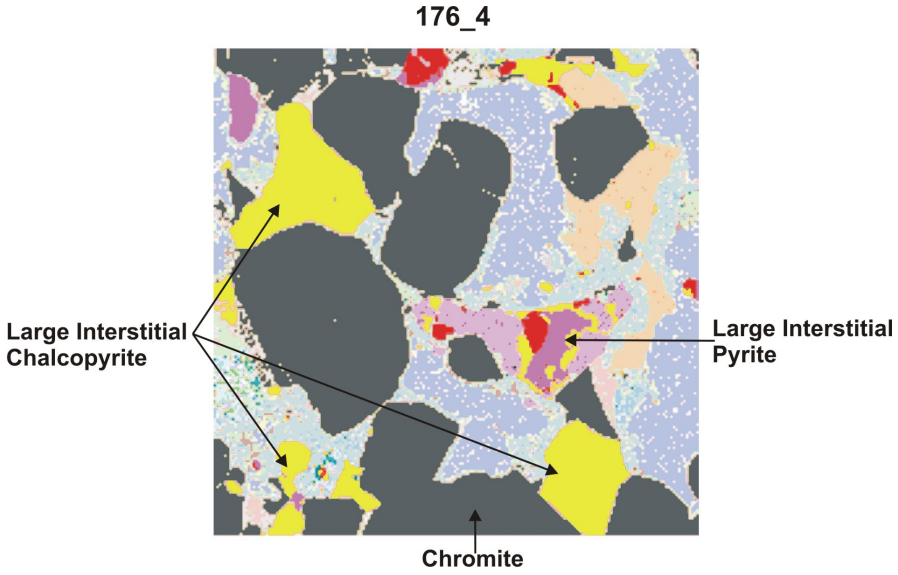
176_4
Large Interstitial
Chalcopyrite
Large Interstitial
Pyrite
Chromite

(E)

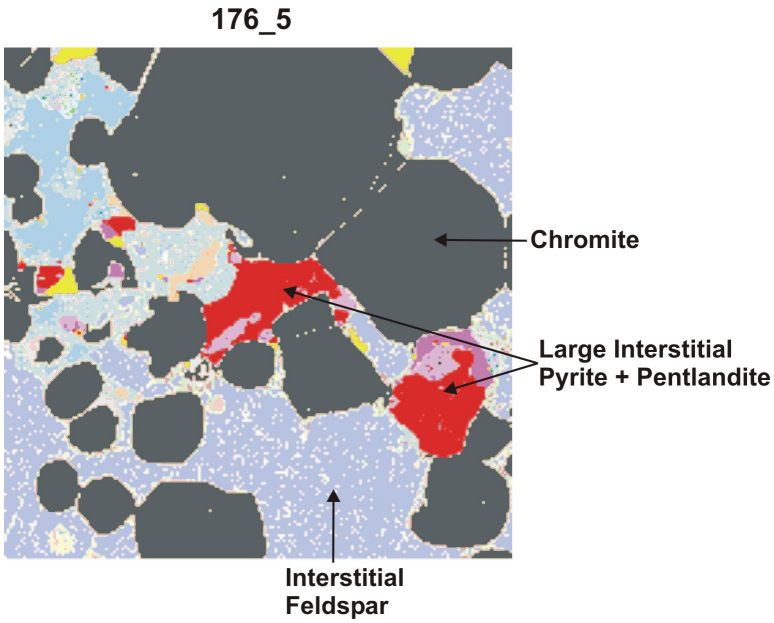

Figure 8.19: Zoomed in Qem-scan map images from sample 176 (Area is ~0.5mm across).

Sample 176 (Figure 8.18) is taken from the base of ZG219 D1 UG2. The overall texture comprises a matrix-supported chromite packing structure. The chromites appear to be fine grained with a number of larger grains scattered randomly with no distinct grain-supported zones. Figures 8.19 A to E provide an excellent documentation of the setting of the sulphide particles. These particles (which form an assemblage of pentlandite-pyrite-chalcopyrite) dominantly occur as interstitial to the cumulus chromite grains. This includes them being distributed in small areas or pockets between chromites as well as in the general open matrix. Figure 8.19 C does also show a sulphide particle locked within a chromite (although this is not the dominant setting). The sulphides appear to be large and well-developed (note the cubic pyrite in Figure 8.19 D). The textural setting and association of the sulphide assemblage will be documented in more detail in the next section.

8.3.4 Discussion

The ZG219 D1 UG2 comprises a bulk mineralogical composition of mainly chromite with lesser plagioclase and orthopyroxene. Variable amounts of hydrous minerals (~5 %) and base metal sulphides (~1 %) are also found to exist within the chromitite.

The primary hydrous phases (talc, amphibole, chlorite and phlogopite) are suggested to represent postcumulus primary phases which have formed by primary entrapment of the residual liquid during the final stages of crystallization. A variety of incompatible elements (including water) have become trapped within this interstitial residual liquid, and eventually crystallized out to form the hydrous mineral phases. These

phases can therefore be used to monitor the degree of trapped liquid within the chromitite. There are therefore three distinct zones containing higher amounts of trapped intercumulus liquid – at the base of the chromitite, around the middle and a major zone near the top of the chromitite. These zones are interpreted to represent areas where a greater degree of residual liquid became trapped, during compaction, in the intercumulus pore spaces, where it eventually crystallized out to form the hydrous minerals.

Texturally, the UG2 chromitite comprises a framework of cumulus chromite within an interstitial matrix of silicate. The packing structure ranges from open (matrix supported), which is the common type, to closed (chromite supported) which is more rare. Some of the chromites are substantially larger than the ordinary chromite grains, and hence are termed 'supergrains'. It is suggested that these supergrains formed in areas of greater pore space where they were allowed to crystallize in an open environment, and therefore form larger grains. During compaction these grains were then forced together and coalesced to form substantially larger grains. Therefore the formation of the chromite supergrains is suggested to be a combination of primary crystallization in an open environment (i.e. zones of greater pore space) as well as post-cumulus coalescence of grains during primary compaction. The base metal sulphides are present mainly within the intercumulus matrix or, rarely, as locked within the chromites

The CIPW norm programme was then used to calculate the theoretical bulk mineralogy for the study section using chemistry data. The normative mineralogical profiles revealed the presence of two major trends within the UG2 unit – a basal normal trend capped by a reverse trend at the level of the UG2 leuconorite. These trends, as defined by normative mineralogical distributions, are suggested to represent primary fractionation processes.

Therefore the UG2 unit is seen to comprise a lower normal fractionation trend, in which the resident liquid within the chamber, despite still been replenished by intermittent injections of more primitive magma, is, as a result of fractional crystallization, trending toward more evolved compositions. This overall normal trend is mirrored by local intra-lithological normal fractionation trends within the UG2 footwall and UG2 hanging wall middle and upper feldspathic pyroxenite units. At the level of the upper contact of the UG2 hanging wall middle feldspathic pyroxenite unit there is a reversal in fractionation trends. Through the overlying UG2 leuconorite and upper feldspathic pyroxenite units exists an upward trend toward more primitive compositions (as reflected by a more mafic mineral distribution). This is suggested to represent a period of increased magma addition into the chamber. Therefore the process of magma replenishment of the chamber is suggested to now be the dominant process – as opposed to that of acquiescence and fractional crystallization (punctuated by intermittent injections) during the normal trend.

8.4 Base–Metal Sulphide Mineralogy

The BMS (base-metal sulphide) assemblages were quantified using a Qem-Scan BMS measurement. This is an automated measurement whereby the machine searches for the BMS phases using their back-scattered electron (BSE) grey level (which is higher than for silicate and chromite) and then analyses the grains using x-ray analysis. This then generates distribution data for the sulphides within the UG2. The BMS assemblages were then documented using a series of microphotos (documenting the textural setting of the sulphides) which were taken on the Optimas (using reflected light techniques).

8.4.1 BMS Distribution

The ZG219 D1 UG2 comprises a sulphide assemblage of mainly pentlandite, chalcopyrite and pyrite with lesser amounts of pyrrhotite (Table 8.5 and Figure 8.20).

Table 8.5: Overall BMS distribution for the ZG219 D1 UG2.

BMS Species	ZG219 D1 UG2
Bornite	0.1
Chalcopyrite	32.2
Pentlandite	40.4
Pyrite	17.4
Pyrrhotite	9.9
Total	100.0

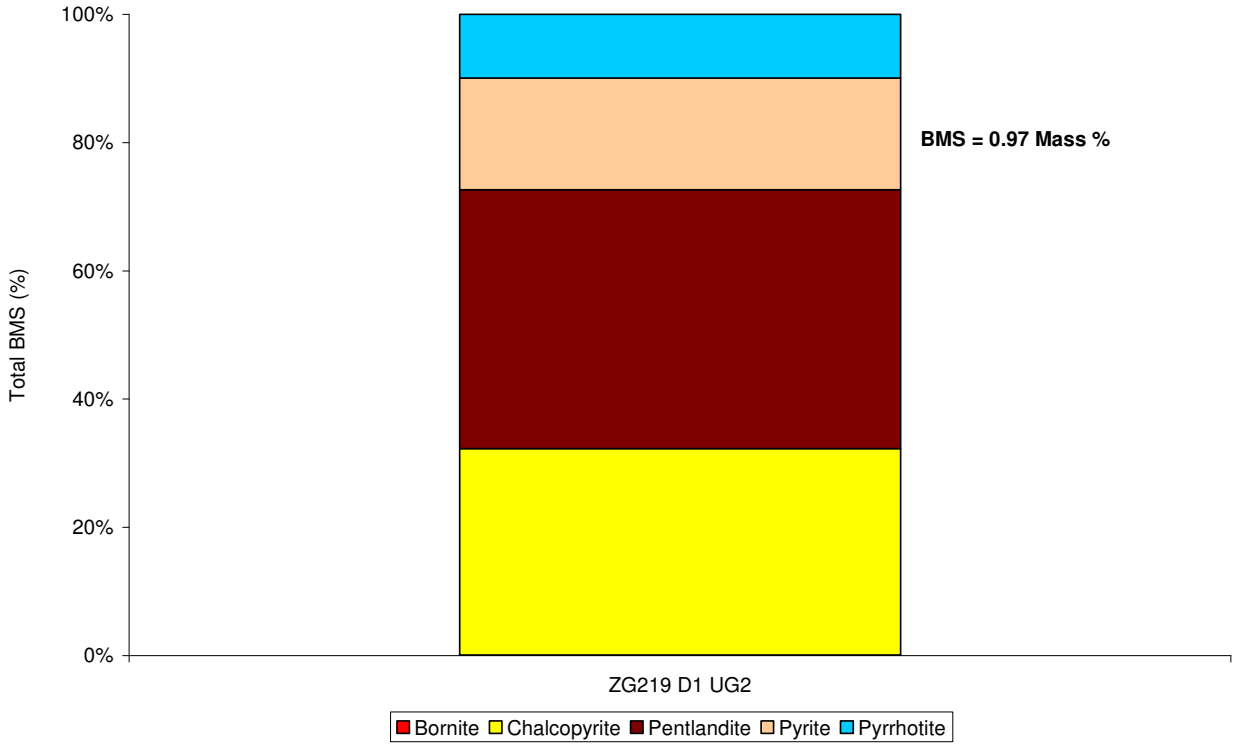

Figure 8.20: Overall BMS distribution for the ZG219 D1 UG2.

The vertical distribution profile of the BMS though the chromitite is documented in Tables 8.6 and 8.7 and in Figure 8.21.

Table 8.6: BMS distribution for the upper half of the ZG219 D1 UG2 chromitite.

BMS Species	161	162	163	164	165	166	167	168
Chalcopyrite	34.6	28.2	42.2	28.0	28.0	35.3	37.9	39.7
Pentlandite	35.7	42.3	27.5	55.3	50.3	37.5	42.5	30.2
Pyrite	14.7	12.3	14.7	16.8	16.6	18.5	19.5	30.2
Pyrrhotite	15.0	17.3	15.7	0.0	5.1	8.6	0.0	0.0
Total	100.0	100.0	100.0	100.0	100.0	100.0	100.0	100.0
Mass %	2.7	2.8	1.0	0.2	0.2	0.5	0.9	0.6

Table 8.7: BMS distribution for the lower half of the ZG219 D1 UG2 chromitite.

BMS Species	169	170	171	172	173	174	175	176
Bornite	0.0	0.0	0.0	0.0	0.0	0.0	0.6	0.0
Chalcopyrite	27.5	21.6	34.2	51.7	38.7	19.8	32.2	41.8
Pentlandite	38.6	56.9	30.6	34.3	43.5	55.0	43.5	34.4
Pyrite	26.3	21.6	30.6	14.0	15.7	14.5	15.6	22.1
Pyrrhotite	7.6	0.0	4.6	0.0	2.1	10.7	8.1	1.7
Total	100.0	100.0	100.0	100.0	100.0	100.0	100.0	100.0
Mass %	1.7	0.3	0.2	0.1	0.4	1.3	1.9	0.8

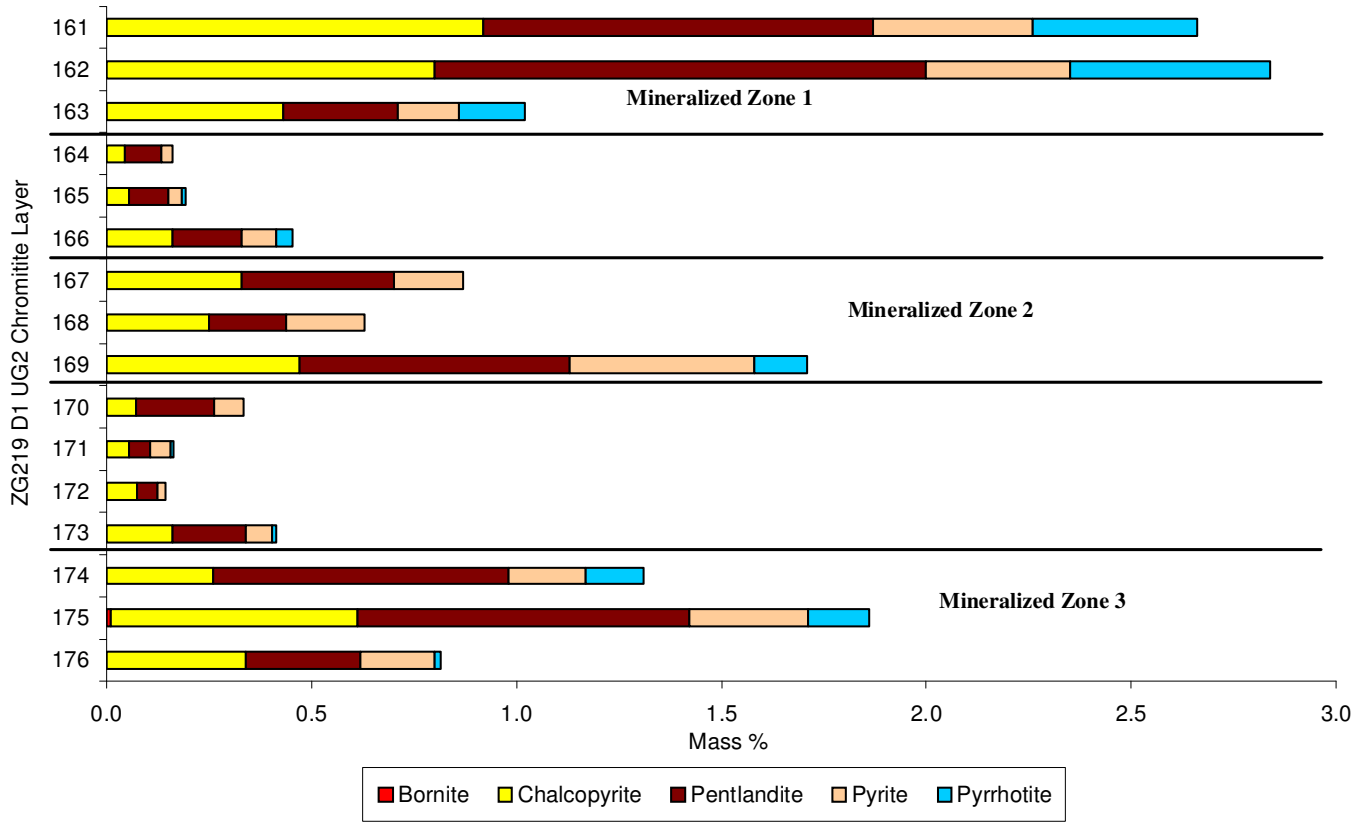

Figure 8.21: Vertical BMS distribution profile, as a function of total mass %, through the ZG219 D1 UG2 chromitite layer.

From the vertical BMS distribution profile through the chromitite (Figure 8.21) it is clear that the sulphide mineralization is concentrated into three distinct zones. For the purposes of this study these zones are classified as 'Mineralized Zone 1, 2 or 3' (from top down), with the mineralized zones containing > 0.5 mass % BMS whilst the background comprises < 0.5 %. The general BMS mineralization profile is a top-loaded one with Mineralized Zone 1 at the top of the chromitite containing the most sulphide (in terms of mass %). The two other zones include the Mineralized Zone 2, in the middle of the UG2, and Mineralized Zone 3, which comprises the basal portion of the UG2. The sulphide assemblage of chalcopyrite, pentlandite and pyrite remains approximately constant throughout the chromitite, although the three mineralized zones appear to be slightly more enriched in pyrrhotite compared to the background.

8.4.2 Textural Characteristics

Several photomicrographs of sulphide assemblages from sample 162 and sample 172 were taken using the Optimas (Figures 8.22 and 8.23 respectively) and are used here to describe the textural characteristics and association of the sulphide assemblages.

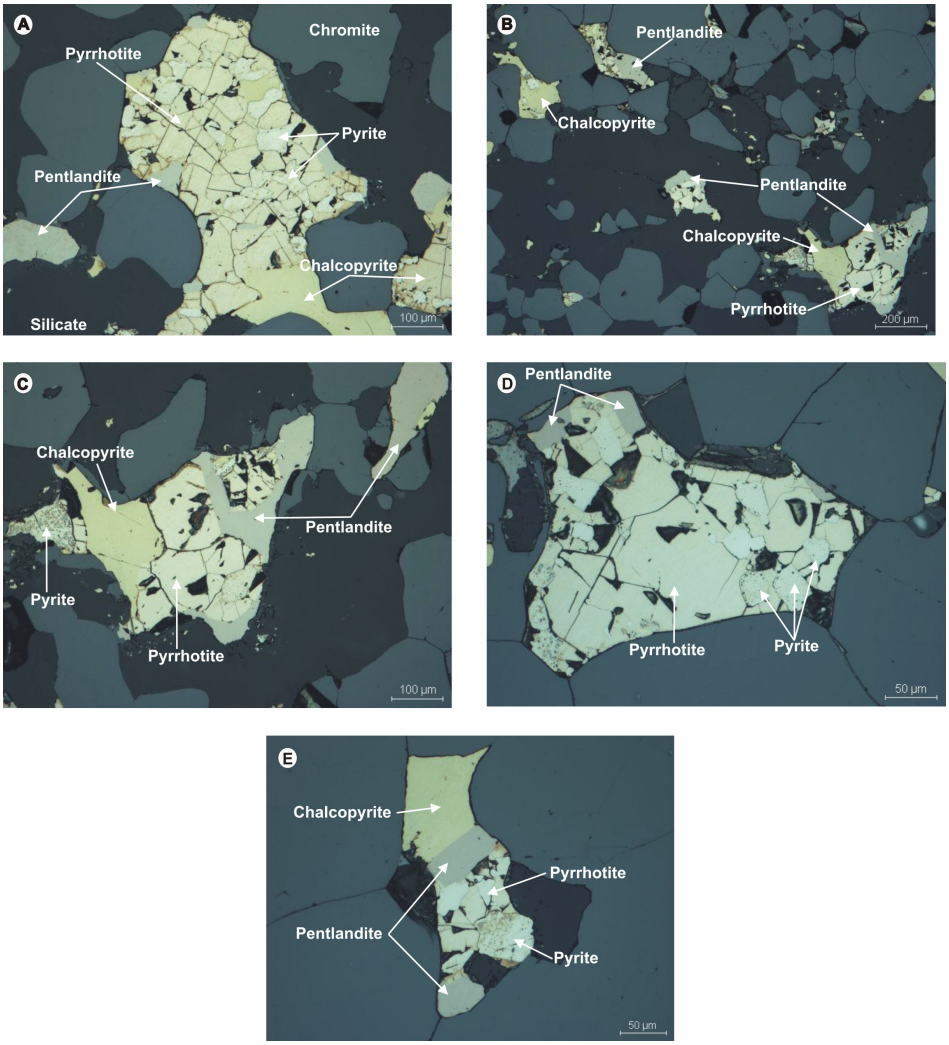

Figure 8.22: Reflected light microphotos of a variety of BMS assemblages from sample 162.

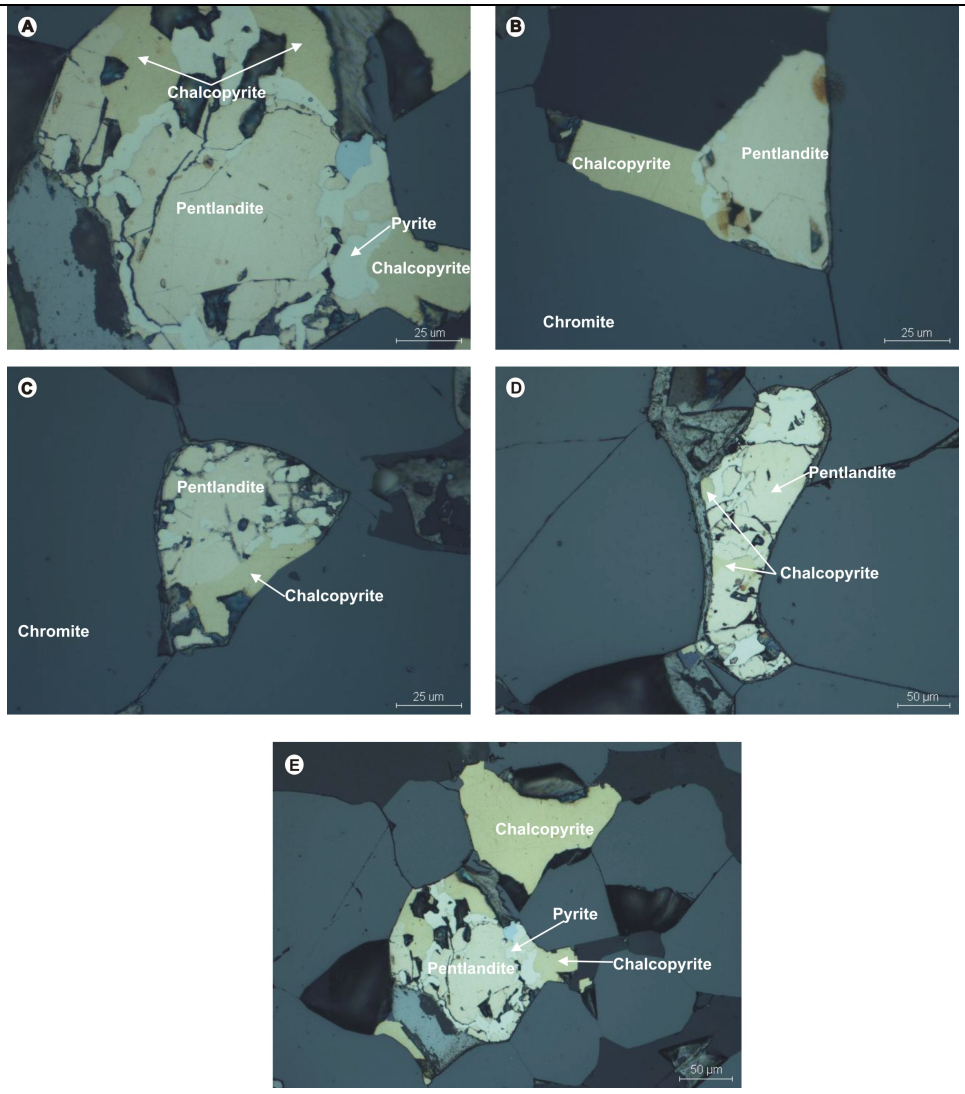

Figure 8.23: Reflected light microphotos of a variety of BMS assemblages from sample 172.

The sulphide particles range in size from ~25 µm up to ~200 µm (large composite particles containing several phases). They are mainly concentrated in the interstitial matrix between the cumulus chromite and silicate grains, whilst some sulphides are also found to be fully enclosed (locked) within chromite grains. The dominant sulphide phases present in sample 162 are pyrrhotite, chalcopyrite, pentlandite and pyrite whilst in 172 the dominant phases are chalcopyrite and pentlandite with lesser pyrite. This corresponds to the quantitative results generated for these samples (Figure 8.21).

The sulphide assemblages exhibit a distinct primary magmatic texture with pyrrhotite and pyrite closely associated with pentlandite. Pyrrhotite and pentlandite are intergrown with each other whilst pyrite appears to have been exsolved from the pentlandite as it occurs mainly as rims along the edge of the pentlandite grains (Figure 8.23). Chalcopyrite, however, occurs as large (> 25 µm), grains which are either separate from, or

occur along the boundary of, the main composite sulphide particles. This intricate magmatic texture is a primary texture formed during the initial crystallization of the sulphides. It therefore confirms that there has been no subsequent reworking or alteration of the sulphides by late-stage circulating fluids.

8.4.3 Discussion

The sulphide mineralization in the ZG219 D1 UG2 is therefore concentrated in three main zones termed Mineralized Zones 1 – 3. These zones represent areas of greater primary enrichment, and provide evidence of an original top-loaded BMS profile within the UG2.

The general sulphide assemblage comprises pentlandite, chalcopyrite and pyrite with pyrrhotite also present in the three mineralized zones (whilst only present in negligible amounts in the background). Texturally the sulphides range in size from a ~25 µm to large composite particles of ~250 µm in size and they are mainly concentrated in the interstitial matrix between the cumulus chromite and silicate particles. Some sulphide particles are also found to be fully enclosed (locked) within chromite grains

Within the composite sulphide assemblages the Fe-sulphides (pyrite and pyrrhotite) and Ni-sulphides (pentlandite) display an intricate intergrowth texture in which the Fe-sulphides have been exsolved from the Ni-sulphides to form zones or blebby areas hosted within the Ni-sulphide (Figure 8.23). This texture is dominant throughout the chromitite layer. The Cu-sulphides (chalcopyrite), however, don't play any part in this texture and are present as separate, discrete phases (either individually or along the boundaries of larger composite sulphide particles). This intricate texture was formed during the primary magmatic phase and is direct evidence that there has been no subsequent reworking of the sulphides by late-stage circulating fluids.

Therefore the sulphide textures and distribution profiles are all representative of the primary characteristics of the UG2 which were formed during primary fractional crystallization.

8.5 Platinum-Group Mineralogy

The PGE (platinum-group element) mineralization in the ZG219 D1 UG2 was quantified using the spl-lite measurement on the MLA (mineral liberation analyser). More than 1000 PGMs (platinum-group minerals) were analyzed and documented and listed in Table 8.8. The PGMs encountered were analysed and compositional, association and textural data was obtained for each.

8.5.1 PGM Distribution

The PGMs were subdivided into six main groups: (1) PGE-sulphides, (2) Pt/Pd-tellurides, (3) Pt/Pd-arsenides, (4) PGE-sulpharsenides, (5) PGE-alloys and (6) Au and Ag bearing phases. The number of particles of each PGM type was recorded. Several unconstrained phases were identified and their general composition recorded.

Table 8.8: Name and ideal formulae of all occurrences of PGM and Au-Ag minerals grouped into the six predominant PGM-species groups.

PGM Group	Mineral Name	Formula	No. of Particles
(1) PGE-Sulphides	Cooperite	PtS	361
	Braggite	(Pt,Pd)S	269
	Laurite	RuS_2	228
	Unconstrained Phase	Pt-Rh-Cu-S	108
	Unconstrained Phase	Pd-S-Ni	1
(2) Pt/Pd Tellurides/Bismuthides	Unnamed Phase	PtTeBi	82
	Unconstrained Phase	Pt-Te-Bi-Fe-Ni	76
	Michenerite	PdBiTe	41
	Moncheite	$PtTe_2$	29
(3) Pt/Pd Arsenides	Sperrylite	$PtAs_2$	2
	Palladoarsenide	Pd_2As	1
(4) PGE Sulpharsenides	Platarsite	PtAsS	6
	Hollingworthite	RhAsS	1
	Unconstrained Phase	Pt-Rh-Ru-S-As	1
(5) PGE-Alloys	Pt-Fe Alloy	Pt_2Fe	7
	Unconstrained Phase	Fe-Pt-Cu	6
	Plumbopalladanite	Pd_3Pb_2	3
	Unnamed Phase	PdGe	1
(6) Au and Ag Bearing Phases	Electrum	Au,Ag	20
	Native Gold	Au	19
		Total	*1262*

The overall PGM distribution for the ZG219 D1 UG2 is graphically represented in Figure 8.24 whilst the vertical distribution profile is presented in Figures 8.25 and 8.26. The distribution data was initially calculated without the presence of laurite (RuS_2) (which is standard procedure for Anglo Platinum due to the uneconomic status of Ruthenium metal). However, it was decided that, for academic reasons, this PGE-sulphide phase is important and therefore the data has been reprocessed (to include Ruthenium) and presented in Figures 8.27, 8.28 and 8.29.

Table 8.9: Overall PGM distribution for the ZG219 D1 UG2(Area %).

Mineral Species	ZG219 D1 UG2
Pt-sulphide	32.9
PtPd-sulphide	45.0
PtRh-sulphide	9.4
Pt-telluride	8.1
Pd-telluride	1.5
Pt-arsenide	0.2
Pd-arsenide	0.2
Ferroplatinum	1.3
Pd-alloys	0.1
PGE-sulpharsenides	0.1
Gold	1.2
Total	100.0
No. of particles examined	1111

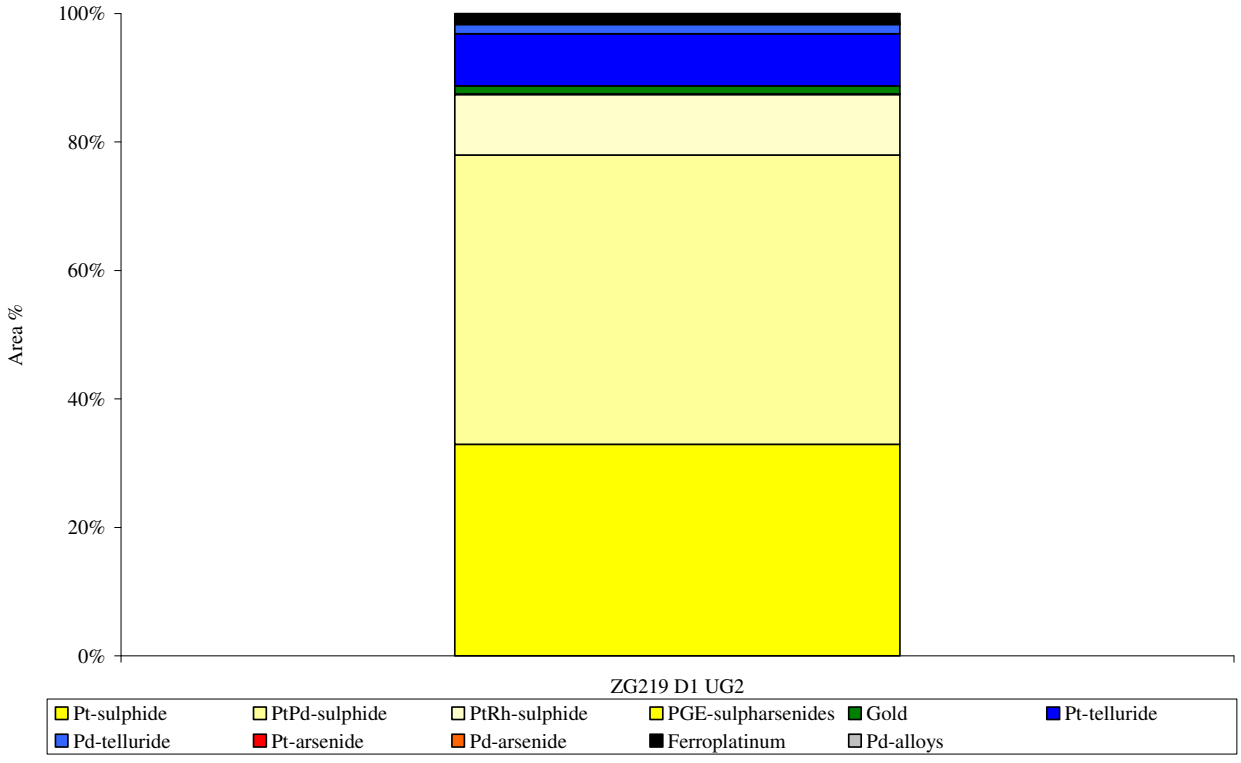

Figure 8.24: Overall PGM distribution for the ZG219 D1 UG2.

The overall PGM distribution for the ZG219 D1 UG2 (Figure 8.24) reveals a predominance of PGE-sulphide species. Braggite, cooperite and Pt-Rh-sulphide species dominate the PGM assemblage. Next most abundant are the PGE-telluride species, especially the unnamed PtTeBi phase. Lesser amounts of gold, ferroplatinum, PGE-arsenide, PGE-sulpharsenide and PGE-alloy phases were also identified.

Table 8.10: PGM distribution for the upper half of the ZG219 D1 UG2.

Mineral Name	161	162	163	164	165	166	167	168
Pt-sulphide	12.8	9.0	19.1	76.0	70.0	30.7	54.2	65.2
PtPd-sulphide	55.4	73.0	54.2	3.3	6.2	49.1	19.7	16.1
PtRh-sulphide	0.1	0.0	1.0	19.5	11.7	6.3	14.3	12.1
Pt-telluride	22.9	12.8	21.3	1.0	5.8	1.7	8.4	5.3
Pd-telluride	6.3	2.9	1.0	0.0	6.2	0.0	0.0	1.0
Ferroplatinum	0.0	0.0	0.0	0.2	0.0	12.1	0.0	0.3
PGE-sulpharsenides	0.0	0.8	0.0	0.0	0.0	0.0	0.0	0.0
Gold	2.5	1.5	3.5	0.0	0.0	0.0	3.4	0.0
Total	100.0	100.0	100.0	100.0	100.0	100.0	100.0	100.0
No. of particles examined	88	49	40	44	68	55	56	60

Table 8.11: PGM distribution for the lower half of the ZG219 D1 UG2.

Mineral Name	169	170	171	172	173	174	175	176
Pt-sulphide	8.0	29.8	27.6	51.8	34.6	13.0	9.4	15.7
PtPd-sulphide	70.6	55.7	24.3	32.4	42.6	77.5	72.8	67.6
PtRh-sulphide	0.8	8.8	42.6	12.3	13.3	0.6	1.4	5.2
Pt-telluride	12.4	3.3	3.8	1.7	4.8	4.9	13.7	5.7
Pd-telluride	1.3	2.5	0.3	0.4	0.5	0.4	0.9	0.3
Pt-arsenide	2.7	0.0	0.0	0.0	0.0	0.0	0.0	0.0
Pd-arsenide	2.4	0.0	0.0	0.0	0.0	0.0	0.0	0.0
Ferroplatinum	0.8	0.0	0.0	0.9	3.5	1.5	0.0	0.9
Pd-alloys	0.0	0.0	0.0	0.4	0.0	1.2	0.0	0.0
PGE-sulpharsenides	0.0	0.0	0.0	0.0	0.0	0.0	0.6	0.9
Gold	1.0	0.0	1.3	0.0	0.7	0.9	1.2	3.7
Total	100.0	100.0	100.0	100.0	100.0	100.0	100.0	100.0
No. of particles examined	96	47	80	58	88	75	125	82

Firstly, as already mentioned, the overall UG2 shows a predominance of PGE-sulphides. It is the variation of the non-PGE-sulphides (especially tellurides), however, through the chromitite (Figures 8.25 and 8.26) which reveals an interesting distribution pattern. The PGE-tellurides appear to be concentrated in three main zones within the chromitite. The highest abundance of PGE-tellurides occurs at the top of the chromitite whilst there are two lesser zones in the middle and at the base of the chromitite.

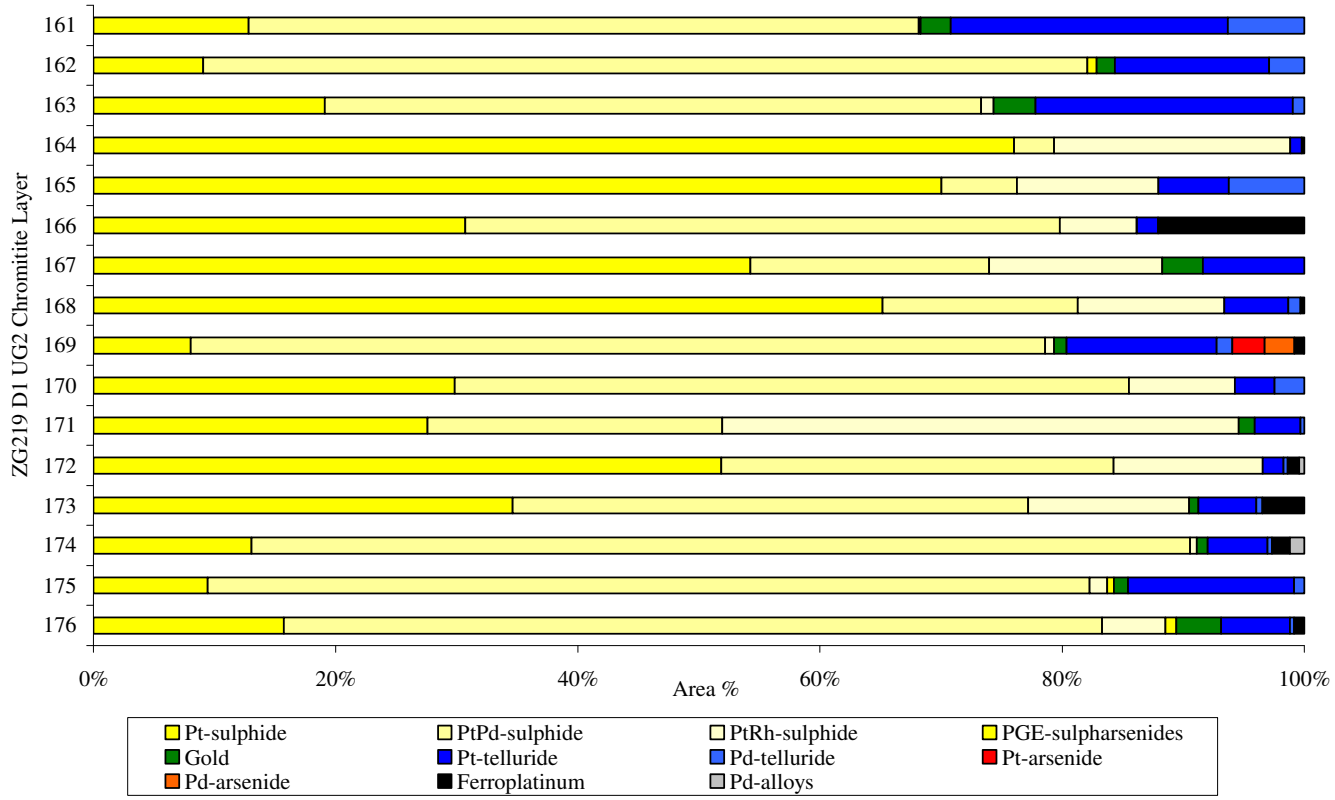

Figure 8.25: Vertical PGM distribution profile for the ZG219 D1 UG2.

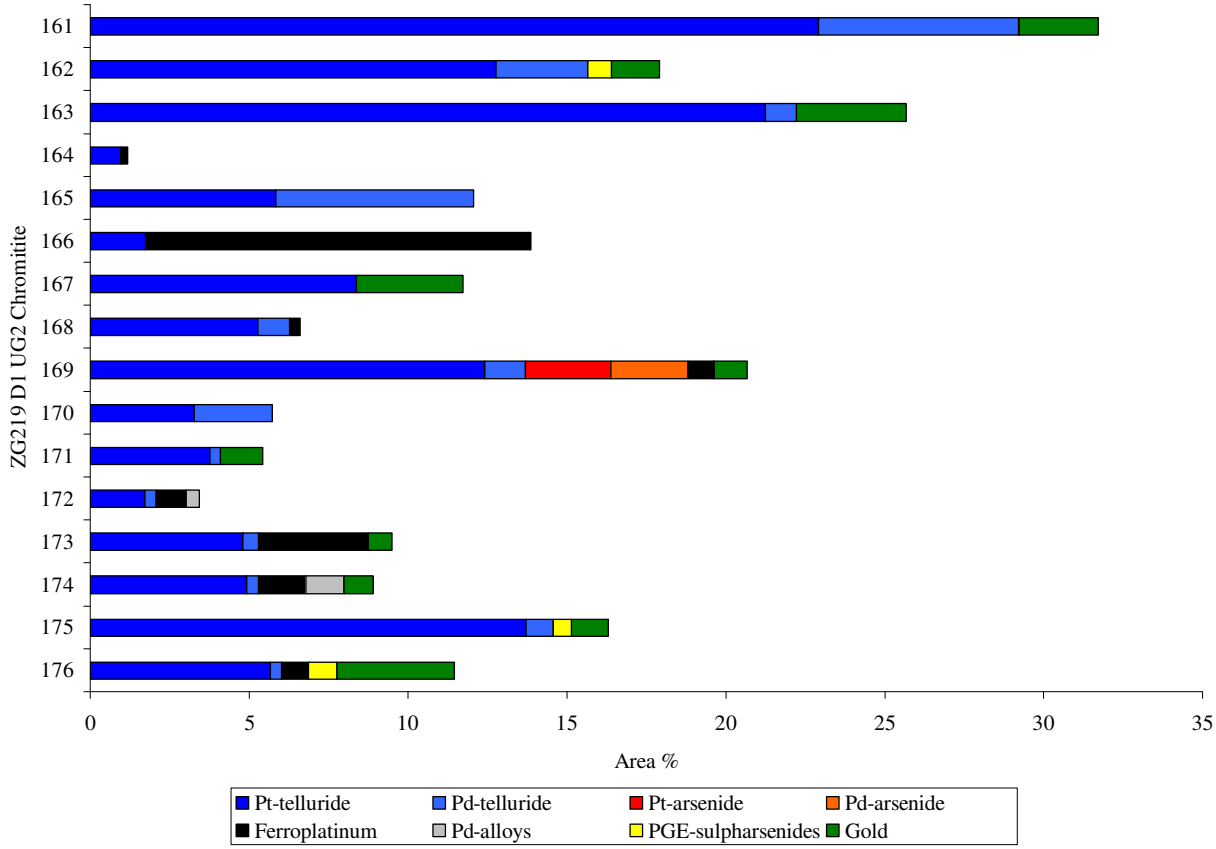

Figure 8.26: Vertical PGM distribution profile for the ZG219 D1 UG2 (excluding the PGE-sulphides).

The PGM distribution data was then reprocessed to include the laurite (RuS_2) species. The new distribution data (Figure 8.27) confirms the previous data in that the ZG219 D1 UG2 comprises a PGE-sulphide dominated PGM assemblage with lesser PGE-tellurides and only trace amounts of the remaining PGM species.

Table 8.12: PGM distribution (with laurite included) for the ZG219 D1 UG2.

Mineral Species	ZG219 D1 UG2
Pt-sulphide	24.0
PtPd-sulphide	35.6
Ru-sulphide	23.8
PtRh-sulphide	6.6
Pt-telluride	6.5
Pd-telluride	1.1
Pt-arsenide	0.2
Pd-arsenide	0.1
Ferroplatinum	0.9
Pd-alloys	0.1
PGE-sulpharsenides	0.1
Gold	1.0
Total	100.0
No. of particles examined	1348

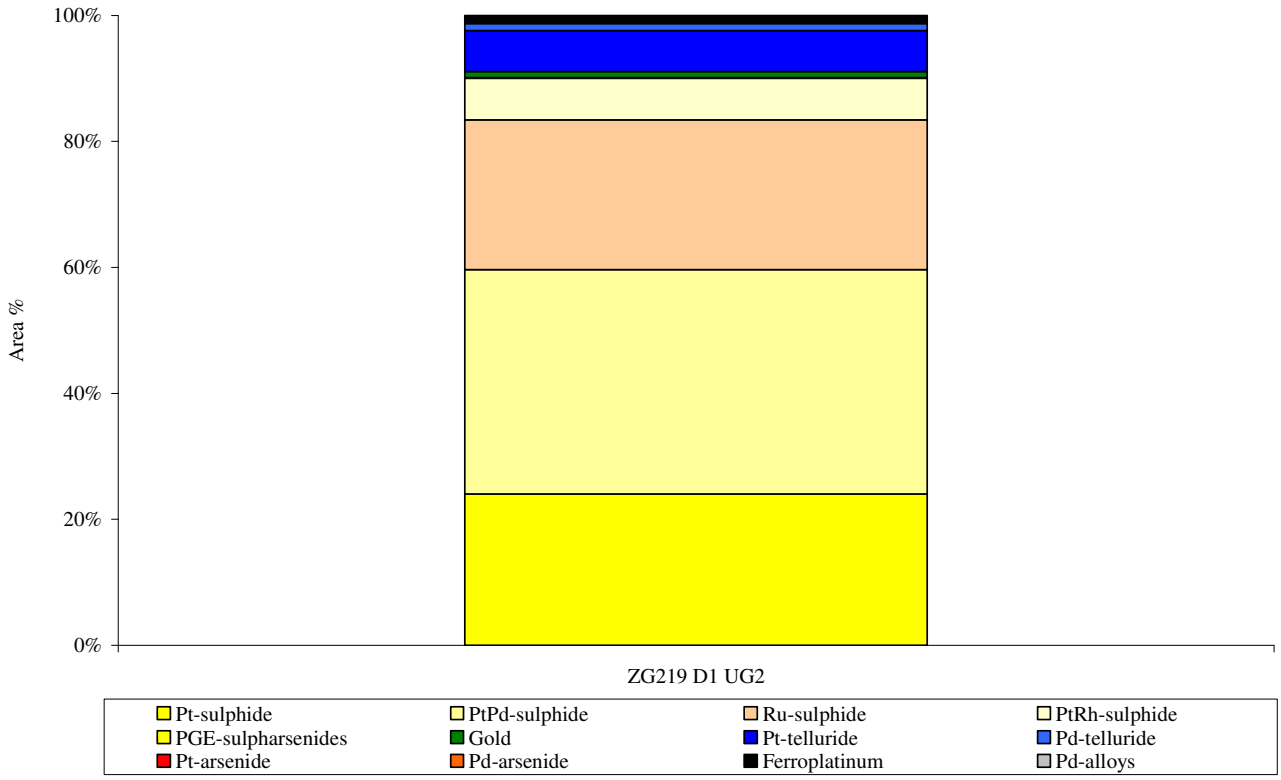

Figure 8.27: PGM distribution (with laurite included) for the ZG219 D1 UG2.

Table 8.13: PGM distribution (with laurite included) for the upper half of the ZG219 D1 UG2.

Mineral Name	161	162	163	164	165	166	167	168
Pt-sulphide	9.9	8.5	17.4	60.3	49.0	21.2	31.2	48.6
PtPd-sulphide	43.0	69.0	49.5	2.6	4.4	33.9	11.3	12.0
Ru-sulphide	22.3	6.4	8.7	20.7	30.0	31.0	42.5	25.4
PtRh-sulphide	0.1	0.0	0.9	15.4	8.2	4.4	8.2	9.0
Pt-telluride	17.8	11.5	19.4	0.8	4.1	1.2	4.8	3.9
Pd-telluride	4.9	2.6	0.9	0.0	4.4	0.0	0.0	0.7
Ferroplatinum	0.0	0.0	0.0	0.2	0.0	8.3	0.0	0.3
PGE-sulpharsenides	0.0	0.7	0.0	0.0	0.0	0.0	0.0	0.0
Gold	1.9	1.3	3.2	0.0	0.0	0.0	1.9	0.0
Total	100.0	100.0	100.0	100.0	100.0	100.0	100.0	100.0
No. of particles examined	98	56	47	54	82	72	69	68

Table 8.14: PGM distribution (with laurite included) for the bottom half of the ZG219 D1 UG2.

Mineral Name	169	170	171	172	173	174	175	176
Pt-sulphide	7.3	17.8	18.4	38.2	26.2	10.5	7.9	12.0
PtPd-sulphide	63.9	33.2	16.2	23.9	32.3	62.2	60.7	51.8
Ru-sulphide	9.5	40.3	33.4	26.3	24.2	19.8	16.6	23.4
PtRh-sulphide	0.7	5.2	28.4	9.1	10.1	0.5	1.2	4.0
Pt-telluride	11.2	1.9	2.5	1.3	3.6	4.0	11.4	4.3
Pd-telluride	1.2	1.5	0.2	0.3	0.4	0.3	0.7	0.3
Pt-arsenide	2.4	0.0	0.0	0.0	0.0	0.0	0.0	0.0
Pd-arsenide	2.2	0.0	0.0	0.0	0.0	0.0	0.0	0.0
Ferroplatinum	0.7	0.0	0.0	0.7	2.6	1.2	0.0	0.7
Pd-alloys	0.0	0.0	0.0	0.3	0.0	1.0	0.0	0.0
PGE-sulpharsenides	0.0	0.0	0.0	0.0	0.0	0.0	0.5	0.7
Gold	0.9	0.0	0.9	0.0	0.6	0.7	1.0	2.8
Total	100.0	100.0	100.0	100.0	100.0	100.0	100.0	100.0
No. of particles examined	109	61	104	76	106	106	145	95

The reprocessed vertical PGM distribution profile (with laurite included), presented in Figures 8.28 and 8.29, confirms the intricate pattern described earlier. The non-PGE-sulphides (predominantly the PGE-tellurides) are concentrated in three distinct zones, with the highest abundance, once again, occurring near the top of the chromitite, whilst two other zones exist at the middle and at the base of the layer.

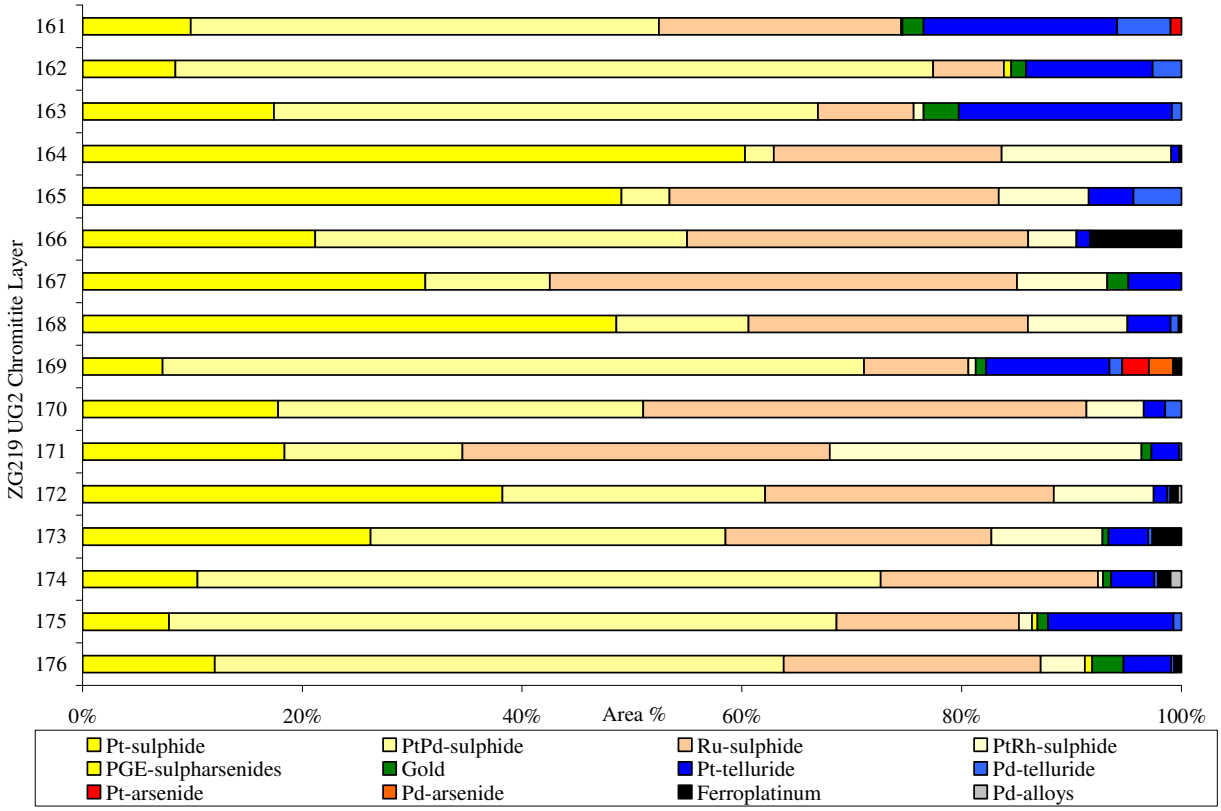

Figure 8.28: Vertical PGM distribution (with laurite included) through the ZG219 D1 UG2.

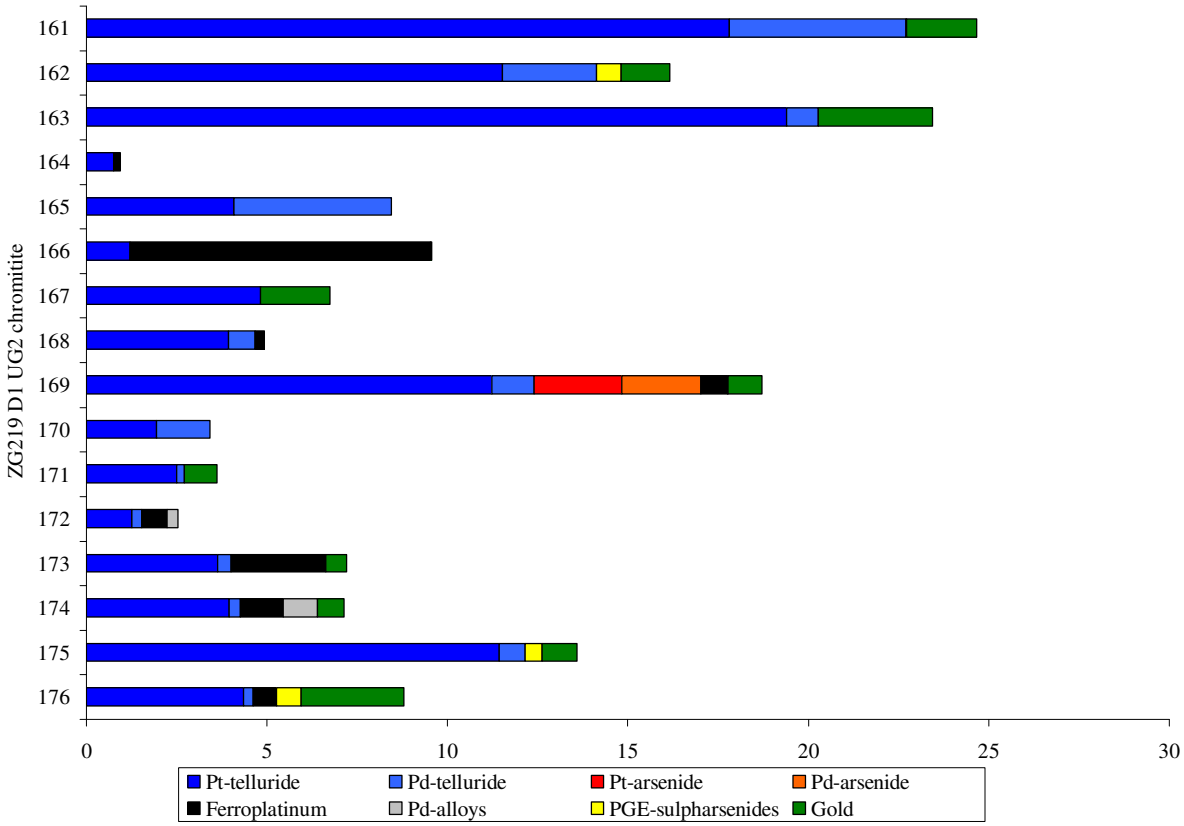

Figure 8.29: Vertical PGM distribution (with laurite included) through the ZG219 D1 UG2 (excluding the PGE-sulphides).

8.5.2 PGM Grain Size

The PGM grain size distribution is presented in Tables 8.15 and 8.16 and in Figure 8.30.

Table 8.15: PGM grain size distribution for the upper half of the ZG219 D1 UG2.

Size Class (µm)	161	162	163	164	165	166	167	168
38	-	59.6	-	-	-	-	-	-
27	-	-	-	-	-	-	-	-
19	31.7	-	36.5	-	-	22.5	-	-
13.5	-	-	-	24.4	19.7	43.9	-	-
9.6	23.4	15.1	18.2	33.7	8.4	8.2	-	30.4
5.7	17.8	11.0	11.4	12.5	23.7	3.8	27.4	20.9
4.1	24.4	12.9	30.8	25.0	37.5	17.2	56.7	43.1
2	2.2	1.3	2.9	3.7	10.1	4.0	15.4	5.4
1	0.4	0.1	0.1	0.7	0.6	0.1	0.5	0.1
p50*	6.3	27.8	6.4	6.4	4.2	11.7	3.4	4.2

*p50 is defined as the grain size through which 50 % of the PGMs pass.

Table 8.16: PGM grain size distribution for the bottom half of the ZG219 D1 UG2.

Size Class (µm)	169	170	171	172	173	174	175	176
38	-	-	-	-	-	63.5	-	-
27	-	-	-	-	-	-	-	30.5
19	28.6	-	16.9	27.5	-	-	9.3	13.9
13.5	-	-	19.8	19.3	25.7	10.2	18.5	10.2
9.6	26.9	25.4	21.0	-	30.4	-	32.8	2.6
5.7	20.8	33.8	15.3	21.3	13.6	10.4	19.8	21.1
4.1	18.0	31.1	24.4	27.3	26.6	12.2	14.7	17.4
2	4.8	9.6	2.3	3.8	3.2	3.3	4.5	3.8
1	0.9	0.2	0.4	0.9	0.5	0.3	0.3	0.5
p50*	6.1	4.7	6.9	4.8	6.1	28.1	7.3	12.4

*p50 is defined as the grain size through which 50 % of the PGMs pass.

The PGMs are fine-grained and have an average grain size (p50) of less than 10 µm. Two samples, however, (162 and 174) display a very coarse average grain size of ~28 µm each, which is far higher than for the rest. This can be attributed to the presence of very large, well formed braggite (PtPdS) grains as is evident in Figures 8.25F, 8.43C and 8.44D.

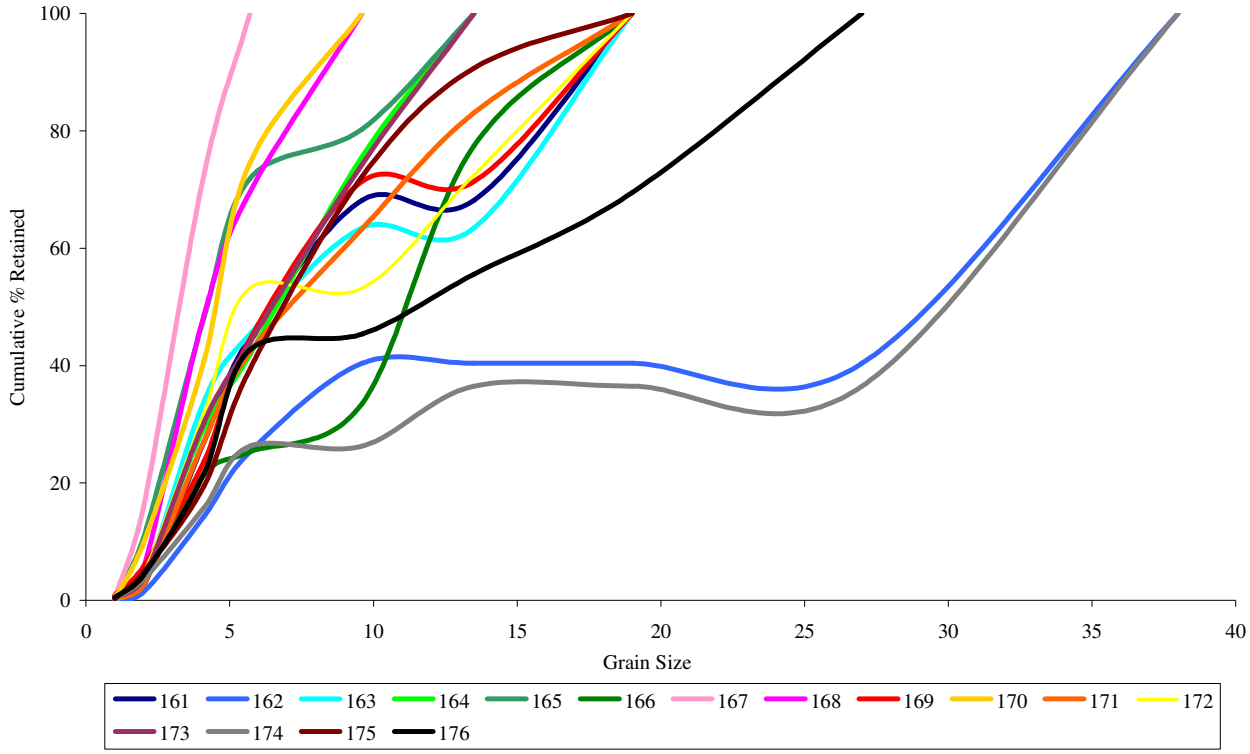

Figure 8.30: PGM grain size distribution for the ZG219 D1 UG2.

8.5.3 PGM Association and Textural Characteristics

The association and textural characteristics of the PGMs are documented here through a variety of back-scattered electron (BSE) images from each sample. The general location and association of the PGMs, as well as any interesting textures, are then described in further detail.

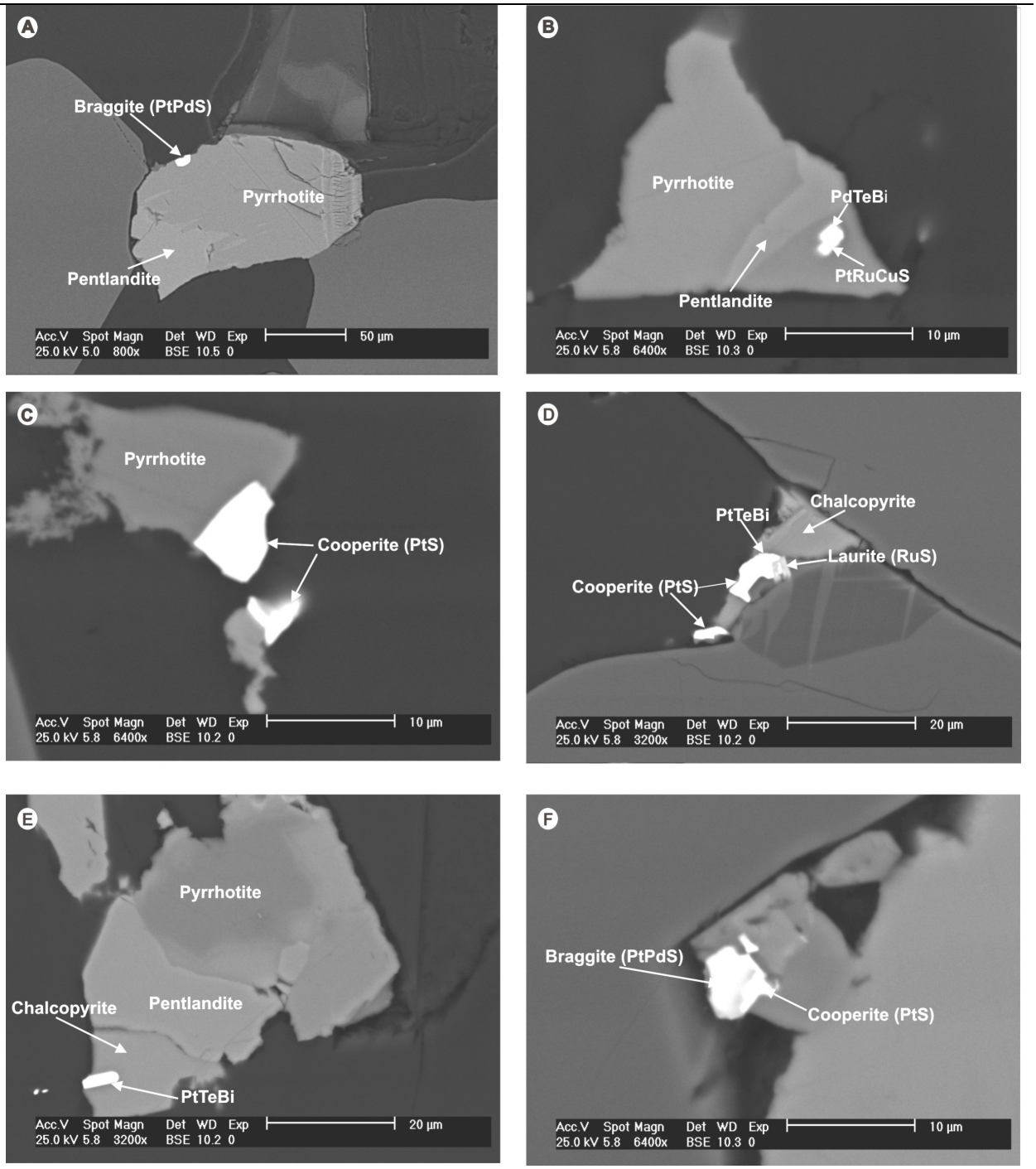

Figure 8.31: MLA BSE image of PGM occurrences within sample 161 (1st batch).

All the PGMs in Figure 8.31 are sulphide associated (especially with the pentlandite-pyrrhotite sulphide assemblage). The PGMs appear to be preferentially found near the edges of the sulphide grains. The PGM-bearing sulphides also are often interstitial to the cumulus chromites (Figure 8.31 D and F). Note also that the PGMs often occur as composite particles comprising more than one PGM phase i.e. as in Figure 8.31 B (PtTeBi and PtRuCuS) and D (PtTeBi, laurite and cooperite).

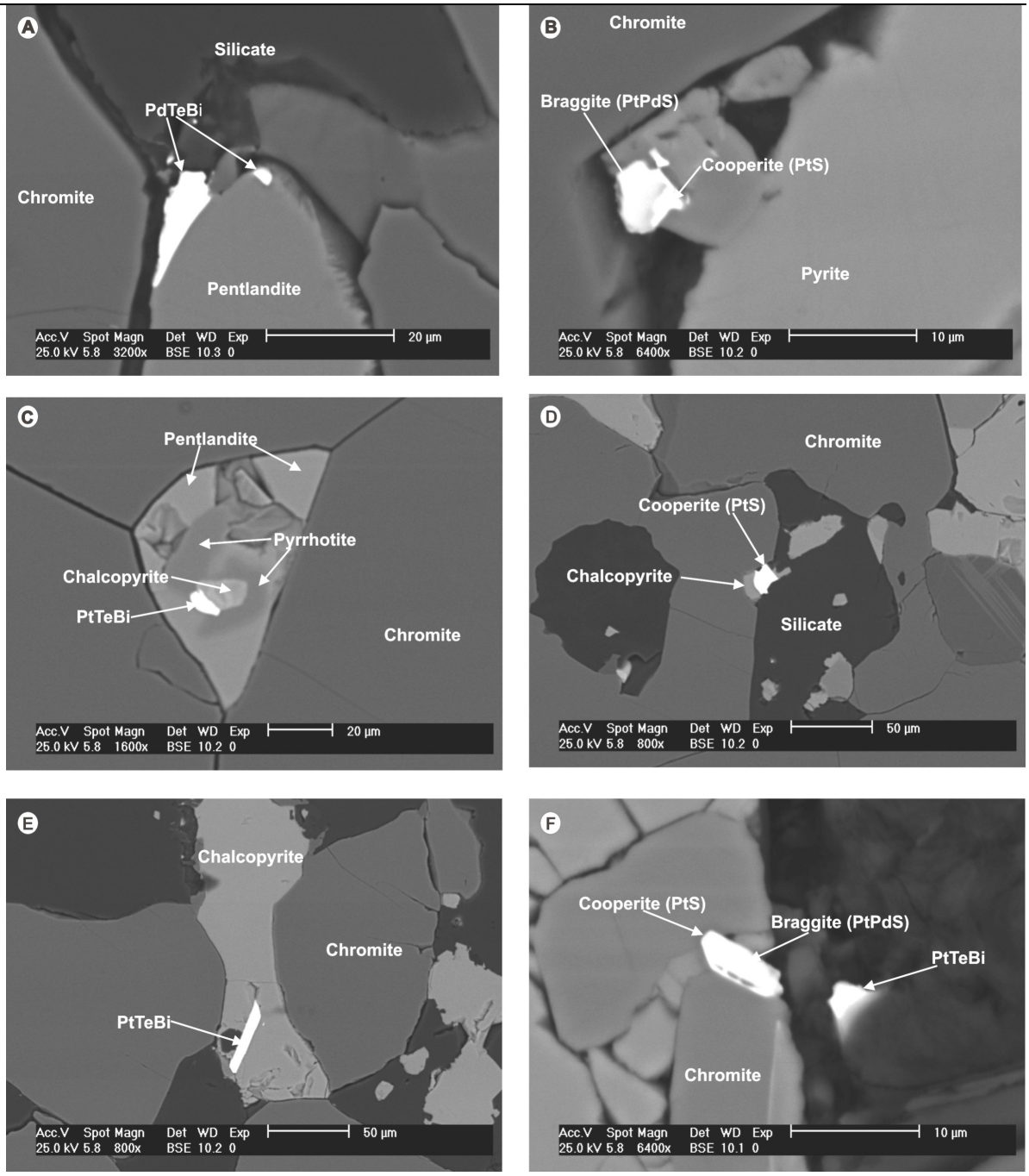

Figure 8.32: MLA BSE image of PGM occurrences within sample 161 (2nd batch).

The moncheite (PdTeBi) grain in Figure 8.32 A, the cooperite in Figure 8.32 D and the PtTeBi phase in Figure 8.32 F all occur within the interstitial silicate. The moncheite particle especially appears to have crystallized along the boundary between the pentlandite and the chromite grains (Figure 8.32 A). The remaining PGMs are all also sulphide associated. The important point to note is that the PGM often occurs along the grain boundary between sulphide phases within a composite sulphide grain i.e. as in Figure 8.32 C (PtTeBi along the chalcopyrite phase boundary).

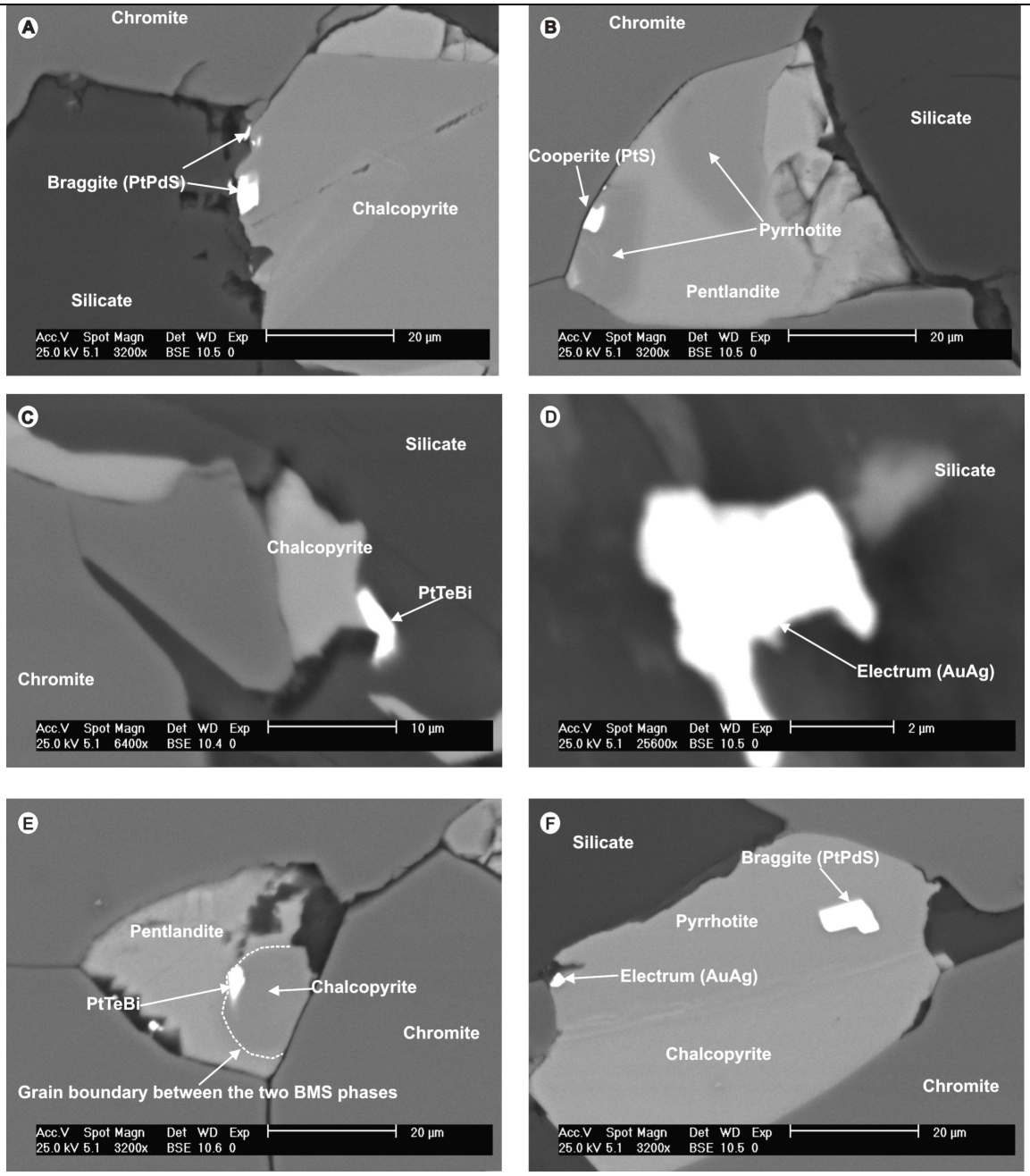

Figure 8.33: MLA BSE image of PGM occurrences within sample 162 (1st batch).

The PGMs in Figure 8.33 C and D both occur in the interstitial silicate (the PtTeBi particle existing along the boundary between chalcopyrite and silicate). The remaining PGMs are all sulphide associated and all occur at the grain boundary of the sulphide phases. In Figure 8.33 A and B the PGM occurs at the edge of the sulphide boundary to a silicate and chromite respectively, whilst in Figure 8.33 E the PGM (PtTeBi) exists at the phase boundary between pentlandite and chalcopyrite. In Figure 8.33 F the larger braggite particle is enclosed within the pyrite whilst the smaller electrum particle is positioned at the edge next to the triple point junction with chromite and silicate.

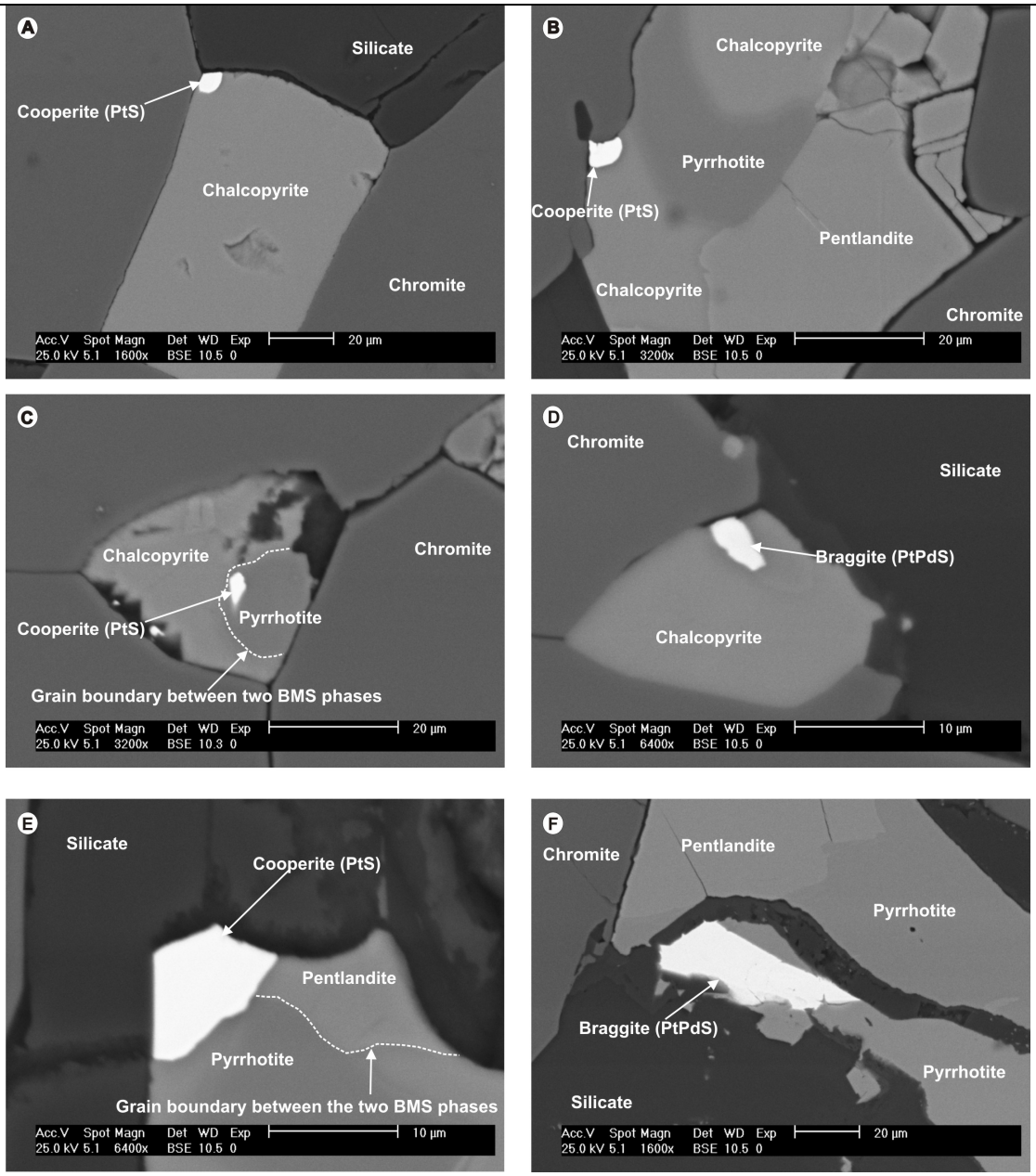

Figure 8.34: MLA BSE image of PGM occurrences within sample 162 (2nd batch).

The second batch of PGMs from sample 162 are dominated by PGE-sulphides of the cooperite and braggite varieties (Figure 8.34). The coarse grain size of the PGMs (p50 = 28 µm) is a result of these large, well formed braggite grains (i.e. Figure 8.34 F).

Once again all the PGMs present show a strong sulphide association and are often closely positioned to the edges of the sulphides, and have an especially strong affinity for triple point junctions. The PGE-sulphides in Figure 8.34 A, D and E all are located at a triple point junction whilst the PGE-sulphides in Figure 8.34 B and F are at the edge of the sulphide next to chromite and silicate respectively. The cooperite phase in Figure 8.34 C, whilst enclosed in sulphide, is positioned at the phase boundary between pyrite and chalcopyrite.

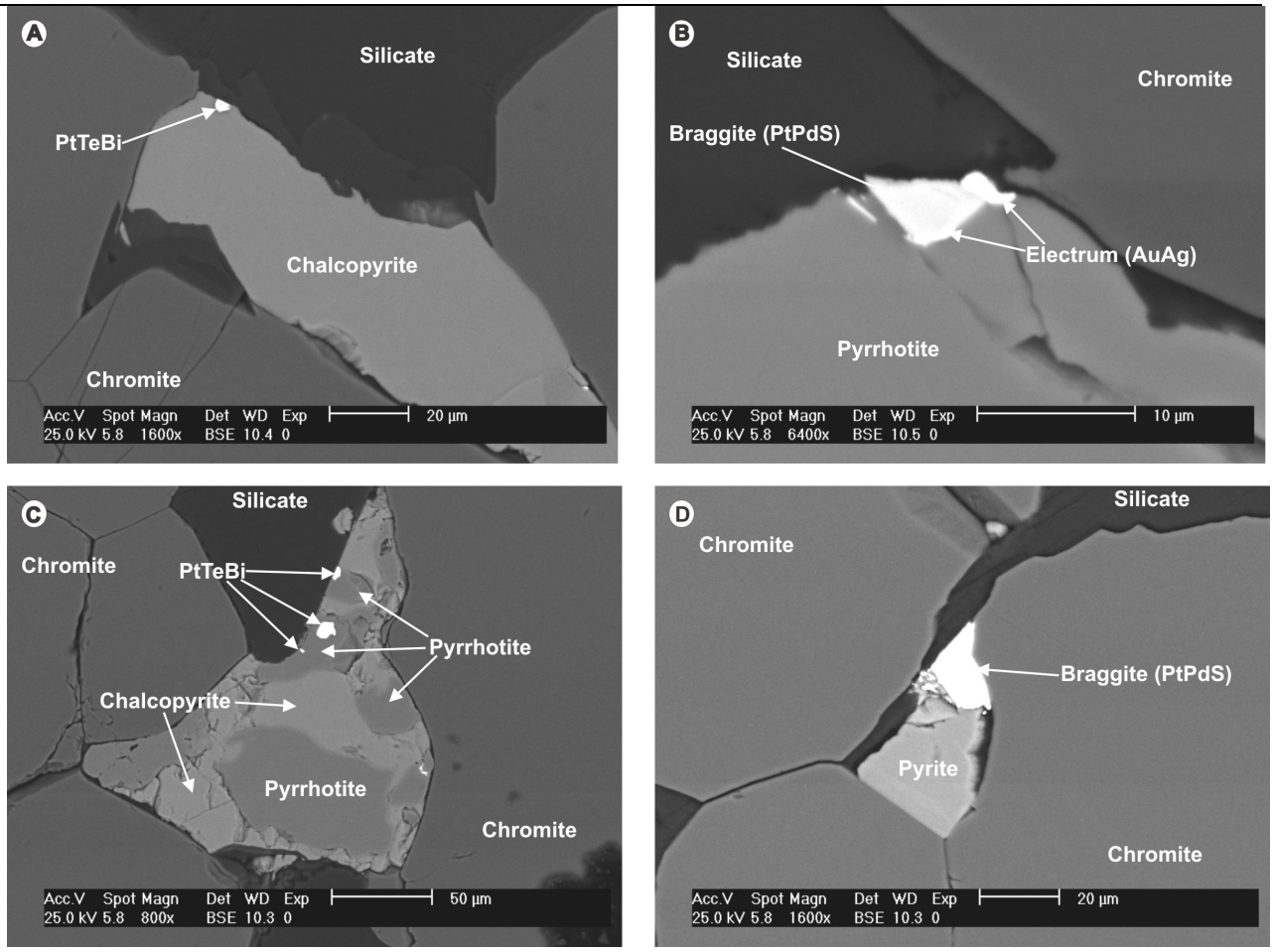

Figure 8.35: MLA BSE image of PGM occurrences within sample 163.

In sample 163 the PtTeBi grains in Figure 8.35 A and C are, once again, closely linked to sulphides in the form of chalcopyrite in A and a chalcopyrite-pyrite assemblage in C. Both PGMs also occur near, or at, the contact boundary of the sulphide phase with silicate. In Figure 8.35 B the braggite-electrum composite PGM also exists at the edge of a pyrite grain at a triple point junction between the pyrite, chromite and silicate. In Figure 8.35 D the large, well formed braggite grain occurs perfectly interstitial to the surrounding chromite grains (is located within the interstitial silicate).

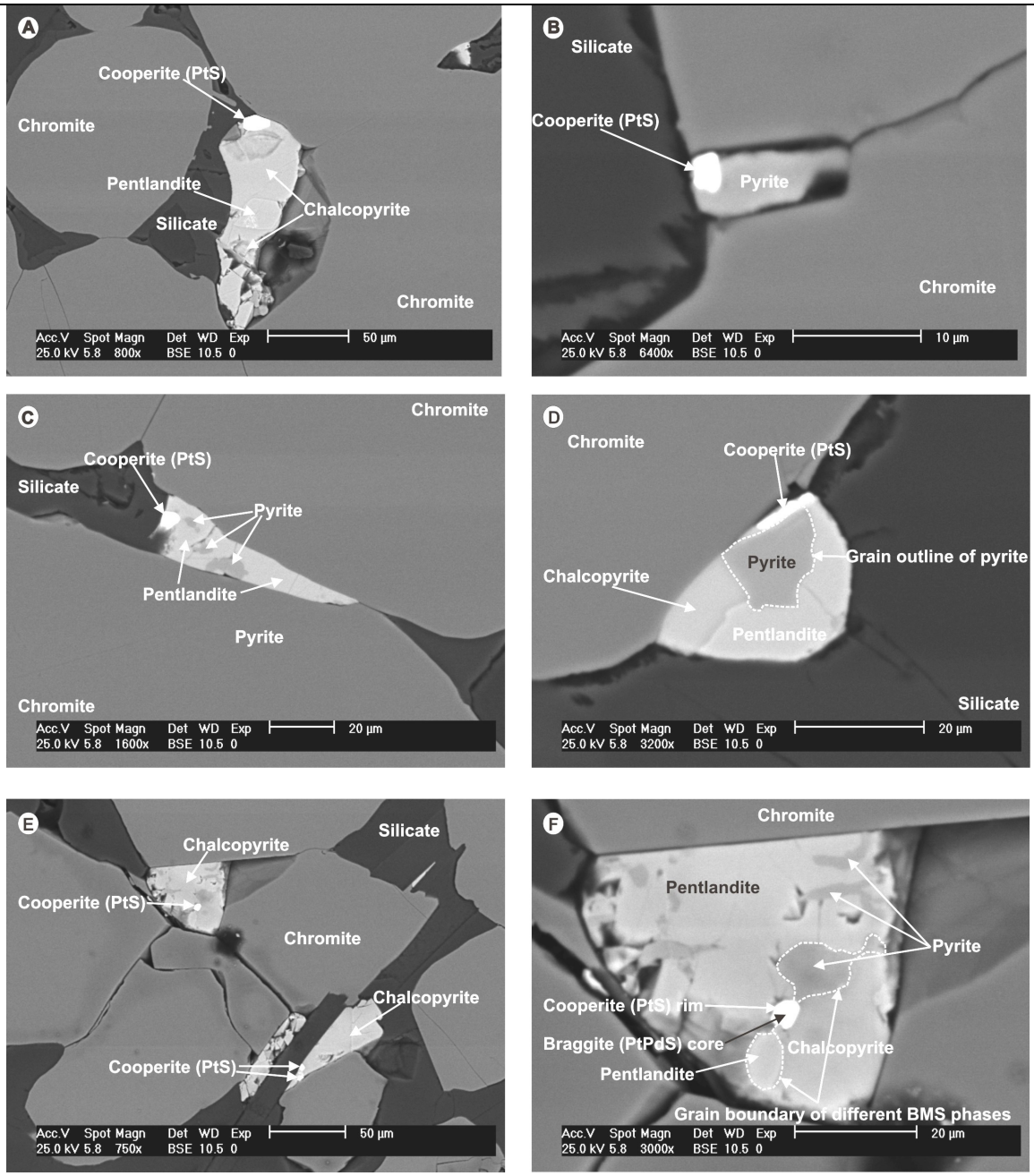

Figure 8.36: MLA BSE image of PGM occurrences within sample 164 (1st batch).

Figure 8.36 shows a series of PGE-sulphide phases which all occur within the sulphide assemblage of chalcopyrite-pentlandite-pyrite. In Figure 8.36 A – D the cooperites all occur near the outskirts of the sulphide particle, in close vicinity, or at, a triple point junction between the sulphide, chromite and silicate. Figure 8.36 E shows the PGM-bearing sulphide particles to be located within the interstitial silicate and which are enclosed by chromites. Figure 8.36 F is a zoomed in image (3000x) of the upper sulphide in Figure 8.36 E. Note the complex textures of the sulphide as well as the intricate exsolution zonation of the PGM i.e. a cooperite rim surrounding a braggite core, with the PGM occurring at the boundary between two sulphide phases.

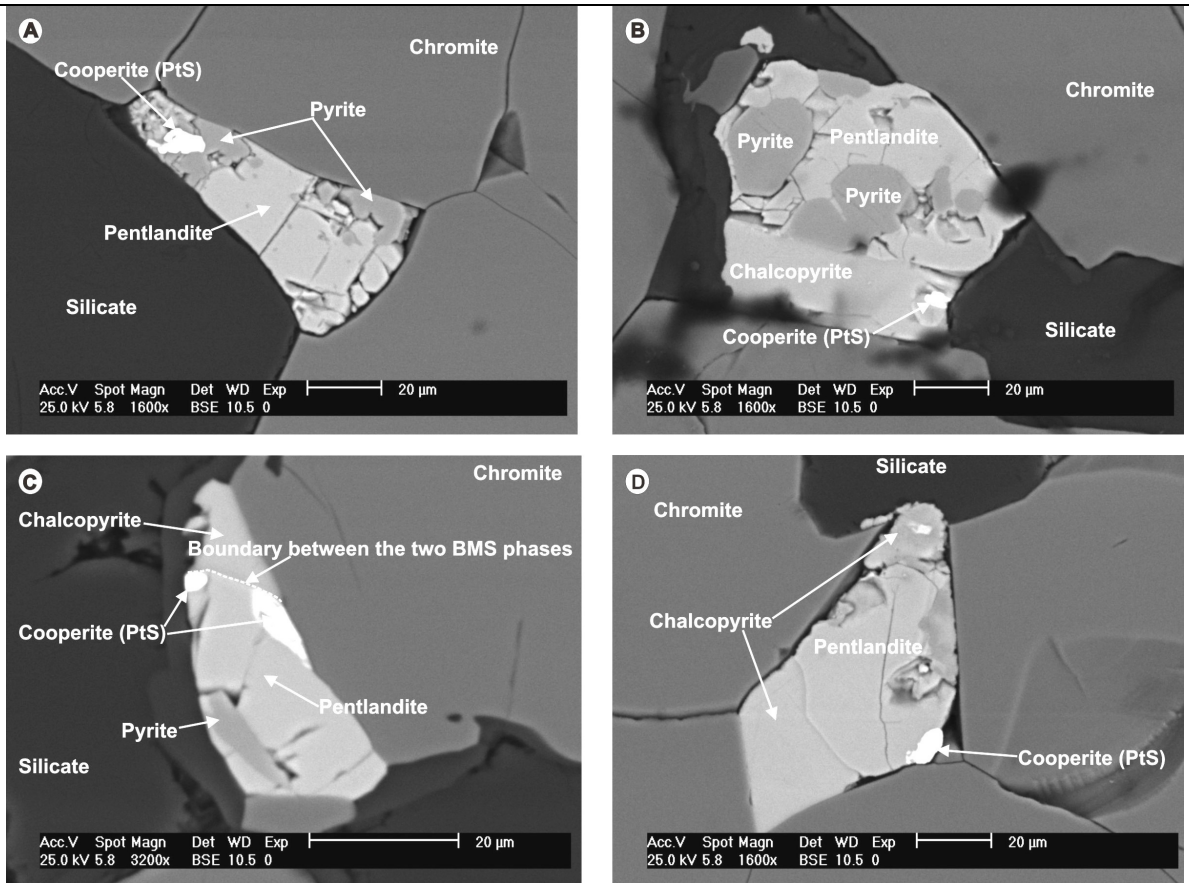

Figure 8.37: MLA BSE image of PGM occurrences within sample 164 (2nd batch).

In the second batch of sample 164 photos there is, once again, a predominance of sulphide-hosted cooperites particles (Figure 8.37). In Figure 8.37 A and B the cooperite phases are fully enclosed by the sulphide whilst in Figure 8.37 D the cooperite exists at the edge of a pentlandite grain at a triple point junction with two chromites. In Figure 8.37 C, two cooperite particles occur intimately at the phase boundary between chalcopyrite and pentlandite at the edge of the sulphide.

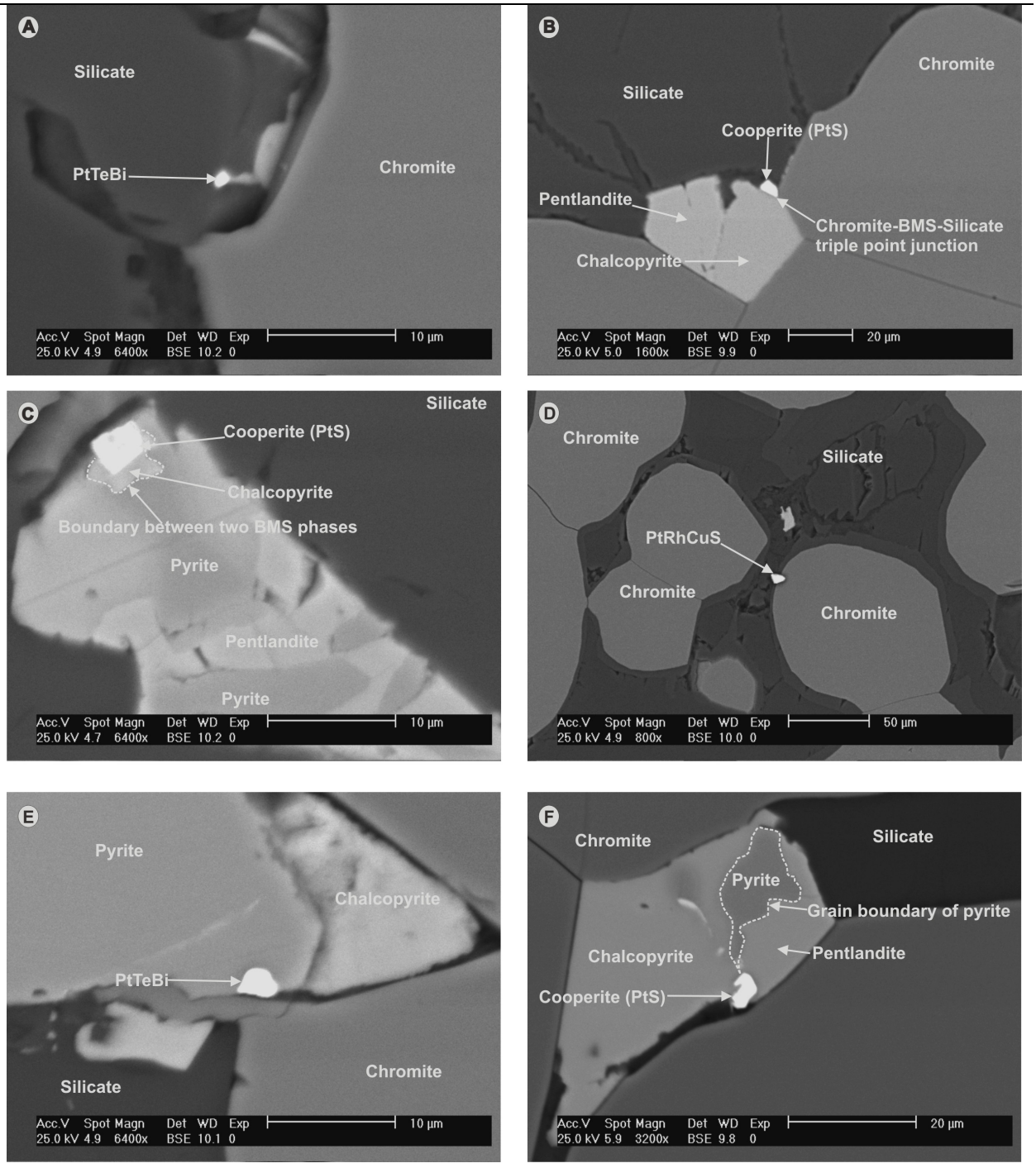

Figure 8.38: MLA BSE image of PGM occurrences within sample 165 (1st batch).

Apart from the PtTeBi phase in Figure 8.38 A, which is locked in silicate, and the PtRhCuS phase in Figure 8.38 D, which is attached to a chromite grain, the remaining PGMs all exist near the edge of sulphide phases. In Figure 8.38 B the cooperite particle sits at a triple point junction whilst in Figure 8.38 C the cooperite phase exists near the edge of the sulphide particle and at the chalcopyrite-pyrite boundary. In both Figure 8.38 E and F the PGMs occur near the outskirts of sulphides.

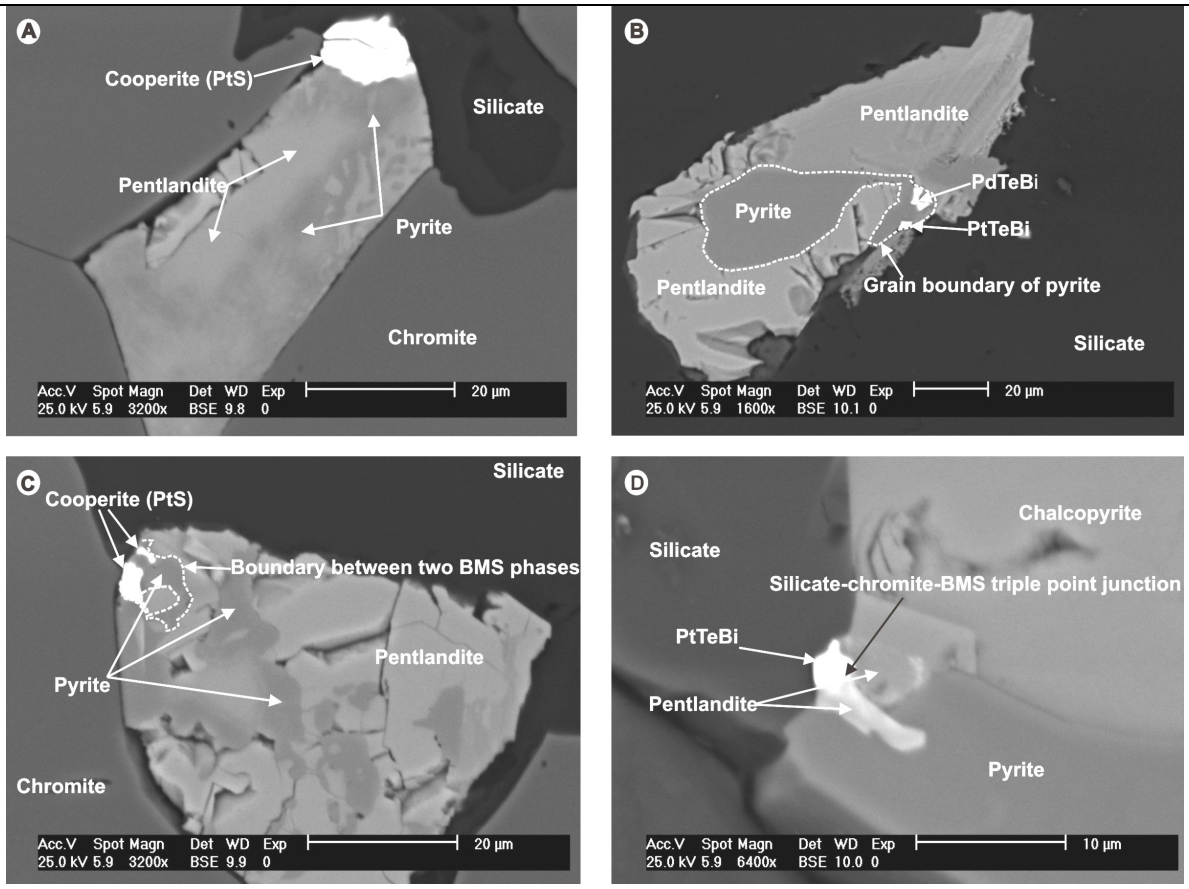

Figure 8.39: MLA BSE image of PGM occurrences within sample 165 (2nd batch).

The cooperite particles in Figure 8.39 A and C as well as the PtTeBi phase in Figure 8.39 D all exist at triple point junctions between sulphide, chromite and silicate whilst the moncheite and PtTeBi phases in Figure 8.39 B occur at the phase boundary between pyrite and pentlandite.

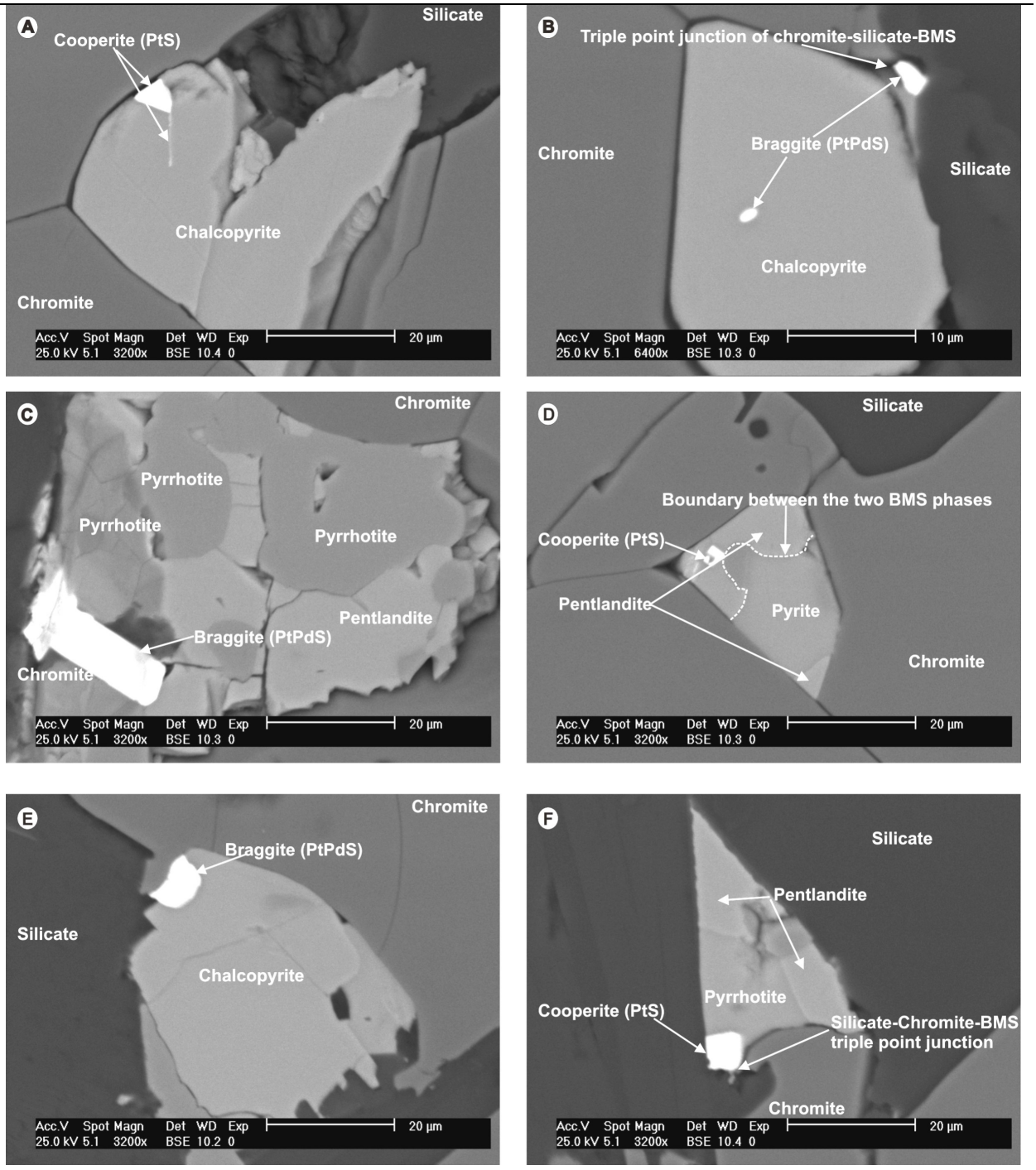

Figure 8.40: MLA BSE image of PGM occurrences within sample 166 (1st batch).

In Figure 8.40 B, E and F the PGMs all exist at a triple point junction. Figure 8.40 B also shows another braggite particle which is fully enclosed within the chalcopyrite. The cooperite in Figure 8.40 A and the large braggite in Figure 8.40 C both occur at the outskirts of the sulphide whilst the cooperite particle in Figure 8.40 D, although locked in sulphide, exists at the phase boundary between pyrite and pentlandite.

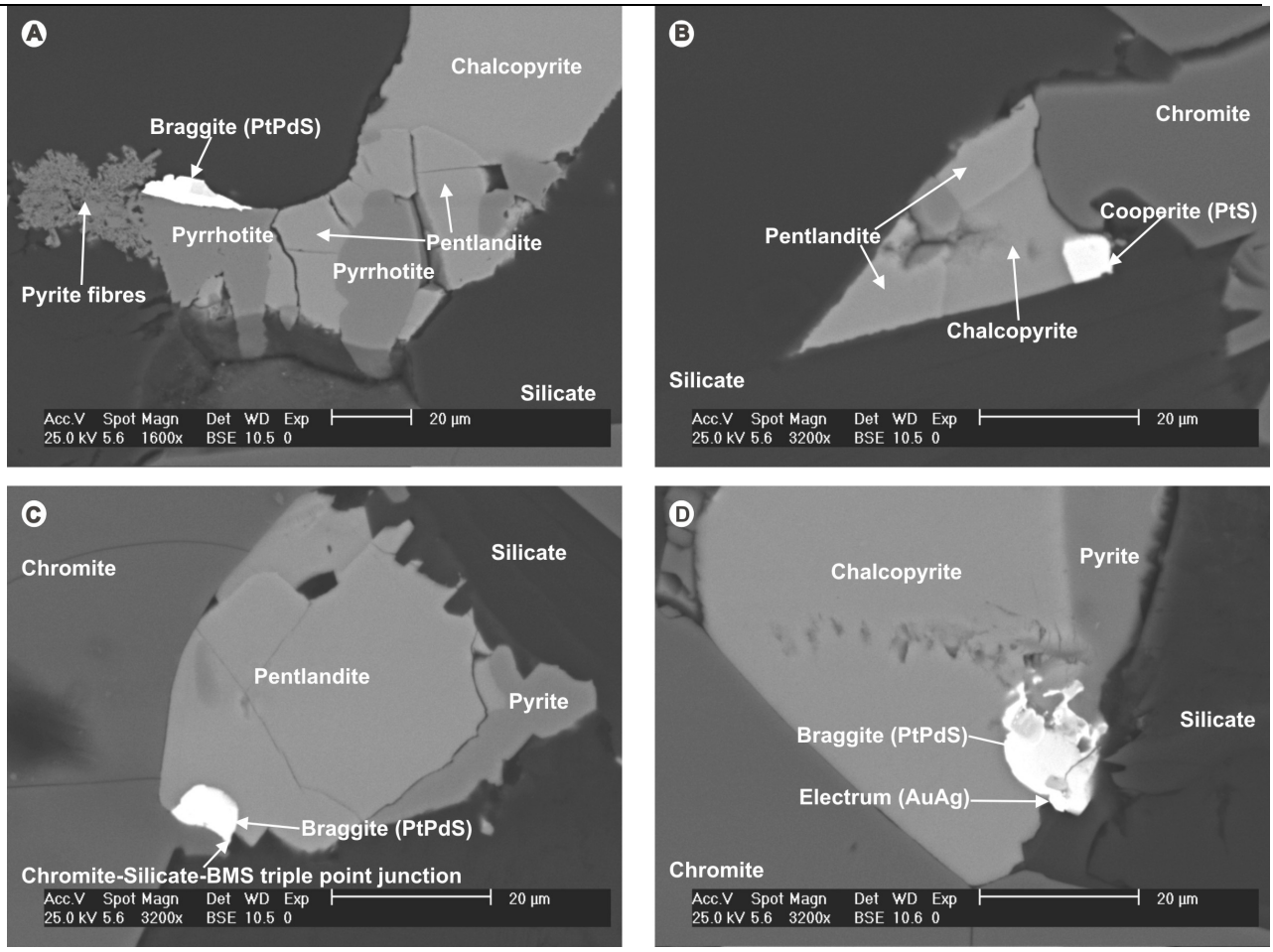

Figure 8.41: MLA BSE image of PGM occurrences within sample 166 (2nd batch).

The PGE-sulphides in Figure 8.41 B and in C both exist at triple point junctions. The braggite phases in both Figure 8.41 A and D (along with the smaller electrum phase) both occur at the boundary between the sulphide grain and the interstitial silicate.

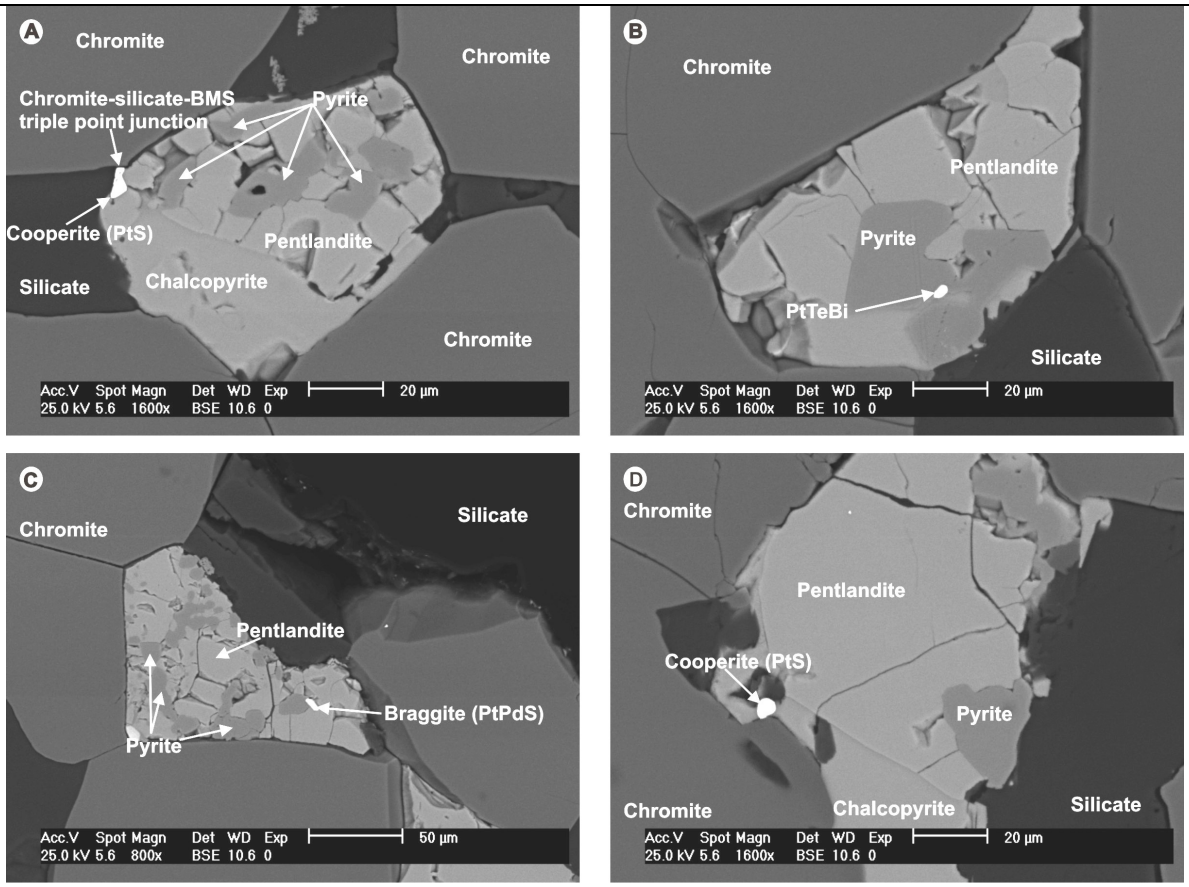

Figure 8.42: MLA BSE image of PGM occurrences within sample 167 (1st batch).

Although the cooperite phase in Figure 8.42 A occurs at a triple point junction and the cooperite in Figure 8.42 D occurs at the outskirts of the sulphide near chromite, both the PtTeBi phase in Figure 8.42 B and the braggite phase in Figure 8.42 C are fully enclosed within sulphide particles.

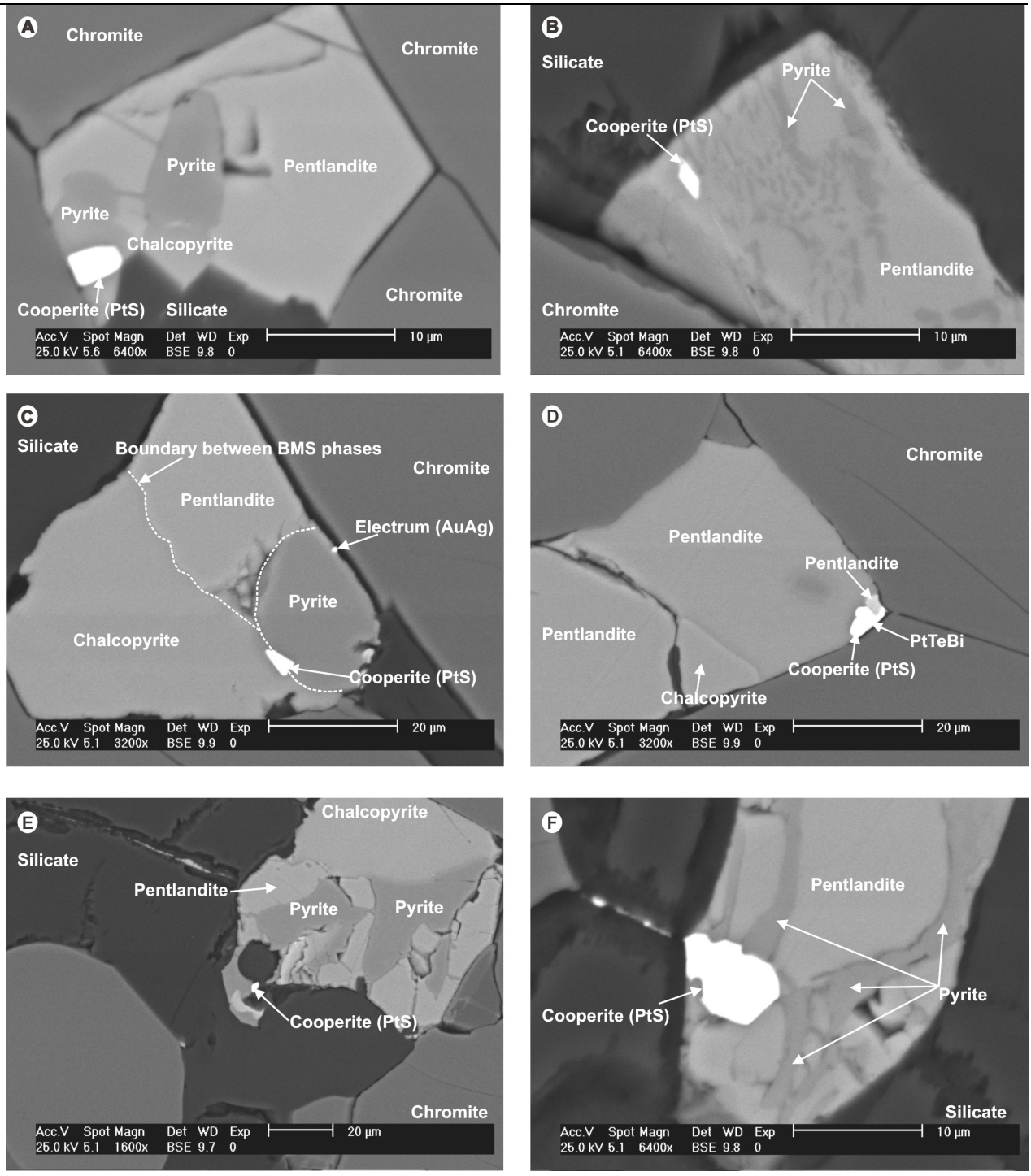

Figure 8.43: MLA BSE image of PGM occurrences within sample 168 (1st batch).

The cooperite - PtTeBi composite PGM in Figure 8.43 D exists at a triple point junction whilst the cooperite phases in Figure 8.43 A, E and F are all located at the edge of sulphide phases. The two cooperite particles in Figure 8.43 B and C, however, are both fully enclosed within sulphide whilst the one in C sits at the phase boundary between pyrite and chalcopyrite.

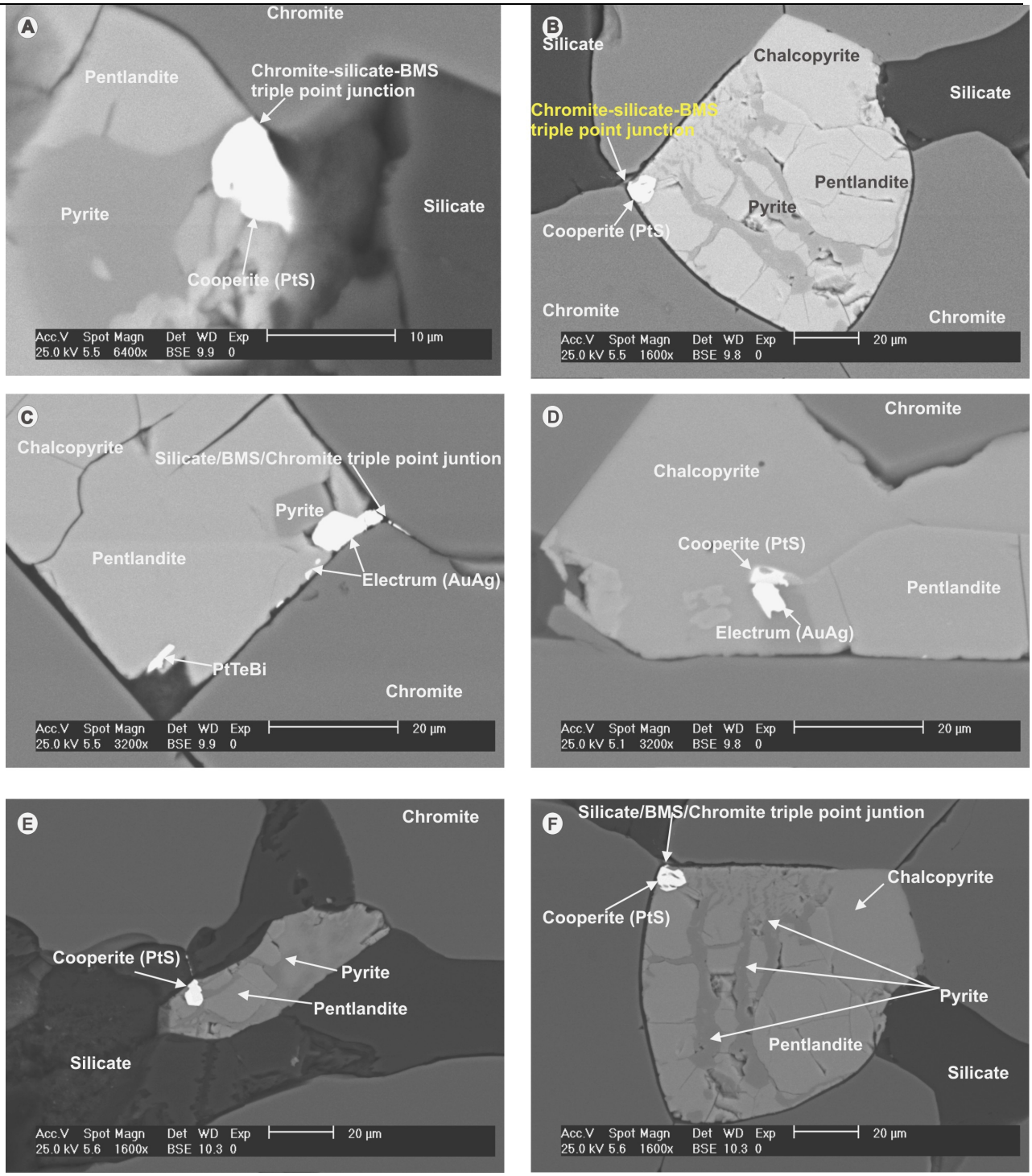

Figure 8.44: MLA BSE image of PGM occurrences within sample 168 (2nd batch).

The cooperite phases in Figure 8.44 A, B and F, as well as the electrum grain in Figure 8.44 C, all exist at triple point junctions. Note the presence of the PtTeBi and electrum phases in Figure 8.44 C which all occur at the sulphide edge. The cooperite-electrum composite in Figure 8.44 D and the cooperite in Figure 8.44 E are all enclosed in sulphide but occur at distinct phase boundaries.

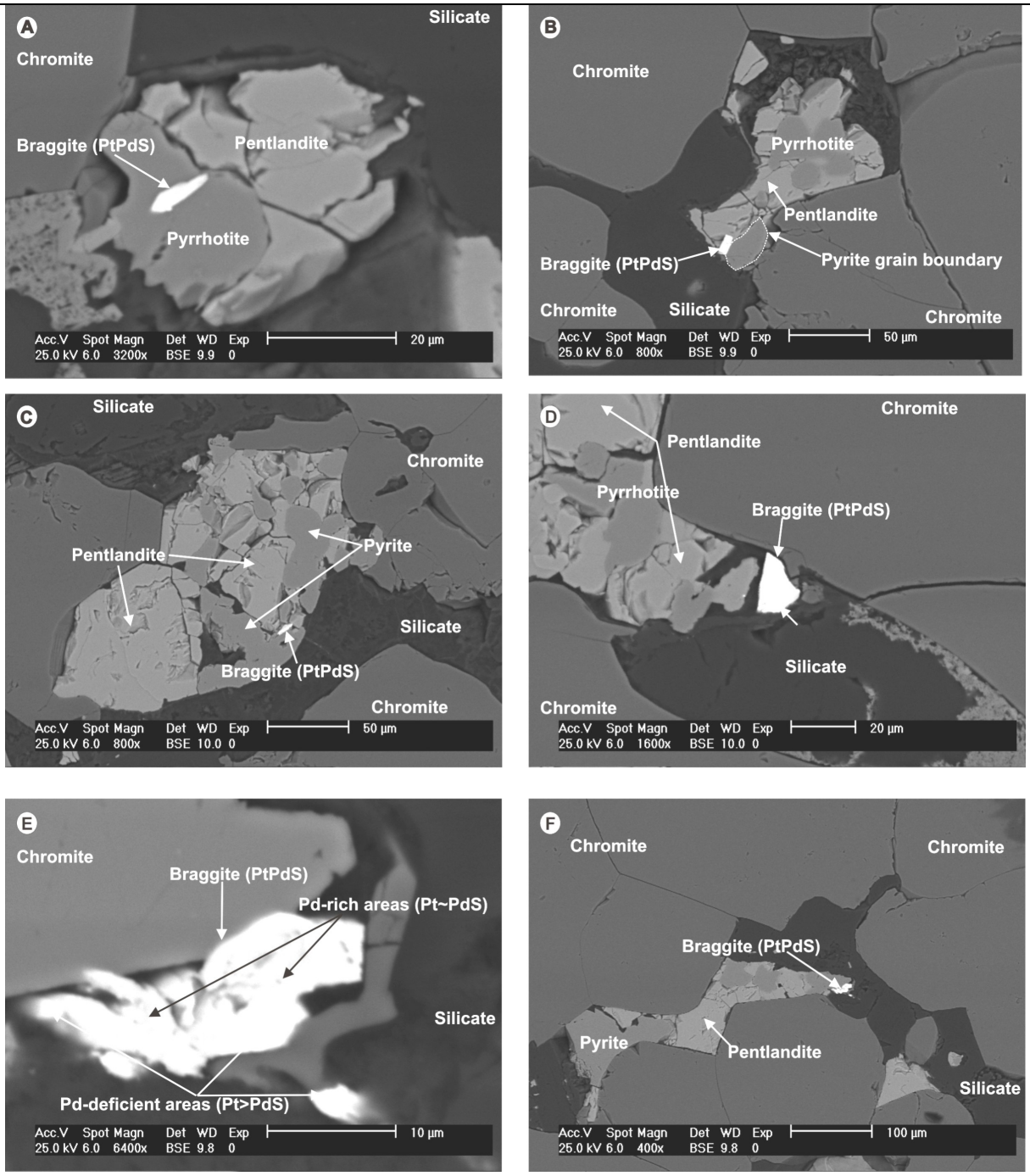

Figure 8.45: MLA BSE image of PGM occurrences within sample 169.

Both the braggite particles in Figure 8.45 A and C are enclosed in pyrite whilst in Figure 8.45 B the braggite is located at the pyrite boundary with pentlandite and silicate. The braggite particle in Figure 8.45 D, however, sits perfectly in the interstitial space between sulphide, chromite and silicate whilst the braggite phase in Figure 8.45 F is at the edge of pentlandite and silicate. Figure 8.45 E is a close up of Figure 8.45 F and it shows the intricate solid solution zonations in the braggite-cooperite particle.

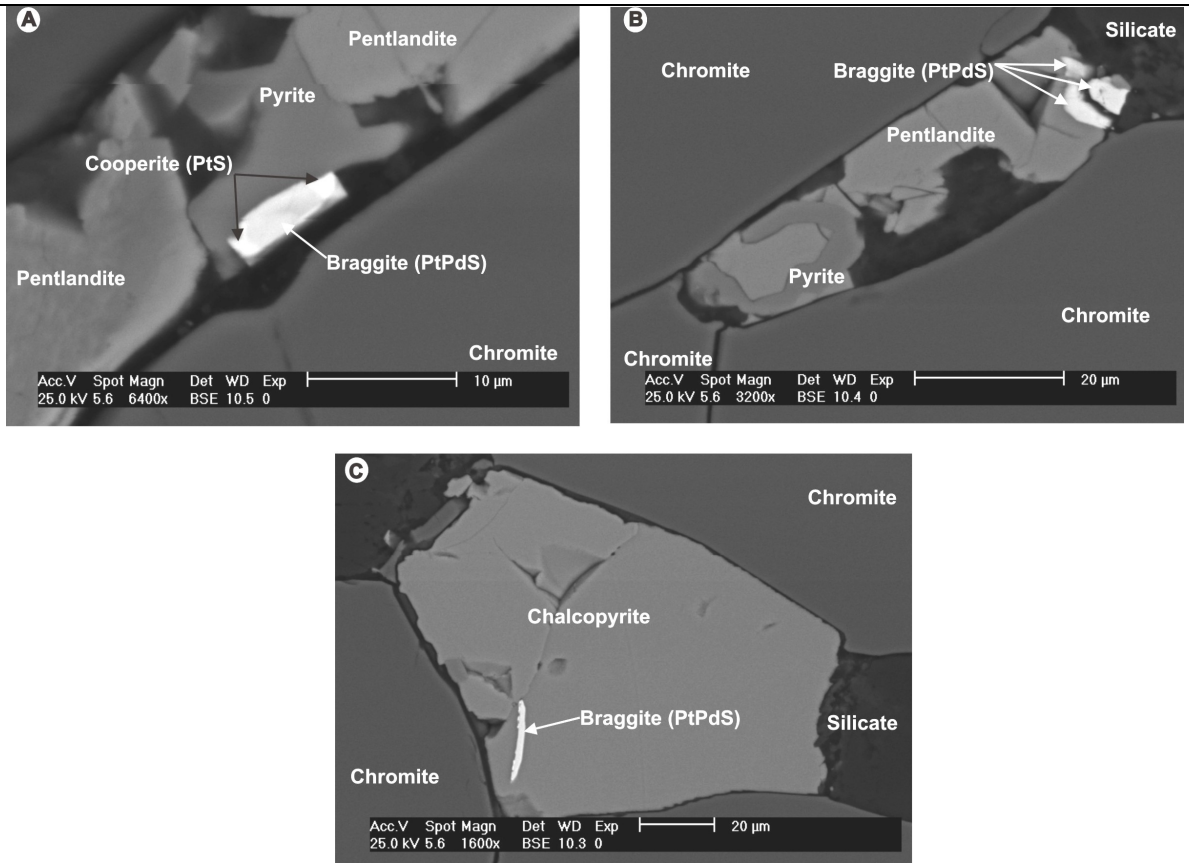

Figure 8.46: MLA BSE image of PGM occurrences within sample 170.

Both the braggite particles in Figure 8.46 A and B are attached to the edge of a sulphide grain. Note the zonation in A where cooperite is formed on the edges surrounding a core of braggite. The braggite grain in Figure 8.46 C, however, is fully enclosed within the chalcopyrite particle.

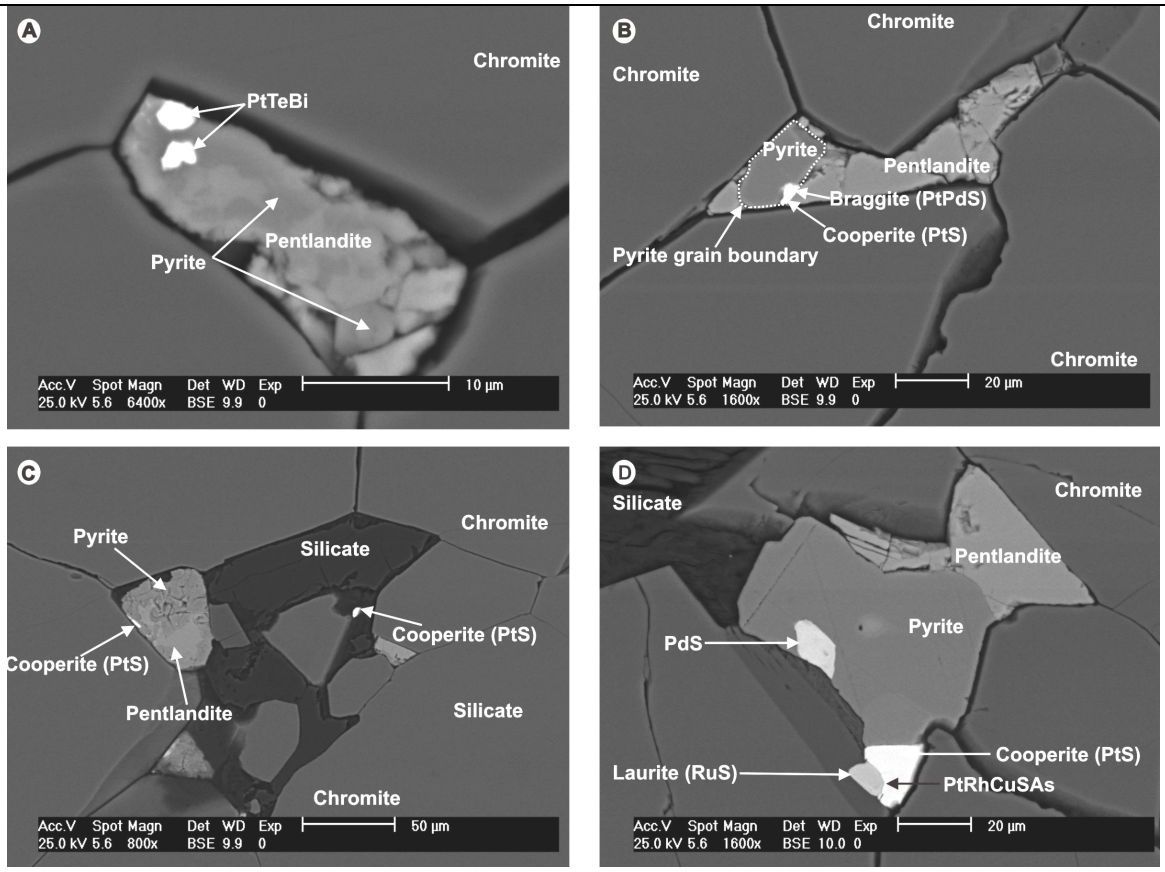

Figure 8.47: MLA BSE image of PGM occurrences within sample 171 (1st batch).

Note that all the PGMs in Figure 8.47, bar the lower PtTeBi in A, which is enclosed in the sulphide, and the cooperite in C, which exists in the interstitial silicate, occur at the edge of major sulphide phases. The cooperite-PtRhCuSAs-laurite composite PGM in Figure 8.47 D exists perfectly in the triple point junction between pyrite and two chromites.

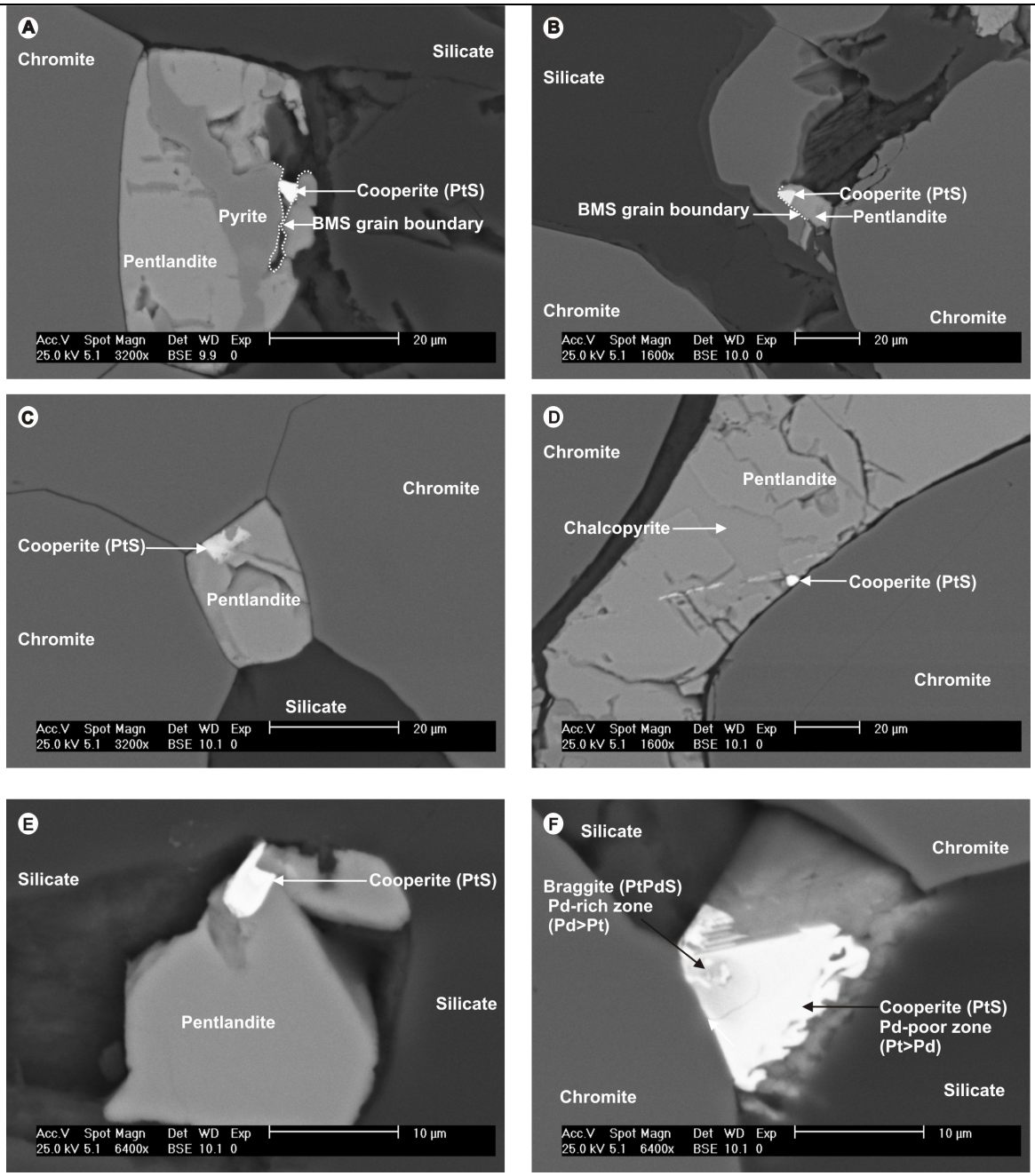

Figure 8.48: MLA BSE image of PGM occurrences within sample 172 (1st batch).

The majority of the PGMs in Figure 8.48 exist near the edge of sulphide particles – near, or at, the contact with silicate or chromite. The cooperite in Figure 8.48 A occurs interstitially between the pyrite and pentlandite phases whilst the cooperite-braggite phase in Figure 8.48 F also exists at a triple point junction between several particles.

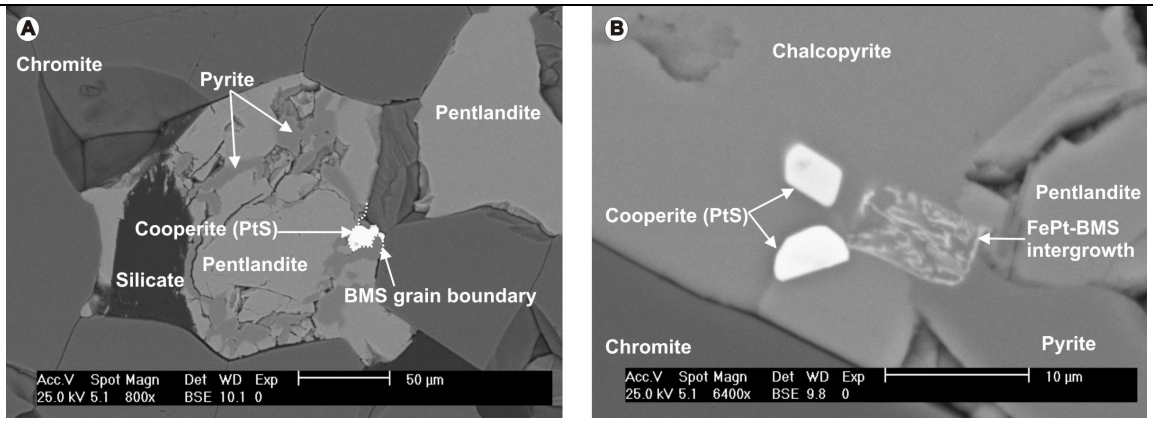

Figure 8.49: MLA BSE image of PGM occurrences within sample 172 (2nd batch).

The cooperite in Figure 8.49 A also exists at a triple point junction whilst in Figure 8.49 B, two cooperites and the ferroplatinum-BMS intergrowth are all enclosed in sulphide. The intergrowth exhibits an intricate pattern termed 'brain texture'. The rectangular, euhedral shape of the ferroplatinum remains but the PGM itself comprises a pattern of irregular and contorted zones of PGM surrounded by sulphide.

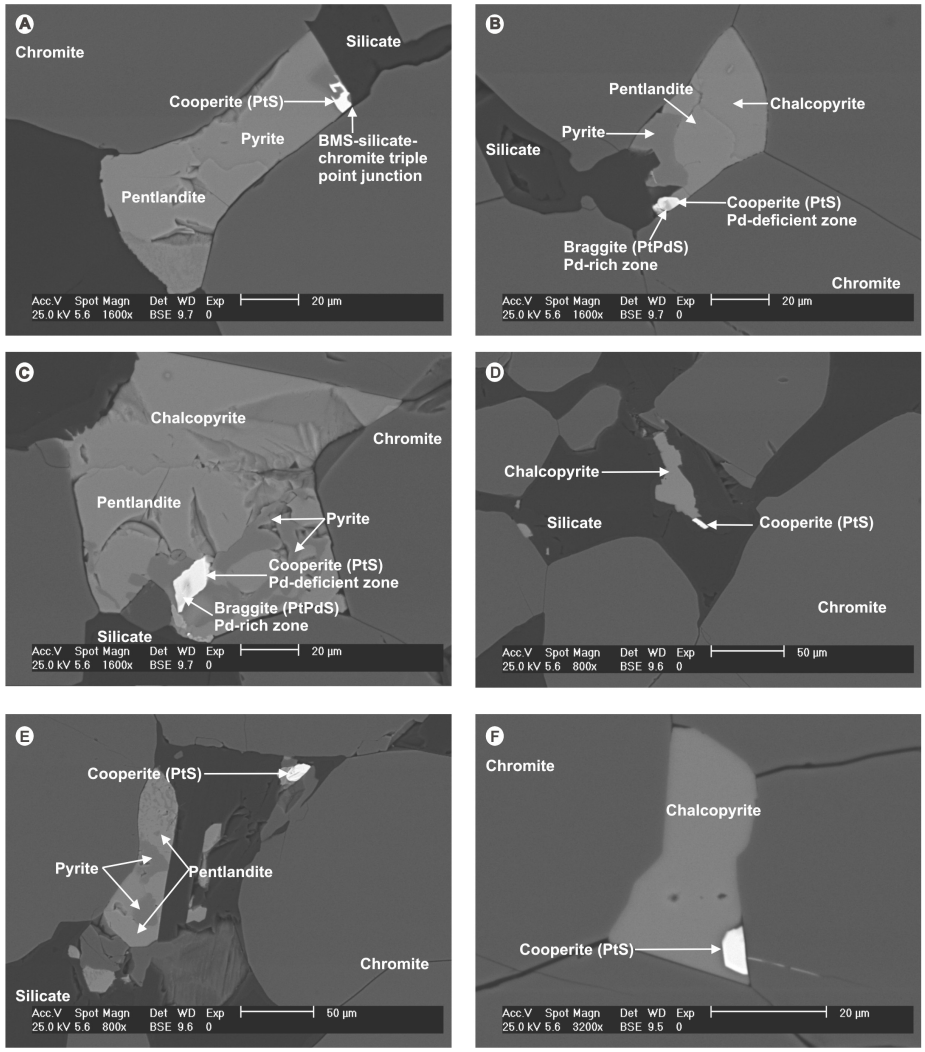

Figure 8.50: MLA BSE image of PGM occurrences within sample 173 (1st batch).

The PGE-sulphide phases in Figure 8.50 A, B, E and F are all located at triple point junctions and are all associated with sulphide. The PGE-sulphide phase in Figure 8.50 C, however, is fully enclosed in the pyrite-pentlandite assemblage whilst the cooperite in Figure 8.50 D is attached to the chalcopyrite in the interstitial silicate. Note the solid solution zonations in the PGE-sulphides in Figure 8.50 B and C.

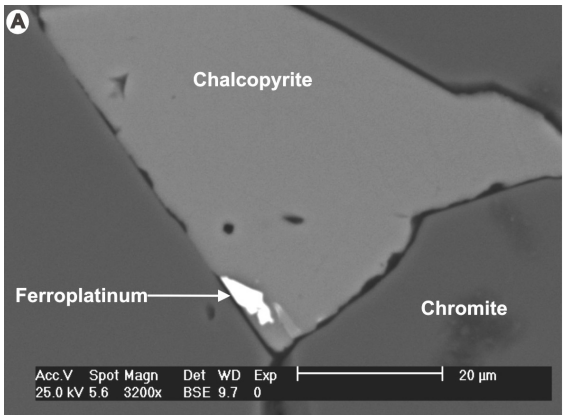

Figure 8.51: MLA BSE image of PGM occurrences within sample 173 (2nd batch).

The ferroplatinum alloy in Figure 8.51 exists at the edge of the chalcopyrite grain at the boundary with chromite.

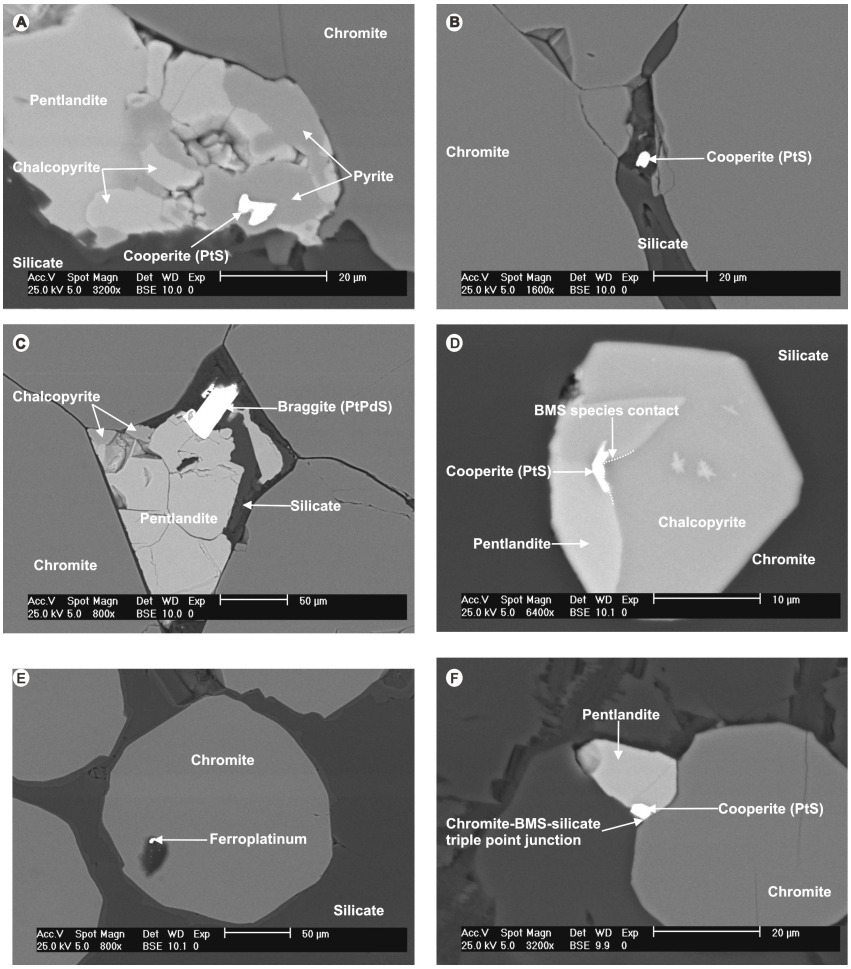

Figure 8.52: MLA BSE image of PGM occurrences within sample 174 (1st batch).

The cooperite in Figure 8.52 A is fully enclosed within the pyrite-pentlandite assemblage whilst the cooperite particle in Figure 8.52 B exists within interstitial silicate between chromite grains. The large, well formed, euhedral braggite in Figure 8.52 C is attached to a sulphide particle and exists within the interstitial silicate (a small pocket of interstitial silicate surrounded by cumulus chromites). The cooperite phase in Figure 8.52 D is fully enclosed in sulphide but it sits exactly at the phase boundary between pyrite and chalcopyrite. It distinctly appears to bend and follow the contact. This could possibly provide evidence of the PGM being exsolved and crystallizing out from the sulphide liquid during advanced fractional crystallization. Also note the presence of pentlandite 'flames' in the chalcopyrite to the right of the PGM. The ferroplatinum particle in Figure 8.52 E appears to be locked in a hole within the chromite grain, whilst in Figure 8.52 F, the cooperite exists at a triple point junction between pentlandite, chromite and silicate.

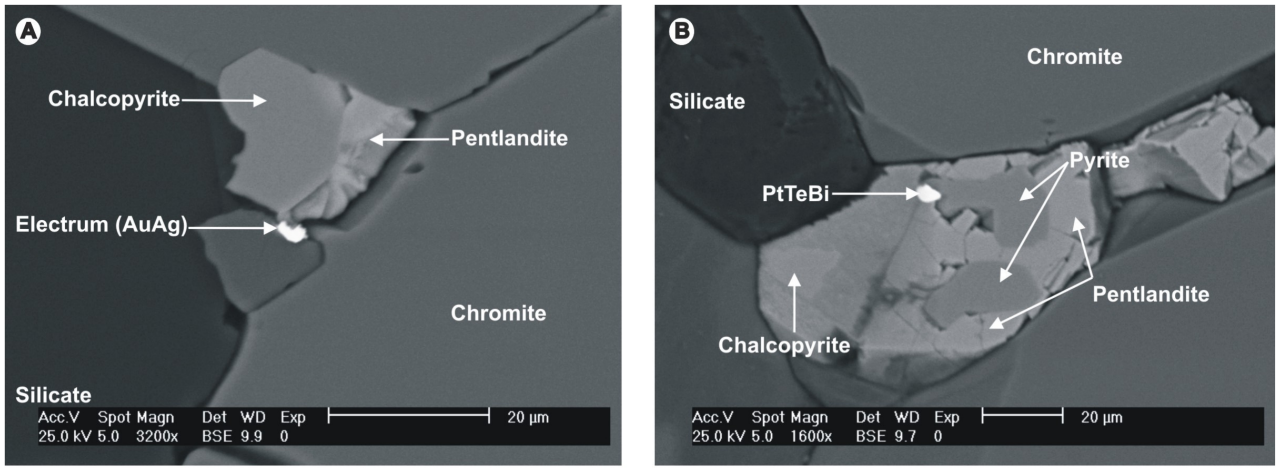

Figure 8.53: MLA BSE image of PGM occurrences within sample 174 (2nd batch).

In Figure 8.53 A the electrum particle sits in the gap between the chromite and sulphide, whilst in Figure 8.53 B the PtTeBi phase is fully enclosed in sulphide but exists at the boundary between pyrite and pentlandite.

The PtTeBi and laurite phases in Figure 8.54 A and C as well as the braggite phases in Figure 8.54 B and D, all occur near the edge of sulphide particles. Note, especially, the occurrence of PtTeBi in C where the fractures between the sulphides clearly postdate the main crystallization event. The PGE-sulphides in Figure 8.54 E and F are both locked in sulphides. In both these photos one can see that the sulphide phase is trapped interstitially between the chromites. In E, especially, the sulphide bends and weaves its way between the chromite.

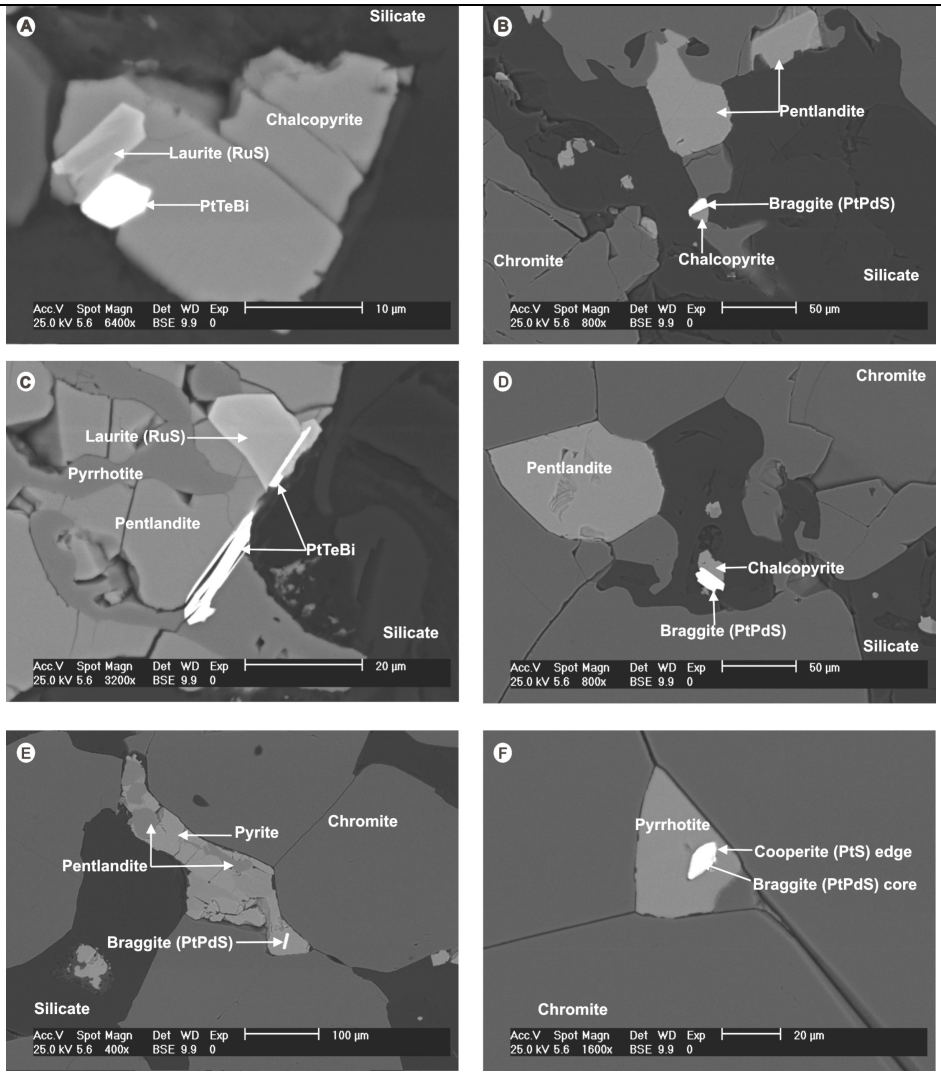

Figure 8.54: MLA BSE image of PGM occurrences within sample 175 (1st batch).

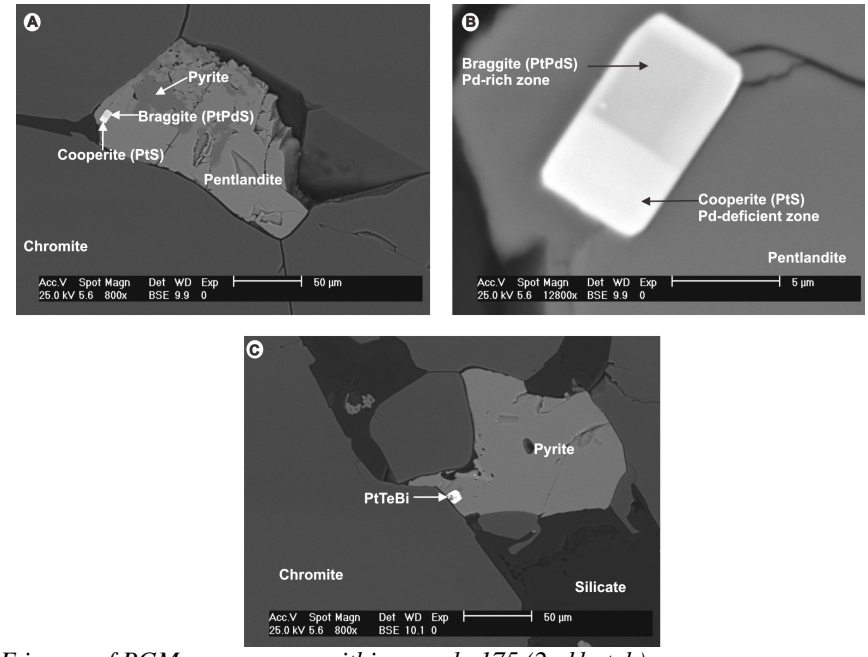

Figure 8.55: MLA BSE image of PGM occurrences within sample 175 (2nd batch).

Figure 8.55 B is a zoomed in image (12800x) of the PGE-sulphide in Figure 8.55 A, which is enclosed in pentlandite. Note the euhedral character and the perfect zoned areas of braggite and cooperite. The PtTeBi particle in Figure 8.55 C sits near the edge of the sulphide, next to the boundary with chromite.

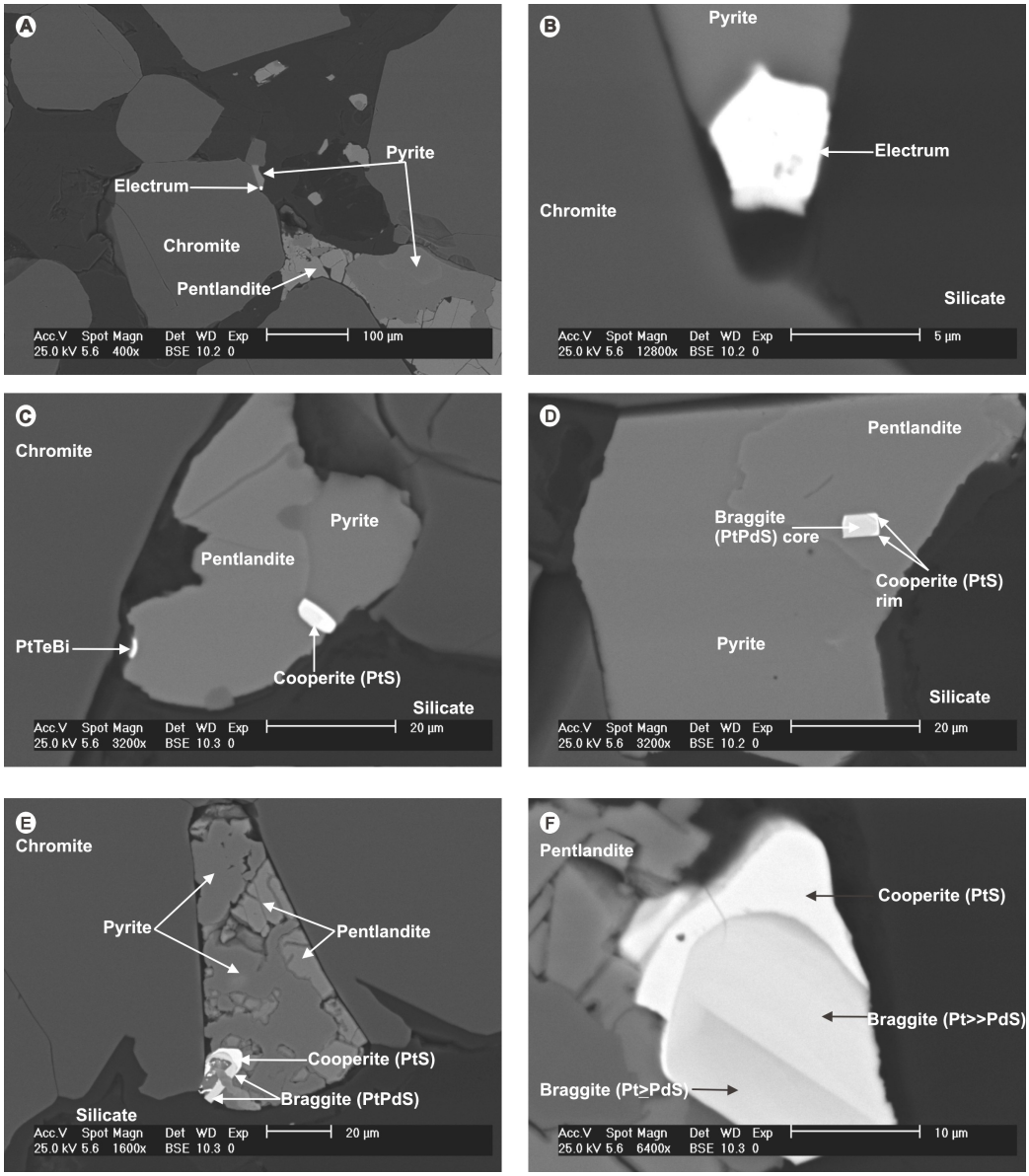

Figure 8.56: MLA BSE image of PGM occurrences within sample 176.

The electrum, zoomed in in Figure 8.56 B, grain in Figure 8.56 A occurs at the triple point junction between pyrite, chromite and silicate. The PGE-sulphides in Figure 8.56 C, E and F all exist near the edge of a sulphide. In C the cooperite is at the edge of the sulphide as well as is positioned perfectly at the phase contact between pentlandite and pyrite. In E the PGM is intergrown with pentlandite – providing evidence that the PGM crystallized at the same time as the sulphide. Note the perfectly exsolved solid solution zonations in Figure 8.56 D, E and F. Photo F, in particular, shows superb euhedral zoning and, even within the braggite, there are zones defined by varying Pt:Pd ratios.

8.5.4 Discussion

The PGE mineralization in the ZG219 D1 UG2 comprises a PGE-sulphide dominated assemblage. Lesser amounts of PGE-tellurides, as well as trace amounts of PGE-arsenides, PGE-alloys, PGE-sulpharsenides and gold, are also present. The vertical PGM distribution profile through the chromitite shows that the PGE-tellurides appear to be concentrated into three zones, with the highest abundance existing at the top of the chromitite with two lesser zones occurring in the middle and at the base of the chromitite. This interesting distribution pattern will be further investigated in the next section.

The PGMs are fine-grained and have an average p50 of less than 10 µm. The PGMs themselves often exist as composite particles comprising two or more phases, like the sulphides. From a textural point of view it is evident that the PGMs are often sulphide associated or located within the interstitial matrix – often at triple point junctions. The PGMs present within the sulphides also show a strong propensity to contact boundaries between different sulphide phases. This intricate texture shows that the PGMs are strongly sulphide associated and are intimately linked to the location and textural association of the different sulphide phases (and therefore genetically linked to the crystallization of the sulphides).

The cooperite – braggite series is well-developed and these PGE-sulphides are seen to form large, euhedral crystals with a well-developed exsolution zonation comprising a Pd-rich core (braggite) and a Pt-rich rim (cooperite). These phases are almost always sulphide associated.

The large, well developed, euhedral nature of these PGM crystals, their close association with sulphides (and especially the propensity for sulphide phase contacts) as well as the well developed intricate exsolution zonation in these minerals are all direct evidence that these PGE-sulphides formed the original PGM assemblage (or the majority of it). Should these PGE-sulphides have been affected by secondary processes in any way, then the intricate exsolution textures would have been destroyed.

The PGE mineralogy of the UG2 has been previously studied by McLaren and De Villiers (1982), Kinloch (1982), Peyerl (1982), Von Gruenewaldt *et al.,* (1990), Grinbeek (1995) and Penberthy and Merkle (1999). Their data also shows that the PGE-sulphides form the predominant PGM assemblage found in the UG2. Rixom (2005) summarized the data from the Anglo Platinum routine mineralogical examinations of the UG2 from borehole core drilled both on the Atok mine property, as well as throughout the north-eastern Bushveld. His summarized results show a largely fresh, unaltered UG2 orebody in the Atok area with a PGM assemblage dominated by PGE-sulphides with lesser PGE-tellurides (Rixom, 2005). Further south, however, there is evidence of localized fluid flow with subsequent alteration, remobilization and recrystallization of the original PGE-sulphide dominant assemblage to one containing higher amounts of PGE-alloys, ferroplatinum, PGE-arsenides and PGE-sulpharsenides (all alteration products) (Rixom, 2005). These PGM types are therefore seen to represent the products of secondary alteration and recrystallization of the orginal PGM assemblage by circulating volatile rich hydrothermal fluids. Therefore borehole ZG219 confirms the

mineralogical data from 38 borehole cores from Atok (Rixom, 2005) that the Atok UG2 is a fresh, unaltered ore body with a PGM assemblage comprising mainly PGE-sulphides and lesser PGE-tellurides. This assemblage represents the original magmatic assemblage which has not been affected in any way since crystallization.

8.6 Discussion

The ZG219 D1 UG2 comprises a bulk mineralogical composition of mainly chromite with lesser plagioclase and orthopyroxene. Variable amounts of hydrous minerals (~5 %) and base metal sulphides (~1 %) are also found to exist within the chromitite.

The primary hydrous phases (talc, amphibole, chlorite and phlogopite) are suggested to represent postcumulus primary phases which have formed by primary entrapment of the residual liquid during the final stages of crystallization. There are therefore three distinct zones containing higher amounts of trapped intercumulus liquid – at the base of the chromitite, around the middle and a major zone near the top of the chromitite. These zones are interpreted to represent areas, where a greater degree of residual liquid became trapped, during compaction, in the intercumulus pore spaces, where it eventually crystallized out to form the hydrous minerals.

Texturally, the UG2 chromitite comprises a framework of cumulus chromite within an interstitial matrix of silicate. The packing structure ranges from open (matrix supported), which is the common type, to closed (chromite supported) which is more rare. Some of the chromites are substantially larger than the ordinary chromite grains, and hence are termed ‘supergrains’. It is suggested that these supergrains formed in areas of greater pore space where they were allowed to crystallize in an open environment, and therefore form larger grains. During compaction these grains were then forced together and coalesced to form substantially larger grains. Therefore the formation of the chromite supergrains is suggested to be a combination of primary crystallization in an open environment (i.e. zones of greater pore space) as well as post-cumulus coalescence of grains during primary compaction. The base metal sulphides are present mainly within the intercumulus matrix or, rarely, as locked within the chromites.

The normative mineralogical profiles (calculated from chemistry data using the CIPW norm programme) reveal the presence of two major trends within the UG2 unit – a basal normal trend capped by a reverse trend at the level of the UG2 leuconorite. These trends, as defined by normative mineralogical distributions, are suggested to represent primary fractionation processes.

Therefore the UG2 unit is seen to comprise a lower normal fractionation trend, in which the resident liquid within the chamber, despite still been replenished by intermittent injections of more primitive magma, is, as a result of fractional crystallization, trending toward more evolved compositions. This overall normal

trend is mirrored by local intra-lithological normal fractionation trends within the UG2 footwall and UG2 hanging wall middle and upper feldspathic pyroxenite units. At the level of the upper contact of the UG2 hanging wall middle feldspathic pyroxenite unit there is a reversal in fractionation trends. Through the overlying UG2 leuconorite and upper feldspathic pyroxenite units exists an upward trend toward more primitive compositions (as reflected by a more mafic mineral distribution). This is suggested to represent a period of increased magma addition into the chamber. Therefore the process of magma replenishment of the chamber is suggested to now be the dominant process – as opposed to that of acquiescence and fractional crystallization (punctuated by intermittent injections) during the normal trend.

The sulphide mineralization in the ZG219 D1 UG2 is concentrated in three main zones termed Mineralized Zones 1 – 3. These zones represent areas of greater primary (sulphide) enrichment, and provide evidence of an original top-loaded BMS profile within the UG2.

The general sulphide assemblage comprises pentlandite, chalcopyrite and pyrite with pyrrhotite also present in the three mineralized zones (whilst only present in negligible amounts in the background). Texturally the sulphides range in size from a ~25 µm to large composite particles of ~250 µm in size and they are mainly concentrated in the interstitial matrix between the cumulus chromite and silicate particles. Some sulphide particles are also found to be fully enclosed (locked) within chromite grains. The intricate texture exsolution exhibited by the sulphides was formed during the primary magmatic phase and is direct evidence that there has been no subsequent reworking of the sulphides by late-stage circulating fluids.

The PGE mineralization in the ZG219 D1 UG2 comprises a PGE-sulphide dominated assemblage. Lesser amounts of PGE-tellurides, as well as trace amounts of PGE-arsenides, PGE-alloys, PGE-sulpharsenides and gold, are also present. The vertical PGM distribution profile through the chromitite shows that the PGE-tellurides appear to be concentrated into three zones, with the highest abundance existing at the top of the chromitite with two lesser zones occurring in the middle and at the base of the chromitite.

The PGMs are fine-grained and have an average p50 of less than 10 µm. The PGMs themselves often exist as composite particles comprising two or more phases, like the sulphides. From a textural point of view it is evident that the PGMs are often sulphide associated or located within the interstitial matrix – often at triple point junctions. The PGMs present within the sulphides also show a strong propensity to contact boundaries between different sulphide phases. This intricate texture shows that the PGMs are strongly sulphide associated and are intimately linked to the location and textural association of the different sulphide phases (and therefore genetically linked to the crystallization of the sulphides).

The cooperite – braggite series is well-developed and these PGE-sulphides are seen to form large, euhedral crystals with a well-developed exsolution zonation comprising a Pd-rich core (braggite) and a Pt-rich rim (cooperite). These phases are almost always sulphide associated.

The large, well developed, euhedral nature of these PGM crystals, their close association with sulphides (and especially the propensity for sulphide phase contacts) as well as the well developed intricate exsolution zonation in these minerals are all direct evidence that these PGE-sulphides formed the original PGM assemblage (or the majority of it). Should these PGE-sulphides have been affected by secondary processes in any way, then the intricate exsolution textures would have been destroyed. Because the intricate exsolution textures are magmatic in origin any influence on them from migrating fluids would result in these textures been reworked and ultimately destroyed.

This has served to summarize the major mineralogical findings. All the mineralogical evidence confirms an original primary magmatic mineralogical assemblage which has not been affected by any secondary processes. The mineral distribution profiles are therefore indicative of the primary, original mineral distribution patterns are formed directly from primary, magmatic processes. The mineral profiles can therefore be used to investigate the primary processes occurring during the formation of the UG2 chromitite. Intricate distribution patterns were exhibited by the hydrous minerals, the base-metal sulphides as well as the PGE-tellurides vertically through the UG2 chromitite. The strong similarities between these three profile patterns necessitated an investigation into whether they are all genetically linked (i.e. whether the patterns are reflecting the same primary processes). The vertical hydrous mineral distribution profile, BMS profile as well as the vertical PGM profile (excluding PGE-sulphides) are presented in Figures 8.57, 8.58 and 8.59 respectively.

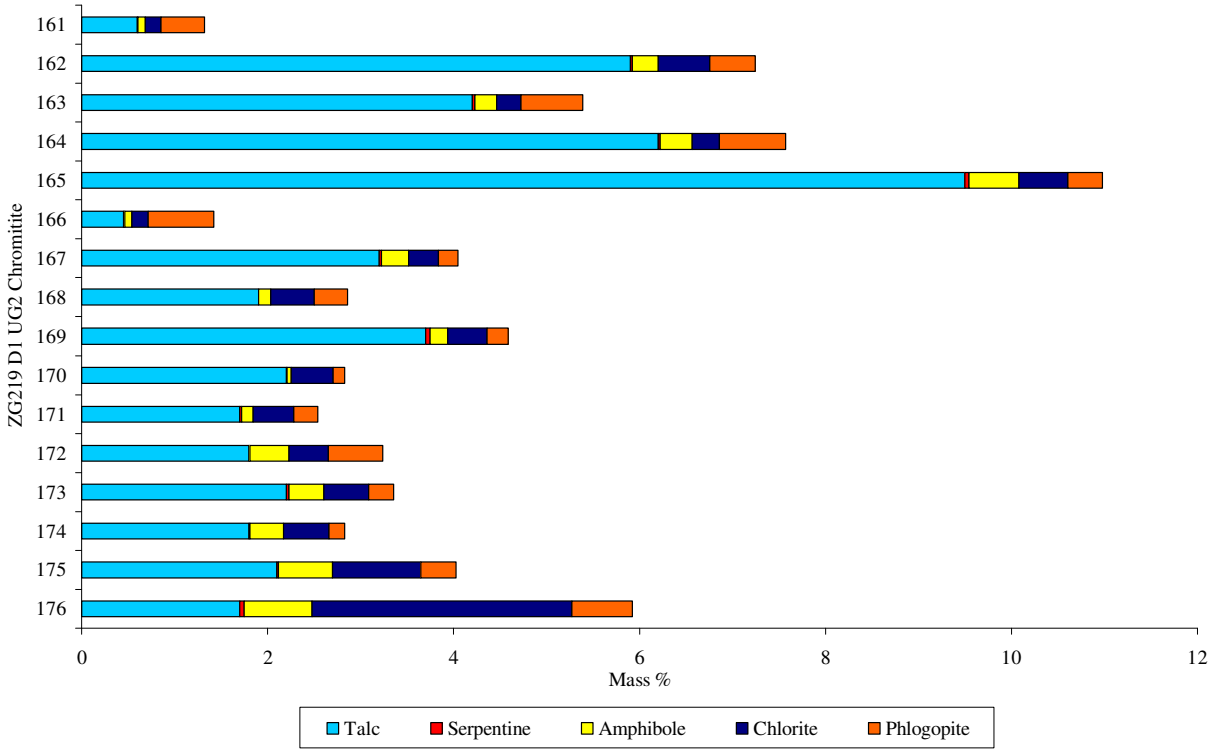

Figure 8.57: Vertical hydrous mineral distribution profile through the ZG219 D1 UG2 chromitite layer.

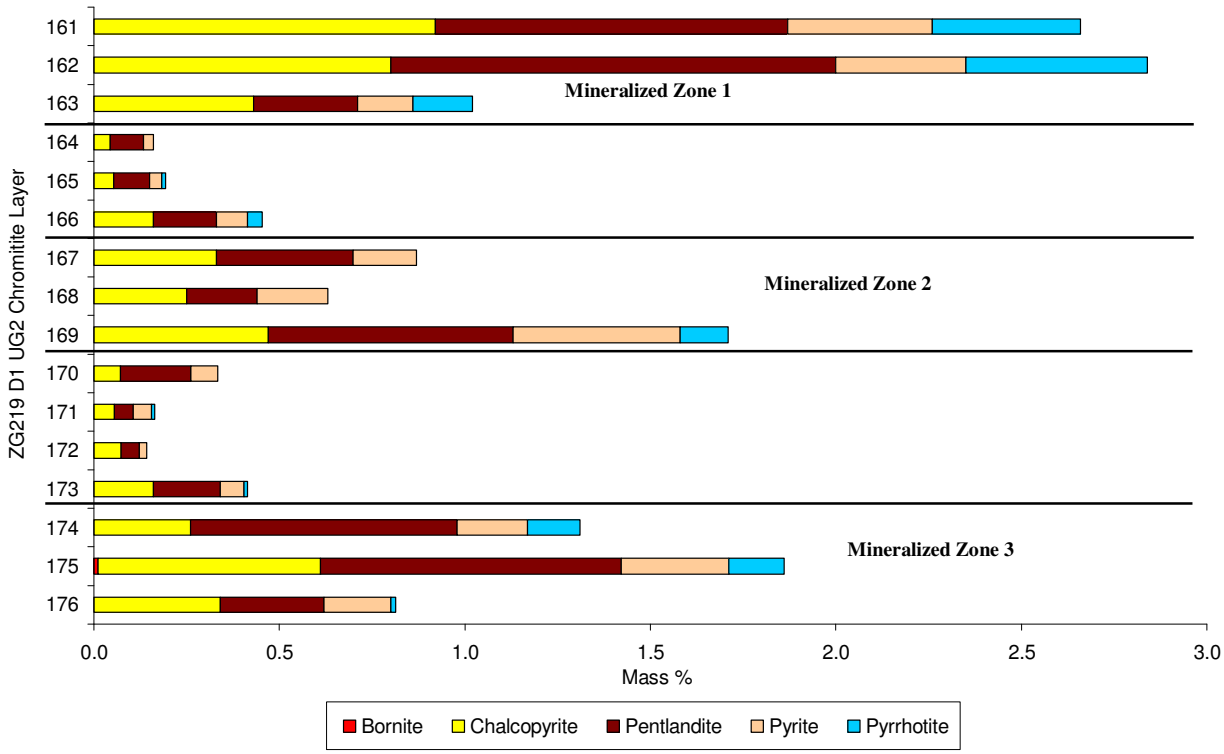

Figure 8.58: Vertical BMS distribution profile, as a function of total mass %, through the ZG219 D1 UG2 chromitite layer.

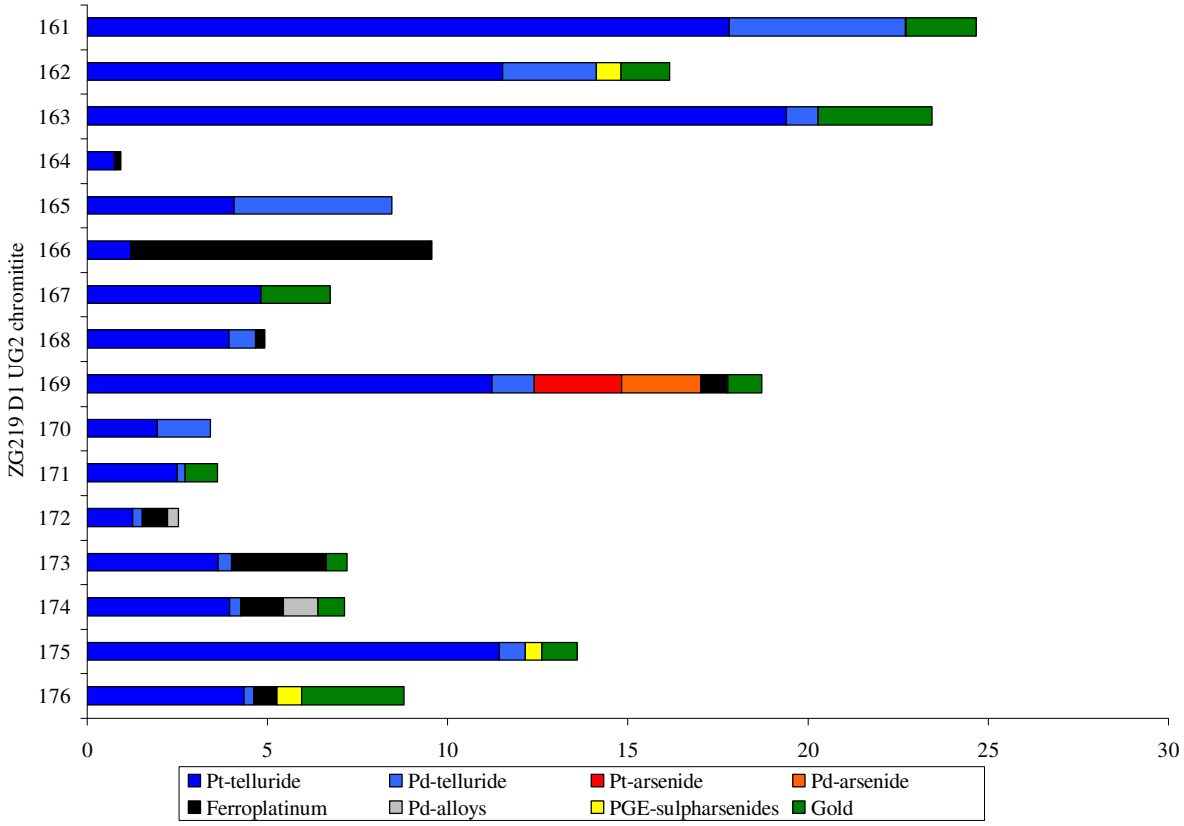

Figure 8.59: Vertical PGM distribution (with laurite included) through the ZG219 D1 UG2 (excluding the PGE-sulphides).

Firstly, as mentioned, the sulphide mineralization is concentrated in three main zones in the chromitite – termed 'Mineralized Zones 1, 2 and 3' (see Figure 8.58). These mineralized zones are located at the top of the layer (1) – which comprises the greatest abundance, near the middle of the layer (2) as well as at the base of the chromitite (3). It is clear that the hydrous minerals (Figure 8.57) and PGE-tellurides (Figure 8.59) reveal similar distribution profile patterns to the sulphides. A series of x/y plots were used to test the strength of the relationship between these 3 parameters (Figures 8.60 – 8.54).

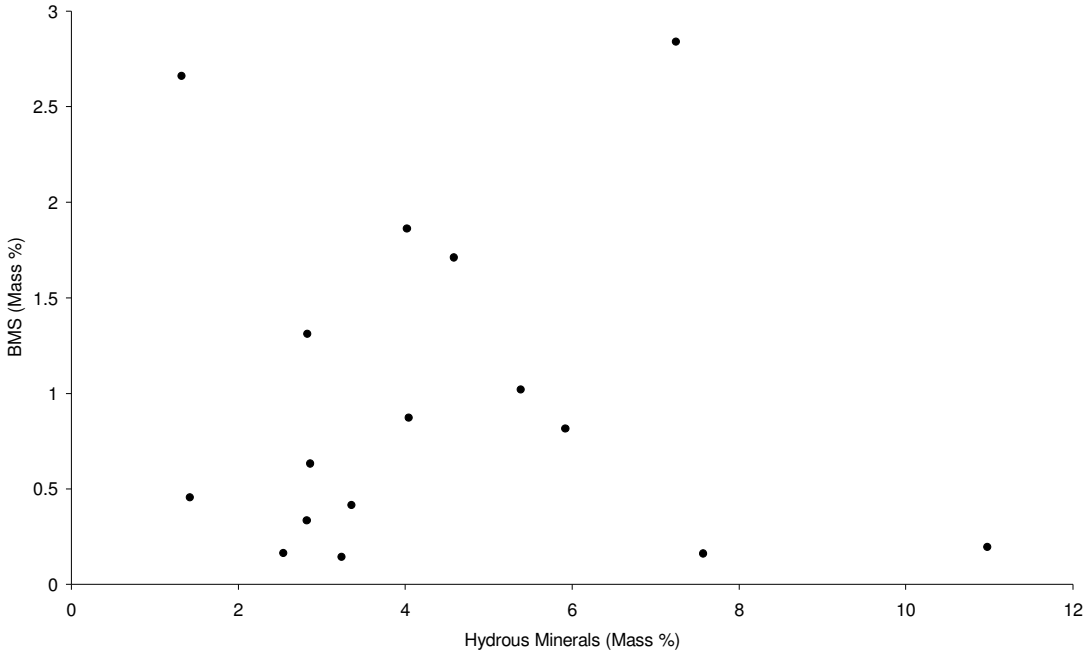

Figure 8.60: Plot of total BMS (mass %) against total hydrous mineral abundance (mass %).

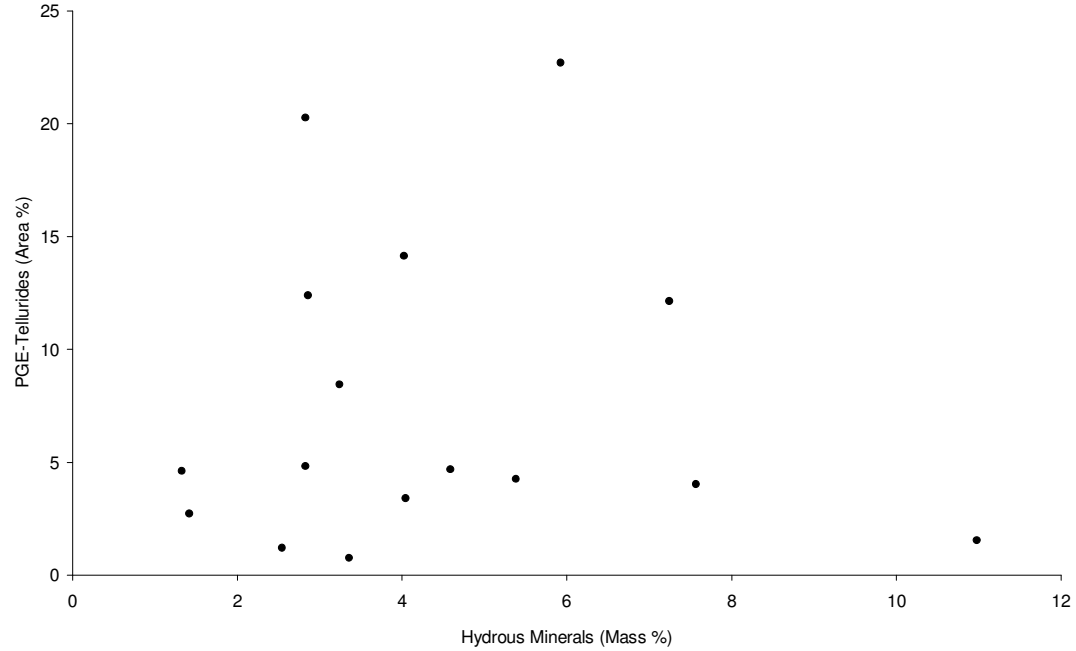

Figure 8.61: Plot of PGE-tellurides (area %) against total hydrous mineral abundance (mass %).

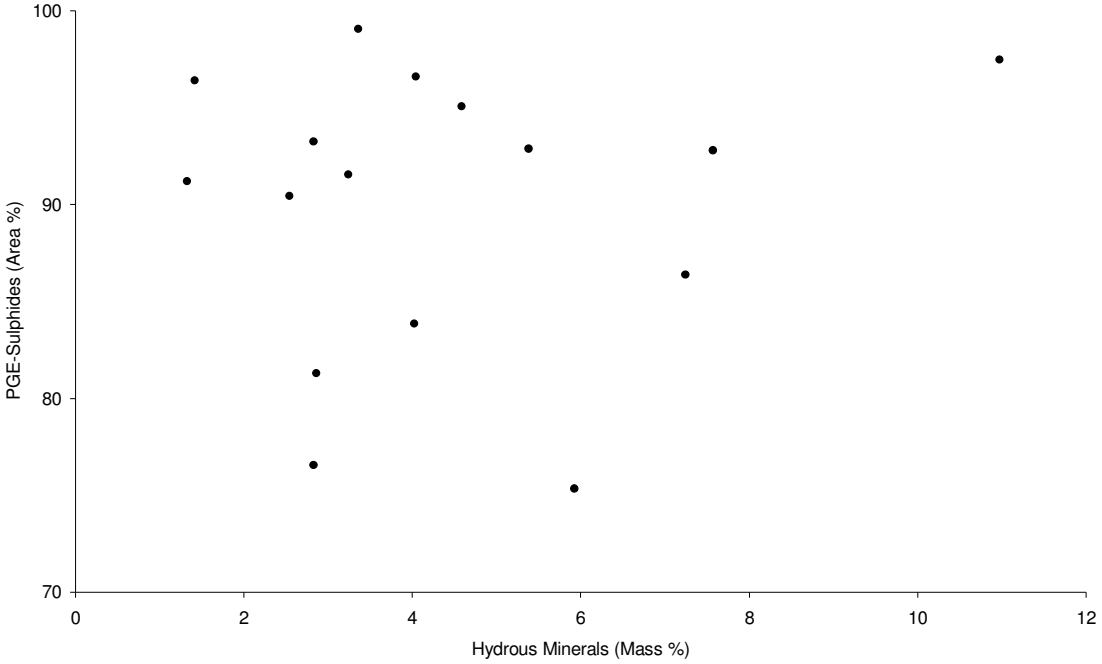

Figure 8.62: Plot of PGE-sulphides (area %) against total hydrous mineral abundance (mass %).

By plotting each of total BMS, PGE-tellurides and PGE-sulphides against the total hydrous mineral abundance, a largely random plot is produced. There may be a very slight positive relationship between the BMS, as well as the PGE-tellurides, and the hydrous minerals, and a negative one between the PGE-sulphides and the hydrous minerals, but these aren't strong at all and the plots can instead be classified as largely random. Therefore the hydrous minerals have a negligible relationship between either of the sulphides or the PGE-telluride species – thereby indicating there formation by secondary (late stage) processes.

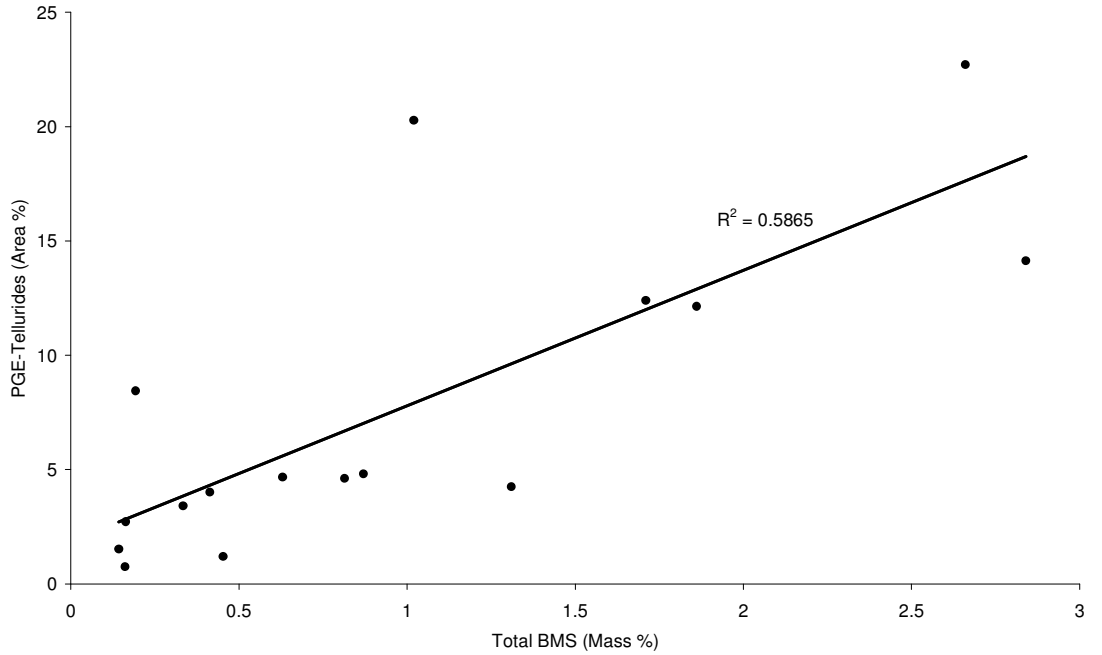

Figure 8.63: Plot of PGE-tellurides (Area %) against total BMS (Mass %).

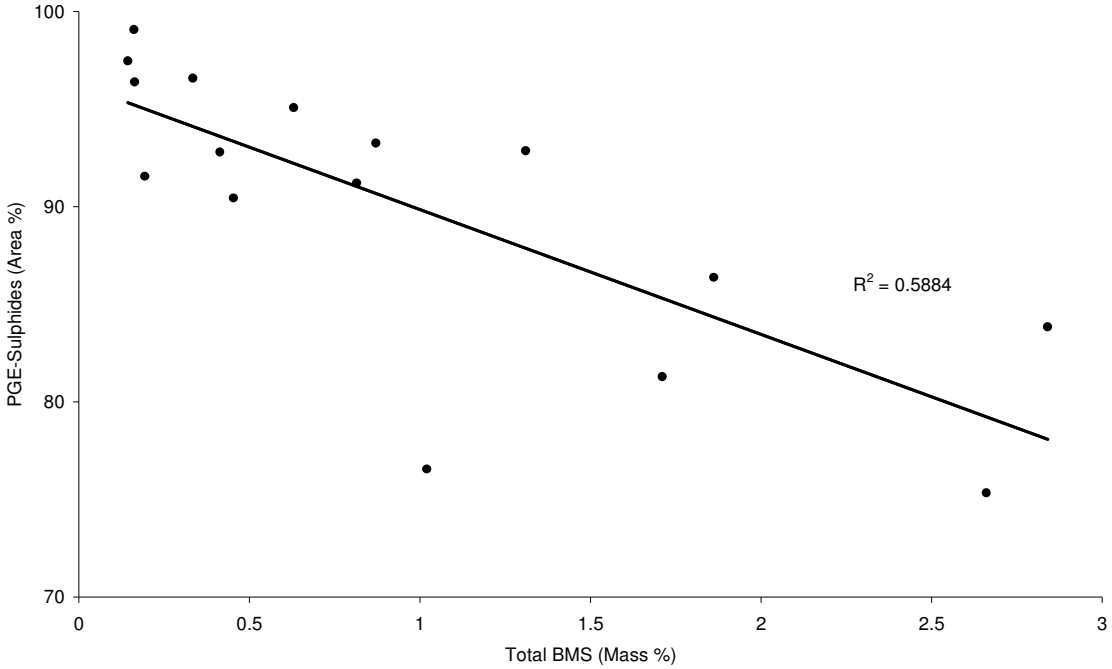

Figure 8.64: Plot of PGE-sulphides (Area %) against total BMS (Mass %).

There is, however, a moderately strong positive linear relationship between the PGE-tellurides and the total BMS (Figure 8.63), as well as a moderately strong negative linear relationship between the PGE-sulphides and the total BMS (Figure 8.64).

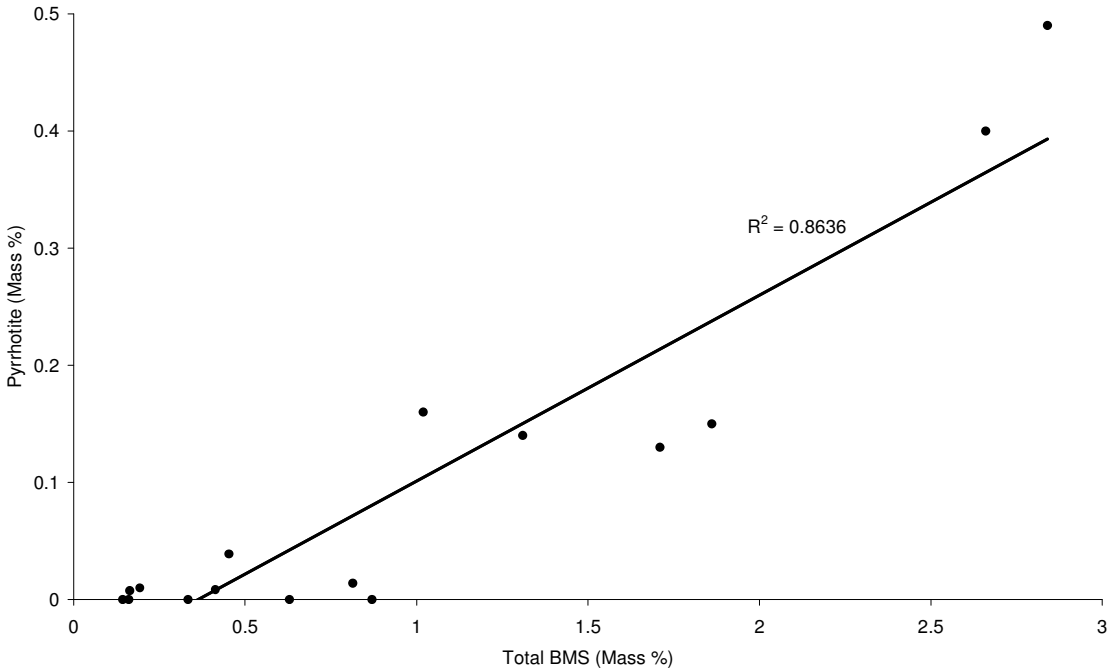

Figure 8.65: Plot of pyrrhotite (Mass %) against total BMS (Mass %).

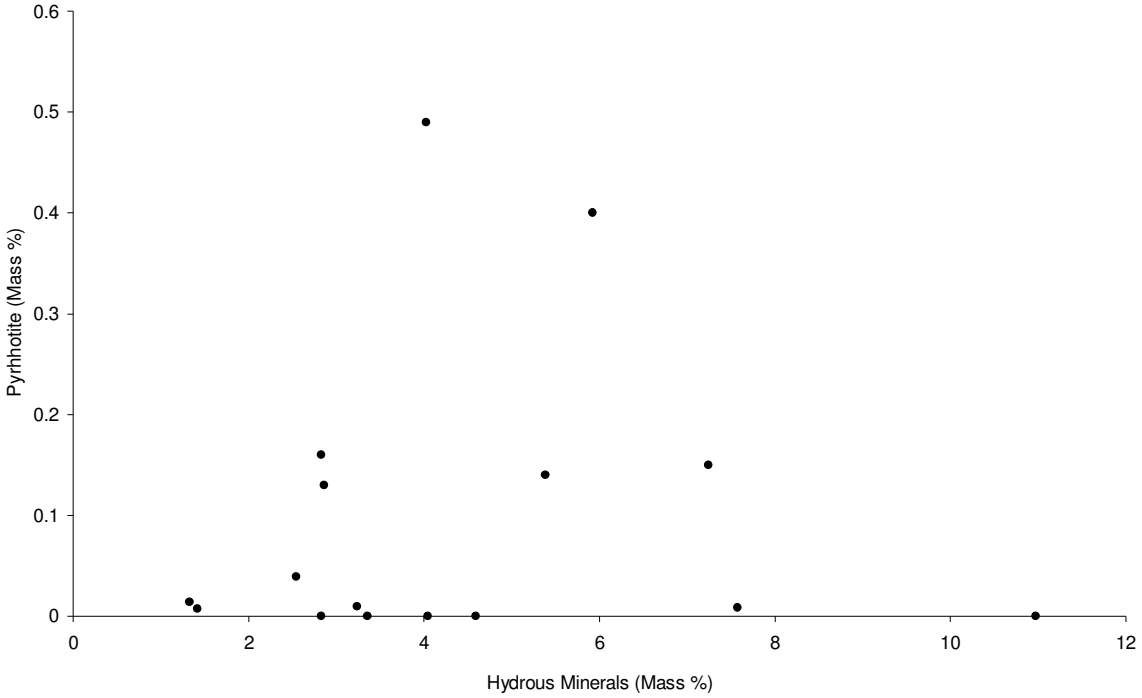

Figure 8.66: Plot of pyrrhotite (Mass %) against total hydrous mineral abundance (Mass %).

Figure 8.66 confirms that pyrrhotite displays no relation to the hydrous minerals. There is, however, a strong relationship between pyrrhotite and total BMS (Figure 8.65). This confirms earlier suggestions that pyrrhotite does occur in higher levels in the sulphide mineralized zones. There is also a moderately strong positive linear relationship between pyrrhotite and the PGE-tellurides (Figure 8.67).

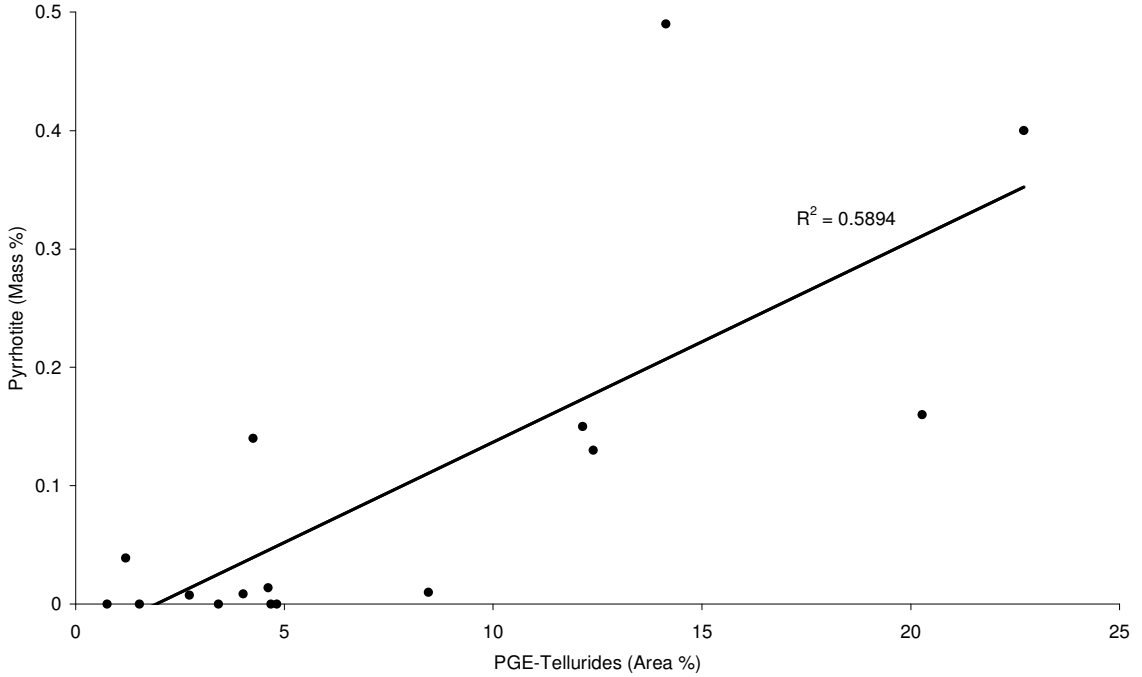

Figure 8.67: Plot of pyrrhotite (Mass %) against PGE-tellurides (Area %).

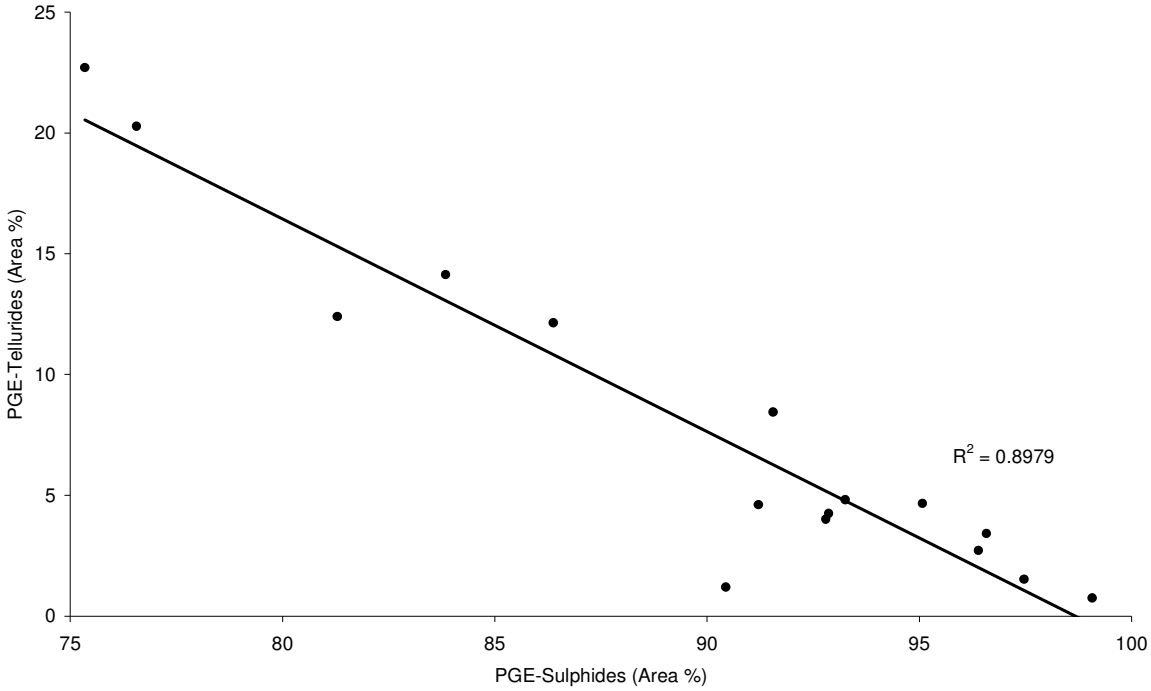

Figure 8.68: Plot of PGE-tellurides (Area %) against PGE-sulphides (area %).

The strong linear negative relationship between the PGE-sulphides and the PGE-tellurides is evident in Figure 8.68. This strong negative relationship simply confirms the fact that the PGM distribution is a strongly bimodal one (comprising mainly PGE-sulphides and PGE-tellurides).

Therefore, it csn be confirmed that the hydrous minerals display no direct relationships with either the sulphides or the PGE-tellurides. Therefore the processes that controlled the proportion of trapped liquid (i.e. most likely pore space etc) within the chromitite had no influence on the sulphide mineralization process as well as the control on the PGE-telluride distribution. The strong relationship between the PGE-sulphides and the PGE-tellurides reflects the strong bi-modality of the PGM distribution within the chromitite i.e. the PGE-tellurides are concentrated in three zones (at the expense of the PGE-sulphides). Therefore, whilst the PGE-sulphides form the dominant PGM type, the PGE-tellurides form the next abundant PGM but, more importantly, are concentrated into three main zones. These zones essentially reflect the sulphide mineralization zones and, as such, the PGE-tellurides exhibit a moderately strong relationship to the BMS (as do the PGE-sulphides due to the fact that they are inversely related to the PGE-tellurides). Therefore the PGE-telluride species are concentrated into the three broad zones where the sulphides are concentrated, and thus the processes controlling the BMS mineralization also controlled the distribution of the PGE-tellurides. This is not too difficult to imagine as the strong relationship between the sulphides and the PGMs suggest that they were both intimately associated during fractional crystallization.

Therefore, from the mineralogical evidence available, the following model (describing the general formation of the UG2 unit as well as the mineralization process of the sulphides and the PGM within the UG2) is proposed:

In terms of the overall UG2 unit, it is evident (from normative mineral distribution data) that a normal fractionation trend exists and is overlain by a reverse trend. Therefore, the UG2 unit was formed by an injection of more primitive magma into the chamber which began mixing within the resident liquid (which crystallized out the UG1 unit) and which began crystallizing the UG2 footwall pyroxenite sequence. During the early stages of crystallization of the UG2 unit the resident liquid within the chamber, despite still been replenished by intermittent injections of more primitive magma, as a result of fractional crystallization, trended toward more evolved compositions. This overall normal trend is mirrored by local intra-lithological normal fractionation trends within the UG2 footwall and UG2 hanging wall middle and upper feldspathic pyroxenite units.

At the level of the upper contact of the UG2 hanging wall middle feldspathic pyroxenite unit a reversal in fractionation trends occurred. Through the overlying UG2 leuconorite and upper feldspathic pyroxenite units an upward trend toward more primitive compositions existed (as reflected by a more mafic mineral distribution). This is suggested to represent a period of increased magma addition into the chamber. Therefore the process of magma replenishment of the chamber is suggested to now be the dominant process – as opposed to that of quiescence and fractional crystallization (punctuated by intermittent injections) during the normal trend. The UG2 unit thus experienced an increased influx of more primitive magma during its formation. Nevertheless, the chromitite layers (including the UG2 and the stringers present in its hanging wall) are suggested to represent injections of batches of more primitive magma into the chamber (as described in chapter 9).

In terms of the mechanism of mineralization, it is suggested the PGE were present in an immiscible sulphide liquid within the UG2 magma. The mechanism of PGE enrichment into the sulphide liquid was most likely a result of sulphide scavenging i.e. as the immiscible sulphide liquid separated from the silicate liquid and percolated downward through the pile it scavenged and collected PGE from the magma (i.e. Naldrett, 1989). The sulphide liquid was then concentrated within intercumulate pockets during advanced crystallization.

At magmatic temperatures the segregated sulphide melt, enriched in PGMs, would have begun to crystallize *mss* (monosulphide solid solution) (i.e. von Gruenewaldt *et al.,* 1989). As the temperature dropped the *mss* converted into pyrrhotite and pentlandite (i.e. Durazzo and Taylor, 1982). As the temperature dropped further the pyrrhotite exsolved out pyrite which grew as individual, euhedral grains. This is confirmed by the exsolution sulphide textures where pyrite occurs as a rim around pyrrhotite in some cases (see Chapter 8).

Therefore the sulphide assemblage is also representative of the original magmatic assemblage. No late stage alteration has affected the sulphide assemblage (with a common low temperature sulphide product being millerite, especially further south in areas of intense local fluid activity) (i.e. Rixom, 2005).

During cooling, the PGE originally incorporated into the *mss* diffused to the sulphide grain boundaries to form PGMs (mainly PGE-sulphides and PGE-tellurides) (i.e. von Gruenewaldt *et al.,* 1986). This explains the close sulphide-PGM association, as well as the propensity of the PGM to be located at phase boundaries (especially triple point junctions). Some of the PGM remained in solid solution in the sulphide phases (ie. Pd in pentlandite). During this stage, appreciable amounts of Pd and Au partitioned into the BMS minerals (due to their strong chalcophile tendencies) to occur in a solid solution state within the BMS minerals. The remaining PGE all partitioned strongly into the PGM. This explains the close relationship between Pd and Au and the BMS as well as the remaining PGE with each other (see Chapter 7). Negligible geochemical evidence for any postcumulus alteration or remobilization exists. This mechanism of mineralization is therefore one of a primary, magmatic origin.

Therefore the proposed model suggests that the formation of the UG2 unit comprised a multitude of magma injections within the chamber, which increased over time. In terms of the process of sulphide and PGM mineralization it is envisaged that a PGE-impregnated sulphide liquid separated out from the silicate magma and, due to its immiscibility, was concentrated in the interstitial liquid where, during the final stages of crystallization, both the base-metal sulphides and the PGMs crystallized out.

9. Summary of the Mechanisms for the Origin of PGE Mineralization in Layered Intrusions – With Reference to the Bushveld Complex

9.1 Introduction

The origin of platinum-group element (PGE) mineralization in layered intrusions is a highly debated and unresolved issue. A variety of models have been proposed and these can largely be divided into (1) a primary magmatic model in which the PGE are removed from the melt early on, and (2) late-stage remobilization, modification and precipitation of the PGE by upward moving magmatic fluids.

9.2 Primary Magmatic Model

The first model suggests that PGE deposits were formed by the segregation of an immiscible sulphide melt which then scavenged the individual PGE or PGE-alloy complexes from the mafic-ultramafic magma in a dynamic magmatic system.

9.2.1 Sulphide Scavenging

The close association of PGE with sulphides in many layered intrusions (i.e. the Main Sulphide Zone of the Great Dyke, the Merensky and UG2 Reefs of the Bushveld Complex and the J-M Reef of the Stillwater Complex) indicates that liquid sulphide probably acted as a collector for these metals (Coghill and Wilson, 1993). It was initially Campbell *et al.* (1983) who proposed that the PGE were scavenged from the silicate magma by an immiscible sulphide melt which segregated at a point of sulphur-saturation within the magma. Campbell and Barnes (1984) proposed that Nernst distribution coefficients required for such a process were very high, as high as 10^5. Thus each PGE may have had a slightly different distribution coefficient value, which is reflected in the relative displacement of the individual PGE and BMS peaks for the Great Dyke (Prendergast and Keays, 1989; Wilson and Tredoux, 1990) and also for the Munni Munni Complex (Barnes *et al.,* 1990). Therefore the primary magmatic 'sulphide scavenging' model is highly successful in explaining the observed 'offset profiles' (metal peaks are stratigraphically displaced from each other) of the PGE and BMS in the Great Dyke and the Munni Munni Complex.

When searching for a model to explain the origin of PGE mineralization in layered intrusions it is important to note that the process must be highly efficient in order to account for the extreme enrichment of PGE i.e. Macdonald (1987) proposed that for the formation of an economic sulphide-hosted PGE deposit, enrichment factors for a normal basaltic magma are required to be in the order of ~10^3. The high Nernst distribution coefficients alone are most likely insufficient to account for the enrichments observed in PGE deposits (Coghill and Wilson, 1993). The concept of the *R*-factor, which was introduced by Campbell and Naldrett (1979), expresses the ratio of the mass of the host magma to sulphide liquid necessary to produce this enrichment (Coghill and Wilson, 1993). The concept of the *R*-factor suggests that, in order to produce an

economic deposit, the sulphide liquid has to come into contact, and interact with, a large volume of silicate magma. Campbell *et al.* (1983) explain that mixing and turbulence in magma are the dominant control in achieving a high *R*-factor. Thus, the injection of a new magma pulse into the chamber with subsequent mixing may be a viable mechanism of PGE-enrichment (discussed in further detail in the next section). Coghill and Wilson (1993), also point out that the general occurrence of PGE-rich sulphide horizons at or near the base of cyclic units may imply that their genesis is linked to injections of magma into the chamber.

9.2.1.1 Mechanisms of Sulphide Precipitation

The mechanism of sulphide precipitation in a silicate magma is also an unresolved, and hotly disputed, issue. The original favoured model, being that of magma mixing (Naldrett *et al.,* 1983, Li *et al., 2001*) has recently being disputed (Cawthorn, 2002). This model provides a very likely mechanism of sulphide precipitation but some of its underlying premises have been show to be incorrect using binary diagrams. Another proposed model suggests crustal contamination to be the initiator of sulphide precipitation (Brenan and Li, 2000; Li *et al.,* 2000; Li *et al., 2002*). Both models, as well as the debate between Cawthorn (2002) and Li *et al.,* (2000, 2002), are summarized here.

9.2.1.1.1 Magma Mixing

Naldrett *et al.* (1983) were the first to suggest that magma mixing can cause sulphide precipitation in a silicate melt. The evidence for such a model includes the fact that the turbulence associated with mixing of new plumes of magma can produce a very high *R*-factor value (which is necessary for PGE enrichment), platiniferous sulphide horizons that are often situated at the base of cyclic units (which are believed to represent new magma injections into the chamber) as well as with chromite concentrations (thus indicating a genetic relationship with magma influxes) and the fact that it also provides a feasible mechanism of initiating sulphur saturation in a silicate melt (Naldrett *et al.,* 1983). Naldrett and von Gruenewaldt (1989) then proposed that the magma mixing model was responsible for the formation of PGE mineralization associated with chromite and sulphide in the Bushveld Complex. Cawthorn (1999) argued this suggestion and concluded that the concave upward sulphur solubility curve of a fractionated basaltic magma, which is central to this model, does not exist and he also pointed out that both the hanging wall and footwall sequences of the Merensky Reef formed from sulphur undersaturated magma as opposed to the sulphide saturated magma predicted by the model. He also argued that there is a significant mass-balance problem with the model (Cawthorn, 1999). Li *et al.* (2001) then attempted to use thermodynamic calculations and binary diagrams to prove that the magma mixing model was indeed responsible for the PGE mineralization in the Bushveld Complex. They recalculated the sulphur solubility limits for the evolving magmas based on the empirical equation:

$S = 1431 + 221 \times (FeO - 9) = 5 \times (T - 1200)$

Where S is sulphur solubility in ppm, FeO is molar %, and T is temperature in ◦C (Cawthorn, 2002). This equation emphasizes the major role of iron and temperature in controlling sulphur solubility as originally shown by Haughton *et al.* (1974). Naldrett and von Gruenewaldt (1989) presented a figure relating the solubility of sulphide to the % of fractionation of the Bushveld parent magma. Li *et al.* (2001) altered this diagram and plotted Zr, instead of % fractionation, as the abscissa and produced the following figures:

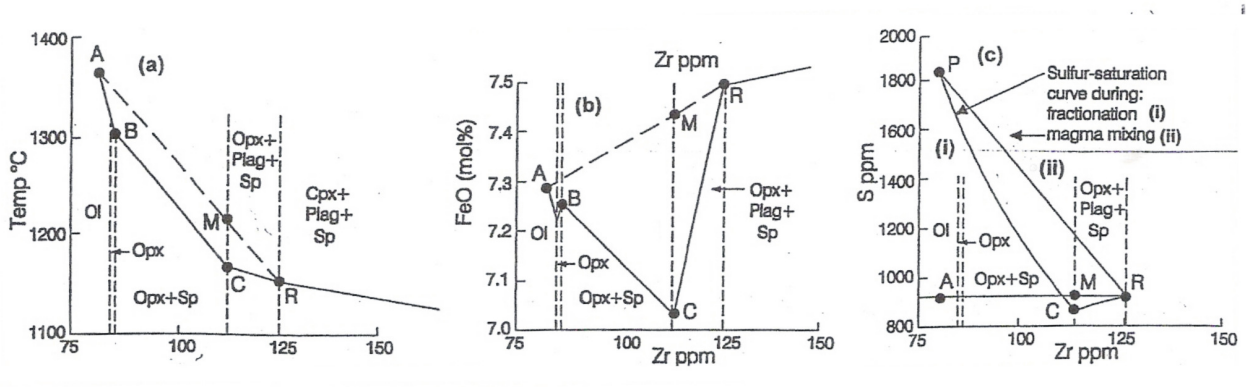

Figure 9.1: Sulphur solubility as a function if various parameters related to the evolution of the parental magma to the Bushveld Complex (Li et al., 2001). Zr is used as the abscissa in all plots. In all diagrams, A is the parental magma to the Bushveld complex, B is the composition of orthopyroxene and spinel saturation, C is the composition at which plagioclase begins to crystallize, R is the residual magma present in the chamber prior to the formation of the Merensky Reef, M is a mixed magma calculated to have the same Zr content as C (Li et al., 2001).

Figure 9.1 shows how fractionation of composition A produces a trend through B, C to R, whilst mixing between A and R produces a trend through M (Cawthorn, 2002). Thus the mixing of A into R produces liquids that are still saturated with both plagioclase and orthopyroxene until point M is passed. Cawthorn (2002) agrees that this is incorrect and that compositions C and M are chemically different (Figure 9.1) and thus cannot be assumed to have the same sulphur saturation limits, and therefore cannot be plotted together on Figure 9.1.

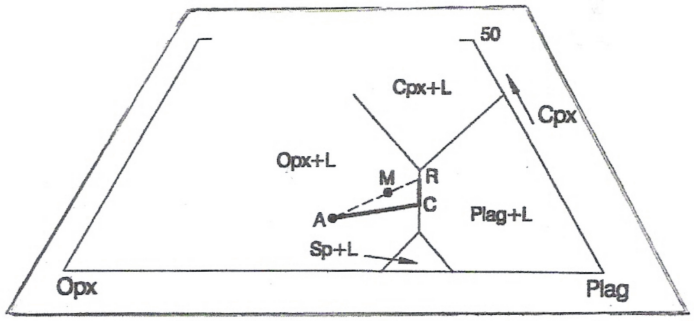

Figure 9.2: Phase relations in the system orthopyroxene-clinopyroxene-plagioclase (Cawthorn, 2001). The points A, C, R, and M are the same as in Figure 9.1. Note that the compositions of a mixed magma, M, and that of the fractionated magma, C, are very different (Cawthorn, 2001).

Thus Li *et al.* (2002) have assumed that because compositions C and M have the same Zr content they will have the same sulphur saturation limit, which is incorrect. In Figure 9.1 A it can e seen that the mixing of compositions A and R produces a series of liquids that have higher temperatures than those produced during fractionation of composition A. In Figure 9.1 B we can see that the mixing curve RMA yields mixed magmas with higher FeO contents than fractionated magmas along curve ABCR. The combined affect of higher temperature and higher FeO content during mixing results in higher sulphur solubility's (according to equation 1) than for a fractionating magma (Li *et al,* 2001). Figure 9.1 C shows that the sulphur solubility's for magmas produced during mixing define a straight line from R to P (the latter being the sulphur solubility of magma A), which exceeds the solubilities of the iron-depleted fractionation trend PR (Cawthorn, 2002). As a result point M (which s the product of mixing resident and new magmas) lies below the sulphur saturation curve for mixed magma, but above the sulphur solubility curve for fractionating magmas (Li *et al.,* 2001). Thus the mixing of residual magma R with an added magma A is a mixed magma M which has a different composition to that produced during fractionation (Li *et al.,* 2001). As a result the mixed magmas (RMA) have greater sulphur solubility than the fractionated magmas (ABCR), and as a consequence the mixed magmas are not sulphur saturated (Li *et al.,* 2001).

Two errors were noticed by Cawthorn (2001) and were later acknowledged by Li *et al.,* (2001). The first is a typographical error in the calculation of the sulphur solubility of a fractionated magma (point C), resulting in a slight change to the sulphur solubility curve (Li *et al.,* 2001) (Figure 9.3). The corrected curve does not support the concept that the fractionating magma may go through a phase of sulphide undersaturation (Cawthorn, 2001).

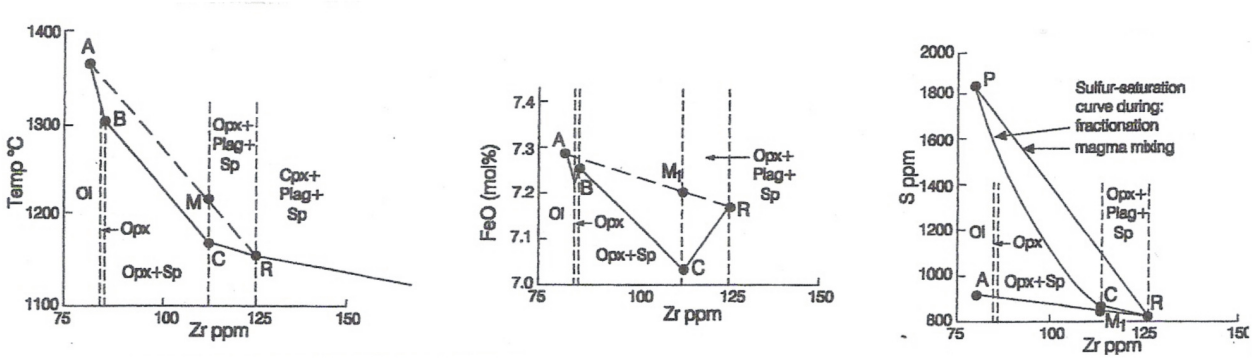

Figure 9.3: Modified version of Figure 9.2 (Cawthorn, 2001). Note the shape of the sulphur solubility curve is changed between C and R relative to Figure 9.2.

The second error is that the sulphur solubility of a mixed magma is not the same as that of a fractionated magma and thus to evaluate the affect of magma mixing on sulphur solubility , the content of sulphur in the hybrid magma must be compared to the sulphur solubility of the hybrid magma itself, and not

to that of a fractionated magma with the same Zr content (Cawthorn, 2002). Figure 9.4 shows the corrected figure and it is clear that the sulphur solubility of a mixed magma is always higher than its sulphur content (Cawthorn, 2002). From this we can conclude that magma mixing could not have triggered sulphide supersaturation in the Bushveld Complex.

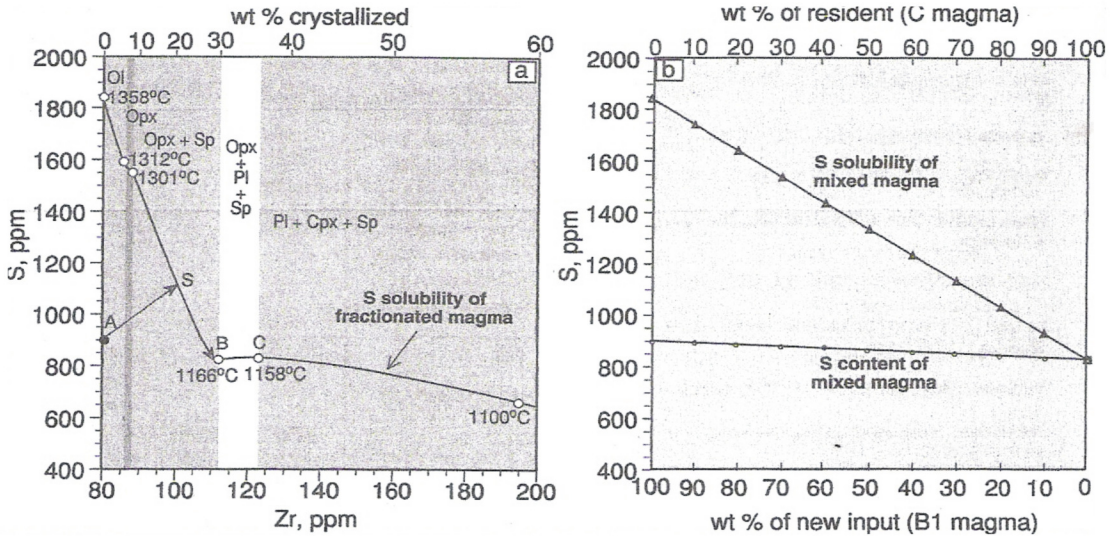

Figure 9.4: Sulphur solubility of magma by fractionation (a) and mixing (b) (Li et al., 2001).

Therefore binary diagrams have been used to define sulphur saturation limits in order to support the concept that magma mixing can generate the production of an immiscible sulphide melt. The basis of the study by Li *et al.,* (2001) was that the same sulphur saturation curve was used for fractionating magmas and for their products of mixing between end-members. Cawthorn (2002) explains that this is invalid as the two magma series have different compositions. A reassessment of magma mixing shows that mixed magmas of Bushveld affinity do not reach sulphur saturation (Cawthorn, 2002). The layered cumulates above the Merensky and UG2 Reefs are not sulphide bearing (Cawthorn, 2002). This situation is not consistent with the hypothesis of magma mixing, with the concept that the fractionating magma may experience a phase of sulphur undersaturation not supported by a detailed examination of the geometry of the phase diagram (Cawthorn, 2002).

The concept of magma mixing is certainly a favourable process for the generation of an immiscible sulphide melt. There are, however, several features which cannot be explained by this model i.e. the sulphur undersaturated cumulates above the Merensky and UG2 Reefs (Cawthorn, 1999).

9.2.1.1.2 Contamination

Taking this into account Li *et al.,* (2002) then changed their attention to crustal contamination as a possible initiator of sulphide saturation in the Bushveld Complex. Previously Li *et al.,* (2000) demonstrated the importance of crustal contamination in the formation of the sulphide ores of the Voiseys Bay and Mushuau Intrusions in Canada. Here they used isotopic systems to determine the nature and amount of crustal assimilation and concluded that Voiseys Bay parental magmas were only moderately affected by contamination during ascent through the crust and probably did not undergo early sulphide separation, whilst the Mushuau Intrusion was probably extensively contaminated with hot restites from intracrustal melting and/or granitoid melts and did reach early sulphide saturation (Li *et al.,* 2000). It is therefore clear that crustal contamination is the probable process responsible for initiating sulphide saturation in several layered intrusion hosted sulphide deposits, as shown by Li *et al.,* (2000).

Li *et al.,* (2002) then investigated the possibility of crustal contamination as an initiator of sulphide saturation in the Bushveld Complex. They explain that three mechanisms of contamination may trigger sulphide supersaturation i.e: (1) addition of external SiO_2 by assimilation of siliceous partial melts of country rocks, thereby lowering the sulphur solubility of the magma, (2) addition of external sulphur by means of devolatization, partial melting, or bulk assimilation of sulphidic country rock, or (3) an increase in oxygen fugacity resulting in the lowering of the FeO content and thus the sulphur carrying capacity of the magma (Li *et al.,* 2002). The latter mechanism may be particularly relevant where the magma intrudes and devolatizes dolomite such as in the case of the Platreef in the Northern Limb (Mokopane area) of the Bushveld Complex. (Li *et al.,* 2002). Li *et al.* (2002) explain that the Bushveld magmas have a distinct crustal signature derived from contamination either in a lower staging chamber or in the Bushveld chamber itself. Sills in the floor of the complex that are thought to represent the parental magmas are sulphide and PGE-poor and thus suggest that contamination at depth did not trigger sulphur saturation (Li *et al.,* 2002). They suggest that crustal contamination may have initiated sulphide saturation in the Bushveld Chamber (Li *et al.,* 2002), but no evidence is produced to support this. Thus crustal contamination is indeed an important mechanism of sulphide saturation in many sulphide ore deposits (i.e. Li *et al.,* 2000), but it has not yet been proven for the Bushveld Complex.

Therefore it is clear that the exact mechanism of sulphide saturation in a silicate melt is a hotly debated and, as yet, unresolved subject. The concepts of magma mixing and crustal contamination do explain many observed features but lack firm, substantial evidence. The authour favours the magma mixing model but it has several shortcomings when attempting to model using phase diagrams.

9.2.2 PGE Clusters

Tredoux *et al.* (1995) explained that there are difficulties involved with modeling PGE as partitioning into sulphides or chromite in the conventional sense, and they suggest that the siderophilic nature of the PGE may allow them to occur in the silicate melt as metallic clusters of 50 – 100 atoms. They propose that the metallic clusters could be stabilized by an outer 'envelope' of ligands (i.e. S, As, Sb, Te), and this may lead to their incorporation into a segregated sulphide melt or into chromite (Tredoux *et al.,* 1995). This is an alternative model for the behaviour of PGE in the magma and it is not controlled by any crystal-chemical compatibility (as required by other primary, magmatic models for the enrichment of PGE in a silicate melt).

The previously discussed "sulphide scavenging" model treated the PGE as largely chalcophilic elements and was based on the chemical compatibility between the PGE and a sulphide melt at magmatic temperatures. It suggested that the PGE would be collected and concentrated by a segregated sulphide melt due to the large positive bulk partition coefficients of the PGE for the sulphide, and thus the fate of the PGE in the magma would be controlled by the same parameters as those which control the formation of the immiscible sulphide melt (Tredoux *et al.,* 1995). This model has proved successful enough to allow first-order modeling of the behaviour of Pt and Pd (Wilson *et al.,* 1989), however, they are much less successful when applied to the behaviour of the other PGE (Wilson and Tredoux, 1990; Peach *et al.,* 1990). It must be remembered that high PGE concentrations are also seen in chromitite layers and in olivine – rich ultramafic rocks apart from sulphide – rich layers (Tredoux *et al.,* 1995). In some cases, the enrichment has been ascribed to high bulk partition coefficients in favour of olivine and/or chromite. Tredoux *et al.,* (1995), however, suggested that the siderophile tendency of the PGE might well dominate even in the presence of sulphide.

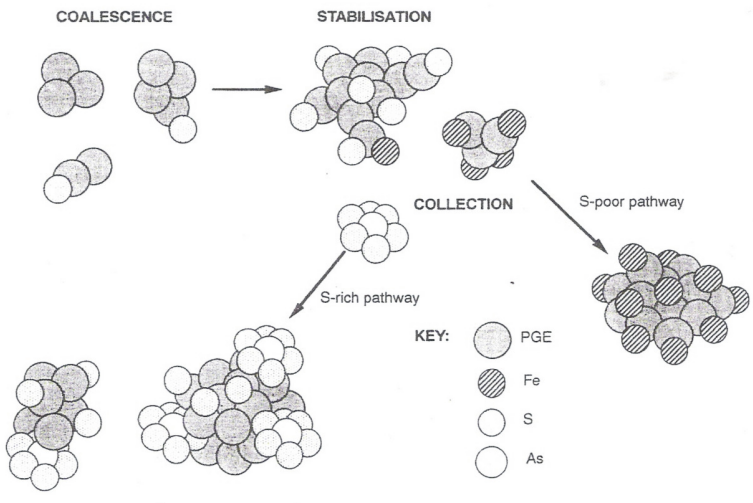

Figure 9.5: Schematic diagram of the behaviour of PGE clusters in a magmatic system (Tredoux et al., 1995).

Their model comprises the following (see Figure 9.5): the PGE are present initially in the silicate melt as metallic clusters which are stabilized by an outer envelope of ligands (Tredoux *et al.,* 1995). They suggest that in sulphur-rich environments, the PGE clusters remain associated with the sulphide melt until they coalesce and precipitate out to form PGE arsenides, tellurides, alloys and complex sulphides (Tredoux *et al.,* 1995). In sulphur-poor environments the clusters will remain in the silicate melt until they coalesce to form alloys, and if the coalescence occurs early enough the resulting PGM might provide nucleation centres for early forming silicates and oxides (Tredoux *et al.,* 1995). Evidence for this is in the form of the close association of Os and Ir with early crystallites (Tredoux *et al.,* 1995). Tredoux *et al.,* (1995) also suggest that PGE clusters which remain too dispersed to precipitate as PGM, could provide the source of late-stage remobilized PGE enrichments seen in the dunite pipes of the Eastern Bushveld Complex.

Their model certainly provides a unique alternative to the previously discussed models. It does not rely on partitioning behaviour and treats the PGE enrichment process as mainly a physical process. It does explain the enrichment of PGE in different settings (i.e. olivine-rich ultramafic rocks, chromitite layers, sulphide-rich layers and dunite pipes) as well as the mineralogical associations of the PGE.

Therefore, the primary magmatic model has sufficient evidence to suggest that it is possibly the main mechanism of PGE enrichment in layered intrusions. The primary model relies on an immiscible sulphide melt, which scavenges and collects PGE, or PGE clusters, in the silicate melt. The model is able to explain the offset peaks observed in the Great Dyke and in the Munni Munni Complex, the close association of PGM with sulphides in mineralized layers and it also provides a feasible mechanism to account for the extreme PGE enrichment in mineralized layers (i.e. a segregated sulphide melt scavenging PGE/PGE clusters from a large volume of silicate magma).

9.3 Late-Stage Hydrothermal Model

The second model proposes a hydrothermal origin of PGE deposits. Evidence for this model is provided in the form of the association of PGM with hydrous silicate phases and altered primary silicates, increased amounts of graphite and chlorite, and textures indicating recrystallization (pegmatoids) and fluid movement (Ballhaus and Stumpfl, 1986; Boudreau, 1988). Coghill and Wilson (1993) explain that this model involves complexation of PGE with a Cl-rich fluid which is capable of transporting the metals to the zone of concentration, notably a sulphide-rich layer. Due to the highly incompatible nature of PGE they tend to be concentrated in the trapped, intercumulus silicate liquid during magmatic differentiation. Ballhaus and Stumpfl (1986) suggest that the PGE (and other precious metals) fractionated into the Cl-rich fluid as Cl-complexes. They therefore suggest that the PGE now exist as Cl-complexes, which are notably efficient transport devices (Ballhaus and Stumpfl, 1986). During crystallization of the magma pile, the density of the pile increases, resulting in compaction. This compaction process is responsible for the exsolution and

expulsion of the evolved intercumulus silicate liquid (Figure 9.6). This 'layer' of liquid then percolates upward through the crystal pile and Boudreau *et al.,* (1986) show how the liquid will be progressively enriched as it encounters pockets of liquid that had not reached saturation of halogens. Once the migrating liquid reaches a sulphide layer, the precious metals precipitate along the boundaries of sulphide melt droplets as the liquid continues rising through the crystal mush (Ballhaus and Stumpfl, 1986). This model is backed by textural and mineralogical evidence observed in several mineralized layers and it also provides a feasible enrichment mechanism of PGE.

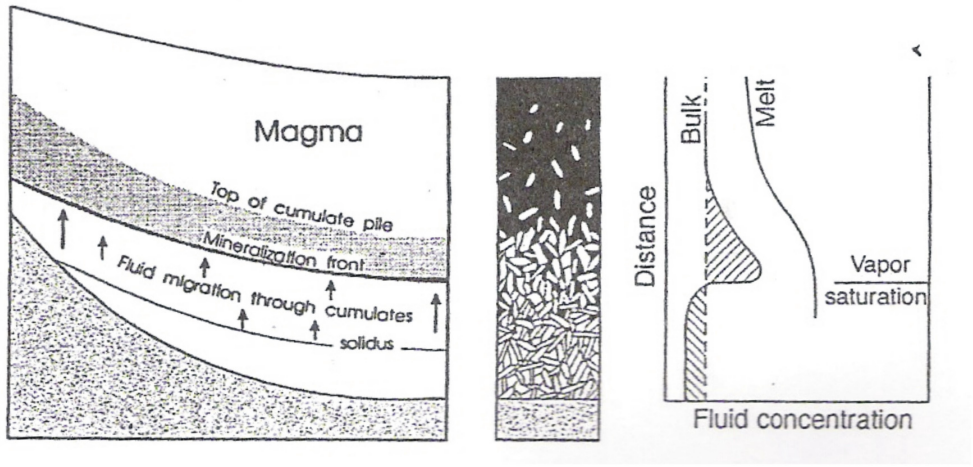

Figure 9.6: Model of Boudreau and McCallum (1992) for the origin of PGE-enriched sulphide zones. This Cl-rich fluid migrates upward and carries with it the fluid compatible elements (S, PGE, Cu, Ni, As, Te) which were originally contained in a minor sulphide phase. The upward migration of fluid is limited to the level at which the interstitial liquid is fluid saturated. As the crystal pile thickens, the fluid saturation boundary moves upwards until it encounters a lithological discontinuity or a sulphide-rich zone (Lee, 1996).

9.4 Application to the Bushveld Complex

From the evidence presented it is believed that no single model is likely to account for all the PGE mineralization present in all layered intrusions. Instead, it is suggested that both processes (primary magmatic vs. later hydrothermal) are inter-related with one process being more dominant in one layered intrusion whilst the other process may be more dominant in another intrusion. This section aims to apply these models to the Bushveld Complex.

The Bushveld Complex is a good base from which to study PGE mineralization mechanisms as it contains three economically PGE-mineralized horizons in the form of the Merensky Reef, the UG2 Reef and the Platreef. The Merensky and UG2 Reefs have been suggested by some (Ballhaus and Stumpfl, 1986; Boudreau and McCallum, 1986) to have undergone hydrothermal PGE enrichment at a late stage. There are

several textural and mineralogical fsctors which suggest a hydrothermal origin for the PGE, and these are summarized by Barnes and Campbell (1984) and Ballhaus and Stumpfl (1986). This evidence includes the presence of pegmatitic textures, intergrowth of sulphides with intercumulus volatile-rich phases, high Cl content in volatile-bearing phases, and association with graphite and fluid inclusions (Campbell and Barnes, 1984). Campbell and Barnes (1984) explain how these textures and mineral associations are not the result of hydrothermal processes but rather the result of late-stage modification and remobilization by postcumulus processes in the orthocumulate layers. The close association of these two PGE rich layers with the bases of cyclic units and with chromitite concentrations, which indicates a genetic relation to new magma influxes i.e. Scoon and Teigler, (1994), the great lateral persistence and uniformity of grade of the Merensky Reef and UG2 chromitite, and systematic stratigraphic controls on PGE tenors of sulphides within the Upper Critical Zone of the Bushveld Complex, particularly within the UG2 chromitite (Naldrett *et al.,* 1986; Hiemstra, 1985, 1986) indicate that the PGE concentrations of the UG2 chromitite and the Merensky Reef are both a result of primary magmatic cumulus processes, whilst the observed hydrothermal features are the result of late stage postcumulus processes superimposed on these two layers (Barnes and Campbell, 1984). Another factor which disproves the hydrothermal model of PGE enrichment in the Bushveld Complex is the presence of the Platreef layer near the base of the complex and also the close stratigraphic spacing of several PGE enriched (compared to the host rock) chromitite layers in the Critical Zone.

9.5 Conclusions

Therefore a multicriterion model of PGE mineralization is suggested for the Bushveld Complex. This model is envisaged to have a dominant primary magmatic component (from the lateral persistence and uniformity of grade of the mineralized layers and the close association of the mineralized layers with the base of cyclic units and with chromitite concentrations to name two points of evidence) along with a late-stage postcumulus component which had a modifying affect on the mineralized layers (especially the textural and mineralogical characteristics of the layers).

10. Implications for Chromitite Petrogenesis in Layered Intrusions – with Particular Reference to the UG2 Chromitite

10.1 Introduction

Chromitite layers are mono-mineralic layers of cumulus chromite in layered intrusions. Despite their relatively simple field occurrence a diverse range of hypotheses have been proposed to explain their origin. This section serves to briefly list these theories and discusses their respective shortcomings and advantages. The origin of the footwall pegmatoidal feldspathic pyroxenite layers is also discussed. Finally, a comprehensive petrogenentic model for the entire UG2 cyclic unit is proposed.

10.2 Setting of the Bushveld Chromitites

10.2.1 Classification and the Characteristics of the Bushveld Chromitites

The main feature of the Bushveld chromitites is that they are confined to the critical zone. Cameron (1978) noted that despite having chromite as a cumulus phase the lower zone contains no chromitite seams. Although Hulbert and von Gruenewaldt (1982) noted that in the northern lobe south of Mokopane there are minor occurrences in the lower zone, these occurrences, however, are minimal compared to the numerous, laterally vast seams within the critical zone. The Bushveld chromitites are subdivided up into three stratigraphic groups (Cousins and Feringa, 1964) namely the lower group (LG), comprising seven layers hosted within feldspathic pyroxenite, the middle group (MG) comprising four layers which straddle the upper – lower critical zone boundary, and the upper group (UG), which consists of two to four layers (depending on geographic location).

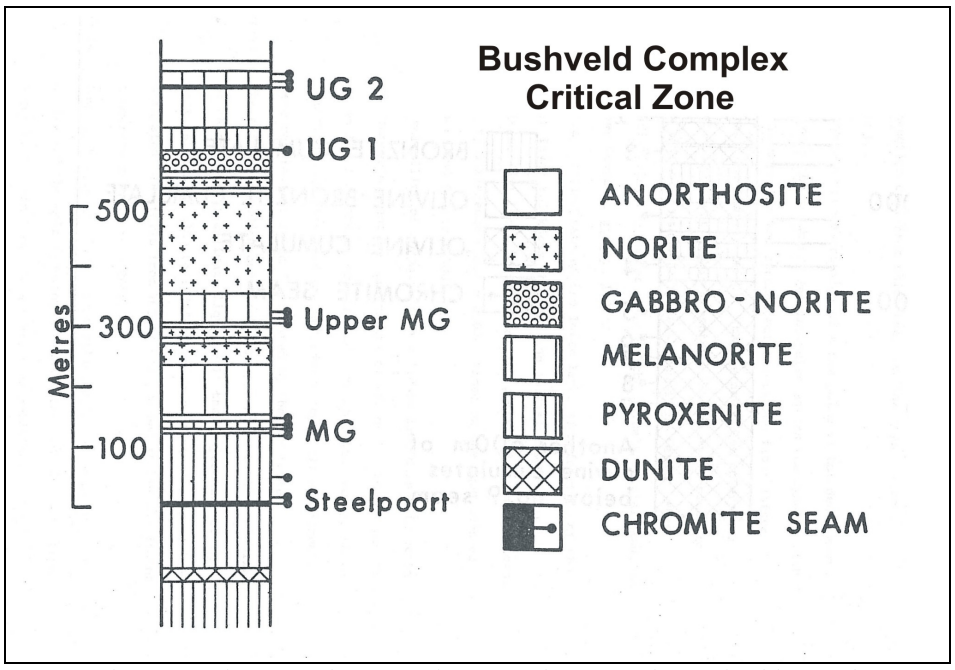

Figure 10.1: Location of the major chromitite layers of the Critical Zone of the Bushveld Complex.

The lower group (LG) chromitites occur within a continuous sequence of feldspathic pyroxenites, usually with no obvious connection between the position of the seam and the start of the cyclic unit. The LG1 to LG4 seams are associated with the appearance of cumulus olivine – a feature that distinguishes them from overlying chromitites (Hatton and von Gruenewaldt, 1989). The thickest of the lower group chromitites is the LG6, also known as the Steelpoort Seam, which is a 1 m thick seam of massive chromite (Cameron, 1980). Cameron (1980) also describes how the LG6, in certain areas, is divided up into two seams separated by a pyroxenite (usually pegmatitic) parting up to 2 m thick and 45 m long.

The middle group (MG) chromitites commonly comprise four seams, although multiple layers of each may develop, for example the MG1 may comprise two thinner chromitites below a 1 m thick chromitite, whilst at Tweefontein mine in the Eastern Bushveld a seam designated MG0 is locally developed below the MG1 (Kinnaird *et al,* 2002). The MG layers straddle the upper – lower critical zone boundary with MG1 and MG2 occurring below the first anorthosite and MG3 and MG4 above.

The UG usually comprises two chromitites (UG1 and UG2), although in the Eastern Bushveld the UG3 and UG3A layers are also recognized. The UG1 is found at the base of the UG1 cyclic unit and it comprises a feldspathic pyroxenite hanging wall and an anorthositic footwall. It outcrops at the world famous Dwars River heritage site where it forms a main upper layer and a complicated assemblage of footwall layers, stringers and lenses separated by partings of anorthosite. These complex bifurcations and interconnections of chromite separated by anorthosite give the UG1 its distinctive appearance, and are indeed present in the study area. The UG2, which is the focus of this study, has already been described in detail. The UG3 is found only in the Eastern Bushveld where it is suggested to occupy a position approximately equivalent to the Pseudo Reef of the Western Bushveld (Campbell and Murck, 1984). It occurs at the base of a cyclic unit and it comprises a feldspathic pyroxenitic hanging wall and an anorthositic footwall.

10.2.2 Lateral Variation in UG2 Cyclic Unit Stratigraphy

Despite the vast lateral continuity of individual chromitite layers along strike (Cawthorn and Webb, 2001) it is more difficult to correlate layers between the different lobes. It can, however, be done using the thickness of the individual layers as well the type and amount of interlayer silicates. Although there is considerable lateral variation in the occurrence and thickness of the chromitite layers between the different lobes as well as between the northern and southern portions of the eastern and western lobes (Kinnaird *et al,* 2001) it is, however, still possible to correlate packages of chromitite rather than individual layers.

The UG2 chromitite layer and its cyclic unit also display some variation both in lithostratigraphy and character between different areas/lobes. The UG2 in the SW Bushveld lies close to the base of a cyclic unit and it comprises a pyroxenitic hanging wall and an anorthositic footwall, whilst in the NW Bushveld the UG2

is commonly separated from the UG1 by 15 m of feldspathic pyroxenite (Campbell, 1978). There is, however, a sporadic development of anorthosite in the immediate footwall to the UG2 in the NW Bushveld (Mitchell and Scoon, 2007). In the Eastern Bushveld, however the UG2 occurs some 100 m above the UG1 and about 6 m above the base of the UG2 cyclic unit, where Mitchell and Scoon (2007) have also documented sporadic development of anorthosite.

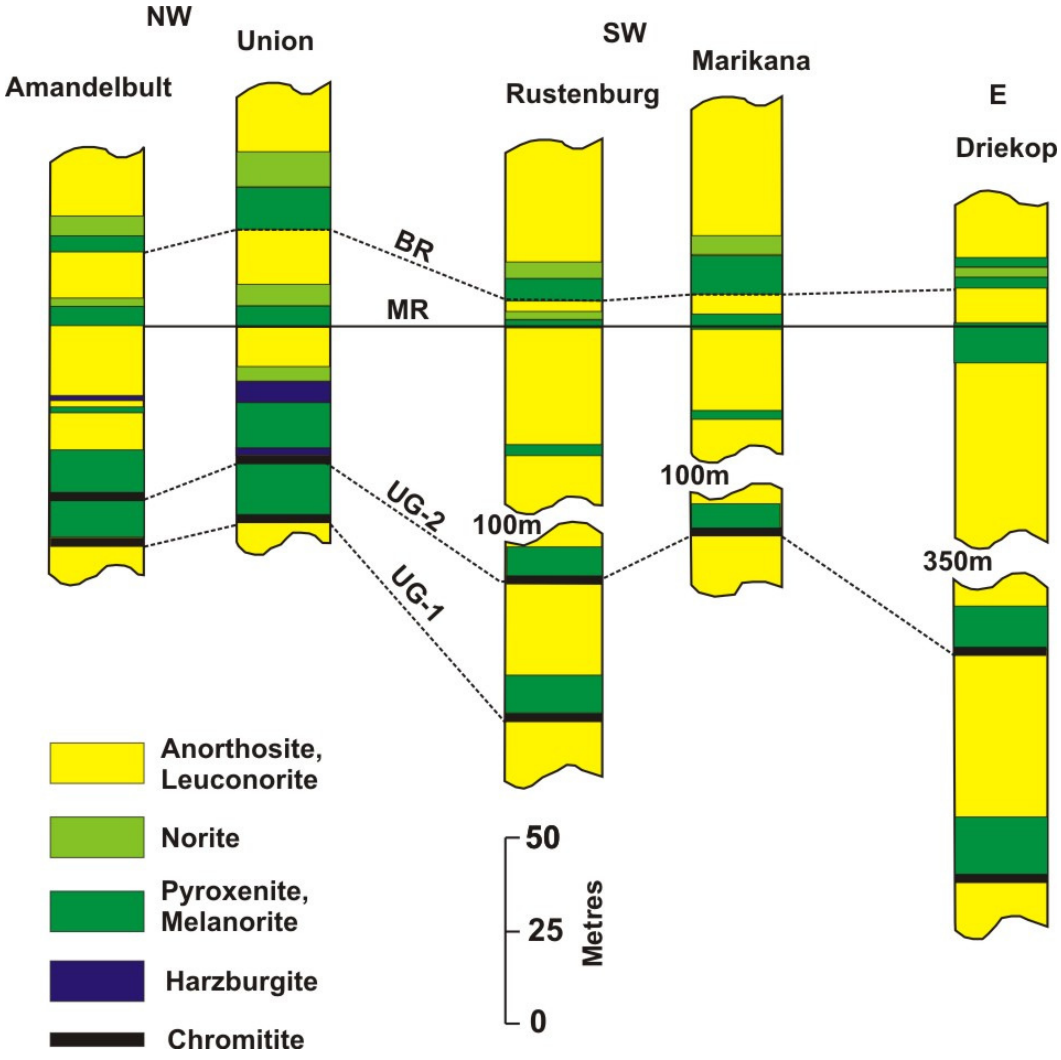

Figure 10.2: Lateral variation in upper critical zone stratigraphy from different lobes (areas) of the Bushveld Complex (from Campbell and Murck, 1984).

10.3 The Chromitite Problem

10.3.1 Introduction

A wide range of hypotheses have been proposed to explain the origin of chromitite layers in layered intrusions. The major challenge when developing a model to account for the formation of these layers is to somehow take an element (Cr^{3+}), which is present in the silicate melt in very low abundances (500 ppm), and enrich it to the extent that a monomineralic layer, built up predominantly of the incompatible element in question, is crystallized out of the silicate melt.

10.3.2 Review of Past Models

A diverse range of theories have been proposed including:

1) Mixing between a resident and a new magma within the chamber (Irvine, 1977).
2) Contamination by a siliceous component (Irvine, 1975).
3) Pressure changes within the chamber (Cameron, 1977).
4) Increases in oxygen fugacity by country rock degassing (Cameron and Desborough, 1969).
5) Gravity induced separation, crystal sorting and settling (Wager and Brown, 1968).
6) Immiscibility of a Cr-rich liquid (Sampson, 1932)
7) Lateral growth with a stratified magma column (Irvine *et al*, 1983)
8) Introduction of chromite as suspended micro-xenoliths in new magma influxes (Eales, 2000)

Each of these theories has been extensively discussed in the literature. There are advantages and disadvantages to each and, as such, no single favoured model exists.

As Campbell and Murck (1984) pointed out, the problem is largely a kinetic one: how does a chromite seam up to 1 m thick containing over 40 % Cr_2O_3 form from a silicate melt with a chromite content of only ~ 500 ppm. It is important to note that the ore/silicate melt concentration factor required to form a major chromitite layer is similar to that required to form an economic PGE-mineralized sulphide horizon (such as the Merensky Reef) in a layered intrusion. This fact is extremely important as the mechanisms resulting in the formation of chromitite layers and those producing the PGE-mineralized sulphide horizons may have important similarities and may be intimately related.

10.4 Field Observations and General Characteristics of the UCZ Chromitites

This section serves to summarize the main characteristics and field relations of the chromitite layers encountered in the study area (which is discussed in detail in Chapter 3). This will form the basis (along with

the geochemistry results) in developing a petrogenetic model for the formation of the observed chromitite layers.

Firstly, from a regional point of view it is important to note that the Bushveld – hosted chromitite layers are all concentrated in the critical zone – well above the base of the layered sequence. This is consistent with all the major chromite seams, which are all found to exist well above the base of layered intrusions. The only exception is the B chromite seam of the Stillwater Complex which is ~20 cm thick and occurs close to the base of the intrusion (Campbell and Murck, 1984). The B seam is, however, small in comparison to the larger G and H chromite seams of the same intrusion (Campbell and Murck, 1984). Therefore most major chromite seams are either absent from the lowermost cyclic units (basal portions of layered intrusions) or, if present, are minor. Many of the afore-mentioned theories have failed to provide an acceptable explanation for this very important fact. It is in the authours opinion that an acceptable mechanism of chromitite petrogenesis *must* be able to explain this feature. As Campbell and Murck (1984) point out, the absence of chromitite layers from the lowermost portions of layered intrusions is surprising as Cr^{3+} partitions strongly into the early cumulus spinels and pyroxenes and, as a consequence, the Cr^{3+} content of the silicate melt is rapidly depleted through fractional crystallization. Therefore one would expect chromitite layers to occur in the lowermost cyclic units which formed when the Cr^{3+} content of the melt was the highest.

Secondly, it is important to note that the three major chromitite layers encountered in the study area are intimately associated with cyclic layering. Therefore the process that accounts for the formation of chromitite layers must also account for, or play a part in, the general cyclical layering found in the cyclic units which host the chromitite layers.

Extending the above point we can also say that the three major chromitite seams all occur at, or near, the base of a cyclic unit. The UG1 and UG3 layers occur at the very base of cyclic units which are characterized by an upward lithological progression of chromitite→feldspathic pyroxenite→gabbronorite→anorthosite. The UG2 chromitite, however, occurs some 5 m above the base of the UG2 cyclic unit. The very base of the UG2 cyclic unit is marked by a cm-scale chromitite stringer.

The UG2 chromitite is separated from the base of the UG2 cyclic unit by a medium grained feldspathic pyroxenite and two distinct phases of pegmatoidal feldspathic pyroxenite. These two pegmatoidal feldspathic pyroxenite are strongly orthocumulate in nature and contain as much as 50 % intercumulus liquid trapped between the cumulate grains. This is particularly true for the top of these two units (chapter 4).

Another point is that the main chromitite layers often occur as multiple seams or have several leader seams a short distance above the main layer.

The final point that requires due consideration is the vast lateral extent of the chromite layers. This means that a petrogenetic model needs to have operated on a 'chamber-wide' scale and have affected the entire magma chamber.

The above describes several important characteristics and field relations of the three main chromitite layers found in the study area. A suitable mechanism of chromitite petrogenesis must be able to explain all these observed features.

10.5 Development of a Petrogenetic Model

10.5.1 A Single Petrogenetic Model for Chromitite Layers

As already mentioned, there are a variety of mechanisms suggested for the formation of chromitite layers in layered intrusions. All of these theories have been extensively discussed in the literature and each has inherent advantages and shortcomings. Instead of summarizing each and every model here, this section will be used to discuss a recently proposed model (i.e. Kinnaird *et al.,* 2002) as well as the authours preferred model, that being Irvine's 1977 magma-mixing model, and its application to the study section. One final point to note is that the formation of chromite layers is most likely closely related to the mechanism of PGE mineralization as most Bushveld chromites contain high PGE concentrations.

The model suggested by Kinnaird *et al*., (2002) attempts to combine both mixing of a newly injected magma into the chamber with residual magma along with contamination by the roof rock (Rooiberg felsites) melt. The result is a three way compositional contrast (residual magma, new primitive magma and roof rock melt) which is suggested to have initiated chromite superaturation (Kinnaird *et al.*, 2002) (Figure 10.3).

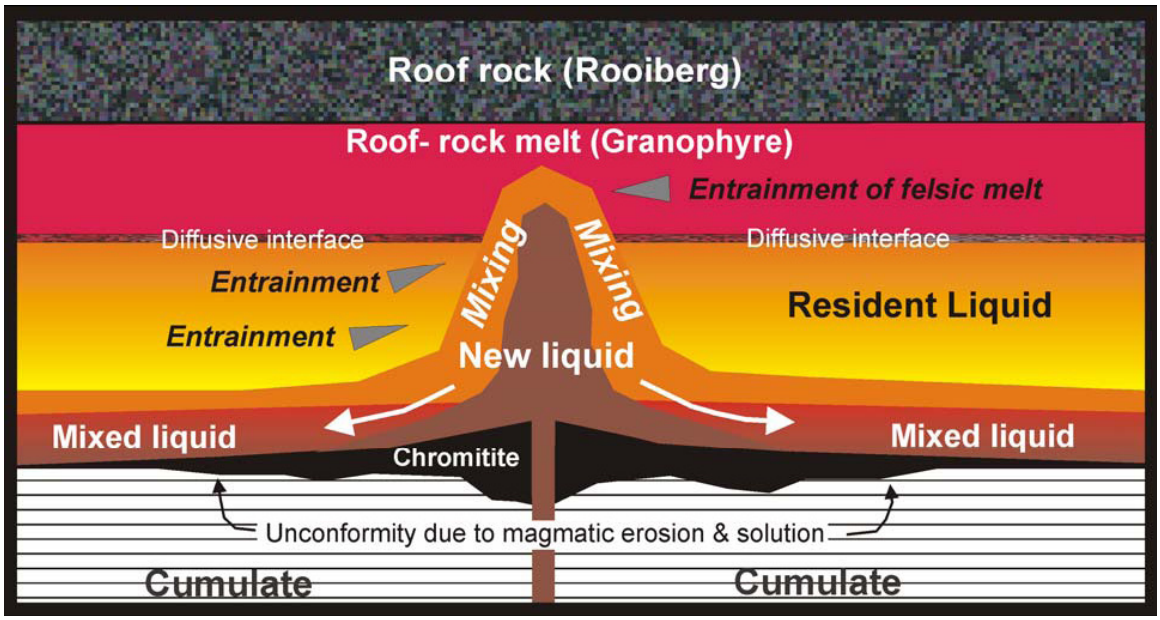

Figure 10.3: The model of Kinnaird et al., (2002). A new injection of magma into the chamber rises up and entrains roof rock, resulting in a three way compositional contrast (Kinnaird et al., 2002).

The author has reservations about the ability of such a contamination process to occur on a basin wide scale and to produce chromitite layers of such a vast lateral extent and also of such a uniformity as that of the Bushveld chromitites. The authour believes Irvine's 1977 magma mixing model to hold true and believes it is the only model which can explain all the features displayed by the Bushveld chromitites:

Irvine's 1977 Magma – Mixing Model

A main problem in formulating a mechanism of origin for chromitite layers in layered intrusions is to account for their vast lateral extent. This is particularly relevant to the Bushveld Complex due to its vast size. Irvine (1977) explained that improbable amounts of contamination of the Bushveld magma by a granitic melt would have to occur to advance from olivine to orthopyroxene crystallization. He also added that the trend of marked iron enrichment of the Bushveld, along which olivine crystallization resumed at high Fe^{2+}/Mg, can most likely develop only in relatively uncontaminated tholeiitic liquid (i.e. poor alkalis) (Irvine, 1977). Irvine (1977) thus established a new mechanism of origin for chromitite layers based on the phase diagram model of the liquidus reactions of chromite, olivine and orthopyroxene (Figure 10.4).

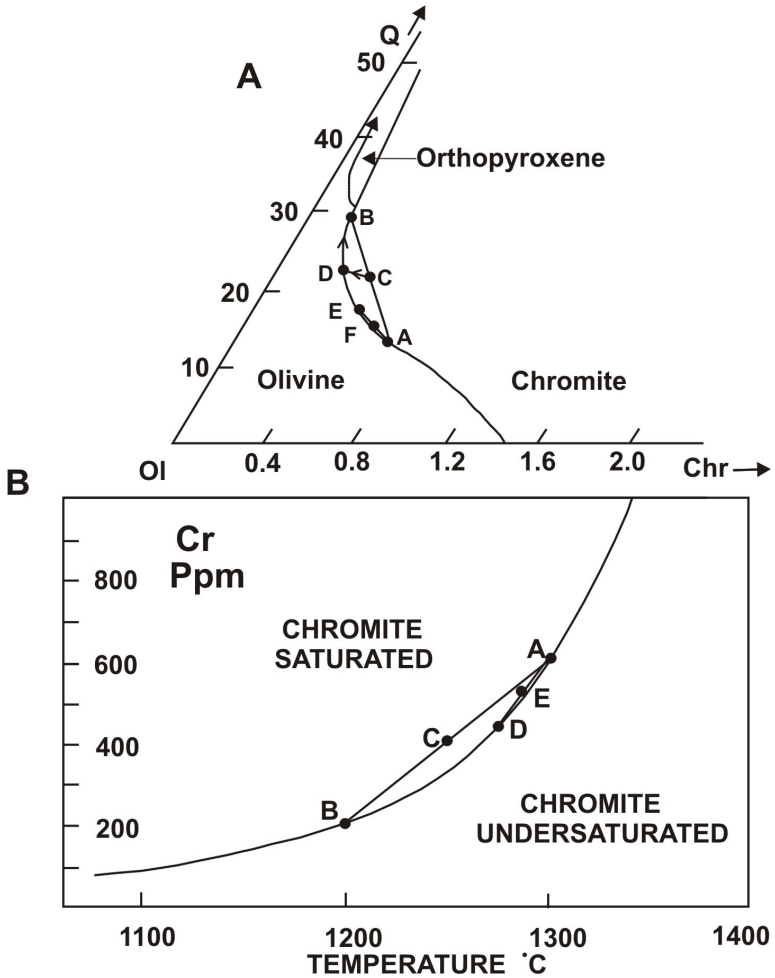

Figure 10.4: (A) Part of the system olivine (Ol) – chromite (Chr) – Quartz (Q) showing calculated and inferred phase boundaries for the Muskox magma. (B) The effect on chromite solubility of mixing two chromite-saturated melts (Irvine, 1977).

The diagram is modeled after the system MgO-Cr_2O_3-SiO_2 (Keith, 1954) and is based on relations of the minerals observed in the Muskox Layered Series. A main feature of the phase relations is the cotectic boundary for olivine and chromite. Irvine (1977) explains that it is curved in such a way that when the two minerals coprecipitate, the ratio of chromite to olivine gradually decreases, as observed in two principal repeated stratigraphic units of the layered series, cyclic units 5 and 6. These units exhibit notably well developed differentiation trends of Fe^{2+}/Mg and Ni, and the chromite modal variations parallel the Ni trends (Irvine and Baragar, 1972; Irvine, 1975).

The crystallization of a mono-mineralic layer of chromite requires not only the precipitation of chromite but also the cessation of crystallization of the other cotectic mineral, normally olivine. Irvine's (1977) magma mixing model provides an attractive mechanism for achieving this:

Assume that the parent magma for a layered intrusion is represented by point A on the diagram (Figure 10.4). As the magma cools it will crystallize olivine and chromite and will proceed along the cotectic boundary to a point B. If the fractionated resident magma within the chamber now receives a new pulse of fresh, undifferentiated parent magma and the two are mixed in a ratio of 1:1, the resulting melt will have the composition C. This melt now lies in the chromite primary field and, for a short period of time, chromite will crystallize alone thereby resulting in the formation of a chromitite seam. Chromite crystallization will then drive the system back to the olivine-chromite cotectic at D.

This model can also be used to explain the great variation in thickness of chromitites i.e. from 1 mm up to several m. For example, if the parent magma is less fractionated than in the previous example, and it has reached the point E on the cotectic before the introduction of a new pulse, and the magmas mix in the ratio of 1:1, the resulting melt will have the composition F, which lies just in the chromite field. Chromite crystallization will thus only occur for a very short period of time (before the system is driven back to the cotectic) resulting in a thin chromitite stringer. Therefore the greater the compositional and temperature contrast between the magamas, the thicker the chromitite seam.

This 'phase-diagram model' proposed by Irvine (1977) certainly has its merits. It is based on the concept of magma-mixing, which has shown to occur in most layered intrusions through the presence of cyclic units. The fact that cyclic units are sharply defined and are constant in stratigraphy over long distances indicates that the newly injected primitive liquid spreads through the intrusions with remarkable efficiency (Irvine, 1977). The observation that some cyclic units can be closely simulated by fractional crystallization models in terms of not only crystallization order but also modal abundance and mineral composition trends (Irvine and Smith, 1967) demonstrates that the minerals accumulate as they precipitate, with little or no sorting, and implies that the liquid was well mixed or homogenized while it crystallized (Irvine, 1977).

This model provides an answer to the lateral persistence and sharp contacts of the chromitite layers. It has also been demonstrated (Irvine, 1977) that it is able to reproduce the stratigraphies of the chromitite layers

present in the Muskox, Stillwater, Great Dyke and Bushveld Complex intrusions. In essence the model relies on the blending of different magmatic liquids to initiate precipitation of certain phases (i.e. chromite) at stages of differentiation when such phases would not ordinarily have formed by fractional crystallization.

It also explains why major chromitite seams occur well above the base of layered intrusions: during the filling of a magma chamber the early magma pulses feeding the chamber will have a similar temperature and composition to the magma within the chamber as there hasn't been enough time for appreciable cooling and fractionation to have occurred yet. Later pulses, however, which enter the chamber differ sharply in temperature and composition to the resident magma as a result of it having undergone extensive cooling and fractionation. An even larger temperature and composition contrast between the two magmas will force the system further into the chromite phase field resulting in a layer of chromitite being produced (Campbell and Murck, 1984).

Application of Irvine's 1977 Magma Mixing Model to the UG2 Cyclic Unit

Although the UG2 chromitite doesn't itself occur at the base of the UG2 cyclic unit, the base of the cyclic unit is still marked by a chromitite stringer. The reason why the UG2 occurs some 5 m above the base of the cyclic unit is most likely a result of one of two reasons:

(1) cyclic unit stratigraphy exhibits a slight time delay in representing magma chamber processes, or

(2) the UG2 cyclic unit was built up from not just one single large injection but rather from a number of smaller magma pulses.

The second reason above is favoured here and it is believed that the intricate detail in both stratigraphy and geochemistry through the study succession can only be explained by an evolving resident liquid within the chamber which is added to by a number of smaller injections during its evolution.

Another point is that potholes are common in the UG2 (i.e. Hahn and Ovendale, 1994) thereby implying that the base of the UG2 chromitite is an angular unconformity and that pre-existing layers of norite and/or anorthosite at the top of the underlying cyclic unit may have been partly or completely eroded away, as in the case of the Merensky Reef. An example is that the anorthosite found by Mathez and Mey (2005) in the immediate footwall to the UG2 could represent the remnant of a pre-existing, now almost completely eroded anorthosite unit at the base of the UG2 (and not a xenolith as suggested). This would lend itself to reason number 2 as described above.

This then means that the evolving Bushveld chamber would have been crystallizing out the UG1 anorthosite when a number of minor magma pulses were injected into the chamber (Nex, 2004). The crystallizing system was then forced into the chromite field for a short period, resulting in a small chromitite stringer being crystallized out (i.e. Irvine, 1977; Naldrett, 1989). Chromite crystallization then drove the

system back into the orthopyroxene phase field from where it resumed orthopyroxenite crystallization. During this time the basal feldspathic pyroxenite unit would have been built up.

The system was then forced back into the chromite phase field either by a single large injection of magma or by a build up of smaller pulses injected into the chamber during the formation of the basal pyroxenite (Irvine, 1977) (Figure 11.3). The UG2 chromitite was therefore most likely a result of a build up of several smaller magma pulses (not of sufficient volume to force the system into the chromite phase field) (i.e. von Gruenewaldt *et al.*, 1990). This process is in line with Hiemstra's (1985) elegant model for the precipitation of chromite in the UG2 from successive influxes of magma streaming into the chamber as thin sheets. The system would have been forced into the chromite phase field (further than the previous occurrence, therefore producing a larger amount of chromite) resulting in chromite crystallization to form the UG2 layer (Irvine, 1977).

The chromite crystals, once formed, descended to the floor of the chamber, due to their greater density compared to the silicate melt (Kinnaird *et al.,* 2002). The chromite slurry then moved away from the source as a turbidity flow (Kinnaird *et al*., 2002). This flow could have spread across the entire current chamber floor and therefore would explain the vast lateral persistence of the layers (Kinnaird *et al.,* 2002). The mixed liquids would have been in disequilibrium with the floor cumulates and would have eroded the footwall to form an unconformity (Kinnaird *et al.,* 2002).

Crystallization solely of chromite would have then forced the system back into the orthopyroxene field, where orthopyroxenite crystallization resumed.

The hanging wall sequence therefore represents a classic continuous evolving fractionating open magma system in which normal evolutionary cooling and fractionation processes were punctuated by small, sharp injections of primitive magma resulting in the formation of chromitite stringers (i.e. Irvine, 1977; Eales *et al.,* 1990). The presence of a reverse fractionation trend at the level of the UG2 leuconorite (Sections 3 and 4) as opposed to a normal trend as exhibited by the lower portion of the UG2 unit, suggests an increase in the amount and size of the magma injections into the chamber during the formation of the unit.

10.5.2 The Petrogenesis of the Footwall Pegmatoidal Feldspathic Pyroxenite Units

The formation of pegmatoidal feldspathic pyroxenite units in layered intrusions is another debated issue. Nevertheless in attempting to unravel the geological history of the study succession the footwall pegmatoidal feldspathic pyroxenite unit(s) below the UG2 also need explaining.

Firstly, as mentioned in Section 3, there are generally two distinct units of pegmatoidal feldspathic pyroxenite (although there can also be just one unit) below the UG2 chromitite. Its main features are its texture and coarse grain size, and it comprises large (1 – 5 cm) orthopyroxene oikocrsysts in a matrix of fine grained plagioclase feldspar. Also present are scarce clinopyroxene oikocrsysts as well an abundance of

accessory phases i.e. phlogopite, hornblende, apatite, quartz and orthoclase. These units are also highly irregular and have sinuous top and bottom contacts.

Bodies of mafic/ultramafic pegmatoidal feldspathic pyroxenites are common in layered intrusions – especially below layers of massive chromitite or anorthosite (Jackson, 1970). Jackson (1961) noted that the thickness and grain size of the pegmatites are loosely related to the thickness of the overlying chromitite. Mathez and Mey (2005) compared the UG2 footwall pegmatoidal pyroxenite to a pegmatite within the Stillwater Complex, namely Hess's (1960) 'pillow troctolite'. They note that, like the UG2 footwall pegmatoidal feldspathic pyroxenite units the troctolite exists below a massive, essentially monomineralic layer (anorthosite in the Stillwater case), are laterally vast and possess a sinuous and discordant contact with the underlying gabbro (Mathez and May, 2005). McCallum *et al.,* (1977) proposed that the troctolite formed as a result of incongruent melting of pyroxene and crystallization of olivine due to invasion of the gabbro protolith by a hydrous mobile phase, which had ponded below the relatively impermeable anorthosite.

Cawthorn and Barry (1992) rejected the ponding of hydrous melt/fluid and consequent recrystallization below the UG2 chromitite on the basis that the pegmatoidal feldspathic pyroxenite has a similar bulk composition to the surrounding feldspathic pyroxenites and that it should contain higher concentrations of incompatible elements if it represents a zone metasomatized by an evolved melt. They proposed that the UG2 chromitite marked an influx of new magma and that the pegmatoidal feldspathic pyroxenite formed as a result of the injection of hot magma into a chamber with a cooler floor (Cawthorn and Barry, 1992). They suggest that the solidified floor partially melted, and the partially molten layer then remained as a mixture of crystals plus liquid for a longer period of time to allow larger crystals to grow (Cawthorn and Barry, 1992).

But, as Mathez and May (2005) explain, this theory does not explain the discordant and highly sinuous contact between the pegmatoidal feldspathic pyroxenite and the regular feldspathic pyroxenite units. The author suggests that, based on field relations as well textural and geochemical evidence, the model of Mathez and May (2005) in which a hydrous melt percolated up through the partially molten crystal pile (driven by compaction), and then ponded beneath an impermeable UG2 chromitite and metasomatized and partially melted the surrounding rocks, which later cooled to form the pegmatoidal feldspathic pyroxenite unit(s), stands firm. Mathez and May (2005) used phase relational evidence (specifically the presence of water) to show why an upward percolating liquid may melt its way through an orthopyroxene – dominated assemblage and won't react with a plagioclase-cemented chromitite. This can be used to explain why the UG2 chromitite was an impermeable barrier to the flow of interstitial melt in the compacting Bushveld crystal pile, and why such a well developed pegmatoidal feldspathic pyroxenite unit exists at its base (Mathez and May, 2005). They also suggest that the melt composition was continuously buffered by its continuous reaction with the surrounding mineral assemblage thereby resulting in a similar bulk composition to the original feldspathic

pyroxenite (Mathez and May, 2005). Therefore, instead of becoming evolved in terms of major elements the melt became enriched in incompatible trace elements, including water (Mathez and May, 2005).

Therefore the footwall pegmatoidal feldspathic pyroxenite most likely represents a pooling of interstitial liquid and later metasomatization and recrystallization of the primary orthopyroxenite. Sometimes, however this unit does not exist directly beneath the UG2 chromitite, or whilst one unit does exist beneath it, another one occurs a few metres below it. Therefore, although the UG2 chromitite did act as an impermeable barrier which resulted in a 'pooling' of interstitial liquid, this did not necessarily occur everywhere. Where the top unit is not directly below the chromitite and where the bottom pegmatoidal feldspathic pyroxenite unit exists shows that the upward percolating melt may just have been slowed and eventually halted within the feldspathic pyroxenite, and slowly start to metasomatize and recrystallize the surrounding rock. It is likely that this rising melt may have begun to slow down, either due to advanced crystallization of the cumulate pile or simply due to a lack of upward velocity. Once the fluid started to slowly metasomatize and recrystallize the surrounding protolith, the upward ascent of the liquid would have slowed inititally and then halted altogether. Therefore the metasomatizing and recrystallizing fluid at the top would, itself, have acted as an impermeable barrier to upward rising fluid below.

This theory provides an explanation for the position and location of the pegmatoidal feldspathic pyroxenite units and, importantly, why its contacts, especially the bottom contact, with the surrounding feldspathic pyroxenite are so sinuous and discordant. The collection and ponding of an upward rising fluid would produce a highly sinuous bottom contact (with large variations and 'fingers') as is indeed observed in the field relations. The ponding of a fluid beneath the UG2 also certainly explains why the pegmatoidal feldspathic pyroxenite is almost as laterally vast as the UG2 itself. It has also seen evidence, in drill core from the north-eastern Bushveld, many examples of pooling of pegmatoidal feldspathic pyroxenites beneath large, well developed chromitite layers below the UG2. These smaller layers, although not as large as the UG2, would also prove impermeable to an upward moving melt and would result in pooling, metasomatzation and recrystallization to produce a pegmatoidal feldspathic pyroxenite directly below it. The fact that pegmatoidal feldspathic pyroxenite units are found below footwall chromitites, where larger footwall chromitite layers exist, provides direct evidence that the pegmatoidal feldspathic pyroxenites are a product of an upward percolating melt.

This mechanism can also be used to explain both the presence of large amounts of disseminated chromite in the footwall directly below the UG2, as well as the highly sinuous nature of the BRC as opposed to the TRC. It is envisaged that fragments of the dense chromitite may have collapsed into the less dense melt-rich zone accumulating below (Cawthorn and Barry, 1992, Mathez and May, 2005). This explains the large amount of disseminated chromitite in certain areas as well as the sinuous BRC - as fragments from the

bottom portion of the UG2 gradually collapsed into the melt, the previously regular BRC would appear more sinuous and discordant.

10.5.3 An Overall Petrogenetic Model for the UG2 Cyclic Unit

The petrogenesis of the UG2 cyclic unit represents a combination of primary and secondary magma chamber processes. By studying the field relations, textures and geochemical profile of the unit we have been able to interpret and unravel the processes occurring within the Bushveld chamber at that time.

Major findings include the suggestion that the UG2 cyclic unit was built from a number of magma injections into the chamber, and not just one large intrusion. The building up of the UG2 cyclic unit is therefore an excellent display of the dynamic interplay between injections of fresh magma and the overall evolution of the resident chamber liquid. It can also be said that the UG2 cyclic unit represents a combination of both primary and secondary magmatic processes. Whilst the crystal pile was cooling, a hydrous melt was forced up through the cumulate rocks to eventually slow, possible pond beneath an impermeable layer (i.e. the UG2) and then metasomatize and recrystallize the surrounding rock to form the secondary pegmatoidal feldspathic pyroxenite units. This process happened after the UG2 cyclic unit had been formed and was partially crystallized.

In conclusion, the UG2 cyclic unit represents a dynamic interplay of evolving, cooling and fractionating resident liquids within the chamber along with repetitive influxes of fresh, undifferentiated primitive magma. These primary processes were then superseded by later secondary processes of compaction, metasomatization and recrystallization to form the pegmatoidal feldspathic pyroxenite units.

11. Conclusions

11.1 Introduction

The final conclusions and results for the entire project are listed in a summarized format here. These constitute the major findings from the project. Finally, all the results are integrated and used to form a model of petrogenesis for the formation of the UG2 cyclic unit as well as a model of mineralization for the PGE mineralization within the UG2 ore body.

11.2 Summarized Results

Underground mapping carried out at the Atok Mine revealed that:

- The UG2 chromitite exists as a ~60 cm thick layer which is underlain by a pegmatoidal feldspathic pyroxenite unit and is overlain by a medium grained feldspathic pyroxenite.
- Irregular zones of recrystallized euhedral coarse chromite exist throughout the UG2 against a background of fine grained chromite.
- The planarity of the top and bottom reef contacts differ greatly with the top reef contact highly planar whilst the bottom reef contact is irregular, sinuous and often contains micropotholes.
- The footwall pegmatoidal feldspathic pyroxenite is highly irregular and often exists as the direct footwall to the reef. There are also often two units of pegmatoidal feldspathic pyroxenite below the UG2.

Surface field mapping of a weathered road outcrop at Atok showed that:

- The highly weathered nature of the outcrop assisted in identifying distinct individual units within seemingly monotonous sequences. This is due to the weatherability of the lithologies being a direct function of its pyroxene:plagioclase ratio (i.e. the amount of interstitial plagioclase present). In this respect the hanging wall feldspathic pyroxenite was seen to be more mafic (higher pyroxene:plagioclase ratio) than the footwall feldspathic pyroxenite unit. The hanging wall sequence also shows slight variations in pyroxene:plagioclase ratio across the chromite stringers – confirming the hanging wall pyroxenite sequence to be composed of several individual units bound by chromite stringers.
- The UG2 itself appears bifurcated and comprises numerous lenses. The weathering has affected the UG2 by oxidizing the base-metal sulphides (producing copper staining) as well as by accentuating a nodular texture in the chromitite. This texture comprises oikocrysts of orthopyroxene and chromite which have formed resistant, circular nodules which stand out against the more friable, fine-grained matrix.

- The UG3, however, differs from the UG2 by not containing any nodular type texture or any sulphide oxidation. Overall, the UG3 also contained no lenses (in contrast to the UG2) and it exists as a solid planar band of fine-grained chromite.
- The highly weathered hanging wall gabbronorite sequence is seen to contain a relatively high amount of interstitial material (with a lower pyroxene:plagioclase ratio).

An investigation of the UG2 cyclic unit stratigraphy using fresh drill core material from borehole ZG219 proved highly complementary to the fieldwork carried out on predominantly weathered outcrop. The geological logging allowed visual traits to be identified whilst the density measurements provided quantitative information and allowed the accurate identification of trends in seemingly monotonous sequences. The final conclusions include:

- The geological logging revealed the cores to contain a strongly differentiated cumulate package comprising the topmost portion of the UG1 cyclic unit, as well as the entire UG2 cyclic unit. Both cyclic units exhibit normal fractionated sequences, i.e. an upward evolving sequence that tends to become more felsic further upsection, and both display an upward evolving lithological sequence of chromitite→feldspathic pyroxenite→gabbronorites→anorthosite. Several mm scale chromite stringers have also been identified in the hanging wall feldspathic pyroxenite. Subtle changes in texture, crystal size and pyroxene:plagioclase ratio were seen to occur across these chromite stringers in the pyroxenite.
- The density measurements revealed the overall UG2 unit to display a normal fractionation trend (as defined by a normal density trend), although, superimposed on this overall normal fractionation trend are a number of well developed local trends present with certain individual units i.e. The UG2 hanging wall lower and middle feldspathic pyroxenite, and UG2 gabbronorite, units also display well developed local normal fractionation trends. Above the hanging wall middle feldspathic pyroxenite, however, the UG2 leuconorite shows a well developed reverse fractionation trend – possibly indicating increased magma injections into the chamber at this level.
- The variation in density regularity of the hanging wall units compared with the footwall units (ie. The footwall units display relatively constant density variations whilst the hanging wall exhibits a more ragged, irregular profile) possibly indicates an increased intensity of magma replenishment during the formation of the hanging wall sequence. The denser, and hence more mafic, character of the hanging wall feldspathic pyroxenite units compared with the footwall units could also indicate that the hanging wall sequence is a crystallization product of a larger, more primitive magma batch – possible at the level of the UG2.

The petrography portion of the study showed:

- The dominant cumulus minerals found in the lithologies to be orthopyroxene, plagioclase and clinopyroxene with accessory phases such as phlogopite and chromite also present. Modally there is a series ranging from pure plagioclase cumulates (anorthosites) through progressively more mafic, pyroxene-rich leuconorites, norites and eventually feldspathic pyroxenites which still contain ~10 % plagioclase. Apart from the modal abundances there are also pronounced variations in crystal size and the general texture between the different lithologies. Certain units also show slight variations in these characteristics up through the unit (defining possible fractionation trends).

The main aim of the whole-rock geochemical analysis was to provide a continuous geochemical profile through the entire mother hole drill core. The behaviour of the major and trace elements were investigated through the study section. The elemental profile patterns were then used to investigate the processes occurring within the chamber during the formation of the UG2 unit. The whole rock geochemical analysis revealed the following:

- The major element profiles are seen to define a lower normal fractionation trend (which straddles the UG1 – UG2 boundary) and an overlying reverse fractionation trend (at the level of the UG2 leuconorite).
- The UG2 footwall feldspathic pyroxenite and the UG1 leuconorite units both show enriched incompatible element abundances due to their high proportion of trapped intercumulus liquid (with the UG2 footwall feldspathic pyroxenite containing the highest abundance of trapped liquid in the study section and the UG1 leuconorite the second most).
- The base metals plus sulphur (Cu, Ni and S) all show strong relationships with each other and define elevated levels of mineralization within the UG2 chromitite, the hanging wall chromitite stringers and, to a lesser extent, the footwall pegmatoidal pyroxenite.

One of the major aims of this project was the presentation of high precision PGE compositional data for 54 closely spaced samples from throughout the ZG219 MH ‘ore zone’ (which refers to the UG2 chromitite, its footwall pegmatoidal feldspathic pyroxenite unit, as well as the hanging wall lower feldspathic pyroxenite unit, including the chromitite stringers). This allowed a detailed study of the PGE mineralization within the UG2 ore zone, and also allowed a possible mineralization model to be formulated. The high precision PGE analysis revealed:

- The PGE + Au grade to be concentrated in a (bottom loaded) triple peaked profile pattern through the ore zone.

- The individual PGE profiles differ somewhat from each other, although all show a strong bottom peak (at the bottom reef contact) and an upper peak at the top reef contact (separated by a zone of lower abundance).
- The base metals plus sulphur distribution is similar to the PGE + Au pattern apart from the bottom peak which is slightly higher up than the PGE + Au bottom peak.
- The individual base metals plus sulphur (Cu, Ni and S) show an almost identical pattern as the total base metal plus sulphur pattern (Cu + Ni + S).
- High precious metals tenors, expressed on a relative basis as ((PGE + Au)/S) exist in the footwall and also occur as three distinct peaks within the chromitite. These three peaks correlate directly with the troughs in the Cu, Ni and S profiles through the chromitite. There is also a systematic upward decreasing trend through the chromitite and the hanging wall. This trend is reversed midway up through the hanging wall pyroxenite.
- The individual PGE and Au tenors show similar patterns with three peaks present within the chromitite although Pd, Au and Rh have a stronger bottom peak whilst the other PGE have larger middle peaks.
- The ratio (Pt + Pd + Rh)/(Os + Ir + Ru) shows a peak in the footwall as well as the characteristic triple peaks within the chromitite. There is a systematic upward increase through the upper portion of the chromitite up to the UT2 stringer. A trough then exists followed by a second upward increasing trend through the hanging wall pyroxenite.
- The Pt/Pd ratio shows a sawtooth type profile with the three peaks present within the chromitite, although the bottom peak is slightly higher than for the previous plots. There is a systematic upward decreasing trend through the upper portion of the chromitite up to the UT2 with the overlying hanging wall pyroxenite exhibiting relatively high values.
- The chondrite normalized PGE patterns reveal four sets of pattern types (lithologically related). The UG2 chromitite shows the most constrained pattern whilst the pegmatoidal pyroxenite and, especially, the hanging wall pyroxenite, show a larger variation. Pd forms the peak element for the UG2 chromitite, the UT1 stringer and the hanging wall pyroxenite whilst Rh is the peak for the pegmatoidal pyroxenite and stringers UT2 – 4.
- There is a negative correlation between the PGE and the Cr_2O_3 abundance (and density). This is related to the textural framework of the rock as the PGE (and BMS) occur interstitially to the chromite in interstitial gaps and thus the more open the packing of the chromitite the less the abundance of Cr_2O_3 and the greater the amount of interstitial PGE and BMS.
- The base metals plus sulphur show very strong positive correlations with each other.

- Of the PGE only Pd and Au show strong correlations with the base metals plus sulphur. This is attributed to their stronger chalcophile character. The remaining PGE are all more siderophile in nature and show poor to average correlations with the base metals plus sulphur and good overall relationships with each other.

11.3 Discussion

This section is a discussion of the features summarized in 11.2 and is an attempt to construct a suitable petrogenetic model for the UG2 unit. A final model is then provided and is described in detail in section 11.4.

11.3.1 A Single Chromitite Petrogenesis and PGE Mineralization Model

The close association of chromite and PGE along with the fact that all chromitite layers are enriched in PGE relative to the host rocks (Kruger, 2002) leads the authour to believe that their presence may be the result of a single, dynamic process. It is problematic trying to apply one model to account for chromitite petrogenesis and another separate model for PGE mineralization genesis and then to try and have them coincide during the formation of the Critical Zone. Therefore a suitable model to account for UG2 style chromitite hosted PGE mineralization needs to incorporate, and be able to account for, both the mechanism of chromitite petrogenesis and the genesis of the PGE mineralization. Although the LG, MG and UG1 and UG3 layers are not as enriched in PGE as the UG2 they are still enriched compared to the host silicate rocks (Kruger, 2002).

11.3.2 Discussion on Chromitite Petrogenesis in Layered Intrusions

Several models have been proposed for the formation of chromitite layers (summarized in chapter 10). These include: (1) Mixing between a resident and a new magma within the chamber (Irvine, 1977); (2) Contamination by a siliceous component (Irvine, 1975); (3) Pressure changes within the chamber (Cameron, 1977); (4) Increases in oxygen fugacity by country rock degassing (Cameron and Desborough, 1969); (5) Gravity induced separation, crystal sorting and settling (Wager and Brown, 1968); (6) Immiscibility of a Cr-rich liquid (Sampson, 1932) and (7) Lateral growth with a stratified magma column (Irvine *et al*, 1983). All these models have certain advantages and drawbacks and are fully summarized in Chapter 10. The main features which a mechanism of chromitite petrogenesis needs to account for is, firstly, the vast lateral extent of the chromitite layers (i.e. Cawthorn, 1999) i.e. the process must be able to operate affectively on a regional (chamber wide) scale. Secondly the close association of chromitite layers with cyclical layering (i.e. Naldrett *et al.*, 1983) needs to be accounted for. Although there are several other important features these, according to the authour, are the most important and require explanation when forming a petrogenetic model.

Although several models have previously been proposed for the petrogenesis of chromitite layers the two most favoured models are that of magma mixing (i.e. Irvine, 1977) and crustal contamination (i.e. Irvine, 1975). Both these models work similarly in that they both produce a sharp compositional contrast, and it is this sharp compositional contrast which is believed to force the magmatic system into the chromite phase field

(i.e. Irvine, 1977). The most recent model (Kinnaird *et al*., 2002) attempts to combine both mixing of a newly injected magma into the chamber with residual magma along with contamination by the roof rock (Rooiberg felsites) melt. The result is a three way compositional contrast (residual magma, new primitive magma and roof rock melt) which is suggested to have initiated chromite superaturation (Kinnaird *et al.*, 2002). The authour has reservations about the ability of such a contamination process to occur on a basin wide scale and to produce chromitite layers of such a vast lateral extent and also of such a uniformity as that of the Bushveld chromitites. The author believes Irvine's 1977 magma mixing model to hold true and believes it is the only model which can explain all the features displayed by the Bushveld chromitites:

Evidence suggesting that magma mixing was responsible for the formation of the chromitite layers include the fact that the chromitite layers are intimately associated with cyclical layering (Naldrett *et al.,* 1983) and often occur at, or near, the base of cyclic units (Campbell and Murck, 1984). Cyclic units are thought to represent a new influx of magma into the chamber (i.e. Jackson, 1970; Naslund and McBirney, 1996). Therefore the formation of chromitite layers must be closely associated with new influxes of magma into the chamber. The presence of potholes, which have been recently suggested to be the result of a downward collapse of crystal mush into pull-apart sites resulting from tensional deformation due to the loading affects of major new magma additions (Carr *et al*., 1999), within the UG2 chromitite layer have also been observed and mapped by the authour, and documented by Mathez and Mey (2005) in the study area. Studies on the bifurcations of the UG1 (Nex, 2004) and also the fact that often the Eastern Bushveld UG2 can be separated into a lower and an upper layer on the basis of distinct textural and modal differences (von Gruenewaldt *et al*., 1990) suggest that the formation of thick chromitite layers may have been episodic rather than a single event. Although texturally and petrologically the Atok UG2 appears uniform, the distinct triple-peaked base metal sulphide and platinum group element mineralization pattern (Figure 7.2) lends itself to a multi-influx magma mixing process to account for the PGE mineralization.

Although local chromite crystallization may be initiated by magma contamination from country rock xenoliths (i.e. Kinnaird e*t al*., 2002; Mathez and Mey, 2005), it is questionable whether this process can occur on a scale the size of the Bushveld chamber and be able to generate such laterally vast, continuous chromitite layers. The author is therefore in favour of Irvine's 1977 magma mixing model and suggests repeated, episodic magma influxes into the chamber to have initiated chromite crystallization and hence formed the chromitite layers (Eales *et al.,* 1988). Indeed repeated influxes of silicate magma into the chamber during Lower and Critical Zone development has been suggested to have occurred by Eales *et al*., (1990) on the basis of cycles of increasing Mg # in pyroxene. Therefore the proposed model for the formation of chromitite layers corresponds well to the overall suggestion (by Eales *et al.,* 1990) for the petrogenetic evolution of the Lower and Critical Zones.

11.3.3 Discussion on PGE Mineralization Mechanisms in Layered Intrusions

A variety of models have been proposed to account for PGE enriched layers in layered intrusions and these can largely be divided into (1) a primary magmatic model in which the PGE are removed from the melt early on, and (2) late-stage remobilization, modification and precipitation of the PGE by upward moving magmatic fluids.

The Merensky and UG2 Reefs have been suggested by some (Ballhaus and Stumpfl, 1986; Boudreau and McCallum, 1992) to have undergone hydrothermal PGE enrichment at a late stage. There are several textural and mineralogical factors which suggest a late-stage hydrothermal origin for the PGE, including the presence of pegmatitic textures, intergrowth of sulphides with intercumulus volatile-rich phases, high Cl content in volatile-bearing phases, and association with graphite and fluid inclusions (Barnes and Campbell, 1984; Ballhaus and Stumpfl, 1986). Campbell and Barnes (1984) explain how these textures and mineral associations are not the result of hydrothermal processes but rather the result of late-stage modification and remobilization by postcumulus processes in the orthocumulate layers. The close association of these two PGE rich layers with the bases of cyclic units (i.e. Naldrett *et al.,* 1983) and with chromitite concentrations (which is hereby suggested to have a genetic relation to new magma influxes) (Scoon and Teigler, 1994; Eales *et al.,* 1993), the great lateral persistence and uniformity of grade of both the Merensky Reef and the UG2 chromitite (Cawthorn, 1999), and the systematic stratigraphic controls on PGE tenors of sulphides within the Upper Critical Zone of the Bushveld Complex, particularly within the UG2 chromitite (Naldrett *et al.,* 1986; Hiemstra, 1985, 1986) leads the authour to believe that the PGE concentrations of the UG2 chromitite and the Merensky Reef are both a result of primary magmatic cumulus processes, whilst the observed hydrothermal features are the result of late stage postcumulus processes superimposed on these two layers (Barnes and Campbell, 1984). Another factor which disproves the hydrothermal model of PGE enrichment in the Bushveld Complex is the presence of the Platreef layer near the base of the complex and also the close stratigraphic spacing of several PGE enriched (compared to the host rock) chromitite layers in the Critical Zone (Kruger, 2002).

The close mineralogical association of the PGM with the BMS (see chapter 8) also suggests the PGE were scavenged by a downward percolating exsolved sulphide melt (from which they later crystallized out) (i.e. Naldrett, 1989). This orthomagmatic model in which an immiscible sulphide phase separating from a silicate magma scavenged base and precious metals (Campbell *et al.*, 1983; Maier and Barnes, 1999; Naldrett, 1983a; Naldrett, 1983b) is favoured by the authour. Frequent influxes of new magma into the chamber, and the subsequent mixing of the resident and new magmas, is suggested to have initiated sulphur supersaturation (Naldrett *et al.,* 1983; Naldrett and von Gruenewaldt, 1989). Although details of this model need fine tuning and various forms of evidence need explaining, such as phase diagram geometry (Cawthorn, 2002) and the presence of sulphur undersaturated cumulates above the UG2 layer (Cawthorn, 1999), the authour still favours

the magma mixing model due to its ability to produce a very high R-factor value (Campbell and Naldrett, 1979), and the fact that if it initiated both chromite crystallization and sulphur supersaturation (which produced a segregated sulphide phase which then scavenged base and precious metals) then it explains the close association of chromitite layers with elevated PGE abundances (i.e. Kruger, 2002). The intimate mineralogical association of PGM with BMS in the UG2 (chapter 8) is direct evidence that the PGE were most likely scavenged by a sulphide melt (with those PGM found enclosed in or at the boundary of silicates suggested to be the result of low temperature re-equilibration). Although details on what triggered sulphide supersaturation remain vague it is clear that magma mixing processes had an integral role to play due to the close association of chromitite layers and enriched PGE abundances

11.3.4 Linking Chromitite Petrogenesis and PGE Mineralization Using a Single Model

Repeated, episodic influxes of magma into the chamber occurred during the formation of the lower and critical zones (Eales *et al.,* 1990). The process of magma mixing has hereby been suggested to be able to initiate chromite crystallization and therefore be responsible for the formation of chromitite layers (Irvine, 1977). In terms of PGE mineralization, the close association between chromite layers and PGE enrichments (Kruger, 2002) suggest that a single, dynamic process be responsible for both. It is clear, due to the close mineralogical association of the PGM and BMS (chapter 8), that the PGE were most likely scavenged and extracted from the silicate magma by a sulphide melt (i.e. Naldrett, 1989), and although various finer details need to be clarified, such as phase diagram geometry (Cawthorn, 2002), and why the cumulates above are sulphur undersaturated (Cawthorn, 1999), the results of this work show that the process of sulphur supersaturation must have been intimately linked with magma mixing. The model of magma mixing would then be able to initiate both chromite crystallization, and therefore form the chromitite layers, and sulphur supersaturation (due to the sharp compositional contrast produced by the mixing). The segregated sulphide melt would then percolate down through the silicate magma and scavenge base and precious metals (i.e. Naldrett, 1989), with the resulting metal impregnated sulphide melt eventually being caught up in the chromite slurry at the base of the chamber (and hence would be intimately linked with the formation of the chromitite layer) (Kinnaird *et al.,* 2002).

Kinnaird *et al.,* (2002) suggest magma mixing to have initiated both chromite and PGM crystallization. This, however, does not explain the close mineralogical link with the PGM and the BMS (see chapter 8). The authour therefore believes the magma mixing process would have initiated chromite crystallization and also sulphur supersaturation. The PGE and base metals, which are present in the silicate liquid, would then have been scavenged by the downward percolating segregated sulphide melt (Naldrett, 1989). This would therefore explain both the close association between PGE and chromitite layers and, especially, the mineralogical relationship between the PGM and BMS (which can not be explained using the Kinnaird *et al.,* 2002 model). Kinaird *et al.,* (2002) then suggest the PGM to be incorporated into a chromite slurry on the floor of the

chamber. The authour agrees with this model however suggests that it was the downward percolating metal-impregnated sulphide melt which was incorporated into the chromite slurry, and not simply just PGM. The sulphide enriched chromite slurry (the sulphide itself enriched in metals) then moved away from the source as a turbidity flow (Kinnaird *et al.,* 2002). This flow could have spread across the entire current chamber floor and would therefore explain the vast lateral persistence and uniformity (both in terms of structure but also grade – due to the metal-impregnated sulphide melt having been well 'mixed' with the slurry). The mixed liquids would have been in disequilibrium with the floor cumulates and would have eroded the footwall to form an unconformity (Kinnaird *et al.,* 2002).

It is also suggested that the UG2 layer be made up not of a single influx event but of three successive magma influxes. This would explain the distinctive triple peaked metal mineralization profiles. The chromite stringers in the hanging wall would have been formed in the same way but would represent only a single, much smaller magma influx. Finally, a late-stage postcumulus component is suggested to have had a modifying affect on the mineralized layers (especially the textural and mineralogical characteristics of the layers).

11.3.5 Final Proposed UG2 Cyclic Unit Petrogenetic Model

The final petrogenetic model for the UG2 cyclic unit is described here in detail:

It is envisaged that the evolving Bushveld chamber would have been crystallizing out the UG1 anorthosite (Nex, 2004) when a number of minor magma pulses were injected into the chamber (i.e. Eales *et al.,* 1990). The crystallizing system would have then been forced into the chromite field for a short period, resulting in a mm scale chromitite stringer being crystallized out (i.e. Irvine, 1977; Naldrett, 1989) (Figure 11.1). This chromitite stringer forms the base of the UG2 cyclic unit.

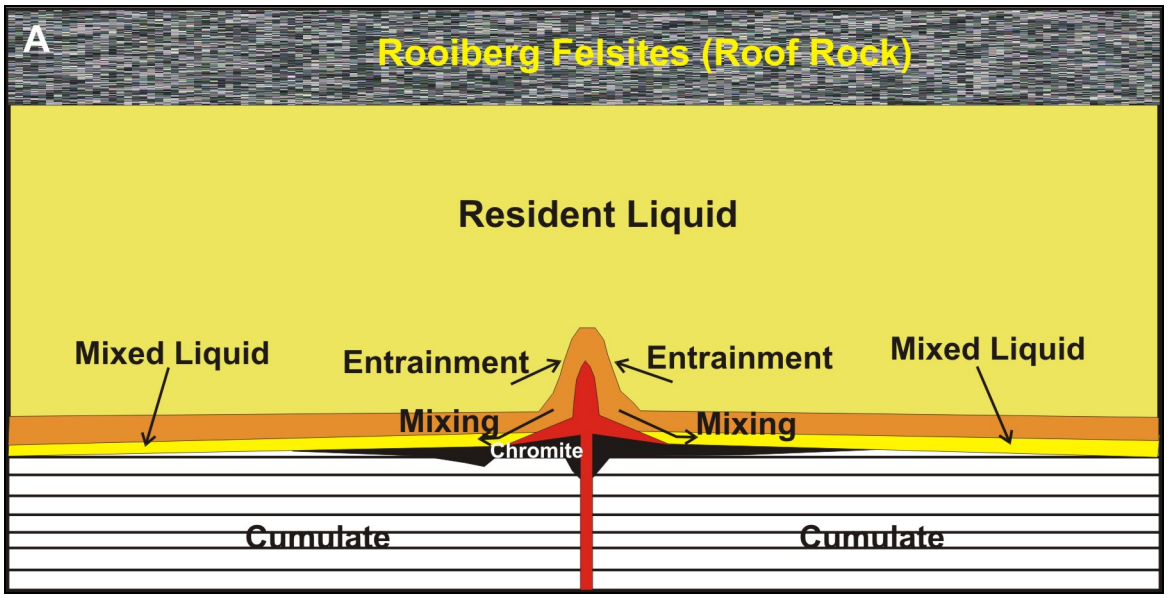

Figure 11.1: The beginning of the UG2 cyclic unit: An initial injection of magma nto the Bushveld chamber initiates chromite crystallization, resulting in the formation of a chromitite stringer which forms the base of the UG2 unit (modified after Kinnaird et al., 2002).

Chromite crystallization then drove the system back into the orthopyroxene phase field from where it resumed orthopyroxenite crystallization (Irvine, 1977). During this time the UG2 footwall feldspathic pyroxenite unit would have been built up (Figure 11.2)

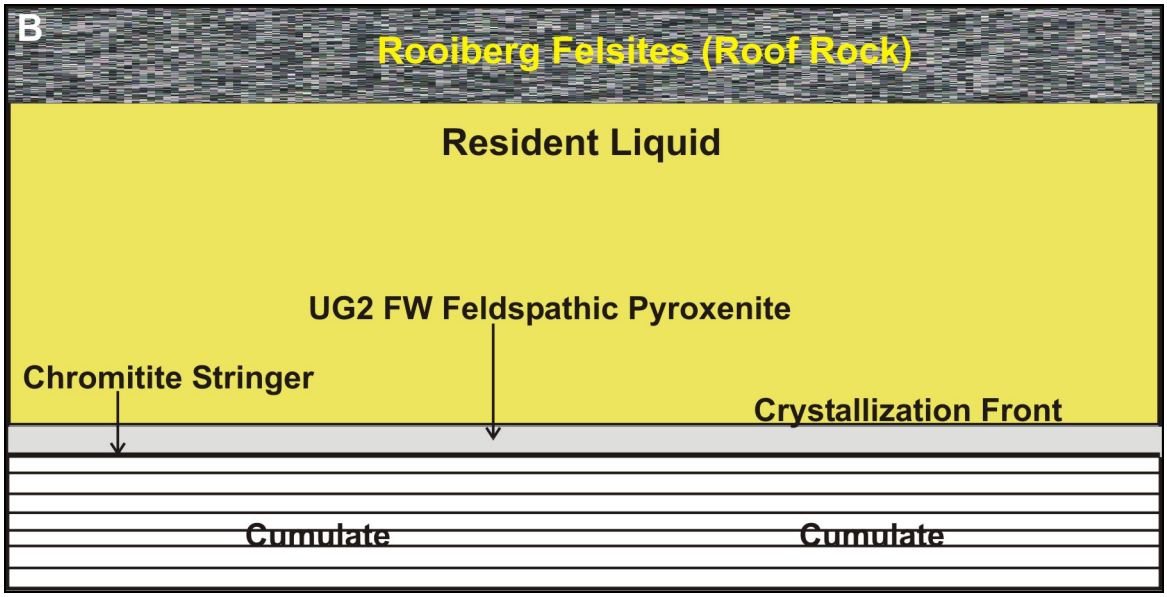

Figure 11.2: Following the initial injection of magma a period of acquiescence occurred during which time the magmatic system continued to evolve and the UG2 footwall feldspathic pyroxenite unit was formed (modified after Kinnaird et al., 2002).

The system was then forced back into the chromite phase field either by a single large injection of magma or by a build up of smaller pulses injected into the chamber during the formation of the basal pyroxenite (Irvine, 1977) (Figure 11.3). The UG2 chromitite was therefore most likely a result of a build up of several smaller magma pulses (not of sufficient volume to force the system into the chromite phase field) (i.e. von Gruenewaldt *et al.*, 1990). The system would have been forced into the chromite phase field (further than the previous occurrence, therefore producing a larger amount of chromite) resulting in chromite crystallization to form the UG2 layer (Irvine, 1977). The chromite crystals, once formed, descended to the floor of the chamber, due to their greater density compared to the silicate melt (Kinnaird *et al.,* 2002).

The influx of magma into the chamber, and subsequent mixing, would, along with causing chromite crystallization, have initiated sulphur supersaturation (Naldrett *et al*., 1983; Naldrett and von Gruenewaldt, 1989). The segregated sulphide melt then percolated down through the silicate magma and scavenged base and precious metals (Naldrett, 1989). This is confirmed by the intimate mineralogical association of the PGM with BMS in the UG2 (chapter 8). The metal impregnated sulphide liquid would then eventually reach the floor of the chamber where it would be caught up and mixed with the chromite slurry (Kinnaird *et al.,* 2002).

At magmatic temperatures the segregated sulphide melt, enriched in PGMs, would have begun to crystallize *mss* (monosulphide solid solution) (i.e. von Gruenewaldt *et al.,* 1989). As the temperature dropped

the *mss* converted into pyrrhotite and pentlandite (i.e. Durazzo and Taylor, 1982). As the temperature dropped further the pyrrhotite exsolved out pyrite which grew as individual, euhedral grains. This is confirmed by the exsolution sulphide textures where pyrite occurs as a rim around pyrrhotite in some cases (see Chapter 8). Therefore the sulphide assemblage is also representative of the original magmatic assemblage. No late stage alteration has affected the sulphide assemblage (with a common low temperature sulphide product being millerite, especially further south in areas of intense local fluid activity) (i.e. Rixom, 2005).

During cooling, the PGE originally incorporated into the *mss* diffused to the sulphide grain boundaries to form PGMs (mainly PGE-sulphides and PGE-tellurides) (i.e. von Gruenewaldt *et al.,* 1986). This explains the close sulphide-PGM association, as well as the propensity of the PGM to be located at phase boundaries (especially triple point junctions) (see Chapter 8). Some of the PGM remained in solid solution in the sulphide phases (i.e. Pd in pentlandite). During this stage, appreciable amounts of Pd and Au partitioned into the BMS minerals (due to their strong chalcophile tendencies) to occur in a solid solution state within the BMS minerals. Therefore, the remaining PGE all partitioned strongly into the PGM. This explains the close relationship between Pd and Au and the BMS as well as the remaining PGE with each other (see Chapter 7). Negligible geochemical evidence for any postcumulus alteration or remobilization exists. This mechanism of mineralization is therefore one of a primary, magmatic origin.

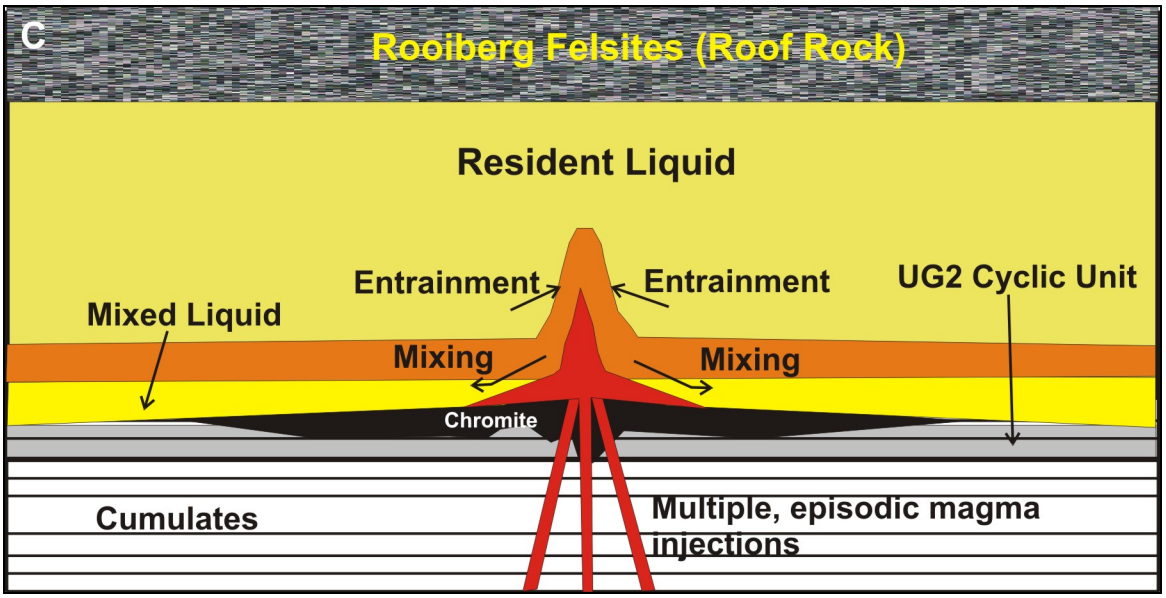

Figure 11.3: The formation of the UG2 layer comprised a sequence of several rapid injections (probably three) of magma into the chamber. The system was forced substantially further into the chromite phase field than for the initial chromitite stringer. This resulted in the ~60 cm thick laterally persisitant UG2 chromitite layer crystallizing out. The magma injections also initiated sulphur supersaturation with the resulting segregated sulphide melt scavenging and extracting base and precious metals from the magma and, eventually, becoming caught up and mixed in with the chromite slurry (modified after Kinnaird et al., 2002).

The sulphide enriched chromite slurry (itself enriched in metals) then moved away from the source as a turbidity flow (Kinnaird *et al*., 2002). This flow could have spread across the entire current chamber floor and therefore would explain the vast lateral persistence and uniformity (both in terms of structure but also grade –

due to the metal-impregnated sulphide melt having been well 'mixed' with the slurry) (Kinnaird *et al.,* 2002). The mixed liquids would have been in disequilibrium with the floor cumulates and would have eroded the footwall to form an unconformity (Kinnaird *et al.,* 2002).

Crystallization solely of chromite would have then forced the system back into the orthopyroxene field, where orthopyroxenite crystallization resumed (Figure 11.4).

The hanging wall sequence therefore represents a classic continuous evolving fractionating open magma system in which normal evolutionary cooling and fractionation processes were punctuated by small, sharp injections of primitive magma resulting in the formation of chromitite stringers (i.e. Irvine, 1977; Eales *et al.,* 1990).

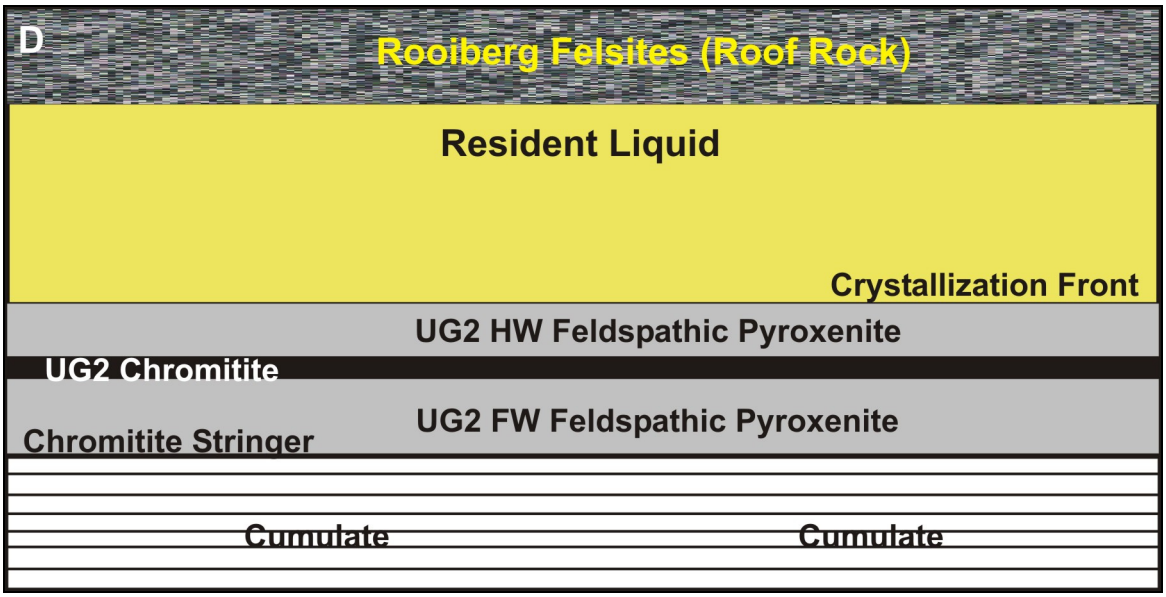

Figure 11.4: Following the formation of the UG2 chromitite layer the magmatic system continued to evolve. The UG2 hanging wall comprises an upward evolving system manifested in the form of a series of feldspathic pyroxenite and norite units. The evolving system was punctuated by a series of minor magma injections (as per Figure 11.1) which resulted in the formation of a series of chromitite stringers (modified after Kinnaird et al., 2002).

Therefore, the UG2 cyclic unit was most likely formed by a number of injections of more primitive magma into the chamber which began mixing within the resident liquid (which crystallized out the UG1 unit) and which began crystallizing the UG2 footwall pyroxenite sequence (i.e. Eales *et al.,* 1990). During the early stages of crystallization of the UG2 unit the resident liquid within the chamber, despite still been replenished by intermittent injections of more primitive magma, as a result of fractional crystallization, trended toward more evolved compositions. This overall normal trend is reflected by local intra-lithological normal fractionation trends within the UG2 footwall and UG2 hanging wall middle and upper feldspathic pyroxenite units.

At the level of the upper contact of the UG2 hanging wall middle feldspathic pyroxenite unit a reversal in fractionation trends occurred. Through the overlying UG2 leuconorite and upper feldspathic pyroxenite

units an upward trend toward more primitive compositions existed (as reflected by a more mafic mineral distribution). This is suggested to represent a period of increased magma addition into the chamber. Therefore the process of magma replenishment of the chamber is suggested at this stage to be the dominant process – as opposed to that of quiescence and fractional crystallization (punctuated by intermittent injections) - during the normal trend. The UG2 unit thus experienced an increased influx of more primitive magma during its formation. Nevertheless, the chromitite layers (including the UG2 and the stringers present in its hanging wall) are suggested to represent injections of batches of more primitive magma into the chamber (as described in chapter 9) (i.e. Irvine, 1977).

The proposed model suggests that the formation of the UG2 unit comprised a multitude of magma injections within the chamber, which increased as the unit developed. In terms of the process of sulphide and PGM mineralization it is envisaged that a segregated sulphide liquid would have scavenged and extracted base and precious metals from the silicate magma as it percolated through (i.e. Naldrett *et al.,* 1983). The metal impregnated sulphide liquid would have then become concentrated in the chromite slurry and become mixed in with the chromite crystals (i.e. Kinnaird *et al.,* 2002).

Once the crystal pile had partially crystallized and the primary processes that were responsible for the building up of the UG2 unit as well as the formation of the PGE mineralization within the UG2 ore body had ceased a series of late-stage, postcumulus processes combined to produce the UG2 footwall pegmatoidal feldspathic pyroxenite unit. Apart from this, it is envisaged that these postcumulus processes had a negligible affect on the primary geochemical and mineralogical signature of the UG2 unit (including the PGE patterns and distributions within the ore zone). Nevertheless, these postcumulus processes were responsible for the formation of the pegmatoidal pyroxenite unit (i.e. the pegmatoidal pyroxenite is hereby suggested to be a result of postcumulus stage recrystallization) as well as a number of other footwall features including the irregular bottom reef contact of the UG2 chromitite and the distribution of disseminated chromite mineralization within the footwall:

It is suggested that, based on field relations as well as textural and geochemical evidence, the model of Mathez and May (2005) in which a hydrous melt percolated up through the partially molten crystal pile (driven by compaction), and then ponded beneath an impermeable UG2 chromitite and metasomatized and partially melted the surrounding rocks, which later cooled to form the pegmatoidal feldspathic pyroxenite unit(s), is favoured. Mathez and May (2005) used phase relational evidence (specifically the presence of water) to show why an upward percolating liquid may melt its way through an orthopyroxene – dominated assemblage but would not react with a plagioclase-cemented chromitite. This can be used to explain why the UG2 chromitite was an impermeable barrier to the flow of interstitial melt in the compacting Bushveld crystal pile, and why such a well developed pegmatoidal feldspathic pyroxenite unit exists at its base (Mathez and May, 2005). They also suggest that the melt composition was continuously buffered by its continuous

reaction with the surrounding mineral assemblage thereby resulting in a similar bulk composition to the original feldspathic pyroxenite (Mathez and May, 2005). This is confirmed by the whole – rock geochemical analysis results of this project (see Chapter 6) which shows the UG2 pegmatoidal feldspathic pyroxenite unit to have a similar chemical composition to the various other feldspathic pyroxenite units found in the UG2 unit.

Therefore, the footwall pegmatoidal feldspathic pyroxenite unit represents a postcumulus recrystallization product of the primary orthopyroxenite lithology which, although texturally very different, is chemically similar to the UG2 footwall feldspathic pyroxenite from which it was derived (as expected). This theory fully explains the position and location of the pegmatoidal feldspathic pyroxenite unit and, importantly, why its contacts, especially the bottom contact, with the surrounding feldspathic pyroxenite are so sinuous and discordant. The collection and ponding of an upward rising fluid would produce a highly sinuous bottom contact (with large variations and 'fingers') as is indeed observed in the field relations. The ponding of fluid beneath the UG2 also certainly explains why the pegmatoidal feldspathic pyroxenite is so laterally persistent below the UG2.

This mechanism can also be used to explain both the presence of large amounts of disseminated chromite in the footwall directly below the UG2, as well as the highly sinuous nature of the bottom reef contact as opposed to the top reef contact. It is envisaged that fragments of the dense chromitite may have collapsed into the less dense melt-rich zone accumulating below (Mathez and May, 2005). This explains the large amount of disseminated chromitite in certain areas as well as the sinuous bottom reef contact - as fragments from the bottom portion of the UG2 gradually collapsed into the melt, the previously regular bottom reef contact would appear more sinuous and discordant.

11.3.6 End Note

The petrogenesis of the UG2 cyclic unit is therefore considered to represent a combination of primary and secondary magma chamber processes. By studying the field relations, textures and geochemical profile of the unit the authour has been able to interpret and unravel the processes occurring within the Bushveld chamber at that time.

Major findings include the fact that the UG2 cyclic unit was built from a number of magma injections into the chamber, and was not formed by a single emplacement event. The building up of the UG2 cyclic unit is therefore an excellent display of the dynamic interplay between injections of fresh magma and the overall evolution of the resident chamber liquid. While a specific magma type has been associated with Critical Zone of the Bushveld Complex (Harmer and Sharpe, 1985) it is also possible that other magmas may have been involved (Wilson and Chunnet, 2006). It can also be said that the UG2 cyclic unit represents a combination of both primary and secondary magmatic processes. Whilst the crystal pile was cooling, a hydrous melt was forced up through the cumulate rocks to eventually slow, possibly pond beneath an impermeable layer (i.e.

the UG2) and then metasomatize and recrystallize the surrounding rock to form the secondary pegmatoidal feldspathic pyroxenite units. This process happened after the UG2 cyclic unit had been formed and was partially crystallized.

The mechanism of mineralization, however, is suggested to be the result solely of primary magmatic processes with little or no role played by late stage postcumulus processes. It is envisaged that a segregated sulphide liquid would have scavenged and extracted base and precious metals from the silicate magma as it percolated through (i.e. Naldrett *et al.,* 1983). The metal impregnated sulphide liquid would have then become concentrated in the chromite slurry and become mixed in with the chromite crystals (i.e. Kinnaird *et al.,* 2002).

Therefore the major chromitite hosted PGE deposits of the Bushveld Complex are associated with the episodic addition, and subsequent mixing, of multiple batches of magma into the chamber. Each chromitite layer is therefore a product of a magma injection(s), and mixing, into the chamber (with the size of the magma batch determining how thick the eventual chromitite layer will be).

In conclusion, the UG2 cyclic unit represents a dynamic interplay of evolving, cooling and fractionating resident liquids within the chamber along with repetitive influxes of fresh, undifferentiated primitive magma. These primary processes were then superseded by later secondary processes of compaction, metasomatization and recrystallization to form the pegmatoidal feldspathic pyroxenite units.

12. Acknowledgements

This thesis is the product of three and a half years of detailed research. A great deal of work was carried out at Lebowa Platinum Mine in the NE Bushveld, Anglo Research in Johannesburg and at the University of KwaZulu-Natal in Durban. A number of people need to be thanked for providing guidance and assistance throughout the project.

Firstly, I would like to thank my supervisor and academic mentor Prof. Allan Wilson. I have thoroughly enjoyed working under his guidance during both my Honours and Msc projects and believe his enthusiasm and knowledge of mafic magma systems is unmatched. I wish him all the best for his new position at Wits University and look forward to possible future work under his supervision.

From Anglo Platinum I would like to thank Gordon Chunnett for providing funding and hence making this project possible. Ray Brown is to be thanked for providing the borehole core material and for many informative discussions. Adam Cooper, Douglas Siboza, Ian McCutcheon and Clive Ackhurst are also thanked.

The mineralogical research portion of the project enabled me to work closely with several esteemed mineralogists in Johannesburg. Jacques Roberts is thanked for many informative discussions and for assisting in interpreting the PGM results. Peter Hey, Robert Schouwstra, Gerda Gloy, Corne Schalkwyk, Odette Smith, Vannessa Clark-Mostert, Yolanda Scharnek, Solomon Dlamini and Solly Mabogwani are all thanked for their help and assistance.

From the University of KwaZulu-Natal all the technicians (especially Pat, Roy, Mukesh and Rob) are thanked for their tireless work in terms of sample preparation, geochemical analysis and many other aspects of the drill core study. Mark Davis is also thanked for his assistance.

To my family and close friends I would also like to say a big thank you. I received constant support and motivation from everyone, and for this I am most appreciative.

Finally, I would like to dedicate this thesis to my beautiful fiancé Samantha. I look forward with great enthusiasm as we open the next chapter of our lives and embark on the great adventure together that is marriage. The journey thus far has been a happy one and I can promise many more happy memories to come.

13. References

Ballhaus, C. G. and Stumpfl, E.F. 1986. Sulphide and platinum mineralization in the Merensky Reef: evidence from hydrous silicates and fluid inclusions. *Contr. Mineral. Petrol.* **94**. 193 – 204.

Barnes, S.J., McIntyre, J.R., Nisbet, B.W., and Williams, C.R. 1990. Platinum-group element mineralization in the Munni Munni Complex, Western Australia. *Contr. Mineral. Petrol.* **42**. p 141 – 64.

Boudreau, A.E. 1988. Investigations of the Stillwater Complex IV. The role of volatiles in the petrogenesis of the J-M Reef, Minneapolis Adit section. *Ibid*. **26**. p 193 – 208.

Boudreau, A.E., Mathez, E.A., and McCallum, I.S. 1986. Halogen geochemistry of the Stillwater and Bushveld Complexes: Evidence for transport of the platinum group elements by Cl-rich fluids. *Journal of Petrology*. **27**. p 967 – 986.

Boudreau, A.E., and Mccallum, I.S. 1992. Concentration of platinum-group elements by magmatic fluids in layered intrusions. *Econ. Geol.* **87**. p 1830 – 1848.

Brenan, J.M., and Li, C. 2000. Constraints on oxygen fugacity during sulfide segregation in the Voiseys Bay Intrusion, Labrador, Canada. *Econ. Geol.* **95 (4)** p 901 – 915.

Brown, R.T., and Nowak, D. 2003. *Lebowa UG2 Geological CBE Report.* Unpublished Anglo Platinum Exploration Geology Report. 1-72 pp.

Brown, R.T. 2004. *The Eastern Bushveld Complex.* Unpublished Anglo Platinum Exploration Geology Report. 1-24 pp.

Buick, I.S., Maas, R., and Gibson, R. 2001. Precise U – Pb titanite age constraints on the emplacement age of the Bushveld Complex, South Africa. *Journal of the Geological Society, London.* **158**. p 3 – 6.

Burger, A.J., and Coertze, F.J. 1975. Age determinations: April 1972 – March 1974. *South Africa Geol. Survey Annals,* **10**. p 135 – 141.

Cameron, E. N. 1977. Chromite in the central sector of the Eastern Bushveld Complex, South Africa. *Amer. Mineral.* **62**, 1082 – 1096.

Cameron, E.N. 1978. The Lower Zone of the Eastern Bushveld Complex in the Olifants River Trough. *J. Petrology.* **19**. p 437 – 462.

Cameron, E.N. 1980. Evolution of the Lower Critical Zone, central sector, eastern Bushveld Complex, South Africa. *American Mineralogist.* **75**. p 845 – 871.

Cameron, E. N. 1982. The upper critical zone of the Eastern Bushveld Complex – Precursor of the Merensky Reef. *Econ. Geol.,* **77**, 1307 – 1327.

Cameron, E. N and Desborough, G. A. 1969. Occurrence and characteristics of chromite deposits – eastern Bushveld Complex. *Econ. Geol. Monogr.* **4**, 23 – 40.

Campbell, I.H., and Barnes, S.J. 1984. A model for the geochemistry of the platinum-group elements in magmatic sulphide deposits. *Canadian Mineralogist*. **22**. p 151 – 160.

Campbell. I.H., and Murck, B.W. 1984. A model for chromite seams in layered intrusions. *In:* Campbell, I.H. (ed). *Layered Complexes: Mineralization and Mechanisms.* Wits University Geology Dept.

Campbell, I.H., Naldrett, A.J., and Barnes, S.J. 1983. A model for the origin of the platinum sulfide horizons in the Bushveld and Stillwater Complexes. *J. Petrology.* **24**. 133 – 65.

Carr, H.W., Kruger, F.J., Groves, D.I., and Cawthorn, R.G. 1999. The petrogenesis of Merensky Reef potholes at the Western Platinum Mine, Bushveld Complex: Sr-isotopic evidence for synmagmatic deformation. *Mineralium Deposita.* **34 (4)**. P335 – 347.

Cawthorn, R. G. 1999. Platinum-group mineralization in the Bushveld Complex – a critical reassessment of geochemical models. *S. Afr. J. Geol.,* **102**. 268 – 81.

Cawthorn, R.G. 2002. The role of magma mixing to the genesis of PGE mineralization in the Bushveld Complex: thermodynamic calculations and new interpretations – a discussion. *Econ. Geol.* **97**. p 663 – 667.

Cawthorn, R.G., and Barry, S.D. 1992. The role of intercumulus residua in the formation of pegmatoid associated with the UG2 chromitite, Bushveld Complex. *Austr. J. Earth Sci.,* **39**, 263 – 276.

Cawthorn, R.G., and Webb, S.J. 2001. Connectivity between the western and eastern limbs of the Bushveld Complex. *Tectonophys.,* **330**. 195 – 209.

Coetzee, H., and Kruger, F.J. 1989. The geochronology, Sr- and Pb- isotope geochemistry of the Losberg Complex, and the southern limit of the Bushveld Complex magmatism. *S. Afr. J. Geol.* **92**. p 37 – 41.

Coghill, B.M., and Wilson, A.H. 1993. Platinum-group minerals in the Selukwe subchamber, Great Dyke, Zimbabwe – implications for PGE collection mechanisms and post-formation redistribution. *Mineralog. Mag.* **57**. p 613 – 633.

Cousins, C.A. 1959. The structure of the mafic portion of the Bushveld Igneous Complex. *Trans. Geol. Soc. S. Afr.,* **62**. p 179 – 189.

Cousins, C.A., and Feringa, G. 1964. The chromite deposits of the western belt of the Bushveld Complex. In Haughton, S.H. ed. *The geology of some ore deposits in southern Africa. Spec. Publ. Geol. Soc. S. Afr.,* **2**. 183 – 202.

Daltry, V.D.C., and Wilson, A.H. 1997 Review of Platinum-Group Mineralogy: Compositions and Elemental Associations of the PG-Minerals and Unidentified PGE-phases. *Mineral. And Petrol.* **60**. 1185 – 229.

Davey, S.R. 1992. Lateral variations within the upper Critical Zone of the Bushveld Complex on the farm Rooikoppies 297JQ, Marikana, South Africa. *S. Afr. J. Geol.,* **95**, 141 – 149.

Durazzo, A., and Taylor, L.A. 1982. Exsolution in the mss-pentlandite system: textural and genetic implications for Ni-sulphide ores. *Mineralium Deposita.* **17**. pp 313 – 332.

Eales, H.V., Field, M., De Klerk, W.J. and Scoon, R.N. 1988. Regional trends of chemical variation and thermal erosion in the Upper Critical Zone, western Bushveld Complex. *Mineralogical Magazine.* **v52**, p63-79.

Eales, H.V., de Klerk, W.J., and Teigler, B. 1990. Evidence for magma mixing processes within the Critical and Lower Zones of the north-western Bushveld Complex, South Africa. *Chem. Geol.,* **88**. p261 – 278.

Eales, H.V., Botha, W.J., Hattingh, P.J., De Klerk, W.J., Maier, W.D. and Odgers, A.T.R. 1993. The mafic rocks of the Bushveld Complex: a review of emplacement and crystallization history in the light of recent data. *Journal of African Earth Sciences,* **16**, p121 – 142.

Eales, H.V., and Cawthorn, R.G. 1996. The Bushveld Complex. *In*: Cawthorn, R.G (ed.). *Layered Intrusions*. Elsevier Science. 531 pp.

Eales, H.V. 2000. Implications of the chromium budget of the Western limb of the Bushveld Complex. *S. Afr. J. Geol.,***v103**, p141-150.

Fourie, J.N., and von Gruenewaldt, G. 1979. Zaaiplats project. *Pretoria Univ., Pretoria Inst. Geol. Research Bushveld Complex,* Ann. Report 1978, p 11 – 15.

Grinbeek, J.C. 1995. *The effect of the Vaalkop replacement pegmatoid on the sulphide mineralogy at Western Platinum Mine in the Mooinooi District.* M.Sc. thesis (unpubl.)., Univ. Pretoria, S. Afr., 110 pp.

Gu, Y. 2003. Automated scanning electron microscope based mineral liberation analysis: An introduction to JKMRC/FEI mineral liberation analyser. *J of Minerals & Metals Characterization & Engineering.* **2**.pp 33 – 41.

Hahn, U.F. and Ovendale, B. 1994. UG2 chromitite layer potholes at Wildebeestfontein North Mine, Impala Platinum Limited. *XVth CMMI Congress,* Johannesburg, SAIMM, **v3**, pp195-200.

Haughton, D.R., Roeder, P.L., and Skinner, B.J. 1974. Solubility of sulphur in mafic magmas. *Econ. Geol.* **69**. p 451 – 457.

Hamilton, P. J. 1977. Sr isotope and trace element studies of the Great Dyke and Bushveld mafic phase and their relation to early Proterozoic magma genesis in southern Africa. *J. Petrology,* **18**. 24 – 52.

Harmer, R.E., and Sharpe, M.R. 1985. Field relations and strontium isotope systematics of the marginal rocks of the eastern Bushveld Complex. *Econ. Geol.,* **80**. 813 – 37.

Hatton, C.J. and von Gruenewaldt, G. 1989. *The geological setting and petrogenesis of the Bushveld chromitite layers*. In: Chromite deposits through time. Ed. C. W. Stowe.International Geological Congress, Washington, 109-142.

Hess, H.H. 1960. Stillwater Igneous Complex, Montana. *Geological Society of American Memoir*. **80**. 230p.

Hiemstra, S.A. 1985. The distribution of some platinum-group elements in the UG-2 chromitite layer of the Bushveld Complex. *Economic Geology*. **80**. p 944 – 957.

Hiemstra, S.A. 1986. The distribution of chalcophile and platinum-group elements in the UG-2 chromitite layer of the Bushveld Complex. *Econ. Geol.* **81**. p 1080 – 1086.

Hulbert, L.J. and von Gruenewaldt, G. 1982. Nickel, copper and platinum mineralization in the Lower Zone of the Bushveld Complex, south of Potgietersrus. *Economic Geology*, **77**. p1296-1306.

Irvine, T. N., and Barager, W.R.A. 1972. Muskox Intrusion and Coppermine River Lavas, Northwest Territories, Canada. *Internat. Geol. Cong., 24th Montreal, Field Excursion A29 Guidebook.* 70p.

Irvine, T.N. 1982. Terminology for Layered Intrusions. *J. Petrology.* **23**. p 127 – 162.

Irvine, T.N., and Smith, C.H. 1967. The ultramafic rocks of the Muskox intrusion. In: Wyllie, P.J., (ed). *Ultramafic and related rocks.* New York, John Wiley and Sons. p 38 – 49.

Irvine, T.N. 1975 Crystallization sequences in the Muskox intrusion and other layered intrusions-II. Origin of chromitite layers and similar deposits of other magmatic ores. *Geochimica et Cosmochimica Acta* **39,** 991-1020.

Irvine, T.N. 1977. Origin of chromitite layers in the Muskox intrusion and other stratiform intrusions: a new interpretation. *Geology* **5,** 273-277.

Irvine, T.N., Keith, D.W. and Todd, S.G. 1983. The J-M platinum-palladium Reef of the Stillwater Complex, Montana: ll Origin by double diffusive convective magma mixing and implications for the Bushveld Complex. *Econ. Geo*l. **7**8, 1287-1334.

Jackson, E.D. 1961. Primary textures and mineral associations in the Ultramafic zone of the Stillwater Complex, Montana. *US Geological Survey*. **358**. p1 – 106.

Jackson, E.D. 1970. The cyclic unit in layered intrusions – a comparison of the repetitive stratigraphy in the ultramafic parts of the Stillwater, Muskox, Great Dyke and Bushveld Complexes. *Geol. Soc. South Africa Spec. Pub.* **1**. p 391 – 424.

Jones, M.P. 1987. Applied mineralogy:a quantitative approach. London; Graham and Trotman.

Keith, M.L. 1954. The system MgO-Cr_2O_3-SiO_2. *Am. Ceramic. Soc. Jour.,* **37**. 490 – 496.

King, R. P. 1993. Basic image analysis for mineralogy. *ICAM '93 Demonstration Workshop Manual,* pp 119 – 139.

Kinloch, E.D. 1982. Regional trends in the platinum-group mineralogy of the Critical Zone of the Bushveld Complex, South Africa. *Econ. Geol.* **85**. p 537 – 555.

Kinnaird, J.A., Kruger, F.J., Nex, P.A.M., and Cawthorn, R.G. 2002. Chromitites of the Bushveld Complex – Process of Formation and PGE Enrichment. *Economic Geology Research Institute. Information Circular*, **369**, University of the Witwatersrand. P 26.

Kruger, F.J. 1990. The stratigraphy of the Bushveld Complex: a reappraisal and the relocation of the Main Zone boundaries. *S. Afr. J. Geol.* **93**, 376 – 381.

Kruger, F.J. 1991. Authors reply to discussion on the stratigraphy of the Bushveld Complex: a reappraisal and relocation of the Main Zone boundaries. *S. Afr. J. Geol.* **94**, 187 – 190.

Kruger, F.J., Jinnaird, J.A., Nex, P.A.M., and Cawthron, R.G. 2002. Chromite is the key to PGE. *9th Int. Pt Symposium,* Stillwater, USA.

Kruger, F. J. 2005. Filling the Bushveld Complex magma chamber: lateral expansion, roof and floor interaction, magmatic unconformities, and the formation of giant chromitite, PGE and T-V-magnetite deposits. *Mineralium Deposita,* **40**, 451 – 472.

Lee, C.A., and Butcher, A.R. 1990. Cyclicity in Sr-isotope stratigraphy through the Merensky and Bastard reef units, Atok section, eastern Bushveld Complex. *Econ.Geol.* **85**. p 173 – 190.

Li, C., Maier, W.D., and de Waal., S.A. 2001a. The role of magma mixing to the genesis of PGE mineralization in the Bushveld Complex: thermodynamic calculations and new interpretations. *Econ.. G.eol*. **96**. p 653 – 662.

Li, C., Maier, W.D., and de Waal., S.A. 2001b. The role of magma mixing to the genesis of PGE mineralization in the Bushveld Complex: thermodynamic calculations and new interpretations-erratum. *Econ. Geol*. **96**. p 1487.

Li, C., Lightfoot, P.C., Amelin, Y., and Naldrett. 2000. Melting reactions of gneissic inclusions with enclosing magma at Voiseys Bay: implications with respect to ore genesis. *Econ. Geol.* **95**. p 815 – 830.

Li, C., Maier, W.D., Barnes, S.J. 2002. A re-evaluation of the role of crustal contamination in the formation of magmatic sulfides in the Bushveld Complex. *9th International Platinum Symposium: Abstracts.*

Macdonald, A.J. 1987. Ore Deposit Models #12. The platinum-group element deposits: classification and genesis. *Geoscience Canada.* **14**. p 155 – 166.

Mathez, E.A., and Mey, J.L. 2005. Character of the UG2 chromitite and petrogenesis of its footwall rocks, eastern Bushveld Complex. *Econ. Geol.* **V.100**. p1617-1630.

Maier, W.D., and Eales, H.V. 1994. Plagioclase inclusions in orthopyroxene and olivine of the UG2 – Merensky Reef interval: regional trends in the western Bushveld Complex. *S. Afr. J. Geol.* **97**. p 408 – 414.

Maier, W.D., and Bowen, M.P. 1996. The UG2 – Merensky Reef interval of the Bushveld Complex northwest of Pretoria. *Mineralium Deposita.* **31**. p 386 – 393.

Maier, W.D., and Barnes, S.J. 1998. Concentrations of rare earth elements in silicate rocks of the Lower, Critical and Main Zones of the Bushveld Complex. *Chemical Geology*, **150**,pp 85-103.

Maier, W.D., and Barnes, S.J. 1999. Platinum-group elements in silicate rocks of the lower, critical and main zones at Union Section, western Bushveld Complex. *J. Petrology,* **10**, 1647 – 1671.

McCallum, I.S., Raedeke, L.D., and Mathez, E.A. 1977. Stratigraphy and petrology of the Banded zone of the Stillwater Complex, Montana. *Transactions of the American Geophysical Union.* **58**. 1245p.

McLaren, C.H., and De Villiers, J.P.R. 1982. The platinum-group chemistry and mineralogy of the UG2 Chromitite layer of the Bushveld Complex. *Econ Geol.,* **77**, 1348 – 1366.

Mitchell, A.A. and Scoon, R.N. 2007. Origin of the UG2 chromitite layer, Bushveld Complex. *J. Petrology,* **102**, part 5, *in press*.

Mossom, R.J. 1986. The Atok Platinum Mine. *In*: Anhaueser, C.R., and Maske, S (eds) *Mineral Deposits of Southern Africa*, **2**, Johannesburg: geol. Soc. S. Afr., 1143-54.

Naldrett, A.J. 1989. Stratiform PGE deposits in layered intrusions. *Rev. Econ. Geol.,* **4**, 135 – 166.

Naldrett, A.J., and von Gruenewaldt, G. 1989. Association of platinum-group elements with chromitite in layered intrusions and ophiolite complexes. *Econ. Geol.* **84**. p 180 – 187.

Naldrett, A.J., Hoffman, E.L., Green, A.H., Chou, C.L., Naldrett, S.R., and Alcock., R.A. 1979. The composition of Ni-sulfide ores, with particular reference to their content of PGE and Au. *Can. Mineal.* **17**. p 403 – 415.

Naldrett, A. J., Gasparrini, E.C., Barnes, S.J., von Gruenewaldt, G., and Sharpe, M.R. 1983. The upper critical zone of the Bushveld Complex and the origin of Merensky – type ores. *Econ. Geol.*. **81**. p 1105 – 1117.

Naldrett, A.J., and Wilson, A.H. 1990. Horizontal and vertical variations in noble-metal distribution in the great dyke of Zimbabwe: A model for the origin of the PGE mineralization by fractional segregation of sulfide. *Chemical Geology.* **88.** p279 – 300.

Naslund, H.R., and McBirney, A.R. 1996. Mechanisms of Formation of Igneous Layering. *In:* Cawthorn, R.G. (ed). *Layered Intrusions.* Amsterdam, Elsevier Science pp 1 – 44.

Nex, P.A.M. 2004. Formation of bifurcating chromitite layers of the UG1 in the Bushveld Igneous Complex, an analogy with sand volcanoes. *Journal of the Geol. Soc. (London).* **161**. p 903 – 909.

Norrish, K., and Hutton, J.T. 1969. An accurate X-ray spectrographic method for the analysis of a wide range of geological samples. *Geochemica et Cosmochimica Acta.* **33 (4)**. p 431 – 453.

Peach, C.I., Mathez, E.A., and Keays, R.R. 1990. Sulfide melt – silicate melt distribution coefficients for noble metals and other chalcophile elements as deduced from MORB: implications for partial melting. *Geochemica et Cosmochima Acta.* **54**. p 3379 – 3389.

Penberthy, C.J. 2001. *The effect of mineralogical variation in the UG2 chromitite on recovery of platinum-group elements*. Unpublished phd thesis. Univ. of Pretoria. 1-410 pp.

Penberthy, C.J., and Merkle, R.K.W. 1999. Lateral variations in the platinum-group element content and mineralogy of the UG2 chromitite layer, Bushveld Complex. *S. Afr. J. Geol.,***102**. p 240 – 250.

Petruk, W. 2000. Applied mineralogy in the mining industry. Amsterdam; New York, Elsevier Science BV.

Petruk, W. 1988. Automatic image analysis for mineral beneficiation. *J. Metals,* **40**, pp 29 – 31.

Petruk, W. 1986. The MP-SEM_IPS image analysis system. *CANMET Report* 87 – 1E (CANMNET, Dept Energy, Mines and Resources, Canada).

Peyerel, W. 1982. The influence of the Driekop Dunite Pipe on the platinum-group mineralogy of the UG-2 chromitite in its vicinity. *Econ. Geol.* **77**. p 1432 – 1438.

Prendergast, M.D., and Keays, R.R. 1989. Controls of platinum-group element mineralization and the origin of the PGE-rich Main Sulphide Zone in the Wedza Subchamber of the Great Dyke, Zimbabwe:

implications for the genesis of, and exploration for, stratiform PGE mineralization in layered intrusions. In: Prendergast, M.D., and Jones, M.J. (eds). *Magmatic Sulphides – the Zimbabwe Volume.* London: Institution of Mining and Metallurgy, pp 43 – 69.

Rixom, 2005. *Geometallutrgical Characterisation of the UG-2 Reef in the North-Eastern Bushveld.* Anglo Research Mineralogy Report No. M/05/110.

Rollinson, H. 1990. *Using geochemical data: evaluation, presentation, interpretation.* Longman Scientific & Technical, London, 352 pp.

Sampson, E. 1932. Magmatic chromitite deposits in Southern Africa. *Econ. Geol.,* **27**. 113 – 44.

Scoon, R.N. and Teigler, B. 1994. Platinum-group element mineralization in the Critical Zone of the western Bushveld Complex: I. Sulfide-poor chromitites below the UG-2. *Economic Geology,* **89**, p1094-1121.

Schurmann, L.W. 1993. The geochemistry and petrology of the Upper Critical Zone of the Boshoek section of the Western Bushveld Complex. *Bulletin 113 of the Geological Survey of South Africa.*

Sharpe, M.R., 1981. The chronology of magma influxes to the eastern compartment of the Bushveld Complex as exemplified by its marginal border groups. *J. Geol. Soc. Lond.* **138**, 307-26 pp.

Snowden. 2003. *Middelpunt UG2 expansion project.* Snowden Mining Industry Consultants (Pty) Ltd, Johannesburg. Report no. JR-008-01-2002, 8pp.

Streckeison, A.L. 1973. Plutonic rocks: classification and nomenclature. *Geotimes,* Oct., 26-30.

Tankard, A.J., Jackson, M.P.A., Hunter, D.R., Erikkson, K.A., Minter, W.E.L., and Hobday, D.K. 1982. *Crustal evolution of Southern Africa: 3.8 Billion Years of Earth History.* Springer-Verlag, New York, 523pp.

Tredoux, M., Lindsay, N.M., Davies, G., and McDonald, I. 1995. The fractionation of platinum-group elements in magmatic systems, with the suggestion of a novel causal mechanism. *S. Afr. J. Geol*. **98**. p 157 – 167.

Vermaak, C.F. 1976. The Merensky Reef: thoughts on its environment and genesis. *Econ. Geol.* **71**. 1270-1298.

Vermaak, C.F., and Hendriks, L.P. 1976. A review of the mineralogy of the Merensky Reef, with special reference to new data on the precious metal mineralogy. *Econ. Geol.,* **71**, 1244 – 1269.

Viljoen, M.J., De Klerk, W.J., Coetzer, P.M., Hatch, N.P., Kinloch, E. and Peyerl, W. 1986. The Union Section of Rustenburg Platinum Mines Limited with reference to the Merensky Reef, in

Anhaeusser, C.R., and MAske, S., eds., *Mineral Deposits of Southern Africa.* Johannesburg. Geological Society of South Africa, **2**, p. 1061 – 1090.

Von Gruenewaldt*, G.,* Hatton, C.J., Merkle, R.K.W., and Gain, S.B. 1986. Platinum-group element-chromitite associations in the Bushveld Complex. *Econ. Geol.,* **81**, 1067 – 1079.

Von Gruenewaldt, G., Dicks, D., de Wet, J., and Horsch, H. 1990. PGE mineralization in the western sector of the eastern Bushveld Complex. *Mineralogy and Petrology.* **42**. p 71 – 95.

Wager, L.R., and Brown, G.M. 1968. *Layered igneous rocks.* Oliver and Boyd. Edinburgh. 326p.

Walraven, F. 1986. A note on the stratigraphic terminology of the Bushveld Complex, *In*: Anhaueser, C.R., and Maske, S (eds) *Mineral Deposits of Southern Africa*, **2**, Johannesburg: geol. Soc. S. Afr., 1039-1040

Wilson, A.H., Naldrett, A.J., and Tredoux, M. 1989. Distribution and controls of platinum group element and base metal mineralization in the Darwendale Subchamber of the Great Dyke, Zimbabwe. *Econ. Geol.* **85**. p 556 – 584.

Wilson, A.H., and Tredoux, M. 1990. Lateral and vertical variation of the platinum-group elements, and petrogenetic controls on the sulphide mineralization in the P1 Pyroxenite Layer of the Darwendale Subchamber of the Great Dyke, Zimbabwe. *Econ. Geol.,* **85**. p 556 – 584.

Wilson, A.H., Lee, C.A., and Brown, R.T. 1999. Geochemistry of the Merensky Reef, Rustenburg Platinum Mine, Bushveld Complex: controls on the silicate framework and distribution of trace elements. *Mineralium Deposita.* **34**, 657-672.

Wilson, A.H., Jermy, C.A., Ridgeway, M., and Chunnett, G. 2005. Rock-strength and physical properties of norites of the Merensky and Bastard units, Western Bushveld Complex. *S. Afr. J. Geol.* **108**. p 525 – 540.

Wilson, A. H. & Chunnett, G., 2006. Trace element and platinum group element distributions and the genesis of the Merensky Reef, western Bushveld Complex, South Africa. *Journal of Petrology*, **47**, 2369-2403.